VOLUME 76 OCTOBER 26, 1972 NUMBER 22

JPCHAx

THE JOURNAL OF PHYSICAL CHEMISTRY

PUBLISHED BIWEEKLY BY THE AMERICAN CHEMICAL SOCIETY

THE JOURNAL OF

PHYSICAL CHEMISTRY

AMERICAN CHEMICAL SOCIETY, *1155 Sixteenth St., N.W., Washington, D. C. 20036*

Books and Journals Division
JOHN K CRUM, *Director*
JOSEPH H. KUNEY, *Head, Business Operations Department*
RUTH REYNARD, *Assistant to the Director*

 Published biweekly by the American Chemical Society at 20th and Northampton Sts., Easton, Pa. 18042. Second-class postage paid at Washington, D. C., and at additional mailing offices.

All manuscripts should be sent to *The Journal of Physical Chemistry,* Department of Chemistry, University of Minnesota, Minneapolis, Minn. 55455.

Additions and Corrections are published once yearly in the final issue. See Volume 75, Number 26 for the proper form.

Extensive or unusual alterations in an article after it has been set in type are made at the author's expense, and it is understood that by requesting such alterations the author agrees to defray the cost thereof.

The American Chemical Society and the Editor of *The Journal of Physical Chemistry* assume no responsibility for the statements and opinions advanced by contributors.

Correspondence regarding accepted copy, proofs, and reprints should be directed to Editorial Production Office, American Chemical Society, 20th and Northampton Sts., Easton, Pa. 18042. Manager: CHARLES R. BERTSCH. Assistant Editor: EDWARD A. BORGER. Editorial Assistant: JOSEPH E. YURVATI.

Advertising Office: Centcom, Ltd. (formerly Century Communications Corporation), 142 East Avenue, Norwalk, Conn. 06851.

Business and Subscription Information

Remittances and orders for subscriptions and for single copies, notices of changes of address and new professional connections, and claims for missing numbers should be sent to the Subscription Service Department, American Chemical Society, 1155 Sixteenth St., N.W., Washington, D. C. 20036. Allow 4 weeks for changes of address. Please include an old address label with the notification.

Claims for missing numbers will not be allowed (1) if received more than sixty days from date of issue, (2) if loss was due to failure of notice of change of address to be received before the date specified in the preceding paragraph, or (3) if the reason for the claim is "missing from files."

Subscription rates (1972): members of the American Chemical Society, $20.00 for 1 year; to nonmembers, $60.00 for 1 year. Those interested in becoming members should write to the Admissions Department, American Chemical Society, 1155 Sixteenth St., N.W., Washington, D. C. 20036. Postage to Canada and countries in the Pan-American Union, $5.00; all other countries, $6.00. Single copies for current year: $3.00. Rates for back issues from Volume 56 to date are available from the Special Issues Sales Department, 1155 Sixteenth St., N.W., Washington, D. C. 20036.

This publication and the other ACS periodical publications are now available on microfilm. For information write to: MICROFILM, Special Issues Sales Department, 1155 Sixteenth St., N.W., Washington, D. C. 20036.

Notice to Authors last printed in the issue of June 22, 1972

THE JOURNAL OF

PHYSICAL CHEMISTRY

Volume 76, Number 22 October 26, 1972

JPCHAx 76(22) 3099–3302 (1972)

COMMUNICATIONS TO THE EDITOR

AUTHOR INDEX

In papers with more than one author the name of the author to whom inquiries about the paper should be addressed is marked with an asterisk in the by-line.

ANNOUNCEMENT

On the last two pages of this issue you will find reproduced the table of contents of the October 1972 issue of the *Journal of Chemical and Engineering Data.*

THE JOURNAL OF
PHYSICAL CHEMISTRY

VOLUME 76, NUMBER 22 OCTOBER 26, 1972

Reduction of Diffraction Data for Molecules with Large Amplitude Motions. An Approximate, General Analysis

by S. H. Bauer* and A. L. Andreassen

Department of Chemistry, Cornell University, Ithaca, New York 14850 *(Received January 24, 1972)*

For unsymmetrical molecules and for those in which the inherent thermal motions introduce large fluctuations in the internuclear separations, gas-phase electron diffraction data alone cannot provide unique parameter assignments. We propose to separate the data reduction step that leads to an $\{r_{ij}^{\mp}; l_{ij}^{\mp}\}$ matrix, which accurately represents the diffraction data, from the structure interpretation step which requires the exploration of the shape of the potential energy surface in the vicinity of its minima. The procedure is particularly applicable to molecules in which the internal motions are highly anharmonic and the root-mean-square amplitudes are large. Four examples are presented. These include two cases with single rotators (trifluoronitrosomethane and perfluoroethyl iodide) and two with two rotators (perfluoroisopropyl iodide and acetone). New diffraction data for trifluoronitrosomethane gave the following r_g parameters: (C–F) = 1.326 ± 0.003 Å; (C–N) = 1.546 ± 0.008 Å; (N=O) = 1.197 ± 0.005 Å; ∠CNO = 113.2 ± 1.3°; ∠NCF = 109.0 ± 0.4°. The minimum energy conformation has a coplanar (ONCF) group; the estimated barrier to rotation about C–N is approximately 1100 cal/mol.

Introduction

It is necessary to review briefly the data reduction procedures currently in use in order to delineate the difficulties associated with large amplitude motions (LAM). For an n-atomic molecule in its κth electronic state there is a function $V_\kappa[q_1 \ldots q_{3n-6}]$ which relates the total energy of the nuclei plus electrons to the $(3n - 6)$ q's, the independent nuclear position variables. There are few exceptions to this Born–Oppenheimer approximation, and the situations wherein it fails are well known. The objectives of a "structure determination" are therefore: (i) for each set of electronic quantum numbers (κ), and particularly for the one of lowest energy, to locate precisely all the minima in this surface (the position variables $[q_1^{(e)} \ldots q_{3n-6}^{(e)}]$ for the lowest minimum are of primary interest); (ii) to measure the curvature of the surface at these minima; and, if possible, (iii) to obtain estimates of the barrier heights which separate adjacent minima. It is obvious that for a gaseous sample at any finite temperature those experimentally observed quantities that are not state selective are averages over all rotational and vibrational states, for all the low-energy conformations, with the latter populations weighted with corresponding Boltzmann distribution factors. Hence, in the diffraction of radiation by a dilute assembly of randomly oriented molecules, the structure-dependent portion of the scattered intensity is a superposition of all atom pair contributions.

$$I[s; r_{ij}^{(e)} \cdots \varphi_{ij}] \propto \sum_{\substack{\text{all pairs} \\ \text{in a} \\ \text{molecule}}}{}' f_i(s) f_j(s) \int_0^\infty P[r_{ij} - r_{ij}^{(e)}; \varphi_{ij}] \frac{\sin sr_{ij}}{sr_{ij}} \, dr_{ij} \quad (1)$$

$s \equiv (4\pi/\lambda) \sin(\theta/2)$ and $f_i(s)$ is the atom form factor for atom i (including the phase shift term) and specifies the scattering of the incident radiation by the nucleus plus electron cloud. [This equation does not take into account intramolecular plural scattering and polarization corrections, which are significant for very heavy atoms, nonspherical electron density distributions about

the nuclei, and other subtle effects.] The probability density function for each (i,j) pair, $P[r_{ij} - r_{ij}^{(e)};\ \varphi_{ij}]$, gives the net distribution of distances about $r_{ij}^{(e)}$; it depends not only on parameters φ_{ij} which characterize the V surface in the vicinity of the minimum, but it is also a function of the temperature; *i.e.*

$$P[r_{ij} + r_{ij}^{(e)};\ \varphi_{ij}] = \frac{1}{Q} \sum_{\text{all states } \eta} [\exp(-\beta E_\eta)] \times p_\eta(r_{ij} - r_{ij}^{(e)};\ \varphi_{ij});\ \beta = 1/kT \quad (2)$$

Here η stands for a collection of quantum numbers which identify the individual rotational and vibrational state with energy E_η above zero-point level, Q is the partition function, and $p_\eta(r_{ij} - r_{ij}^{(e)})$ is the intrinsic probability distribution of r_{ij} about $r_{ij}^{(e)}$ when the molecule is in the state η. To obtain the best estimates for $[q_1^{(e)} \ldots q_{3n-6}^{(e)}]$ it is necessary to perform two operations. For each molecular specie, (i) express the p_η's parametrically in terms of a selected set of $(3n - 6)$ independent q's, and sum over all the states to evaluate the pair distribution functions, $P[\ ]$, according to eq 2; and (ii) deduce $I[s;\ r_{ij}^{(e)};\ \varphi_{ij}]$ from eq 1 by integration, and estimate the q parameters by least-squares fitting of the calculated diffraction pattern to the experimental one.

The data reduction problem has been solved for the case when the lowest minimum in the $V[\ ]$ surface is considerably deeper than the others; then the molecules are essentially restricted to a single stable conformation, the curvature at the bottom is nearly quadratic, and the molecular vibrations are harmonic or only slightly anharmonic.[1,2] It is customary, after correcting the intensity pattern for the s dependence of the $f_i(s)$, $f_j(s)$'s, to evaluate a fourier transform of $I(s)$, designated by $f_z(r)$, which is a good approximation to the superposed $P[r_{ij} - r_{ij}^{(e)}]$'s. This may be resolved into an internally consistent set of skewed Gaussians, one for each atom pair. To facilitate the resolution of $f_z(r)$ for small amplitude motions (SAM) the half-widths of the peaks may be estimated from the known masses and vibrational force constants derived from spectroscopic data.[1] However, it would be misleading not to emphasize that for nearly all but the simplest molecules, the structural parameters generally deduced from the $f_z(r)$ function are *thermally averaged* on the basis of the *nearly harmonic approximations* (*tanha*), and therefore do not strictly correspond to the lowest point in the V surface. It is very difficult to insert anharmonicity and shrinkage[2] corrections in the resolution of the radial distribution function. To distinguish the *tanha* values, designate them by $P[r_{ij} - r_{ij}^{\pm};\ \varphi_{ij}]$. The molecular parameters derived by resolution of $f_z(r)$ may be refined by least-squares fitting of calculated $I[s;\ r_{ij}^{(e)};\ \varphi_{ij}]$ or $I[s;\ r_{ij}^{\pm};\ \varphi_{ij}]$ curves to the experimental molecular scattering curve. Were a model available, for the molecule under investigation, which includes the force constants for vibration and other parameters that characterize the conformational motions, and an analytic form could be inserted in eq 1 and 2 for integration, then a least-squares fitting of the experimental $I[\ ]$ function would lead directly to the desired molecular parameters. Interpretation of experimental intensity curves in this manner is laborious even for small symmetric molecules, and entirely impractical for large floppy ones.

Molecules which have shallow minima and low barriers between adjacent minima may execute, in part, large amplitude motions. Then several practical (rather than conceptual) difficulties arise. (α) Since $I(s)$ is not available over the complete half-plane, corrections must be inserted in the fourier inversion for the finite integration range ($s_{min} \approx 2$; $s_{max} \approx 40$); the corrections are unavoidably dependent on the test model used and consequently the uncertainty in $f_z(r)$ is largest in the long r_{ij} region which contains the information on the LAM's. (β) Since the $f_i(s)$ and $f_j(s)$'s are sufficiently different in shape for atom pairs which have substantially different atomic numbers, corrections for the nonnuclear scattering[3] can be made only when the peaks in the $P[\ ]$ curve are adequately resolved. The proper resolution of superposed atom pair contributions which constitute the experimental $f_z(r)$ function clearly is the crux of the problem for LAM. However, obtaining the correct total $f_z(r)$ is limited not only by α and β but also by (γ) the ambiguities associated with estimating the background scattering function. Indeed, all proposed procedures for obtaining the background curve are to some extent model dependent. Thus, to estimate the potential function parameters, φ_{ij}, one must obtain the shape of $P[r_{ij} - r_{ij}^{(e)};\ \varphi_{jj}]$, and unless the atom pair of interest is clearly separated in the distance spectrum from all the others, one must know the shapes of all but the desired atom pair contributions which constitute the given peak. Of course, if all but one of the atom pairs execute SAM, their contributions can be assumed to be, to a good approximation, skewed Gaussians.

The direct evaluation of molecular parameters by least-squares fitting of a theoretical to an experimental molecular scattering function is the preferred procedure for a molecule with LAM, as for one in which only SAM is present. However, this necessitates that the flexible molecule be subjected to a normal mode analysis, which has been carried out for a relatively small number of cases. Good examples are bicyclo[2.2.2]-

(1) (a) S. J. Cyvin, "Molecular Vibrations and Mean Square Amplitudes," Elsevier, Amsterdam, 1968; (b) K. Kuchitsu, *Bull. Chem. Soc. Jap.*, **40**, 498, 505 (1967); (c) R. A. Bonham and L. S. Su, *J. Chem. Phys.*, **45**, 2827 (1966); (d) K. Kuchitsu, "Molecular Vibrations and Structure Studies," S. J. Cyvin, Ed., Elsevier, Amsterdam, 1972, Chapter 12.

(2) Y. Morino, *Acta Crystallogr.*, **13**, 1107 (1960); O. Bastiansen, *ibid.*, 1108 (1960).

(3) T. Iijima and R. A. Bonham, *J. Phys. Chem.*, **68**, 3146 (1964).

octane,[4] disulfur dichloride,[5] and carbon suboxide.[6,7] In general, an adequate normal mode analysis for molecular vibrations when perturbed by the presence of several minima which are separated by low barriers in the potential energy surface is quite difficult. There are no general analytical expressions that incorporate the potential surface characteristics as well as the temperature in a form suitable for the summation in eq 2, and the integration indicated by eq 1. The computational procedure developed in our laboratory is an attempt to provide a rapid, semiquantitative alternative analysis of diffraction data for molecules in which some large amplitude motions, superposed on the nearly harmonic oscillations, may lead to unacceptable converged parameters when one follows the conventional procedures. It was tested with four compounds, acetone, trifluoronitrosomethane, perfluoroethyl iodide, and perfluoroisopropyl iodide; new diffraction data were recorded for three of them. The method is applicable to molecules for which the barrier heights which separate potential minima are of the order of $RT/5$ or greater. Thus, in its present form, it does not apply to molecules in which there are freely rotating groups, but an appropriate extension can be incorporated. The major advantage of the method is its generality, the ease of computation, and particularly its usefulness in reinterpreting molecular parameters derived without regard for LAM by least-squares reduction of diffraction data. *Tanha* structures now in the literature are not unambiguous because of unavoidable correlations between the various geometrical parameters and associated root-mean-square amplitudes. No one has yet proposed a scheme for estimating error limits for moderate size unsymmetrical molecules that is free from objections. Hence it is essential that reliable data be reported in a manner such that they may be reexamined by anyone who has a modest computer at his disposal (in our case an augmented DEC PDP-9) and a molecular model which he wished to test. The procedure leans heavily on the concept that LAM may be separated from SAM and the former treated classically, while the dynamic parameters for the latter are estimated from the large amount of structural data now in the literature involving molecules for which root-mean-square amplitudes are known. While this is the first detailed exposition of the procedure, the concept is not novel; it has been applied by several previous investigators, for example, in the analysis of the structures of B_2Cl_4,[8] Cl_3CCCl_3,[9] and $H_3C \cdot CO \cdot C_2H_5$.[10]

Outline of Procedure

Subject to the condition that the barrier heights which separate adjacent minima in the potential energy surface are equal to or greater than $RT/5$, we assert that whether a molecule has a semirigid framework or is flexible, its *reduced molecular intensity* pattern,[1c] $M(s)$, can be accurately *represented* by a summation of products of exponential and trigonometric functions

$$\frac{I_T - I_B}{I_B} \leftrightarrow M(s) \equiv \frac{\sum_i \sum_j{}' (Z - F)_i (Z - F)_j \cos(\eta_i - \eta_j) \exp[-l_{ij}^{\pm 2} s^2/2]}{\sum_i \{(Z - F)_i^2 + S_i\}} \sin\left\{ sr_{ij}^{\pm} - \frac{s l_{ij}^{\pm 2}}{r_{ij}^{\pm}} - \frac{s^3 \alpha l_{ij}^{\pm 4}}{6} \right\} \Big/ sr_{ij}^{\pm} \quad (3)$$

In this program, the elastic, F_i, and inelastic, S_i, scattering factors of Tavard, *et al.*,[11,12] were inserted in conjunction with the Bonham–Ukaji phase shift values, η_i.[13] The anharmonicity corrections, α,[14] were estimated to be 2.0 $Å^{-1}$ for the bonded atom pairs and zero for the nonbonded pairs. A "best" set of elements in the matrix $\{r_{ij}^{\pm};\ l_{ij}^{\pm}\}$ can be evaluated by least-squares fitting a calculated $sM(s)$ function to the corresponding experimental $sM_x(s)$. The least-squares program used in this laboratory includes the modification suggested by Bonham,[15] and a weighting matrix that incorporates the first off-diagonal terms, calculated in the manner suggested by Morino.[16] The precision of this fitting must attain (or exceed) the estimated level of precision for the recorded diffraction data, at which point it is no longer meaningful to search for a "better fit." The resulting set of $\{r_{ij}^{\pm};\ l_{ij}^{\pm}\}$ values represents one of several structures that is compatible with the diffraction data. Whether this one or another is accepted as the "correct" structure for the compound of interest must then be decided on the basis of additional (nondiffraction) data. Note that for molecules with large amplitude motions $\{r_{ij}^{\pm};\ l_{ij}^{\pm}\}$ probably does not give values which describe a structure at the the lowest potential energy minimum; hence the designation with the $\pm$ superscript. However, this matrix correctly specifies the observed pattern to the available

(4) A. Yokozeki, K. Kuchitsu, and Y. Morino, *Bull. Chem. Soc. Jap.*, **43**, 2017 (1970).

(5) S. J. Cyvin, *et al.*, *J. Chem. Phys.*, **49**, 3561 (1968).

(6) A. Clark and H. M. Seip, *Chem. Phys. Lett.*, **6**, 452 (1970).

(7) M. Tanimoto, K. Kuchitsu, and Y. Morino, *Bull. Chem. Soc. Jap.*, **43**, 2776 (1966).

(8) R. R. Ryan and K. Hedberg, *J. Chem. Phys.*, **50**, 4986 (1969).

(9) J. Karle, *ibid.*, **45**, 4149 (1966).

(10) M. M. Abe, K. Kuchitsu, and T. Shimanouchi, *J. Mol. Struct.*, **4**, 245 (1969).

(11) C. Tavard, D. Nicholas, and M. Rouault, *J. Chim. Phys.*, **64**, 540 (1967).

(12) L. Schäfer, A. C. Yates, and R. A. Bonham, *J. Chem. Phys.*, **55**, 3055 (1971).

(13) R. A. Bonham and T. Ukaji, *ibid.*, **36**, 72 (1962).

(14) L. S. Bartell, *ibid.*, **23**, 1219 (1955); K. Kuchitsu and L. S. Bartell, *ibid.*, **35**, 1945 (1961); K. Kuchitsu, *Bull. Chem. Soc. Jap.*, **40**, 498 (1967).

(15) T. G. Strand, D. A. Kohl, and R. A. Bonham, *J. Chem. Phys.*, **39**, 1307 (1963).

(16) Y. Murata and Y. Morino, *Acta Crystallogr.*, **20**, 605 (1966).

Table I: Structural Parameters (Å) for CS_2

	This work	Electron diffraction[a]	Spectroscopy[a]
r_g(C=S)	1.5582 ± 0.0021	1.5592 ± 0.0022	1.5580 ± 0.0005
r_g(S···S)	3.1102 ± 0.0024	3.1126 ± 0.0044	3.1090 ± 0.0010
l(C=S)	0.0383 ± 0.0021	0.0364 ± 0.0040	0.0391
l(S···S)	0.0453 ± 0.0018	0.0448 ± 0.0038	0.0412
δ_g[b]	0.0062 ± 0.0032	0.0058 ± 0.0042	0.0070

[a] Y. Morino and T. Iijima, *Bull. Chem. Soc. Jap.*, **35**, 1661 (1962). Note that the spectroscopic distances listed are also r_g. [b] δ_g is defined as $[2r_g(C{=}S) - r_g(S\cdots S)]$.

level of precision, and consequently it also represents its fourier transform ($G^{\pm}$ below).

The problem is now reduced to developing a systematic and easily performed procedure for *relating* an $\{r_{ij}^{(e)};\ \varphi_{ij}\}$ matrix to the available $\{r_{ij}^{\pm};\ l_{ij}^{\pm}\}$ matrix. One representation of the latter is a superposition of skewed Gaussians, $G(r_{ij} - r_{ij}^{\pm};\ l_{ij}^{\pm})$, each centered at $r_{ij}^{\pm}$, of area $(n_{ij}Z_iZ_j/r_{ij})$ and width at half maximum of $[(4\gamma^2 + 2l_{ij}^{\pm 2})^{1/2} \ln 2/2]$

$$G^{\pm}(r) \equiv \sum_i \sum_j{}' [\pi/(4\gamma^2 + 2l_{ij}^{\pm 2})]^{1/2} \times \left(\frac{Z_iZ_j}{r}\right) \exp[-(r - r_{ij}^{\pm})^2/(4\gamma^2 + 2l_{ij}^{\pm 2})] \quad (4)$$

In eq 4 γ is an artificial damping factor such that $\exp[-\gamma^2 s_{max}^2] \approx 0.1$. *Over the range 1 to 7 Å the $G^{\pm}$ curve is very close to the usually calculated $f_x(r)$*, which suffers from termination errors and incomplete corrections for nonnuclear scattering. For testing any model, a corresponding *equivalent* weighted sum of skewed Gaussians ($\Sigma\omega G$) can be readily calculated, taking into account (classically) the presence of large amplitude motions. We now introduce the assumption that small errors which are present in computing $\Sigma\omega G$ are *compensated* by corresponding small errors in $G^{\pm}$ because both functions are evaluated on the same basis.

The sought-for $\Sigma\omega G$ function is obtained as follows. Calculate sets of distances $\{r_{ij}^{(e)}\}$ for a model specified by a sequence of fixed LAM parameters[17] $[\varphi_m - \varphi^0]$, where φ is, perhaps, a torsional angle about a bond; φ^0 is at the potential minimum, and $m = 1,2,\ldots$. Treat atom pairs which undergo SAM in the conventional manner. For each m compute a contributing radial distribution function $G(r^{(e)};\ [\varphi_m - \varphi^0])$ by superposing Gaussians centered at $r_{ij}^{(e)}$. At this stage one should insert shrinkage corrections[1] estimated from similar known compounds, and use half-widths $[(\ln 2/2)(l_{ij}^2/2 + \gamma^2)^{1/2}]$, where the l_{ij}'s are root-mean-square amplitudes, carried over from known similar structures without LAM. This procedure permits one to adjust the magnitudes of $r_{ij}^{(e)}$ and l_{ij} to the specific value of φ_m, whenever a theoretical basis for such a dependence is available. Then give each $G(r^{(e)};\ [\varphi_m - \varphi^0])$ a weight

$$\omega_m = g(\varphi_m) \exp[-V(\varphi_m - \varphi^0)/kT] / \Sigma g(\varphi_m) \exp[-V(\varphi_m - \varphi^0)/kT] \quad (5)$$

and sum to cover the full range in φ_m, for specified φ^0's. A selection of the "best" parameters is then made by varying $\{r_{ij}^{(e)};\ l_{ij};\ \varphi^0;\ V_0\}$ until a minimum in the difference function $[\Sigma\omega G - G^{\pm}]$ is obtained. Four examples are given below.

Experimental Section

A sample of CF_3NO was obtained from Penninsular ChemResearch, Gainesville, Fla.; its purity was checked by infrared.[18] Sectored diffraction photographs were recorded on Kodak electron image plates, with a beam accelerating voltage of 65 kV. The nozzle to plate distances were 25.26 (HVL) and 12.50 cm (HVS). These combinations gave diffraction patterns over the q range from 4 to 55 $Å^{-1}$ and from 35 to 120 $Å^{-1}$, respectively $[q \equiv (10/\pi)s]$. The background pressure in the apparatus was maintained at less than 2×10^{-6} Torr. The plates were scanned on a Jarrell-Ash densitometer fitted with a rotating stage; the plates were spun about their centers at about 10 cps. The photometer output (integrated at each radial position for 3 sec) is interfaced to an A-D Data Systems converter and digitizing unit. The HVL transmittances were recorded at 200 μm intervals, while the HVS plates at 100 μm increments. Such sampling provides (five–six) points for each q interval from which we interpolate (six-point Lagrangian scheme) the density at integral q values. Each plate chosen for analysis was traced several times and the densities averaged. Tracings that differed significantly from the average (always on the low side in peak positions) were eliminated and the remaining scans averaged again. This procedure minimizes the error in locating the scan diameter and significantly improves the signal-to-noise ratio. Data reduction and conversion to intensities[19] were performed on an DEC PDP-9 computer. The scale factor was determined from MgO powder patterns, taken concurrently with the gas sample plates.

(17) R. L. Hilderbrandt, *J. Chem. Phys.*, **51**, 1654 (1969).
(18) J. Mason and J. Dunderdale, *J. Chem. Soc.*, 754 (1956).
(19) J. L. Hencher and S. H. Bauer, *J. Amer. Chem. Soc.*, **89**, 5527 (1967).

Further checks were obtained from companion CS_2 photographs, which were analyzed in parallel with the patterns of the compounds under investigation. The results for carbon disulfide are presented in Table I; no further comments are needed. The intensity data and the refined background for CF_3NO are shown in Figure 1; tabulated values are listed in Tables II and III.

Table II: CF_3NO

	λ = 0.04918 Å; L = 252.63 mm				λ = 0.04918 Å; L = 125.04 mm		
q	Intensity	q	Intensity	q	Intensity	q	Intensity
4	1.1793	47	1.1379	35	1.6546	78	1.6287
5	0.8738	48	1.1413	36	1.6705	79	1.6258
6	0.6828	49	1.1371	37	1.6808	80	1.6224
7	0.6002	50	1.1297	38	1.6701	81	1.6184
8	0.5929	51	1.1189	39	1.6325	82	1.6172
9	0.6032	52	1.1097	40	1.5742	83	1.6192
10	0.6206	53	1.1028	41	1.5142	84	1.6200
11	0.6335	54	1.0995	42	1.4773	85	1.6182
12	0.6521	55	1.0976	43	1.4718	86	1.6165
13	0.6683			44	1.4967	87	1.6134
14	0.6841			45	1.5361	88	1.6117
15	0.7218			46	1.5780	89	1.6111
16	0.8058			47	1.6065	90	1.6139
17	0.9250			48	1.6219	91	1.6194
18	1.0375			49	1.6185	92	1.6260
19	1.1449			50	1.6060	93	1.6326
20	1.1755			51	1.5879	94	1.6372
21	1.1492			52	1.5736	95	1.6356
22	1.0882			53	1.5665	96	1.6310
23	1.0182			54	1.5683	97	1.6219
24	0.9734			55	1.5748	98	1.6135
25	0.9760			56	1.5785	99	1.6077
26	1.0155			57	1.5760	100	1.6072
27	1.0642			58	1.5686	101	1.6090
28	1.1071			59	1.5624	102	1.6145
29	1.1325			60	1.5594	103	1.6219
30	1.1442			61	1.5653	104	1.6280
31	1.1455			62	1.5775	105	1.6301
32	1.1387			63	1.5934	106	1.6313
33	1.1344			64	1.6129	107	1.6293
34	1.1382			65	1.6251	108	1.6277
35	1.1508			66	1.6300	109	1.6274
36	1.1651			67	1.6265	110	1.6272
37	1.1738			68	1.6186	111	1.6274
38	1.1698			69	1.6052	112	1.6261
39	1.1546			70	1.5937	113	1.6234
40	1.1325			71	1.5847	114	1.6200
41	1.1039			72	1.5845	115	1.6159
42	1.0867			73	1.5897	116	1.6140
43	1.0816			74	1.6008	117	1.6180
44	1.0912			75	1.6123	118	1.6220
45	1.1096			76	1.6226	119	1.6262
46	1.1264			77	1.6275	120	1.6345

Results

CF_3NO. Davis, *et al.*, reported[20] on their electron diffraction investigation of trifluoronitrosomethane. They found that a model with the oxygen atom eclipsing one of the fluorines is preferable to one with a staggered conformation. In addition, the direction of the C–N bond appeared to deviate from the pyramid axis of the CF_3 group by 1.3°. In our investigation we considered three models: (A) the C–N bond coincides with the pyramid axis, and the oxygen atom is located in the eclipsed position; in (B) the constraint to an eclipsed conformation was relaxed; and in model (C) both torsional motion about the C–N bond and its deviation from colinearity with the pyramid axis were permitted. The z axis was placed along the pyramid axis. In model C no attempt was made to vary the individual NCF angles, only the zCF angle was eval-

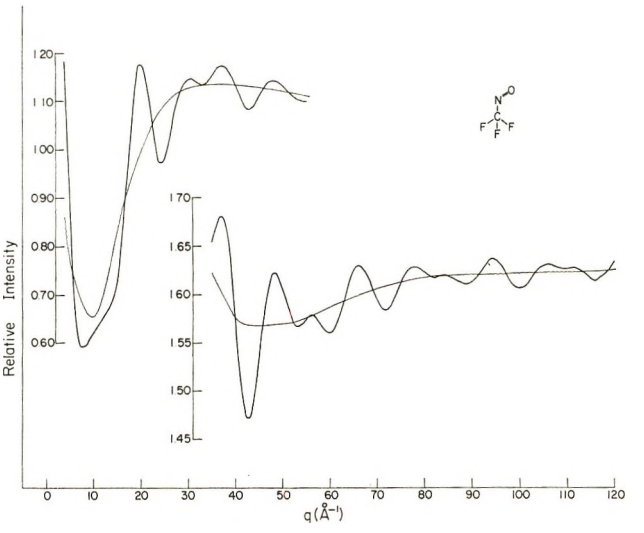

Figure 1. The relative intensity for trifluoronitrosomethane has been plotted as a function of the scattering variable q. The refined background has also been plotted.

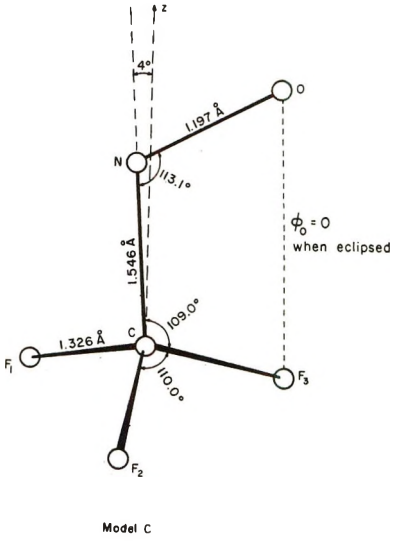

Figure 2. A schematic of the atom positions for trifluoronitrosomethane. The parameters listed are those from model C.

(20) M. I. Davis, J. E. Boggs, and D. Coffey, Jr., *J. Phys. Chem.*, 69, 3727 (1965).

Table III: Error Matrix for CF_3NO (Model B)

	C–N	N=O	∠CNO	C–F	∠ZCF	φ(F₃CNO)	l(C–N)	l(N=O)	l(C–F)	l(FF)	l(NF)	l(OF₃)
C–N	0.0028											
N=O	−0.0012	0.0016										
∠CNO	−0.0111	−0.0103	0.4058									
C–F	−0.0011	0.0008	−0.0083	0.0008								
∠ZCF	−0.0149	0.0089	−0.1159	0.0088	0.1177							
φ(F₃CNO)	0.0229	0.0085	−0.4872	0.0091	0.0990	1.0788						
l(C–N)	0.0015	−0.0010	0.0102	−0.0011	−0.0118	−0.0096	0.0042					
l(N=O)	−0.0003	0.0004	−0.0071	0.0007	0.0062	0.0102	−0.0013	0.0021				
l(C–F)	0.0006	−0.0005	−0.0029	0.0002	−0.0007	0.0063	−0.0009	0.0010	0.0009			
l(FF)	−0.0004	−0.0002	0.0063	−0.0002	−0.0037	−0.0019	0.0003	0.0001	0.0000	0.0008		
l(NF)	0.0001	0.0001	0.0038	0.0003	−0.0047	0.0101	−0.0003	0.0004	0.0002	0.0009	0.0015	
l(OF₃)	−0.0011	−0.0003	0.0149	−0.0004	−0.0054	−0.0217	0.0005	−0.0004	−0.0003	0.0008	0.0013	0.0044

CF_3NO: cartesian coordinates for model B

	x	y	z
C	0.0	0.0	0.0
N	0.0	0.0	1.5335
O	1.0505	0.0	2.1012
F1	−0.9938	0.7655	−0.4226
F2	−0.1660	−1.2434	−0.4226
F3	1.1598	0.4779	−0.4226

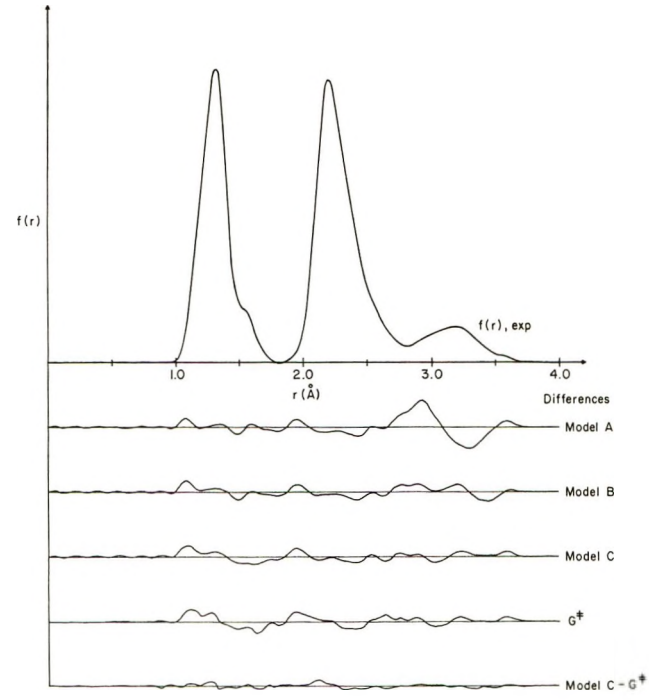

Figure 3. Comparison of experimental radial distribution curve with those computed for models A, B, and C. The difference curves are plotted at twice the scale of the $f(r)_{exp}$ curve. The lowest curve is $[f(r)_{cal}$ (model C) $- G^{\pm}(r)]$.

uated. Where the tilt angle is greater than 0°, the nitrogen is bent back between F_1 and F_2. The torsion angle, $\varphi(F_3CNO)$, is measured away from F_3 with the eclipsed conformation set at zero. Figure 2 is a schematic of the atom positions. In Figure 3 the refined experimental radial distribution function $f(r)$ is compared with those calculated for models A, B, C, and with the $G^{\pm}$ function of model C. The results from least-squares fitting of the $sM(s)$ curve with the aforementioned constraints are listed in Table IV. Davis' values are included for comparison. As the geometrical constraints were relaxed, only the CNO angle was found to vary appreciably; all other parameters lie within each others error limits. The large change in the CNO angle, accompanied by small variations in the other parameters, serve to keep the $O\cdots F_3$ and the average $O\cdots F_1$ and $O\cdots F_2$ distances nearly constant. Note that for a semirigid frame (models B and C) allowing for torsion about the C–N bond away from the eclipsed position results in a substantial improvement in the standard deviation of the fit (σ). This is apparent from Figure 4, which is a plot of the experimental $qM(q)$ curve and of the residuals for the three models under consideration.

The $\{r_{ij}^{\pm};\ l_{ij}^{\pm}\}$ values derived from the least-squares calculation for model C (which best represents the observed diffraction pattern) were used to construct a $G^{\pm}$ curve in accordance with eq 4. We then calculated superposition of Gaussians for several combinations of parameters $\{r_{ij};\ l_{ij};\ \varphi^0;\ V_0\}$. A threefold

Table IV: Least-Squares Parameters for CF_3NO from $sM(q)$ Function[d]

	Model A	Model B	Model C	Davis
C–N, Å	1.5288 (0.0123)	1.5335 (0.0084)	1.5464 (0.0090)	1.555 ± 0.015
N=O, Å	1.1926 (0.0069)	1.1941 (0.0048)	1.1967 (0.0045)	1.171 ± 0.008
C–F, Å	1.3227 (0.0036)	1.3237 (0.0024)	1.3258 (0.0024)	1.321 ± 0.004
∠ZCF, deg	108.511 (0.506)	108.618 (0.353)	108.984 (0.387)	107.0 ± 0.6[c]
∠CNO, deg	120.674 (1.461)	118.386 (1.217)	113.156 (1.246)	121.0 ± 1.6
∠ZCN, deg	[0][a]	[0][a]	4.372 (0.745)	1.3 ± 0.8
φF_3CNO, deg	[0][a]	22.394 (3.236)[b]	21.822 (3.331)[b]	
l(C–N), Å	0.069 (0.019)	0.067 (0.013)	0.063 (0.011)	
l(N=O), Å	0.030 (0.009)	0.030 (0.006)	0.032 (0.006)	
l(C–F), Å	0.045 (0.004)	0.045 (0.003)	0.046 (0.002)	
l(FF), Å	0.061 (0.004)	0.061 (0.002)	0.059 (0.003)	
l(NF), Å	0.085 (0.007)	0.087 (0.005)	0.074 (0.006)	
$l(OF_3)$, Å	0.095 (0.021)	0.091 (0.013)	0.091 (0.012)	
$l(OF_{1,2})$, Å	[0.150][a]	[0.150][a]	[0.150][a]	
σ	0.02978	0.02263	0.02016	

[a] Parameter was constrained in the least-squares calculation to the value in square brackets. [b] $d_0 = 0$ with the oxygen atom eclipsing F_3. [c] Calculated from values in ref 20. [d] *Note regarding estimation of error limits.* The numbers listed in parentheses are three times the calculated least-squares uncertainties. These, rather than the uncertainties, are given to provide the general reader with a more realistic estimate of the reliability of the parameters deduced *for the particular model* which is tested. The following arguments provide the basis for selecting the factor of 3. In the error analyses published by Hilderbrandt and Bauer [*J. Mol. Struct.*, **3**, 325 (1969)] and by Oberhammer and Bauer [*J. Amer. Chem. Soc.*, **91**, 10 (1969)], the many possible sources of error (both random and systematic) were enumerated and some magnitudes estimated. For instance, the uncertainty in the (λL) calibration, which establishes the overall scale, is now less than 0.1%; this introduces a corresponding uncertainty for internuclear distances of $\leq$ 0.002 Å (refer to Table I). Noncentering of the plates during microdensitometry affects the scale as well as the recording of correct diffraction intensities; this source of error has been considerably reduced during the past 2 years (see text). Since the operational noise level of the digitizing densitometer is less than $5/10^4$, the major unresolved problem is the presence of correlation between the magnitudes of adjacent points of the scattered intensities used in the $qM(q)$ tables. While correlation in the *measured photographic densities* has been minimized by the interpolation procedure based on recording 5 times as many measured points as q values used, larger correlations are introduced by "drawing-in" the backgrounds, by unrecognized presence of faint local blotches in the plate due to extraneous radiation, and particularly by errors in the dependence of the tabulated atom form factors on q. The effects of these correlations are reduced by use of nondiagonal weighting terms in the least-squares analyses (ref 16). It has been estimated from studies of a number of relatively simple molecules [M. A. MacGregor and R. K. Bohn, *Chem. Phys. Lett.*, **11**, 29 (1971), and references quoted therein] that the effect of these errors are encompassed by the factor of 3 in the calculated uncertainties, provided these are larger than the error due to the uncertainty in the overall scale (≈0.002 Å). For molecules which have a large number of different values in their $\{r_{ij}\}$ matrix, the error limits which one may quote depend on the certainty with which a particular model is accepted. The choice of model, at the present stage of developments of the electron diffraction discipline, is still highly subjective. The σ and R factors are published to provide each reader with sufficient information to check his selection against the one made by the authors. The latter claim no prescience in this process.

cosine potential was assumed to describe the barrier to rotation about the C–N bond.

$$V(\varphi - \varphi_0) = (V_0/2)[1 - \cos 3(\varphi - \varphi_0)] \quad (6)$$

The frame parameters deduced by least squares *via* eq 3 were used without change. In Figure 5, we plotted $G^{\pm}$ (calculated from model C parameters) and the $[\Sigma\omega G - G^{\pm}]$ difference curves for several combinations of V_0 and φ_0. The first five difference curves were computed for models with B frame parameters; for the last five curves we used model C frame parameters. To obtain a quantitative measure of the fit of the weighted curves $\Sigma\omega G(V_0, \varphi^0)$ to $G^{\pm}$, an R factor[21] defined below was calculated for each model. These results are summarized in Table V. It follows that when the $G^{\pm}$

$$R^2 \equiv \frac{\sum_r [\sum \omega G(V_0,\varphi^0)_r - G_r^{\pm}]^2}{\sum_r (G_r^{\pm})^2} \quad (7)$$

Table V: CF_3NO[a]

V_0, cal/mol	d_0, deg	R
800	0	0.02807
1000	0	0.02742
1200	0	0.02794
1400	0	0.02922
1200	22.39	0.03131
800	0	0.01439
1000	0	0.01052
1200	0	0.00812
1400	0	0.00869
1200	21.82	0.02344

[a] The first five values correspond to model B parameters, the last five correspond to model C parameters.

(21) W. C. Hamilton, "Statistics in Physical Science," Ronald Press, New York, N. Y., 1964, p 158.

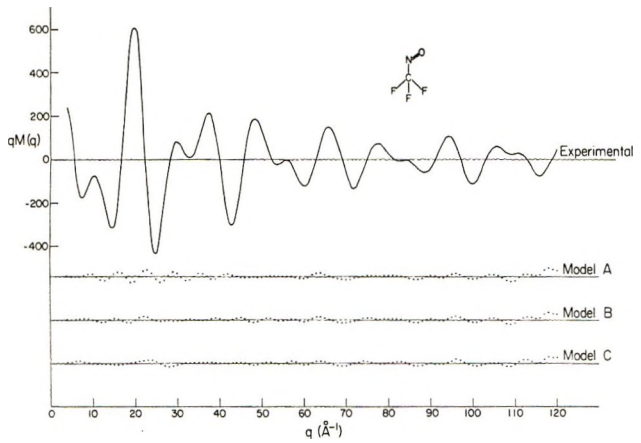

Figure 4. The experimental $qM(q)$ curve for trifluoronitrosomethane plotted as a function of q. The experimental − theoretical difference values for models A, B, and C are presented.

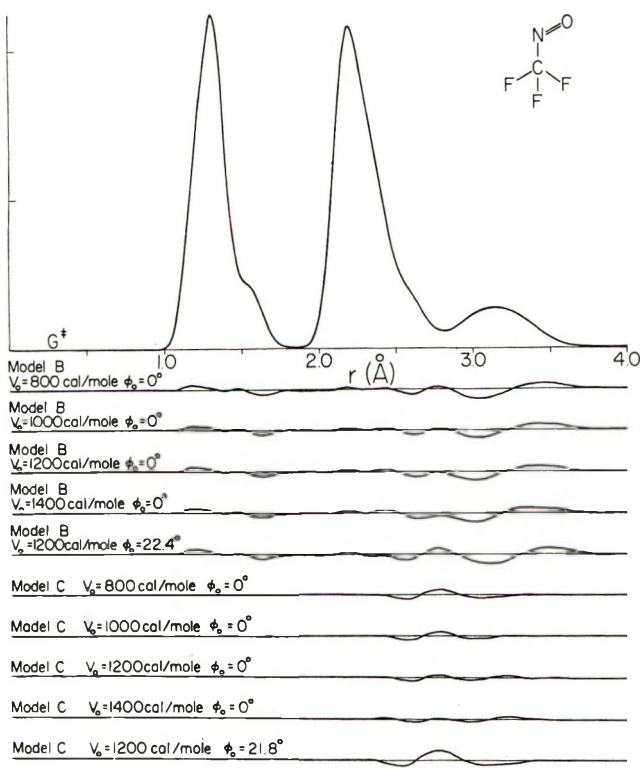

Figure 5. The $G^{\mp}$ curve calculated from model C. The difference curves $[\Sigma\omega G - G^{\mp}]$ are plotted below for several combinations of structural parameters, rotational barrier heights, and configurations.

curve was reinterpreted, allowing for large amplitude motion about C–N, both model B and C parameters favored the *eclipsed* conformation, with a barrier between 1000 and 1200 cal/mol. The eclipsed conformation agrees with that found for the hydrogen analog, and the barrier is also close to that obtained by Coffey, *et al.*,[22] for CH_3NO. The long C–N bond compensates for the replacement of the hydrogens by fluorines.

Concerning the tilting of the C–N bond away from the pyramid axis, it appears to us that this deviation is an example of "vibrational shrinkage." The inclusion of this angle in the analysis merely served to improve the fit to the experimental data ($G^{\mp}$). The frame parameters were not significantly affected when this parameter was unconstrained.

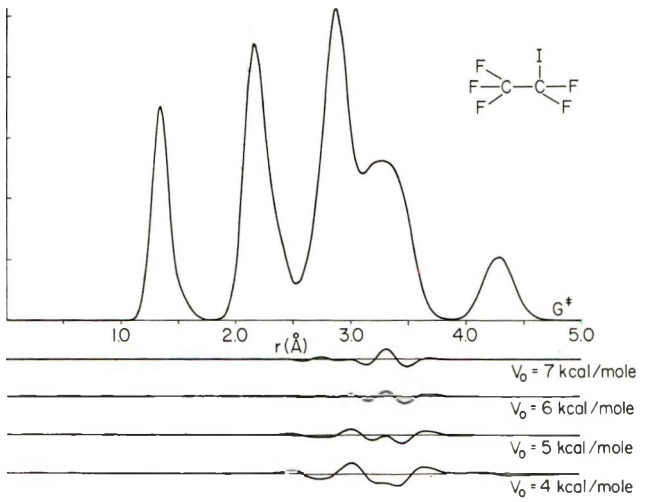

Figure 6. The $G^{\mp}$ curve for perfluoroethyl iodide. Difference curves were plotted for four barrier heights for the model with the staggered conformation ($\varphi_0 = 60°$).

CF_3CF_2I. A structure has been determined for perfluoroethyl iodide[23] on the basis of *tanha*. The conformation which followed from the converged least-squares reduction of the $sM(s)$ data deviated from the expected staggered conformation by approximately 8°. Attempts to obtain a least-squares fitting of the $sM(s)$ curve for a model that was constrained to the staggered conformation consistently failed to converge, but with the torsional angle as a parameter [eclipsed form assigned zero angle], the least-squares calculation converged to a value of 68.15 ± 1.61°, with an overall standard deviation of 0.01196. A $G^{\mp}(r)$ curve was then calculated for the parameters derived from this analysis; it is plotted in Figure 6. Various curves were obtained for a threefold potential function, eq 6, in which the minimum was set at the staggered conformation; no allowance was made for the possibility that the torsional motions couple to the frame vibrations and alter the assigned l_{ij}'s. The R factors for these were plotted in Figure 7. The best fit was obtained for $\varphi_0 = 60°$, with an estimated barrier of 5.8 kcal/mol.

$(CH_3)_2C{=}O$. A *tanha* structure for acetone was recently redetermined by electron diffraction.[24] The molecular conformation which gave the lowest standard deviation is one with a torsional angle of the

(22) D. Coffey, Jr., C. O. Britt, and J. E. Boggs, *J. Chem. Phys.*, **49**, 591 (1968).

(23) A. L. Andreassen and S. H. Bauer, *ibid.*, **56**, 3802 (1972).

(24) R. L. Hilderbrandt, A. L. Andreassen, and S. H. Bauer, *J. Phys. Chem.*, **74**, 1586 (1970).

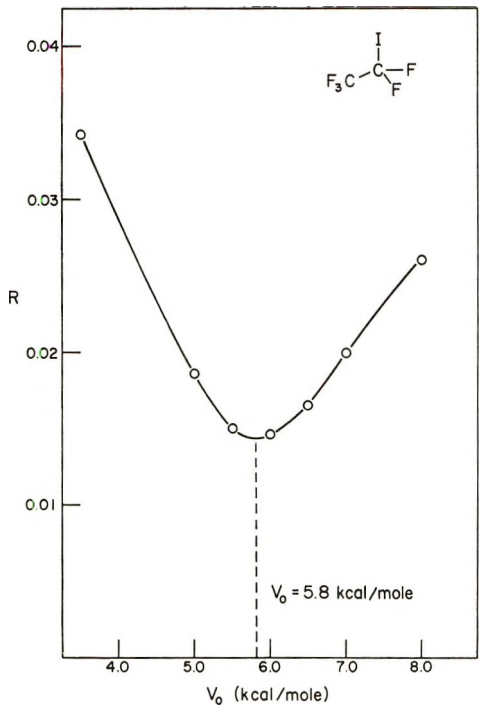

Figure 7. The R factor for the staggered conformation (φ_0 = 60°) of perfluoroethyl iodide plotted as a function of the barrier to internal rotation.

CH_3 groups about the C–C bonds of 32.63° (0° represents a configuration in which a proton from each CH_3 group eclipses the oxygen). To treat a molecule with two independent rotors according to our method, it is necessary to introduce the following expression for the weighting

$$\{\omega_1; \omega_2\} = \frac{g(\varphi_1)g(\varphi_2) \exp[-V_1(\varphi_1 - \varphi_{01})/kT] \times \exp[-V_2(\varphi_2 - \varphi_{02})/kT]}{\sum g(\varphi_1)g(\varphi_2) \exp[-V(\varphi_1 - \varphi_{01})/kT] \times \exp[-V_2(\varphi_2 - \varphi_{02})/kT]} \quad (8)$$

This weights all configurations for each rotor under the assumption that their motions are independent. An interaction term of the form $[V_3^0 \sum_{l,m} \exp(-R_{lm}/a)]$ could be introduced if the two rotators are forced by geometry to be too close as, for example, in a *tert*-butyl halide. In the case of acetone, with two identical rotors, V_1 and V_2 as well as φ_{01} and φ_{02} were taken to be equal. A barrier height of 750 cal/mol, consistent with several spectroscopic determinations,[25,26] was assumed. It is interesting to note that while the configuration about the C–C bond has not been determined,[25,27] several authors assumed in their calculations[27,28] that the torsional angle was zero. The $G^{\pm}$ curve was plotted in Figure 8. The $[\Sigma\omega G(\varphi_1; \varphi_2) - G^{\pm}]$ difference curves were calculated for V_0 = 750 cal/mol, with φ_0 set at 0 and 32.6°. The R factor obtained for the 0° conformation is 0.00947 while that for the 32.6° conformation is 0.00684. It is likely that the minimum potential conformation does not correspond

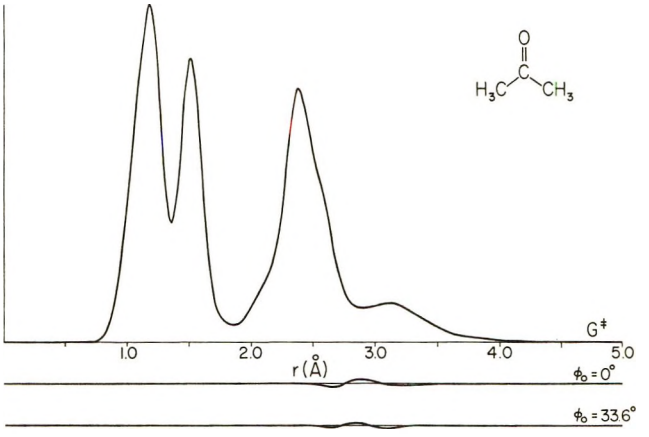

Figure 8. The $G^{\pm}$ curve for acetone. A barrier of 750 cal/mol was assumed for φ_0 (minimal potential energy position for the torsional angle) of 0 and 33.6°.

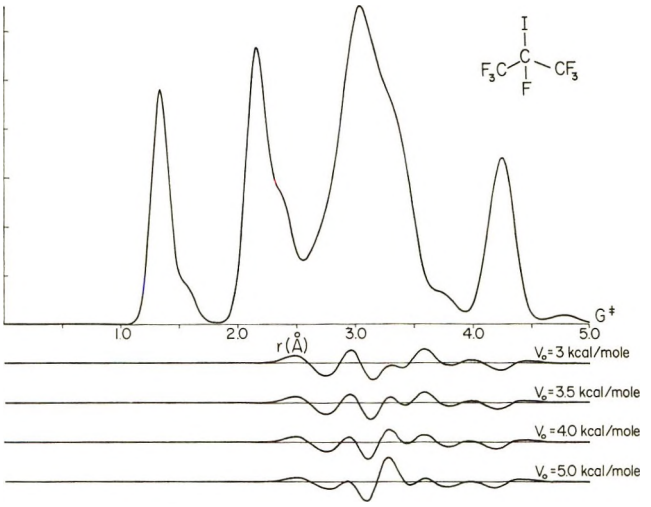

Figure 9. The $G^{\pm}$ curve for perfluoroisopropyl iodide. The four difference curves are calculated for the indicated barrier heights, assuming a staggered conformation (φ_0 = 60°).

to φ_0 = 32.6°, since the shape of the torsional potential is unknown and the rotators are probably not independent; nevertheless, it appears to us that a twisted model of some form is a better representation of the structure than the eclipsed conformation.

$(CF_3)_2CFI$. Analysis of the perfluoroisopropyl iodide $\{r_{ij}^{\pm}; l_{ij}^{\pm}\}$ matrix[23] was carried out in a manner similar to that used for acetone. A set of weighted Gaussians were calculated as per eq 8. In this case also, the heights of both barriers were assumed to be equal, the rotators with minima at the same φ_0's and moving independently. As can be seen from the curves presented in Figure 9 a complete reduction was

(25) R. Nelson and L. Pierce, *J. Mol. Spectrosc.*, **18**, 344 (1965).
(26) J. D. Swalen and C. C. Costain, *J. Chem. Phys.*, **31**, 1562 (1959).
(27) T. Iijima, *Bull. Chem. Soc. Jap.*, **43**, 1049 (1970).
(28) P. Cossee and J. H. Schachtschneider, *J. Chem. Phys.*, **44**, 97 (1966).

not obtained, possibly because the rotators are not independent. To that approximation, a staggered conformation and a barrier height somewhat less than 4.0 kcal/mol is indicated. One should anticipate a lower barrier height to internal rotation in $(CF_3)_2CFI$, compared to CF_3CF_2I, since the C–C bond length is shorter (1.554 *vs.* 1.523 Å) in the latter. The error curves in Figure 9 are larger than those found for CF_3CF_2I, and the R factors for the isopropyl compound are roughly twice (0.04) those found for the ethyl. However, we anticipate the R values to increase with the number of rotors, while the inclusion of an interaction potential energy term would improve the agreement with the experimental diffraction data. In addition, had spectroscopic information on the magnitude of the shrinkage corrections been inserted, the fit would have been further improved.

Conclusions

In this paper we propose a *modus operandi* for analyzing, reporting, and interpreting electron diffraction data for molecules with potential energy surfaces $V[q_1 \ldots q_{3n-6}]$ characterized by several adjacent minima of comparable depth, separated by low barriers ($12RT > V_0 > RT/5$). It is becoming increasingly clear, with the investigation of many atomic molecules that have structures of low symmetry, that the diffraction data alone may not lead to a unique determination of the molecular parameters that correspond to the deepest minimum in the potential energy surface. We propose that the best least-squares matrix $\{r^{\pm};\ l_{ij}{}^{\pm}\}$ be accepted as a representation of the diffraction data, and that the corresponding $G^{\pm}$ superposition of skewed Gaussians be used for exploration of models compatible with other structural information. While the above four cases demonstrate the utility of this approach, it is not our intention to argue that these results are the ultimate solutions of their structures. Indeed, our position is that the $G^{\pm}$ curves invite continued reinterpretation by anyone who has a modest computer and a new model to test.

Acknowledgments. We gratefully acknowledge financial support from the Advanced Research Projects Agency (Material Science Center, Cornell University). We thank Professor R. A. Bonham for helpful correspondence regarding this proposed procedure for diffraction data reinterpretation.

Vibrational Relaxation in CO_2 with Selected Collision Partners. I. H_2O and D_2O

by M. I. Buchwald and S. H. Bauer*

Department of Chemistry, Cornell University, Ithaca, New York 14850 *(Received May 16, 1972)*

Publication costs assisted by Cornell University

Density gradients were measured with a laser-schlieren technique in CO_2–H_2O and CO_2–D_2O mixtures behind incident shocks, at temperatures from 380 to 1200°K. Shock pressures ranged from 100 to 400 Torr; water concentrations from 1 to 9%. These data were reduced to vibrational relaxation times which were found to increase with rising temperature, and which are in good agreement with recent ultrasonic measurements. At 400°K, $(P\tau_{CO_2\text{-}D_2O}) \approx 4(P\tau_{CO_2\text{-}H_2O})$. The vibrational relaxation times approach a common value of 4×10^{-8} sec/atm at 1000°K, and then decrease slowly with temperature. The shock tube results are compared with previous measurements and theoretical predictions.

Introduction

For the last three decades carbon dioxide, in its pure state and in mixtures with a large variety of gases, has served as a "guinea pig" system for exploration of the fundamental processes which account for energy transfers in molecular collisions. Recently, the measurement of the detailed energy exchange processes in CO_2 and its theoretical interpretation have assumed practical importance because of the development of the CO_2 laser.

To maximize the efficiency and power of this laser system (electrically pumped, GDL, or DF transfer) it is evident that the roles of the following two basic processes should be well established.

$$CO_2^{\ddagger} + M \longrightarrow CO_2(000) + M + \text{kinetic energy} \quad (1)$$

$$CO_2(00^01) + M \longrightarrow CO_2(mno) + M + \text{kinetic energy} \quad (2)$$

The superscript ‡ designates the "Fermi resonant" combination of symmetric stretching (01^00) and bending (02^00) vibrations, generally assumed to equilibrate with each other much more rapidly than they do with the asymmetric stretching mode. Processes 1 and 2 describe the depletion of the lower and the upper states, respectively, of the lasing transition. For clear-cut checks on the success of any proposed model data should be available for a selected variety of M's over a wide range of temperatures. While dependence of the efficiency of reaction 2 on the nature of the collision partner has been extensively explored (Figure 1), generally by means of fluorescence quenching, we must recognize that with respect to laser operation this is only half of the story. For a medium to be effective in maintaining an inverted population the net rate for step one must be greater than that for step two at least by as much as the lasing transition rate. It is now established that the bottle-neck in the deexcitation of the ‡ states is the vibration–translation relaxation of the (01^00) bending mode, since the v–v process (02^00) + (00^00) → 2(01^00) requires on the average only about 20 collisions.

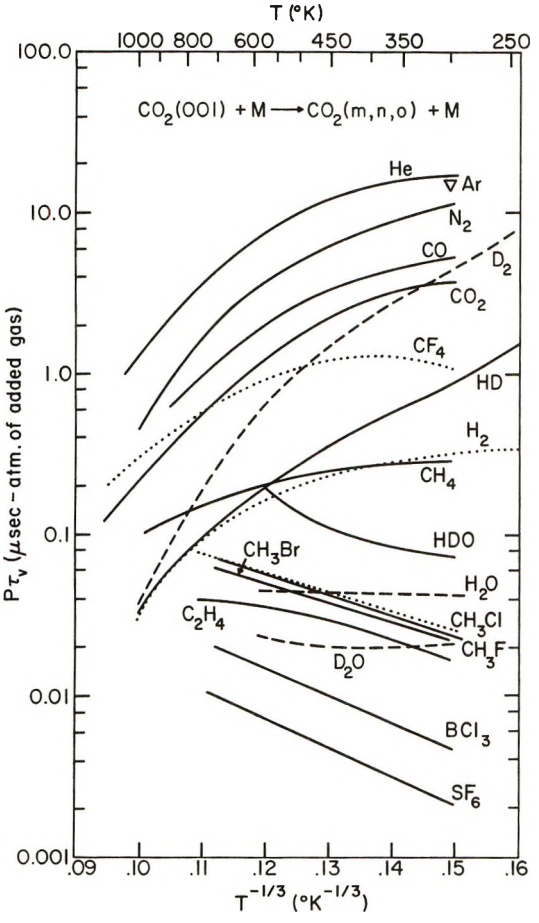

Figure 1. Summary of relaxation times for the deexcitation of $CO_2(00^01)$, as a function of temperature, for various collision partners: (M = N_2) W. A. Rosser, A. D. Wood, and E. T. Gerry, *J. Chem. Phys.*, **50**, 4996 (1969); (CO) W. A. Rosser, R. D. Sharma, and E. T. Gerry, *ibid.*, **54**, 1196 (1971); (H_2O, D_2O, HDO) D. F. Heller and C. B. Moore, *ibid.*, **52**, 1005 (1970); (Ar) G. Kamimoto and H. Matsui, *ibid.*, **53**, 3990 (1970); (SF_6, C_2H_4, BCl_3, CH_3F, CH_3Cl, CH_3Br, CH_3I) J. C. Stephenson and C. B. Moore, *ibid.*, **52**, 2333 (1970); (CO_2, He, H_2, D_2, HD) J. J. Hinchen, UAC, private communication.

When selecting collision partners for measurement of the rates of deexcitation of (01^00), it is instructive to list the factors which have been proposed at various times to account for the obvious departures of this process from the classical Landau–Teller mechanism.[1] In addition to the parameters that appear directly in the L–T expression (reduced mass, vibrational energy level spacing, and the characteristic distance for the repulsive potential) the possibility that the collision partner may have vibrational and/or rotational spacings in near-resonance with the deexcitation energy gap must be considered. The role of rotation–vibration transfers which appear to be particularly effective when the collision partners have low moments of inertia has been discussed.[2] Finally, all molecular parameters that determine the three-dimensional shape of the potential function, such as the presence of dipole and quadrupole moments, and the magnitudes of collision partner polarizabilities should be explored. The present studies provide data for the efficiencies of vibrational deexcitation of carbon dioxide in the (010) state with a variety of collision partners selected to test the relative effectiveness of the listed factors. It is interesting to note that most of the previous investigations involving CO_2 with H_2O and D_2O were carried out *via* ultrasonic techniques,[3,4] with the exception of a recent impact tube measurement at room temperature[5] and shock tube measurements at 450°K by Smiley and Winkler,[6] who used a Mach–Zehnder interferometer.

Shock tube techniques have the advantage of allowing the study of vibrational relaxation rates over a wide range of densities and temperatures. In addition, since most of the uncertainty in the water content is

(1) L. Landau and E. Teller, *Phys. Z. Sowjetunion*, **10**, 34 (1936).

(2) C. Bradley Moore, *J. Chem. Phys.*, **43**, 2979 (1965).

(3) (a) A. Eucken and R. Z. Becker, *Z. Phys. Chem. (Leipzig) B*, **27**, 235 (1934); (b) A. Eucken and E. Z. Neuman, *ibid.*, **36**, 163 (1937); (c) F. A. Gutowski, *J. Accoust. Soc. Amer.*, **12**, 255 (1940); (d) A. Van Itterbeck and P. Mariens, *Physica*, **7**, 125 (1940); (e) I. M. Metter, *Phys. Z. Sowjetunion*, **12**, 233 (1937); (f) V. O. Knudsen and E. Fricke, *J. Accoust. Soc. Amer.*, **12**, 255 (1940); (g) A. Van Itterbeck, P. DeBruyn, and P. Mariens, *Physica*, **6**, 511 (1939); (h) W. H. Pielmeier, H. L. Saxton, and D. J. Telfain, *J. Chem. Phys.*, **8**, 106 (1940); (i) D. Sette and J. C. Hubbard, *J. Accoust. Soc. Amer.*, **25**, 994 (1953).

(4) R. W. Higgs and R. H. Torborg, *ibid.*, **42**, 1038 (1967).

(5) M. Huetz and P. Chevalier, *Advan. Mol. Relaxation Processes*, **2**, 110 (1970).

(6) E. F. Smiley and E. H. Winkler, *J. Chem. Phys.*, **22**, 2018 (1954).

thought to be due to variable extents of absorption on surfaces, the shock tube has an obvious advantage; the walls always remain at the same low temperature. The introduction of new techniques for water vapor determination has made it possible to estimate accurately small water vapor concentrations.

In order to investigate in detail the mechanism of energy transfer the temperature dependence of the relaxation times must be established. Two sets of ultrasonic measurements have been reported over a large temperature interval, one from 300 to 500°[7] and the other from 300 to 700°.[3b] Differing relaxation times were found but both investigations displayed a temperature dependence opposite to that predicted by the L-T model; *i.e.*, the relaxation time was found to increase with temperature. In addition, one investigator reported a pronounced minimum in the relaxation time near room temperature which has not yet been duplicated. Recently, in studies made directly on CO_2 lasers, Carbone and Witteman[8] and Ochkin and Shubina[9] investigated the effects of added H_2O in the laser discharge. They estimated ambient electron temperatures, and considered the concurrent chemical reactions and the relaxation processes. By studying the decay of lasing in a pulsed, sealed CO_2 laser Bulthuis and Ponsen[10] attempted to measure the relaxation time of the CO_2 (01^10) level over the temperature range 600 to 1000°K.

Several theories were proposed to account for the high efficiencies of relaxation of CO_2 by water, and of the unexpected temperature dependence. Early qualitative explanations were based on the assumption that some form of chemical interaction between CO_2 and H_2O led to a deep attractive potential between the two, and thus to effective coupling between the vibrations of the carbon dioxide and the relative translational energy of the colliding pair. Widom and Bauer[11] showed that a negative temperature dependence is predicted on the basis of a long-range attractive potential, when proper account is taken of small impact parameter collisions. Marriott[12] studied the scattering of CO_2 by H_2O, using as a model a spherically symmetric (Lennard-Jones) potential. Application of Moore's[2] model for vibrational–rotational energy transfer was found to be unsatisfactory in this case. Recently Sharma[13] calculated the temperature dependence of the energy transfer probability. He found that the temperature dependence can be explained by the presence of long-range forces and that energy is readily transferred between rotational states of H_2O and the bending mode of CO_2.

The substitution of D_2O for H_2O leaves the intermolecular potential for CO_2–water collisions unchanged. Measurement of both the CO_2–H_2O and the CO_2–D_2O relaxation times provides an important test for any theory of vibrational energy transfer. Shields and Burkes[14] measured ultrasonic absorption and dispersion in CO_2–D_2O as well as in CO_2–H_2O from 300 to 500°K. They found that the Widom–Bauer theory can account for the CO_2–H_2O data, but the CO_2–D_2O relaxation time values could not be fitted with the same interaction potential parameters. In turn, they formulated a theory which incorporated the Widom–Bauer emphasis of low-impact parameter collisions, and an assumed factor in the expression for the interaction force function which depends on the rotational frequency of the collision partner. They were then able to fit the relaxation times for both CO_2–H_2O and CO_2–D_2O pairs from 300 to 500°K using only one adjustable parameter. However, since their formulation starts with an explicit form for the time dependence of the forcing function, it is incomplete in the sense that a detailed collision model is not available.

Experimental Section

The shock tube and driver section are square, 12 cm on a side. Nitrogen or helium were used as driver gases, as needed. The driver section of 2 m is sufficiently long to delay the arrival of the rarefaction wave at the schlieren window (9-m downstream) so as to permit an adequate test period. Shock waves were initiated by increasing the driver pressure until a prescored mylar diaphragm burst. A barium titanate pressure transducer was mounted in the tube wall to trigger the velocity measuring oscilloscope. Three heat transfer gauges (70 ohm platinum thin-film sensors) indicate shock arrival times. The four detection stations are equidistant (at 254 mm) with the last heat gauge 20-mm downstream of the laser beam path. A Tektronix Model 535 oscilloscope was modified to generate a raster, which was calibrated in 1 μsec units. Transit times could be read to 0.5 μsec accuracy.

The optical system is similar to that described by Kiefer and Lutz[15] (Figure 2). A Spectra-Physics helium–neon laser, operating in the TMS_{00} mode with an output of 7 mW, was used for the light source. The beam had a divergence of 1 mradian. The beam width was 0.7 mm at the window near the laser and 0.8 mm at the exit window. In order to avoid distortion of the Gaussian intensity distribution and extraneous scattering by lens imperfections no telescopes were used in the system. The optical path from the tube center to

(7) J. W. Lewis and K. P. Lee, *J. Accoust. Soc Amer.*, **38**, 813 (1965).

(8) R. C. Carbone and W. J. Witteman, *IEEE J. Quantum Electron.*, **5**, 442 (1969).

(9) T. K. Ochkin and N. A. Shubina, *Khim. Vys. Energ.*, **6**, 26 (1972).

(10) K. Bulthius and G. J. Ponsen, *Phys. Lett., A*, **36**, 123 (1971).

(11) B. Widom and S. H. Bauer, *J. Chem. Phys.*, **21**, 1670 (1953).

(12) R. Marriott, *Proc. Phys. Soc., London*, **88**, 83 (1966).

(13) R. D. Sharma, *J. Chem. Phys.*, **54**, 810 (1971).

(14) F. D. Shields and J. A. Burkes, *J. Accoust. Soc. Amer.*, **43**, 510 (1968).

(15) J. H. Kiefer and R. W. Lutz, *J. Chem. Phys.*, **44**, 658 (1966).

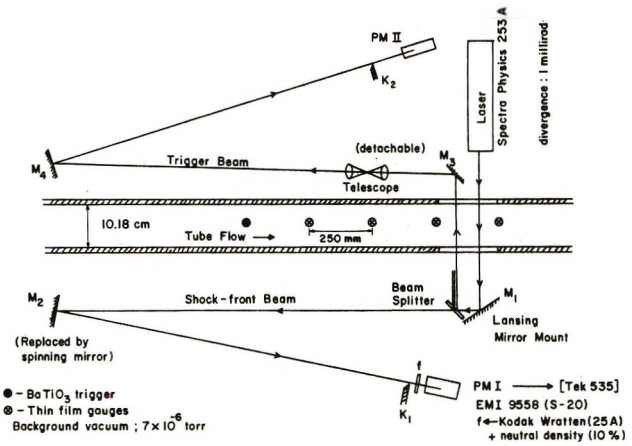

Figure 2. Schematic for schlieren optical arrangement. [For additional details refer to I. R. Hurle, M. I. Buchwald, and S. H. Bauer, Laboratory of Plasma Studies, Report LPS No. 51 (1970).]

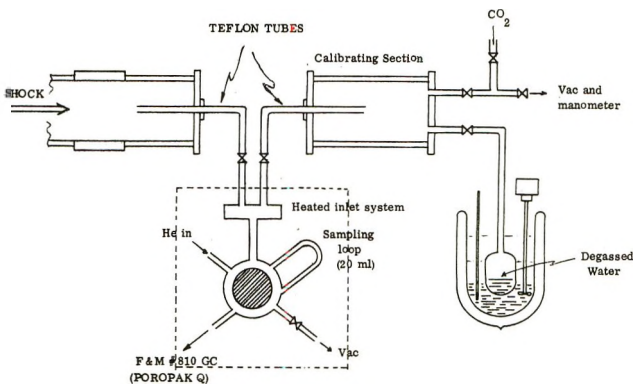

Figure 3. Schematic for calibration and measurement of water content in shock heated samples. The gc column was programmed for a temperature rise of 60°/min from injection at 85°.

the knife edge was 6.5 m. The phototube assembly was placed immediately behind the knife edge. Six dynodes of an EMI 9558 phototube (S-20) were used. The output from an emitter follower was ac coupled to a Tektronix 535 oscilloscope with a type H preamplifier. The rise time of the laser–schlieren system was measured using a gallium arsenide light emitting diode driven by a high-speed pulser, and found to be 200 nsec.

Oscilloscope patterns were recorded on Polaroid 107 film. The photographs were enlarged and traced on large pieces of graph paper (50 cm × 30 cm); then the displacement *vs.* time points were read. The oscilloscopes were calibrated using a digital voltmeter standardized with an NBS standard cell. The time mark generator and scope time-base-line were calibrated by comparison with a crystal controlled 1-μsec time mark generator. Enlargements of schlieren photographs showed less than 0.4% distortion.

The shock tube, together with the pumping lines, were leak tested with a helium leak detector. Using a liquid nitrogen trapped 4-in. diffusion pump with Dow-Corning 705 oil, the ultimate pressure in the lines plus tube was 7×10^{-6} Torr. Between shocks the tube was pumped to approximately 1.5×10^{-5} Torr. The background shock tube pressure rose about 4×10^{-5} Torr/min. A typical gas sample resided in the shock tube about 20 min so that impurities due to leakage (or degassing) attained approximately 1 μ. Adsorption of degassing impurities was minimized by flushing the tube with Coleman grade CO_2 while changing diaphragms.

The water used was glass distilled. D_2O was supplied by International Chemical and Nuclear Corp.; its purity was listed as 99.82%. Both liquids were degassed under vacuum. Test mixtures were prepared manometrically with Coleman Instrument grade CO_2 in a glass-lined hot water heater that had been thoroughly degassed. The mixtures were allowed to stand for 24 hr before being used in the shock tube. The leak rate in the mixing tank was less than 3 μ/day. Special care was taken with D_2O which was isolated from contact with atmospheric water. All lines and the shock tube were thoroughly cleaned and degassed and conditioned before the D_2O runs to minimize exchange with adsorbed H_2O.

Analysis for H_2O and D_2O in the shock tube fill was first attempted with an electronic hygrometer. (Principle of operation: the sensor changes impedance due to absorbed water.) It was deemed necessary to isolate the fragile detector from the shock tube. The readings were found to be erratic and unreliable in these experiments even with frequent calibrations. Water concentrations were measured successfully by gas chromatography (Figure 3). The column material was Poropak Q, 50–80 mesh. Matched 3 ft × $^1/_8$ in. copper columns were used; water was detected by measuring the thermal conductivity of the gas stream. Samples were injected from a 20-ml heated stainless steel cell. The cell was filled through a 0.25-in. teflon tube which was inserted into the shock tube to a position just downstream of the last shock speed sensing gauge, about 30 mm from the laser beam path. The chromatograph, F & M Model 810, was temperature programmed to rise at 60°/min from 85°, at injection. Helium was the carrier gas.

To allow the water vapor concentration in the shock tube to reach an equilibrium level the sample was extracted from the tube 10 min after introducing the water–CO_2 mixture. To ensure that the samples were representative the cell and the sampling tube were flushed repeatedly before each measurement with the shock tube gas mixture. The measured water concentration usually reached a constant value in 10 min and were fully equilibrated in 15 min. An analysis was termed "satisfactory" when three measurements over a space of 10 min were consistent to better than 10%. Equilibration was hastened when the shock tube was

flushed once with the water–CO_2 mixture, after the tube was pumped and before the mixture to be shocked was introduced.

The chromatograph was calibrated frequently using a cell made from a section of pipe identical with that from which the shock tube was constructed. After pumping, water vapor was introduced into the cell from a small bulb containing ice that was immersed in a stirred constant temperature cold bath. Two hours were allowed for the calibration cell to equilibrate. The cell was then isolated and dry CO_2 was admitted to various pressures, spanning the experimental range of initial conditions. No dependence on CO_2 pressure was found. Peak height calibrations were made from dew points between −35 and 0°. Plots of log of peak height *vs.* dew point were straight lines. The vapor pressures of D_2O were related to dew points using the data of Van Hook.[16]

Initial shock sample pressures were varied from 5 to 150 Torr. Final shock temperatures ranged from 370 to 1250°K. Low-temperature shocks (< 450°K) were made using nitrogen for the driver gas and with high initial sample pressures (up to 750 mm). Water concentrations were varied from 0.5 to 5% by volume.

Analysis of Data

Vibrational relaxation times were extracted from the laser–schlieren traces by two methods. The tracings were first analyzed by the "exact method," introduced by Simpson,[17] which allows for continuously changing translational temperature and density in the relaxation zone. This procedure yields translational temperatures and relaxation times as a function of distance behind the shock front. A modification of the expression derived by Blackman[18,19] directly relates the vibrational relaxation time to an apparent density relaxation time. Both procedures are solutions of the master equation.

$$\frac{d\epsilon_{vib}}{dt} = \frac{\epsilon_{vib}^{eq}(T) - \epsilon_{vib}}{\tau_{vib}} \tag{3}$$

where ϵ_{vib} = total energy in vibration, ϵ_{vib}^{eq} = equilibrium amount of energy, (T) = translational temperature, and τ = vibrational relaxation time at temperature T and p. The exact analysis corresponds to integrating eq 3 point by point on the laser–schlieren curve. Simultaneous solution of the conservation equations and the equation of state for the gas mixture relates the changing translational temperature, density, and heat capacity. In addition to the schlieren data one must insert the thermodynamic functions for CO_2,[16,20] H_2O, and D_2O.[17,21]

Study of the oscilloscope traces showed that the relaxation zone probed in these experiments corresponds very nearly to vibrational equilibrium, with the translational temperature and density departing only 4°K and 0.5%, respectively, from their equilibrium values. In addition, semilog plots of schlieren curves show little or no deviation from linearity, further justifying the use of the modified Blackman expression

$$\tau_{vib} = \frac{C_p^{eq}}{C_p^{frozen}} \frac{\rho^{eq}}{\rho^0} \tau_\rho \tag{4}$$

where τ_ρ = apparent relaxation time for gas density (laboratory frame); ρ^{eq}/ρ^0 = equilibrium density ratio, to correct from laboratory to particle time; C_p^{eq} = heat capacity at constant pressure, at equilibrium; and C_p^{frozen} = heat capacity at constant pressure excluding the relaxing degree of freedom. Water vibrations were assumed to relax rapidly with translation and rotation while the CO_2 vibrations remain frozen. The exact method of Simpson and the modified Blackman procedure give the same calculated relaxation times. Because of proximity to equilibrium and the small density changes measured, the small calculated dependence of relaxation times on translational temperatures was not significant. Simpson's data show that the changing vibrational relaxation times during individual shocks are in excellent agreement with the relaxation time corresponding to the best-fit curve through the entire experimental range (including all the runs). The significance of the near collinearity (within experimental error) of the relaxation time *vs.* translational temperature curves for each shock, and the overall curve are clear evidence that, in the measured range, the vibrational relaxation time depends on translational temperature alone. Vibrational relaxation times in pure CO_2 were measured from 350 to 1300°K and found to be in excellent agreement with the Mach–Zender interferometer and laser–schlieren results of Simpson, *et al.*[17,22] (Lab Plasma Studies, Report 51, 1970).

The reduced relaxation time ($\tau_{CO_2-H_2O}$) corresponds to the relaxation of CO_2 at infinite dilution in water. The following expression was used to extract these values from the measured times.

$$\frac{1}{\tau_{obsd}} = \frac{1 - \chi}{\tau_{CO_2-CO_2}} + \frac{\chi}{\tau_{CO_2-H_2O}} \tag{5}$$

where χ = mole fraction of water and $\tau_{CO_2-CO_2}$ = vibrational relaxation time for pure CO_2.

Equations 4 and 5 imply that only the CO_2 vibrations were relaxing. It was assumed that the vibrational temperature of the water is the same as the ambient translational temperature, since vibrational relaxation in pure water is much faster than in pure CO_2.[23] When

(16) W. A. Van Hook, *J. Phys. Chem.*, **72**, 1234 (1968).

(17) C. J. S. M. Simpson, T. R. D. Chandler, and A. C. Strawson, *J. Chem. Phys.*, **51**, 2214 (1969).

(18) W. Griffith, I. D. Brick, and V. Blackman, *Phys. Rev.*, **102**, 1209 (1956).

(19) V. Blackman, *J. Fluid Mech.*, **1**, 61 (1956).

(20) H. W. Wooley, *J. Res. Nat. Bur. Stand.*, **52**, 289 (1954).

(21) A. S. Friedman and L. Haar, *J. Chem. Phys.*, **22**, 2051 (1954).

(22) C. J. S. M. Simpson, K. B. Bridgman, and T. R. D. Chandler, *ibid.*, **49**, 513 (1968).

the relaxation times were calculated under other assumptions (for instance, if one assumes that the H_2O vibrationally relaxes along with the CO_2) only slightly different values were found for $\tau_{CO_2-H_2O}$. This is a consequence of the low H_2O concentrations and its small vibrational heat capacity. $\tau_{H_2O-H_2O}$ has been measured; it is 1.5×10^{-2} μsec atm at room temperature. On this basis, eq 5 is satisfactory for concentrations of water less than, or equal to, 10%. Actually, this relation was used in the analysis of the ultrasonic measurements for mixtures containing up to 24% H_2O[4] and was found to give a satisfactory reduction of the experimental results.

With the assumption of rapid energy exchange between the vibrational modes we can find the specific relaxation time for CO_2 in the first excited bending mode (τ_{01^10})

$$\tau_{01^10} = \tau_{CO_2-H_2O}\left(\frac{C_{01^10}}{C_{vib}}\right) \quad (6)$$

where C_{vib} = total vibrational heat capacity and C_{01^10} = vibrational heat capacity due to the (01^10) state alone.

The rate constant for deexciting the (01^10) state is then given by

$$k_{10} = (\tau_{01^10})^{-1}[1 - \exp(-h\nu/kT)]^{-1} \quad (7)$$

where ν is the bending frequency. The probability of a $(01^10) \rightarrow (000)$ transition during a collision (P_{10}) is estimated by dividing the transition rate constant by the collision rate. Thus

$$P_{10} = k_{10}/Z_{CO_2-H_2O} \quad (8)$$

Equation 6 is known as the Schafer relation,[24] and implies that the (01^10) state is the "gating" mode through which all the vibrational energy passes *enroute* to equilibration. If vibrational energy does not enter the molecule *via* any other route, *i.e.*, directly to (10^00) or (00^01), eq 6 accurately yields τ_{01^10}. The Schafer equation is satisfactory at low temperatures when the major portion of the varying specific heat is associated with the (01^10) state.

Results and Discussion

Our experimental results are presented in Tables I and II. The relaxation times were calculated by the modified Blackman procedure; the vibrational states of water were assumed to be in equilibrium with the translational temperature. Final temperatures and pressures correspond to equilibrium beyond the relaxation zone. In Figure 4 these results are compared with values extracted from the literature. There is good agreement for CO_2–H_2O, where our measurements overlap in temperature with the shock tube investigations of Smiley and Winkler,[6] and the ultrasonic data of Lewis and Lee[7] and of Higgs and Torborg.[4] This appears to be the first report based on shock tube measurement of CO_2 relaxation times that show the negative Landau–Teller temperature dependence previously demonstrated by ultrasonic techniques. The present results on the CO_2–D_2O system are also consistent with the ultrasonic values published by Shields and Burkes.[14] Whereas a small negative temperature dependence appears in our data, these authors reported that the relaxation time increased more rapidly with temperature in CO_2–D_2O than in CO_2–H_2O mixtures, in the lower temperature regime. In the combined $p\tau_v$ *vs.* T plots there is no indication of the minimum in the reduced relaxation times reported by Eucken and Neuman.[3b] In addition to our work recent measurements[4] confirm the results of Lewis and Lee.

Table I: CO_2–H_2O

Run No.	P_1, Torr	$P_{2(eq)}$, Torr	T_2, °K	$P\tau_v$, μsec atm, as measured	$P\tau_v$, μsec atm (reduced) CO_2–H_2O	x_{H_2O}
1	26.75	179	512	0.35	0.0083	0.021
2	29.72	215	529	0.48	0.015	0.026
3	30.00	215	527	0.41	0.013	0.028
4	31.30	237	540	0.51	0.014	0.024
5	46.00	275	490	0.54	0.013	0.021
6	47.10	201	432	0.22	0.056	0.024
7	27.70	137	466	0.41	0.0068	0.015
8	31.81	155	454	0.36	0.0061	0.015
9	29.10	300	622	1.18	0.0016	0.002
10	38.05	269	524	0.36	0.0063	0.016
11	31.07	382	677	1.21	0.0026	0.011
12	29.10	423	741	1.07	0.0027	0.013
13	21.72	258	667	1.00	0.029	0.017
14	22.04	264	671	0.61	0.014	0.017
15	25.69	290	652	0.53	0.014	0.020
16	18.10	251	723	0.68	0.020	0.020
17	18.42	272	748	0.65	0.016	0.017
18	16.60	231	726	0.55	0.018	0.024
19	13.10	213	789	0.58	0.018	0.022
20	10.02	205	902	0.59	0.024	0.026
21	7.30	202	1083	0.58	0.037	0.036
22	7.10	208	1117	0.43	0.024	0.037
23	11.57	261	958	0.28	0.033	0.098
24	8.60	225	1042	0.27	0.018	0.055
25	7.18	241	1165	0.25	0.023	0.073

The experimental results are compared with various theories in Figure 5. Sharma's analysis contains no adjustable parameters; for CO_2–H_2O he calculated P_{10} as a function of temperature. His P_{10}'s were converted to relaxation times on the basis of a hard-sphere model for the collision number ($\pi\sigma^2 = 44.2$ Å^2). Widom and Bauer's predictions are plotted for the potential function parameters that gave a best fit with the results of Eucken and Neuman. Lewis and Lee,[7]

(23) Y. Fujii, R. B. Lindsay, and K. Urushihana, *J. Accoust. Soc. Amer.*, **35**, 961 (1963).

(24) F. D. Shields, *ibid.*, **47**, 1262 (1969).

Table II: CO_2–D_2O

Run No.	P_1, Torr	$P_{2(eq)}$, Torr	T_2, °K	$P\tau_v$, μsec atm, measured	$P\tau_v$, μsec atm (reduced) CO_2–D_2O	x_{D_2O}
1	96.90	282	377	0.75	0.021	0.024
2	100.40	282	380	1.22	0.016	0.010
3	102.50	298	383	1.10	0.016	0.011
4	89.90	264	386	0.55	0.017	0.027
5	96.90	313	396	0.81	0.025	0.025
6	42.10	159	415	0.73	0.017	0.020
7	45.16	176	420	0.86	0.027	0.026
8	45.67	179	423	0.71	0.019	0.023
9	46.12	256	477	0.71	0.024	0.028
10	43.52	255	487	0.67	0.019	0.024
11	42.30	311	533	1.06	0.034	0.022
12	41.52	312	536	0.78	0.030	0.029
13	32.20	353	638	0.57	0.022	0.030
14	25.60	312	671	1.09	0.052	0.027
15	21.13	291	714	1.12	0.054	0.025
16	22.02	306	721	0.58	0.027	0.035
17	25.07	354	725	0.63	0.027	0.031
18	26.00	373	734	0.60	0.029	0.036
19	29.32	433	740	0.88	0.060	0.041
20	26.17	396	755	0.43	0.022	0.041
21	24.82	430	814	0.73	0.034	0.029
22	20.08	367	834	0.75	0.027	0.021
23	12.00	221	844	0.40	0.030	0.059
24	13.85	324	969	0.55	0.047	0.054
25	15.08	356	976	0.41	0.031	0.055
26	13.55	346	1019	0.46	0.027	0.040
27	8.15	251	1152	0.43	0.033	0.049
28	7.19	238	1211	0.41	0.042	0.068

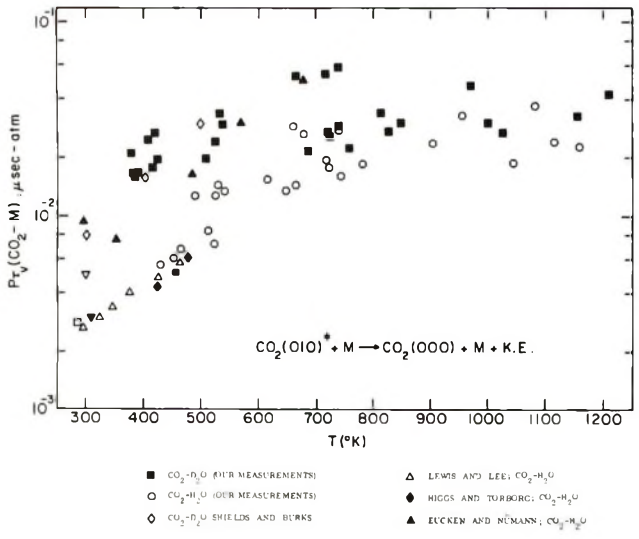

Figure 4. Relaxation times for the deexcitation of $CO_2(01^10)$. Experimental values obtained in this study are compared with the relevant literature.

with slight changes in these parameters, were able to fit their CO_2–H_2O data to the Widom–Bauer theory. However, Shields and Burkes were unsuccessful in fitting ultrasonic results for both CO_2–H_2O and CO_2–D_2O, using the same parameters. It is clear that the

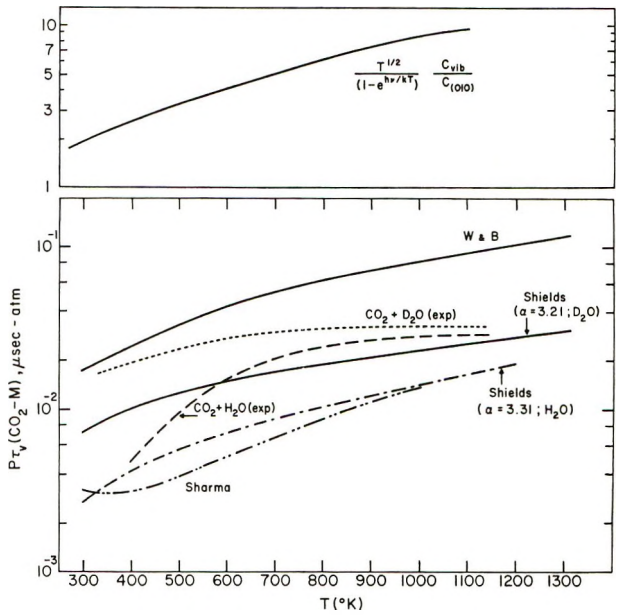

Figure 5. Comparisons of our experimental results with proposed theories. The top graph shows the relative temperature dependence which the relaxation time would show were P_{10} independent of T; this effect is due primarily to the collision frequency. $C_{(01^10)}$ is the heat capacity of the bending mode and ν is the corresponding frequency.

Widom–Bauer theory cannot account for the large observed isotope effect, since the isotope shift enters only as a change in reduced mass of the collision partners. Sharma's theory seems flexible enough to account for this difference because it takes into consideration the large differences in their rotational level separations. However, he has not yet published detailed calculations of P_{10} for CO_2 with D_2O as a collision partner.

Shields proposed that the time-dependent force exerted by the water molecule on the bending mode of CO_2 is of the form

$$F(t) = F_0 \exp(-\alpha^2 t^2) \cos(2\omega t + \varphi) \qquad (9)$$

For the maximum force he chose $F_0 = 24\epsilon/\sigma$, the slope of the Lennard-Jones potential function at $r_{CO_2-H_2O} = \sigma$; α is an adjustable inverse interaction-time parameter; ω = angular rotational velocity of the collider (H_2O or D_2O), and φ is an arbitrary phase angle. To obtain an optimum fit for both the light and heavy water, we used $F_0 = 24\epsilon/1.5\sigma$. Shields proposed for CO_2 with collision partners H_2O, D_2O, H_2S, and D_2S that

$$\alpha_i = (1.18 \times 10^{14})/(\mu_i)^{1/2} \qquad (10)$$

[μ_i is the reduced mass for the collision pair].

In the Widom–Bauer formulation the high- and low-impact parameter collisions were treated separately. It was assumed that high relative kinetic energy collisions (greater than 0.8ϵ) are only effective with impact parameters smaller than the maximum value for or-

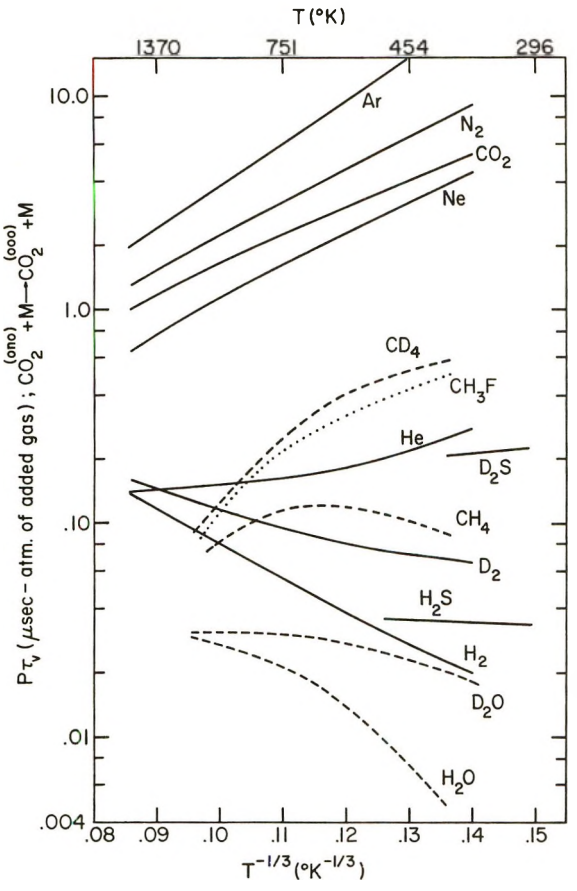

Figure 6. Compilation of data for $CO_2(0n0)$ relaxation: (M = CO_2, Ar) C. J. S. M. Simpson, T. R. D. Chandler, and A. C. Strawson, *J. Chem. Phys.*, **51**, 2214 (1969); (N_2, H_2, D_2, Ne, He) C. J. S. M. Simpson and T. R. D. Chandler, *Proc. Roy. Soc., Ser. A*, **317**, 265 (1970); (H_2S) F. D. Shields, *J. Acoust. Soc. Amer.*, **45**, 481 (1968); (D_2S) F. D. Shields and G. P. Carney, *ibid.*, **47**, 1269 (1970); (CD_4, CH_4, CH_3F) P. M. Walsh and S. H. Bauer, unpublished results; (D_2O, H_2O) this work.

biting. The contribution of low-energy collisions is thus given special importance. The somewhat arbitrary cut off energy between high- and low-energy collisions of 0.8ϵ (which is applicable to interaction potentials such as L-J, 6/12) corresponds to 215°K. With an interaction distance of 0.1 Å this implies an interaction time of 2.1×10^{-14} sec for CO_2–H_2O collisions. This essential aspect of the model was incorporated in Shield's formulation.

Figure 6 is a compendium of the available data on $CO_2(01^10)$ relaxation times, covering a range of temperatures and collision partners. It is clear from this plot that the efficient relaxers do not exhibit L–T temperature dependence, with the most efficient colliders deviating the most from the usual $T^{-1/3}$ form. The principal interaction in these cases is not properly represented by an exponential repulsive term. Shields formulation does not directly involve the interaction potential, and thus provides no connection with the controlling factor in the energy transfer process. The temperature dependence of the transition probabilities are masked by the effect of temperature on the effective collision cross sections. The question remains whether any theory can provide predictions at the level of precision with which current experiments are performed if the estimates for energy transfer probability are obtained by first calculating collision orbits as though the colliders followed a central force interaction, and then superposing a vibrator–collider interaction potential, possibly with arbitrarily builtin asymmetries. The obvious but more difficult approach is to generate a semiempirical potential energy surface for the minimum number of "centers" required to characterize the collision [for example, $CO_2 + H_2O$ needs (3 + 2), if one represents the water molecule as a polar ellipsoid of revolution], and to compute collision dynamics on that surface by Monte Carlo techniques.

Acknowledgments. The authors express their appreciation for help in designing the apparatus to Dr. Ian Hurle. Professor C. J. S. M. Simpson and Dr. R. Taylor supplied helpful discussions and data. They also thank the Advanced Research Projects Agency of the Department of Defense, monitored by the Office of Naval Research under Contract No. N00014-67-A-0077-0006, for support which made this study possible.

Formation of, by Termolecular Reactions, and Bond Dissociation Energy, Structure, and Bond Length for OH^-H_2O and O^-H_2O[1]

by Charles E. Melton

Chemistry Department, University of Georgia, Athens, Georgia 30601 *(Received May 12, 1972)*

Publication costs assisted by the U. S. Atomic Energy Commission

The termolecular reactions of O^- and OH^- with H_2O to produce O^-H_2O and OH^-H_2O have been studied in the mass spectrometer. The rate constant for the former is 2.1×10^{-27} cc^3 sec^{-1} and that for the latter is 1.8×10^{-27} cc^3 sec^{-1}. The bond dissociation energy of OH^-H_2O was calculated to be 1.1 eV. The internuclear distance for R(O—H) was calculated to be 1.22 Å. The formation of the complexes is discussed in terms of both the energy transfer and bound complex mechanism.

Introduction

When water vapor at high pressure (~0.1 Torr) is bombarded with electrons (or any other ionizing media), solvated or associate OH^- ions and H^+ ions of empirical formula $OH^-(H_2O)_n$ and $H^+(H_2O)_n$ (n = 1, 2) are formed. Comparable ionic association in solution is a basic phenomenon that has been known for many years. However a study of the statics, energetics, and kinetics of ionic interactions in solution is difficult because the data must be obtained by indirect methods. Furthermore, the dielectric constant of the solution must be known to calculate the free energy of solvation of the ion. This quantity is usually unknown because average dielectric constants are not valid in the immediate vicinity of an ion. Even the hydration number for various ions in solution is uncertain. Consequently, to make further progress on the general problem of solvation a new approach is required. The present approach to the problem involves a study of solvated species in the gas phase. Specifically, we will consider the OH^- ion attached to a single solvent molecule of H_2O at a distance r from its center.

A study of solvation in the gas offers a direct method for determining the statics, kinetics, and energetics of ionic solvation. Several years ago work was initiated at this laboratory to determine quantitively each of the above parameters for pure water vapor. Our work has been principally concerned with solvation of OH^-. Since OH^- is not produced predominately as a primary product, considerable background information on the production of OH^- must be obtained prior to considering the solvation problem. Previous work[2-4] has shown that OH^- is formed in water vapor by electron impact by four different processes. They are

$$H_2O + e \longrightarrow OH^- + H \quad (1a)$$

$$H_2O + e \longrightarrow OH^- + H^+ + e \quad (1b)$$

$$H_2O + e \longrightarrow H^- + OH \quad (2a)$$

$$H^- + H_2O \longrightarrow OH^- + H_2 \quad (2b)$$

$$H_2O + e \longrightarrow O^- + H_2 \quad (3a)$$

$$O^- + H_2O \longrightarrow OH^- + OH \quad (3b)$$

An experimental determination of the rate constant by mass spectrometry for the reaction of OH^- with solvent to produce OH^-H_2O in the gas phase involves a knowledge of the rate constants involved in the production of the reactant OH^- by reactions 1–3. Accordingly accurate values for these quantities are needed. Several different laboratories[4-13] have studied reaction 2a and the experimental results are in reasonable agreement. In contrast to the good agreement found for reaction 2a, values[3,14-17] for the rate constants and cross sections for reaction 2b differ by three orders of magnitude. However, values agree to within an order

(1) Supported by the U. S. Atomic Energy Commission under Contract No. AT-(38-1) 640 with the University of Georgia.

(2) (a) C. E. Melton, *J. Chem. Phys.*, in press; (b) *ibid.*, **74**, 582 (1970).

(3) C. E. Melton and G. S. Neece, *J. Amer. Chem. Soc.*, **93**, 6757 (1971).

(4) C. E. Melton and G. S. Neece, *J. Chem. Phys.*, **55**, 4665 (1971).

(5) B. C. Cox, Ph.D. Thesis, University of Liverpool, 1953.

(6) M. M. Mann, A. Hustrulid, and J. T. Take, *Phys. Rev.*, **58**, 340 (1940).

(7) W. W. Lozier, *ibid.*, **36**, 1417 (1930).

(8) I. S. Buchel'nikova, *Zh. Eksp. Teor. Fiz.*, **35**, 1119 (1959); *Sov. Phys. JETP*, **8**, 783 (1959).

(9) F. H. Dorman, *J. Chem. Phys.*, **44**, 3856 (1966).

(10) M. Cottin, *J. Chim. Phys.*, **56**, 1024 (1959).

(11) G. J. Schulz, *J. Chem. Phys.*, **33**, 1661 (1960).

(12) J. L. Moruzzi and A. V. Phelps, *ibid.*, **45**, 4617 (1966).

(13) R. N. Compton and L. G. Christophorou, *Phys. Rev.*, **154**, 110 (1967).

(14) J. H. D. Stockdale, R. N. Compton, and P. W. Reinhardt, *ibid.*, **184**, 81 (1969).

(15) J. F. Paulson, Nineteenth Annual Conference of Mass Spectrometry and Allied Topics, Atlanta, Ga., 1971.

(16) R. Tassa and C. Lifshitz, Annual Meeting of Israel Chemical Society, 1971.

(17) L. B. Yound, E. Lee-Ruff, and D. K. Bohme, *Can. J. Chem.*, **49**, 979 (1971).

of magnitude for the two groups[3,14] who have also determined the cross section for reaction 2a. Furthermore, results obtained by two groups[3-15] utilizing pressure techniques of mass spectrometry agree to within about $\pm 10\%$. Thus, pending evidence to the contrary, conventional pressure techniques[18] of mass spectrometry appear to give good results for rate constants for ionic processes. These arguments appear to justify further use of conventional pressure techniques for higher order reactions in water vapor. It should be noted that the principal source of error for reaction 2b is the determination of the pressure. Indirect methods for determining the pressure may well account for the discrepancy in the results reported in the literature.

Perhaps the most important quantity in ionic solvation is the heat of solvation. Several investigators[19-21] have attempted to measure by various means heats of solvation of OH^- in the gas phase. Previous experimental results are somewhat uncertain because the state of excitation of the ionic species was unknown. The amount of excitation is determined largely by the mode of formation of the species. For $OH^-(H_2O)$, at least four possible processes must be considered. They are

$$OH^- + H_2O \longrightarrow OH^-H_2O \quad (4)$$

$$OH^- + (H_2O)_2 \longrightarrow OH^-H_2O + H_2O \quad (5)$$

$$OH^- + H_2O \rightleftarrows OH^-H_2O^* \quad (6a)$$

$$OH^-H_2O^* + H_2O \longrightarrow OH^-H_2O + H_2O \quad (6b)$$

$$e + (H_2O)_2 \longrightarrow OH^-H_2O + H \quad (7)$$

Should OH^-H_2O be formed by association or clustering, reaction 4, the species would be highly excited unless the excess energy were lost by radiation. Formation of OH^-H_2O by reactions 5, 6, or 7 would most likely produce the species in essentially the "ground state." Thus, an accurate knowledge of the mode of formation can be used as evidence for the amount of excitation of the ion. In this study, we expected to determine both the mode of formation and the rate constant for the process and to combine the results with other data[19] to obtain a value for the bond energy of the species OH^-H_2O.

Should OH^-H_2O be formed by association, other associated species might also be formed. For example, $O^-H_2O^*$ is a possible long-lived intermediate complex for reaction 3b. Thus, the occurrence of O^-H_2O in the system was to be explicitly considered.

Experimental Section

Mass spectrometry has proved to be an extremely versatile tool for the study of bimolecular ion–molecule reactions in the gas phase. Most of the systems studied have involved positive ions at relatively low pressure. The study of ionic solvation requires extending the pressure range to much higher values.

The apparatus that we have developed for high-pressure studies of gaseous systems consists of two somewhat different 6-in. radius 90° sector type of research mass spectrometers. The analyzer tubes, source, and collector envelopes are constructed from inconel and stainless steel. Differential pumping with oil diffusion pumps is utilized between the source envelope and the analyzer tube. Base pressure of the instruments is about 4×10^{-7} Torr without liquid nitrogen in the traps. The pressure is decreased to about 1×10^{-8} Torr with liquid N_2 cooling.

Ions are produced in a high-pressure ion source described elsewhere.[3] In these experiments the apertures for admission of the electron beam and exit of the ions were holes of 0.007-in. diameter. Ionizing electrons were produced by a hot thoria iridium filament[22] and collimated by permanent magnets of about 500 G strength. The current from the filament was about 300 μA and the collimated electron beam was about 10 μA. The emission from the filament was electronically controlled to maintain a constant value. The potential of the ion repeller, with respect to the ion chamber, was variable by ± 20 V. Ions were accelerated by a constant potential of 6500 V. High-accelerating potentials were necessary because the electron multiplier delector was maintained at a potential of -3000 V. Thus, the energy of the negative ions at the first dynode was 3500 eV. Pressure in the ion source was determined by a MKS baratron pressure gauge. No correction was made for any possible drop in pressure between the ion chamber and gauge head.

Ions were detected by a 14-stage electron multiplier coupled to a vibrating capacitor electrometer and a strip chart recorder. The gain of the multiplier was about 10^6 and assumed to be constant for all of the ions under investigation.

The sample of water was introduced from a 5-l. borosilicate glass expansion reservoir. The reservoir was connected to the ionizing chamber by a molecular leak about 0.001 in. in diameter.

Since both Cl^- and $OH^-(H_2O)$ appear at mass 35, particular care had to be exercised to avoid Cl in the sample. Ultimately, we triply distilled a sample of natural spring water to avoid the Cl contamination.

Ion–molecule reactions were identified by "standard" appearance potential and pressure techniques.[23]

(18) C. E. Melton, "Principles of Mass Spectrometry and Negative Ions," Marcel Dekker, New York, N. Y., 1970, p 273.

(19) S. Golub and B. Steiner, *J. Chem. Phys.*, 49, 5191 (1968).

(20) J. L. Moruzzi and A. V. Phelps, *ibid.*, 45, 4617 (1966).

(21) M. De Paz, A. Guidoni Giardini, and L. Friedman, *ibid.*, 52, 687 (1970).

(22) C. E. Melton, *Rev. Sci. Instrum.*, 29, 250 (1958).

(23) C. E. Melton, "Ion Molecule Reactions," in "Mass Spectra of Organic Ions," F. W. McLafferty, Ed., Academic Press, New York, N. Y., 1963, p 82.

Results and Discussion

Three different types of experiments on water vapor were performed. The first was designed to determine the pressure dependence of the species O^-H_2O and OH^-H_2O and involved measuring the intensity of each ion as a function of pressure. The second was designed to determine the origin of the hydrated species and involved determining the ionization efficiency curve of the species for comparison with known curves for primary and secondary ions, and the third experiment was designed to measure the rate constants by a careful measurement of the absolute value of the pressure.

Results for the first series of experiments are presented in Figure 1. It can be seen that the intensity of each of the ions, O^-H_2O and OH^-H_2O, is a function of the fourth power of the pressure. The data show some scatter because of the high-pressure range required for the experiments. Useful data could not be obtained below a pressure of about 0.05 Torr. At pressures above about 0.1 Torr, the OH^-H_2O intensity failed to increase with increasing pressure according to the P^4 law. This observation was interpreted on the basis of OH^-H_2O loss to form $OH^-(H_2O)_2$. These results clearly show that the rate-limiting step in the formation of $OH^-(H_2O)$ and O^-H_2O is a termolecular reaction.

The next series of experiments involved a determination of the ionization efficiency curves for O^-H_2O and OH^-H_2O. Results are shown in Figures 2 and 3, together with results for O^- and OH^-. All intensities are adjusted to give approximately the same maximum. These data show that O^- is the precursor for O^-H_2O and OH^- is the precursor for OH^-H_2O. The appearance potential data for OH^- are for secondary OH^-. Primary OH^- has an entirely different ionization efficiency curve as shown in Figure 4.

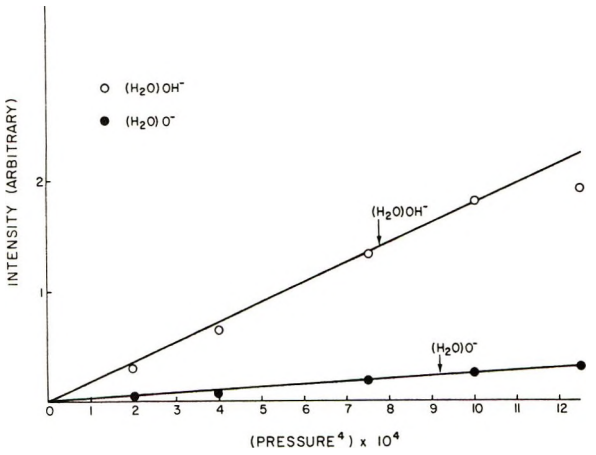

Figure 1. Abundance of H_2OOH^- and H_2OO^- as a function of pressure. The temperature was constant at 50° and the relative energy was constant at 0.5 eV.

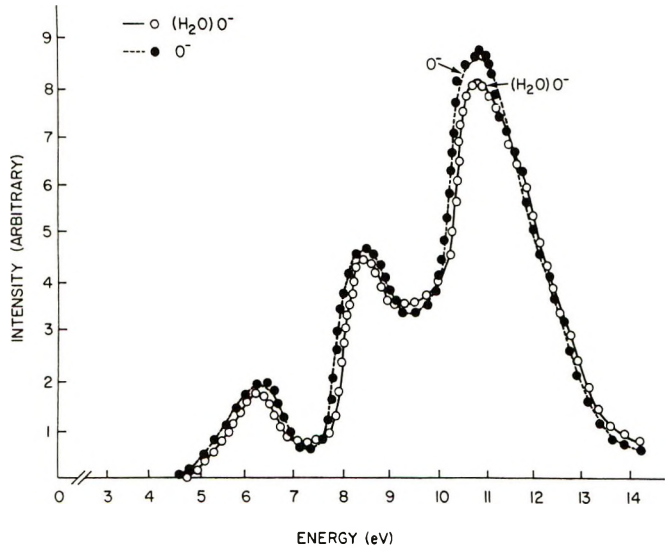

Figure 2. Ionization efficiency curves for primary O^- and H_2OO^-. Pressure in the reaction chamber was 0.08 Torr.

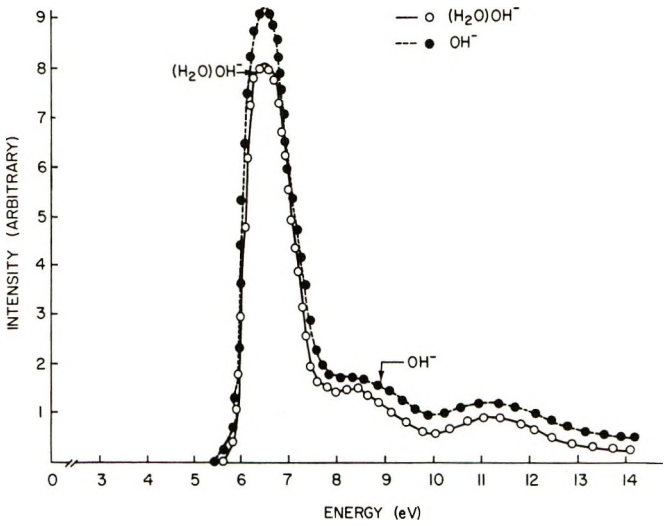

Figure 3. Ionization efficiency curves for secondary OH^- and H_2OOH^-. The pressure in the reaction chamber was 0.08 Torr.

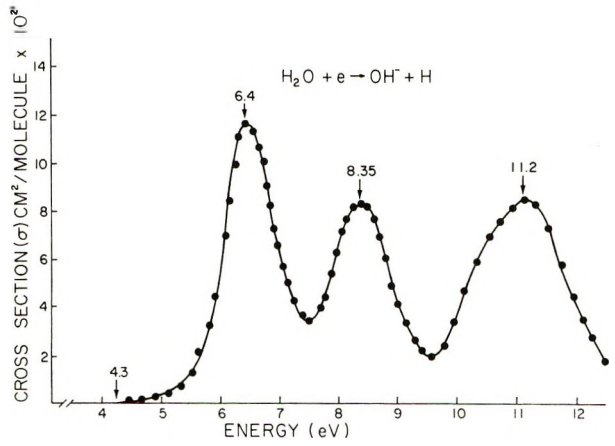

Figure 4. Ionization efficiency curve for primary OH^-. The pressure in the ionization chamber was 6×10^{-7} Torr.

The third series of experiments was directed toward a determination of the rate constants for the termolecular reactions. Experimentally the rate constant is obtained from the expression

$$k = 6.95 \times 10^5 \frac{[AB_p^-]}{[AB_R^-][AB]^2 x}\left(\frac{Ex}{M_{AB_R^-}}\right)^{1/2} \quad (8)$$

where AB_p^- is the product ion, AB_R^- is the reactant ion, [AB] is the concentration of neutrals, x is the reaction path in cm, M is the mass in atomic mass units, and E is the electric field in volts cm^{-1}. The species OH^-H_2O is produced from both primary H^- and O^-. However, by suitably adjusting the electron energy the reactions could be easily differentiated. For example, production *via* O^- was determined with 11.1-eV ionizing electrons (see Figure 2) and production *via* H^- was determined with 6.4-eV ionizing electrons. Equal collection efficiencies were assumed for the ions O^-, OH^-, O^-H_2O, and OH^-H_2O. This assumption is probably reasonable for all ions except O^- which is initially formed with kinetic energy. Results for the rate constants are given in Tables I–III. Values for the rate constants and cross sections for primary and secondary steps of the reaction are taken from previous work.[2a,3,4]

Table I: Formation of OH^-H_2O *via* H^- in Water

Reaction (6.4 eV)	Cross sections (σ), 10^{-18} cm^2 molecule^{-1}	Rate constant, k
$e + H_2O \xrightarrow{\text{primary}} H^- + OH$	6.6	
$H^- + H_2O \xrightarrow{\text{secondary}} OH^- + OH$	3800	3.8×10^{-9} cc sec^{-1}
$OH^- + H_2O \xrightleftharpoons{\text{termolecular}} OH^-(H_2O)^*$		
$OH^-(H_2O)^* + H_2O \rightarrow OH^-H_2O + H_2O$		1.8×10^{-27} cc^3 sec^{-1}

Table II: Formation of OH^-H_2O *via* O^- in Water

Reaction (11.2 eV)	Cross section (σ), 10^{-18} cm^2 molecule^{-1}	Rate constant, k
$e + H_2O \xrightarrow{\text{primary}} O^- + H_2$	0.57	
$O^- + H_2O \xrightarrow{\text{secondary}} OH^- + OH$	1350	1.4×10^{-9} cc sec^{-1}
$OH^- + H_2O \xrightleftharpoons{\text{termolecular}} OH^-(H_2O)^*$		
$OH^-(H_2O)^* + H_2O \rightarrow OH^-H_2O + H_2O$		1.8×10^{-27} cc^3 sec^{-1}

Table III: Formation of O^-H_2O in Water

Reaction (11.2 eV)	Cross section (σ), 10^{-18} cm^2 molecule^{-1}	Rate constant, k
$e + H_2O \rightarrow O^- + H_2$	0.57	
$O^- + H_2O \rightarrow O^-H_2O^*$		
$O^-H_2O^* + H_2O \rightarrow O^-H_2O + H_2O$		2.1×10^{-27} cc^3 sec^{-1}

Let us now combine the results from this study to estimate the bond energy $D(OH^-–H_2O)$. Both modes of formation of OH^-H_2O involve a termolecular reaction. This mode of formation usually produces a product with little excess vibrational energy. Thus, one can combine the electron affinity for OH^-H_2O as measured by Golub and Steiner[19] with that for OH^- as reported by Branscomb[24] to obtain the dissociation energy for the species. The results are

$$OH^-H_2O \longrightarrow OH^- + H_2O \qquad 1.12 \text{ eV}$$

This value is about 35% lower than that obtained by indirect methods.[21]

A knowledge of the dissociation energy can be used to estimate the internuclear separation for the ion and the molecule. Consider the ion of charge e interacting with a water molecule at a distance r from its center. Let α be the polarizability and μ the dipole moment of the water molecule. The energy of interaction, ϵ, is

$$\epsilon = Ar^{-9} - Br^{-4} - Cr^{-2} \quad (9)$$

assuming the energy of repulsion varies inversely as the ninth power of the separation. The coefficients for water are defined as

$$A = \left(\frac{4}{9}\right)Br_0^5 + \left(\frac{2}{9}\right)Cr_0^7$$

$$B = {}^1/_2\alpha e^2$$

$$C = \mu e$$

Evaluating eq 9 by minimizing with respect to r, we obtain a value of 2.18 Å for r_0. If we assume a linear structure of $OH^-(H_2O)$ of the type

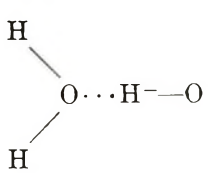

and take the usual[25] ROH bond distance of 0.9572 Å, then the RO···H bond distance becomes 1.22 Å. This distance is considerally shorter than that[26] of about 1.7

(24) L. M. Branscomb, *Phys. Rev.*, **148**, 11 (1966).

(25) W. S. Benedict, N. Gallas, and E. K. Plyler, *J. Chem. Phys.*, **24**, 1139 (1956).

Å for dimeric H_2O. If, as expected,[26] the ROH bond length increased in OH^-H_2O species to about 1 Å then the R(O···H) bond distance is about 20% greater than that of R(O–H).

The formation of OH^-H_2O by a termolecular reaction can be discussed in terms of two mechanisms. On the one hand, we can consider the energy transfer mechanism

$$OH^- + H_2O \rightleftarrows OH^-H_2O^* \quad (10)$$

$$OH^-H_2O^* + H_2O \longrightarrow OH^-H_2O + H_2O \quad (11)$$

on the other hand, there is the intermediate complex process

$$OH^- + 2H_2O \rightleftarrows OH^-H_2O + H_2O \quad (12)$$

Several investigators[27-31] have developed theories to describe termolecular reactions. The bound-complex theory obtains an equilibrium constant for reaction 12 of the form

$$K = \frac{[OH^-H_2O]}{[OH^-][H_2O]} = \frac{Q_{OH^-H_2O}}{Q_{OH^-}Q_{H_2O}} \exp(\epsilon/kT) \quad (13)$$

where the Q's refer to partition functions. The translational partition functions are easily obtained, but the vibrational partition function for OH^-H_2O cannot be easily obtained from a harmonic oscillator function. Bunker and Davidson[27] suggested the use of a phase integral of the form

$$Q_{int} = 4\pi \int_0^\infty \int_0^\infty \int_0^\infty \times \exp\, p^2/2\mu kT \, dp_x dp_y dp_z \int_0^{r_1} \exp\, -\epsilon/kTr^2 dr \quad (14)$$

If one substitutes reasonable parameters into eq 13 and 14, the theoretical results give the same order of magnitude as that for the experimental results.

On the other hand, if one evaluates the rate constant by the energy transfer theory as proposed by Rabinowitch,[32] one again obtains agreement to within an order of magnitude. Thus, the theories can not be evaluated with sufficient accuracy to distinguish between the energy transfer and bound complex mechanisms for the formation of OH^-H_2O.

These results were obtained for a temperature of approximately 50° in the reaction chamber. The reaction could not be studied as a function of temperature in the present apparatus.

The energy of the reactant ions was 0.5 eV. Because of experimental difficulties, the reactions were not examined as a function of energy.

In conclusion, the species $OH^-(H_2O)$ is formed in the gas phase by a termolecular reaction with little excess internal energy. The bond energy of 1.1 eV indicates that the species is quite stable with respect to autodissociation at room temperature. The species O^-H_2O appears to be equally stable although no quantitative data on stability were obtained. The calculated internuclear distance of 1.2 Å is considerably less as expected than the reported value for dimeric H_2O of 1.7 Å.

(26) D. Hadzi and H. W. Thompson, Ed., "Hydrogen Bonding," Pergamon Press, Oxford, 1959.

(27) D. L. Bunker and N. Davidson, *J. Amer. Chem. Soc.*, **80**, 5090 (1958).

(28) E. Wigner, *J. Chem. Phys.*, **5**, 720 (1938).

(29) J. C. Keck, *ibid.*, **29**, 410 (1958).

(30) J. C. Light, *ibid.*, **36**, 1016 (1962).

(31) G. Porter, Z. G. Szabo, and M. G. Townsend, *Proc. Roy. Soc., Ser. A*, **270**, 493 (1962).

(32) E. Rabinowitch, *Trans. Faraday Soc.*, **33**, 283 (1937).

Spontaneous and General Base-Catalyzed Iodination of Pyruvic Acid and Alkyl Pyruvates. Activation Parameters and Solvent Deuterium Isotope Effects

by M. Hegazi and J. E. Meany*

Department of Chemistry, Central Washington State College, Ellensburg, Washington 98926 *(Received December 28, 1971)*

Publication costs assisted by the Central Washington State Research Fund

The iodinations of pyruvic acid and the methyl and ethyl pyruvate esters have been studied using a spectrophotometric method by following the disappearance of the triiodide anion at 353 nm. The spontaneous rates were determined over a wide range of temperatures from which the activation parameters were determined in H_2O and D_2O. For pyruvic acid, the free energy, $\Delta G^{\pm}$, enthalpy, $\Delta H^{\pm}$, and entropy, $\Delta S^{\pm}$, of activation were found to be very similar to the corresponding values as determined for the esters. The catalytic components, k_{cat}, involved in the general base-catalyzed iodination of methyl pyruvate in formate, acetate, and diethyl malonate buffers were determined and these values along with the value associated with the solvent-catalyzed component at 25.0° allowed the estimation of the Brønsted coefficient, $\beta = 0.55 \pm 0.06$.

Introduction

A recent report from this laboratory described a comparative study of the *iodinations* of pyruvic acid and methyl and ethyl pyruvate,[1] wherein the similarity of spontaneous rates of iodination for all substrates as obtained at a single temperature, 25.0°, suggested that the intramolecular acid-catalyzed enolization of pyruvic acid by the carboxyl group (a mode not available in the corresponding reaction of the esters) is not the dominant reaction pathway. In the present work, we have extended our studies to include kinetic determinations over a wide range of temperatures thereby allowing the evaluation of the activation parameters for the enolization processes associated with pyruvic acid and the pyruvate esters. Similar investigations were carried out in deuterium oxide for the same substrates and the solvent deuterium isotope effects are deduced. Finally, the sensitivity of the iodination of methyl pyruvate toward general base catalysis was studied *via* application of the Brønsted catalysis law.

Experimental Section

The substrates used in the present work were obtained from commercial sources and purified as described in earlier work.[1] The concentration of the distilled pyruvic acid was checked prior to use by titration with a previously standardized sodium hydroxide solution. Diethylmalonic acid was prepared by the saponification of its diethyl ester[2] and all other chemicals were obtained from commercial sources in analytical or reagent grade. Buffer solutions were prepared either in deionized water or in deuterium oxide (ICN Chemical Co.) with the appropriate quantities of sodium chloride added to obtain an ionic strength of 0.1 M.

The kinetic runs were generally inititated by injecting 0.050 ml of a solution formally 2.05×10^{-3} M in iodine and 1.00 M in potassium iodide into 3 ml of the reaction mixture. The iodination of the carbonyl compounds was monitored on a Beckman Kintrac VII spectrophotometer, the cell compartment of which is thermostated to ±0.02° by means of a Beckman Thermocirculator Accessory. The disappearance of the triiodide (ϵ 24,500 M^{-1} cm^{-1})[3] ion was followed at 353 nm and the reaction velocities were calculated from the linear traces obtained.[1,3] The initial "burst" in the uptake of iodine by the pyruvic acid–pyruvate system as noted by earlier workers[3] was minimal when the pyruvic acid concentration rather greatly exceeded that of its conjugate base (Table I). This "burst" was not observed in the corresponding iodinations of the alkyl pyruvates.

The rate constants, $k_{obsd} = v/[\text{substrate}]$, were calculated by taking into account that the carbonyl compounds are partially hydrated and that the extent of hydration varies with temperature as well as the concentration. The fractions hydrated at the experimental concentrations ([MeP] = 0.0185 M; [EtP] = 0.0165 M; [PA] < 0.01 M) and temperatures were calculated for each run.[4,5] A spectrophotometric method[5] was used to determine the fraction of hydration of methyl pyruvate; it was essentially the same in both light and heavy water at all temperatures studied.

For the pyruvic acid work, the concentration of undissociated pyruvic acid was calculated from the thermodynamic dissociation constant $K_a = (a_{P^-})(a_{H^+})/$

(1) J. E. Meany, *J. Phys. Chem.*, **75**, 150 (1971).

(2) Y. Pocker and J. E. Meany, *J. Amer. Chem. Soc.*, **89**, 631 (1967).

(3) W. J. Albery, R. P. Bell, and A. L. Powell, *Trans. Faraday Soc.*, **61**, 1194 (1965).

(4) Y. Pocker, J. E. Meany, B. J. Nist, and C. Zadorojny, *J. Phys. Chem.*, **73**, 2879 (1969).

(5) Y. Pocker, J. E. Meany, and C. Zadorojny, *ibid.*, **75**, 792 (1971).

Table I: Spontaneous Rate of Iodination of Pyruvic Acid at 25.0°

pH or pD	[P⁻]/[HP]	[HP] × 10⁴, *M*	v_{obsd} × 10⁹, *M* sec⁻¹	k_0 × 10⁶, sec⁻¹
		H_2O		
1.85	0.28	71	3.07	1.31
1.75	0.24	76	3.84	1.54
1.54	0.15	73	3.14	1.30
1.49	0.13	83	3.84	1.40
1.38	0.10	85	3.95	1.40
1.38	0.10	70	3.04	1.31
1.20	0.063	64	3.79	1.33
		D_2O		
1.14	0.022	97	2.55	0.69
1.23	0.026	97	2.34	0.70
1.36	0.027	97	2.27	0.71

a_{HP} for each temperature at which the kinetic runs were carried out. The value $K_a = 3.24 \times 10^{-3}$ *M* was used at 25.0° [6] and the dissociation constant values at the other temperatures studied were calculated from the enthalpy of ionization of pyruvic acid as reported by Öjelund and Wadsö, $\Delta H = 2.90$ kcal/mol.[7] The dissociation constant for pyruvic acid in D_2O ($K_a = 1.12 \times 10^{-3}$ *M*) was obtained from pD measurements observed during the titration of a solution of pyruvic acid in D_2O with a previously standardized solution of 0.100 *M* NaOD. These and all other measurements of pH or pD were carried out using a Beckman Century SS pH meter, the reproducibility of which is 0.01 pH units. For measurements in heavy water, the glass electrode correction formula, pD = (pH reading) + 0.41 was applied.[8] Ionic activity coefficients, $\gamma_\pm$, were calculated in the usual manner[9] at the various temperatures studied. Since the dielectric constant and the density of D_2O are essentially the same as that for H_2O, activity coefficients were taken to be identical for the two solvents at a given temperature (*e.g.*, $\gamma_\pm = 0.76$ at 0.0°; $\gamma_\pm = 0.74$ at 50.0° at $\mu = 0.1$ *M*).

A more complete description of experimental details and techniques may be found in ref 1.

Results

Iodinations of Pyruvic Acid, Methyl Pyruvate, and Ethyl Pyruvate as a Function of Temperature. In Table I typical values of the spontaneous rate of iodination of pyruvic acid at 25.0° are presented. It will be noted that the values of k_0 for the different values of pH are in good agreement, indicating the absence of any significant catalytic contribution by hydroxide, hydronium, or pyruvate ion. Values of k_0 were similarly obtained over a temperature range from 8 to 40° and the Arrhenius plot for the spontaneous iodination of pyruvic acid is shown in Figure 1. The activation parameters calculated from the figure are tabulated in Table II.

Table II: Activation Parameters for the Spontaneous Iodination of MeP and EtP in Both D_2O and H_2O

	H_2O			D_2O	
	HP	MeP	EtP	MeP	EtP
$k_0 \times 10^6$, sec⁻¹ [a]	1.38	2.10	1.70	1.03	0.80
E_a, kcal mol⁻¹	18.6	18.8	18.9	18.9	19.0
$\Delta H^\ddagger$, kcal mol⁻¹	18.0	18.2	18.3	18.3	18.4
$\Delta G^\ddagger$, kcal mol⁻¹	25.6	25.3	25.4	25.8	25.9
$\Delta S^\ddagger$, eu	25	24	24	25	25

[a] Data at 25.0°.

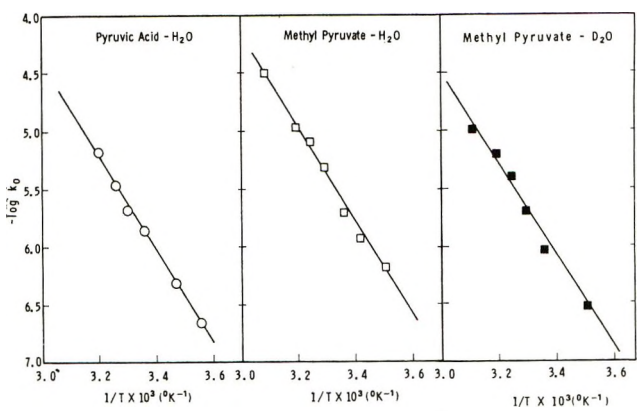

Figure 1. Arrhenius plot for spontaneous iodination of (○) pyruvic acid in H_2O, (□) methyl pyruvate in H_2O, and (■) methyl pyruvate in D_2O.

The overall rate constants associated with the iodinations of methyl and ethyl pyruvate, $k_{obsd} = k_0 + k_{HCO_2^-}[HCO_2^-]$, were determined as a function of formate concentration at several temperatures. Plots of k_{obsd} *vs.* the concentration of formate were constructed and the specific rate coefficients for formate, $k_{HCO_2^-}$, and the spontaneous rates, k_0, were evaluated from the slopes and intercepts of the resultant straight lines (see, for example, Figure 2). The activation parameters associated with the spontaneous iodinations of methyl and ethyl pyruvate were obtained in the usual way (see Figure 1 and Table II).

Solvent Deuterium Isotope Effects. The spontaneous rate of iodination of pyruvic acid was obtained in deuterium oxide in the same manner as that described for the corresponding determinations in H_2O. The data obtained are summarized in Table I from which the average value of the spontaneous rate constant in D_2O at 25.0° was evaluated, $k_0 = 0.7 \times 10^{-6}$ sec⁻¹. The solvent deuterium isotope effect, $k_0^{H_2O}/k_0^{D_2O}$, associated with the iodination of pyruvic acid is *ca.* 2.0.

(6) G. Kortum, W. Vogel, and K. Andresson, "Dissociation Constants of Acids in Aqueous Solution," Butterworths, London, 1961, p 335.

(7) G. Öjelund and I. Wadsö, *Acta Chem. Scand.*, **21**, 1410 (1967).

(8) P. K. Glasoe and F. A. Long, *J. Phys. Chem.*, **64**, 188 (1960).

(9) J. N. Brønsted, *Z. Phys. Chem.*, **102**, 169 (1922); **115**, 337 (1925).

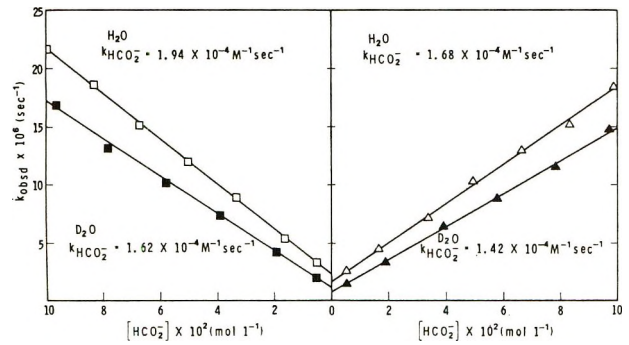

Figure 2. Catalysis of the iodinations of methyl pyruvate (□) and ethyl pyruvate (△) in formate buffers. Open symbols refer to work in H_2O, dark symbols in D_2O.

The spontaneous rates of iodination of methyl and ethyl pyruvate were determined in formate buffer solutions in heavy water at a buffer ratio of unity. The values obtained at 25.0° (Figure 2) are given in Table II. From these data, the solvent deuterium isotope effects were evaluated, $k_{H_2O}/k_{D_2O} = 2.1$ for both esters.

The spontaneous catalyzed iodinations of the pyruvate esters in D_2O were similarly investigated over a wide temperature range. The Arrhenius plot constructed from the data obtained from the methyl pyruvate studies is shown in Figure 1. The corresponding activation parameters for both methyl and ethyl pyruvate are summarized in Table II.

General Base Catalysis. The sensitivity of the iodination of methyl pyruvate toward catalysis by general bases was investigated. The formate-catalyzed process has already been discussed. A series of runs were carried out in acetate buffers (buffer ratio = 1) at 0.1 M ionic strength at 25.0°. Since acetic acid is a weaker acid than formic acid, it was assumed, as was observed to be the case for the latter, that catalysis by acetic acid under the experimental conditions employed was negligible. The observed rate constants for the iodination of methyl pyruvate are plotted against the concentration of acetate ion in Figure 3. The catalytic coefficient $k_{CH_3CO_2^-} = 2.8 \times 10^{-4}\ M^{-1}\ \text{sec}^{-1}$ was obtained from the slope of the resultant straight line.

Trial runs were also made in malonate buffers for the iodination of methyl pyruvate at 25.0°. It was observed, however, that the buffer consumed the triiodide so rapidly that the iodination of pyruvate itself is difficult to monitor. To avoid this difficulty, which presumably arises from the capacity of the malonate system to enolize, 2,2-diethylmalonate buffers were employed. Again, it was logically assumed that, under our experimental conditions, the catalysis by the acid component was negligible. The data obtained are shown in Figure 3, from which the specific rate coefficient for the dianion of 2,2-diethylmalonic acid, $k_{DEM^{2-}} = 32 \times 10^{-4}\ M^{-1}\ \text{sec}^{-1}$, was calculated. It will be noted that the extrapolation of each of the plots in Figure 3 to zero buffer concentration yields a common

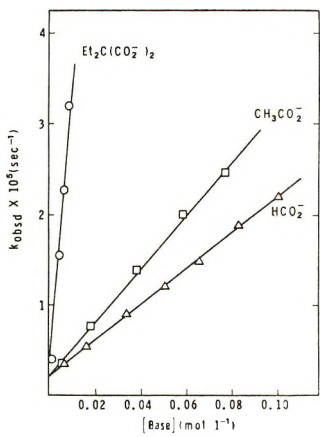

Figure 3. Catalysis of the iodination of methyl pyruvate by by formate (△), $k_{HCO_2^-} = 1.94 \times 10^{-4}\ M^{-1}\ \text{sec}^{-1}$; acetate (□), $k_{CH_3CO_2^-} = 2.8 \times 10^{-4}\ M^{-1}\ \text{sec}^{-1}$; and the dianion of 2,2-diethylmalonic acid (○), $k_{DEM^{2-}} = 32 \times 10^{-4}\ M^{-1}\ \text{sec}^{-1}$ at 25.0°.

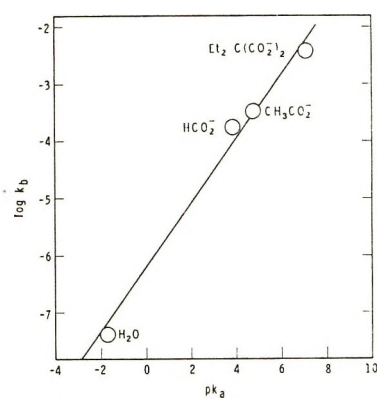

Figure 4. Brønsted plot for the general base-catalyzed iodination of methyl pyruvate: the slope of the line, $\beta = 0.55 \pm 0.06$; for H_2O, $k_{H_2O} = k_0/55.5$. Statistical corrections[10] were not used.

intercept (2.1×10^{-6} sec^{-1}) indicating that even at pH 7.2, catalysis by the hydroxide ion is too small to be detected.

Brønsted plots[10] were constructed by plotting the logarithms of the catalytic rate coefficients associated with water, $k_0/55.5\ M$, formate, acetate, and the dianion of 2,2-diethylmalonic acid *vs.* their respective values of pK_a. The slope of the straight line depicted in Figure 4 corresponds to a Brønsted coefficient, $\beta = 0.55 \pm 0.06$.

Discussion

It has been proposed by earlier workers, that the relatively rapid spontaneous rates of both the hydration[11] and enolization[3] of pyruvic acid are the result of intramolecular catalysis by the carboxyl group. Re-

(10) J. N. Brønsted, *Chem. Rev.*, **5**, 322 (1928).

(11) M. Eigen, K. Kustin, and H. Strehlow, *Z. Phys. Chem.* (*Frankfurt am Main*), **31**, 140 (1962); H. Strehlow, *Z. Elektrochem.*, **66**, 3921 (1962).

cently published comparative rate studies of pyruvic acid and methyl and ethyl pyruvates indicate that their spontaneous enolizations at 25.0° proceed at comparable rates.[1] In the case of the esters there is no possibility of intramolecular acid catalysis. The spontaneous *hydrations* of pyruvic acid and the alkyl pyruvates proceed at similar rates at 0°. Unfortunately, in the case of the hydration studies, rate comparisons at higher temperatures are precluded because the relatively large catalytic component associated with hydronium ion interfere with the accurate determination of k_0 for pyruvic acid. On the other hand, the enolization of pyruvic acid is less sensitive toward specific acid catalysis, and the spontaneous rate constants associated with this process may be deduced over a wide temperature range. The activation parameters associated with the spontaneous enolizations of pyruvic acid, methyl pyruvate, and ethyl pyruvate have been deduced, making possible a direct comparison of their relative magnitudes. The free energies, enthalpies, and entropies of activation for pyruvic acid and the alkyl pyruvates are tabulated in Table II.

The values of the solvent deuterium isotope effects for the spontaneous iodinations of pyruvic acid and the alkyl pyruvates are all basically the same, k_{H_2O}/k_{D_2O} = *ca.* 2. It may be noted that similar solvent deuterium isotope effects have been observed for the spontaneous halogenations of other carbonyl compounds with acidic protons (*e.g.*, for acetylacetone, k_{H_2O}/k_{D_2O} = 1.9).[12] Furthermore, the Brønsted coefficients associated with such processes (acetylacetone, β = 0.48; acetoacetic ester, β = 0.59)[13] are in the same range as that approximated for the iodination of methyl pyruvate (β = *ca.* 0.55) in the present work.

The closeness of the activation parameters for the three substrates studied in the present work as well as the similarity in the respective deuterium isotope effects suggest that the enolizations of pyruvic acid and pyruvate esters proceed through parallel mechanisms. Hence it is suggested that intramolecular catalysis for the former is of little importance. The relatively low value of the Brønsted coefficient associated with the general base-catalyzed enolization of methyl pyruvate is consistent with this interpretation. For these systems, the electron-withdrawing inductive effect caused by the carboxy or carbalkoxy group facilitates proton removal. This explanation precludes the necessity of either intra- or intermolecular acid catalysis, and adequately explains the rapidity with which the enolizations of pyruvic acid and the pyruvate esters proceed.

Well-founded cases of intramolecular-catalyzed enolization reactions in aqueous solution are cited in the literature.[14,15] It now appears that the least ambiguous models for this mode of catalysis are those in which the atoms participating in the bond making and breaking processes are suitably directed toward one another. Rate enhancement resulting from other proximity effects, such as inductive effects, should not be confused with that arising from intramolecular catalysis in the strict sense.

Acknowledgment. The authors wish to thank Drs. L. C. Duncan, W. C. Emken, and the other members of the Department of Chemistry of this institution who assisted in the preparation of this manuscript.

(12) F. C. Nachad, *Z. Phys. Chem. (Leipzig), A*, **182**, 193 (1938).

(13) R. P. Bell, "The Proton in Chemistry," Methuen, London, 1959, pp 155–182.

(14) E. T. Harper and M. L. Bender, *J. Amer. Chem. Soc.*, **87**, 5625 (1965).

(15) J. K. Coward and T. C. Bruice, *ibid.*, **91**, 5339 (1969).

Hydrogen Fluoride Elimination Chemical Laser from Deuterated *N,N*-Difluoromethylamine

by Thomas D. Padrick and George C. Pimentel*

Chemistry Department, University of California, Berkeley, California 94720 *(Received April 25, 1972)*

Publication costs assisted by the U. S. Air Force Office of Scientific Research

Hydrogen fluoride and deuterium fluoride chemical laser emission has been observed due to elimination from *N,N*-difluoromethylamine and its deuterated analogs. Gaseous methyl iodide–N_2F_4–Ar mixtures at or near 250°K are photolyzed through Vycor. Hydrogen fluoride laser emission is observed from CH_3NF_2†, CH_2DNF_2†, and CHD_2NF_2† and equal-gain temperature measurements indicate a vibrational population ratio $N_1/N_0 = 0.47 \pm 0.02$ from each precursor. Deuterium fluoride laser emission is observed from CD_3NF_2† and CHD_2NF_2† with population ratio $N_2/N_1 = 0.66$ from each precursor, but no DF emission was observed from CH_2DNF_2†. The relative intensities and population ratios indicate that laser emission is associated with the first elimination step only, CH_3NF_2† → $CH_2{=}NF + HF$†, and that in the mixed H–D precursors, HF elimination is 2.5 times more probable than DF elimination. The average vibrational energy imparted to HF is, within experimental uncertainty, equal to the average internal energy per vibrational degree of freedom, in accord with statistical theories of unimolecular decomposition.

Introduction

Laser emission has been reported[1] due to the elimination of vibrationally excited HF from CH_3NF_2 produced in the reaction between CH_3 and N_2F_4. In the earlier work (which will, hereafter, be called I) a number of interesting questions were raised concerning the detailed chemical processes that are involved. Chemical studies have shown that HCN is produced,[2,3] but they do not indicate whether the elimination occurs in one or in two steps. Nor, of course, do they indicate how the vibrational excitation might be apportioned if two steps are involved. We report here experiments based upon isotopically substituted methyl radicals that bear upon these questions.

Experimental Section

The experimental apparatus described in I was used with only slight modifications. All experiments used a Vycor laser tube fitted with NaCl Brewster angle windows. The deuterated methyl iodides, CD_3I (ICN Chemical & Radioisotope Div.), CH_2DI (Isotopes), and CHD_2I (Thompston Packard, Inc.), were purified by low temperature, bulb-to-bulb distillation *in vacuo*.

Results

As background for the interpretation of laser emissions from the deuterated difluoromethylamines, a number of additional experiments were performed with the CH_3I–N_2F_4 system. The effect of added inert gas, noted in I, was studied in more detail and the equal-gain temperature measurement[4] was repeated under conditions of better control. These results are reported first, followed, in turn, by those involving CD_3I, CH_2DI, and CHD_2I.

CH_3I–N_2F_4. Figure 1 shows the effect of inert gas (argon or methane) on the intensity and time to threshold for CH_3I–N_2F_4 mixtures photolyzed at 253°K. While the partial pressures of N_2F_4 and CH_3I were held constant (respectively at 0.27 and 1.1 Torr) the argon partial pressure was increased from 5.6 (Figure 1a) to 10.7 Torr (Figure 1b) and then to 15.7 Torr (Figure 1c). The time to threshold increased from 15 to 23 μsec and then to 31 μsec while the intensity steadily decreased. With 20 Torr argon, no laser emission occurred. Figure 1d shows the laser emission obtained with 1.1 Torr CH_4 and 5.5 Torr argon. Both the intensity and the time to threshold, 23 μsec, suggest that 1 Torr CH_4 has an effect equivalent to at least 5 Torr Ar. In agreement with this conclusion, a mixture that contained 2 Torr CH_4 and 5 Torr Ar gave no laser emission.

To permit detailed comparison of the laser emissions of the various isotopically substituted difluoromethylamines, it was necessary to establish more accurately the equal-gain temperature, T_{eg}, for CH_3NF_2. The problem of poor reproducibility in equal-gain temperature experiments has been under study in these laboratories[5] and has clearly been related to mode spacing. In I, a 1-m optical cavity was used, which provides a longitudinal mode spacing of 0.005 cm^{-1} (150 MHz).

(1) T. D. Padrick and G. C. Pimentel, *J. Chem. Phys.*, **54**, 720 (1971). (This reference is called I in the text.)

(2) J. W. Frazer, *J. Inorg. Nucl. Chem.*, **16**, 63 (1960).

(3) C. L. Bumgardner, E. L. Lawton, and H. Carmichael, *Chem. Commun.*, 1079 (1968).

(4) J. H. Parker and G. C. Pimentel, *J. Chem. Phys.*, **51**, 91 (1969).

(5) M. J. Molina and G. C. Pimentel, *ibid.*, **56**, 3832 (1972); see also, M. J. Molina, Ph.D. Dissertation, University of California, Berkeley, 1972.

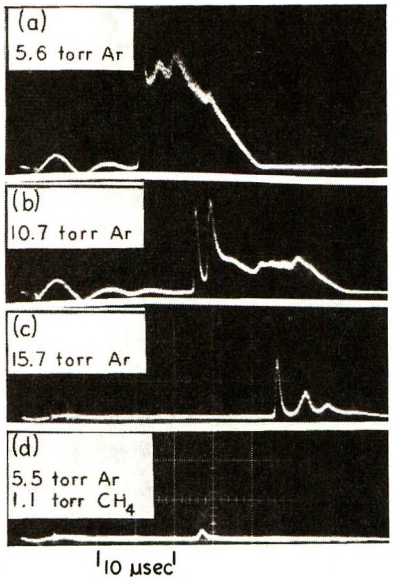

Figure 1. Total HF laser emission from 0.27 Torr N_2F_4, 1.1 Torr CH_3I, and various pressures of buffer gas: 253°K, 490 J flash energy; (a) 5.6 Torr argon; (b) 10.7 Torr argon; (c) 15.7 Torr argon; (d) 5.5 Torr argon plus 1.1 Torr CH_4.

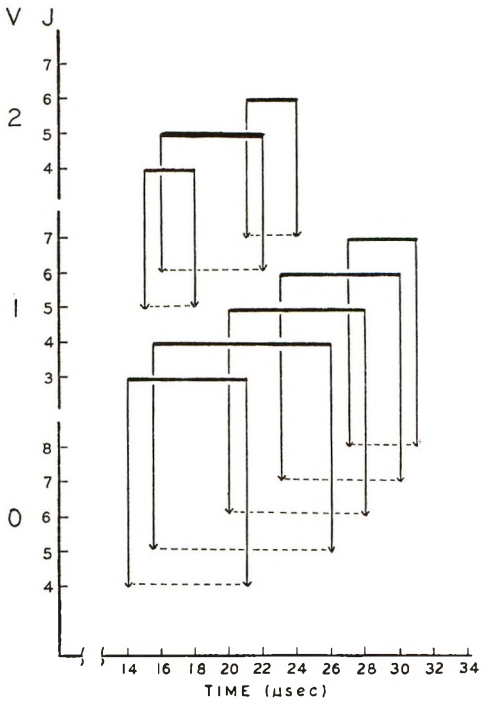

Figure 2. Sequencing of the HF transitions observed in the photolysis of 12 Torr of a 1:4:20 mixture of N_2F_4:CH_3I:Ar: 248°K, 490 J flash energy.

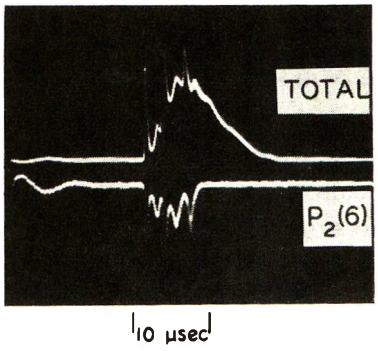

Figure 3. DF laser emission observed in the photolysis of 12 Torr of a 1:4:20 mixture of N_2F_4:CD_3I:Ar: 248°K, 490 J flash energy.

This implies that, in an equal-gain experiment, the highest-gain longitudinal mode for either of the two transitions may miss the line center by as much as 0.0025 cm^{-1}. Since this is comparable to line widths under our experimental conditions, the gain of both transitions can vary capriciously from experiment to experiment due to slight cavity length changes. With the 1-m cavity, this caused the measured value of T_{eg} to vary over a range of 60°. To correct this difficulty, the experiments were repeated with a 2-m optical cavity, halving the mode spacing. Reproducibility was very much better and measurements over a 20° range were sufficient to establish T_{eg} reliably.

Clues to the effectiveness of rotational equilibrium, which is essential to the equal-gain technique, are provided by the sequencing of the observed transitions.[6] Figure 2 shows the sequencing observed in the photolysis of 12 Torr of a 1:4:20 mixture of N_2F_4:CH_3I:Ar at 248°K. The first transition is $P_{1-0}(4)$. The second transition to reach threshold is $P_{2-1}(5)$, preceding by 5 μsec the emission by $P_{1-0}(6)$, the 1 → 0 transition that directly pumps $P_{2-1}(5)$. This shows there is not strong communication between connected transitions, which means that rotational equilibration is good.

Eleven equal-gain determinations were carried out with a 1:4:20 mixture of N_2F_4:CH_3I:Ar. The total pressure was varied from 7 to 22 Torr and no pressure dependence could be discerned. Except for one measurement at 235°K, all values were in the range 246–255°K. The absence of pressure dependence implies that J-dependent pressure-broadening effects and vibrational relaxation are negligible. The average value of T_{eg} for the $P_{1-0}(4)$ and $P_{1-0}(5)$ transitions is 249°K with a standard deviation σ = 5.4° (σ_{11} = 1.6°K). From this value of T_{eg} and the equal-gain temperature equations,[4,5] we calculate N_1/N_0 = 0.47 ± 0.01 for the CH_3NF_2 elimination laser.

CD_3I–N_2F_4. Figure 3 shows the total DF laser emission and also that due to $P_{2-1}(6)$, as observed after photolysis of 12 Torr of a 1:4:20 mixture of N_2F_4:CD_3I:Ar at 248°K. The DF laser emission reached threshold about 4 μsec later than the HF emission shown in Figure 2, but the integrated detector signal exceeded that for HF under exactly the same conditions. In three pairs of experiments, the DF/HF integrated intensity ratio averaged 1.55 with an average

(6) K. L. Kompa, J. H. Parker, and G. C. Pimentel, *J. Chem. Phys.*, 49, 4257 (1968).

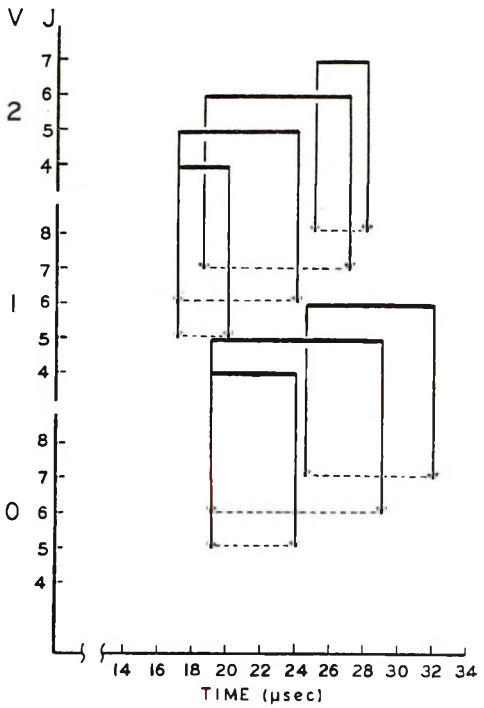

Figure 4. Sequencing of the DF transitions in the N_2F_4:CD_3I:Ar experiment shown in Figure 3.

deviation of 0.26. We shall use such area ratios as relative measures of the amounts of HF and DF emission in the mixed isotope experiments; the ratios are not directly interpretable because the DF gain is undoubtedly lower than that for HF but the detector is more sensitive in the DF spectral region. Figure 4 shows the sequencing; the first v = 1–0 transitions to reach threshold were $P_{1-0}(5)$ and $P_{1-0}(6)$, each about 2 μsec after $P_{2-1}(5)$ and $P_{2-1}(6)$.

Table I lists the results of equal-gain determinations. The average value of T_{eg} for the $P_{2-1}(5)$ and $P_{2-1}(6)$ transitions is 242°K with estimated uncertainty ±6°K. This value of T_{eg} corresponds to $N_2/N_1 = 0.66 \pm 0.01$.

CH_2DI–N_2F_4. Photolysis of 12 Torr of a 1:4:20 mixture of N_2F_4:CH_2DI:Ar at 253°K produced HF laser emission but no DF emission, even at higher total pressure, 24 Torr. The HF emission included the same transitions as CH_3I and it displayed threshold time, intensity, and duration that were all quite similar to those obtained from CH_3I (compare Figure 5a and 1a). Equal-gain determinations, listed in Table I, gave $T_{eg} = 254 \pm 6$°K for the $P_{1-0}(4)$ and $P_{1-0}(5)$ transitions. This corresponds to $N_1/N_0 = 0.48 \pm 0.01$.

CHD_2I–N_2F_4. Figure 5b shows the total emission observed from 12 Torr of a 1:4:20 mixture of N_2F_4:CHD_2I:Ar at 253°K. Both HF and DF emission are included, as shown in Figure 5c, which is the total laser emission transmitted by an interference filter, which blocks all HF emission and transmits about 73% in the DF spectral range. In six pairs of experiments like that shown in Figures 5b and 5c, the DF/HF area ratio was measured to provide an estimate of the relative

Table I: Equal-Gain Temperatures for N_2F_4 Plus Methyl Iodide

Isotopic species	Total pressure,[a] Torr	HF/DF	Transition	T_{eg},[b] °K
CH_3I	7–22[c]	HF	$P_{1-0}(4)/P_{1-0}(5)$ Av	249 ± 3
CD_3I	8	DF	$P_{2-1}(5)/P_{2-1}(6)$	241
	8	DF		236
	12	DF		249
			Av	242 ± 6
CH_2DI	10	HF	$P_{1-0}(4)/P_{1-0}(5)$	252
	12	HF		255
	17	HF		254
			Av	254 ± 6
CHD_2I	12	HF	$P_{1-0}(4)/P_{1-0}(5)$	241
	12	HF		238
	12	HF		255
	15	HF		235
			Av	242 ± 5
	12	DF	$P_{2-1}(5)/P_{2-1}(6)$	249
	16	DF		238
			Av	243.5 ± 8

[a] All methyl iodides were studied at the same relative composition, N_2F_4:$CH_nD_{3-n}I$:Ar = 1:4:20. [b] Uncertainties specified are $2\sigma_n$ where $\sigma_1 = 5.4$°K, taken from the CH_3I experiments and $\sigma_n = \sqrt{5.4/n}$ where n is the number of measurements averaged. [c] Eleven measurements, $\sigma_1 = 5.4$°K, $\sigma_{11} = 1.6$°K (see text).

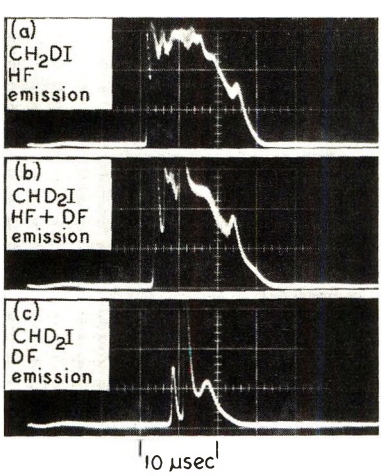

Figure 5. Laser emission from photolysis of N_2F_4 and partially deuterated methyl iodides: 253°K, 490 J flash energy; (a) HF emission from 12 Torr of a 1:4:20 mixture of N_2F_4:CH_2DI:Ar; (b) HF + DF emission from 12 Torr of a 1:4:20 mixture of N_2F_4:CHD_2I:Ar; (c) DF emission only from sample b (73% transmission filter).

probability of DF and HF elimination. The DF area was divided by the filter transmission factor, 0.73, and then subtracted from the combined HF and DF area to give the HF area. The six experiments gave an average DF/HF intensity ratio of 0.36 with a standard

deviation of 0.16. If we interpret this ratio with the aid of the area ratio obtained from CD_3NF_2 and CH_3NF_2, 1.55, the results suggest that 19 ± 8% of the hydrogen fluorides eliminated from CHD_2NF_2 are DF and 81 ± 8% are HF. The first transitions to reach threshold were the same as for CH_3I and CD_3I, *i.e.*, $1 \rightarrow 0$ transitions for HF and $2 \rightarrow 1$ transitions for DF.

Equal-gain studies were conducted for both the HF and DF emissions, as summarized in Table I. For HF from CHD_2NF_2, T_{eg} = 242 ± 5°K for the $P_{1-0}(4)$ and $P_{1-0}(5)$ transitions, to give N_1/N_0 = 0.46 ± 0.01. For DF from CHD_2NF_2, T_{eg} = 243.5 ± 8°K for the $P_{2-1}(5)$ and $P_{2-1}(6)$ transitions, to give N_2/N_1 = 0.66 ± 0.01.

Discussion

The sequence of reactions we must consider is as follows.

$$CH_3 + N_2F_4 \longrightarrow CH_3NF_2\dagger + NF_2 \quad (1)$$

$$CH_3 + NF_2 \longrightarrow CH_3NF_2\dagger\dagger \quad (1a)$$

$$CH_3NF_2\dagger \longrightarrow CH_2{=}NF\dagger + HF\dagger \quad (2)$$

$$CH_2{=}NF\dagger \longrightarrow HCN + HF\dagger \quad (3)$$

The energy available for elimination depends upon whether reaction 1 or 1a is operative, so that question is considered first. Then the effect of argon will be discussed, again because of its importance to the laser performance. Thereafter, the significance of the laser emissions observed from the isotopically substituted species can be assessed.

Production of $CH_3NF_2\dagger$. In I, it was assumed that reaction 1 initiates the elimination that accounts for the laser emission. In contrast, Brus and Lin feel that (1a) accounts for the HF elimination, both in their room temperature studies[7] and in I. This proposal is plausible under their experimental conditions, where the N_2F_4/NF_2 ratio is maintained near 50 by the dimerization equilibrium. In a footnote (and without details) Brus and Lin[7] refer to an RRKM estimate of $k_{1a}/k_1 \sim 100$ at 300°K. If this estimate is accepted, it can be coupled with the room temperature N_2F_4/NF_2 equilibrium ratio to indicate that the CH_3NF_2 formed by (1a) is twice that formed by (1).

The experimental conditions used in I and in the present work give quite a different picture. With temperatures in the range 240–255°K, and N_2F_4 pressures near 1 Torr (as were used in some experiments), the N_2F_4/NF_2 ratio is near 1000 and the NF_2 equilibrium pressure has dropped to 10^{-3} Torr. This must slow down reaction 1a 20-fold and, if (1a) were the dominant pumping reaction, there should be a dramatic increase in the time to reach threshold, which is not observed. Furthermore, the NF_2 pressure is now one or two orders of magnitude lower than the CH_3 partial pressure produced by the flash.[8] Since (1a) probably has about the same rate constant as the $CH_3 + CH_3$ reaction, the amount of CH_3 consumed in (1a) would decrease to only a small fraction of that lost to ethane formation, again drastically impairing laser performance. Since overall laser gain attributable to elimination is rather little affected by temperature, reaction 1a cannot be the dominant pumping reaction at the low temperatures.

These difficulties are eliminated if reaction 1 is also a significant pumping reaction. The $k_{1a}/k_1 \sim 100$ estimate, if applicable at the low temperatures, would indicate that the CH_3NF_2 produced by (1) would be ten times larger than that formed by reaction 1a. There is, however, significant reason for believing that k_{1a}/k_1 is much smaller than 100. The reactions $CH_3 + X_2 \rightarrow CH_3X + X$ can be regarded as prototypes for reaction 1. In the series Cl_2, Br_2, and I_2, as the X_2 bond energy decreases from 57 to 45 kcal, and then to 35 kcal, the activation energy decreases from 3.6 to 0.7 kcal and then to 0 kcal.[9] Since the bond energy of N_2F_4, 20 kcal, is even lower than that of I_2, the comparison indicates that reaction 1 has zero activation energy. This implies that k_{1a}/k_1 is probably nearer unity and not much dependent upon temperature. With this estimate, over 99% of the CH_3NF_2 comes from reaction 1 at 250°K and (1a) becomes unimportant. We conclude that, at the low temperatures used in our experiments, reaction 1 is both the dominant source of $CH_3NF_2\dagger$ and the effective pumping reaction.

Effect of Inert Gases. The delay and weakening of the laser emission caused by added argon or methane (see Figure 1) implies a deactivation process. This cannot be attributed to HF vibrational deactivation by argon because argon is known to be quite ineffective. Airey and Fried[10] estimate that more than 2×10^4 argon–HF collisions are needed, on the average. In the conditions appropriate to Figure 1b, there are about 100 HF–argon collisions per microsecond (at 10 Torr pressure) but the time to threshold is nearly double the 15 μsec threshold time observed at 5 Torr total pressure. Yet in 15 μsec, an average HF molecule would have encountered no more than about 750 argon atoms, an order of magnitude too low to account for the delay.

Deactivation of excited $CH_3NF_2\dagger$ before elimination offers another possible explanation of the inert gas pressure effect. Ross and Shaw[11] have estimated the rate constant for the elimination of HF from excited $CH_3NF_2\dagger\dagger$ to be $10^{10.3}$ sec^{-1}, which gives a half-time of

(7) L. E. Brus and M. C. Lin, *J. Phys. Chem.*, **75**, 2546 (1971).

(8) T. Ogawa, G. A. Carlson, and G. C. Pimentel, *ibid.*, **74**, 2090 (1970).

(9) (a) See H. S. Johnston and P. Goldfinger, *J. Chem. Phys.*, **37**, 100 (1962); (b) see A. F. Trotman-Dickenson and G. S. Milne, *Nat. Bur. Stand. (U. S.), Data System*, **9** (1967), from $E^{\ddagger}(M/HBr) - E^{\ddagger}(M/Br_2)$ = 2.0, $E^{\ddagger}(M/HBr) - E^{\ddagger}(M/I_2)$ = 1.0 (av), M = CH_3; (c) M. C. Flowers and S. W. Benson, *J. Chem. Phys.*, **38**, 882 (1963). Note: measured value $E^{\ddagger}$ = 1.5 considered by authors to be ≈ 1 kcal high.

(10) J. R. Airey and S. F. Fried, *Chem. Phys. Lett.*, **8**, 23 (1971).

(11) D. S. Ross and R. Shaw, *J. Phys. Chem.*, **75**, 1170 (1971).

3.6×10^{-11} sec. This half-time means that at 10 Torr, with one collision every 10^{-8} sec, elimination could not be affected by collisions. It must be remembered, of course, that Ross and Shaw are dealing with CH_3NF_2†† formed from $CH_3 + NF_2$ (reaction 1a), rather than from $CH_3 + N_2F_4$, as in the present experiments. Hence our excitation is lower by the N–N bond energy in N_2F_4, 20 kcal, and by whatever energy is partitioned into the NF_2 fragment, which we estimate to be 10 kcal or more. With perhaps 30 kcal less excitation, the rate of elimination could be appreciably slower. Nevertheless, we do not regard this as a likely explanation of the argon effect.

The observations are consistent with the interpretation that methyl radicals with excess translational and/or internal energy are required in reaction 1. In I, the activation energy, $E_2^{\ddagger}$, for elimination from CH_3NF_2 was shown to exceed 30 kcal on the basis of the known stability of CH_3NF_2. Ross and Shaw[11] offer two additional estimates based on deactivation studies, RRK or RRKM modelling, and the usual array of assumptions about collision efficiency, effective number of oscillators, and the nature of the transition state. These estimates place $E_2^{\ddagger}$ between about 35 and 42 kcal/mol. Brus and Lin[7] offer another estimate, 38 kcal, also based upon RRKM modelling. We will use this last value as a mean, with an uncertainty fixed by the range, $E_2^{\ddagger} = 38 \pm 5$ kcal/mol.

The internal energy available for elimination depends upon ΔH_1, the exothermicity of reaction 1 and the energy division between the product fragments. In I, ΔH_1 was estimated to be about −60 kcal, assuming that the CN bond energy is the same as in methylamine, 85 kcal (as derived from tabulated heats of formation[12] for CH_3NH_2, CH_3, and NH_2). However, Dykstra, *et al.*,[13] have presented kinetic evidence that suggests the difluoromethylamine CN bond energy is only 56 kcal while Ross and Shaw[11] estimate 60 kcal. Accepting the latter figure implies that $\Delta H_1 = -40$ kcal. As indicated in I, the CH_3NF_2 might receive about 83% of the energy that goes into vibration (at most, 33 kcal) and only 44% of the energy that goes into translation. Thus, the lower CN bond energy, taken with the 38 kcal activation energy estimate, implies that reaction 1 produces CH_3NF_2† that cannot eliminate HF. The energy deficit, which would probably be in the range 5–15 kcal, might be made up by reactions involving "hot" methyl radicals.

The energy imparted to a photolytic CH_3 can be estimated. If photolysis occurs near 2576 Å (the peak of the CH_3I absorption band), the quanta carry 111 kcal/mol of energy, 57 kcal more than the C–I bond energy. Hancock and Wilson[14] have measured the energy distribution between the photolysis products and conclude that about $^5/_6$ of the bond ruptures give excited iodine atoms, $I(^2P_{1/2})$, and $^1/_6$ give ground state atoms, $I(^2P_{3/2})$. When $I(^2P_{1/2})$ is formed, the CH_3 fragment receives about 27 kcal of translational energy and 5.5 kcal of internal energy (vibration and rotation). When $I(^2P_{3/2})$ is formed, Hancock and Wilson find that the CH_3 fragment is given about 41 kcal of translational energy and 11 kcal of internal energy.[14] The internal energies lodged in CH_3, 5.5 and 11 kcal, compare favorably to the 10 kcal estimate of Bass and Pimentel.[15] This estimate is based on the assumption that the Franck–Condon principle is operative, which suggests that most of the internal energy is placed in vibrational excitation of the ν_2 "umbrella" mode. The work of Callear and Van den Bergh[16] also supports this contention. These workers found that vibrationally excited methyl radicals are produced in the photolysis of dimethylmercury.

The $Ar:N_2F_4$ and $CH_3I:N_2F_4$ ratios are 20 and 4, respectively. This suggests that most of the CH_3 translational energy will be lost in collisions with Ar or CH_3I before a reactive collision occurs. Removal of vibrational energy is more difficult, however. Callear and Van den Bergh[16] found that it takes about 200 Ar collisions or 35 CH_4 collisions to deactivate their vibrationally excited methyl radicals. This relative deactivation efficiency is reasonably consistent with the observation, shown in Figure 1, that CH_4 delays and attenuates the laser emission about 4 to 8 times as effectively as does Ar. All of the data are consistent with the interpretation that excited methyl radicals are formed and that they contain internal energies of 5 to 10 kcal, probably enough to activate the difluoromethylamine above its critical energy for HF elimination.

This conclusion implies that the energy held by CH_3NF_2† just before elimination is quite close to the activation energy, which we have taken to be 38 ± 5 kcal.

Isotopic Comparisons. Table II summarizes the vibrational populations implied by the equal-gain temperature data in Table I. For both HF and DF, the derived population ratios are found to be independent of the parent. This fact, coupled with the observation that DF emits weakly from CHD_2NF_2 and not at all from CH_2DNF_2, permits some conclusions about the elimination process. For example, consider a two-step elimination in which HF† excitation is identical with the two steps (reactions 2 and 3). Such a model would explain the constancy of the population ratios, but the DF emission from CHD_2NF_2 would be expected to be

(12) D. D. Wagman, *et al.*, *Nat. Bur. Stand. (U. S.), Tech. Note*, 270-1 (1965).

(13) A. J. Dykstra, J. A. Kerr, and A. F. Trotman-Dickenson, *J. Chem. Soc. A*, 105 (1967).

(14) G. Hancock and K. R. Wilson, Proceedings of the Esfahan Symposium on Fundamental and Applied Physics, Ali Javan, Ed., Aug 29–Sept 5, 1971.

(15) C. D. Bass and G. C. Pimentel, *J. Amer. Chem. Soc.*, **83**, 3754 (1961).

(16) A. B. Callear and H. E. Van den Bergh, *Chem. Phys. Lett.*, **5**, 23 (1970).

between $^1/_2$ and $^2/_3$ as intense as observed from CD_3NF_2, depending upon whether HF elimination is strongly favored or whether HF and DF elimination are equally probable. (The k_H/k_D ratio found for the fluoroethanes,[17] $k_H/k_D = 3.1$, would give DF emission 0.55 times that from CD_3NF_2.) The observed intensity, 19% of the CD_3NF_2 emission, contradicts this model. If a two-step elimination is pictured in which reaction 3 gives a lower vibrational excitation than reaction 2, the weakness of the DF emission from CHD_2NF_2 can be explained by assuming that H is preferentially eliminated in the first step, as suggested by the behavior of the fluoroethanes.[17] However, this leads to the expectation that the N_1/N_0 ratio for HF should be higher from CHD_2NF_2 than from CH_3NF_2 and that the N_2/N_1 ratio for DF should be lower than from CD_3NF_2. The constancy of the population ratios is now in conflict with the model. These contradictions are not avoided by assuming simultaneous ejection of two hydrogen fluorides.

Table II: Vibrational Populations[a] Deduced from Equal-Gain Temperatures

Isotopic species	HF N_1/N_0	DF N_2/N_1
CH_3NF_2	0.47	
CH_2DNF_2	0.48	
CHD_2NF_2	0.46[b]	0.66[b]
CD_3NF_2		0.66

[a] All population ratios carry an estimated uncertainty of ±0.01. [b] Intensities suggest that 81% of eliminations give HF and 19% give DF.

We are left with the interpretation that reaction 3 does not occur within the time scale of our observations. Since only reaction 2 is effective in pumping, the constancy of population ratios becomes reasonable. The CH_2DNF_2 and CHD_2NF_2 results merely indicate a preferential elimination of H over D, as would be expected in any case. The DF intensity from CHD_2NF_2 suggests that HF elimination per H atom is 2.5 times more probable than DF elimination per D atom. This is in reasonable accord with the fluoroethane result[17] quoted earlier, $k_H/k_D = 3.1$.

Energy Distribution. The RRKM theory of unimolecular decomposition contains the postulate that the internal energy is randomly distributed among the internal degrees of freedom of the energized molecule.[18] Our data furnish some information about the energy disposed in one degree of freedom and, hence, an opportunity to test this statistical hypothesis. This was attempted in I, but with the premise that the sum of the exothermicities of reactions 2 and 3 was accessible. Since the present work indicates only the first step, reaction 2, is involved in the pumping, the significance of the data must be reassessed.

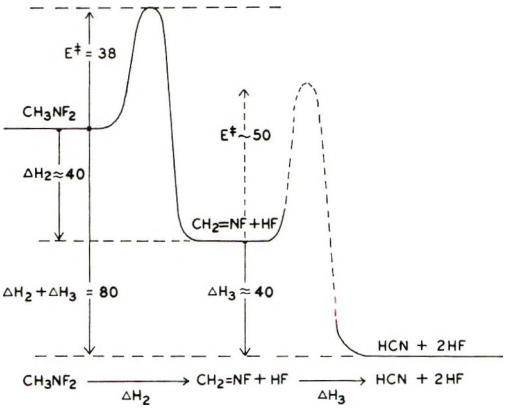

Figure 6. Energy diagram for HF elimination from CH_3NF_2.

Figure 6 shows a schematic representation of the thermochemistry for reactions 2 and 3. We assume that $CH_3NF_2\dagger$ contains just the 38 ± 5 kcal needed to surmount the presumed activation energy barrier. The exothermicity of reaction 2 and reaction 3 is relatively well known; the most uncertain element is the C–N bond energy, as mentioned earlier.

$$\Delta H_2 + \Delta H_3 = \Delta H_f^\circ(\mathrm{HCN}) + 2\Delta H_f^\circ(\mathrm{HF}) + D_0(\mathrm{CH_3}\text{–}\mathrm{NF_2}) - \Delta H_f^\circ(\mathrm{CH_3}) - \Delta H_f^\circ(\mathrm{NF_2}) =$$
$$32.3 + 2(-64.8) + 60 - 33.2 - 10.3 = -80.8 \text{ kcal}$$

The exothermicity of reaction 2 is more difficult to guess. If the C=NF bond energy is taken to be double that of $C\text{–}NF_2$, as is consistent with the relative magnitudes of CN bond energies listed by Cottrell,[19] then ΔH_2 is −33 kcal. If the overall exothermicity is assumed to be equally divided between reactions 2 and 3, then $\Delta H_2 = -40$ kcal. We will take the latter figure as our best estimate.

This value of ΔH_2 leads to an internal energy in $CH_3NF_2\dagger$ equal to 38 + 40 = 78 kcal with an uncertainty of perhaps 10 kcal. If this energy is divided equally among the 15 vibrational degrees of freedom, there is about 5.2 kcal/degree of freedom.

This result can be compared to the information provided by our equal-gain temperature measurements. For HF, we find $N_1/N_0 = 0.47$. Furthermore, the observation that $v = 1 \rightarrow 0$ reaches threshold before the $v = 2 \rightarrow 1$ transition implies that $N_2/N_1 \leq 0.45$. If no higher levels are excited, the average energy in vibration is ≤6.0 kcal. If the N_2/N_1 ratio were 0.25 and $N_3/N_2 = 0$, the average energy would drop to 5.0 kcal, but it would rise to 5.5 again if N_3/N_2 also were 0.25.

(17) G. O. Pritchard and M. J. Perona, *Int. J. Chem. Kinet.*, **2**, 281 (1970).

(18) See, for example, K. Dees, D. W. Setzer, and W. S. Clark, *J. Phys. Chem.*, **75**, 2231 (1971).

(19) T. L. Cottrell, "The Strengths of Chemical Bonds," Butterworths, London, 1958.

The DF ratio, $N_2/N_1 = 0.66$, gives similarly reasonable results. For example, if we assume for DF that $N_1/N_0 = N_2/N_1 = 0.66$ and $N_3 = N_4 = 0$, the average energy is 6.0 kcal; if $N_1/N_0 = N_3/N_2 = 0.33$ and $N_2/N_1 = 0.66$, the average energy is 5.0 kcal. Plainly, these indications of the average energy in the HF or DF vibrational motion are consistent with the statistical estimate within the uncertainty that must be ascribed to the comparison.

Elimination from CH_2=NF. The conclusion that reaction 3 plays no role in the laser emission must be rationalized with the chemical evidence that hydrogen cyanide is a final product.[2,3,11] In this regard, it is perhaps significant that in all of this earlier work, reaction 1a was probably responsible for much of the CH_3NF_2† formation. It is possible that CH_3NF_2† from reaction 1 will eliminate only one HF molecule (reaction 2) while CH_3NF_2†† from reaction 1a can eliminate two (reaction 2 followed by reaction 3). Another possibility is that reaction 3 occurs even in our experiments, but on a much slower time scale than needed to affect the laser emission.

To evaluate these alternatives, it becomes interesting to try to estimate the energy received by CH_2=NF†. A natural starting point, in the light of the previous section, is to assume a statistical distribution among the degrees of freedom. As reaction 2 occurs, five of the fifteen vibrational degrees of freedom of CH_3NF_2 become translations and rotations. We might assume that these degrees of freedom will receive $^5/_{15}$ of the available 80 ± 10 kcal, or 27 kcal. This energy will mainly go to the light fragment but, in any case, will probably be ineffective in aiding elimination. The remaining 53 kcal might be divided between CH_2=NF and HF in proportion to the numbers of vibrational degrees of freedom, in which case CH_2=NF would receive 90%, or 48 kcal. This estimate is somewhat larger than the 38 kcal activation energy deduced for elimination from CH_3NF_2†. However, the activation energy for elimination from the imine is probably at least 10 kcal higher than for the difluoroamine, judging by the activation energy for elimination from vinyl fluoride, estimated to be ~71 kcal/mol by Simmie, *et al.*,[20] and ~81 kcal/mol by Cadman and Engelbrecht,[21] compared to that for fluoroethane, 60 kcal/mol.[22] These considerations all suggest that the energy available for elimination from CH_2=NF† is marginally close to the activation energy. This makes creditable the explanation that two steps of elimination can occur from CH_3NF_2†† formed in reaction 1a but only one step from CH_3NF_2† formed in reaction 1.

Conclusions

These experiments lead then to the rather unexpected, hence interesting, conclusion that the reaction between CH_3 and N_2F_4 is only marginally effective in initiating elimination from CH_3NF_2† and it does not encourage significantly the second step elimination from CH_2=NF†. Reaction 2 needs energetic assistance from "hot" methyl radicals and reaction 3 does not seem to occur at all on the time scale of the laser experiment.

With this clarification of the important processes, it is possible to verify, for the CH_3NF_2 elimination, that the energy entering the HF vibrational degree of freedom is close to what is expected on the basis of a statistical energy distribution. This not only adds a useful experimental tiepoint for statistical theories of unimolecular decomposition but it also provides a working hypothesis for understanding the low vibrational excitation already displayed in elimination reactions[1,23-26] and for predicting the behavior of new, similar reactions.

Acknowledgment. We gratefully acknowledge support of this research by the U. S. Air Force Office of Scientific Research.

(20) J. M. Simmie, W. J. Quiring, and E. Tschuikow-Roux, *J. Phys. Chem.*, **74**, 992 (1970).

(21) P. Cadman and W. J. Engelbrecht, *Chem. Commun.*, 453 (1970).

(22) P. Cadman, M. Day, A. W. Kirk, and A. F. Trotman-Dickenson, *ibid.*, **4**, 203 (1970).

(23) M. J. Berry and G. C. Pimentel, *J. Chem. Phys.*, **49**, 5190 (1968).

(24) M. J. Berry and G. C. Pimentel, *ibid.*, **53**, 3453 (1970).

(25) P. N. Clough, J. C. Polanyi, and R. T. Taguchi, *Can. J. Chem.*, **48**, 2919 (1970).

(26) M. C. Lin, *J. Phys. Chem.*, **75**, 3642 (1971).

Electron Transfer Mechanism of Fluorescence Quenching in Polar Solvents. II. Tetracyanoethylene and Tetracyanobenzene as Quenchers[1]

by K. H. Grellmann, A. R. Watkins, and A. Weller*

Max-Planck-Institut für Biophysikalische Chemie, Spektroskopie, 34 Göttingen, Nikolausberg, Germany
(Received February 18, 1972)

Publication costs assisted by the Max-Planck-Institut für Biophysikalische Chemie

Flash studies of quenched systems are reported, with the strong electron acceptors tetracyanoethylene and tetracyanobenzene as quenchers. The results generally confirm the supposition that fluorescence quenching occurs chiefly by electron transfer, but, in contrast to the results with dicyanobenzene as quencher (part I of this series), no detectable formation of triplets of the fluorescer occurs. This is shown to be consistent with the change in energy relationships in going from dicyanobenzene to tetracyanoethylene and tetracyanobenzene as quenchers.

In a preceding paper[1] we reported an investigation of the fluorescence quenching properties of the electron acceptor *p*-dicyanobenzene (DCB) with a series of polynuclear aromatic hydrocarbons. The results confirmed that the initial step in the quenching reaction in polar solvents was an electron transfer leading to the radical ions of the fluorescer and quencher. It could be shown that, for these systems, the free energy of the solvated radical ions formed in the quenching reaction lies, in all cases studied, above the lowest triplet energy level of the aromatic hydrocarbon, and flash experiments showed that, in fact, the hydrocarbon triplet was formed as a general rule. There is evidence to show that the mechanism leading to triplet formation is a recombination reaction of the solvated radical ions[2]

$$D_s^+ + A_s^- \longrightarrow {}^3D^* + A \qquad (1)$$

The free energy change associated with this reaction, ΔG_2, can be calculated from the electrochemical data for the donor D (in this case the fluorescing hydrocarbon) and the acceptor A (in this case the quencher).

$$-\Delta G_2 = \Delta E_{00}({}^3D^*) - [E_{1/2}(D/D^+) - E_{1/2}(A^-/A)] \qquad (2)$$

$E_{1/2}(D/D^+)$ and $E_{1/2}(A^-/A)$ are the electrochemically determined half-wave potentials for the one-electron oxidation of D and the one-electron reduction of A, respectively; $\Delta E_{00}({}^3D^*)$ is the zero-point energy of the lowest triplet state of D. The energy of the lowest triplet of A was so high that its formation from the radical ions in a reaction analogous to reaction 1 could be ruled out on energetic grounds. It is, of course, clear that reaction 1, besides leadingt o the formation of ${}^3D^*$, will also produce D in its ground state.

In this paper we report a similar investigation, this time with tetracyanobenzene (TCB) and tetracyanoethylene (TCE) as quenchers. The corresponding reduction potentials (*vs.* sce) are $E_{1/2}(A^-/A) = -0.66$ V for TCB[3] and $E_{1/2}(A^-/A) = +0.24$ V for TCE;[4] comparison with *p*-dicyanobenzene ($E_{1/2}(A^-/A) = -1.65$ V[5]) shows that TCB and TCE are considerably more powerful electron acceptors. In other words the initial electron transfer

$$^1D^* + A \longrightarrow D_s^+ + A_s^- \qquad (3)$$

will be energetically more favorable than in the case where the acceptor is DCB, since the energy of the free ions will be lower with TCB and TCE as quenchers. The free energy change associated with reaction 3 will be given by[6]

$$-\Delta G_1 = \Delta E_{00}({}^1D^*) - [E_{1/2}(D/D^+) - E_{1/2}(A^-/A)] \qquad (4)$$

where $\Delta E_{00}({}^1D^*)$ is the zero-point energy of the first excited singlet state (the state populated in solution by the initial excitation of D) estimated from available absorption and fluorescence data.[7]

The low-lying ions produced with TCB and TCE lead to a more significant change in the energy relationships: the value of ΔG_2, associated with the triplet-production step 1, becomes positive; *i.e.*, the triplet levels of the aromatic hydrocarbons now lie *above* the energy levels of the corresponding free ions. This

(1) Part I: K. H. Grellmann, A. R. Watkins, and A. Weller, *J. Phys. Chem.*, **76**, 469 (1972).

(2) H. Schomburg, H. Staerk, and A. Weller, to be published.

(3) P. H. Rieger, I. Bernal, W. H. Reinmuth, and G. K. Fraenkel, *J. Amer. Chem. Soc.*, **85**, 683 (1963).

(4) M. E. Peover, *Trans. Faraday Soc.*, **58**, 2370 (1962).

(5) D. van der Meer, Thesis, Technical University Twente, 1970.

(6) D. Rehm and A. Weller, *Ber. Bunsenges. Phys. Chem.*, **73**, 834 (1969).

(7) J. B. Birks, "The Photophysics of Aromatic Molecules," Wiley-Interscience, London, 1970.

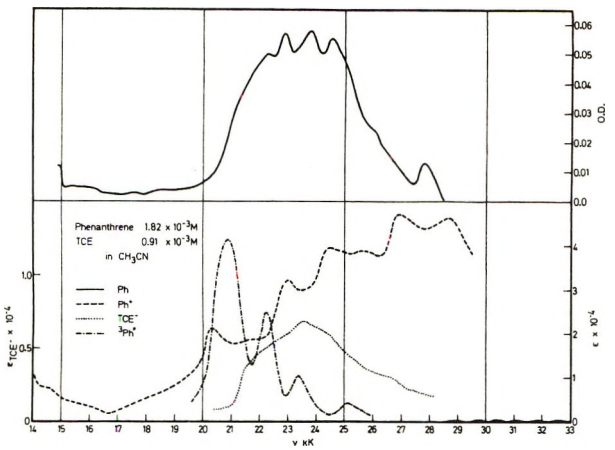

Figure 1. Transient absorption spectrum obtained on flashing phenanthrene–TCE (upper half) together with the relevant literature spectra (lower half).

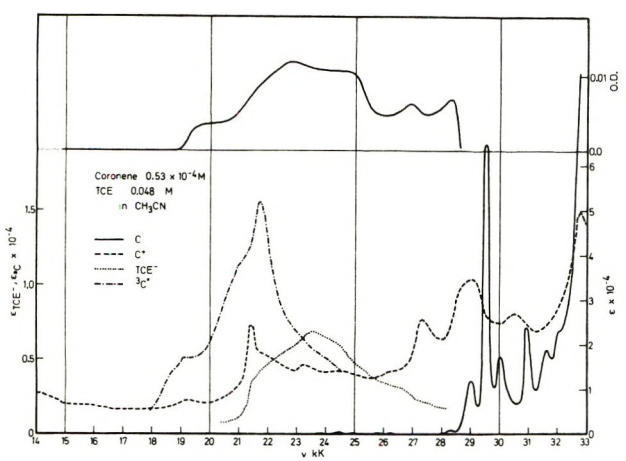

Figure 2. Transient absorption spectrum obtained on flashing coronene–TCE (upper half) together with the relevant literature spectra (lower half).

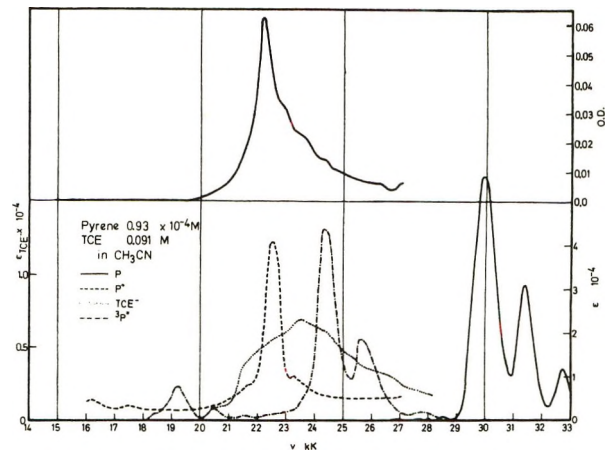

Figure 3. Transient absorption spectrum obtained on flashing pyrene–TCE (upper half) together with the relevant literature spectra (lower half).

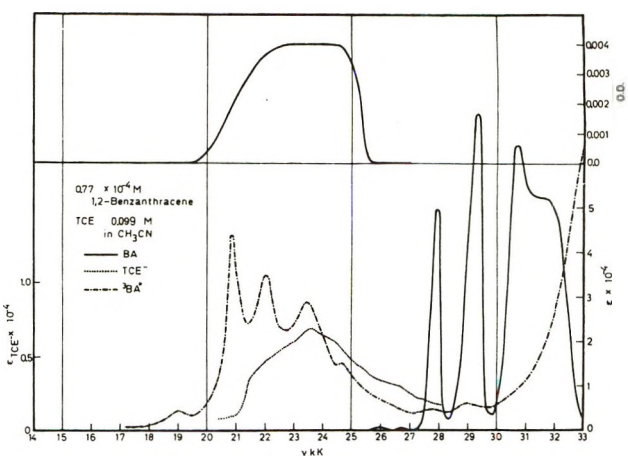

Figure 4. Transient absorption spectrum obtained on flashing 1,2-benzanthracene–TCE (upper half) together with the relevant literature spectra (lower half).

leads clearly to a situation in which one route for the disappearence of the radical ions, reaction 1, is no longer available. We therefore expect that, in the systems reported here, no detectable triplet production will take place. Some earlier results[8] suggest that this expectation is experimentally justified; the investigation reported here is an attempt to explore the range of validity of this model for the underlying mechanism of electron-transfer fluorescence quenching.

Experimental Section

The aromatic hydrocarbons used were purified as described previously.[1] Tetracyanoethylene (Schuchardt) was purified by recrystallization from chlorobenzene followed by sublimation. Tetracyanobenzene (Frinton) was purified by recrystallization. The solvents and experimental techniques used in obtaining the transient spectra were as described previously,[1] flash experiments being carried out with glass filters (Schott WG305 for the systems with TCE, WG320 for those with TCB) in order to exclude direct excitation of the acceptor, which could lead to the production of the corresponding radical anions by photoionization.[9] The flash and fluorescence quenching experiments reported here were all carried out in degassed acetonitrile solution.

Results

Figures 1–5 (upper half) show the transient absorption spectra from the flash photolysis experiments with TCE, and Figures 6–10 the spectra with TCB as quencher. The lower half of each figure shows the corresponding literature spectra, the sources being as previously indicated,[1] with the exception of the TCE and TCB radical anions.[10] In some cases transient absorp-

(8) K. H. Grellmann, A. R. Watkins, and A. Weller, *J. Lumin.*, **1,2**, 678 (1970).

(9) M. Sofue and S. Nagakura, *Bull. Chem. Soc. Jap.*, **38**, 1048 (1965).

(10) A. Ishitani and S. Nagakura, *Theor. Chim. Acta*, **4**, 236 (1966); W. Liptay, G. Briegleb, and K. Schindler, *Z. Elektrochem.*, **66**, 331 (1961).

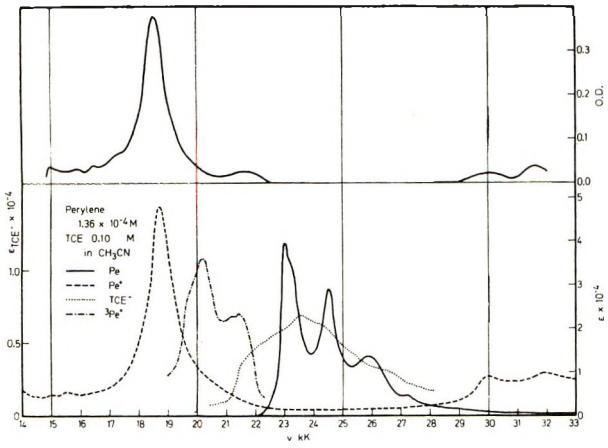

Figure 5. Transient absorption spectrum obtained on flashing perylene–TCE (upper half) together with the relevant literature spectra (lower half).

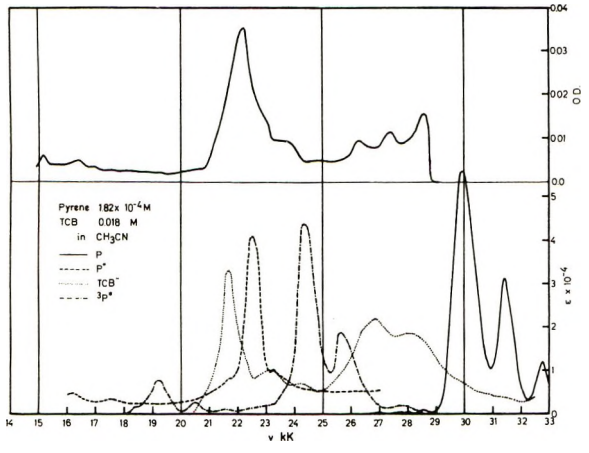

Figure 6. Transient absorption spectrum obtained on flashing pyrene–TCB (upper half) together with the relevant literature spectra (lower half).

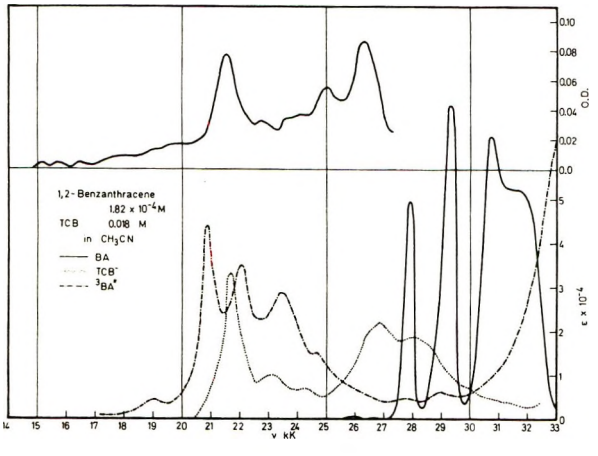

Figure 7. Transient absorption spectrum obtained on flashing 1,2-benzanthracene–TCB (upper half) together with the relevant literature spectra (lower half).

tions occur in a spectral region where absorption of the hydrocarbon in the ground state is quite considerable and as a result the absorption measurements in these

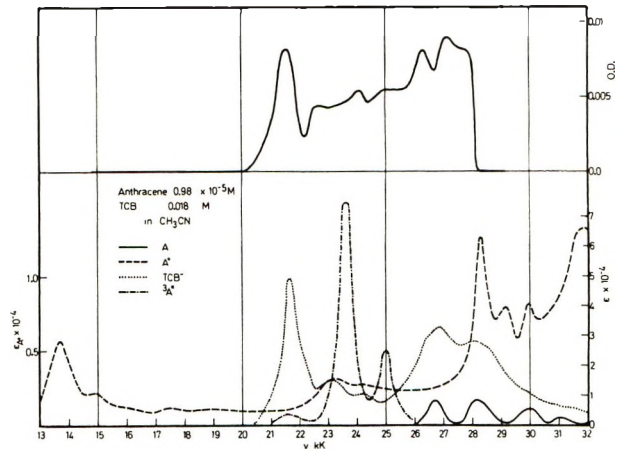

Figure 8. Transient absorption spectrum obtained on flashing anthracene–TCB (upper half) together with the relevant literature spectra (lower half).

Table I: Quenching Constants (in Oxygen-Free Acetonitrile) and Extent of Fluorescence Quenching for the Systems Studied

Acceptor	Donor	Quenching constant, M^{-1}	% quenching in flash experiments
TCE	Phenanthrene	1370	57
	Coronene	2900[a]	99
	Pyrene	5600[a]	>99
	1,2-Benzanthracene	1040[a]	99
	Perylene	260	96
TCB	Pyrene	4600	99
	1,2-Benzanthracene	1090	95
	Anthracene	160	75
	Perylene	200	95
	Tetracene	160	89

[a] D. Rehm, private communication.

regions will be less reliable. Table I gives the measured Stern–Volmer quenching constants (for oxygen-free solution) and the extent of quenching in the flash experiments.

The systems anthracene–TCE and tetracene–TCE appeared to undergo photochemical decomposition (other authors have reported similar effects with anthracene–TCE[11]), and were not further investigated. Naphthalene–TCE, on flashing, gave a transient absorption centered on 25 kK which was, however, too weak to be positively identified. The system phenanthrene–TCE was flashed at quencher concentrations of 10^{-3} M, since at higher concentrations marked complex formation in the ground state takes place. No complex formation or photochemical decomposition could be detected with the other systems with TCE as quencher.

(11) G. Schenk and N. Radke, *Anal. Chem.*, **37**, 910 (1965).

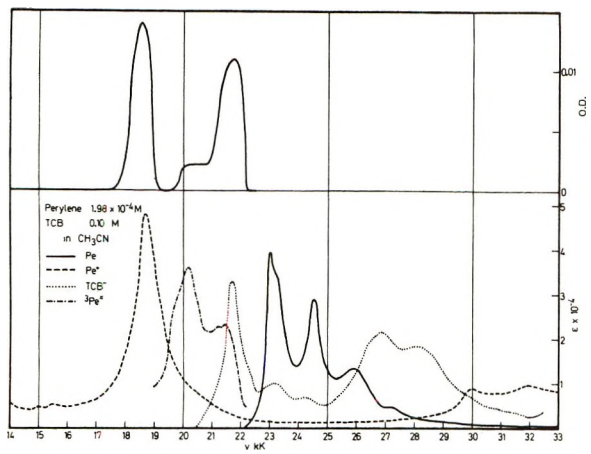

Figure 9. Transient absorption spectrum obtained on flashing perylene–TCB (upper half) together with the relevant literature spectra (lower half).

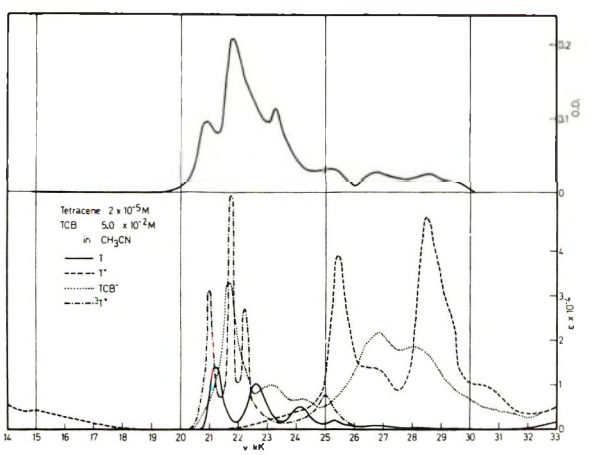

Figure 10. Transient absorption spectrum obtained on flashing tetracene–TCB (upper half) together with the relevant literature spectra (lower half).

Weak complex formation in the ground state was also observed with TCB as quencher (with pyrene the formation constant is 0.05 M^{-1}) and most flash experiments were carried out with a TCB concentration of about 0.02 M, at which complex formation can be disregarded.

Discussion

The flash spectra for the systems pyrene–TCE and perylene–TCE show quite clearly absorptions which are due to the respective hydrocarbon radical cations (these results for pyrene–TCE, already briefly reported,[8] have recently been confirmed[12]); hydrocarbon radical cations can also be identified, although not so unambiguously, in the spectra of coronene–TCE and phenanthrene–TCE. The weak absorption of the TCE anion radical makes it somewhat difficult to identify; it appears to be the main component of the transient spectrum of 1,2-benzanthracene–TCE (the radical cation of 1,2-benzanthracene has no reported spectrum in the wavelength region accessible in these measurements). Quenching in the system phenanthrene–TCE

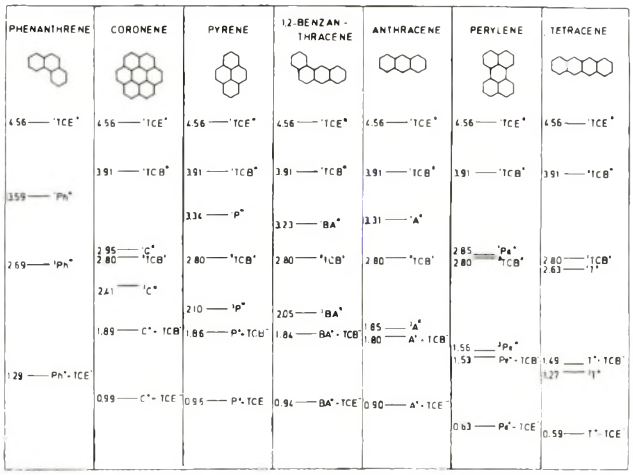

Figure 11. Schematic representation of the energy levels (in eV) of the electronic states and free radical ions for the systems investigated.

is by no means complete; however, triplets formed directly by intersystem crossing from the primarily excited phenanthrene singlet will react rapidly (too quickly to be detected in the flash spectra) with TCE to produce radical ions.[8,13] From these spectra it can be concluded that the electron transfer mechanism is, in all systems studied here, responsible for fluorescence quenching.

In all five systems with TCE the hydrocarbon triplet is absent, within the limits of experimental error. At first sight this result appears to confirm the mechanism of triplet formation outlined in the introduction; however, one explanation for this phenomenon could be that TCE, always considerably in excess, possesses a low-lying triplet which rapidly (compared to the lifetime of the flash) depopulates the hydrocarbon triplet. Although no measurement of the triplet energy of TCE has to date appeared in the literature, Evans[14] has measured a triplet energy of 3.56 eV for ethylene, and TCE, by analogy, would be expected to have a triplet energy lying considerably above most of the hydrocarbon triplet levels in the systems studied.

A similar situation prevails in the systems with TCB as acceptor with regard to the relative positions of radical-ion and triplet energy levels. In every case the hydrocarbon triplet lies above the radical ions, with the single exception of tetracene–TCB (see Figure 11). Examination of the flash spectra (Figures 6–10) shows that the TCB radical anion (with absorption peaks at 22 and 26.5 kK) is present in all cases, and the radical cations of the aromatic hydrocarbon can be identified in the spectra obtained with pyrene–TCB (somewhat overlapped, Figure 6) and perylene–TCB

(12) T. Okada, H. Oohari, and N. Mataga, *Bull. Chem. Soc. Jap.*, **43**, 2750 (1970).

(13) M. Pinsky, H. Staerk, and A. Weller, to be published.

(14) D. F. Evans, *J. Chem. Soc.*, 1735 (1960).

(Figure 9). Once again, the aromatic hydrocarbon triplet cannot be detected, as in the spectra with TCE as quencher, with the exception of the system tetracene–TCB (Figure 10). (The overlap of the spectra in this last case, together with the incomplete quenching, makes it difficult to say how much of the triplet comes from the quenching reaction. The situation is further complicated by the absorption of tetracene in the ground state, which occurs in the same region as the triplet-triplet absorption spectrum.)

The flash spectra obtained with TCB as quencher can be compared with the energy level scheme shown in Figure 11. Two important facts stand out. First, the nonappearence of the aromatic hydrocarbon triplet in the systems with TCB (with the exception of tetracene–TCB) cannot be explained in terms of a triplet–triplet energy transfer between the aromatic hydrocarbon triplet and TCB. The lowest triplet state of TCB has an energy of 2.80 eV[15] and lies too high in energy for such a triplet–triplet energy transfer to be effective. Secondly, we can say that the reason for the nonappearence of the aromatic hydrocarbon triplet is in fact connected with the inversion of the radical-ion and triplet energy levels, and is in all probability a consequence of the unfavorable free energy requirement of reaction 1 ($\Delta G_2 > 0$), not only in the case of the systems with TCB, but also in the systems with TCE as quencher. The possibility and extent of triplet formation in the systems with TCB as quencher do actually appear to be governed by the sign and magnitude of ΔG_2. The quite strong triplet formation with tetracene–TCB corresponds to a free energy change $\Delta G_2 = -0.22$eV (see Figure 11) in favor of reaction 1, and the slight indications of triplet formation in the spectra of the systems perylene–TCB (at 20.3 kK) and anthracene–TCB (the badly resolved absorption between 23 and 25 kK) can reasonably be interpreted as a thermally activated triplet formation from the radical ions (the additional free energy required for reaction 1 for these systems amounts to $\Delta G_2 = 0.03$ and 0.05 eV, respectively).

A further significant feature of these flash spectra is the low quantum yield of ion formation. Although a quantitative comparison with the results obtained with DCB is difficult, the quantum yields of ion formation in the latter case are always higher, sometimes by a factor of 5, than for TCB and TCE as quenchers. In order to understand which factors are decisive in bringing about this difference, it must be realized that reaction 3 actually consists of a number of consecutive steps: the diffusion of the ions together to form a collision complex, the transfer of an electron from D to A to form an ion pair, and the subsequent diffusional separation of the ion pair. The ion pair, in addition to diffusing apart to form the free solvated radical ions, has only one remaining reaction pathway: it can convert to the ground state by means of a reverse electron transfer. This is summarized in the reaction scheme shown in eq 5. It should be pointed out that hetero-

$$\begin{array}{ccc} {}^1D^* + A & \longrightarrow & {}^1D^* \cdots A \\ & & \downarrow \\ D_s^+ + A_s^- & \xleftarrow{k_{sep}} & D^+ \cdots A^- \\ & & \downarrow k_g \\ D + A & \longleftarrow & D \cdots A \end{array} \qquad (5)$$

excimer formation can be neglected in the systems studied here; the ion pair is to be considered as a loose association of the two solvated radical ions.

If we assume that the steps leading to the ion pair take place with unit efficiency (a reasonable assumption in view of the high quencher concentrations used here) the quantum yield of radical ion formation will depend on the yield ϕ_i of radical ions from the ion pair. The radical ion yield can therefore be expressed as

$$\phi_i = k_{sep}/(k_{sep} + k_g) \qquad (6)$$

Since k_{sep} can be taken to be a constant which does not depend on the chemical properties of D and A, variations in ϕ_i will be a result of variations in k_g

$$\phi_i = \frac{1}{1 + \dfrac{k_g}{4 \times 10^9}} \qquad (7)$$

where k_{sep} has been set equal to the previously calculated value[16] of 4×10^9 sec^{-1} in acetonitrile.

The step k_g will involve the conversion of a large amount of electronic energy into vibrational energy, and the efficiency with which this occurs will be determined by the appropriate Franck–Condon factors for the ion pair.[17] These will, in turn, be a function of the energy separation between ion pair and ground state (which is given by $E_{1/2}(D/D^+) - E_{1/2}(A^-/A)$), so that k_g will be expected to increase, and ϕ_i decrease, as the energy of the ion pair sinks to lower values. The results presented here and in part I are qualitatively in agreement with this picture; experiments are in progress with the aim of investigating quantitatively the radical ion yields in these systems.

We have looked for confirmation of these observations on triplet formation in previously reported studies of fluorescence quenching. In addition to radical ions, the corresponding hydrocarbon triplets are formed on flashing perylene–diethylaniline, coronene–diethylaniline, anthracene–diethylaniline, and tetracene–diethylaniline in acetonitrile.[16,18] Calculations show that, in these four systems, the triplet energy lies below

(15) H. Hayashi, S. Iwata, and S. Nagakura in "Molecular Luminescence," E. C. Lim, Ed., W. A. Benjamin, New York, N. Y., 1969.

(16) H. Knibbe, D. Rehm, and A. Weller, *Ber. Bunsenges. Phys. Chem.*, **72**, 257 (1968).

(17) R. A. Marcus, *Ann. Rev. Phys. Chem.*, **15**, 155 (1964).

(18) H. Leonhardt and A. Weller, *Z. Phys. Chem.*, **29**, 277 (1961).

the free energy of the radical ions ($\Delta G_2 > 0.4$ eV). Similarly, the flash spectrum of pyrene–dimethylaniline in acetonitrile[12] shows the presence of the pyrene radical anion, the pyrene triplet, and possibly the dimethylaniline radical cation, once again in accordance with the fact that the radical ions lie about 0.8 eV above the pyrene triplet. The observation of Nakato, *et al.*,[19] that the naphthalene triplet and the TMPD radical cation are formed on flashing the system TMPD–naphthalene in ethanol (where the free ions certainly lie above the naphthalene triplet) is also to be expected. Examples where the energy of the free ions formed in the reactions is lower than that of the lowest triplet are provided by the system *p*-dimethoxybenzene–chloranil[20] (the chloranil triplet lying more than 1 eV above the ions) and *N*,*N*-dimethyl-2-naphthylamine dimethylisophthalate[21] (where the dimethylnaphthylamine triplet lies about 0.2 eV above the ions). In these two cases only ions are seen in the flash spectrum, and in the second case it can be concluded that no triplet (the spectrum of which was known) was formed in the reaction. These observations generally confirm the experimental findings reported here.

Acknowledgments. The authors wish to express their gratitude to Mrs. S. Reiche for her assistance with much of the experimental work, and one of us (A. R. W.) wishes to thank the Alexander-von-Humboldt-Stiftung for the award of a fellowship, during the tenure of which part of this work was carried out. Thanks are also due to Dr. W. Kühnle, who purified the solvent used in this work.

(19) Y. Nakato, N. Yamamoto, and H. Tsubomura, *Bull. Chem. Soc. Jap.*, **40**, 2480 (1967).

(20) K. Kawai, N. Yamamoto, and H. Tsubomura, *ibid.*, **42**, 369 (1969).

(21) M. Koizumi and H. Yamashita, *Z. Phys. Chem. (Frankfurt am Main)*, **57**, 103 (1968); H. Yamashita, H. Kokubun, and M. Koizumi, *Bull. Chem. Soc. Jap.*, **41**, 2312 (1968).

Viscosity Effects on the Photohydration of Pyrimidines

by Wm. A. Summers, Jr., and John G. Burr*

Chemistry Department, Oklahoma University, Norman, Oklahoma 73069 *(Received February 25, 1972)*

Publication costs assisted by the National Cancer Institute

A study of the effects of viscosity change on the photohydration quantum yield of uracil and dimethyluracil has been carried out to help evaluate possible mechanisms for these reactions. The results indicate that the rate of photoaddition of water to the 5,6 double bond of these pyrimidines changes only slightly with increasing viscosity and thus is not diffusion controlled. In light of known effects of pH, deuterium isotope effects, enhanced reactivity with stronger nucleophiles, and energy transfer data, these results suggest that the precursor for photohydration is longer lived than the π,π^* fluorescent singlet.

Introduction

The change in quantum yield with viscosity change for the photohydration of uracil and dimethyluracil was measured in the following two types of solutions: (1) aqueous solutions of polyethylene oxide (Union Carbide WSR-301 and WSR-205), and (2) aqueous solutions of glycerine. The former are characterized by large changes in viscosity and small changes in water activity, while the latter by small changes in viscosity and large changes in water activity. These studies were performed at a uniform temperature of 16°. The relationship of diffusion constant to viscosity was measured for each type of solution.

Experimental Section

Water was doubly distilled from glass; acetonitrile (Eastman, spectroquality) and glycerine (Baker) were used without further purification. Uracil, dimethyluracil, and 2-hydroxypyrimidine were obtained from Cyclo Chemical Co. The polymers were a gift from Union Carbide Corp.

Viscosities were measured with an Ostwald viscosimeter. Light intensities were determined with the ferrioxalate[1] and dimethyluracil[2,3] actinometers. The light source was an array of six symmetrically arranged GE 15-W germicidal lamps. A jacketed cell

(1) C. G. Hatchard and C. A. Parker, *Proc. Roy. Soc., Ser. A*, **235**, 518 (1956).

(2) J. G. Burr, B. R. Gordon, and E. H. Park, *Photochem. Photobiol.*, **8**, 73 (1968); *cf.* the discussion in ref 3 regarding this actinometer.

(3) J. G. Burr, E. H. Park, and A. Chan, *J. Amer. Chem. Soc.*, **94**, 5866 (1972).

holder (totally of Vycor) of special design served to mount the cuvet for irradiation, maintain constant temperature, and filter the light.

The formation of hydrate was determined by the "heat recovered uracil" method[2] and by chromatographic separation on cellulose using [2-^{14}C]uracil in butanol–water at 0°. Chromatographic separation of photohydrate was only effective with the glycerine–water systems.

A Sargent Model XVI polarograph was used to determine i_d for 2-hydroxypyrimidine in both glycerine–water solutions and polymer–water solutions. These polarographic reductions were carried out in borate buffered (pH 7) solutions with 10^{-3} M 2-HP. The $E_{1/2}$ was observed to decrease with added polymer (−1.35 to −1.67 V) but no change was observed with glycerine, indicating some phenomenon occurring at the solvent–electrode interface which inhibits electron transfer. The diffusion current determined is related to the diffusion coefficient by the Ilkovic equation, $D = (i_d/km^{1/3}t^{1/6}nC)^2$.

Tracer labeling was used to determine the diffusion coefficients of glucose (standard) and uracil. The device used consisted of a thermostated 200-ml flask with a side arm for periodic sampling. The labeled material, in a solution of known viscosity, was allowed to diffuse into the large volume of solution of the same viscosity, which was stirred mechanically, through a large porosity sintered glass disk. The change in concentration with time was determined by liquid scintillation and related to the diffusion coefficient by Fick's second law $dc/dt = d(D\,dc/dx)/dc$.

Results

The quantum yield normalized to unit water activity for photohydration of uracil and dimethyluracil as a function of viscosity, in the polymer solutions, increases slightly (Figure 1). The polymer solutions were very dilute, 1.5% (w/w) for the 10^4 cP solution, and the water activity was found to decrease by about 8% over the range. Quantum yields for solutions of water–polymer–acetonitrile (Figure 2) also revealed a slight increase at high viscosity. These data suggest that the photohydration process is relatively insensitive to viscosity changes. The slight increases in quantum yield at high viscosity will be discussed later.

For the glycerine–water mixtures, the variation of the quantum yields (based on heat recovery) as a function of viscosity are shown in Figures 3 and 4 for uracil and dimethyluracil, respectively. When data, based on the chromatographic separation of the uracil photohydrate, are normalized to unit water activity and plotted against viscosity (Figure 5) the quantum yield is found to increase about 30%. This increase implies greater efficiency in more viscous media.

The usual S-shaped curves (Figures 3 and 4) are believed to result from another reaction of photoexcited pyrimidine with glycerine. This product might be similar to the methanol adduct,[4] which is also heat labile. A second spot was observed on the tlc plates using the labeled uracil but it could not be separated from unreacted uracil. It was felt that this might be the glycerine–water adduct.

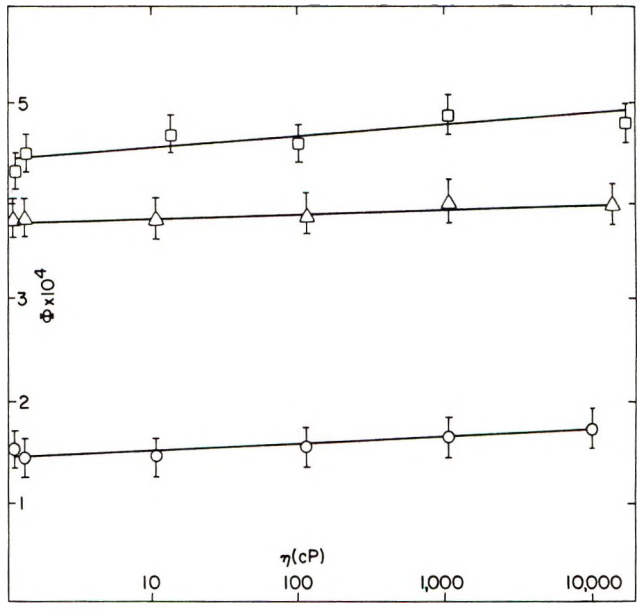

Figure 1. Quantum yields, Φ, for photohydration *vs.* viscosity in water–polymer solutions; Φ is normalized to unit water activity: □, uracil, pH 2; △, 1,3-dimethyluracil, pH 7; ○, uracil, pH 7.

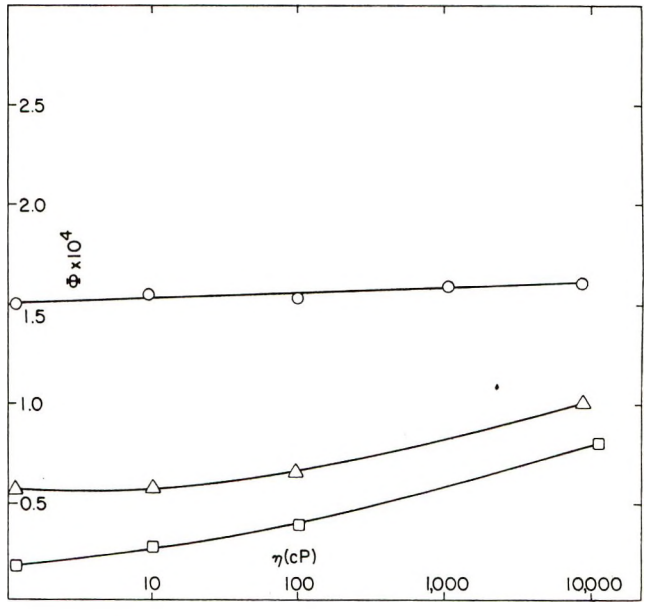

Figure 2. The quantum yields, Φ, for photohydration of uracil *vs.* viscosity in mixtures of water, acetonitrile, and polymer WSR 301; pH = 7: ○, water and polymer only; △, water–acetonitrile (1:1, v/v) and polymer; water–acetonitrile (1:3,v/v) and polymer (lowest line).

(4) S. Y. Wang, *Nature (London)*, **184**, 184 (1959).

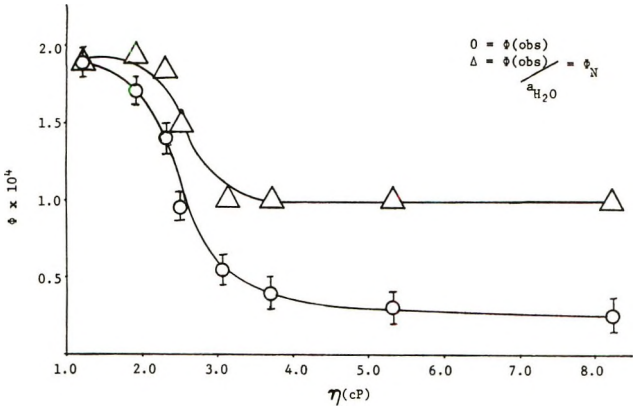

Figure 3. Quantum yield for photohydration (uracil) *vs.* viscosity, Φ based on heat reversible product.

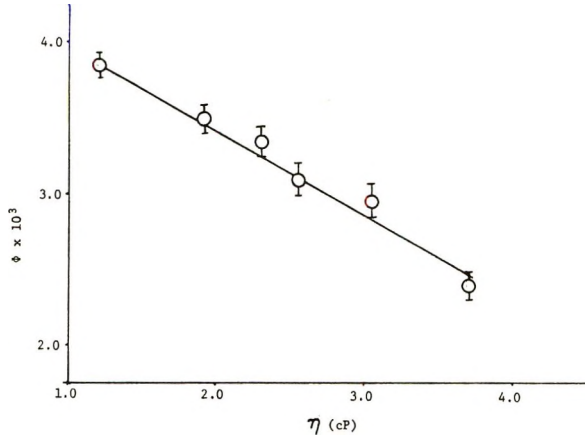

Figure 4. Normalized quantum yield of photohydration (DMU) *vs.* viscosity, Φ based on heat reversible product.

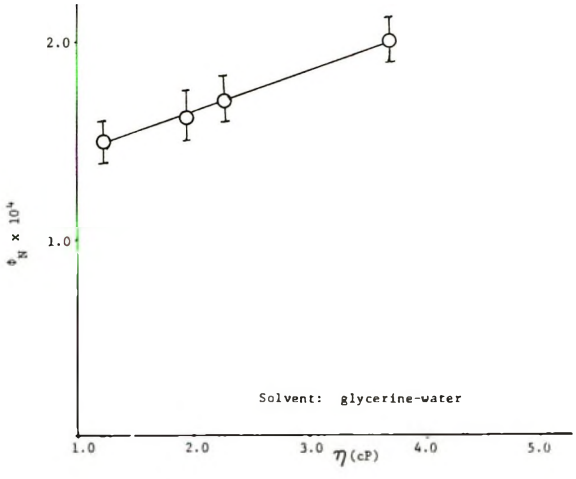

Figure 5. Quantum yield for photohydration (uracil) (normalized to unit water activity) *vs.* viscosity, Φ based on chromatographic separation.

In order to clarify the relation of viscosity to diffusion coefficient in these solvent systems, a determination of the diffusion coefficients in each type of solution was carried out. Tables I and II list the observed values compared to calculated values using the Stokes–Einstein equation, $D = RT/6\pi rN\eta$. The data indicate that polymer–water solutions are not classical with respect to the Stokes–Einstein equation but glycerine–water solutions are. In any case a change in diffusion coefficient does occur with polymer–water solutions which should be reflected by a decrease in the reaction rate, if the reaction were diffusion controlled. Little change in quantum yield was observed for these systems and a definite increase was observed in the glycerine mixtures.

Table I: Polarographic Determination of Diffusion Coefficient for Uracil Based on the Ilkovic Equation

Solvent	Temp, °C	Viscosity, cP	D_{obsd}[a]	D_{calcd}[b]	Φ[c]
Water	16	1.19	6.2	5.8	1.5
Glycerine–water	16	3.1	1.85	1.8	1.0
0.2% WSR-301 water	16	7.0	4.9	0.97	1.56
0.6% WSR-301 water	16	122.0	2.25	0.06	1.57

[a] All values multiplied by 10^{-6} cm² sec^{-1}. [b] Based on Stokes–Einstein equation, all values multiplied by 10^{-6} cm² sec^{-1}. [c] Quantum yield "observed" for photohydration of uracil; all values multiplied by 10^4.

Discussion

The data presented in this paper lead to the conclusion that the photohydration of uracil and dimethyluracil is not a diffusion-controlled process. The reaction must be either very fast (a rearrangement) or slower than diffusion controlled (not occurring at every collision). The observed effects of pH on the photohydration rate,[3,5] deuterium isotope effects,[6] enhanced reactivity with stronger nucleophiles,[7,8] and the kinetic dependence of photohydration rate on water concentration,[6] all suggest that the excited state precursor is long enough lived to become "aware" of its molecular environment in solution. This would correspond to a "slow" bimolecular process, indicated as step 4 in Scheme I.

The possibility of a very fast (rearrangement) reaction is suggested by the lifetime (10^{-12} sec) of the uracil (and thymine) fluorescent (π,π^*) singlet, estimated from observation of the very faint fluorescence ($\Phi = 10^{-4}$ to 10^{-5}) of these substances.[9] Such a very fast

(5) (a) W. R. Moore, *Advan. Polymer Sci.*, in press; (b) J. G. Burr, B. R. Gordon, and E. H. Park, *Advan. Chem. Ser.*, **No. 81**, 418 (1968).

(6) (a) J. G. Burr, *Advan. Photochem.*, in press; (b) J. G. Burr and E. H. Park, *Advan. Chem. Ser.*, **No. 81**, 421 (1968).

(7) A. M. Moore, *Can. J. Chem.*, **36**, 281 (1958).

(8) J. G. Burr, R. L. Letsinger, W. A. Summers, and C. Enwall, manuscript in preparation.

(9) M. Daniels and W. Hauswirth, *Science*, **171**, 675 (1971).

Table II: Direct Determination of Diffusion Coefficient Using Tracer Labeling

Solvent	Temp, °C	Viscosity, cP	D_{obsd}	Solute	D_{calcd}
Water	16	1.19	6.73[a]	[^{14}C]Glucose	
			10.7	[^{14}C]Uracil	5.8
0.2% WSR-301 water	16	7.0	4.70	[^{14}C]Glucose	
			7.50	[^{14}C]Uracil	0.97
0.6% WSR-301 water	16	122	0.3	[^{14}C]Glucose	
			1.77	[^{14}C]Uracil	0.06
0.4% WSR-205 water	16	4.7	9.0	[^{14}C]Uracil	1.4
0.9% WSR-205 water	16	13.5	2.2	[^{14}C]Uracil	0.5

[a] Standard for apparatus, 2.2×10^{-2} M glucose in water, $D = 6.73 \times 10^{-6}$ cm^2 sec^{-1}.

Scheme I

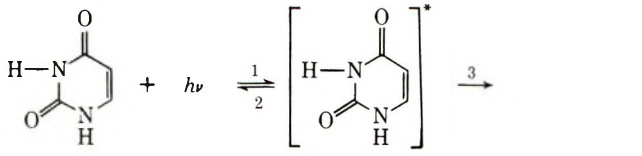

I. π,π^* singlet

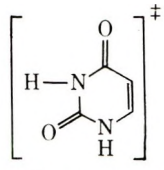

II. n,π^* singlet (?)

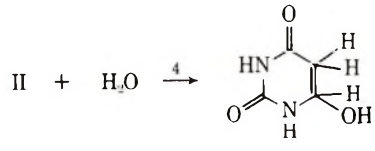

reaction might be the rearrangement of an excited state water–pyrimidine complex, shown by the reactions in Scheme II. Work is currently underway in our

Scheme II

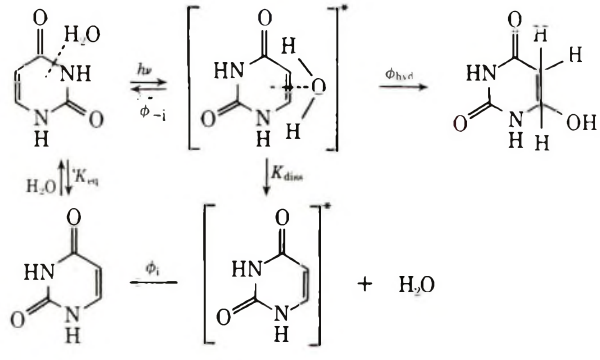

laboratory to identify such a complex, measure its formation constants, and evaluate its contribution to uracil photochemistry. We do have evidence for deuterium exchange between the H on N-3 of 1-cyclohexyluracil and D_2O at low concentrations in carbon tetrachloride; the thermodynamics of such exchanges are being determined.[10] In view of the first-order dependence of uracil photohydration yield with water activity (in acetonitrile solution),[6] the kinetic importance of such a complex in the photohydration reaction may be limited.

There are several indications that the fluorescent singlet state and the excited state precursor to the photohydrate may not be the same state. Whitten and coworkers report[11,12] no correlation between the fluorescence quenching of DMU by water and the photohydration rate of DMU. We have reported[13] that europium(III) ion emission can be sensitized by uridine monophosphate, but that the photohydration of this nucleotide is not quenched by europium ion.

In conjunction with the other characteristics of uracil photohydration, we feel that the relative independence of photohydration yield on viscosity provides justification for suggesting that the excited state precursor of the photohydrate of uracil and DMU is a state which is longer lived than the fluorescent singlet, and which is not the triplet state (since that state is known to lead only to photodimer). This state could be an n,π^* singlet, using one of the oxygen lone pair electrons (a "hidden" n,π^* singlet).[14,15] The lone pair electrons of the nitrogens are in π orbitals perpendicular to the plane of the ring, making these diketopyrimidines eight-electron, antiaromatic systems, and are thus not "n" electrons. Another possibility could be a tautomeric form of the fluorescent singlet formed in sort of a nonvertical excitation. The n,π^* singlet would likely be populated by intersystem crossing from the fluorescent state and would be longer lived. A precedent for this suggestion is the observation that the excited state of azaanthracene which is photore-

(10) W. A. Summers, J. G. Burr, and S. D. Christian, manuscript in preparation.

(11) O. G. Whitten, J. W. Happ, G. L. B. Carlsen and M. T. McCall, *J. Amer. Chem. Soc.*, **92**, 3499 (1970).

(12) D. G. Whitten and Y. J. Lee, *ibid.*, **93**, 961 (1971).

(13) J. G. Burr and A. Sarpotdar, 27th Southwest Regional Meeting of the American Chemical Society, San Antonio, Tex, Dec 1–3, 1971.

(14) D. G. Whitten and Y. J. Lee, *J. Amer. Chem. Soc.*, **92**, 415 (1970).

(15) Y. J. Lee, D. G. Whitten, and L. Pedersen, *ibid.*, **93**, 6330 (1971).

duced by hydrogen abstraction from the solvent is not the π,π^* fluorescent singlet but a lower lying, n,π^* singlet state;[12] Lee, *et al.*, have summarized the importance of η,π^* singlet states in N heterocycles.[15,16]

Formation of this other longer-lived singlet is shown as step 3 in Scheme I, a step which competes with fluorescence (step 2), formation of the triplet ($\Phi = 10^{-3}$), and with radiationless decay processes which are the predominant reactions depopulating the excited state. Only about 0.3% of the excited molecules are engaged in step 3 and 0.01% of them in step 2 so that steps 3 and 2 are not competitive (for a limited supply of the fluorescent singlet).

In conclusion, the slight increase in photohydration quantum yield with increasing viscosity may be construed as increasing the probability that the photohydration process is a relatively slow bimolecular reaction, since such an increase could be the result of a solvent cage which increases in effectiveness with increasing viscosity.

Acknowledgments. The authors are indebted to Dr. S. D. Christian for stimulating discussion during the preparation of this manuscript. Also, the gift of polyethylene oxide, WSR-301 and WSR-205, from Union Carbide Corp. was greatly appreciated. This work was supported by Grant CA 11418 from the National Cancer Institute, whose assistance is gratefully acknowledged.

(16) A referee has suggested that this photohydrate precursor might be a ground state rearrangement product. Such a possibility is not excluded by the available facts but we have difficulty in visualizing a suitable candidate, at least for DMU, since the enol is the most likely candidate.

Electron Paramagnetic Resonance Spectroscopic Study of the Photoinitiated Polymerization of Alkyl Methacrylates[1]

by P. Smith* and R. D. Stevens

Paul M. Gross Chemical Laboratory, Department of Chemistry, Duke University, Durham, North Carolina 27706
(Received April 14, 1972)

Publication costs assisted by the National Science Foundation

Within a continuous-flow system, dilute oxygen-free solutions of 2,2′-azobis[isobutyronitrile], RN:NR, have been irradiated with near-ultraviolet mercury radiation, this occurring as the liquid passed through the cavity of an X-band electron paramagnetic resonance, epr, spectrometer. By this means transient radicals have been observed. The solvents used were toluene, methyl methacrylate, ethyl methacrylate, isobutyl methacrylate, *n*-butyl methacrylate, and separate mixtures of toluene with each of these esters. The flow rate was varied 30-fold and the temperature from 25 to 39° with little appreciable effect, except as noted. With toluene as the solvent, the only epr signal observed was that from the R· radical. As the toluene was replaced by an increasing proportion of methyl methacrylate keeping the other reaction conditions unchanged, the signal from the R· radical fell in intensity and a new absorption took its place, growing progressively more intense so that when the solvent was undiluted methyl methacrylate there was only a small signal from the R· radical. The new absorption is consistent with addition radicals of structure $R\text{-}(\text{-}CH_2\text{-}C(COOCH_3)\text{-}CH_3\text{-})_n\text{-}CH_2\text{-}\dot{C}(COOCH_3)CH_3$ with the size of n unknown. Kinetic arguments are given which suggest that the average of n may be at least about ten. The results obtained with the use of the other alkyl methacrylates were very similar to those found for methyl methacrylate and are interpretable in a like fashion.

Introduction

There have been many[2-20] electron paramagnetic resonance (epr) studies of liquid systems containing short-lived free radicals of the sort which occur in radical polymerization processes. Most of these studies[2-8,10-17] have been based on rapid-mixing continuous-flow methods of the type discovered by Dixon and Norman[2a] in which the primary radicals are generated with the use of a thermal-redox reaction, and others have relied on the photochemical generation of primary

(1) This work was supported by National Science Foundation Grants No. GP-7534 and GP-17579.

(2) (a) W. T. Dixon and R. O. C. Norman, *J. Chem. Soc.*, 3119 (1963); (b) R. O. C. Norman, P. M. Storey, and P. R. West, *J. Chem. Soc. B*, 1087 (1970); (c) R. O. C. Norman and P. R. Storey, *ibid.*, 1009 (1971); (d) D. J. Edge, B. C. Gilbert, R. O. C. Norman, and P. R. West, *ibid.*, 189 (1971); (e) R. O. C. Norman, *Chem. Soc., Spec. Publ.*, **No. 24**, 117 (1970).

radicals by ultraviolet irradiation.[9,18-20] A variety of unsaturated polymerizable substrates have been investigated with the use of several radical-generating methods of the thermal-redox type.[2-8,10-17] In the case of those polymerizable substrates for which successful results have been reported so far, epr spectra attributed to monomeric addition radicals formed, for example, by addition of a primary radical originating from the redox reaction to a substrate molecule, have been observed and, for some substrates, the epr spectra of polymeric addition radicals have been observed also.

As might be expected, the studies with the use of thermal-redox radical-generating methods have been restricted mostly to reactions in water as the solvent. In principle, this restriction may be circumvented more easily for those reaction systems in which the primary radicals are generated photochemically. However, few radical addition reactions involving[9,18-20] simple aliphatic species have been reported with the use of photochemical methods and in none of the systems[9,20] studied have polymeric addition radicals been observed.

In this present work we have been able to employ a photo-flow method to successfully observe radicals resulting from the addition of a photolytically generated primary radical to each of four methacrylic esters. The primary radical was the 2-cyano-2-propyl radical

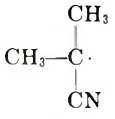

1

produced by the photodecomposition of 2,2′-azobis-[isobutyronitrile], RN:NR[21,22]

$$RN{:}NR + h\nu \longrightarrow N_2 + 2R\cdot \qquad (1)$$

where R· is radical **1**. The methacrylic esters used were of general formula $CH_2{:}C(COOY)CH_3$ where Y was methyl, ethyl, isobutyl, and *n*-butyl. For each ester two epr spectra were observed, one due to R· and the other assigned to addition radicals of general formula

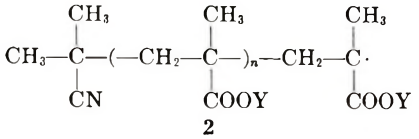

2

with $n \geq 0$. The epr spectrum of R· has been well characterized already[23-29] and our results for this radical are in general agreement with those in previous reports. The coupling constants of the addition radicals are similar to those of the few comparable species successfully characterized with the use of thermal-redox methods.[8,13]

Experimental Section

The epr measurements were made using a standard X-band epr spectrometer system equipped with a V-4531 multipurpose cavity bearing a 60% transmission grid on the front face, the spectra being recorded as the first derivative. As in all our previous epr investigations with the use of this spectrometer system,[30] the Fieldial was calibrated with the use of peroxylamine disulfonate anion in aqueous solution on the assumption that the nitrogen hyperfine coupling constant equals exactly 13.0 G.[31] The sample cells were fashioned from Suprasil to the style of the Varian V-4548 aqueous solution cell but with the internal path length between the two plane faces varying from 0.5 to 2.0 mm and the internal breadth being 9.0 mm. In use, a sample

(3) H. Fischer, *Z. Naturforsch. A*, **19**, 866 (1964).

(4) H. Fischer, *J. Polymer Sci., Part B*, **2**, 529 (1964).

(5) C. Corvaja, H. Fischer, and G. Giacometti, *Z. Phys. Chem. (Frankfurt am Main)*, **45**, 1 (1965).

(6) H. Fischer, *Makromol. Chem.*, **98**, 179 (1966).

(7) H. Fischer and G. Giacometti, *J. Polymer Sci., Part C*, **16**, 2763 (1967).

(8) H. Fischer, *Advan. Polymer Sci.*, **5**, 463 (1968).

(9) H. Hefter and H. Fischer, *Ber. Bunsenges. Phys. Chem.*, **73**, 633 (1969).

(10) P. Smith and P. B. Wood, *Can. J. Chem.*, **45**, 649 (1967).

(11) H. Yoshida and B. Rånby, *J. Polymer Sci., Part C*, **16**, 1333 (1967).

(12) (a) K. Takakura and B. Rånby, *J. Polymer Sci., Part B*, **5**, 83 (1967); (b) *J. Polymer Sci., Part C*, **22**, 939 (1969).

(13) (a) K. Takakura and B. Rånby, *Advan. Chem. Ser.*, **No. 91**, 125 (1969); (b) *J. Polymer Sci., Part A-1*, **8**, 77 (1970).

(14) W. E. Griffiths, G. F. Longster, J. Myatt, and P. F. Todd, *J. Chem. Soc. B*, 530 (1967).

(15) B. D. Flockhart, K. J. Ivin, R. C. Pink, and B. D. Sharma, *J. Chem. Soc. D*, 339 (1971).

(16) T. Kawamura, M. Ushio, T. Fujimoto, and T. Yonezawa, *J. Amer. Chem. Soc.*, **93**, 908 (1971).

(17) A. T. Bullock, G. M. Burnett, and C. M. L. Kerr, *Eur. Polym. J.*, **7**, 791 (1971).

(18) R. Livingston and H. Zeldes, *J. Chem. Phys.*, **44**, 1245 (1966).

(19) R. Livingston and H. Zeldes, *J. Amer. Chem. Soc.*, **88**, 433 (1966), and later papers by these authors.

(20) (a) J. K. Kochi and P. J. Krusic, *ibid.*, **90**, 7157 (1968); (b) J. K. Kochi and P. J. Krusic, *Chem. Soc., Spec. Publ.*, **No. 24**, 147 (1970).

(21) G. Oster and N.-L. Yang, *Chem. Rev.*, **68**, 125 (1968).

(22) (a) P. Smith and A. M. Rosenberg, *J. Amer. Chem. Soc.*, **81**, 2037 (1959); (b) P. Smith and S. Carbone, *ibid.*, **81**, 6174 (1959); (c) P. Smith, N. Muller, and W. C. Tosch, *J. Polymer Sci.*, **57**, 823 (1962); (d) G. S. Hammond, C.-H. S. Wu, O. D. Trapp, J. Warkentin, and R. T. Keys, *J. Amer. Chem. Soc.*, **82**, 5394 (1960); (e) T. Mill and R. S. Stringham, *Tetrahedron Lett.*, 1853 (1969).

(23) (a) J. T. Pearson, P. Smith, and T. C. Smith, *Can. J. Chem.*, **42**, 2022 (1964); (b) P. Smith and S. E. Richard, unpublished work.

(24) A. A. Bichutinskii, A. I. Prokof'ev, and V. A. Shabalkin, *Zh. Fiz. Khim.*, **38**, 983 (1964).

(25) T. S. Zhuravleva, Ya. S. Lebedev', and V. F. Shuvalov, *Zh. Strukt. Khim.*, **5**, 786 (1964).

(26) S. A. Weiner and G. S. Hammond, *J. Amer. Chem. Soc.*, **90**, 1659 (1968); **91**, 986 (1969).

(27) R. Livingston and H. Zeldes, *J. Mag. Resonance*, **1**, 169 (1969).

(28) S. Brumby, *Z. Naturforsch. A*, **25**, 12 (1970).

(29) A. T. Bullock, G. M. Burnett, and C. M. L. Kerr, *Eur. Polym. J.*, **7**, 1011 (1971).

(30) *E.g.*, P. Smith, W. M. Fox, D. J. McGinty, and R. D. Stevens, *Can. J. Chem.*, **48**, 480 (1970).

(31) H. Fischer in "Landolt-Bornstein," Vol. 1, K.-H. Hellwege, Ed., New Series, Group II, Springer-Verlag, Verlin, 1965, p 19.

cell was oriented with its plane faces parallel to the cavity grid. Unless specified otherwise, all the results refer to cells of internal path length 1.0 mm. g values were taken using a wavemeter by comparison with 2,2′-diphenyl-1-picrylhydrazyl on the assumption that its g value is exactly 2.0036,[32] the maximum uncertainty of the results so obtained being ±0.0002. In these determinations a small quantity of polycrystalline 2,2′-diphenyl-1-picrylhydrazyl (Eastman reagent) was placed within a thin-walled Pyrex capillary tube held to the side of the sample cell out of the way of the light beam.

The light source was a convection air-cooled 1-kW Mazda Type ME/D extra-high-pressure mercury discharge lamp (Thorn Electrical Industries, Ltd., London) located in a vented aluminum housing and run from a rectified dc supply with the use of a variable series resistance to control the output.

The arc in this type of mercury lamp operates between the pointed tips of two vertical solid tungsten electrodes within a quartz bulb of nominal diameter 48.0 mm and provides a roughly cylindrical light source which is effectively *ca.* 6.5 mm high and *ca.* 2.5 mm in diameter. The center of the arc was located so that the line between it and the center of the transmission grid of the cavity was perpendicular to the latter and was as short as possible, *viz.* 38 cm. The arc output was focussed on the sample cell with the use of two clear fused-quartz biconvex lenses each of focal length 65 mm and aperture 55 mm located with their centers on and their principal planes perpendicular to the line of centers of the arc, grid, and sample cell. The arc center was at the focal plane of one of these lenses and the sample cell was at that of the other. This arrangement of arc, lenses, cavity, and sample cell was similar to that employed by Livingston and Zeldes[18] but the mercury lamp we used was different from the one in their work.

In between the two lenses there was a cylindrical filter cell with plane fused-quartz faces and of internal path length 7.5 cm through which tap water was flowed, and immediately in front of the grid one or two Corning glass filters were located. One of these filters was of Pyrex (2.0 mm) and the second, of colored glass (Corning CS No. 7-54, 3.0 mm). For most of the work, both glass filters were used, so restricting the radiation reaching the sample cell to the range 290–410 mμ which roughly encompasses the absorption band of the solutions to be photolyzed.[32a] In use, the No. 7-54 filter was prone to suffer thermal fracture, but this possibility was considerably reduced by locating it between the Pyrex filter and the cavity grid. However, for the dilution studies with methyl methacrylate, the No. 7-54 filter was omitted so as to increase the signal intensity. The effectiveness of a lamp as a radical source fell over its operating life, this being compensated by varying the series resistance so that all the data with the use of a given set of filters relate to roughly the same irradiation conditions.

The solution to be irradiated was freshly prepared by dissolving RN:NR in the desired solvent. This solution was deoxygenated by agitating for about 30 min while dispersing a fine stream of bubbles of nitrogen (Matheson, Prepurified) from a fritted gas-dispersion tube, following which, while still under nitrogen, it was drawn through Teflon tubing attached to the lower or entrance tube of the sample cell and, from there, through the sample cell where it was irradiated. The liquid flow was maintained by a partial vacuum, controlled to ±1 cm by means of a manostat and maintained in a 10-l. bottle which was part of the flow system beyond the upper or exit tube of the sample cell. The flow rate was controlled by a Teflon-stemmed glass needle valve and was continuously monitored with a calibrated flow meter.

Temperature measurements of the flowing irradiated solution stream were made by means of a thermocouple with the hot junction in the upper half of the sample cell close to but outside the irradiated zone. Use of the water and glass filters reduced the need for a direct method of sample cooling. The rise in temperature of the stream in passing through the sample cell was less than 0.2° if flow rates of no less than 0.10 ml sec^{-1} were employed and if both glass filters were used, or if the flow rate was no less than 0.12 ml sec^{-1} and the No. 7-54 filter was omitted. However, omission of the No. 7-54 filter while keeping other variables constant caused the signal intensities to increase 10–20%. Variable-temperature measurements were obtained with the inclusion of a heat exchanger in the flow system immediately before the lower entrance tube of the sample cell.

Fresh samples of 2,2′-azobis[isobutyronitrile] (E. I. du Pont de Nemours and Co., Vazo), thiophene-free toluene (Eastman Organic Chemicals, White Label), methyl methacrylate, ethyl methacrylate, isobutyl methacrylate, and *n*-butyl methacrylate (Rohm and Haas Co.) were used without further purification. The RN:NR was shown to be at least 99% pure by ultraviolet absorbance measurements of its solutions in toluene and absolute ethanol both before and after recrystallization from absolute ethanol.[22a] The methacrylic esters contained small concentrations of added inhibitors, but control experiments showed them to have no effect on the observed epr spectra. These control experiments were carried out using ester samples freed of inhibitors by bulb-to-bulb distillation within a high-vacuum line and collecting the middle 80% fraction.

The first measurements were made on 0.4 M solutions of RN:NR in toluene–methyl methacrylate mixtures ranging in concentrations from 0.10 to 1.00 vol-

(32) Reference 31, p 46.

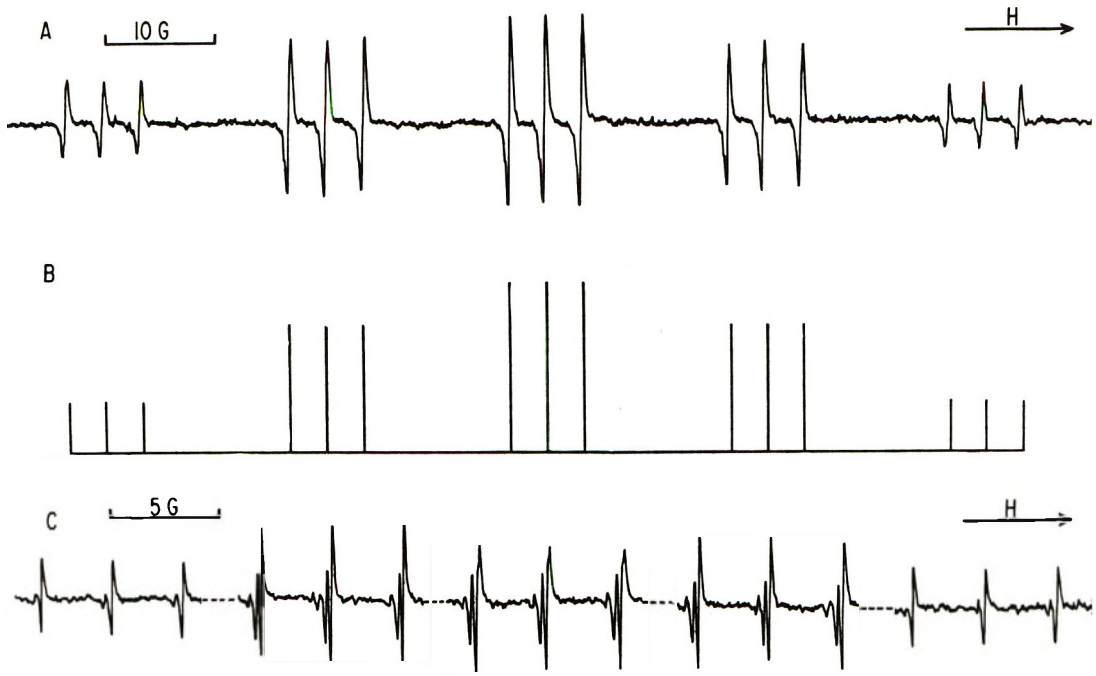

Figure 1. (A) Epr spectrum for the photolysis of RN:NR in toluene: temperature, 25°; [RN:NR], 0.2 *M*; flow rate, 0.10 ml sec^{-1}. Only the central 15 lines are shown. (B) Stick plot for A, the central 15 lines of a septet (1:6:15:20:15:6:1) or triplets (1:1:1) consistent with the radical $(CH_3)_2\dot{C}CN$. (C) The absorption in A with the use of the same chart speed but with the field scan rate halved and the microwave power and amplitude attenuated so as to resolve the second-order spectrum.

ume fraction in methyl methacrylate in roughly 0.10 volume-fraction steps.[33] These solutions were photolyzed at 25 ± 1 and 39 ± 1° at flow rates from 0.12 to 0.50 ml sec^{-1}, the sample cells being of internal path length 1.5 mm for mixtures of less than 0.5 volume fraction of methyl methacrylate. Most of the measurements taken were for 0.2 *M* solutions of RN:NR in toluene, each of the undiluted esters, and equivolume mixtures of toluene and each ester. These solutions were all photolyzed at 25 ± 1 and 39 ± 1°, and intermediate temperatures over the flow rate range 0.10–*ca.* 3.3 ml sec^{-1} with the use of both glass filters; control experiments under these reaction conditions and employing neat methacrylic esters in the absence of RN:NR showed no detectable epr signals.

In runs using neat esters as solvent the ratio [R·]/[A·] where [A·] represents the sum of the concentrations of all the addition radicals present was estimated by comparing peak heights adjusted with respect to degeneracy.[34] For this comparison, a single well-resolved line of similar width from R· and the addition radical were chosen in the same part of the field, due allowance being made for the contribution from noise. For a given ester and temperature, [R·]/[A·] was found to be reproducible to ±10%, the peak heights themselves ranging by ±15% for the same spectrometer recording conditions, and repetitive measurements of [R·]/[A·] on the same reaction mixture showed a standard deviation of 5%. In view of the uncertainties involved in such comparisons, especially with the use of spectra of such low intensity and quality, these estimations are considered to be accurate to ±30–40%.

Results

I. Photolysis of 2,2′-Azobis[isobutyronitrile] in Toluene. The photolysis of RN:NR alone in toluene solution at 25° gave the epr spectrum of radical **1**.[23–29] The signal intensity was high enough to allow an almost completely resolved second-order spectrum to be obtained. The peak-to-peak line width in the absence of second-order splitting was 0.1 G. These spectra are comparable to the best of those observed previously.[28–29] Typical results are given in Figure 1.

The structure of the spectrum and the coupling constants were independent of the temperature over the range 25–39°. The only noticeable effect of raising the temperature from 25 to 39° at constant flow was a slight reduction in peak-to-peak signal intensity, *e.g.*, *ca.* 2% when the flow rate was 0.10 ml sec^{-1}. The peak-to-peak signal intensity at constant temperature was marginally dependent on the flow rate and at the highest flow rates, *ca.* 3.3 ml sec^{-1}, was reduced by *ca.* 5% from that at 0.10 ml sec^{-1}. It was shown

(33) At 25° toluene and methyl methacrylate are both 9.4 *M*, have similar coefficients of thermal expansion [(a) Y. P. Castille in "Polymer Handbook," J. Brandrup and E. H. Immergut, Ed., Interscience, New York, N. Y., 1966, Section VIII.1; (b) J. Timmermans, "Physiochemical Constants of Pure Organic Compounds," Vol. 1, Elsevier, New York, N. Y., 1950, p 152 and Vol. 2, 1965, p 100], and mix with negligible volume change.

(34) P. Smith, J. T. Pearson, P. B. Wood, and T. C. Smith, *J. Chem. Phys.*, **43**, 1535 (1965).

that, at 25° and flow rates of 0.10 ml sec^{-1}, freshly prepared solutions and solutions which had been run once already gave indistinguishable results, showing that the percentage consumption of RN:NR during one pass through the flow system was probably small.

The coupling constants and the g value for radical **1** from our study are compared with those from previous reports in Table I. It will be seen that there is reasonable agreement between our data and the others[26,28] taken under conditions most similar to those of our work.

Table I: Hyperfine Coupling Constants and g Values for the 2-Cyano-2-propyl Radical

Coupling constants, G		g value	Ref
a_N	$a_{\beta\text{-}H}^{CH_3}$		
3.42	20.82	2.0030	23b[a]
3.1	19.5		24[b]
3.5	22		25[c]
3.3	20.3		26[d]
3.35	20.72	2.00290	27[e]
3.3	20.4		28[f]
3.35	20.50	2.0029	g
3.39	21.05	2.00289	29[h]

[a] $TiCl_3$–H_2O_2 radical-generating method,[23a] 0.3 M solution of isobutyronitrile in water, 25°. These data were taken essentially as previously described[23a] except that the epr spectrometer and procedures used were those of the present work. These coupling constants are more reliable than those we previously reported.[23a] The maximum uncertainty in the a values is *ca.* 0.05 G. [b] Thermal decomposition, 10% solution of RN:NR in benzene, 128°. [c] Thermal decomposition, RN:NR in diphenyl or *tert*-butylbenzene, 100–110°. [d] Photolysis, RN:NR in benzene, room temperature. [e] Photolysis, 1 v/v % solution of hydrogen peroxide in isobutyronitrile, 36°. [f] Photolysis, 0.30 M solution of RN:NR in benzene, 20°. [g] Present work, 25°, taken from the first-order spectrum. The maximum uncertainty in the a values is *ca.* 0.05 G. [h] Thermal decomposition, RN:NR in diphenyl, 100°.

II. Photolysis of 2,2′-Azobis[isobutyronitrile] in the Presence of Alkyl Methacrylates. Methyl Methacrylate. The epr spectra resulting from the photolysis of RN:NR in neat methyl methacrylate were complex and essentially independent of flow rate, 0.10–*ca.* 3.3 ml sec^{-1}, at constant temperature but somewhat dependent on temperature at constant flow rate.

Figure 2B shows a typical spectrum observed at 25°. Some of the lines present are from **1** but the contribution from **1** to the whole spectrum is clearly small. The value of $[R\cdot]/[A\cdot]$ at 25° determined from eight scans was 0.25. The remaining lines are centered on a g value slightly higher than that of radical **1** and may be interpreted as being due to the presence of one other radical. The high-field lines are sharper than the low-field lines, an effect which is well known for certain radicals, for example, addition radicals formed from substituted ethylenes in aqueous solution.[3] Also, superimposed upon this trend, certain groups of lines are severely broadened even at high-field values. This second effect is discussed below.

The radical products expected[8,13,21] from this reaction system are of general formula **2** with –Y equal to $-CH_3$. The results of previous investigations[8] of radical addition to this and similar methacrylic esters suggest that for such radicals one would expect strong hyperfine interactions from the protons in the β-CH_3 and $-CH_2$ groups, and a weak, long-range interaction with the three δ-CH_3 group protons.[34] The observed spectrum agrees with expectation, if the two β-CH_2 group protons are assumed to be inequivalent, and may be satisfactorily interpreted as a quartet (1:3:3:1) of doublets (1:1) of quartets (1:3:3:1). With this interpretation, the (1:1) doublets from each of the β-CH_2 group protons form a quartet (1:1:1:1) with the central pair of lines of each quartet accounting for the broadening phenomenon described above. Few radicals similar to **2** have been characterized by epr[8,13] in the liquid phase and, of these, the most comparable is the polymeric addition radical of methacrylic acid formed in aqueous solution and first observed by Fischer.[3,4,8] The nonequivalence of the two protons and broadening of the inner two lines of each β-CH_2 group quartet (1:1:1:1) we have observed is very similar to what Fischer found for the analogous radical of polymethacrylic acid.[3,4,8] This point is discussed below.

A typical spectrum taken at 40° is given in Figure 2C. The spectrum from the addition radical component is essentially the same as that at 25° save that the broadening of the inner two lines of the (1:1:1:1) quartets is reduced. The resulting improvement of the resolution of these groups of inner lines enabled more reliable measurement of the coupling constants. Close inspection of Figure 2 shows that the intensity of the minor signal from R· appears to fall as the temperature is raised. The value of $[R\cdot]/[A\cdot]$ at 39° determined from five scans was 0.16.

The photolysis of RN:NR in toluene–methyl methacrylate mixtures at 25 and 39° gave spectra similar to those reported above for neat methyl methacrylate. As with the use of neat methyl methacrylate, the spectra did not depend appreciably on flow rate. When the concentration of methyl methacrylate was less than *ca.* 1.9 M, the only observable radical was **1** but, as the concentration of methyl methacrylate was increased by roughly 1 M steps to 9.4 M while keeping the temperature constant,[33] this spectrum was gradually replaced by that assigned to radicals of type **2**. The most detailed measurements were carried out at a flow rate of 0.50 ml sec^{-1}. Within experimental accuracy, the structure and line positions of the secondary spectrum were independent of the methyl methacrylate concentration and the flow rate but there was present a temperature-dependent line width phenomenon similar to that noted above. However, the pos-

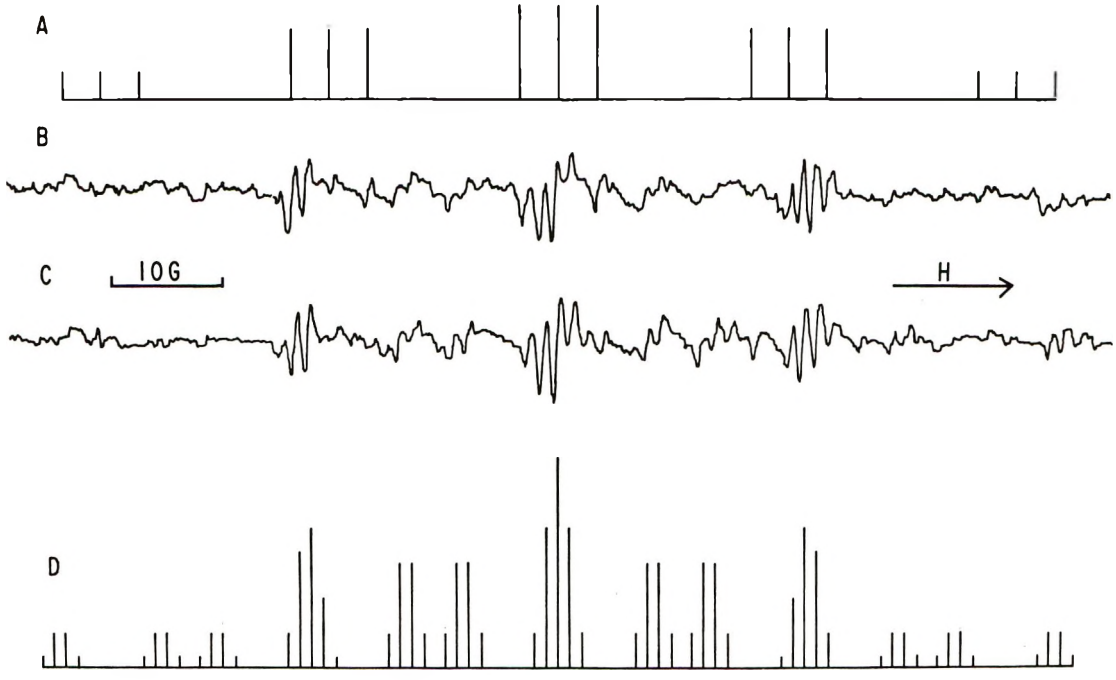

Figure 2. (A) Stick plot as for Figure 1B. (B) Epr spectrum for the photolysis of RN:NR in neat methyl methacrylate: temperature, 25°; [RN:NR], 0.2 *M*; flow rate 0.10 ml sec^{-1}. (C) As for B with the use of the same reaction and recording conditions except that the temperature was 40°. (D) Stick plot for a quartet (1:3:3:1) of doublets (1:1) of doublets (1:1) of quartets (1:3:3:1) consistent with a radical of terminal structure $-CH_2-\dot{C}(COOCH_3)CH_3$.

sible significance of these observations is limited by the low intensity of the contribution from the addition radical component to the total spectrum when the methyl methacrylate concentration was low.

Ethyl, Isobutyl, and n-Butyl Methacrylates. The photolysis of RN:NR in neat ethyl methacrylate gave complex epr spectra. As in the comparable work with methyl methacrylate, the intensity and form of these spectra and, in particular, the positions of the lines and their respective line widths were essentially independent of flow rate, 0.10–*ca.* 3.3 ml sec^{-1}, at constant temperatures, and, on varying the temperature at constant flow rate, the spectra from the addition radical component remained essentially the same except that some groups of lines which were severely broadened at 25° become progressively less broadened as the temperature was raised to 39°. The analysis of the spectrum was similar to that for the case of neat methyl methacrylate, *viz.* in terms of two species, **1**, present to only a minor extent, and a radical of general formula **2** with –Y equal to $-CH_2CH_3$ and for which the temperature-dependent line width effect arises from the inner two lines of the quartets (1:1:1:1) from the two β-CH_2 protons. When the above experiments were repeated with equivolume mixtures of ester and toluene in place of neat ester, the results remained essentially unchanged except that the signal intensity from **1** had grown at the expense of that from the addition radical component.

The results obtained with the use of isobutyl methacrylate and *n*-butyl methacrylate were essentially the same as those described in the case of ethyl methacrylate. Figure 3 gives typical spectra obtained with the use of neat *n*-butyl methacrylate as the solvent.

The data for all the addition radicals observed are presented in Table II. It will be seen that the comparable data for these radicals are very similar. This similarity of the spectroscopic data and the general similarity of all of the results found with these four alkyl methacrylates noted above is not surprising. This follows because these esters differ to only a moderate extent with respect to the alkoxyl group and such differences in the alkoxyl group would not be expected to greatly affect either the kinetic rate constants of the chemical and physical processes taking place in these systems or the epr spectroscopic constants of the radicals formed. This view is supported, for example, by the available data on the relevant polymerization

Table II: Hyperfine Coupling Constants and *g* Values[a] at 39 ± 1° for Addition Radicals of Terminal Structure $-CH_2-\dot{C}(COOY)CH_3$

Alkyl group, –Y	Proton coupling constants, G[b] $a_\beta^{CH_2}$	$a_\beta^{CH_3}$	a_γ^{COOY}
$-CH_3$	14.18, 9.27	22.19	1.13
$-CH_2CH_3$	14.04, 9.33	22.18	1.19
$-CH_2CH(CH_3)_2$	14.32, 9.32	22.14	1.22
$-CH_2CH_2CH_2CH_3$	14.18, 9.22	22.23	1.19

[a] *g* values were all equal to 2.0034. [b] Maximum uncertainty, *ca.* 0.05 G.

rate constants[35] of these alkyl methacrylates and on the coupling constants of related radicals.[3,34]

Discussion

We have been able to observe radicals formed as a consequence of the addition of a primary photolytically generated radical to an ethylenic double bond. Recent epr studies of radical addition to substituted ethylenes using thermal-redox and photochemical radical-generating techniques[2-20] have provided structural and kinetic information useful to an understanding of polymerization processes. However, most of these studies have been by thermal-redox radical-generating methods.[2-8,10-17] The nature of such methods so far found successful has limited the kind of solvent used, water being the usual choice, and hence also the type of substrate and the range of reaction conditions investigated. Another limitation of these thermal-redox methods has stemmed from the necessary presence in the reaction mixture of the components of the redox system, for commonly these components may be the source of secondary processes liable to complicate the overall kinetic analysis of the reactions taking place and, at the same time, may reduce the spectroscopic resolution attainable.[10,15,36]

This new method we report here allows study of radical polymerization processes in nonaqueous solvents more favorable for epr measurements and in which many polymeric addition radicals of interest are more likely to be soluble. Also, our radical-generating system introduces few serious kinetic complications,[37] avoids the possibility of spectroscopic interference from transition metal ions which is a disadvantage commonly accompanying the use of thermal-redox radical-generating methods, and has the added simplicity of rate control inherent to a single-stream, photochemical method compared with that of a double-stream, thermal-reaction method. This last feature of simplicity should make for easier study of the kinetic aspects of the reactions taking place, although this feature was not exploited here.

The structure of the addition radicals we have observed is discussed in Section I and this is followed in Section II by a simple kinetic analysis reaction of our reaction system.

I. Structure of the Radicals Formed. Fischer[3-5,7,8] and his coworkers have extended the accepted rationalization[38-40] of the hyperfine coupling constant of a β proton in a CH group bonded to an sp^2-hybridized α-carbon atom of a radical to account for the epr spectra of addition radicals of structure

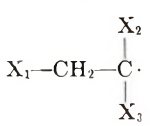

3

formed by the addition of a radical $X_1\cdot$ to a substituted ethylene, $CH_2{:}CX_2X_3$. They have shown that the observed β-CH_2 proton coupling constants can be explained in terms of restricted rotation, incurred by the size and shape of the groups X_1, X_2, and X_3, and the resultant lifetimes of the preferred conformations about the X_1CH_2–$\dot{C}X_2X_3$ bond. For such a radical, the two preferred conformers are schematically represented in Figure 4. Since the molecular geometry about the β-CH_2 carbon atom is fixed, going from one conformation to the other results in the two β-CH_2 protons interchanging their arrangement relative to the $2p_z$ orbital and consequently their coupling constants. From a consideration of the magnitude of the modulation of the hyperfine coupling constants and the lifetimes of conformers A and B in Figure 4 and the theory of rate effects associated with magnetic resonance, they concluded the following.

(a) When the average lifetime of the preferred conformers is small compared to the difference in size of the two β-CH_2 proton coupling constants, the observed spectrum would consist of a triplet (1:2:1).

(b) When the average lifetime of the preferred conformers is large compared to the difference of the size of the two β-CH_2 proton coupling constants, the observed spectrum is a quartet made up of a doublet (1:1) of doublets (1:1) unless, of course, the two β-CH_2 proton coupling constants happen to be equal, *i.e.*, in Figure 4, θ' equals θ''.

(c) When the average lifetime is of intermediate value compared to those of conditions a and b then, as the lifetime in b decreases, the two inner lines of the quartet broaden and move together, finally resulting in coalescence, initially as a broad line and then as a sharp line corresponding to condition a. Throughout these changes the outer lines remain sharp, although their positions change.[41]

All the addition radicals of our study would be expected to be of type **2** and their epr spectra support this view. On the basis of Fischer's model, the observed magnetic inequivalence of the β-CH_2 protons indicates that either a fixed conformation about the X_1CH_2–$\dot{C}X_2X_3$ bond exists or condition b holds. Both conclusions are virtually the same since the former is a limiting case of the latter. Such conclusions are consistent with radicals having bulky X_1 groups and

(35) (a) J. Ulbricht, ref 33a, Section II, 2 and 3; (b) L. J. Young, G. Brandrup, and J. Brandrup, ref 33a, Section II.5.

(36) *E.g.*, P. Smith and P. B. Wood, 151st National Meeting of the American Chemical Society, Pittsburgh, Pa., 1966, Abstract N 90; R. O. C. Norman and P. R. West, *J. Chem. Soc. B*, 389 (1969); R. E. James and F. Silicio, *J. Phys. Chem.*, **75**, 1326 (1971).

(37) *E.g.*, under our reaction conditions, RN:NR and solvents such as toluene are not readily attacked by radicals, see W. A. Pryor and T. P. Fiske, *Macromolecules*, **2**, 62 (1969), and ref 22a–c.

(38) C. Heller and H. M. McConnell, *J. Chem. Phys.*, **32**, 1535 (1960).

(39) J. P. Colpa and E. De Boer, *Mol. Phys.*, **7**, 333 (1964).

(40) E. W. Stone and A. H. Maki, *J. Chem. Phys.*, **37**, 1326 (1962).

(41) R. W. Fessenden and R. H. Shuler, *ibid.*, **39**, 2147 (1963).

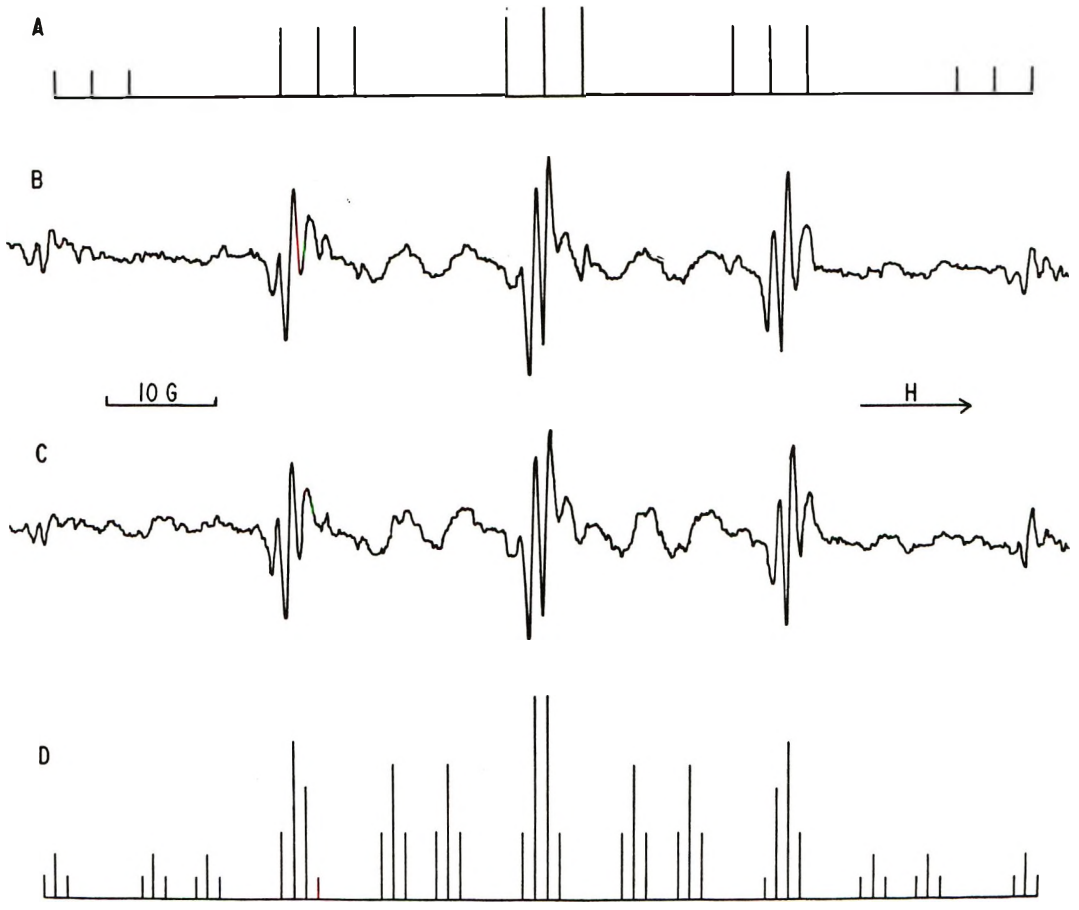

Figure 3. (A) Stick plot as for Figure 1B. (B) Epr spectrum for the photolysis of RN:NR in neat *n*-butyl methacrylate: temperature, 25°; [RN:NR], 0.2 *M*; flow rate 0.27 ml sec^{-1}. (C) As for B with the use of the same reaction and recording conditions except that the temperature was 39°. (D) Stick plot for a quartet (1:3:3:1) of doublets (1:1) of doublets (1:1) of triplets (1:2:1) consistent with a radical of terminal structure $-CH_2-\dot{C}(COOCH_2CH_2CH_2CH_3)CH_3$.

consequently we consider the observed radicals to have structure **2**.

It should be emphasized here that under our experimental conditions the observed spectra are probably made up from contributions from radicals with a range of values of n including zero. In other epr studies[3,5-8,10,13,15] of the homopolymerization processes in the liquid phase where the primary initiating radical was small, such as ·OH, it has been possible to distinguish between the monomeric addition radical and the higher addition radicals, *i.e.*, those for which n is respectively zero and greater than zero, the coupling constants of these two classes of radicals being different.[42] However, in most cases only the coupling constants for the monomeric addition radical have been reported. Table III illustrates the data obtained and includes those for the three cases where the coupling constants for the polymeric addition radical have been assigned.[43]

Included in Table III are related data[12,13a] taken with the simultaneous use of two unsaturated substrates, $CH_2{:}CX_2X_3$ and $CH_2{:}CX_2'X_3'$ in aqueous solution. The reaction conditions were such that the coupling constants could be determined for only one polymeric addition radical

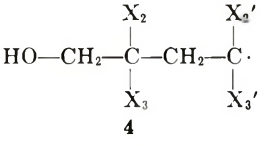

4

this being codimeric. A radical such as **4** is formally similar to the first member of the radical **2** series, n equal to zero, a specific example of **4** in Table III which is perhaps the most similar being

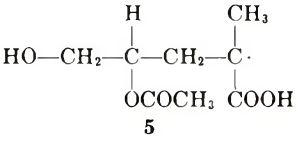

5

Radical **5** has β-CH_2 proton couplings which are unequal and of size similar to those we find for type **2** radicals. On the other hand, the replacement of the

(42) Also, it has been possible[8] to distinguish spectroscopically between the radicals for which n is 0, 1, and >1.

(43) See also ref 10 and P. Neta, *J. Phys. Chem.*, 75, 2570 (1971).

Table III: α and β Proton Coupling Constants of Selected Addition Radicals[a]

Radical	Proton	Proton coupling constants (X_1–), G: HO–	CH_3–[b]	NH_2–[c]	$CH_2(OH)$–[c]	P–[d]	V(OH)–[e,f]	I(OH)–[e,g]
X_1–CH_2–$\dot{C}$(H)(CN)	β-CH_2	28.15[h]	25.19	23.75	22.89			
		28.2[e]					20.6	19.3
	α-H	20.10[h]	20.10	20.45	20.08			
		20.1[e]					20.3	20.0
X_1–CH_2–$\dot{C}$(H)(COOH)	β-CH_2	27.58[h]	23.78	25.03	22.81	21.34[h,i]		
		27.8[e]				22.6[e]	21.2	
	α-H	20.45[h]	20.17	20.17	20.23	22.62[h,i]		
		20.6[e]				21.1[e]	20.4	
X_1–CH_2–$\dot{C}$(H)($COOCH_3$)	β-CH_2	26.62[h]						
	α-H	20.19[h]						
X_1–CH–$\dot{C}$(H)($COOCH_2CH_3$)	β-CH_2	26.67[h]						
	α-H	20.19[h]						
X_1–CH(CH_3)–$\dot{C}$(CN)	β-CH_2	23.92[h]	21.83	19.24	17.82			
	β-CH_3	21.12[h]	19.79	22.35	21.22			
X_1–CH_2–$\dot{C}$(CH_3)(COOH)	β-CH_2	19.98[h]	15.37	16.98	14.45	11.04, 13.75[i]		
		19.9[e]				11.0, 13.8[e]	9.5, 15.5	
	β-CH_3	23.03[h]	21.83	24.19	22.27	22.45[i]		
		23.0[e]				22.4[e]	22.4	
X_1–CH_2–$\dot{C}$(CH_2)($COOCH_3$)	β-CH_2	20.12[h]		16.75				
	β-CH_3	23.01[h]		23.92				
X_1–CH_2–$\dot{C}$(CH_3)($COOCH_2CH_3$)	β-CH_2	18.80[h]						
	β-CH_3	23.02[h]						

[a] All data were taken with the use of $TiCl_3$-based continuous-flow systems, pH *ca.* 1. Unless specified otherwise, the reaction mixture was largely water (monomer concentrations less than 0.6 *M*) at *ca.* 15°. In the interests of brevity, some[2b-d,16] of the available data for monomeric addition radicals from acrylonitrile and acrylic acid which are not readily comparable with the rest of the data in the table have been omitted. [b] Reference 7. [c] Reference 5. When the group X_1– was $CH_2(OH)$– reaction mixture was largely methanol. [d] For a polymeric addition radical analogous in structure to radical 2. [e] References 12 and 13a, at 22 ± 2°. [f] V(OH)– ≡ $CH_2(OH)$–CH($OCOCH_3$)–, from vinyl acetate. [g] I(OH)– ≡ $CH_2(OH)$–C($OCOCH_3$)CH_3–, from isopropenyl acetate. [h] Reference 3. [i] The same spectrum for the polymeric radical was obtained with the use of the $TiCl_3$–H_2O_2[3] and the $TiCl_3$–NH_2OH[5] radical-generating systems. Another estimate for $a_{\alpha-H}^{CH_2OH}$ is perhaps 22.06 G, with the corresponding value of $a_{\alpha-H}^{H}$ being 20.67 G (see ref 3 and 5). [j] References 3 and 4, at 47°; within experimental error the *a* values remain unchanged at 39°.

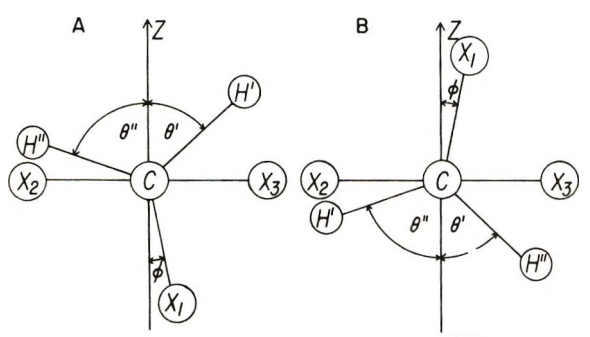

Figure 4. Steric conformations of the X_1–CH_2–$\dot{C}(X_2)X_3$ radical. In the figure, the symbols C and Z, respectively, refer to the α-C–β-C bond with its axis perpendicular to the plane of the paper and to the axis of the $2p_z$ orbital.

α-CH_3 group in **5** with a single hydrogen atom causes the β-CH_2 protons to become magnetically equivalent, consistent with the α-H being smaller than the corresponding α-CH_3 group in **5**. An analogous difference is shown in Table III for the polymethacrylic acid and polyacrylic acid radicals. These examples and other data in Table III and elsewhere[8,13a,44] for similar radicals indicate that, under our experimental conditions, the epr spectra of all members of a given radical **2** series might be indistinguishable.[45] Our experimental results do not conflict with this possibility.

Thus, for the addition radicals in the present investigation where $n \geq 0$, we can reasonably expect β-CH_2

(44) H. Fischer, *Z. Naturforsch. A*, **20**, 428 (1965).

(45) That polymethacryonitrile radicals and polyalkyl methacrylate radicals may have similar steric properties is supported by the available thermodynamic data, *e.g.*, see K. J. Ivin, ref 33a, Section II.9. The extension of this idea to include copolymeric radicals of methacrylonitrile and an alkyl methacrylate seems reasonable.

proton coupling constants of about 10–20 G and β-CH_3 proton coupling constants of *ca.* 23 G. However, *a priori* it is not known for certain whether the coupling constants of the β-CH_2 group protons should be unequal or equal. Hence, our interpretation of the spectrum attributed to all the radical **2** series is not inconsistent with expectation. However, it is still possible that the CH_2 proton coupling constants for **2** when n equals zero are equal or unequal and appreciably different from those for the higher members of the series and for this not to be clearly evident in the spectrum. For example, the relative concentration of the monomeric addition radical may be low; or, if this is not low, fortuitous overlap takes place between the spectrum of the monomeric addition radical and that from the rest of the radical **2** series. Even under conditions which were the most favorable to the observation of monomeric addition radicals, we observed no spectra which could not be interpreted in terms of radical **1**, and the radicals to which we have assigned $n \geq 0$. Although we cannot rigorously exclude contributions to the observed spectra from radicals with n equal to zero, it is reasonable to suppose that the proportion of such radicals relative to the total other addition radicals could be small. This view is supported by the kinetic arguments given in Section II.

The epr spectra of the addition radicals we observed exhibited a similar, anomalous intensity distribution for the β-CH_2 proton quartet. On the basis of Fischer's model, this anomalous intensity distribution indicates that the radicals conform to Fischer's case c but approach his case b. Fischer noticed a similar intensity distribution phenomenon in his investigation of the polymerization in aqueous solution of methacrylic acid initiated with the use of the titanous chloride–hydrogen peroxide radical-generating system.[3,4,8] As the temperature is raised, keeping the other reaction variables constant, we observe a sharpening of the inner lines of the β-CH_2 proton quartet. This can only happen if the motion about the X_1CH_2–$\dot{C}X_2X_3$ bond becomes more restricted, allowing the lifetimes of the preferred conformers to approach values which will more closely satisfy those needed for case b to be operative. One effect possibly contributing to the apparent increase in the restriction to rotational motion about the X_1CH_2–$\dot{C}X_2X_3$ bond on so raising the temperature of the reaction mixture is that the X_1 group becomes larger, *i.e.*, in the sense of occupying a bigger effective volume even if the size of n remains unchanged. There are sufficient data available in the case of methyl methacrylate to develop this point further. Methyl methacrylate is a good solvent for polymethyl methacrylate molecules, the θ temperature being $-163 \pm 50°$.[46] Consequently, there will be a tendency for the X_1 group in such molecules to expand with increase in temperature.[47] However, because the solvent is good, it is possible that this expansion would have little effect on the steric hindrance to motion about the X_1CH_2–$\dot{C}X_2X_3$ bond. While less is known about the comparable solubility data for the other alkyl methacrylates[47] it is not unlikely that similar considerations would apply to them. A second possibly contributing effect is that, as argued in Section II, the average size of n in radical **2** will probably tend to rise as the temperature is raised while keeping the other reaction variables unchanged. This rise would also tend to increase the volume of the X_1 group and so perhaps act in the same sense as the temperature induced expansion discussed above. But, here again, because the solvent is good, the consequential effect on the steric hindrance to rotation about the X_1CH_2–$\dot{C}X_2X_3$ bond might not be large. A third effect, which will tend to oppose the other two postulated effects, stems from the fact that the rotational motion about X_1CH_2–$\dot{C}X_2X_3$ bond in the absence of the first two phenomena would be expected to have the positive energy of activation usually associated with a hindered internal rotation.[48] Examples of this effect in the case of simple radicals in solution are well known.[2e,3,8,20b]

Our observation for all the type **2** radicals was that the central two lines of the (1:1:1:1) quartets sharpened as the temperature was raised while keeping the other reaction variables constant, indicating a decrease in rotational freedom about the X_1CH_2–$\dot{C}X_2X_3$ bond. On the basis of the three effects discussed above, this observation suggests that, over the limited temperature range covered in our work, the first two outweigh the third.[49] The results in the literature most comparable to ours are those of Fischer[3,4,8] for the polymeric addition radical from methacrylic acid in aqueous solution. Fischer's results include those of a fragmentary investigation of the effect of varying the temperature over the range 39 to 47°, these appearing to be similar to those in our work.

It would have been rewarding to study these systems over a temperature range wider than that employed here. Unfortunately, at lower temperatures, the azo compound is less soluble, resulting in signals which were insufficiently intense and, at higher temperatures, the reaction solutions thermally polymerize too quickly for them to be examined. This problem might be resolved with the use of different azo compounds. Use of different azo compounds would be interesting for another reason. For example, a sym-

(46) H.-G. Elias, G. Adank, Hj. Dietschy, O. Etter, U. Gruber, and F. W. Ibrahim, ref 33a, Section IV.4.

(47) P. J. Flory, "Principles of Polymer Chemistry," Cornell University Press, Ithaca, N. Y., 1953, Chapter 14.

(48) F. A. Bovey, "Polymer Conformation and Configuration," Academic Press, New York, N. Y., 1969; H. Morawetz, "Macromolecules in Solution," Interscience, New York, N. Y., 1965.

(49) Of course, it is possible that our observation stems partly from effects we have not considered, for example, perhaps one likely to be significant for macroradicals of moderately large molecular weight in a good solvent of low viscosity. We prefer to delay speculation on such effects until we have more extensive experimental results available.

metrical azo compound, R'N:NR', other than 2,2'-azobis[isobutyronitrile] would result in the formation of radicals of structure **2** but with R'– in place of R–. With a suitable choice of azo compounds, the epr spectrum of R'– initiated radicals would be expected[3-5,7,8] to depend on the identity of R' if n were equal to zero but to be insensitive to the identity of R' if the average value of n were large.[50]

II. Elementary Kinetic Analysis of the Reaction System. The usual simple mechanism for radical polymerization[51] applied to an alkyl methacrylate, M_1, would involve step 1 plus initiation, propagation, and termination steps with rate constants k_i, k_p, and k_t, respectively, k_p and k_t being assumed independent of radical size. Hydrogen-atom transfer processes between a radical and a nonradical, such as M_1, may be neglected because no epr evidence for these was found, in agreement with the relevant kinetic information in the literature.[35b,37]

During stationary-state conditions the average lifetime of a kinetic chain, τ, and the kinetic chain length, ν, respectively, are given[51] by

$$\tau = 1/(2k_t[C\cdot]) \quad (2)$$

$$\nu = k_p[M_1]/(2k_t[C\cdot]) \quad (3)$$

where $[C\cdot]$ is the stationary-state concentration of addition radicals of all values of n. From the intensity of the spectra we observed, $[C\cdot]$ may be estimated to be *ca.* 1×10^{-6} M. Reliable rate constant data applicable to the above mechanism are available for methyl methacrylate, for which k_p and $2k_t$ at 25° are 2×10^2 and 2×10^7 M^{-1} sec^{-1}, respectively.[35,52] The corresponding rate constant data for the other esters studied are less well known than but similar to those for methyl methacrylate.[35] Hence, the discussion will be confined to methyl methacrylate. It follows from eq 2 and 3 that for methyl methacrylate at 25° undiluted with toluene, τ is 5×10^{-2} sec and ν is 1×10^2.

The flow-rate range used was 0.10–*ca.* 3.3 ml sec^{-1} which corresponds to a velocity range through the sample cell of 1.1–*ca.* 37 cm sec^{-1}. The irradiated zone of the sample cell being 2 cm long, the residence time of a flowing element of the reaction mixture within the irradiated zone may be estimated to be 1.8–*ca.* 0.053 sec. The dependence of the local concentration of propagating radicals, $[C\cdot]_L$, on residence time, t, within the irradiated zone under constant reaction conditions is given[51] by

$$[C\cdot]_L = [C\cdot] \tanh (t/\tau) \quad (4)$$

From eq 4, when (t/τ) is 1.0–2.0, $[C\cdot]_L/[C\cdot]$ equals 0.76–0.96. Clearly, at the flow rate most commonly employed, 0.10 ml sec^{-1}, the stationary state is essentially realized over all but the first 5–10% of the irradiated zone. Also, there is the possibility that τ might be less than 5×10^{-2} sec, so making the stationary-state concentration apply to an even higher percentage of the irradiated zone. Such might be the case if the polymeric radicals were predominately of very short chain length, for there is evidence that k_t tends to increase as the chain length falls,[6,26,51,53] the extent of the increase being perhaps as much as one or two powers of 10. However, there is evidence that this increase in k_t is possibly[6,9,51] accompanied by a parallel increase of comparable magnitude in k_p so that the size of ν may not change much. Nevertheless, the evidence available clearly suggests that *perhaps* ν could be between 1×10 and 1×10^2.

The above reaction scheme does not allow for the possibility that primary radical termination[51] occurs, the rate constant being k_t'. It is plausible to assume that the values of k_t and k_t' would be determined by the rate of diffusion together of the reacting radicals through the reaction medium,[51,54] and the smaller the radicals the larger the k value. Consequently, we may crudely assume that, under the same reaction conditions, the reactivity of the R· radical is of the same order of magnitude as that of the monomeric addition radical, in which case the possible contribution of primary radical termination to our reaction system may be incorporated without important modification to our conclusions above.

When considering the possible effect of primary radical termination, the value of k_i becomes significant. There appear to be no data for k_i in the literature. However, it seems[55] that long-chain polymethacrylonitrile radicals and long-chain polymethyl methacrylate radicals are similar in reactivity. Consequently, k_i and k_p for addition radicals of short chain length may be assumed to be roughly equal. This assumption amounts to regarding R· as kinetically equivalent to a propagation radical and, hence, its adoption also leads to no serious changes to our conclusions.

Another possible complication stems from the probability that the formation of R· in step 1 is *via* the consecutive steps

$$\textit{trans}\text{-RN:NR} + h\nu \longrightarrow \textit{cis}\text{-RN:NR} \quad (5)$$

$$\textit{cis}\text{-RN:NR} \longrightarrow N_2 + 2R\cdot \quad (6)$$

the trans isomer being the expected form of the starting material.[22e] As far as we are aware, the rate con-

(50) Experiments of this sort are in progress, these indicating that the average value of n is large: P. Smith, R. A. DeLorenzo, and L. B. Gilman, unpublished results.

(51) A. M. North, "The Kinetics of Free Radical Polymerization," Pergamon Press, Oxford, 1966, Chapters 1–6.

(52) G. V. Schulz, G. Henrici-Olivé, and S. Olivé, *Z. Phys. Chem. (Frankfurt am Main)*, **27**, 1 (1960).

(53) See also ref 9 and G. Czapski, *J. Phys. Chem.*, **75**, 2957 (1971).

(54) P. E. M. Allen and C. R. Patrick, *Makromol. Chem.*, **47**, 154 (1961).

(55) C. H. Bamford and A. D. Jenkins, *Trans. Faraday Soc.*, **59**, 530 (1963).

stant for step 6 is not known.[22e] However, because the intensity of the epr signals observed was not found to depend significantly on the flow rate, the rate of step 6 was not considered to be limiting.[56]

The influence of temperature on ν may be considered with the use of the expression

$$\nu = k_p[M_1]/(2Rk_t)^{1/2} \quad (7)$$

which follows from eq 3 if R is the rate of production *via* step 1 of R· radicals available for the initiation and primary radical termination processes. The temperature dependence of the right-hand side of eq 7 is probably determined largely by that of $k_p/(k_t)^{1/2}$ because the temperature dependence of $[M_1]$ is comparatively insignificant[57] and that of R is likely to be small also.[47,58,59] The overall Arrhenius energy of activation for the term $k_p/(k_t)^{1/2}$ is probably[35] 3–5 kcal mol^{-1} indicating that $\nu_{39°}/\nu_{25°}$ is about 1.3–1.5.

The influence of temperature on τ may be estimated with the use of the relationship

$$\tau = 1/(2Rk_t)^{1/2} \quad (8)$$

which follows from eq 2, 3, and 7. On the assumption that k_t has[35] an Arrhenius energy of activation of 0–4 kcal mol^{-1}, it follows that $\tau_{39°}/\tau_{25°}$ is about 1.0–0.9. This small temperature dependence clearly does not affect the conclusion above that the stationary state is essentially realized in most of the experiments carried out.

The stationary state radical size distribution for the simple mechanism outlined in the first paragraph of this section is given[51] by the function

$$F_x = R(M_1)_x\cdot/[C\cdot] = \nu^{-1}(1 + \nu^{-1})^{-x} \quad (9)$$

where $R(M_1)_x\cdot$ is the addition radical with n equal to $(x - 1)$. It follows that

$$F_1 = R(M_1)_1\cdot/[C\cdot] = 0.01 \quad (10)$$

if ν is 1×10^2. If ν is 1×10–1×10^2, then F_1 becomes 0.01–0.1. If, as implied above, R· may be crudely regarded as the first formed member of the propagation radical series, then $[R\cdot]/[C\cdot]$ for neat methyl methacrylate at 25° equals 0.20 as we found $[R\cdot]/[A\cdot]$ to be 0.25. Bearing in mind the accuracy and reproducibility of our experimental determinations of $[R\cdot]/[A\cdot]$ and all the assumptions made with respect to the applicability of eq 9, there is reasonable agreement between experiment and theory.

Furthermore, it was argued above that $\nu_{39°}/\nu_{25°}$ is about 1.3–1.5, in which case it follows that $(F_1)_{39°}/(F_1)_{25°}$ equals *ca.* 0.7. Our results on the temperature variation of $[R\cdot]/[A\cdot]$ for neat methyl methacrylate give an experimental value for $(F_1)_{39°}/(F_1)_{25°}$ of *ca.* 0.8 which is in accord with the theoretical value. Such good correlation is regarded as somewhat encouraging.

The foregoing kinetic treatment of the reaction system tacitly assumes that the only radicals of concern are within the irradiated zone of the sample cell and that the light flux within this zone is uniformly distributed. The first assumption bears on the correct interpretation of our general observation that the epr signal intensity for a given reaction system was not significantly dependent on flow rate, keeping the other reaction variables constant. If this first assumption were valid then the observed lack of significant dependence of the epr signal intensity on flow rate would suggest τ to be considerably less than 5×10^{-2} sec. A more plausible explanation of this observation is perhaps that in the unirradiated zone[60] of the sample cell immediately following irradiated zone sufficient radicals are detected by the epr spectrometer to help maintain the total signal intensity constant.

Under constant reaction conditions, the average value of the concentration of propagating radicals in the irradiated zone, $[C\cdot]_I$, may be calculated by integrating eq 4 to give

$$[C\cdot]_I = [C\cdot](\tau/t) \ln \{\cosh (t/\tau)\} \quad (11)$$

where the velocity of flow, v, through the sample cell equals $2/t$ because the length of the irradiated zone is 2 cm. Radicals in the unirradiated zone follow a second-order decay law, so that

$$[C\cdot]_L = [C\cdot]_0/(1 + 2k_t t'[C\cdot]_0) \quad (12)$$

where $[C\cdot]_0$ and t', respectively, are the value of $[C\cdot]_L$ at the start[61] of the unirradiated zone and the residence time of the flowing element of reaction mixture within the unirradiated zone. It follows by integrating eq 12 that the average concentration of propagating radicals in the unirradiated zone, $[C\cdot]_U$, is

$$[C\cdot]_U = (\ln \{1 + 2k_t t'[C\cdot]_0\})/(2k_t t') \quad (13)$$

An indication of the size of the effect being considered is provided by the dependence on v of an appropriate expression for the average concentration of propagating radicals in both zones, $[\overline{C\cdot}]$, such as

$$[\overline{C\cdot}] = (2[C\cdot]_I + [C\cdot]_U)/3 \quad (14)$$

This particular expression assumes the length of the unirradiated zone to be 1 cm, which is a reasonable estimate.[60,62] Use of eq 14 with data applicable our reaction systems indicates that this effect could account for the insignificant variation of the signal intensity with change in flow rate.

(56) The dependence of the epr signal intensity on flow rate is taken up below.

(57) *E.g.*, M. S. Matheson, E. E. Auer, E. B. Bevilacqua, and E. J. Hart, *J. Amer. Chem. Soc.*, 71, 497 (1949).

(58) A. M. North, "The Collision Theory of Chemical Reactions in Liquids," Methuen, London, 1964, Chapter 7.

(59) *E.g.*, G. S. Hammond and J. R. Fox, *J. Amer. Chem. Soc.*, 86, 1918 (1964).

(60) The length of the plane-faced section of the sample cell was *ca.* 4.8 cm.

(61) This value of $[C\cdot]_L$ is not necessarily the stationary state value, $[C\cdot]$ (see eq 4).

(62) The center of the irradiated zone was *ca.* 2.2 cm from the upper end of the plane-faced section of the sample cell.

Vacuum-Ultraviolet Photolysis of the C_4H_6 Isomers. V. Methylenecyclopropane

by Kevin L. Hill and Richard D. Doepker*

Department of Chemistry, University of Miami, Coral Gables, Florida 33124 *(Received April 24, 1972)*

The vacuum-ultraviolet photolysis of methylenecyclopropane was carried out in a static system using "gettered" xenon (147.0 nm) and krypton (123.6 nm) resonance lamps. Hydrogen, acetylene, ethylene, allene, and vinylacetylene accounted for nearly 90% of the observable decomposition products. Identification of H atoms and methyl and vinyl radicals was made quantitative by the use of numerous additives such as NO, O_2, H_2S, D_2S, NH_3, and ND_3. Four major primary processes were found and primary quantum yields assigned: $CH_2{=}C(CH_2)_2 + h\nu \rightarrow C_2H_2 + C_2H_4$, $CH_2{=}C(CH_2)_2 + h\nu \rightarrow 2H + C_4H_4$, $CH_2{=}C(CH_2)_2 + h\nu \rightarrow 2C_2H_2 + H_2$, $CH_2{=}C(CH_2)_2 + h\nu \rightarrow CH_2 + C_3H_4$. Formation of allene *via* an H atom reaction channel was established through mercury-photosensitized dissociation of deuterium in the presence of methylenecyclopropane: $CH_2{=}C(CH_2)_2 + D \rightarrow C_3H_4 + CH_2D$.

Introduction

Over the past few years our laboratory has been engaged in a program to determine the primary and secondary reaction channels for the neutral excited (8.4–10.0 eV) C_4H_6 molecules. The vacuum-ultraviolet photolysis of methylenecyclopropane (MCP) reported here was part of this study.

An early investigation by Frey[1] examined the decomposition and isomerization of excited methylenecyclopropane generated through the insertion of a methylene radical into a double bond of allene. Major products were acetylene and ethylene, in equal amounts, and four C_4H_6 isomers: 1,3- and 1,2-butadiene and 1- and 2-butyne. Brinton[2] carried out the direct (253.7 nm) and $Hg(6^3P_1)$ photolysis of methylenecyclopropane and found primarily acetylene and ethylene again in nearly equal amounts. Small yields of allene and hydrogen were also reported. The behavior of methylenecyclopropane in the presence of added oxygen indicated that the mechanism was intramolecular, rather than the result of radical processes. The primary processes postulated by Brinton[2] were as follows

$$\text{MCP} + h\nu \longrightarrow C_2H_2 + C_2H_4 \qquad (1)$$

$$\text{MCP} + h\nu \longrightarrow CH_2 + C_3H_4 \qquad (2)$$

In recent work in our laboratory the vacuum-ultraviolet photolyses of cyclobutene[3] and 1-butyne[4] have been studied. Both of these systems had major primary processes involving the elimination of hydrogen atoms. It was further found that the resulting hydrogen atom added to the parent molecule, producing a (C_4H_7') species with excess internal energy capable of undergoing decomposition.

$$H + \text{c-}C_4H_6 \longrightarrow H + \text{1,3-}C_4H_6 \qquad (3)$$

$$H + \text{1-}C_4H_6 \longrightarrow CH_3 + C_3H_4(\text{allene}) \qquad (4)$$

Although an early study of the vacuum-ultraviolet photolysis of 1,2-butadiene[5] failed to recognize the process, later studies[6] show a similar mechanism for the formation of methylacetylene and allene for 1,2-butadiene.

Experimental Section

Materials. Methylenecyclopropane was prepared by the method of Anderson[7] which was a modification of the method of Gragson, *et al.*[8] This preparation involves the chlorination of methallyl chloride followed by the treatment of the product with Mg in tetrahydrofuran. Purification was achieved through vapor chromatography using a 35-ft dimethylsulfolane column followed by a 25-ft squalane column. A 1% acetylene-ethylene impurity was removed through low-temperature distillation. D_2S, ND_3, and D_2 were obtained from Merck Sharp and Dohme, Montreal, Canada, and used without further purification. Purification of other materials used has been described in previous studies.[3,9]

Irradiation and Analysis. The vacuum-ultraviolet photolysis of methylenecyclopropane was carried out in a "standard" static system using "gettered" xenon (147.0 nm) and krypton (123.6 nm) resonance lamps. Analysis was performed with vapor chromatography (25-ft squalane column) and mass spectrometry (CEC-21-103 C) as reported previously.[3,4] Quantum yields were determined for xenon using 1-butyne $\Phi_{C_4H_4} = 0.34$[4] and for krypton using cyclobutene $\Phi_{C_2H_2} = 0.40$.[3]

(1) H. M. Frey, *Trans. Faraday Soc.*, **57**, (1961).
(2) R. K. Brinton, *J. Phys. Chem.*, **72**, 321 (1968).
(3) A. DeLeon and R. D. Doepker, *ibid.*, **75**, 3656 (1971).
(4) K. L. Hill and R. D. Doepker, *ibid.*, **76**, 1112 (1972).
(5) R. D. Doepker and K. L. Hill, *ibid.*, **73**, 1313 (1969).
(6) R. D. Doepker and J. L. White, to be submitted for publication.
(7) B. C. Anderson, *J. Org. Chem.*, **27**, 2720 (1962).
(8) J. T. Gragson, K. W. Greenlee, J. M. Derfer, and C. E. Boord, *J. Amer. Chem. Soc.*, **75**, 3344 (1953).
(9) R. D. Doepker, *J. Phys. Chem.*, **72**, 4037 (1968).

Results

Using 1-butyne as an actinometer, the quantum yields of the major products from the 147.0-nm photolysis of methylenecyclopropane were determined. Table I reports the quantum yields of the products as determined in these experiments. Moreover, Table II reports similar quantum yields for the products of the 123.6-nm photolysis based on cyclobutene as an actinometer. At both wavelengths the vinylacetylene formation was independent of pressure as well as unaffected by the presence or absence of radical scavengers. Allene, on the other hand, exhibited a moderate pressure dependency.

Table I: Photolysis of Methylenecyclopropane, Quantum Yields at 147.0 nm

c-C_4H_6 P, Torr	Additive (P, Torr)	H_2	C_2H_2	C_2H_4	C_3H_4[a]	C_4H_4
1.0	None	nd[b]	0.53	0.43	0.33	0.21
0.2	NO (0.01)	nd	0.55	0.46	0.51	0.20[c]
0.5	NO (0.03)	nd	0.54	0.44	0.32	0.19
1.0	NO (0.05)	0.078	0.53	0.42	0.25	0.20
5.0	NO (0.25)	nd	0.50	0.43	0.20	0.21
10.0	NO (0.5)	0.075	0.52	0.41	0.16	0.20
23.0	NO (1.5)	nd	0.52	0.43	0.15	0.20
1.0	O_2 (0.05)	nd	0.51	0.41	0.25	0.19
1.0	N_2 (180) NO (0.07)	nd	0.53	0.45	0.12	0.20[c]
1.0	N_2 (255)	nd	0.54	0.40	0.12	0.20[c]

[a] Allene. [b] nd = not determined. [c] Estimated.

Table II: Photolysis of Methylenecyclopropane, Quantum Yields at 123.6 nm

c-C_4H_6 P, Torr	Additive (P, Torr)	H_2	C_2H_2	C_2H_4	C_3H_4[a]	C_4H_4
1.0	None	nd[b]	0.31	0.21	0.21	0.16
0.2	NO (0.01)	nd	0.29	0.21	0.33	0.15[c]
0.5	NO (0.03)	nd	0.32	0.22	0.28	0.15
1.0	NO (0.05)	0.11	0.29	0.21	0.18	0.15
5.0	NO (0.05)	0.09	0.30	0.20	0.14	0.17
10.0	NO (0.5)	0.09	0.28	0.24	0.11	0.14
1.0	O_2 (0.05)	nd	0.25	0.18	0.20	0.15
1.0	N_2 (78)	nd	0.33	0.25	0.068	0.17[c]
1.0	N_2 (226) NO (0.07)	nd	0.28	0.21	0.063	0.15[c]

[a–c] See corresponding footnotes in Table I.

In addition to the data given in Tables I and II, a few general observations should be stated.

(1) When a radical scavenger was present, relative product yields were insensitive to irradiation time. This study corresponded to conversion of from 0.01 to 0.8% decomposition (based on the yield of vinylacetylene). Normal conversions were held to approximately 0.02% when no radical scavenger was present or below 0.5% with either oxygen or nitric oxide present.

(2) An increase in NO from 5 to 20% of the MCP pressure had no noticeable effect on the relative yields of products observed.

(3) Minor products observed in the presence of radical scavenger in the 147.0-nm photolysis included methylacetylene, $\Phi = 0.02$; propylene, $\Phi = 0.01$; and 1,3-butadiene, $\Phi = 0.02$. The same products were observed at 123.6 nm to the following extent, methylacetylene, $\Phi = 0.02$; propylene, $\Phi = 0.02$; and 1,3-butadiene, $\Phi = 0.03$. Both methane and ethane, as well as isobutene, were observed when no radical scavenger was present.

In order to differentiate between a bimolecular reaction channel and a unimolecular one, common practice in radiation chemistry would call for the photolysis of a 1:1 mixture of methylenecyclopropane-d_6:methylenecyclopropane-d_6. Unfortunately, it was not economically possible to obtain methylenecyclopropane-d_6. Therefore, in an attempt to elucidate the formation of hydrogen and allene and to establish the presence of radical species in the photolysis system, a series of experiments were designed to substitute for the unavailability of methylenecyclopropane-d_6.

The mercury-photosensitized dissociation of deuterium in the presence of MCP (Table III) led to the formation of acetylene, ethylene, and allene as major products with allene contributing nearly 50% of the total yield of observable products when NO was present. Methane, ethane, and isobutene become important products when the NO was omitted from the photolysis mixture. Mass spectral analyses of the allene and ethylene fraction are given in Table III. Analysis of the ethane produced in the unscavenged experiments gave nearly 95% ethane-*1,2*-d_2. Methane was not examined.

Table III: Mercury-Photosensitized Dissociation of Deuterium in the Presence of Methylenecyclopropane

Pressure of reactants P, Torr			Relative yields				
			Acetylene	Ethylene		Allene	
c-C_4H_6	D_2	NO	Total	C_2H_3D	C_2H_4	C_3H_3D	C_3H_4
0.30	12.0	0.0	22	5	30	1	99
0.30	12.0	0.1	26	2	36	0	100

In other experiments H_2S and D_2S (Table IV) were used as diagnostic tests for free radicals.[10] Recently Collin, *et al.*,[11] demonstrated the use of H_2S as a quantitative reagent for the determination of radical yields such as CH_3 and C_2H_5 in olefin systems. Table IV

(10) P. Ausloos and S. G. Lias, *J. Chem. Phys.*, **44**, 521 (1966).

(11) G. J. Collin, P. M. Perrin, and C. M. Gaucher, private communication.

Table IV: Photolysis of Methylenecyclopropane in the Presence of H_2S

c-C_4H_6 P, Torr	Additive (P, Torr)	Relative yields, vinylacetylene = 100 Methane	Acetylene	Ethylene	Allene
		147.0 nm			
1.0	None	6	258	202	130
1.0	H_2S (0.06)	114	262	231	126
1.0	H_2S (0.13)	133	268	236	137
1.0	H_2S (0.28)	155	267	220	122
1.0	H_2S (0.42)	168	298	240	124
		123.6 nm			
1.0	None	7	197	128	135
1.0	H_2S (0.08)	181	186	148	136
1.0	H_2S (0.15)	195	186	152	133
1.0	H_2S (0.26)	214	180	160	136
1.0	H_2S (0.40)	220	188	172	140

reports results of similar experiments carried out for methylenecyclopropane.

In a few of the experiments similar to those in Table IV, D_2S was substituted for H_2S, and selected products examined with mass spectrometry. For a 1.0 Torr MCP sample the CH_3D/CH_4 ratio increased from 0.69 to 2.6 when D_2S pressure was raised from 0.1 to 0.15 Torr. The HD/H_2 ratio increased from 0.16 to 0.35 over the same D_2S pressure change. On the other hand the ratio of C_2H_3D/C_2H_4 remained nearly constant at 0.15 from a D_2S pressure of 0.1 to 0.2 Torr. In all cases the allene fraction consisted of purely C_3H_4. All of these experiments were carried out with the krypton resonance radiation.

In an earlier study[3] NH_3 and ND_3 were photolyzed in the presence of cyclobutene as a test for the importance of hydrogen atom in the vacuum-ultraviolet photolysis of cyclobutene. Similar tests were carried out in the case of methylenecyclopropane of which those containing NH_3 are reported in Table V. In addition to those given there, ND_3 was used in the place of NH_3 for a 9/1 mixture of ND_3/MCP. The ethane formed contained appreciable $C_2H_4D_2$, while allene was entirely C_3H_4.

Discussion

When methylenecyclopropane (I.P. = 10.7 eV)[12] absorbs a photon of energy 8.4 eV (147.0 nm) or 10.0 eV (123.6 nm) only electronically excited neutral molecules will be produced. If the lifetime of the resulting excited MCP molecule is less than the collision interval at the pressure range used in this study, fragmentation

$$CH_2{=}C(CH_2)_2 + h\nu \longrightarrow (C_4H_6)^* \qquad (5)$$

of the excited species will occur which is independent of total pressure. A long-lived excited state on the other hand would manifest itself through decreasing fragmentation with increasing total pressure. Brinton[2] observed such a long-lived state in the 253.7-nm photolysis of MCP. In the more recent studies on 1-butyne[4] and cyclobutene,[3] no long-lived state was observed in the vacuum-ultraviolet photolysis.

On examination of Tables I and II only allene exhibits a pressure dependence characteristic of a product from a long-lived excited state. However, this pressure effect is best explained through a hydrogen atom mechanism characteristic of the C_4H_6 isomers thus far studied (see Discussion; Allene Formation).

Vinylacetylene Formation. It was noted in the Results section that vinylacetylene formation was independent of MCP pressure and unaffected by the presence or absence of additives. The formation of vinylacetylene in the vacuum-ultraviolet photolysis of the C_4H_6 isomers thus far studied (1,3-butadiene,[9] 1,2-butadiene,[5,6] cyclobutene,[3] 1-butyne,[4] and 2-butyne[13]) is consistent with a primary process involving the elimination of two hydrogen atoms. This process is also consistent with the data presented for methylenecyclopropane.

$$(C_4H_6)^* \longrightarrow 2H + C_4H_4 \qquad (6)$$

Brinton[2] did not observe this process in the 253.7-nm photolysis. The photon energy at this wavelength is insufficient for the process.

The molecular hydrogen elimination process producing a stable vinylacetylene has been discarded due

$$(C_4H_6)^* \longrightarrow H_2 + C_4H_4 \qquad (7)$$

to energy arguments coupled to the absence of a pressure dependency.[3,4] Even with photon energy of 195 kcal/einstein the resulting C_4H_4 molecule would possess the greater part of 147 kcal/mol excess energy. Fragmentation and pressure stabilization would be expected but the latter is not seen.

Allene Formation. In the 147-0-nm photolysis of cyclobutene[3] it was postulated that the formation of 1,3-butadiene proceeded through hydrogen atom cyclobutene adduct. The resulting $(C_4H_7)^1$ species was found to be pressure stabilized, thus leading to a decreasing yield of 1,3-butadiene with increasing total pressure.

Table V: Photolysis of NH_3 in the Presence of Methylenecyclopropane at 123.6 nm

c-C_4H_6 P, Torr	NH_3 P, Torr	Relative yields, vinylacetylene = 100 Methane	Acetylene	Ethylene	Allene
1.0	0.0	8	196	131	131
0.20	0.80	15	169	135	139
0.10	0.90	18	170	128	201
0.02	0.98	89	200	220	975

(12) J. S. Dewar, *J. Amer. Chem. Soc.*, 89, 3966 (1967).

(13) K. L. Hill, Prasad Koka, and R. D. Doepker, to be submitted for publication.

$$H + \text{cyclobutene} \longrightarrow (C_4H_7)' \quad (8)$$

$$(C_4H_7)' \longrightarrow H + \text{1,3-butadiene} \quad (9)$$

$$(C_4H_7)' + M \longrightarrow C_4H_7 + M \quad (10)$$

Similarly in the 147.0-nm photolysis of methylacetylene Stief, *et al.*,[14] found that acetylene and a methyl radical resulted through displacement by a hydrogen atom.

$$H + CH_3{-}C{\equiv}CH \longrightarrow CH_3 + C_2H_2 \quad (11)$$

In the case of 1-butyne[4] a similar reaction occurs resulting in the formation of allene, except that a pressure effect is observed.

$$H + 1\text{-}C_4H_6 \longrightarrow (C_4H_7)' \quad (12)$$

$$(C_4H_7)' \longrightarrow CH_3 + C_3H_4 \quad (13)$$

$$(C_4H_7)' + M \longrightarrow C_4H_7 + M \quad (14)$$

In an examination of Tables I and II it becomes apparent that at least part of the overall yield of allene is pressure dependent. Further, when deuterium was dissociated in the presence of MCP, allene was found to be the major product (Table III). In those experiments where ammonia (Table V) was used as a hydrogen atom source[3,15] allene increased with the increased ammonia to methylenecyclopropane ratio. In both the D_2 and ND_3 experiments allene was found to be almost entirely allene-h_4.

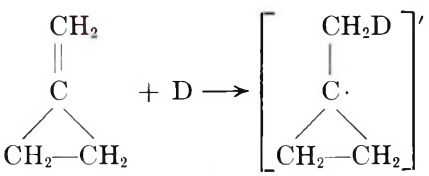

(15)

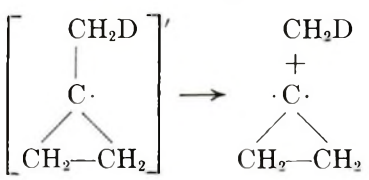

(16)

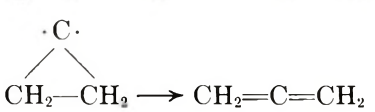

$$\longrightarrow CH_2{=}C{=}CH_2 \quad (17)$$

A second source of allene is also apparent from Tables I and II which involves a primary process. Brinton[2] observed allene formation in the 253.7-nm photolysis of methylenecyclopropane and postulated the direct elimination of a methylene radical. Such a primary process is also consistent with the data presented for the vacuum-ultraviolet photolysis of MCP.

$$(C_4H_6)^* \longrightarrow CH_2 + C_3H_4 \quad (2a)$$

Brinton[2] further pointed out that the methylene radical would insert itself into the double bond of the MCP molecule forming a spiropentane molecule which would contain considerable excess energy and would decompose into allene and ethylene.

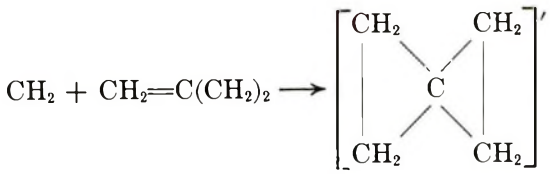

(18)

$$(C_5H_8)' \longrightarrow C_2H_4 + C_3H_4 \quad (19)$$

Spiropentane was not found as a product in the vacuum-ultraviolet study here reported even when the irradiation was carried out under 255 Torr of N_2. It appeared therefore that the high-pressure quantum yield of allene would be double the primary quantum yield of process 2a.

Acetylene and Ethylene. The 147.0-nm photolysis of methylenecyclopropane results in a C_2H_2 to C_2H_4 ratio of nearly 1.2. This ratio is independent of pressure and is nearly independent of additive, but does increase to nearly 1.5 with 123.6-nm photons. The predominant reaction channel for the formation of ethylene and acetylene in the C_4H_6 isomers thus far studied has been attributed to a direct split of the excited parent molecular into ethylene and acetylene. It is interesting to note that such a process in the case of cyclobutane[16] and methylcyclopropane[17] results in the secondary decomposition of a C_2H_4 fragment with a distinctive pressure dependency, where $(C_2H_4)^1$ is a molecule with excess internal energy. On the other hand, cyclobutene[3] as well as the other C_4H_6 isomers does not show a pressure effect on the C_2H_2/C_2H_4 ratio that would be predicted by the methylcyclopropane mechanism. It appears that only a fraction of the ethylene formed in the dissociation of the excited methylenecyclopropane has sufficient energy to eliminate a hydrogen molecule. The lifetime of this species must be shorter than the collision interval at the pressures used in this study.

$$CH_3C(CH_2)_2 + h\nu \longrightarrow C_2H_4 + (C_2H_4)' \quad (20)$$

$$(C_2H_4)' \longrightarrow C_2H_2 + H_2 \quad (21)$$

$$(C_2H_4)' + M \longrightarrow C_2H_4 + M \quad (22)$$

$$CH_2{=}C(CH_2)_2 + h\nu \longrightarrow C_2H_2 + C_2H_4 \quad (1a)$$

$$CH_2{=}C(CH_2)_2 + h\nu \longrightarrow C_2H_2 + C_2H_2 + H_2 \quad (23)$$

In comparing the C_2H_2/C_2H_4 ratio at the two vacuum-ultraviolet wavelengths it can be concluded that the ratio of reaction 23 to 1a increases with increasing photon energy. This would indeed be as expected.

Hydrogen Formation. The hydrogen reported in the 147.0- and 123.6-nm photolysis of methylenecyclo-

(14) L. J. Stief, V. S. DeCarlo, and W. A. Payne, *J. Chem. Phys.*, **54**, 1913 (1971).

(15) J. Magenheimer, R. E. Varnerin, and R. B. Timmons, *J. Phys. Chem.*, **73**, 3904 (1969).

(16) R. D. Doepker and P. Ausloos, *J. Chem. Phys.*, **43**, 3814 (1965).

(17) R. D. Doepker, *J. Phys. Chem.*, **73**, 3219 (1969).

propane (Tables I and II) is produced primarily through the direct elimination of molecular hydrogen and to a very small extent through a hydrogen atom abstraction mechanism. The source of molecular hydrogen is reaction 23 during the elimination of 2 mol of acetylene. This process increases with increasing photon energy, as previously stated.

Radical Formation. The use of hydrogen sulfide as a diagnostic test for the presence of free radicals[10,11] has been used successfully in the earlier studies of the C_4H_6 isomers.[3,4] Due to the unavailability of methylenecyclopropane-d_6 it was necessary to photolyze methylenecyclopropane in the presence of D_2S. This system has many drawbacks related to the competitive kinetics involved. Conversely, H_2S intercepts the great majority of the methyl and vinyl radical produced in the system. Table IV shows an increase in methane with an increase in H_2S/MCP ratio reaching a maximum at a quantum yield of 0.36 for both 147.0 and 123.6 nm. It further appears from this table that ethylene shows a slight increase in quantum yield when H_2S is added to the system. The presence of small amounts of vinyl radicals may be inferred from these data but is most certainly a very minor product. From Table IV it can be determined that H_2S concentration of 15 to 20% of methylenecyclopropane pressure is sufficient to intercept nearly all of the methyl radicals produced in the system. This would seem to be consistent with the results found by Collin, *et al.*,[11] for other unsaturated systems.

Summary of Primary Processes. Based on the above discussion, values presented in the tables of data and the results of previously published and presently unpublished work on the C_4H_6 isomers, estimates of the important primary processes can be attempted.

The formation of vinylacetylene through the elimination of two hydrogen atoms accounts for nearly all of the vinylacetylene observed. The quantum yield

$$CH_2{=}C(CH)_2 + h\nu \longrightarrow 2H + C_4H_4 \qquad (6a)$$

for this process is 0.20 at 147.0 nm and 0.16 with 123.6-nm photons.

A primary process leading to the formation of allene cannot be considered negligible based on the "high"-pressure allene yields obtained and reported in Tables I and II. The upper limit for the quantum yield for

$$CH_2{=}C(CH_2) + h\nu \longrightarrow CH_2 + C_3H_4 \qquad (2a)$$

this process would be one-half of the high-pressure yield of allene, 0.06 at 147.0 nm and 0.03 at 123.6 nm. The assumption is made that all the CH_2 produced in reaction 2a results in an additional molecule of allene.

$$CH_2 + CH_2{=}C(CH_2)_2 \longrightarrow C_2H_4 + C_3H_4 \qquad (18a)$$

The absence of an ethylene pressure effect, the absence of a decreased allene yield with an increased H_2S/MCP ratio, and the results of Brinton[2] for the 253.7-nm study all seem to point to the validity of this assumption.

The formation of ethylene must be attributed to two major reaction channels, one accounting for a quantum yield of 0.06 and 0.03 at 147.0 and 123.6 nm, respectively, from reaction 18a, and a second due to a primary process.

$$CH_2{=}C(CH_2)_2 + h\nu \longrightarrow C_2H_4 + C_2H_2 \qquad (1a)$$

The quantum yield of this process therefore is wavelength dependent, having a value of 0.37 with the xenon resonance line, and 0.27 with krypton.

Acetylene also requires two reaction channels (1a) and a second primary process involving the elimination of molecular hydrogen.

$$CH_2{=}C(CH_2)_2 + h\nu \longrightarrow 2C_2H_2 + H_2 \qquad (23)$$

The quantum yield of this process should equal $^1/_2$ (the total yield of acetylene minus the quantum yield of process 1a). This would result in $\phi_{23} = 0.08$ at 147.0 nm and $\phi_{23} = 0.10$ at 123.6 nm. These values are also consistent with the total hydrogen yields, assuming that the hydrogen is a measure of the molecular hydrogen only. $\Phi_{H_2} = 0.08$ at 147.0 nm, $\Phi_{H_2} = 0.10$ at 123.6 nm.

It is interesting to note that the low-pressure quantum yield for allene minus the high-pressure value is only slightly larger than twice the quantum yield for the formation of vinylacetylene. This is consistent with the assumption that almost all hydrogen atoms add to the unsaturated molecule, which will completely fragment at pressure under approximately 0.2 Torr.

Acknowledgment. The authors wish to thank Dr. Guy Collin for the preprint of his work with H_2S, and Donald Olinger, who helped with some timely experiments. Furthermore, the authors wish to acknowledge the National Science Foundation which supported this investigation under Grants No. NSF-GP-7060 and NSF-GP-20878.

Further Studies of Chemical Reactions on γ-Irradiated Silica Gel and Porous Vycor Glass[1]

by Günter R. Joppien and John E. Willard*

Department of Chemistry, University of Wisconsin, Madison, Wisconsin, 53706 *(Received January 24, 1972)*

Publication costs assisted by the U. S. Atomic Energy Commission

Energy deposited in either silica gel or porous Vycor glass by γ-irradiation can activate adsorbed CH_3Cl, C_2H_5Cl, C_2H_7Cl, C_2H_4, C_2D_4, C_3H_6, and CH_4 with approximately equal effectiveness (G (products) = *ca.* 1 in each case). The products include CH_4 and C_2H_6 from CH_3Cl at 77 and 300°K, C_2H_6 and C_4H_{10} from C_2H_4 at 77 and 300°K, CH_3 radicals from CH_4 at 77°K, C_2D_4H radicals from C_2D_4 at 77°K, and peroxy radicals from O_2–CH_3Cl and O_2–CH_4 mixtures at 77°K. When CH_3Cl and C_2H_4 are present together on the surface they compete for activation by energy absorbed in the gel. O_2 admitted to CH_3 radicals trapped on silica gel at 77°K converts them slowly to peroxy radicals. Sorbed CH_3 radicals exposed to C_2H_4 at 77°K yield propane on analysis at room temperature. The yields of stable products from radiolyses of sorbates on the gel decrease sharply for doses above 4×10^{18} eV g^{-1} at 77°K, but not at 300°K, suggesting a preempting of most of the sensitive energy transfer sites by products at the lower temperature, but release of the sites by desorption at the higher temperature. The influence of gel preparation and sorbate concentration on G values and the effect on the esr spectra of sorbed radicals is illustrated.

Introduction

The discovery of Caffrey and Allen,[2] confirmed and extended by many others,[3] that adsorbed organic molecules can be decomposed by γ-radiation energy deposited in the bulk of various adsorbents has posed many unanswered questions as to the mechanisms of energy transfer to the surface and from the surface to the sorbate, and as to subsequent reactions on the surfaces. Silica gel and porous Vycor (silica) glass are among the substrates most investigated. Radiation G values of unity and higher for reaction of adsorbed molecules (based on the energy absorbed by sorbate plus substrate) are common in these materials. They can be obtained relatively pure, and their surface structures have been investigated in some detail.[4] It has been reported that (1) anion formation by transfer of electrons from the surface can occur during γ-irradiation for sorbates such as tetracyanoethylene (TCNE),[5] galvinoxyl,[6a] napthalene,[6a] biphenyl,[6a] carbon dioxide,[6b] and sulfur dioxide;[6b] (2) easily oxidized sorbates such as tetramethyl-*p*-phenylenediamine can be converted to the cation;[5] (3) methyl halides yield methyl radicals at 77°K[6a] and methane at 273°K;[7] (4) aliphatic hydrocarbons,[2,3] azoethane,[8] ethanol,[9] and isopropylbenzene[10] are decomposed; (5) high yields (G = 4 and 6.5) of benzene and $TCNE^-$, respectively, are obtained when isopropylbenzene[10] and TCNE[5] are added to γ-irradiated silica *after* irradiation; (6) certain active surface centers stable at 77°K decay at 300°K.[10] These observations indicate both the versatility and complexity of silica as a transducer of γ energy to produce chemical change. They show that electrons, positive holes, and/or excitons must be able to travel many angstroms through the irradiated silica to "find" sorbed molecules and that different types of energy and charge transfer occur at the surface. In the present work we have obtained further evidence on the following: (a) the relative ability of silica undergoing irradiation to initiate reactions of sorbate molecules of similar size but contrasting electron affinity (*e.g.*, CH_3Cl and CH_4; CH_3Cl and C_2H_4; C_2H_5Cl and C_2H_4, C_3H_7Cl and C_3H_6), both when the species are present separately and when they are competing on the same surface; (b) reactions of activated sorbate molecules with surface silanol groups; (c) reactions of sorbed free radicals with added C_2H_4 and O_2; (d) the effect of temperature on yields, as a function of dose; (e) post-irradiation polymerization of ethylene; (f) properties of sorbed free radicals and hydrogen atoms.

(1) This work has been supported in part by the U. S. Atomic Energy Commission under Contract No. AT(11-1)-1715, by the W. F. Vilas Trust of the University of Wisconsin, and by the Deutsche Forschungsgemeinschaft.

(2) J. M. Caffrey, Jr., and A. O. Allen, *J. Phys. Chem.*, **62**, 33 (1958).

(3) See review article by H. W. Kohn, "The Radiation Chemistry of Surfaces" in "Actions Chimiques et Biologiques des Radiations," onzième série, Masson and Cie, Paris, 1967, and more recent references included in those cited below.

(4) (a) J. B. Peri and A. L. Hensley, Jr., *J. Phys. Chem.*, **72**, 2926 (1968); (b) M. L. Hair and W. Hertl, *ibid.*, **73**, 4269 (1969).

(5) P. K. Wong and A. O. Allen, *ibid.*, **74**, 774 (1970).

(6) (a) P. K. Wong and J. E. Willard, *ibid.*, **72**, 2623 (1968); (b) P. K. Wong and J. E. Willard, *ibid.*, **73**, 2226 (1969).

(7) N. H. Sagert, J. A. Reid, and R. W. Robinson, *Can. J. Chem.*, **48**, 17 (1970).

(8) J. G. Rabe, B. Rabe, and A. O. Allen, *J. Phys. Chem.*, **70**, 1098 (1966).

(9) L. Abrams and A. O. Allen, *ibid.*, **73**, 2741 (1969).

(10) E. A. Rojo and R. R. Hentz, *ibid.*, **70**, 2919 (1966).

Experimental Section

Materials. The reagents, and the manufacturers' purity specifications, were Matheson CH_3Cl (99.5%), C_2H_5Cl (99.7%), CH_4 (99.99%), and C_2H_4 (99.7%), Aldrich C_2H_5Cl ($n^{20}D$ = 1.3878); Merck Sharp and Dohme C_2D_4 (99% isotopic purity). The silica gel was Davison Chemical Co. Grade 950 with a stated BET surface area of 700 $m^2\ g^{-1}$ and a particle size of 60–200 mesh. Vycor porous glass No. 7930 from Corning was used as glass rods of 2–2.6-mm diameter with a stated BET surface area of 140 $m^2\ g^{-1}$.

Sample Preparation. Prior to degassing, the silica gel was heated in air at 200° for 2 hr, and the Vycor was heated in 500 Torr of dry oxygen at 600° for 2 hr, to remove volatile impurities and physisorbed water. For experiments followed by stable product analysis, portions of *ca.* 7 g of the silica gel were weighed into annular Pyrex irradiation cells with break-seals and degassed for 96 hr at 460° and $<10^{-3}$ Torr. For esr investigations, either 0.2 g of the gel or 30-mm lengths of Vycor rod were placed in 3-mm i.d. Suprasil tubes with graded seals to Pyrex and degassed for 24 hr at 460° and $<10^{-5}$ Torr. A grease-free, mercury-free vacuum line was used. Gaseous samples of all compounds to be adsorbed were dried by passing through a 2-in. column of P_2O_5, degassed by freeze–pump–thaw cycles, metered by a calibrated volume at known PVT, passed through silver powder to remove mercury from the manometer, condensed on the adsorbent at 77°K, and then sealed from the vacuum line. In experiments with CH_4, greaseless stopcocks were used instead of fusion seals, to avoid pyrolysis of the noncondensable CH_4. All samples were stored at room temperature for several hours prior to irradiation to allow random surface distribution of the adsorbates. The silica gel samples were thoroughly mixed by shaking.

In this work the concentrations of adsorbed compounds are expressed as mole fractions (mf), using 60 for the molecular weights of silica gel and Vycor porous glass.

Irradiations. Irradiations were carried out at 77°K or room temperature using a 2-cm high, 1-cm diameter ^{60}Co γ source encapsulated in a stainless steel rod of 18 mm o.d. Annular cells were irradiated with the source in the center. Esr samples were held adjacent to the source by an irradiation rack. In both cases the dose rate was $4.2 \pm 0.1 \times 10^{18}$ eV $g^{-1}\ min^{-1}$. For irradiations at 77°K both the samples and the source were immersed in liquid nitrogen.

The dose rates were determined by Fricke dosimetry using an extinction coefficient of ϵ 2201 $M^{-1}\ cm^{-1}$ at 3040 Å for Fe^{3+} in 0.8 N H_2SO_4 at 25°, and $G(Fe^{3+})$ = 15.5. The energy absorbed per gram of silica was assumed to be 0.9 of that per gram of dosimeter solution, based on the electron density ratio.

To avoid inducing esr signals in the Suprasil sample tubes, the tubes were inverted to place the samples in the Pyrex ends during γ-irradiation.

Analysis for Stable Products. After γ-irradiation of an annular irradiation vessel its break-seal was attached to the vacuum line, and the volatile products and unchanged sorbed compounds were pumped off the silica gel with a Toepler pump while heating the vessel to 120°. Usually compounds not condensable at 77°K were separated from the condensable compounds by a trap immersed in liquid nitrogen. The two fractions were separately analyzed either by an AEI MS-10 mass spectrometer using an electron energy of 35 eV or by a gas chromatograph with flame ionization detector, using a 6-ft Porapak Q column at 80°.

Esr Measurements. Electron spin resonance measurements were made with a V-4500 or E-15 Varian spectrometer. Both were operated in the X-band, using 100-kHz modulation, microwave power levels from 0.25 to 8 mW and a Varian 4531 cavity. The first derivative esr spectra were displayed. Unpaired spin concentrations were determined from the areas of the double integrated spectra compared with that of a standard strong pitch sample having 3.0×10^{15} spins/cm of esr tube length.

Results

Effects of Radiation Dose and Temperature on Yields. Previous investigations[7] of the stable products of methyl halide radiolysis on silica gel have been limited to CH_3I at 273°K using radiation doses of 4×10^{19} eV g^{-1}. Under these conditions CH_3I decomposition to form the major products CH_4 and C_2H_6 was nearly linear with dose. In the present work, using CH_3Cl at 300°K, this near linearity extends to at least 8×10^{20} eV g^{-1} (Figure 1), with indication that the rate of production of CH_4 increases slightly with increasing dose while that of C_2H_6 decreases. About 10% of the CH_3Cl had been radiolyzed at the highest doses used. At 6×10^{-3} mf CH_3Cl the surface coverage was *ca.* 1.7% of a monolayer assuming 20 $Å^2$ per CH_3Cl molecule. At 77°K the initial G value (slope of curve of Figure 1) for CH_4 plus $2C_2H_6$ is similar to that at 300°K, but at doses above *ca.* 4×10^{19} eV g^{-1} G decreases becoming zero above *ca.* 2×10^{20} eV g^{-1}, with indication that the surface concentration of C_2H_6 decreases slowly at higher doses (Figures 1 and 2).

No free radicals are observable by esr on silica gel containing 6×10^{-3} mf CH_3Cl following irradiations with doses of 4×10^{18} to 6×10^{19} eV g^{-1} in 1 to 15 min at 300°K, consistent with previous findings with CH_3Br[6] (but see footnote 11).[12,13] When the gel is irradiated

(11) By contrast, photolysis of CH_3I on Vycor porous glass[12] or silica gel[13] at 300°K produces CH_3 radicals which are stable at 300°K. Recent photolyses of CH_3I on silica gel in our laboratory indicate that these "stable" radicals are produced with about the same yield at 77°K but at the lower temperature are accompanied by about a 100-fold higher yield of radicals which disappear below 300°K when the sample is warmed.

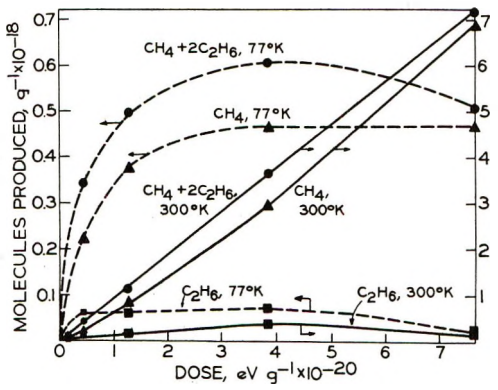

Figure 1. Dose dependence at 300 (solid lines) and 77°K (dashed lines) of product yields from γ-irradiation of silica gel containing 6×10^{-3} mole fraction CH_3Cl. Scale at left is for samples at 77°K, scale at right for those at 300°K.

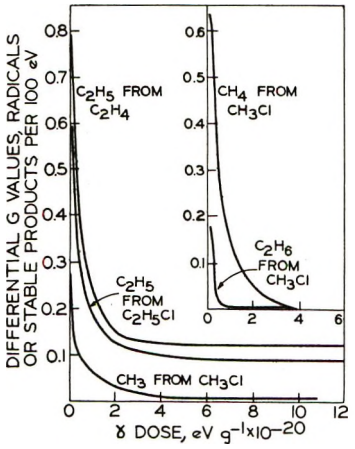

Figure 2. Dose dependence of differential G values of radicals and stable products from γ-irradiation of sorbates on silica gel at 77°K, 3×10^{-2} mole fraction C_2H_4 and C_2H_5Cl, 6×10^{-3} mole fraction CH_3Cl.

at 77°K stable CH_3 radicals are produced from CH_3Cl or CH_4 as the sorbates, C_2H_5 radicals from C_2H_5Cl or C_2H_4, and iso and normal C_3H_7 radicals from sorbed C_3H_6 or C_3H_7Cl. As with stable product G values (inset of Figure 2), the differential G values of radicals decrease rapidly with increasing dose in the range of *ca.* 10^{19} to 10^{20} eV g^{-1} (Figure 2). The curves of Figure 2 show the dose dependence of the slopes of tangents to the experimentally obtained concentration *vs.* dose curves. The initial values of each curve of Figure 2 are the maximum values observed. At doses below about 10^{18} eV g^{-1} there is evidence for lower G values, suggesting an induction period with respect to dose. The surface-stabilized free radicals undergo continued production with nearly constant low G values from 4×10^{20} eV g^{-1} to at least 12×10^{20} eV g^{-1}, in contrast to the zero or negative values for the stable products CH_4 and C_2H_6 in this region.

Effect of Sorbate Concentration and Silica Gel Preparation on Yields of Trapped Radicals. When different concentrations of CH_3Cl or CH_3Br on silica gel were exposed at 77°K to the same γ dose, 4×10^{18} eV g^{-1}, the G values of CH_3 production increased with concentration (Table I). The data of this table indicate the following: (1) the G values of CH_3 radicals increase by a factor of 2 or 3 for an increase by a factor of 10 to 15 in the concentration of CH_3Cl or CH_3Br as sorbate; (2) the yields are higher for the gel degassed at 200° than for that degassed at 460°; (3) the yields from CH_3Cl are higher than those from CH_3Br; (4) the yields of C_2D_4H are independent of C_2D_4 concentration within the limits of error of the measurements in contrast to the yields of CH_3 from the methyl halides. Earlier work using 140–200 mesh gel degassed for 24 hr at 460° and 10^{-3} Torr, rather than the 60–200 mesh degassed for 24 hr at 460° and $<10^{-5}$ Torr in this work, showed $G(CH_3)$ values from CH_3Br which were constant within ±15% over the range from 12×10^{-3} to 75×10^{-3} mole fraction of CH_3Br.[6,14]

Table I: Effect of Sorbate Concentration and Gel Preparation Temperature on Trapped Radical Yields on Silica Gel at 77°K[d]

CH_3Cl,[a] mf × 10^3	$G(CH_3)$	CH_3Br,[a] mf × 10^3	$G(CH_3)$	CH_3Br,[b] mf × 10^3	$G(CH_3)$
0.5	0.17	7.3	0.09	7.3	0.20
6	0.27	12	0.11	14	0.30
20	0.33	29	0.15	29	0.42
40	0.40	46	0.18	47	0.45
50	0.55	69	0.21	70	0.47
90	0.73	81	0.21	93	0.41

C_2D_4, mf × 10^3	$G(C_2D_4H)$	C_2H_4,[a] mf × 10^3	$G(C_2H_5)$	CH_4,[a] mf × 10^3	$G(CH_3)$
On Vycor				On silica gel	
3.7	0.63	30	0.79	1.6	0.059
47	0.76				
410	0.57			38	0.13
On silica gel					
51[c]	0.89				

[a] Gel pretreated by heating 24 hr at 460° at $<10^{-5}$ Torr. [b] Gel pretreated by heating 24 hr at 200° at $<10^{-5}$ Torr. [c] Degassed at 300°. [d] Dose 4×10^{18} eV g^{-1}.

Stable Product Yields from CH_3Cl, C_2H_4, and Their Mixtures. Both at 300 and 77°K the major products from sorbed CH_3Cl are CH_4 and C_2H_6. These are accompanied by relatively trace amounts of C_3H_8 and n-C_4H_{10} (experiments 1 and 5 of Table II). From

(12) J. Turkevich and Y. Fujita, *Science*, **152**, 1619 (1966).

(13) (a) G. B. Garbutt and H. D. Gesser, *Can. J. Chem.*, **48**, 2685 (1970); (b) B. Wiseall, private communication.

(14) There is an error in the labeling of Figure 8 of ref 6. The correct label is now believed to be "eV $g^{-1} \times 10^{-20}$" rather than "eV $g^{-1} \times 10^{-18}$," coupled with a CH_3 radical yield in Table II of 0.14 rather than 1.4.

Table II: Product Yields from γ-Irradiation of CH_3Cl, C_2H_4, and Their Mixtures on Silica Gel at 300 and 77°K[a]

Expt No.	Irradiation temp, °K	Adsorbates: CH_3Cl, mf × 10^3	Adsorbates: C_2H_4, mf × 10^3	Product yields, molecules per 100 eV: CH_4	C_2H_6	C_3H_8	n-C_4H_{10}	Total C atoms	C_2H_4 not recovered, G[b]
1	300	6.0	None	0.76	0.094	0.007	<0.001	0.96	
				f	(0.19)	(0.024)			
2	300	None	6.2	0.024	0.66	0.030	0.23	1.18	15.9
				(0.012)[f]	(0.66)	(0.045)	(0.46)		
3	300	6.6	7.6	0.27	0.2[c]	0.010	*e*		*e*
4	300	0.65	7.4	0.13	0.62	0.044	0.171		18.3
5	77	6.2	None	0.12	0.018	0.001	<0.001		
				f	(0.036)	(0.003)			
6	77	None	6.4	0.019	0.028	0.012	0.018		5.43
				(0.01)[f]	0.028	(0.018)	(0.034)		
7	77	0.64	6.0[d]	0.02	0.003	0.16	0.048		4.12

[a] The adsorbed dose was $(4 \pm 0.2) \times 10^{20}$ eV g^{-1} in all cases. [b] Ethylene unaccounted for in analysis following radiolysis, presumed to be nonvolatile polymer remaining on gel. [c] Determined only by mass spectrometry analysis. [d] Ethylene added at 77°K after γ-irradiation. [e] Not determined. [f] Numbers in parentheses show the value of $G(-CH_3Cl)$ or $G(-C_2H_4)$ required to give the G(product) noted immediately above.

C_2H_4 (experiments 2 and 6 of Table II) the products at 300°K are C_2H_6 and n-C_4H_{10} with much smaller yields of CH_4 and C_3H_8. At 77°K the yields of the four products from C_2H_4 are more nearly equivalent. When coadsorbed mixtures of CH_3Cl and C_2H_4 are irradiated the presence of each compound decreases the yield of the major products of the other (Table II, experiments 3 and 4 as compared to 1 and 2 and Table I).

For the independently adsorbed species, $G(-CH_3Cl)$ may be evaluated as $G(CH_4 + 2C_2H_6 + 3C_3H_8 + 4C_4H_{10}) = 0.96$ and $G(-C_2H_4)$ as $G(^1/_2CH_4 + C_2H_6 + {}^3/_2C_3H_8 + 2C_4H_{10}) = 1.18$. These results suggest that C_2H_4 is as effectively radiolyzed on SiO_2 at 300°K as CH_3Cl and that the two compete on nearly equal terms for excitation transferred from the substrate.

Material Balances and Reactions When Reagent is Added Following Irradiation. Following γ-irradiation of CH_3Cl on silica gel all of the products and most of the CH_3Cl could be removed by pumping at room temperature. Heating to 50° facilitated the desorption process. A temperature of 120° was required to remove the last traces of CH_3Cl within a reasonable time. Following such removal the sum (in numbers of C atoms) of the CH_3Cl plus the products was equal to the CH_3Cl used, within ±1%. When C_2H_4 was present during irradiation (Table II, experiments 2, 4, and 6) or added after irradiation (experiment 7) the sum of carbon atoms in the products plus those in the C_2H_4 recovered by pumping at 120° was always less than equivalent to the C_2H_4 added. The amounts lost were lower for irradiations at 77°K than 300°K but were about the same for C_2H_4 added before ($G \sim 5$, Table II, experiment 6) or after irradiation at 77°K ($G \sim 4$, experiment 7) and for samples with and without CH_3Cl present. This loss is tentatively attributed to formation of a nonvolatile polymer by a chain reaction initiated by trapped charges which do not affect the CH_3Cl. C_2H_4 adsorbed on nonirradiated silica gel could be recovered quantitatively by pumping at 120°, thus excluding irreversible adsorption of part of this sorbate. Only trace amounts ($G < 0.001$) of hydrocarbons were formed when the CH_3Cl was added to gel which had received a dose of 4×10^{20} eV g^{-1} at either 77 or 300°K.

In experiment 7 of Table II the possibility of a reaction of surface-stabilized CH_3 radicals with added C_2H_4 was studied. Formation of C_3H_8 with $G = 0.16$, a value much higher than corresponding values of this product from γ-irradiation of sorbed CH_3Cl, C_2H_4, or their mixtures, indicates such an addition reaction followed by H abstraction from silanol groups. The low CH_4 ($G = 0.02$) and C_2H_6 yield ($G = 0.003$) compared with the higher yields of these products in experiment 5 show that the stabilized CH_3 radicals add to C_2H_4 in preference to combining or forming CH_4 by H abstraction from the surface. In corresponding esr experiments formation of the transient C_3H_7 free radical could not be observed, suggesting prompt reaction with silanol groups to form C_3H_8.

Free Radicals Produced by γ-Irradiation of Silica Gel Containing CH_3Cl or CH_4. Figures 3 and 4 illustrate three features of the esr spectra of CH_3 radicals produced by γ-irradiation of methyl halides on silica gel. One is a pattern of satellite lines (Figure 3A) somewhat similar to that for CH_3 radicals from the photolysis of CH_3I on Vycor,[12] attributed to interactions of the unpaired electron with protons of the silanol groups.[13] Another feature is a reversible change in the spectrum on warming from 77 (Figure 3A) to 129°K (Figure 3B), which occurred primarily above 107°K. The spectrum reverted to that of Figure 3A when the sample was returned to 77°K. When more than 95% of the CH_3 signal of Figure 3 had decayed, as a result of holding the sample at elevated temperatures, a second

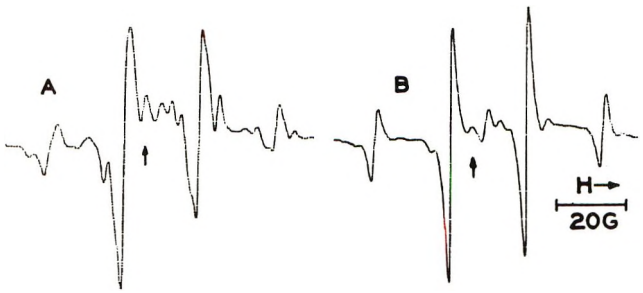

Figure 3. Reversible change of satellite structure and line widths in the esr spectra of methyl radicals on silica gel upon sample warming and recooling: A, measured at 85°K before and after warmup to 129°K; B, measured at 129°K, 6×10^{-3} mf CH_3Cl on silica gel; γ dose 1×10^{20} eV g^{-1} at 77°K, microwave power 8 mW, modulation amplitude 2.0 G, vertical arrows at $g = 2.0028$.

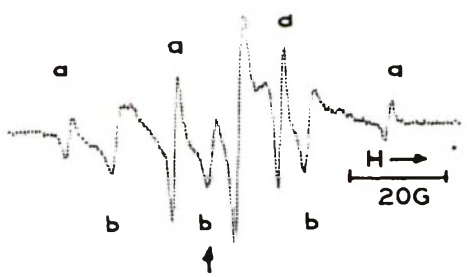

Figure 4. Residual esr spectrum from silica gel containing 6×10^{-3} mole fraction CH_3Cl following γ dose of 2×10^{19} eV g^{-1} at 77°K and 95% decay of the CH_3 radical absorption at 283°K. Signals marked a assigned to CH_3, those marked b attributed to $SiOCH_2$: microwave power 3.1 mW, modulation amplitude 1.3 G, vertical arrow indicates $g = 2.0028$.

radical spectrum (consisting of the three lines designated by b in Figure 4) could be observed. It is tentatively assigned to the species CH_2–O–Si$\lessdot$ formed by addition of methylene radicals to surface oxygen atoms. A three-line esr spectrum with $a_H = 21$ G and a binomial (1:2:1) intensity distribution but a nonbinomial amplitude distribution (1:14:1) observed from a silica gel sample exposed to 365-nm radiation after heating in CH_3OH vapor has also been attributed to this radical.[15] The three-line esr spectrum with $a_H = 20$ G and 1:2:1 intensity ratio observed after photolysis of methanol adsorbed on alumina has been attributed to the Al–O–CH_2 radical.[16] The nonbinomial amplitude ratio of 1:14:1 for the species in ref 15 is due to a different broadening of the central peak compared with that of the extreme components. This is attributed to a loss of some of the degrees of rotational freedom when the radical is stabilized on the surface causing different averaging of the hyperfine structure anisotropy.[11] The three-line spectrum of Figure 4 is also analogous to that of the acetic acid free radical,[17] CH_2COOH, which gives a three-line spectrum with an intensity ratio of 1:2:1 and a splitting constant of 21.8 G.

γ-Irradiation of CH_4 adsorbed on either silica gel or porous Vycor glass generates the CH_3 esr quartet spectrum with satellite lines which vary somewhat with the dose. Typical G values (Table I) are about a factor of 3 less than for CH_3Cl at the same concentration and dose.

Radical Scavenging by Added O_2. When 5×10^{-2} mf O_2 is admitted to a γ-irradiated sample of silica gel containing 6×10^{-3} mf CH_3Cl at 77°K, the CH_3 esr spectrum changes (*ca.* 1% per 2 min) to the peroxy radical spectrum. When the temperature is raised to 160°K conversion is rapid and quantitative and the spin concentration of CH_3O_2 is identical with that of the converted CH_3 radical. When O_2 is present at 5×10^{-2} mf or higher during irradiation of a silica gel–CH_3Cl or silica gel–CH_4 sample at 77°K only peroxy radicals are observable at the end of irradiation. With 6×10^{-3} mf CH_3Cl and a 2×10^{19} eV g^{-1} dose, $G(CH_3O_2) = 0.86$, higher than the yield of stabilized radicals observed in the absence of O_2 and close to the $G(CH_4 + 2C_2H_6)$ observed by stable product analysis. With 8×10^{-3} mf CH_4 and a dose of 4×10^{18} eV g^{-1}, G peroxy radicals was 1.96, as compared with the 0.86 for the similar irradiation of CH_3Cl, suggesting formation of both CH_3O_2 and HO_2.

Ethyl Radical Production from C_2H_5Cl, C_2H_4, and C_2D_4 on Silica Gel and Vycor. γ-Irradiation of 3×10^{-2} mf C_2H_5Cl or C_2H_4 on silica gel at 77°K produced the very similar spectra Figure 5A and B. These are similar to the 12-line spectrum from C_2H_5 radicals with nonequivalent α and β protons which has been reported[18] as giving an intensity ratio of 1:2:3:1:6:3:3:6:1:3:2:1 and splitting constants of $a_\alpha^H = 21$ G and $a_\beta^H = 26.2$ G, consistent with the spectra of Figure 5A and B. These findings indicate that C_2H_5 radicals are formed from the irradiation of silica gel containing either adsorbed C_2H_5Cl or C_2H_4. The yields are similar (Figure 2). Confirmation of the conclusion that excited C_2H_4 molecules abstract H from the silica surface is given by the spectrum of Figure 5D from an irradiation of Vycor containing adsorbed C_2D_4. By comparison with spectra of the free C_2D_4H radical in liquid ethane, recorded at −175°,[18] spectrum 5D can be attributed to the HD_2CCD_2 radical with nonequivalent α and β deuterium atoms giving two sets of 25 hyperfine lines with their centers separated by $a_\beta^H = 29.8$ G. On Vycor the 50 lines are not completely resolved, but the number and distance of the resolved groups of lines compare well with the published spectra. A similar spectrum was produced with silica gel as the substrate. Evidence that the C_2H_5 formation from C_2H_4 does not require an ionic mechanism is given

(15) A. P. Bobrovskii and V. E. Kholmogorov, *Teor. Eksp. Khim.*, 3, 112 (1967).

(16) Y. Ono and T. Keii, *J. Phys. Chem.*, 72, 2851 (1968).

(17) W. T. Dixon, R. O. C. Norman, and A. L. Buley, *J. Chem. Soc.*, 3625 (1964).

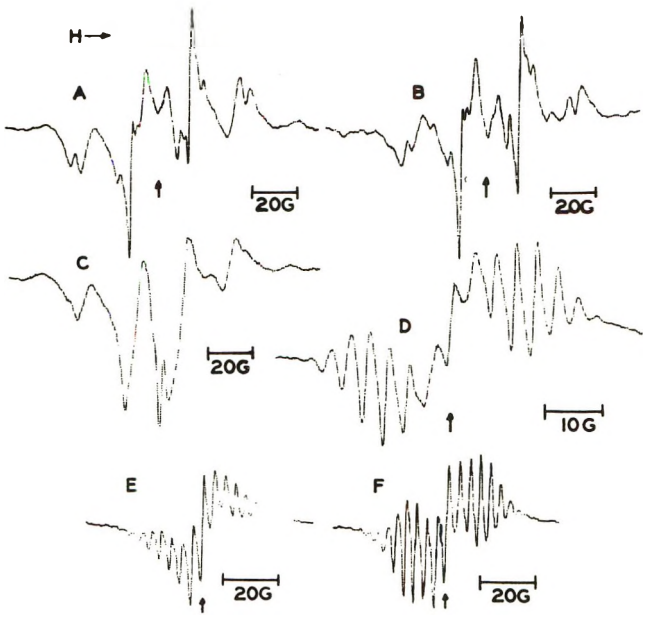

Figure 5. Esr spectra following γ and uv irradiation of selected compounds on silica gel and Vycor porous glass: A, 3×10^{-2} mf C_2H_4 on silica gel, γ dose 4×10^{18} eV g^{-1}, power 8 mW; modulation amplitude 1.3 G, signal level 40, T 77°K; B, 3×10^{-2} mf C_2H_5Cl on silica gel, dose 4×10^{18} eV g^{-1}, power 8 mW, modulation amplitude, 1.3 G; signal level 40, T 77°K; C, 6×10^{-3} mf C_2H_4 on silica gel, dose 2×10^{19} eV g^{-1}, power 1.9 mW, modulation amplitude 1.3 G, signal level 40, T 85°K; D, 4.7×10^{-2} mf C_2D_4 on VPG; dose 4×10^{18} eV g^{-1}, power 1.1 mW, modulation amplitude 1.3 G, signal level 50, T 77°K; E, 3.3×10^{-2} mf C_2D_4 on VPG, photolyzed 12 min with low-pressure mercury lamp, power 1.1 mW; modulation amplitude 1.3 G, signal level 100, T 77°K; F, same sample as E after 48-hr storage at 77°K; vertical arrows indicate $g = 2.0028$.

by Figure 5E which is a spectrum produced by photolysis of 3.3×10^{-2} mf C_2D_4 on Vycor with a low-pressure mercury arc. A similar spectrum was produced by photolysis of C_2D_4 on silica gel.

Spectrum 5F, which was recorded after 48 hr of storage of sample 5E at 77°K, shows a marked increase in line resolution. This must be due to reorientation of the radicals on the surface, and it suggests that the differences of spectra E and D are due to similar orientation effects, which may involve the extent of interaction with surface OH groups.

Figure 5C is an example of the influence of sorbate concentration on radical geometry. The sample used was similar to that of Figure 5A but contained 6×10^{-3} mf C_2H_4 rather than 3.2×10^{-2} mf. The change from a 12-line to a 6-line spectrum with equal spacing of these lines by $a_{av}^{H} = 23$ G and an amplitude ratio close to the binomial ratio 1:5:10:10:5:1 indicates equal coupling of the unpaired electron with the five protons. This observation suggests that at surface coverages above about 2% of a monolayer the added ethylene molecules are sorbed on a different type of site, or form sorbate clusters, favoring a different type of radical geometry than is produced at lower concentrations. Ethyl radicals with nonequivalent α and β protons are observed in the liquid phase.[18]

The data of Table III indicate that $G(C_2H_5)$ is independent of the composition of C_2H_4–C_2H_5Cl mixtures over the range of at least 22 to 80% C_2H_5Cl. The lower value obtained from pure C_2H_5Cl (experiment 6) than from pure C_2H_4 is consistent with the experiments of Figure 2 and is in the direction to be expected if some of the C_2H_5 radicals form C_2H_6 by hot abstraction from silanol groups. It is not obvious why this effect does not cause a downward trend in $G(C_2H_5)$ from the mixtures used in experiments 2 through 5. The slightly higher G values of the experiments of Table III than those of Figure 2 are attributed to differences in sample preparation.

Table III: Ethyl Radical Yields from γ-Irradiation of Ethylene, Ethyl Chloride, and Their Mixtures on Silica Gel[a]

Expt No.	Total concn, mf	% C_2H_5Cl[b]	$[C_2H_6]$, mf × 10^6	$G(C_2H_6)$
1	3.0×10^{-2}	0.0	2.02	1.22
2	2.2×10^{-2}	22	1.79	1.08
3	2.1×10^{-2}	39	1.68	1.01
4	1.8×10^{-2}	60	1.69	1.02
5	2.5×10^{-2}	80	1.79	1.08
6	1.9×10^{-2}	100	0.77	0.46

[a] Absorbed γ dose was 1.65×10^{19} eV g^{-1}; irradiations and esr measurements carried out at 77°K. [b] $100 \times [C_2H_5Cl]/([C_2H_5Cl] + [C_2H_4])$.

Radical Production from C_3H_6 and C_3H_7Cl on Silica Gel. γ-Irradiation of propylene (1.6×10^{-2} mf) on silica gel at 77°K generates an esr spectrum of eight well-resolved lines with a splitting constant of 23 G. On warming to room temperature the six inner lines split into six groups of two giving a 14-line spectrum similar to that reported for the isopropyl radical with equivalent β protons.[18] A similar but somewhat less resolved spectrum is obtained from γ-irradiation of 1.6×10^{-2} mf n-C_3H_7Cl on silica gel at 77°K, at a dose of 2×10^{19} eV g^{-1}. G(radicals) was determined to be 0.8 ± 0.2 from both spectra. In each case the presence of n-propyl radicals could not be excluded.

Trapped Hydrogen Atoms and Paramagnetic Centers in Silica Matrices. γ-Irradiated silica gel and Vycor samples prepared by the methods used in this work show no evidence of the hydrogen atom esr doublet, indicating that $G(H_{tr})$ is $<10^{-4}$ in contrast to some previous observations,[19] but in agreement with oth-

(18) R. W. Fessenden and R. H. Schuler, *J. Chem. Phys.*, **39**, 2147 (1963).

(19) (a) V. B. Kazanskii, G. B. Pariiskii, and V. V. Voevodskii, *Discuss. Faraday Soc.*, **31**, 203 (1961); (b) P. H. Emmett, R. Livingston, H. Zeldes, and R. J. Kokes, *J. Phys. Chem.*, **66**, 921 (1962). See also the review article by E. H. Taylor, *Advan. Catal. Relat. Subj.*, **18**, 148 (1968).

ers.[7,20] With adsorbed CH_4 and C_2D_4 the yields shown in Table IV are obtained. The observation that γ-irradiation of Vycor containing adsorbed C_2D_4 yields trapped H atoms but not D atoms indicates that the sorbate is not the source of the atoms but plays some role in the trapping mechanism. Production of trapped D atoms from sorbed CD_4 and D_2O has, however, been reported.[20]

Table IV: *G* Values of Trapped Hydrogen Atoms from γ-Irradiation of Silica Gel and Vycor Porous Glass Sorbates at 77°K

	Substrate	Sorbate, mf × 10^2	Dose, eV g^{-1} × 10^{-18}	*G*(H trapped) × 10^3
CH_4	Silica gel	CH_4, 0.16	12	0.6
CH_4	Silica gel	CH_4, 3.8	12	0.5
CH_4	Vycor	CH_4, 0.27	4.0	4.3
CH_4	Vycor	CH_4, 7.4	4.0	3.5
CH_4	Vycor	CH_3, 50	4.0	2.3
C_2D_4	Vycor	C_2D_4, 0.37	4.0	1.5
C_2D_4	Vycor	C_2D_4, 4.7	4.0	1.2
C_2D_4	Vycor	C_2D_4, 41	4.0	0.82

γ-Irradiation of Vycor containing 0.5 monolayer of H_2O, C_2H_4, c-C_6H_{12}, and 3-methylhexane has been reported[20] to produce trapped H atoms with *G* values of *ca.* 0.7, 0.6, 0.08, and 0.005.

The central esr signal from γ-irradiated porous Vycor containing adsorbed water has been attributed[20] to HO_2. Since we obtain an almost identical signal following irradiation of porous Vycor degassed by heating for 24 hr at 460° and $<10^{-5}$ Torr, we conclude that a more probable assignment is the interaction of trapped electrons with B atoms (Vycor contains 0.3% B_2O_3) as suggested in other work.[21]

As noted earlier, the high-purity Davison 950 silica gel used in this work contrasts with literature reports on other silica gels in that it does not become colored[22] on irradiation to doses of 7×10^{20} eV g^{-1} at 77 or 300°K, and that the esr spectrum is not bleachable by room light.[23] The measured *G* values for trapped unpaired spins produced by irradiation at 77°K were 0.079, 0.055, and 0.061 at 2×10^{19}, 6×10^{19}, and 1.2×10^{20} eV g^{-1}, respectively, as compared to 0.04 reported earlier for the dose range and gel degassed at somewhat lower vacuum.[7] The *G* values of trapped charges generated in silica gel were at least 10-fold lower when a sorbate was present during irradiation at 6×10^{-3} mf or higher as found by previous workers.[24] The esr spectrum of γ-irradiated silica gel degassed for 24 hr at 460° and $<10^{-5}$ Torr in this work was similar to that of a sample degassed 24 hr at 610° in previous work (ref 17, Figure 5) rather than to that degassed 24 hr at 460° and $<10^{-3}$ Torr (ref 7, Figure 1).

Discussion

G Values and Mechanism of Energy Transfer. In Table V are summarized the *G* values obtained at low doses in this work for radiolysis of alkyl chlorides, olefins, and CH_4 on silica substrates, together with selected values reported in the literature[24-32] for a variety of other compounds irradiated under similar conditions. Of the 38 values (15 for room temperature and 23 at 77°K), 24 lie in the range of 0.5 to 1.5 and most of the remainder are not dramatically different. These results bespeak a nonselective type of energy transport capable of initiating electron transfer, positive charge transfer, or energy transfer to sorbed molecules, dependent on the nature of the molecule, as suggested earlier.[5,10] This is in contrast to the interpretation[6a] that those sorbates with high-electron affinity capture electrons which have migrated as such through long distances in the silica. The conclusion is strongly supported by the nearly equal radical yields from alkyl chlorides (electron affinity *ca.* +3.7 eV), from CH_4 (as deduced from the experiments in the presence of oxygen), and from the olefins (electron affinity *ca.* −1.8 eV). It is also strongly supported by the relatively equal competition between CH_3Cl and C_2H_4 for activation when their mixtures are irradiated on silica gel (Table II), and by the independence of C_2H_5 yield on the composition of C_2H_5Cl–C_2H_4 mixtures on silica gel Table III). Five compounds, N_2O, $(C_2H_5)_2N_2$, CH_3OH, galvinoxyl, and TCNE, stand out in Table V as having *G* values of 3 or higher. There is, as yet, no simple unifying explanation.

Rojo and Hentz[10] have shown that γ-irradiation of silica gel at 77°K yields active surface sites capable of decomposing isopropylbenzene with $G = 4$, when the sorbate is added *after* irradiation and allowed to come to room temperature. When raised to room tempera-

(20) P. K. Wong, *J. Phys. Chem.*, **75**, 201 (1971).

(21) G. M. Muha and D. J. C. Yates, *ibid.*, **70**, 1399 (1966).

(22) (a) H. W. Kohn, *Nature (London)*, **184**, 630 (1959); (b) H. W. Kohn and E. H. Taylor, *Actes Congr. Int. Catal., 2nd, 1960*, **2**, 1461 (1961); (c) G. B. Pariiskii, Yu. A. Mishchenko, and V. B. Kazanskii, *Kinet. Katal.*, **6**, 625 (1965).

(23) P.-O. Kinell, T. Komatsu, A. Lund, T. Shiga, and A. Shimizu, Research Report LF-29, The Swedish Research Councils' Laboratory, Studsvik, Fack, 1970.

(24) P.-O. Kinell, A. Lund, and T. Vänngard, *Acta Chem. Scand.*, **19**, 2113 (1965).

(25) J. W. Sutherland and R. Goodrich, *J. Amer. Chem. Soc.*, **89**, 6779 (1967).

(26) N. H. Sagert and R. W. Robinson, *Can. J. Chem.*, **46**, 2075 (1968).

(27) N. H. Sagert and P. J. Dyne, *ibid.*, **45**, 615 (1967).

(28) O. Edlund, P.-O. Kinell, A. Lund, and A. Shimuzu, *Advan. Chem. Ser.*, **No. 82**, 311 (1968).

(29) P.-O. Kinell, A. Lund, and A. Shimizu, *J. Phys. Chem.*, **73**, 4175 (1969).

(30) R. R. Hentz, *ibid.*, **66**, 1622 (1962); **68**, 2889 (1964).

(31) P. K. Wong, Ph.D. Thesis, University of Wisconsin, Madison, Wis., 1968.

(32) G. M. Zhabrova, V. I. Vladimirova, and B. M. Kadenatsi, *J. Catal.*, **12**, 238 (1968).

Table V: Selected G Values of Stable Products and Radicals from Radiolyses on Silica Gel and Vycor Porous Glass[a]

Sorbate[b]	Concn, mf × 10^3	T, °K	Stable products or radicals formed	Integral G, 100 eV^{-1}
CH_3Cl	6	300	$\Sigma(CH_4 + 2C_2H_6)$	0.81
CH_3Cl	6	77	$\Sigma(CH_4 + 2C_2H_6)$	0.83
CH_3Cl	90	77	CH_3	0.73
$CH_3Cl + O_2$	6, 60	77	CH_3O_2	0.86
CH_3Br	12–75	77	CH_3[6]	1.4
CH_3I	13	273	$\Sigma(CH_4 + 2C_2H_6)$[7]	1.02
C_2H_5Cl	30	77	C_2H_5	0.58
C_3H_7Cl	30	77	i- and n-C_3H_7	0.8
CH_4	38	77	CH_3	0.13
$CH_4 + O_2$	8, 50	77	$^1/_2\Sigma(CH_3O_2 + HO_2)$	0.98
C_2H_4		300	$\Sigma(^1/_2CH_4 + C_2H_6 + {}^3/_2C_3H_8 + 2C_4H_{10})$	1.18
C_2H_4	30	77	C_2H_5	1.22
C_2D_4	62	77	C_2D_4H	0.92
C_2D_4 on VPG	47	77	C_2D_4H	0.78
C_3H_6	13	77	i- and n-C_3H_7	0.8
N_2O	0.55	283	N_2[25]	0.52
N_2O	68	283	N_2[25]	3.1
N_2O	40[c]	273	N_2[26]	3.2
$N_2O + CCl_4$	40,[c] 20[c]	273	N_2[26]	1.0
$N_2O + SF_6$	40,[c] 20[c]	273	N_2[26]	1.0
$N_2O + C_6D_{12}$	0.2,[c] 20[c]	308	N_2[27]	1.0
$(C_2H_5)_2N_2$	6	296	N_2[8]	0.5
$(C_2H_5)_2N_2$	66	296	N_2[8]	4.2
CH_3OH	4–110	293	$HCHO + HOCH_2 - CH_2OH$[32]	4.4
C_2H_5OH on Cabosil	4–30	296	$^1/_2H_2$	1.5
C_6H_6	7	77	$C_6H_5 + C_6H_6^+$[28]	0.95
C_6H_6	36	77	$C_6H_5 + C_6H_6^+$[28]	1.29
C_6H_6	0.3	77	$C_6H_6^-$[31]	2.1
Naphthalene	0.3	77	$C_{10}H_8^-$[6]	2.1
Biphenyl	0.3	77	$C_{12}H_{10}^-$[6]	2.1
Naphthalene	5	77	$C_{20}H_{16}^+ + C_{10}H_9$[29]	*d*
Biphenyl	4	77	$C_{12}H_{10}^+$[29]	*d*
Galvinoxyl	0.005–0.1	300	Galvinoxyl$^-$[6]	4.7
Galvinoxyl	0.005–0.1	77	No product[6]	0.0
TCNE on VPG	≥0.04	77 and 300	$TCNE^-$[5]	6.5
TPA on VPG	0.006–0.7	77	TPA^+[5]	0.76
TMPD on VPG	0.006–0.7	77	$TMPD^+$[5]	1.9
C_5H_{12}	64	298	$\Sigma(C_5H_{10} + 2C_{10}H_{22})$[2]	1.8
Cumene	2	77	C_6H_6[10]	2.2
Cumene on silica–alumina	2	77	C_6H_6[30]	1.45

[a] Data are from work of this paper at a γ dose of ~10^{19} eV g^{-1} except as indicated by reference numbers following formula of the product. [b] Support is silica gel unless stated as VPG. [c] Converted from monolayer units on assumption that 1 monolayer = *ca.* 0.4 mf. [d] Not determined.

ture without the sorbate the sites decay by 50% in a few minutes and then much more slowly, to about 20% of the original value over 3 days. Generation of these sites at 77°K reaches a plateau value at a dose of about 10^{20} eV g^{-1}, similar to the onset of the plateau for production of CH_4 plus C_2H_6 from CH_3Cl (Figure 1). The authors have ascribed the plateau to a steady state in which the active centers are being destroyed by radiation effects as fast as they are produced. This explanation is not applicable to the data of Figure 1, since the sorbate is present during irradiation and is capable of reacting with the active centers as rapidly as they are produced. The rapid initial fall-off in differential G values (Figure 2) suggests that there may be of the order of 5×10^{17} sites per gram from which energy absorbed in the bulk of the gel can be readily transferred to sorbed molecules, with many other sites where the transfer efficiency is much lower. The absence of a fall-off in G with dose at 300°K suggests that the more active sites desorb the product molecules and accept new molecules at this temperature.

Wong and Allen[5] have found that $TCNE^-$ is formed with $G = 4.2$ when TCNE is added to irradiated Vycor at room temperature, indicating trapped active

sites that are apparently more stable to decay than those produced in silica gel at 77°K. Neither the chlorides or hydrocarbons used in the present work show any evidence of such sites on silica gel or Vycor, but, as noted, there is evidence for polymerization of C_2H_4 added following irradiation.

Free Radical Formation and Reactions. As indicated in Table V, significant yields of trapped radicals are formed by γ-irradiation of CH_3Cl, CH_3Br, C_2H_5Cl, or C_3H_7Cl on silica gel at 77°K. In none of these cases was there evidence of appreciable rupture of any bond other than the carbon–halogen bond. The trapped radicals all decayed rapidly at room temperature and no observable radicals were produced by γ-irradiation at 300°K.

The production of ethyl radicals with a G value of 0.8 from both C_2H_4 and C_2D_4 on silica gel, and from C_2D_4 on Vycor (and similar production of iso- and *n*-propyl radicals from propylene on Vycor) indicates a high efficiency for the sequence: silica → excitation; excitation + C_2H_4 → C_2H_4*; C_2H_4* + HOSi → C_2H_5 + OSi, the final step in the sequence being confirmed by the formation of C_2D_4H from C_2D_4. Previously reported paramagnetic products from ethylene present on silica gel during γ-irradiation[33] at 77°K, or added after irradiation,[19a] have been assigned to ethyl radicals although only a tentative assignment was possible because of the poorly resolved esr spectra.

$G(CH_3)$ formed from 6×10^{-3} mf CH_3Cl at 77°K is 0.27 (Table I). The yield of (CH_4 plus $2C_2H_6$) recoverable on warming to 300°K (Table II) is equivalent to that formed by radiolysis at 300°K (*i.e.*, *ca.* 1). If oxygen is present during radiolysis at 77°K trapped peroxy radicals are produced with a yield of 0.86. These data suggest that all CH_4 production is *via* free radicals, $(1 - 0.27)/1$ of which abstract hydrogen from the surface by hot reaction at 77°K and 0.27/1 of which do so by thermal reaction during warm-up. In the presence of the high concentration of O_2 used (60×10^{-3} mf = *ca.* 0.15 monolayer) they all react with adjacent oxygen molecules to form the peroxy radicals. However, the data do not preclude the possibility that the yields of CH_4 and CH_3O_2 in excess of the 0.27 trapped radical yield observed in the absence of O_2 are the result of excited molecule reactions rather than radical reactions (*e.g.*, $CH_3Cl^* + O_2 \rightarrow CH_3O_2 + Cl$). In the presence of a high concentration of O_2 the peroxy radical yield from CH_4 is double that from CH_3Cl, suggesting that HO_2 as well as CH_3O_2 is formed.

The increase in $G(CH_3)$ with increase in methyl halide concentration on the surface (Table I) may result from a lessening of the probability of the freshly formed hot CH_3 radicals abstracting H from silanol groups before moderation, when the silanol groups are shielded by CH_3Cl molecules.

There are two demonstrations from the present work of the ability of methyl radicals stabilized on silica gel to react with reagents added *after* irradiation. One is their quantitative conversion to peroxy radicals when the sample is exposed to oxygen, the other is the formation of propane when C_2H_4 is added (experiment 7, Table II).

Reaction Initiated by Stable Active Sites in Irradiated Silica. When 6×10^{-3} mf of C_2H_4 was added at 77°K to silica gel containing 0.6×10^{-3} mf CH_3Cl which had received a dose of 4×10^{20} eV g^{-1}, an amount equivalent to $G(-C_2H_4) = 4$ was not recoverable on warming (experiment 7, Table II). A similar amount was lost when the C_2H_4 alone was present during irradiation at 77°K and about three times as much when present during irradiation at 300°K. This suggests that stable sites on the surface initiate polymerization chains which form a nonvolatile product, the chains being longer at the higher temperature. Samples of porous Vycor glass with or without adsorbed C_2H_4 or C_2D_4 (4×10^{-3}–4×10^{-1} mf) had a transparent brown color following γ-irradiation at 77°K with doses of 2.4×10^{20} eV g^{-1}. After warming to room temperature the samples containing adsorbed ethylene became translucent within minutes and turned white after *ca.* 30 min. This observation suggests that polymerization occurs during warm-up of samples but not at 77°K.

Variables Which Affect G Values. The variety of variables which influence the G values of reactions induced by irradiation of sorbates on silica gel is a source of difficulty in seeking to define the reaction mechanisms. In the present work this is illustrated by the following: (1) the sensitive dose dependence at 77°K of the G values of stable products and radicals in the range of 1×10^{19} eV g^{-1} to 2×10^{20} eV g^{-1} (Figure 2); (2) the difference in $G(CH_3)$ from CH_3Br for gels prepared at 200 and 400° (Table I); (3) the concentration dependence of $G(CH_3)$ from CH_3Cl and CH_3Br (Table I) as compared to the independence of concentration observed in previous work[6] with similar systems.

(33) Yu. A. Sorokin, V. I. Tupikov, E. A. Borisor, and V. F. Zakharov, *Khim. Vys. Energ.*, 3 (5), 457 (1969).

Annealing and Other Variables Which Affect Observed Decay Rates of Trapped Electrons in 3-Methylpentane Glass[1]

by David Shooter and John E. Willard*

Department of Chemistry, University of Wisconsin, Madison, Wisconsin 53706 *(Received May 2, 1972)*

Publication costs assisted by the U. S. Atomic Energy Commission

The rate of decay at 77°K of trapped electrons produced by γ-irradiation of 3-methylpentane (3MP) glass decreases with time of annealing of the matrix at 77°K before γ-irradiation, and, for short annealing times, is dependent on the geometry of the sample. In quench cooled samples in 2-mm i.d. tubes the initial half-life increases from 10 min without annealing to 60 min for samples annealed for 250 hr, but there is little or no effect of annealing on the yields and absorption spectra of the trapped electrons. Decay rates measured by esr and ir have been compared and sources of error in both types of measurement considered.

Introduction

The yields, decay properties, and spectra of trapped electrons produced in rigid hydrocarbon glasses by γ-irradiation have been studied in a number of laboratories to obtain a better understanding of trapping phenomena.[2] In the present work we have investigated the influence of two experimental variables suspected of having previously unrecognized effects on the results of such studies. These are preirradiation annealing of the matrix and changing microwave power saturation of the trapped electron esr signal as decay progresses. Earlier work[3] suggesting an effect of cooling rate of the matrix on trapped electron decay rates has been extended, and other experimental variables in esr and infrared measurements of trapped electron decay have been reviewed.

Experimental Section

Phillips pure grade 3MP was prepared for use by passage through a column of freshly activated silica gel and storage on the vacuum line over a sodium mirror, from which it was distilled into the Suprasil cells used for irradiation and esr and ir spectrometry. Cylindrical 2-mm i.d. and rectangular 2 mm × 3 mm i.d. cells were used for both esr and ir measurements. Cylindrical 8-mm i.d., rectangular 1 mm × 6 mm i.d., and square 1 cm × 1 cm i.d. cells were also used for ir measurements. γ-Irradiations were made with a ^{60}Co source at dose rates of 3.6×10^{18} eV g^{-1} min^{-1} on the small cells and 2×10^{18} eV g^{-1} min^{-1} on the large cells. During irradiation the samples were immersed in liquid nitrogen maintained at *ca.* 71°K by bubbling He gas.[4]

Trapped electron concentrations were monitored at 1560 or 950 nm, depending on the optical density, using a Cary 14 spectrophotometer modified to pass the infrared analyzing beam through the monochromator before passing through the sample. Esr measurements were made with a Varian 4500 X-band spectrometer equipped with Fieldial, using 100-kHz modulation, a 4531 cavity, and a modulation amplitude of 4 G or less with samples under liquid nitrogen, at 77°K, or at 71°K with the aid of a stream of helium entering the finger of the Varian dewar 3 cm from the bottom. Microwave powers of 0.5 to 600 μW incident on the cavity were obtained with the cavity attached to the low-power arm of the microwave bridge and a resistive terminator attached to the high-power arm. The power passing down the low-power arm to the cavity was determined with a Hewlett-Packard power meter (Model 431c) for powers down to 30 μW. Lower powers were determined from the height of the 3MP radical signal relative to its height in the range above 30 μW, after showing that the radical signal does not saturate in the 30- to 300-μW range (*i.e.*, a plot of radical signal height *vs.* $(power)^{1/2}$ is linear). The spectrometer sensitivity was monitored using a strong pitch sample.

In this work rates of trapped electron decay are indicated by the "initial half-lives" (*i.e.*, the time for half of the electrons to decay starting at a specified short time after a specified short irradiation). The kinetics of the decay[2a] are time-dependent first order, *i.e.*, plots of log $[e^-_{tr}]$ *vs.* t decrease in slope with time but are first order in dose (the decay curves for different doses are superimposable after normalization for dose). This indi-

(1) This work has been supported in part by the U. S. Atomic Energy Commission under Contract No. AT(11-1)-1715 and by the W. F. Vilas Trust of the University of Wisconsin.

(2) For examples and references see: (a) J. E. Willard in "Fundamentals of Radiation Chemistry," P. Ausloss, Ed., Wiley, New York, N. Y., 1968, Chapter 9; (b) A. Ekstrom, *Radiat. Res. Rev.*, **2**, 381 (1971); (c) H. Hase, M. Noda, and T. Higashimura, *J. Chem. Phys.*, **54**, 2975 (1971); (d) D. P. Lin and L. Kevan, *ibid.*, **55**, 2629 (1971); (e) J. Miller, *ibid.*, in press.

(3) (a) J. Lin, K. Tsuji, and F. Williams, *J. Amer. Chem. Soc.*, **90**, 2766 (1968); (b) K. Tsuji and F. Williams, *Int. J. Radiat. Phys. Chem.*, **1**, 383 (1969).

(4) F. W. Lytle and J. T. Stoner, *Science*, **148**, 1721 (1965).

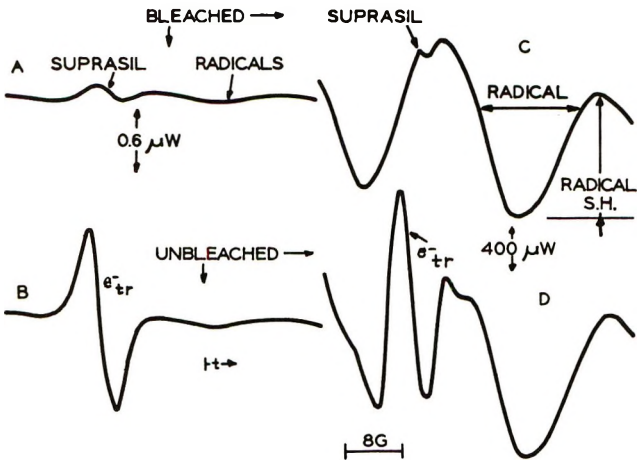

Figure 1. Esr spectra at 71°K of γ-irradiated 3MP at powers of 0.6 and 400 μW before and after bleaching: dose, 1.7×10^{19} eV g^{-1}.

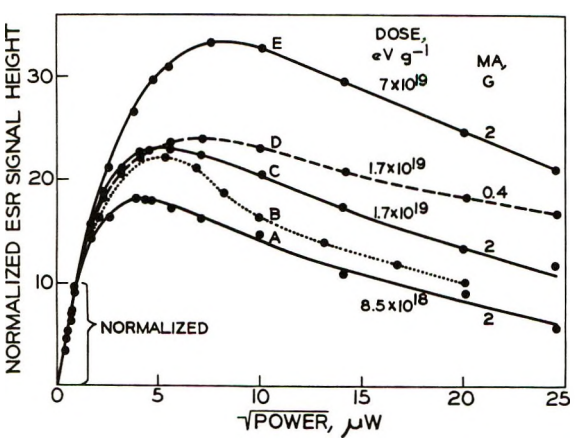

Figure 2. Dose and modulation amplitude dependence of esr power saturation curve of trapped electrons in γ-irradiated 3MP at 71°K. All data are normalized to the low power, nonsaturated data of curve C. Curve B shows results of Williams, *et al.*,[3] obtained at a modulation frequency of 400 Hz and a modulation amplitude of 1.7 G or less after a γ dose of 1.2×10^{19} eV g^{-1}.

cates that essentially all e^-_{tr} combine with a positive ion or radical within the parent spur, and possibly with the geminate positive ion.

Effects of Microwave Power, Dose, and Modulation Amplitude on Esr Signal of Trapped Electrons in 3MP Glass. Figure 1 shows typical (normalized) esr spectra from 3MP glass observed at 71°K following a 1.7×10^{19} eV g^{-1} γ dose at 71°K using microwave powers of 0.6 and 400 μW. Of the three signals contributing to the spectra, (*i.e.*, the radical signal, the Suprasil signal, and the trapped electron signal), only the trapped electron signal was observably affected by the output of a 25-W tungsten lamp. The line width and magnetic field position of the electron signal did not vary in these investigations. The electron concentration was taken as proportional to the change of the vertical distance between the points of zero slope of the electron signal when the signal was exhaustively photobleached, under conditions where the background was small (Figure 1B).

Curves A, C, and E of Figure 2 show normalized signal heights of the trapped electron esr signal as a function of the square root of the microwave power for three samples of 3MP glass in 2-mm i.d. tubes which had received different γ doses. The power range over which the signal is unsaturated and the power at which the maximum of the saturation curve is reached are both greater the higher the dose. These effects are attributable to a decrease in the spin–spin relaxation time with increasing spin concentration. Reduction in the modulation amplitude from 2 to 0.4 G increases the power at which the saturation curve reaches its maximum (curves C and D). Curve B for a modulation amplitude of 1.7 G at 400 Hz is from the work of Williams, *et al.*[3a]

Curves A and B of Figure 3 indicate a shift toward saturation at lower powers as trapped electron decay

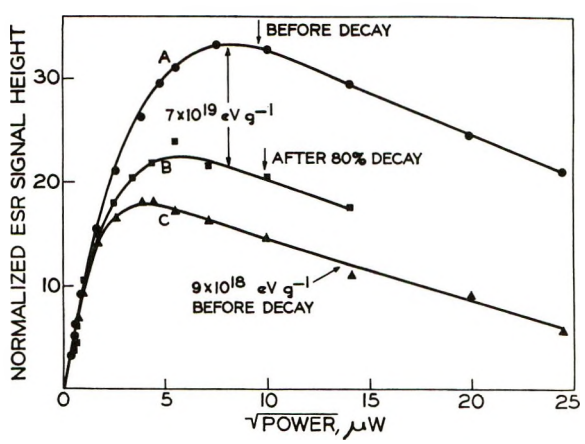

Figure 3. Esr power saturation curves of trapped electrons in 3MP at 71°K: A, 7.2×10^{19} eV g^{-1}, before decay; B, same as A but after 88% decay; C, 9×10^{18} eV g^{-1}, before decay, the trapped electron concentration in C was the same as in B.

progresses. This is attributable to a decrease in spin–spin interaction with decreasing concentration. Curve C of Figure 3 is for a sample which received a dose $^1/_8$ that of the curve A to produce an electron concentration the same as that in the sample of curve B. The higher powers required for saturation of the partially decayed sample (B) which had received the higher dose may be attributed to spin–spin interaction of the trapped electrons with the trapped radicals.

The trapped electron decay plots of Figure 4, obtained from identical 2-mm i.d. samples monitored at 0.7 and 10 μW, show the type of error which results from measurements at a microwave power at which the degree of saturation changes with decay (Figure 3). It is not sufficient to use a power where the signal is initially unsaturated. A power sufficiently low so that the normalized decay plots are independent of power

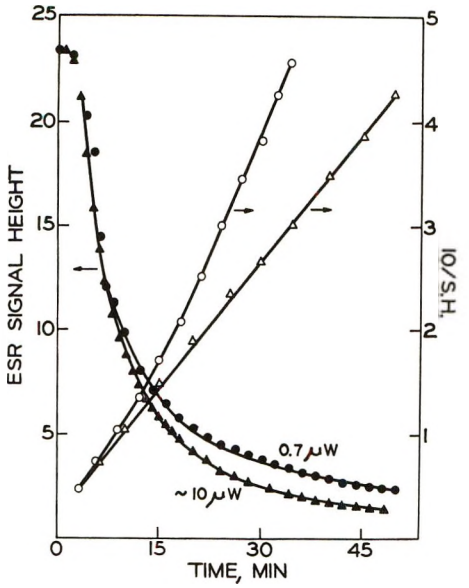

Figure 4. Dependence of decay of trapped electron esr signal from γ-irradiated 3MP at 77°K on microwave power: solid points show linear plot; open points reciprocal plot; open circles 10 μW; open triangles 0.7 μW.

(*i.e.*, superimposable over the whole decay range of interest) must be used.

Effects of Sample Geometry and Preirradiation Annealing of 3MP Glass at 77°K on Decay Rate of Trapped Electrons. Early in the study of the decay of trapped electrons in 3MP glass it was noted that rates observed in 1-cm² cells by ir transmission were slower (half-lives of 35 to 45 min) than those observed in 3-mm i.d. tubes by esr (5 to 10 min). Using an esr cavity which would accommodate a 1-cm² cell, Tsuji and Williams[3] showed that the rates observed by ir and esr are similar when similar sized samples are used, and suggested that the faster decay with small samples is related to a faster rate of cooling of the 3MP.

We have confirmed that the rate of cooling of the 3MP to the glassy state affects the decay rates of trapped electrons produced by subsequent γ-irradiation. Two samples cooled in 2-mm i.d. tubes to 102°K in 15 min and then to 77°K at *ca.* 1° min^{-1} gave initial half-lives of 28 and 27 min, while four identical samples prepared by fast quenching in liquid nitrogen to 77 or 71°K gave half-lives of 10 ± 1.0 min. In each case the half-life was independent of whether measurement was made by ir or esr.

Further experiments have shown that annealing of quench-cooled 3MP at 77°K, like slow cooling, decreases the decay rate of trapped electrons. The initial half-lives in a 2-mm i.d. tube increased from 10 min to over 60 min as the preirradiation annealing time at 77°K was increased from 5 min to 250 hr (Figure 5).

For half-lives >30 min, the half-lives given in the last paragraphs were measured starting 2 min after the end of a 5-min irradiation at 77°K. For shorter half-lives the sample was transferred to an esr dewar at

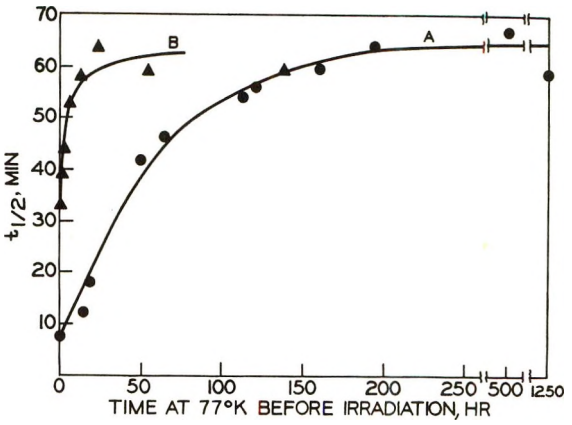

Figure 5. Dependence of initial half-life of trapped electrons in 3MP glass at 77°K on time of preirradiation annealing at 77°K: (A) 2-mm i.d. samples; (B) 1-cm² samples.

71°K after irradiation at 71°K. Zero time for the decay was taken as the time at which the back-extrapolated decay curve reached the electron concentration observed at 71°K. The half-lives from ir measurements in 1-cm² cells irradiated at 77°K, given below, were all >30 min and were measured starting 2 min after a 1.5-min irradiation.

The half-life (as defined above) of the trapped electrons in quench-cooled (*i.e.*, less than 5 min from immersion to beginning or irradiation) 1-cm² samples as measured by ir under our most reproducible conditions was 33 min. This value rises with increasing time of preirradiation annealing to an apparently constant value of slightly over 60 min after approximately 50 hr of annealing (Figure 5B).

Consistent with the trend of decay times described, the half-life for a quench-cooled sample in an 8-mm i.d. cylindrical tube is *ca.* 20 min. Surprisingly, however, the decay time in a quench-cooled sample in a rectangular 2 mm × 3 mm i.d. cell is 35 min, as measured by either esr or ir. Likewise surprising is the 49-min half-life in samples in flat "paddle" cells with internal dimensions of 6 mm × 1 mm and several centimeters high. These results (Figure 6) indicate that trapped electron decay rates in incompletely annealed samples are dependent not only on the thickness (and hence rapidity of cooling) of the sample when it is quenched, but also on its geometry. However, it appears (Figures 5 and 6) that in completely annealed samples the decay rates are independent of the geometry. The data of Figure 6 indicate, somewhat unexpectedly, a tendency for the rate of approach to the completely annealed state to be faster in the samples formed closer to equilibrium than in those farther removed, a feature which may, again, be geometry dependent.

Some additional observations have been made on the decay kinetics of the trapped electrons in unannealed and annealed samples. (1) Plots of log $[e^{-}_{tr}]$ *vs.* time

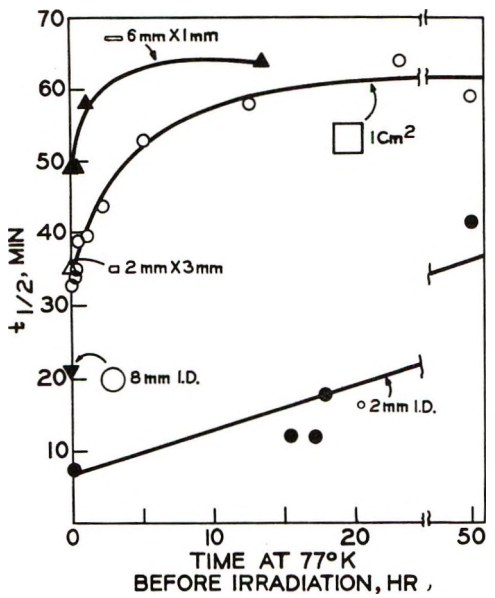

Figure 6. Dependence of initial half-lives of trapped electrons in 3MP glass at 77°K on time of preirradiation annealing at 77°K and on sample geometry. The cross sectional shape of each of the five cells used is depicted with the dimensions adjacent to each curve. The horizontal scale is contracted between 25 and 50 hr.

for decay at 77°K are always curved but, consistent with observations in several laboratories, are first order in dose (*i.e.*, the decay curves are superimposable after normalization for dose) over the range of 3×10^{18} to 1×10^{19} eV g^{-1} and 80% decay for which we have followed them. This is true for both annealed and unannealed samples. (2) Plots of $1/[e^-_{tr}]$ *vs.* time for samples with short trapped electron half-lives (*e.g.*, in quench-cooled, 2-mm i.d. tubes) are always linear, with slopes which vary with the initial concentration (*i.e.*, with the dose). (3) Plots of $1/[e^-_{tr}]$ for unannealed samples with half-lives >30 min (*e.g.*, quench cooled in 1-cm² cells) are curved (Figure 7). However, the curvature decreases as the preirradiation annealing time is increased. For samples in which annealing is nearly complete, the $1/[e^-_{tr}]$ *vs.* time plots are linear from the start. Curvature seems to be observed only when appreciable decay and appreciable annealing (*i.e.*, change in matrix characteristics) occur in the same time period. Thus it is only when the sample is completely annealed or anneals slowly relative to the decay rate that decay is not influenced by simultaneous changes in the matrix.

Within experimental error, the microwave power saturation properties of the trapped electron are the same in a sample in a 2-mm i.d. tube irradiated immediately after quench cooling to 77°K, as in a similar sample irradiated after 200-hr annealing at 77°K. Likewise the trapped electron yield was the same for annealed and unannealed samples, and the trapped electron spectra from 600 to 2160 nm in 1-cm² cells were unaffected by preirradiation annealing.

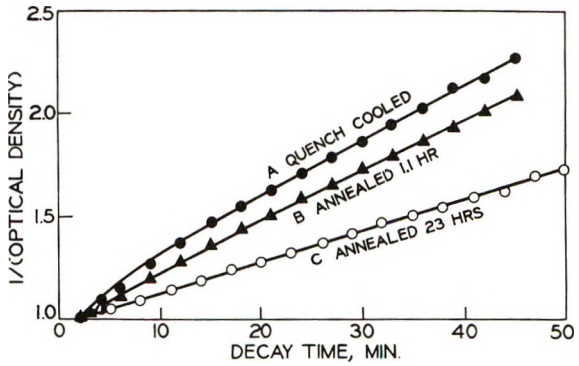

Figure 7. Dependence of second-order plots of trapped electron decay in 3MP on time of preirradiation annealing of 1-cm² samples at 77°K.

Measurement of Trapped Electron Concentration by Ir Absorption. Significant differences in apparent decay rates of trapped electrons observed in identical samples by infrared absorption can result from such factors as (1) changes in optical density resulting from smoothly changing concentrations of ice crystals as more are produced or as they settle out during an experiment and (2) systematic changes in the rate of liquid nitrogen bubbling with resultant changes in "noise" which affects the apparent baseline. Surrounding the top of the dewar with a box of flowing nitrogen gas minimizes ice formation. Bubbling can sometimes be reduced by rinsing the dewar with liquid nitrogen before the final filling. In work at lower temperatures (produced by bubbling helium gas through the liquid nitrogen) nitrogen bubbling is reduced.

In a previous study in our laboratory[5] the effects of both ice and bubbling on the measurement of light transmission by samples at 77°K have been avoided by using Suprasil rods as light pipes to conduct the light through the liquid nitrogen to and from the cell. In some cases the rods were sealed to the optical faces of the cell and in others the cell fit closely between the inner ends of the rods. The outer ends of the rods were sealed through the sides of a styrofoam-lined metal box of liquid nitrogen which could be positioned in the sample compartment of the Cary spectrophotometer. The light pipe technique was completely successful in eliminating ice and bubbling effects and should be generally useful for spectrophotomeric studies under liquid nitrogen.

Discussion

This work has shown that the yields of trapped electrons produced by γ-irradiation of 3MP glass are independent of the time of annealing of the glass at 77°K prior to irradiation and of the sample geometry, but that the decay rate of the electrons is dependent on both of these factors. This dependence is lost when samples have been completely annealed. The absorp-

(5) R. Fass and J. E. Willard, unpublished results.

tion spectrum of the trapped electrons which decay with a half-life of 30 min is indistinguishable from that of those which decay with a half-life of 60 min. These facts suggest that annealing does not change the number or depth of the electron traps but rather involves a change in matrix rigidity on the molecular scale which decreases the rate at which the trapped electrons can diffuse. This decrease is presumed to be due to a decrease in free volume in the glass as it anneals at a temperature at or below the glass transition.

Current work of S. L. Hager in our laboratory indicates that unirradiated 3MP glass shows an endothermic differential thermal analysis peak at 82°K when warmed from 77°K. The magnitude of this peak increases with time of annealing of the sample at 77°K for time intervals similar to those required to produce maximum trapped electron decay times. By analogy with DTA studies[6] on polymeric systems the peak is presumed to reflect the energy necessary for regaining the free volume which is lost while annealing the sample at 77°K.

Preirradiation annealing has been found to change postirradiation phenomena other than electron decay in 3MP glass. It causes a decrease in the luminescence intensity,[7] a decrease in the 3MP radical decay rate,[8] and a lengthening of the observed phosphorescence lifetime of deuteriobenzene solute.[9] Quantitative correlation of the effects relative to annealing times is not possible because of differences in sample size, sample geometry, and rate of cooling.

(6) (a) J. R. McLoughlin and A. V. Tobolsky, *J. Polymer Sci.*, **7**, 658 (1951); (b) Yu. A. Sharonov and M. V. Vol'kenshtein, *Sov. Phys. Solid State*, **5**, 429 (1963).

(7) K. Funabashi, P. F. Herley, and M. Burton, *J. Chem. Phys.*, **43**, 3939 (1965).

(8) W. K. Kam and J. E. Willard, unpublished results.

(9) T. E. Martin and A. H. Kalantar, *J. Phys. Chem.*, **72**, 2265 (1968).

Modifications to a Precision Adsorption Apparatus. Interaction of the Inert Gases with Boron Nitride

by R. N. Ramsey, H. E. Thomas, and R. A. Pierotti*

School of Chemistry, Georgia Institute of Technology, Atlanta, Georgia 30332 *(Received May 8, 1972)*

Publication costs assisted by the U. S. Army Research Office—Durham

A modified high-precision volumetric adsorption apparatus is described. The apparatus incorporates a precision cryostat, the precise pressure-measuring techniques of gas thermometry, and a null capacitance manometer. The use of the capacitance manometer to separate the mercury manometer from the adsorption system is shown to eliminate a number of apparatus corrections and to simplify the acquisition of data. The apparatus is suitable for the investigation of the low-coverage, high-temperature physical adsorption region in which Henry's law behavior and deviations therefrom occur. Measurements are reported for the adsorption of neon, argon, krypton, and xenon on the hexagonal modification of boron nitride at 273°K. The results are analyzed using the gas–solid virial coefficient treatment to give energies of interaction of these gases with boron nitride.

Introduction

Studies of the physical adsorption of the inert gases on graphitized carbon blacks at low surface coverage have yielded important information on the nature of gas–solid interactions.[1] In the analysis the adsorption isotherm data are fitted to a virial equation in which the number of moles of gas adsorbed per gram of adsorbent, n_a, is given by[1]

$$n_a = B_{2s}\left(\frac{f}{RT}\right) + B_{3s}\left(\frac{f}{RT}\right)^2 + \ldots \qquad (1)$$

where f is the fugacity, R is the gas constant, T is the isotherm temperature, and B_{2s}, B_{3s}, ... are the gas–solid virial coefficients. The present analysis is concerned only with B_{2s}, the second gas–solid virial coefficient which is related to the Henry's law constant, and which is characteristic of the interaction between an isolated adsorbate molecule and the adsorbent. The determination of values of B_{2s} requires accurate adsorp-

(1) R. A. Pierotti and H. E. Thomas, "Surface and Colloid Science," Vol. IV, E. Matijević, Ed., Wiley-Interscience, New York, N. Y., 1971, pp 93–259.

tion isotherm data at low surface coverages (less than about 10%).

In this study we have modified the high-precision volumetric apparatus of Halsey and coworkers[2] and used the apparatus to study the adsorption of the inert gases on the hexagonal modification of boron nitride. This adsorbent was chosen because theoretical calculations based upon the lattice structure of boron nitride indicated that one might expect a substantially homogeneous surface.[3] This is a particularly important requirement when the analysis is extended to higher gas–solid virial coefficients. The adsorption of the inert gases was studied so that initially at least the complicating effects of restricted rotation, etc., could be avoided. The results reported here are for the adsorption of neon, argon, krypton, and xenon at 273°K. A detailed account of the modifications to the apparatus is given, and an analysis is presented that yields values of the energies of interaction of the inert gases with boron nitride.

Experimental Section

The precision apparatus, which is shown schematically in Figure 1, used a conventional volumetric technique: a dose of gas was introduced into the calibrated pipet system and a series of measurements of the pressure, volume, and temperature were used to calculate the amount of gas present. This dose of gas was introduced into the sample cell and additional measurements of pressure, volume, and temperature were made to determine the amount of gas adsorbed.

This apparatus is similar to that used by Constabaris, Singleton, and Halsey[2] in their study of the interaction of the inert gases with the graphitized carbon black, P33(2700).[4,5] However, a number of important modifications have been made and these will be described in detail. The main modifications are an improved sample cell and cryostat and the introduction of a null capacitance manometer between the mercury manometer and the pipet system.

Measurements of pressure were made with a precision mercury manometer system in which the meniscus heights were measured relative to etch marks on a standard meter bar using a travelling telescope. The details of the design and construction of the mercury manometer system are substantially the same as those used by Halsey and coworkers[2,6] and will not be described here. The manometer tubes and the standard meter bar were housed in the air thermostat and thermostated at 24.0 ± 0.03°. A series of six to eight measurements were made of each meniscus height. Pressures were measured with a precision of ±0.005 mm and were corrected to standard conditions.

Precise changes in the volume of the system were made by means of a system of accurately calibrated pipets.

The all-metal sample cell was enclosed in a cryostat

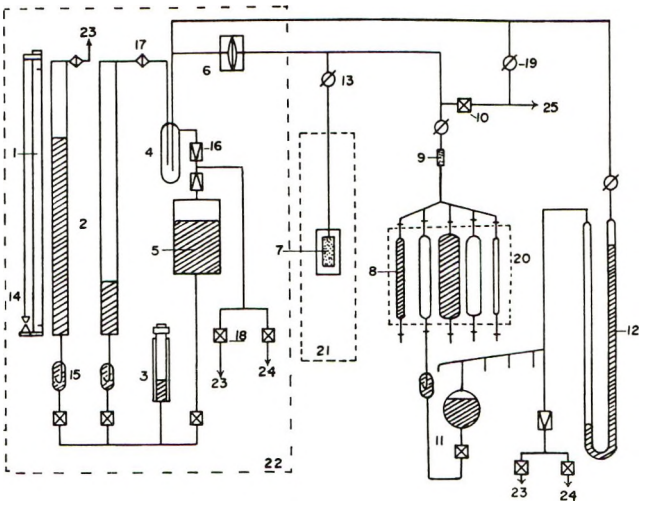

Figure 1. A schematic diagram of the apparatus: (1) standard meter bar; (2) precision mercury manometer; (3) fine mercury level control; (4) cold trap; (5) mercury reservoir (304 stainless steel); (6) null capacitance manometer; (7) nickel sample cell; (8) glass pipets; (9) gold trap; (10) main inlet valve; (11) mercury supply to pipets (one only shown); (12) differential mercury manometer; (13) sample stopcock; (14) plumb line; (15) symbol designates air trap; (16) symbol designates needle valve; (17) symbol designates fritted disk; (18) symbol designates metal stopcock; (19) symbol designates greased Pyrex stopcock; (20) ice box; (21) cryostat; (22) air thermostat; (23) to vacuum; (24) to helium cylinder; (25) vacuum and gas inlet line.

assembly which was used to control the sample temperature to better than 0.005° at any temperature in the range 65–300°K. The temperature of the sample was determined using a platinum resistance thermometer. The thermometer resistance was measured with a Leeds and Northrup thermostated Mueller bridge (Type 8069 B) to 0.0001 ohm (equivalent to 0.001°).

Before describing the calibration of the apparatus we list the details of the apparatus modifications.

Sample Cell. The nickel sample cell, which is shown schematically in Figure 2, had an internal volume of about 80 cm³. The $^1/_{16}$-in. diameter Monel tubing that connected the cell to the dosing system was joined to the cell top by a graded seal (Monel—silver solder—gold–nickel solder—nickel). A stainless steel screw with a $^1/_{16}$-in. axial hole held a small plug of Pyrex wool in a threaded recess to prevent the transport of the adsorbent from the cell by a sudden change in pressure.

The main cylindrical body of the cell had a thermometer well welded to its bottom edge to house the platinum resistance thermometer which was used for the

(2) G. Constabaris, J. H. Singleton, and G. D. Halsey, Jr., *J. Phys. Chem.*, **63**, 1350 (1959).

(3) R. A. Pierotti and J. C. Petricciani, *ibid.*, **64**, 1596 (1960).

(4) J. R. Sams, G. Constabaris, and G. D. Halsey, Jr., *ibid.*, **64**, 1689 (1960).

(5) J. R. Sams, G. Constabaris, and G. D. Halsey, Jr., *J. Chem. Phys.*, **36**, 1334 (1962).

(6) G. Constabaris, Ph.D. Thesis, University of Washington, 1957.

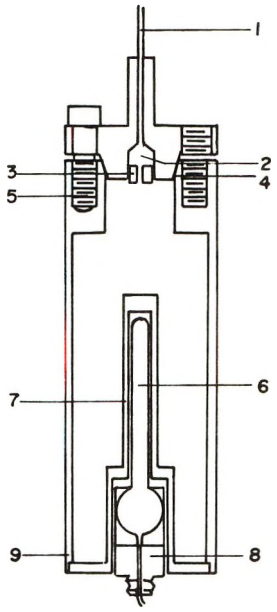

Figure 2. The sample cell: (1) Monel metal gas inlet tube ($^1/_{16}$ in.); (2) Pyrex wool plug; (3) stainless steel screw; (4) copper gasket (0.010 in.); (5) tightening bolt; (6) platinum resistance thermometer; (7) thermometer well; (8) Teflon block; (9) nickel sample cell (4.5 × 1.5 in.).

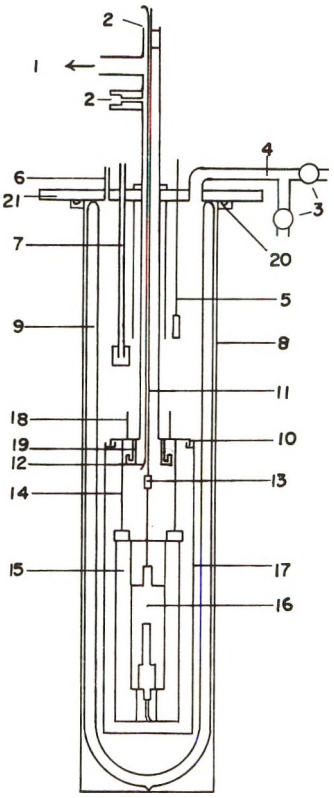

Figure 3. The cryostat: (1) to vacuum pump; (2) wire exit tube; (3) solenoid valves; (4) exhaust manifold (0.5 in.); (5) oxygen vapor-pressure probe; (6) refrigerant vapor-pressure probe; (7) refrigerant liquid level controller and filling tube; (8) outer brass container (32 × 6 in.); (9) glass dewar vessel; (10) Wood's metal seal; (11) gas inlet tube; (12) spare gas inlet tube; (13) Monel metal union; (14) support wire; (15) main copper block (8 × 2.9 in. o.d.); (16) sample cell; (17) inner brass container (14 × 4 in. o.d.); (18) water well; (19) heat exchanger; (20) O-ring seal; (21) brass top plate (18 × 12 × 0.25 in.).

determination of the sample temperature and for the control of the cryostat. The head of the platinum resistance thermometer was encapsulated in a threaded Teflon block which was screwed into the surrounding copper block. Thermal contact between the resistance thermometer and the cell was made with white petroleum jelly.

A vacuum seal between the top and the body of the cell was made by bolting together the two sections on a preformed, well-annealed, 0.010-in. thick copper gasket placed between their tapered (10°) surfaces. This seal remained vacuum tight for many cycles between liquid nitrogen temperature and the outgassing temperature of about 500°. The free clearance holes in the sample cell top for the six tightening bolts were threaded to assist breaking the vacuum seal when dismantling the sample cell. To break the seal the tightening bolts were removed and metal strips were inserted between the main body and the top section. Bolts were threaded into the holes in the top of the cell and tightened so as to bear down on the metal strips and so force the two sections apart. If any copper from the gasket remained on the nickel surfaces it was removed by washing with acid. Thread lubricant was smeared on the bolts to prevent them from seizing during the temperature cycling.

Cryostat. The cryostat, which is illustrated in Figure 3, enabled the sample temperature to be controlled to better than 0.005° at any temperature in the range 65–300°K. The system included many of the details of the cryostats used by Halsey[2] and Morrison[7] but used a modified design for the metal block system and incorporated automatic control of the temperature and level of the refrigerant liquid in the outer dewar vessel.

The main copper block surrounding the sample cell had walls $^5/_8$ in. thick and a mass of 6 kg. Other copper blocks fitted into the spaces above and below the sample cell. Two heaters (each 140 ohm) were wound around the outside surface of the main block and were insulated with baked Glyptal lacquer. The first heater was supplied with a constant current which offset nearly all of the heat lost to the surroundings. Power to the second heater was regulated in the following manner. The resistance of the platinum resistance thermometer was monitored by a thermostated Mueller bridge and a guarded dc null meter (Leeds and Northrup 9834). The signal from the recorder output terminal of the null meter was fed through a 200-kilohm resistance to a galvanometer. A light beam was reflected from the galvanometer mirror toward two photocells which were positioned so as to be operated by the reflected beam

(7) J. A. Morrison and D. M. Young, *Rev. Sci. Instrum.*, **25**, 518 (1954).

when the temperature of the resistance thermometer changed by about 0.0005°. One photocell activated and the other deactivated a relay that fed power to the second block heater.

In the range 65–200°K the outer dewar was filled with liquid nitrogen and its level automatically controlled by a liquid level controller (Linde LL-6). At higher temperatures a Dry Ice–acetone mixture was used.

The temperature of the liquid nitrogen refrigerant was regulated as follows. The exhaust manifold leading from the refrigerant section branched after leaving the cryostat. One branch went through a solenoid valve to the atmosphere and the other went through another solenoid valve to a vacuum pump. The system used to control the temperature of the refrigerant liquid used two vapor pressure thermometers to control these solenoids. The first thermometer monitored the vapor pressure in a probe which was submerged in the refrigerant liquid and the second thermometer monitored the pressure above the refrigerant liquid. The probe was filled with a pure gas with a convenient vapor pressure at the required temperature (*e.g.*, oxygen). For an operating temperature below the normal boiling point of liquid nitrogen the oxygen vapor pressure thermometer operated the solenoid valve leading to the vacuum pump. The temperature was regulated by alternately isolating and pumping on the liquid nitrogen. The other solenoid valve was normally closed but was opened by the second vapor pressure thermometer when the cryostat was being topped up with liquid nitrogen because the normal setting of the vacuum line did not have the capacity to quickly expel the gas then being evolved. The thermal inertia of the system was such that the block temperature was not significantly disturbed by the inevitable pressure and temperature fluctuations caused by the topping up of the refrigerant.

For temperatures above the normal boiling point of nitrogen the system was operated by a control system in which the oxygen vapor pressure thermometer now controlled the solenoid valve leading to the atmosphere.

There are two advantages to these modifications. First the refrigerant could be controlled at temperatures above and below the normal boiling point and secondly the refrigerant temperature did not drift as a result of the change in the concentration of impurities (*e.g.*, oxygen).

Twelve copper–constantan thermocouples were used to monitor different temperatures in the cryostat. Eight were equally spaced along the length of the gas inlet tube; one was placed under and one on top of the sample cell; the other two were placed on the copper block surface, under the heaters.

Capacitance Manometer. In the apparatus design of Halsey and coworkers[2] the main mercury manometer is directly linked to the pipet sample line. In order to achieve the required small and well-defined volume in this section of the apparatus the mercury meniscus must then be set to a constant height, and volume corrections made for any variation in meniscus covolume or mis-set of the meniscus. For the error in these corrections to be small it is advantageous to use a small diameter manometer tube, but this would result in a significant error in the meniscus depression correction and a compromise size must be chosen. Uncertainties in these corrections reduce the accuracy of the apparatus.[2]

To eliminate these corrections the present apparatus incorporated a null capacitance diaphragm manometer between the adsorption system and the main mercury manometer. In this modified arrangement it is possible to measure the pressure without introducing the volume above the mercury meniscus into the adsorption system. The meniscus covolume and mis-set corrections are thus eliminated. Furthermore, the manometer tube is no longer subject to the correction compromise and it was made sufficiently large (25 mm) for the meniscus depression correction to be negligible.

The capacitance manometer (Granville-Phillips, Series 212B)was modified so as to present a small dead space volume to the adsorption system (2.9 cm^3) and was calibrated to account for the small change in the null point capacitance with internal gas pressure. It was carefully thermostated in the air thermostat and during operation great care was taken to avoid large deflections of the diaphragm. With these precautions a sensitivity and a long-term stability of better than ±0.002 mm were achieved. A Dry Ice trap was inserted between the mercury manometer and the capacitance manometer to prevent mercury contamination of the diaphragm head. An additional advantage of the capacitance manometer was that it prevented mercury vapor from the main manometer from reaching the sample.

Although it was no longer necessary to set the lower meniscus to a constant reference height in order to maintain a well-defined volume, the technique was retained for another reason. If the lower meniscus is set to a constant reference height then the uncertainty in the value of this height decreases as the run proceeds because of the large number of repetitive measurements and this results in an increased accuracy in the pressure measurement. The lower mercury meniscus was brought to a constant reference height defined by the cross hairs of a travelling microscope mounted in front of the manometer tube. The travelling microscope (Model 3507-K, Gaertner Scientific Corp.) had a greater sensitivity than the cathetometer telescope (Model M-300P, Gaertner Scientific Corp.). The meniscus level was adjusted using a mercury level control in which a stainless steel piston was driven into a stainless steel cylinder by a fine screw drive.

Other Modifications. A trap containing 2 g of gold

spheres about 2 mm in diameter was inserted in the glass capillary line above the pipets in order to prevent mercury vapor from reaching the sample cell. This trap was chosen rather than a cold trap because the latter would have introduced additional uncertainty in the temperature of this part of the dead space volume. The stopcock situated just above this trap enabled the pipet system to be isolated in the event of a prolonged outgassing of the sample.

The filling of the pipets was found to be difficult because the mercury could not be seen through the thermostating ice. Any overshoot was serious because of the ease with which mercury would fill the capillary tubing or form small droplets which would alter the volume calibration. The solution to this problem utilized the capacitance manometer system. A differential mercury manometer was connected between the reservoirs of the pipet mercury supply and the left-hand side of the capacitance manometer. With the capacitance manometer balanced this mercury manometer monitored the difference in pressure between a pipet and its reservoir and thus indicated the height of the mercury in the pipet. A setting was marked on the manometer to indicate the pressure difference required to just fill each pipet. During operation it was a simple matter to apply the appropriate pressure difference to fill (or empty) a chosen pipet.

Complete details of the adsorption apparatus including lists of components, manufacturer's specifications, and construction and handling techniques are available.[8]

Calibration

The pressure-measuring system, the cryostat, and the resistance thermometer were tested in a preliminary experiment in which the boiling point of pure oxygen was measured. Oxygen was condensed in the sample cell and measurements of vapor pressure were made in the range 32–758.3 mm using the precision mercury manometer. The temperature was determined using the platinum resistance thermometer which had been calibrated by the National Bureau of Standards. The value of the normal boiling point of oxygen was determined to be 90.190°K on the IPTS-68 scale. This is in very satisfactory agreement with the IPTS-68 defined value of 90.188°K. If one assumes that the whole discrepancy is the result of an error in the pressure measurement, which is unlikely, then it follows that this apparatus is capable of measuring the *absolute* pressure to 0.14 mm at a pressure of 760 mm.

A complete volume calibration of the apparatus was carried out prior to the isotherm determinations. The pipets, which had volumes of about 10, 20, 40, 60, and 150 cm^3, were calibrated *in situ* using direct mercury weighing. The average standard deviation on the pipet volumes was ± 0.0008 cm^3. The external dead space volume (*i.e.*, the volume between the top pipet etch marks, the sample stopcock, and the capacitance manometer) was considered in two parts, the division being at the air thermostat wall. The volume of the capacitance manometer and the tubing within the air thermostat was estimated from its geometric dimensions to be 2.931 cm^3. A series of compression–expansion measurements using neon were used to determine the volume of the remaining part of the external dead space volume. Several copper–constantan thermocouples and thermometers, which had been calibrated by reference to the resistance thermometer, were used to obtain a representative mean room temperature for this section. The total external dead space volume was determined to be 4.703 ± 0.004 cm^3. The volume from the top of the massive copper block to the sample stopcock was estimated in ten parts using the sample inlet tube cross section. This degree of volume division was necessary because of the large temperature gradient in this section. Eight thermocouples and a thermometer were used to determine mean temperatures for these sections. The total volume of this connecting tubing was determined to be 0.8517 cm^3. The sample dead space volume was calibrated by means of three series of compression–expansion measurements using helium with the sample thermostated at 0°. The volume was determined to be 40.719 ± 0.009 cm^3. The mass of the boron nitride sample was 83.47 g.

Results

The apparatus was used to measure the adsorption of neon, argon, krypton, and xenon on the hexagonal modification of boron nitride. The sample was obtained from the Refractories and Electronics Division of the Carborundum Co. and was designated HPC (high purity coarse). The adsorption isotherms were determined as follows. With the sample isolated a dose of gas was admitted into the pipet system. Several sets of pressure and temperature measurements were made at various pipet settings to determine the number of moles of gas in the dose. For all such calculations the bulk virial equation was used, neglecting terms following the one in the second bulk virial coefficient. When the amount of gas in the dose had been determined the sample stopcock was opened and a series of pressure and temperature measurements were made at various pipet volumes that were chosen so as to cover the required isotherm pressure range. The amount adsorbed was calculated as the difference between the amount of adsorbate present in the sample cell during isotherm determination and the amount that would be present in the absence of gas–solid interactions (except volume exclusion as determined by the helium calibration). The results reported here are for the adsorption of the inert gases at 0°. The isotherms are shown in Figure 4 and the data are listed in Table I. The gas–

(8) R. N. Ramsey, Ph.D. Thesis, Georgia Institute of Technology, 1970.

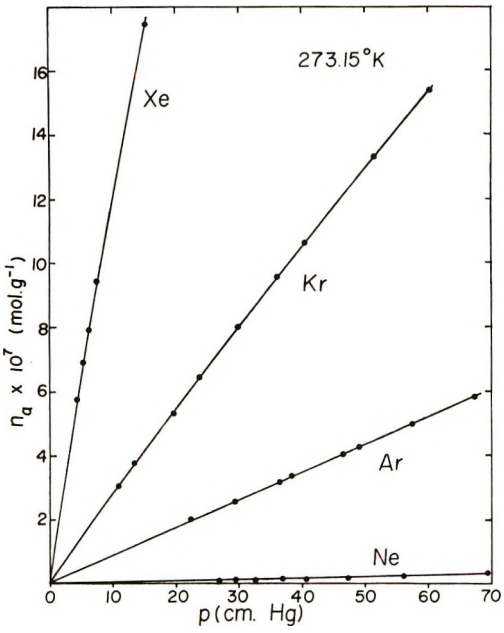

Figure 4. Adsorption isotherms for the inert gases on hexagonal boron nitride at 273.15°K. A value of n_a = 6×10^{-7} mol g^{-1} corresponds to about 1% coverage based upon the BET area.

solid virial coefficients were determined either by computer fitting the data to eq 1 or by plotting the apparent Henry's law constant (n_a/p) *vs.* pressure. In the latter case the intercept at zero pressure yields a value for the second gas–solid virial coefficient, B_{2s}. Values for this coefficient are given in Table II.

Table I: Isotherm Data for the Inert Gases on Boron Nitride at 273.15°K

p, cm	$n_a \times 10^7$, mol/g	p, cm	$n_a \times 10^7$, mol/g
Ne		Ar	
26.7784	0.119	29.3239	2.569
29.5353	0.126	36.3953	3.214
32.6475	0.130	46.4687	4.067
36.8345	0.171	67.1690	5.842
40.6380	0.170	22.2852	2.010
47.3381	0.220	38.3569	3.388
55.8725	0.253	48.9704	4.294
69.3687	0.353	57.4902	5.009
		70.7890	6.170
Kr		Xe	
10.8345	3.051	4.2956	5.760
13.3602	3.781	5.2533	6.879
19.5898	5.328	6.1184	7.921
23.7152	6.435	7.5501	9.450
29.7814	7.992	15.2462	17.473
36.0708	9.567	18.2413	20.402
40.5203	10.669	22.5365	24.419
51.4977	13.320	24.2235	25.826
60.2596	15.389	24.5837	26.323
73.8178	18.582	24.7872	26.446

Table II: Values of B_{2s} for the Inert Gas–Boron Nitride Systems

Gas	T, °K	B_{2s}, cm^3 g^{-1}
Ne	273.15	0.00076 ± 0.00006
Ar	273.15	0.01534 ± 0.00009
Kr	273.15	0.0488 ± 0.0007
Xe	273.15	0.254 ± 0.003

One of the objects of this work was to make adsorption measurements of the same precision as those obtained by Halsey and coworkers, a precision that is some 10 to 100 times better than that obtained with conventional volumetric apparatuses. A comparison of the calibration and isotherm results given above with those of Halsey[2] indicates that results of equal precision have been obtained. The percentage precisions obtained were (with Halsey's values in parentheses) external dead space volume, 0.1% (0.1%); sample dead space volume at 0°, 0.02% (0.01%); B_{2s} for neon–solid at 0°, 7% (7%); and B_{2s} for argon–solid at 0°, 0.6% (0.5%). The volume precision obtained here is thus between 2 and 3 parts per 10,000. The errors on the krypton and xenon values of B_{2s} (about 1.3%) are substantially larger than Halsey's but this is not because the isotherms were less precise. Rather it was found that with these two gases the isotherms had not reached their Henry's law region at the lowest pressure measured. There remained a curvature in the Henry's law plot and extrapolation to zero pressure involved a somewhat greater uncertainty.

It can be noted that the introduction of the capacitance manometer has not resulted in a better precision. Although this modification has eliminated the uncertainty in both the meniscus covolume and the meniscus depression correction this capacitance manometer contributed an almost equal uncertainty in its sensitivity and stability. Capacitance manometers of greater sensitivity and stability are now available and use of one of these would result in a small increase in precision, possibly to about 1 part in 10,000, which is estimated as the limit of the precision of the mercury manometer. The advantages of the capacitance manometer in simplifying the system have already been discussed.

An additional argon isotherm was measured at 90°K. A BET analysis of these data gave a surface area of 4.98 m^2 g^{-1} using an area of 14.1 Å^2 for the adatom.

Analysis

The second gas–solid virial coefficient, B_{2s}, is characteristic of the interaction of an isolated absorbate atom with the surface. If a (m,n) Lennard-Jones potential is assumed between the adsorbate and a structureless, uniform surface then the second gas–

solid virial coefficient can be calculated from the relationship[1]

$$B_{2s} = Az_0 \sum_{\tau=0}^{\infty} (\tau!n)^{-1} \left[\left(\frac{n}{n-m} \right) \left(\frac{n}{m} \right)^{m/(n-m)} \times \left(\frac{\epsilon^*_{1s}}{kT} \right)^{\{\tau(n-m)+1\}/n} \Gamma\{(\tau m - 1)/n\} \right] \quad (2)$$

where A is the surface area of the solid, z_0 is the finite distance at which the interaction energy is zero (the "distance of closest approach"), $m < n$, and $\Gamma\{(\tau m - 1)/n\}$ is a Γ function. This function was calculated for the (3,9) and (4,10) gas–solid potentials and the results are shown in Figure 5. The (3,9) calculation was in agreement with published values.[4,9,10] The (4,10) calculation did not agree with the published values[4,9] which we believe to be in error. Calculated values of the reduced virial coefficient for the (4,10) potential at chosen values of ϵ^*_{1s}/kT are given in Table III. (The data of Halsey, *et al.*,[4] were reanalyzed using this (4,10) tabulation. The results are given in Table IV.)

Table III: Values of B_{2s}/Az_0 at Selected Values of ϵ^*_{1s}/kT for the (4,10) Potential

ϵ^*_{1s}/kT	B_{2s}/Az_0	ϵ^*_{1s}/kT	B_{2s}/Az_0
1.1	0.10602	6.0	88.584
1.5	0.73097	6.5	138.86
2.0	1.8220	7.0	218.35
2.5	3.4220	7.5	344.44
3.0	5.8029	8.0	545.05
3.5	9.3924	8.5	864.90
4.0	14.863	9.0	1376.0
4.5	23.279	9.5	2194.4
5.0	36.323	10.0	3506.5
5.5	56.673		

Table IV: Best-Fit Parameters from the Fit of the Inert Gas–P33(2700) Data of Halsey, *et al.*,[4] to the Corrected (4,10) Potential[a]

Gas	ϵ^*_{1s}/k, °K	$Az_0 \times 10^3$, cm³ g⁻¹	$\sigma(\log Az_0) \times 10^3$
Ne	375	3.134	0.55
Ar	1096	3.274	1.54
Kr	1437	3.381	1.79
Xe	1904	3.588	1.67

[a] Compare parts of Table II, ref 4.

In a conventional analysis[1,4] the temperature dependence of B_{2s} for a given gas–solid system is fitted to a theoretical curve which as one of those in Figure 5 to yield best-fit values of ϵ^*_{1s}/k and Az_0. The present data are different from those used in a conventional analysis in that they consist of values of B_{2s} for different gases at the same temperature. It can be noted that data of the present type cover a wide range of reduced temperature (kT/ϵ^*_{1s}), a wider range in fact than any conventional data. The data were analyzed in a manner that is somewhat different from the conventional analysis. The analysis requires values of σ, the collision diameter, for each adsorbate and independent values of z_0 and ϵ^*_{1s}/k for one of the gas–solid systems and yields a value for the surface area and energies of interaction for the other gas–solid systems.

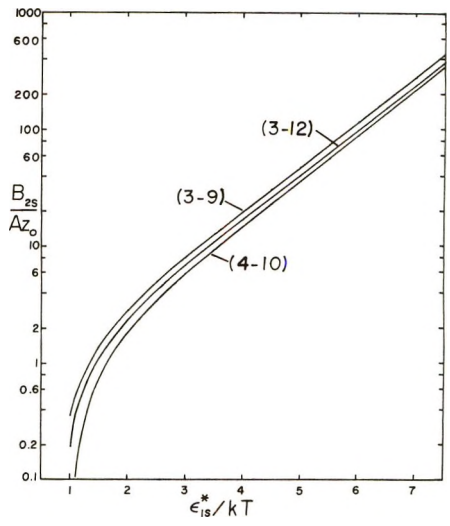

Figure 5. Semilogarithmic plots of B_{2s}/Az_0 *vs.* ϵ^*_{1s}/kT for various (m,n) potential functions.

The values of the parameters required for this analysis were determined as follows. A value of z_0 for the argon–boron nitride system was calculated from the value of the equilibrium separation, $z^* = 3.39$ Å, determined by Crowell and Chang.[11] This value of z_0 was set equal to one-half the sum of the gas-phase collision diameter of argon (σ^{Ar}) and an effective collision diameter for the surface (σ^{BN}). A value for σ^{Ar} was taken from Hirschfelder, Curtiss, and Bird[12] and a value of σ^{BN} calculated. The values of z_0 for the neon–, krypton–, and xenon–boron nitride systems were calculated by adding one-half the gas-phase collision diameter of the gas to one-half of this calculated value of σ^{BN}. Values of z_0 are given in Table V.

The final independent parameter required for the analysis is a value of ϵ^*_{1s}/k for one of the gas–solid systems. A separate determination and conventional analysis of the temperature dependence of B_{2s} for argon on the same sample of boron nitride has been

(9) R. Yaris and J. R. Sams, *J. Chem. Phys.*, **37**, 571 (1962); J. R. Sams, Ph.D. Thesis, University of Washington, 1962.

(10) W. C. DeMarcus, E. H. Hopper, and A. M. Allen, *U. S. At. Energy Comm., Tech. Bull.*, K1222 (1955).

(11) A. D. Crowell and C. O. Chang, *J. Chem. Phys.*, **43**, 4364 (1965).

(12) J. O. Hirschfelder, C. F. Curtiss, and R. B. Bird, "Molecular Theory of Gases and Liquids," Wiley, New York, N. Y., 1967.

Table V: Values of z_0 for the Inert Gas–Boron Nitride Systems[a]

	σ	z_0(3,9)	z_0(4,10)
Ne	2.76	2.50	2.59
Ar	3.41	2.83	2.92
Kr	3.68	2.96	3.05
Xe	4.07	3.16	3.25

[a] Values of σ^{BN} were 2.24 Å for the (3,9) potential and 2.42 Å for the (4,10) potential.

carried out and yielded values for ϵ^*_{1s}/k of 1212 and 1193°K for the (3,9) and (4,10) potentials, respectively.[8]

Using these parameters and the present experimental values of B_{2s} the following method was used to calculate a surface area and values of ϵ^*_{1s}/k for the other three gas–solid systems. The reduced virial coefficient (B_{2s}/Az_0) for the argon–boron nitride system at 273°K was calculated from eq 2 using the value of ϵ^*_{1s}/k and a chosen gas–solid potential. The experimental value of B_{2s} at 273°K was divided by the theoretical B_{2s}/Az_0 to yield a value of Az_0 and hence A. The surface area of the boron nitride was assumed to be constant for all four gases and was used to calculate values of Az_0. The experimental values of B_{2s} were combined with these Az_0 to yield values of B_{2s}/Az_0 and these were used in eq 2 to yield values of ϵ^*_{1s}/k. The results for the (3,9) and (4,10) potentials are given in Table VI together with comparison values obtained in other studies. The calculated values for the surface area of the boron nitride were 1.86 $m^2\,g^{-1}$ for the (3,9) potential and 2.54 $m^2\,g^{-1}$ for the (4,10). The BET area for this sample is equal to 4.98 $m^2\,g^{-1}$.

In order to determine the reliability of the energies and areas calculated in the above manner the data of Halsey and coworkers[2] for the adsorption of the inert gases on P33(2700) at about 273°K were analyzed in the same way. The results were then compared with the values of ϵ^*_{1s}/k and A obtained by Halsey and coworkers[4] from a conventional analysis of their more extensive data which include measurements of the temperature dependence of B_{2s} for each gas–solid system. The results are given in Table VII. The analysis gave surface areas of 8.41 $m^2\,g^{-1}$ for the (3,9) potential and 11.30 $m^2\,g^{-1}$ for the (4,10). Halsey and coworkers calculated areas of 7.41 $m^2\,g^{-1}$ using values of z_0 based upon second virial radii of the adatoms and 8.38 $m^2\,g^{-1}$ using values based upon crystal radii. The BET surface area of P33(2700) is about 12.5 $m^2\,g^{-1}$.

Table VI: Values of ϵ^*_{1s}/k for Inert Gas–Boron Nitride Systems for the (3,9) and (4,10) Potentials (°K)

Source	Ne	Ar	Kr	Xe
Present analysis (3,9)	436	(1212)[f]	1559	2043
Present analysis (4,10)	469	(1193)[f]	1534	2015
a	387	986		
b	433	1047	1409	1855
c	509	1123	1312	1783
d		981		
e		956	1321	

[a] Reference 3 and J. C. Petricciani, M.S. Thesis, University of Nevada, 1960. [b] G. Curthoys and P. A. Elkington, *J. Phys. Chem.*, **71**, 1477 (1967) (calculated). [c] Reference 11 (calculated). [d] R. A. Pierotti, *J. Phys. Chem.*, **66**, 1810 (1962) (experimental, determined from submonolayer data). [e] J. J. McAlpin, Ph.D. Thesis, Georgia Institute of Technology, 1966 (experimental, determined from submonolayer data). [f] Value taken from ref 8.

Table VII: Values of ϵ^*_{1s}/k for the Inert Gas–P33(2700) Systems for the (3,9) and (4,10) Potentials (°K)

Source	Ne	Ar	Kr	Xe
Present analysis,[a] (3,9)	398	(1107)[c]	1444	1915
Reference 4, (3,9)	382	1107	1460	1919
Present analysis,[a] (4,10)	438	(1096)[c]	1426	1893
Reference 4,[b] (4,10)	375	1096	1437	1904

[a] Data from ref 2. [b] Corrected, see Table IV. [c] Value taken from ref 4.

Discussion

The high-precision volumetric apparatus incorporating the modifications described has been shown to yield data of the precision required for the analysis of the high-temperature, low-coverage adsorption region where Henry's law behavior and deviations therefrom occur. This apparatus will be used to investigate a number of gas–solid systems. The experimental study reported here, although limited in its scope in order to emphasize the apparatus and to indicate its experimental capabilities, does yield values of ϵ^*_{1s}/k for a number of inert gases interacting with boron nitride and a value of the surface area.

Prior to discussing the boron nitride results it is worthwhile noting that, in the case of the inert gas–P33(2700) systems, the method of analysis used here to analyze the experimental values of B_{2s} for a number of gases at one temperature yields values of ϵ^*_{1s}/k which are in very good agreement with the values obtained by a conventional analysis of more extensive data which include temperature dependence of B_{2s} for each system (Table VII). The method is a useful one for the preliminary characterization of the interaction of a number of gases with a surface, provided one has a value of ϵ^*_{1s}/k and z_0 for one of these systems from an independent source. The one exception to the good agreement is the value for neon obtained using the (4,10) potential. All the conventional analyses of Halsey and coworkers[4] were calculated in a range of reduced temperature within the range 4–8 where the (3,9) and (4,10)

potential functions yield similar curves for the reduced virial coefficient *vs.* the reduced temperature (see Figure 5). However, the present analysis covers a range of reduced temperature from 1.5 to 7 and extends into the region where the curves have a somewhat different shape. It is possible that the better agreement with the (3,9) potential as opposed to the (4,10) could indicate that the former is a more realistic potential form but this is a very tentative conclusion.

Returning to the boron nitride data we see that a comparison of the values in Table VI indicates a number of features. First the values appear somewhat high when compared with the theoretical values and are considerably higher than other experimental values determined in these laboratories using the significant structures theory to extract ϵ^*_{1s}/k from data in the submonolayer region. The same theory when applied to inert gas–graphite data yields values of ϵ^*_{1s}/k within a few tenths of a per cent of those obtained from the Henry's law analysis of Halsey and coworkers. Secondly, the deviation between the present values and either the calculated or the experimental values becomes larger as the interaction energy increases. These features lead one to believe that the BN sample possesses a small degree of heterogeneity. The theoretical values in Table VI are calculated for the basal plane and the range of coverage in the significant structures analysis results in an energy for the majority of the surface, *i.e.*, the basal plane.

Although one is unable to determine the nature or degree of the heterogeneity with the data presented here, crystallography and electron microscope studies indicate that the BN crystallites are platelets in contrast to the polyhedral particles characteristic of graphitized carbon. These platelets contribute a few per cent of high energy sites to the overall gas–solid interaction.

The analysis of data from the Henry's law region is still valid for a heterogeneous solid, although the values of the interaction parameters extracted are different in that they represent averaged quantities.[1] The higher energy sites for the edges in the BN sample must result in somewhat higher values of ϵ^*_{1s}/k than would be expected for the bulk of the surface, namely, the basal plane. Information concerning the distribution of site energy can be obtained from the temperature variation of B_{2s} if such data are available for several gases on the same solid.[1] In any case, the values of ϵ^*_{1s}/k reported in Table VI are upper limits of the values expected for the inert gas–BN interaction with the basal plane and even at that are in reasonable agreement with the calculated values indicating a relatively small contribution from the surface heterogeneity.

One of the reasons for selecting boron nitride as an adsorbent was that it was hoped that an analysis of the gas–solid virial coefficients of both graphite and BN would yield information about the effect of the external field of the solid on the pair potential for molecules adsorbed on the solid. Information concerning these effects is found by analysis of the third gas–solid virial coefficient, B_{3s} (eq 1). This is a subject of considerable theoretical interest[13,14] and the BN and graphite systems are model systems for making these studies because of the great similarity in their crystallographic and structural properties. The small degree and nature of the heterogeneity found for the BN sample will make these studies very difficult because of the manner in which the spatial distribution of the energy sites enters into B_{3s}.[1,15]

Acknowledgment. The authors gratefully acknowledge support from the Air Force Office of Scientific Research (Project Themis), the U. S. Army Research Office—Durham, and the Petroleum Research Fund of the American Chemical Society.

(13) O. Sinanoğlu and K. S. Pitzer, *J. Chem. Phys.*, **32**, 1279 (1960).
(14) A. D. McLachlan, *Mol. Phys.*, **7**, 381 (1964).
(15) R. A. Pierotti, *Chem. Phys. Lett.*, **2**, 385 (1968).

Infrared Spectra of Carbon Monoxide Chemisorbed on Iron at Low Temperature

by G. Blyholder* and Masako Tanaka

Department of Chemistry, University of Arkansas, Fayetteville, Arkansas 72701 *(Received May 3, 1972)*

The interaction of CO and Fe particles at temperatures down to 43°K has been observed with infrared spectroscopy using a matrix isolation technique. The CO is brought into contact with the Fe particles by diffusion within an Ar matrix at 43°K or by condensing CO on bare Fe left after the Ar has been evaporated. CO and Fe particles do interact at 43°K to produce a very broad infrared band around 1970 cm^{-1} and a band at 570 cm^{-1}, which are like those previously reported for room temperature interaction. While bare Fe particles sinter at 43°K the CO covered particles do not sinter until the temperature reaches the neighborhood of 250°K. Changing the sample temperature from 21 to 150°K and back to 21°K has little effect on the spectrum of chemisorbed CO indicating that the chemisorbed layer is stable in this temperature range. Addition of Ar to a chemisorbed CO layer at 21°K scours CO off the surface.

Introduction

While much useful structural information about molecules adsorbed on metal surfaces has been obtained by infrared spectroscopy,[1-4] most of it has been at or somewhat above room temperature. Low-temperature studies are of particular importance to a fundamental understanding of chemisorption because at low temperatures secondary processes such as surface migration of atoms and adsorbed molecules, decomposition of adsorbed species, and reactions of adsorbed molecules are suppressed so that primary processes can be observed. However, relatively few infrared studies of adsorbed species at low temperatures have been made. Spectra of CO adsorbed on Ir and Ru at 80°K have been reported by Lynds[5] but the CO was apparently adsorbed at 300°K. Infrared spectra of CO adsorbed on Ni films have been obtained[6-8] at temperatures down to 203°K but in these studies the CO is admitted at room temperature to a cold surface so that the interaction temperature is not defined. A matrix isolation technique has been developed in this laboratory and used[9] to examine by infrared spectroscopy the interaction between Ni particles and CO at temperatures down to 44°K. While the low-temperature spectra for CO on Ni resemble those obtained by other methods at room temperature, the possibility of observing changes upon warming to room temperature was obscured by the great decrease in intensity caused by sintering of the Ni particles as the temperature was raised. In this paper the results are reported of using this technique with Fe, which was chosen for study because its melting point is considerably above that of Ni so that we hoped it would sinter less readily.

A variety of evidence points to the existence of distinct low-temperature adsorption states. Sometimes referred to as type C chemisorption, it has been found for hydrogen on Fe, Ni, W, Cr, Pd, and Pt, for nitrogen on W, Fe, Co, and Ni, and for oxygen on W.[10] It has been suggested that type C chemisorption is atomic[11,12] by some and molecular[13,14] by others. The existence of a low-temperature chemisorbed state for CO on W, referred to as virgin CO, has been inferred from flash-filament, field emission, and electron impact desorption data.[15] The idea of a weakly chemisorbed precursor state has been used to analyze data for CO adsorption on Ni.[16,17]

Experimental Section

In the matrix technique the metal is evaporated

(1) M. L. Hair, "Infrared Spectroscopy in Surface Chemistry," Marcel Dekker, New York, N. Y., 1967.

(2) L. M. Little, "Infrared Spectra of Adsorbed Species," Academic Press, New York, N. Y., 1966.

(3) M. R. Basila, *Appl. Spectrosc. Rev.*, **1**, 289 (1968).

(4) G. Blyholder, "Experimental Methods in Catalytic Research," R. B. Anderson, Ed., Academic Press, New York, N. Y., 1968.

(5) L. Lynds, *Spectrochim. Acta*, **20**, 1369 (1964).

(6) A. M. Bradshaw and J. Pritchard, *Surface Sci.*, **17**, 372 (1969).

(7) A. M. Bradshaw and J. Pritchard, *Proc. Roy. Soc., Ser. A*, **316**, 169 (1970).

(8) A. M. Bradshaw and P. Vierle, *Ber. Bunsenges. Phys. Chem.*, **74**, 630 (1970).

(9) G. Blyholder and M. Tanaka, *J. Colloid Interface Sci.*, **37**, 753 (1971).

(10) G. C. Bond, "Catalysis by Metals," Academic Press, New York, N. Y., 1962.

(11) W. A. Pliskin and R. P. Eischens, *Z. Phys. Chem. (Frankfurt am Main)*, **23**, 11 (1960).

(12) P. M. Gundry and F. C. Tompkins, *Trans. Faraday Soc.*, **52**, 1609 (1956).

(13) D. A. Dowden, "Chemisorption," W. E. Garner, Ed., Butterworths, London, 1958, p 3.

(14) J. C. P. Mignolet, *Bull. Soc. Chem. Belg.*, **67**, 258 (1958).

(15) R. R. Ford, *Advan. Catal.*, **21**, 51 (1970).

(16) D. A. Dowden, *J. Chem. Soc.*, 242 (1950).

(17) P. M. Gundry and F. C. Tompkins, *Trans. Faraday Soc.*, **52**, 1612 (1956).

from a heated tungsten filament and condensed in an Ar matrix at 21°K. The tungsten filament is heated to the point at which the iron wire on it just melts. The deposition surface temperature is maintained by a miniature two-stage Jule–Thompson liquefier (Air Products and Chemicals, Inc., Model AC-2-110). This device has some temperature control over the range from 20 to 300°K. The details of the vacuum shroud have been published previously.[9] This vacuum assembly which uses O-rings could be pumped down to 10^{-6} to 10^{-7} Torr. Some experiments were also done using a new vacuum assembly which had the diameter of the connection to the diffusion pump increased and replaced O-ring seals with epoxy resin seals. This pumped down to between 10^{-8} and 10^{-9} Torr.

The CO and Ar were passed over Cu turnings at 400° and then through a liquid-air-cooled charcoal trap to remove any possible O_2 or H_2O contamination.

The matrix isolation technique has the advantages that (1) it gives much greater infrared band intensity than any other clean evaporated metal technique; (2) the entire infrared spectral range is available; (3) the evaporated metal surface is clean except for noble gas contact; and (4) low-temperature adsorbate–adsorbent interactions are readily investigated.

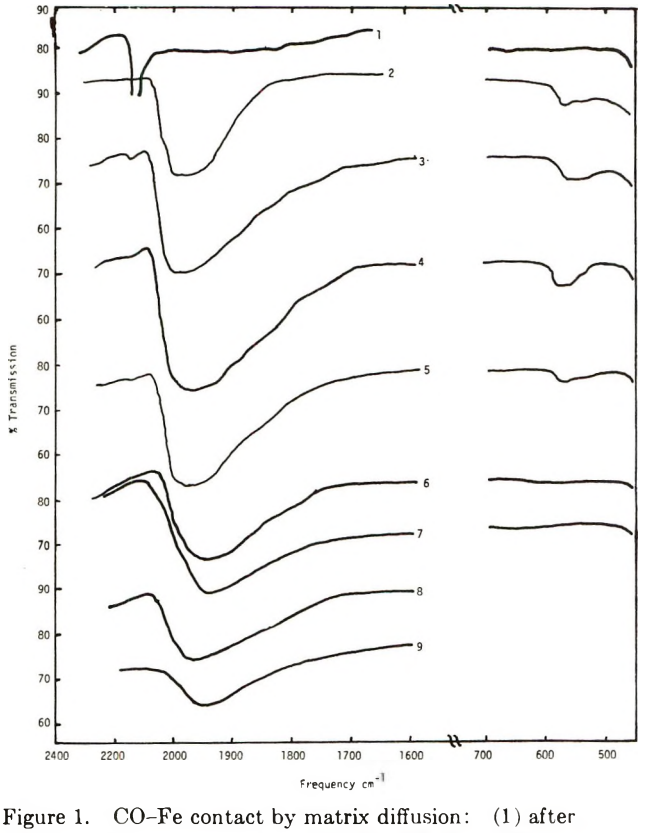

Figure 1. CO–Fe contact by matrix diffusion: (1) after CO–Ar matrix was deposited at 21°K; (2) after 43°K matrix diffusion, spectrum recorded at 21°K; (3) after Ar was removed at 70°K, spectrum recorded at 21°K; (4) at 83°K; (5) at 150–170°K; (6) at 250°K; (7) at room temperature; (8) exposed to 1 Torr CO for 1 night at room temperature; (9) CO evacuated for 30 min at room temperature.

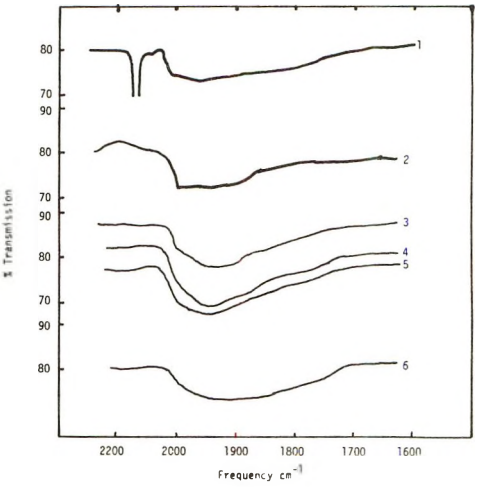

Figure 2. Sample warmed up to 40°K before the CO–Ar matrix was deposited: (1) after deposition of the CO–Ar matrix at 21°K; (2) after 43°K matrix diffusion and cooling to 21°K for recording of the spectrum; (3) at 210–170°K; (4) at 230°K; (5) at 10°; (6) at 20°.

Results

Using the original vacuum shroud Fe was evaporated with an Ar flow of 20 ml/min. Figure 1, curve 1, shows a spectrum after the mixture of Ar and CO was deposited on top of the Fe–Ar matrix at a flow rate of 20 ml/min for 8 min. A band due to CO in the matrix is observed at 2140 cm^{-1}. The sample was warmed at 43°K for 3 min and curve 2 was recorded at 21°K. The band of CO in the matrix at 2140 cm^{-1} disappeared completely. A strong band at 2000–1950 cm^{-1} with a shoulder at 2030 cm^{-1} is observed. In the Fe–C–O bending region weak bands appeared at 565 and 530 cm^{-1}. Then, in order to remove matrix Ar the sample window was warmed to 70°K slowly so that the metal film does not peel off the window. Two hours were used to warm up from 40 to 70°K. After the pressure of the system decreased below 1×10^{-6} Torr at 70°K, indicating that all Ar has been removed, the sample window was cooled to 21°K and curve 3 was recorded. The main band which showed some structure in curve 2 smoothed to one very broad peak at 1985 cm^{-1} with the shoulder at 2030 cm^{-1} no longer being distinct. A weak band which is probably due to recondensed CO from the cell walls is observed at 2140 cm^{-1} again. The transparency of the film was not decreased by the warming. No fine crack-like network occurred on the metal film as was sometimes observed on the Ni films after the evaporation of Ar. The film was warmed up slowly to room temperature by decreasing the flow of N_2 and H_2 in the heat exchanger. Curves 4 to 7 were obtained at 83, 150–170, 250°K, and room temperature, respectively. The band maximum at 1980 cm^{-1} moved to 1950 cm^{-1} at 250°K. The intensity of this band notably increased up to 83°K and decreased again above this temperature. The bands around 570 cm^{-1} also showed the strongest

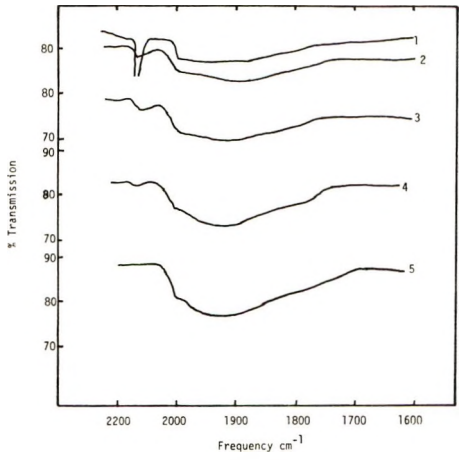

Figure 3. Ar removed before CO addition: (1) after pure CO addition at 21°K; (2) after warming up at 43°K and cooling back to 21°K; (3) at 75–85°K; (4) at 130–210°K; (5) at 270–300°K.

intensity at 83°K, showing three peaks or shoulders at 570, 550, and 525 cm^{-1}. The band shape of curves 6 and 7 at 250 and 300°K are almost the same. Curve 8 shows the spectrum after the film was exposed to 1 Torr of pure CO at room temperature for 1 night. The band center shifted to 1960–1970 cm^{-1} from 1940 cm^{-1} in curve 7. After the CO was evacuated for 30 min at room temperature, it moved back to 1950 cm^{-1}, as shown in curve 9.

For the experiment shown in Figure 2 using the original vacuum shroud Fe was evaporated with an Ar flow of 20 ml/min and the Fe–Ar matrix was immediately warmed to 40°K for 4 min. Then, the sample was cooled to 21°K and the mixture of CO and Ar deposited on top of the Fe–Ar matrix. As shown in curve 1, besides the band for matrix CO at 2140 cm^{-1}, a broad band is observed around 1960 cm^{-1} with a shoulder at 2000 cm^{-1}. After the film was warmed at 43°K for 10 min for matrix diffusion, the band for matrix CO disappeared and the band at 2000–1900 cm^{-1} became strong as shown in curve 2. The sample was warmed to room temperature slowly. Curves 3–6 were recorded at 120–170, 230, 283, and 293°, respectively. The shoulder at 2000 cm^{-1} was as intense as the 1960-cm^{-1} band after matrix diffusion at 43°K but became less intense at higher temperatures. The transmission of this film was poorer than that of the previous experiment. The spectra below 1000 cm^{-1} could not be obtained because of insufficient light transmission to operate the spectrometer.

In the experiment shown in Figure 3, the Ar was completely evaporated from the Fe–Ar matrix before CO was added. The Fe was evaporated with an Ar flow of 20 ml/min and then the Ar was evaporated completely by warming the sample to 70°K. Curve 1 shows the spectrum after pure CO was deposited on top of the bare metal film at a flow rate of 20 ml/min for 3 min. Besides the band due to solid CO at 2140 cm^{-1}, a broad weak band appears at 2000–1900 cm^{-1}. The sample was warmed to 43°K for 10 min and curve 2 recorded at 21°K. A broad band at 1930–1880 cm^{-1} with a shoulder at 2000 cm^{-1} and a weak band at 2140 cm^{-1} are observed. The sample was then warmed to room temperature. Curves 3–5 were recorded at 75–85, 130–210, and 270–300°K, respectively. The weak band at 2140 cm^{-1} remained at 130–210°K. The 2000-cm^{-1} band can be observed even at room temperature as a shoulder. The 1930-cm^{-1} band increased in intensity as the temperature increased to room temperature.

The results of cyclic temperature changes between 21 and 150°K using the new vacuum shroud are shown in Figure 4. Fe was evaporated with 20 ml/min of Ar flow. Curve 1 shows a spectrum after the mixture of Ar and CO was deposited on top of the Fe–Ar matrix. A band for matrix CO was observed at 2140 cm^{-1}. After the matrix diffusion at 37°K for 10 min, curve 2 was recorded at 21°K and shows a band at 1980 cm^{-1}. Then, Ar was evaporated at 70°K and curve 3 was recorded at 21°K and is very similar to curve 8. The sample was then warmed slowly to 150°K. Curves 4, 5, and 6 were recorded at 85–105, 110–120, and 150°K, respectively. The sample was cooled down again to 21°K and curve 7 was recorded. The effect of the temperature change between 21 and 150°K on band in-

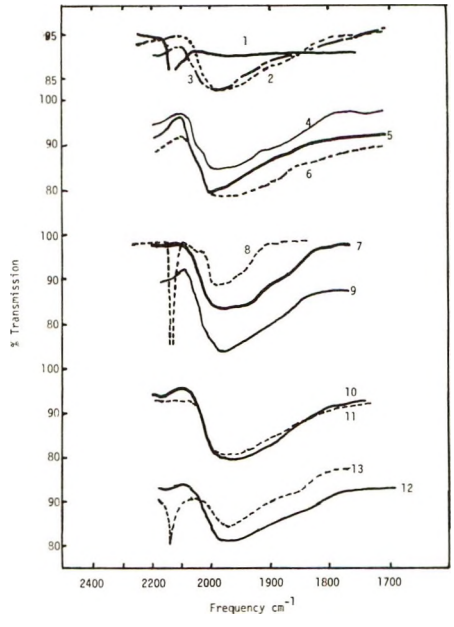

Figure 4. Fe–CO interaction using the high-vacuum system: (1) after CO–Ar matrix was deposited at 21°K; (2) after 43°K matrix diffusion, spectrum recorded at 21°K; (3) after Ar evaporation, spectrum recorded at 21°K; (4) at 85–105°K; (5) at 110–120°K; (6) at 150°K; (7) at 21°K; (8) after more CO–Ar matrix has been deposited at 21°K; (9) after 43°K matrix diffusion, spectrum recorded at 21°K; (10) at 160°K; (11) at 21°K; (12) after pure CO was added at 21°K, warmed to 43°K, and cooled down to record spectrum at 21°K; (13) after pure Ar was deposited at 21°K.

tensity is relatively small (*i.e.*, less than 10%). Curve 8 was recorded after a mixture of Ar and CO was added onto this film at 21°K. The light transmission of the sample changed little and the intensity around 1980 cm^{-1} was reduced considerably. This decrease was restored by matrix diffusion at 37°K for 10 min, as shown in curve 9 which was recorded at 21°K. The recovered intensity is a little higher than that of curve 7. Then, the sample was warmed up and curve 10 recorded at 160°K. No effect of warming up on the band intensity appeared. Following that, the sample was cooled down and curve 11 recorded at 21°K. The band intensity decreased slightly. Curve 12 was recorded after deposit of pure CO at 21°K, warming at 43°K for 10 min, and cooling down to 21°K. The warming to 43°K has as usual allowed the unadsorbed CO to evaporate. The band intensity has remained essentially constant. Argon with a small amount of CO that had remained in the supply line was deposited on the surface at 21°K and curve 13 recorded. The chemisorbed CO band intensity was decreased by this procedure and the sample transmission decreased considerably.

Discussion

One of the immediate results of this study is the indication that CO does chemisorb on Fe at 43°K. Thus, the occurence of an activation energy for adsorption greater than a few tenths of a kilocalorie is most unlikely. Further the chemisorbed state appears to be the same as that produced at room temperature since the large band around 1970 cm^{-1} for the C–O stretch and the band at 580 cm^{-1} for the Fe–C–O bend are the same as found for room temperature adsorption.[18-22] This does not mean that there is necessarily no CO adsorbed in a weakly held precursor state at low temperatures on Fe but that we have found no infrared evidence for it. Since there is good evidence for special low-temperature states for CO adsorbed on W,[15] it would be reasonable to expect them on Fe.

An interesting feature of the spectra in Figure 1 is the increase in intensity of the band for chemisorbed CO as the temperature increases from 21 to 83°K in curves 2 to 4. This intensity change is not believed to be due to a surface transition of adsorbed CO but rather to CO being desorbed from the central cold column of the cell as the temperature is raised. Supporting this interpretation is the appearance of a weak band at 2140 cm^{-1} in curve 3 (recorded at 21°K after the cell had been warmed to 70°K) which was not in curve 2. This increase in intensity also occurs in Figures 2 and 3 recording experiments done with the same vacuum shroud. In Figure 4, where the experiment used the new vacuum shroud that maintains a lower pressure the intensity does not increase nearly as much if at all during the warming up period. The fact that more CO could adsorb during the warming up period of the first three experiments indicates that not all of the surface was covered with CO at 43°K. This could be due either to their being a small intrinsic activation energy for adsorption on some sites or to insufficient time being allowed for the CO to diffuse into contact with all of the surface sites at 43°K. At room temperature all of the surface sites are covered since addition of more CO at room temperature gives no increase in band intensity as shown in curve 8 of Figure 1.

Above 200 to 250°K the intensity of the band for chemisorbed CO decreases. This is apparently due to sintering of the Fe particles. The band intensity decreases fairly uniformly at all wavelengths across the very broad band from 1700 to 2050 cm^{-1} so that the band shape is not appreciably altered. Thus, no major structural changes in the chemisorbed CO are apparent as the iron temperature goes from 21 to 300°K. The interpretation of the intensity decrease being due to sintering is supported by the experiment shown in Figure 2 in which the matrix was warmed to 43°K before the CO was added. This warming without CO allows the metal particles to sinter some so the intensity of the chemisorbed CO band is never as great as in Figure 1. The sintering of Fe particles is much less than that of Ni particles since the chemisorbed CO band intensity for Fe remains at a reasonable level for CO adsorbed at 43°K whereas for Ni the intensity for CO adsorbed at 43°K goes to zero at room temperature unless more CO is added.[9] This difference is ascribed to the higher cohesive energy of Fe as reflected by its higher melting point causing the Fe atoms to be less mobile and therefore the Fe particles less able to sinter than Ni.

In the experiment shown in Figure 3 the Ar was evaporated from the Fe–Ar matrix before any CO was introduced. The criterion used for completeness of Ar removal is that the pressure reduces to 10^{-6} Torr at 70°K. The band intensity for chemisorbed CO is much greater for Fe adsorbent here than it was for Ni. This is again a reflection of less sintering occurring with Fe than with Ni. These results with Fe indicate that it is reasonable to try experiments in which the film is warmed up to several hundred degrees Kelvin to stabilize it before CO addition and still hope to get a satisfactory intensity for chemisorbed CO. This would allow isolating sintering effects from chemisorbed layer changes.

Changing the temperature from 21 to 150°K and back to 21°K is seen in Figure 4 to have relatively little

(18) R. P. Eischens and W. A. Pliskin, *Advan. Catal.*, **10**, 1 (1971).
(19) G. Blyholder, *J. Chem. Phys.*, **36**, 2036 (1962).
(20) G. Blyholder, *ibid.*, **44**, 3134 (1966).
(21) G. Blyholder and L. D. Neff, *J. Phys. Chem.*, **66**, 1464 (1962).
(22) F. S. Baker, A. M. Bradshaw, J. Pritchard, and K. W. Sykes, *Surface Sci.*, **12**, 426 (1968).

effect on the spectrum of CO on Fe. Thus once an Fe film is covered with CO it is relatively stable up to 150°K. However, Figures 1 and 2 indicate that as the film goes above 300°K a reduction in chemisorbed CO band intensity occurs, presumably due to sintering. Curve 8 of Figure 4 shows a large reduction in chemisorbed CO when further Ar–CO matrix is sprayed on a metal film that has had the Ar matrix removed. This reduction is apparently due to a simple scouring process since warming the new Ar–CO matrix to allow CO to diffuse returns the band to its original intensity. The warming from 21 to 160°K and cooling to 21°K was repeated in curves 9–11 to further check the film stability with the same results as before. Addition of pure CO at 21°K did not change the spectrum. If incoming CO did scour some adsorbed CO off, there was more CO immediately available to replace it. After evaporation of the excess CO, pure Ar was admitted. This treatment not only reduced the band intensity but cut the film transmission to about one fourth of its former value. Thus, additions of gas at 300°K to a film at 21°K can scour adsorbed species off of the surface and induce sintering.

The particle size distribution is unknown but is probably quite small. The evaporation of metal from a filament into an inert gas at room temperature gives particles having a maximum at 50–100 Å in their particle size distribution.[23] Such particles collected into an oil film give infrared spectra of adsorbed species very similar to those reported here.[19,20] The spectra observed here are certainly for adsorption on particles and not atoms since the interaction of CO and Ni atoms in an Ar matrix gives sharp lines.[24] Thus, the matrix technique shows great promise for investigating the infrared spectra of species adsorbed on metals at low temperatures.

Acknowledgment. This research was supported in part by a grant from the National Science Foundation.

(23) P. H. Hill and J. Turkevich, *U. S. At. Energy Comm., Tech. Rep.*, NYO-3435 (1956).

(24) R. L. De Kock, *Inorg. Chem.*, **10**, 1205 (1971).

Adsorbed Oxygen Species on Zinc Oxide in the Dark and under Illumination

by Ken-ichi Tanaka*[1] and George Blyholder

Department of Chemistry, University of Arkansas, Fayetteville, Arkansas 72701 *(Received June 16, 1972)*

Temperature-programmed desorption of oxygen adsorbed on zinc oxide, which has been cooled down *in vacuo* after activation, gives two desorption peaks with maxima at 180–190 and 285–295°. The low-temperature peak was identified as O_2^- by esr and the high-temperature peak is probably due to O^-. The O^- is more reactive than O_2^- in reaction with carbon monoxide. Zinc oxide cooled down in an oxygen atmosphere gives no desorption of oxygen to 400° in the dark or under illumination. However after illuminating with oxygen gas present, desorption of oxygen is again observed indicating the generation of electrons available for oxygen adsorption. The oxygen adsorbed on zinc oxide with presorbed hydrogen was identified as O_2^- by esr, but it desorbs at 110–120°, indicating a marked reduction in adsorption strength for O_2^- on the hydrogen presorbed sample. TiO_2, rutile, gave a desorption peak maximum at 150–160°, which is probably due to O_2^-.

Introduction

Two types of adsorbed species of oxygen, O_2^- and O^-, have been proposed for oxygen adsorbed on zinc oxide, and the esr spectrum of O_2^- has been established by several investigators at -190[2] and -196°.[3] The assignment of the spectrum to O^- on zinc oxide[4] is still ambiguous as has been pointed out by Lunsford and coworkers.[5]

In a previous paper,[6] we have suggested that O^- is an intermediate species in the catalytic oxidation of carbon monoxide over zinc oxide, that is, the slow step of the thermal catalytic reaction is the reaction of O^- with weakly adsorbed CO, and the slow step under illumination is the formation of an O^- species.

This paper reports the characteristics of these

(1) To whom correspondence should be addressed at The Institute for Catalysis, Hokkaido University, Sapporo, Japan.

(2) J. H. Lunsford and J. P. Jayne, *J. Chem. Phys.*, **44**, 1487 (1966).

(3) A. J. Tench and T. Lawson, *Chem. Phys. Lett.*, **8**, 177 (1971).

(4) H. Horiguchi, M. Setaka, K. M. Sancier, and T. Kwan, *Int. Congr. Catal., 4th*, 66 (1968).

(5) W. B. Williamson, J. H. Lunsford, and C. Naccache, *Chem. Phys. Lett.*, **9**, 33 (1971).

(6) K. Tanaka and G. Blyholder, *J. Phys. Chem.*, **76**, 1807 (1972); *Chem. Commun.*, 736 (1971).

adsorbed species as studied by combining a temperature-programmed desorption technique with esr spectroscopy. The plausibility of the molecular or atomic reaction mechanism proposed for the thermal catalytic decomposition of N_2O at 400° on zinc oxide[7] is also discussed.

Experimental Section

The apparatus used for the temperature-programmed desorption experiments is shown in Figure 1. The Pyrex glass cell (R), furnace, and illuminating procedure are the same as those used previously.[7] About 1.5–1.6 g of ZnO (Kadox-25) or of TiO_2 (rutile from National Lead Co.) were mounted in the cell and all treatments such as oxidation, evacuation, and adsorption were carried out in the cell. By changing the flow of helium carrier gas from L_2 to L_3 at the time the temperature of the cell reached a desired value, the desorbed oxygen could be detected in a gas chromatograph with a molecular sieve column. The heating rate was about 400°/hr.

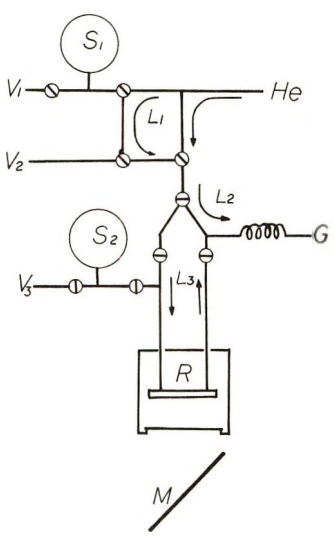

Figure 1. The apparatus of the temperature-programmed desorption: V_1, V_2, and V_3 go to the vacuum line; S_1 and S_2 are sample gas holders; R is the cell; M is the front surface mirror; and G goes to the gas chromatograph.

The reactivity of the adsorbed species, O_2^- and O^-, was examined by passing a small carbon monoxide pulse over the catalyst using lines L_1 and L_3. Esr samples were prepared by connecting a sample tube to a vacuum system with an O-ring stopcock and O-ring joint. The sample was protected from contaminations by using a liquid air trap. Esr spectra were taken at room temperature with a Varian E-4 spectrometer.

Our standard pretreatment of zinc oxide and titanium dioxide consisted of oxidation at 400–435° for several hours, followed by evacuation at the same temperature. The oxide was evacuated for 10 min at room temperature before the desorption experiments.

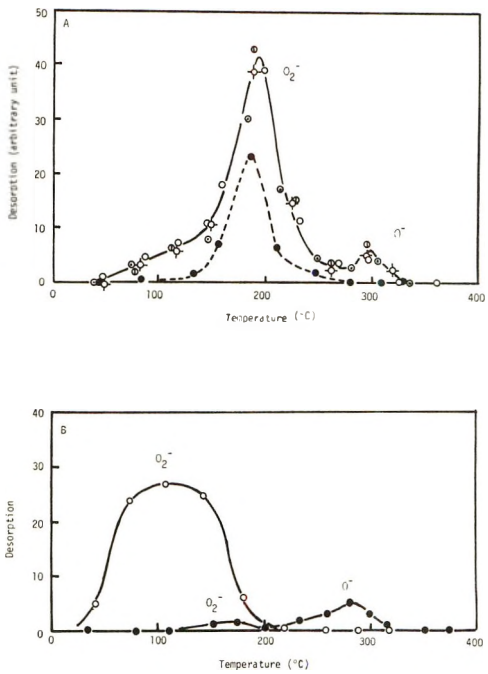

Figure 2. Desorption spectra of oxygen from zinc oxide: (A) solid line represents desorption of oxygen adsorbed on evacuated ZnO and broken line represents desorption of oxygen after CO pulse has been passed through; (B) ○ represents desorption of oxygen adsorbed on hydrogen presorbed ZnO and ● represents desorption of oxygen adsorbed at 200° and cooled to room temperature.

Results

A typical desorption spectrum of oxygen adsorbed by exposure to 8 cm oxygen pressure at room temperature on zinc oxide, which has been outgassed at 415–435° for 5 hr and cooled *in vacuo*, is shown in Figure 2A. Two peaks with maxima at 180–190 and 285–295° were observed, but the high-temperature peak was relatively smaller than that observed previously.[8] It was found that the high-temperature peak is more sensitive than the low-temperature peak to pretreatment and that the ratio of the high-temperature peak to the total oxygen desorption changes some from one sample to another. However, reproducibility is obtained for the same sample as shown in Figure 2A; five repeated experiments giving the approximately constant values of 8.4, 9.2, 8.0, 8.0, and 8.4% for the ratio of the high-temperature peak area to the total desorption. As will be discussed later, the low-temperature peak corresponds to O_2^- and the high-temperature peak is probably due to O^-.

In order to determine the reactivity of these two adsorbed species, a small carbon monoxide pulse was passed at room temperature over zinc oxide on which oxygen had been adsorbed as stated above. The desorption spectrum of oxygen from this sample is

(7) K. Tanaka and G. Blyholder, *Chem. Commun.*, 1130 (1970); K. Tanaka and G. Blyholder, *J. Phys. Chem.*, **75**, 1037 (1971).

(8) K. Tanaka and G. Blyholder, *Chem. Commun.*, 1343 (1971).

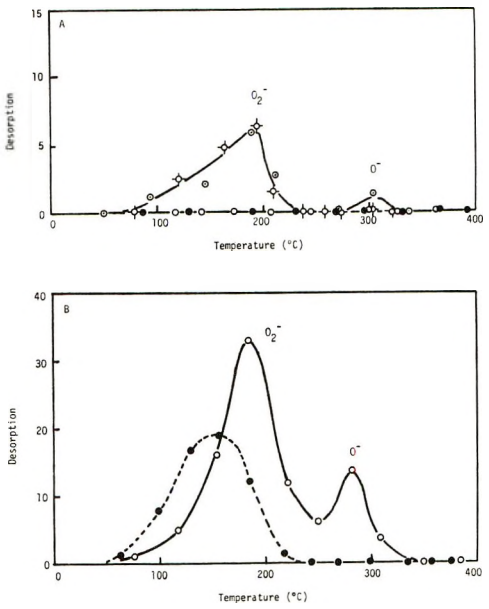

Figure 3. (A) Photo effects on the desorption and on the adsorption of oxygen over the inert zinc oxide: ○ represents desorption from the ZnO under illumination, ● represents desorption from the ZnO in the dark, and ⊙-◇- represents desorption from the ZnO having been illuminated under oxygen; (B) the desorption of oxygen from ZnO and TiO_2: ○ represents desorption of oxygen adsorbed on evacuated ZnO, and ● represents desorption of oxygen adsorbed on evacuated TiO_2.

shown in Figure 2A with a dotted line. The high-temperature peak is missing within the experimental accuracy.

When oxygen was adsorbed at about 200° for 1 hr, instead of at room temperature, and then the sample cooled to room temperature under oxygen, the desorption spectrum is as shown in Figure 2B with solid circles. The lower temperature peak is greatly decreased. If zinc oxide evacuated at 415° for 2 hr was cooled under several centimeters (pressure) of oxygen and kept over night under oxygen, no desorption peaks were observed as shown in Figure 3A with solid circles. A temperature-programmed desorption experiment of this inert surface under illumination gave no desorption of oxygen as shown in Figure 3A with open circles on the abscissa. However, by illuminating the inert surface under several centimeters (pressure) of oxygen at room temperature for 30 min, a desorption spectrum was again observed as shown in Figure 3A.

It was found that the oxygen adsorbed on hydrogen-presorbed zinc oxide desorbs at rather lower temperatures than usual. Figure 2B (open circles) shows a typical desorption spectrum of oxygen from a hydrogen-presorbed surface on which oxygen had been adsorbed at room temperature for 5 hr after exposure to hydrogen at room temperature for 9 hr and evacuation for 1 hr at room temperature. The desorption spectrum is rather broad and has a maximum at 110–120°.

In order to identify the adsorbed species on the evacuated surface and on the hydrogen presorbed surface, esr spectroscopic studies were carried out. Figure 4A shows spectra of zinc oxide evacuated at about 410° for several hours and cooled *in vacuo* (dotted line) and of zinc oxide cooled under oxygen (solid line). The zinc oxide cooled *in vacuo* gives an absorption corresponding to electrons in the conduction band or on interstitial zinc, but the zinc oxide cooled under oxygen gives no such absorption.

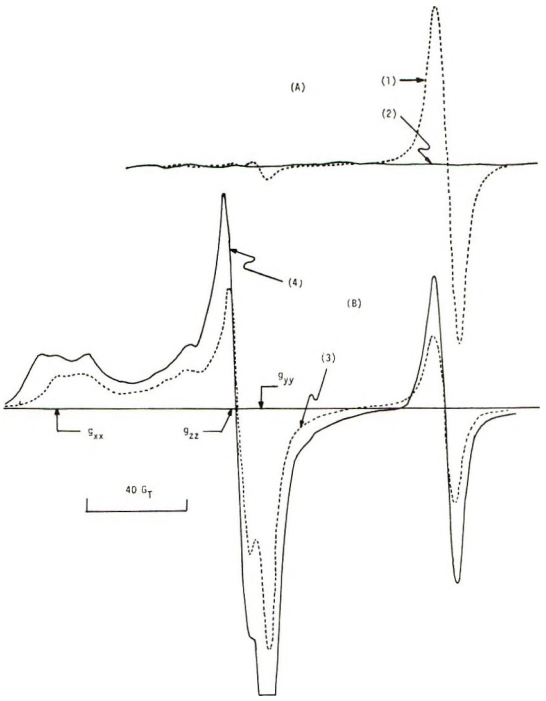

Figure 4. Esr spectra of adsorbed oxygen on zinc oxide at room temperature: (A) broken line represents evacuated ZnO and solid line represents ZnO cooled under oxygen; (B) broken line represents oxygen adsorbed on evacuated ZnO and solid line represents oxygen adsorbed on hydrogen-presorbed ZnO.

Oxygen adsorbed on zinc oxide which has been evacuated at about 410° and cooled *in vacuo* gives the spectrum shown in Figure 4B with a dotted line. This spectrum obtained at room temperature agrees quite well with that obtained at −190° by Lunsford and Jayne,[2] and the g values given by them are indicated in the figure by arrows.

The esr spectrum of oxygen adsorbed on hydrogen-presorbed zinc oxide is very similar to that obtained above and is shown in Figure 4B with a solid line.

The desorption of oxygen from titanium dioxide was also studied. Oxygen was adsorbed at room temperature for 16 hr on titanium dioxide which has been evacuated at about 400° for 4 hr and cooled *in vacuo*. The desorption spectrum has only one peak with a maximum at 150–160° as shown with the dotted line in Figure 3B and no higher temperature peak like zinc oxide. For comparison, a typical desorption spectrum of zinc oxide[8] is shown with a solid line.

Discussion

In the previous paper,[8] the two desorption peaks with maxima at 180–190 and 285–295° were tentatively assigned to O_2^- and O^-, respectively. The temperatures of the desorption spectra are consistent with the reports that the conductivity of evacuated zinc oxide decreased in oxygen and is not returned to its original value by a subsequent evacuation below 261°, but is above 300°.[9] The esr spectrum of oxygen adsorbed on zinc oxide at room temperature, which is shown in Figure 4B with a dotted line, agrees with the spectrum of adsorbed oxygen obtained at −190° and assigned to an O_2^- species on zinc oxide.[2] Thus, the main species of oxygen adsorbed on zinc oxide at room temperature is also most likely O_2^-, and the desorption peak with a maximum at 180–190° is reasonably assigned to O_2^-.

The esr spectroscopic assignment of O^- on zinc oxide is unsettled; the assignment given by Kwan, *et al.*,[4] has some ambiguity as has been pointed out by Lunsford, *et al.*[5] On the other hand, the results of the catalytic oxidation of CO with O_2 and with N_2O over zinc oxide[6] give evidence for assigning the high-temperature peak to O^-. That is, at about 200° both reactions, $CO + {}^1/_2O_2 \rightarrow CO_2$ and $CO + N_2O \rightarrow N_2 + CO_2$, have the same reaction rate and the same kinetics, which are first order in carbon monoxide pressure and zero order in oxygen or nitrous oxide pressure. Furthermore, in the simultaneous competitive reaction of CO with O_2 and N_2O the reaction of CO with N_2O is strongly retarded by O_2, while the over-all carbon dioxide formation rate is the same as that observed in the separate oxidations of CO with O_2 or N_2O. These results suggest for the two reactions a common intermediate which since it comes from O_2 or N_2O seems to us most likely to be O^- and that the active sites are mostly covered by the intermediate species around 200° at which temperature O_2^- species are mostly desorbed. Thus, the desorption peak at 285–295° is reasonably assigned to an O^- species. The result of the pulse experiment shown in Figure 2A supports the assignment of the high-temperature peak to an O^- species which is more reactive with CO than is O_2^-.

The capability of mutual conversion of these two species on zinc oxide should be carefully studied. Kwan, *et al.*,[4] reported that O_2^- on zinc oxide changed to O^- at temperatures above 160° with some activation energy; however, their assignment of O^- has some ambiguity.[5] The results shown in Figure 2B, in which oxygen was adsorbed at about 200° for 1 hr and cooled to room temperature under oxygen, reveal that O^- does not change to O_2^- over zinc oxide at temperatures below 200°, and that the number of electrons available for O_2^- adsorption is decreased by heating up to 200°. The esr spectra also show the decrease in the number of electrons available for O_2^- formation by heating up to 200°, that is, the esr spectrum is not returned to the original intensity by heating and evacuating at about 200°. These results suggest that both species, O_2^- and O^-, are formed on zinc oxide by the adsorption of oxygen at room temperature and that the equilibration between them cannot be established below 200.° This means the conversion of O_2^- to O^- during temperature-programmed desorption will be negligible.

The zinc oxide cooled under oxygen has relatively few electrons available for oxygen adsorption as shown in Figure 4A with a solid line, and actually no oxygen desorption from this surface is observed as shown in Figure 3A with solid circles. Thus this surface is inert for oxygen adsorption. Photodesorption of oxygen from a zinc oxide surface has been observed by several investigators,[10] and was explained as photoreduction of ZnO. This photoreduction process was not observed on the inert zinc oxide surface as shown in Figure 3A with open circles, but rather the electrons produced by illumination over this inert zinc oxide are available for the adsorption of oxygen as shown in Figure 3A. These results make it plausible that the thermal catalytic decomposition of nitrous oxide on zinc oxide near 400° does not include electron transfer processes but only the photocatalytic decomposition proceeds by an electron transfer mechanism.[7]

The adsorption of hydrogen on zinc oxide enhances the amount of oxygen adsorption as O_2^- (Figure 4B), but weakens the adsorption strength of O_2^- (Figure 2B). A rough calculation gives about a 20% decrease in the adsorption strength on a hydrogen-presorbed sample. The lower adsorption strength of O_2^- on hydrogen-presorbed zinc oxide could be caused by field effects at the surface and the board shape of the desorption spectrum suggests the surface field is heterogeneous. The O_2^- species on titanium dioxide are held on the surface more weakly than those on evacuated zinc oxide but stronger than those on hydrogen-presorbed zinc oxide. Thus some of the complexities of gas absorption during catalysis are revealed.

Acknowledgment. This investigation was supported in part by Research Grant No. 00818 from the Air Pollution Control Office, Environmental Protection Agency.

(9) P. Amigues and S. J. Teichner, *Discuss. Faraday Soc.*, **41**, 362 (1966).

(10) Y. Fujita and T. Kwan, *Bull. Chem. Soc. Jap.*, **31**, 379 (1958); T. I. Barry and F. S. Stone, *Proc. Roy. Soc., Ser. A*, **255**, 124 (1960).

An Infrared Spectroscopy Study of Water Adsorption at the Silica–Carbon Tetrachloride Interface

by Willard D. Bascom

Surface Chemistry Branch, Naval Research Laboratory, Washington, D. C. 20390 *(Received April 5, 1972)*

Publication costs assisted by the Office of Naval Research

Suspensions of amorphous silica (Cabosil) in CCl_4 were studied by infrared spectroscopy in the 4000–2500-cm^{-1} region. The silica was predried at 750° so that the only major spectral band was at 3700 cm^{-1}, attributable to isolated surface hydroxyls interacting with the CCl_4 media. Rehydration of the silica in suspension produced bands at 3400 cm^{-1} for adsorbed molecular water and at 3660 cm^{-1} for adjacent, hydrogen-bonded surface hydroxyls. Rehydration did not alter the intensity of the free hydroxyl band at 3700 cm^{-1}, even though the water is adsorbed by hydrogen bonding to the hydroxyl groups. An estimate of the molar absorptivity of the molecular water band (3400 cm^{-1}) gave a value of 53 M^{-1} cm^{-1}, close to that of bulk water.

A large body of literature has developed on the infrared spectra of water chemisorbed and physically adsorbed on silica surfaces. Much of the work stems from the technical and fundamental interest in the silica–water interaction. Also, water adsorption on silica is particularly amenable to infrared studies since silica is transparent in the O–H stretching vibration region (4000–2500 cm^{-1}). There is reasonable agreement as to the band assignments for surface silanols (≥Si–OH) and adsorbed molecular water; nonetheless, there are still details and ambiguities about these bands that deserve attention. The literature dealing with this problem has been reviewed by Little,[1] Kiselev,[2] and Hair.[3]

Most of the infrared spectroscopy of SiO_2 surfaces has been done using thin porous plates or disks of pressed powder. These samples are fragile and because of their particulate structure there is considerable beam scattering which reduces band intensity and resolution. In the work reported here the silica was suspended in carbon tetrachloride. These suspensions can be conveniently handled without contamination by atmospheric water and because of the close match between the refractive indices of CCl_4 and SiO_2 there is negligible beam scattering.

Experimental Section

The SiO_2 powder was a nonporous aerosil (Cabosil, Cabot Corp., Boston) having a surface area of 202 m^2 gm^{-1} after outgassing at 80° for 20 hr to a residual gas evolution of <0.1 μmol hr^{-1} m^{-2}. The SiO_2 was dried at 10^{-3} mm pressure for 24 hr in the drying cell illustrated in Figure 1. The drying temperature was usually 750°, although the effect of drying at other temperatures between 25 and 800° was also studied. All vacuum fittings were copper gasket flanges and all valves were stainless steel with Kel-F seats. Back diffusion of oil from the pumps to the cell was suppressed by a molecular sieve–Dry Ice trap.

After the SiO_2 had been dried the cell was allowed to cool and brought to atmospheric pressure by introducing dried He gas. A Teflon stirring bar, held out of the furnace by a magnet during the heating, was allowed to fall into the silica powder. An appropriate amount of CCl_4 was added through a long, wide-bore (1.5 mm) hypodermic needle that extended from the septum inlet, e, (Figure 1) to the powder, a, (Figure 1). The CCl_4 had been dried by percolation through activated Florisil. Stirring for about 2 hr gave a clear suspension containing 2.00 ± 0.04% silica. The suspension was transparent due to the close match between the refractive indices of SiO_2 (1.46) and CCl_4 (1.463). Because the particle size was about 0.015 μ the rate of settling of the SiO_2 was very slow. The hypodermic needle was left in the cell and used for adding or withdrawing material to or from the suspension. To rehydrate the SiO_2, wet He gas was bubbled through the suspension using the hypodermic needle as a gas inlet tube.

Infrared spectra of the SiO_2–CCl_4 suspensions in the 4000–2500-cm^{-1} region were determined by withdrawing 2.5-ml aliquots with a gas-tight syringe and injecting them into an optical cell having a 1-cm path length. The cell was constructed of Infrasil, a silica with low absorption in the 4000–2500-cm^{-1} region (Amersil Inc., Hillside, N.J.). The spectrometer was a double-beam Perkin-Elmer 457 Model operated at

(1) L. H. Little, "Infrared Spectra of Adsorbed Species," Academic Press, New York, N. Y., 1966, p 228.

(2) A. V. Kiselev and V. I. Lygin, ref 1, pp 213 and 352.

(3) M. L. Hair, "Infrared Spectroscopy in Surface Chemistry," Marcel Dekker, New York, N. Y., 1967, p 79.

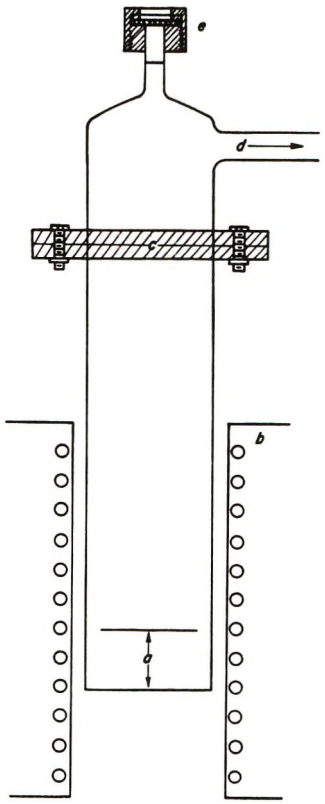

Figure 1. Drying cell: (a) sample area, (b) movable heater, (c) copper gasket flange, (d) vacuum outlet, (e) inlet septum.

a spectral slit width of about 4 cm^{-1}. Compensation for solvent absorption was achieved by placing in the reference beam a matched Infrasil cell containing only CCl_4.

The amount of molecular water in a SiO_2–CCl_4 suspension was determined by titration with the Karl Fisher reagent. The applicability of this method to water on silica has been demonstrated by Kellum and Smith.[4] A 5-ml sample of suspension was injected into approximately 50 ml of a methanol–chloroform solvent (1:3 by volume) and titrated to a minimum, constant conductivity. The major difficulty with this technique is that the Karl Fisher reagent is adsorbed and may react with the SiO_2 surface. To correct for this error the volume of reagent required for a suspension of SiO_2 dried at 750° was subtracted from the volume required for an equivalent sample of rehydrated SiO_2.

Results

The infrared spectra obtained for Cabosil dried at temperatures from 25 to 750° and suspended in CCl_4 are given in Figure 2. The silica that had been dried at 750° (and suspended in CCl_4) was rehydrated by passing wet He gas through the suspension. The resulting spectrum is given in Figure 3. Note that the major spectral change is the appearance of the broad band at 3400 cm^{-1}. The intensity of this band was varied by varying the time of treatment with wet helium

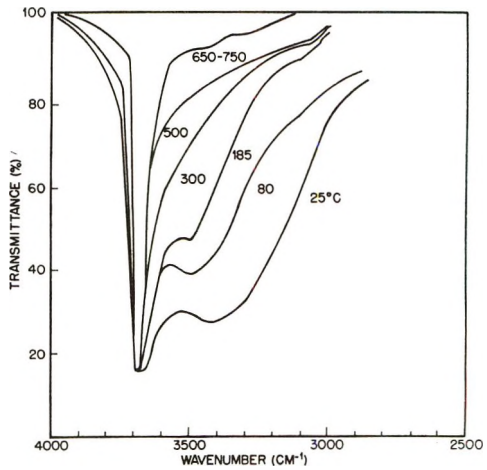

Figure 2. Infrared spectra of SiO_2–CCl_4 suspensions. SiO_2 was dried for 20 hr and 10^{-3} mm pressure at the indicated temperatures.

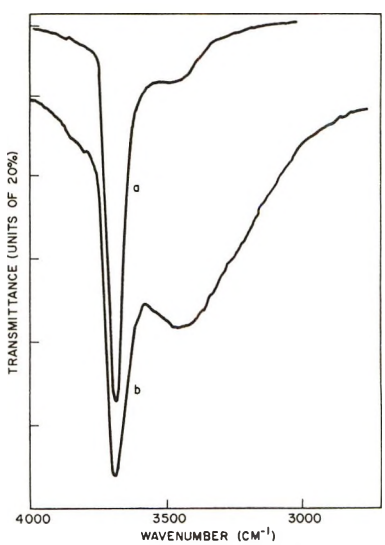

Figure 3. Spectra of SiO_2 suspended in CCl_4: (a) predried at 750°; (b) rehydrated.

and its absorbance ($A = \log 1/T$) was plotted against the moles of adsorbed water, as determined by Karl Fisher titration. The results given in Figure 4 indicate the Beer–Lambert relation ($A = \alpha lc$) was followed over most of the data. In these expressions T is the transmittance, α is the molar absorptivity (g mol^{-1} cm^{-1}), l the cell length (cm), and c the concentration (mol gm^{-1}). The values for T were obtained from the ratio, $T_{\text{rehydrated}}/T_{\text{dried}}$, *i.e.*, the transmittance of the silica at 3400 cm^{-1} before and after rehydration.

The silica dried at 750° was also treated with D_2O. First, before adding CCl_4, the chamber was opened to a side tube of liquid D_2O until the volume taken up was slightly more than required for a monolayer coverage of the powder (0.1 ml of liquid). This procedure of drying followed by D_2O exposure was repeated ten

(4) G. E. Kellum and R. C. Smith, *Anal. Chem.*, 39, 341 (1967).

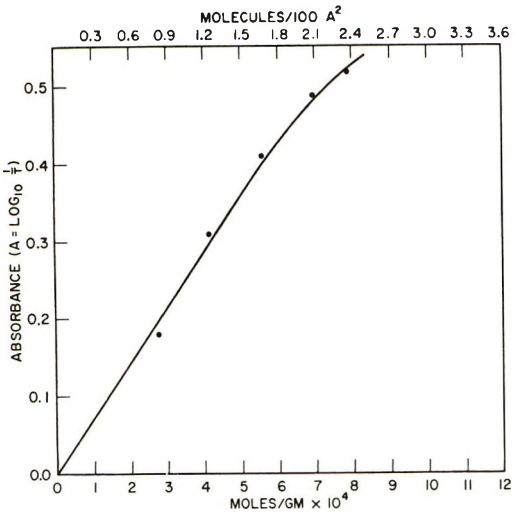

Figure 4. Beers–Lambert plot for the adsorbed water band at 3400 cm^{-1}.

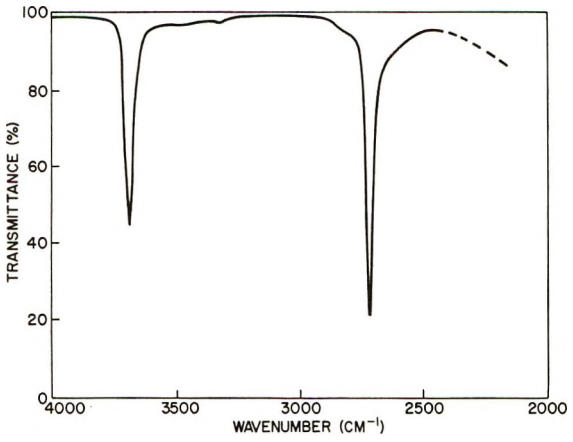

Figure 5. Spectrum of SiO_2 (in CCl_4) that had been repeatedly dried (750°) and exposed to D_2O vapor.

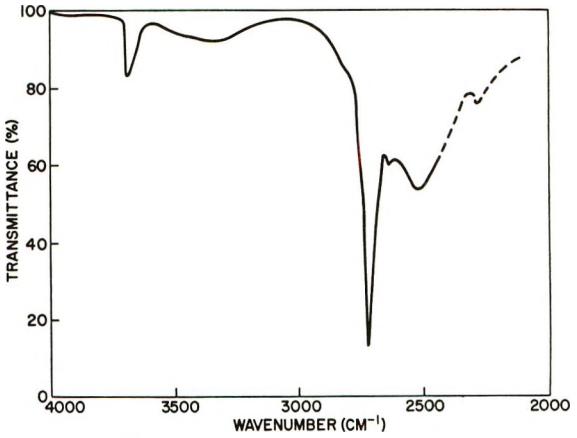

Figure 6. Spectrum of a SiO_2–CCl_4 suspension after treatment with D_2O-saturated He gas.

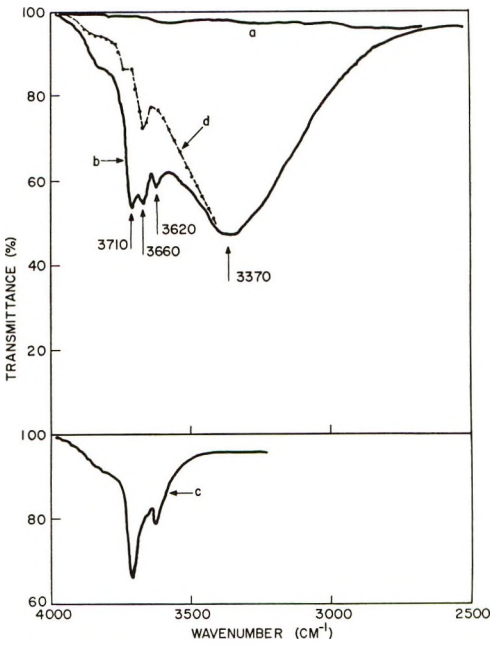

Figure 7. Differential spectra (a) before wet He treatment of sample, (b) 30 min after treatment, (c) filtrate of b, (d) manual subtraction of c from b.

times, then the sample was given a final drying at 750° and suspended in CCl_4 (2% solution). The spectrum of this suspension is given in Figure 5. The silica was then further treated by bubbling D_2O-saturated He gas through the suspension and the resulting spectrum is shown in Figure 6.

A more detailed examination was made of the spectral changes occurring in the rehydration of the silica. Differential spectra were obtained by placing matched samples of SiO_2 (dried at 750°) in CCl_4 in both the sample and reference beams and wet He was passed through the suspension in the sample beam. Spectra were taken after various time intervals over a 2-hr period. Figure 7b is typical of the spectra. In addition to the principle band at 3370 cm^{-1} (attributed to H-bonded molecular water) the three other bands included two (3710 and 3620 cm^{-1}) found to be due to monomeric (non H-bonded) water in the CCl_4 (Figure 7c). Dissolved water in the CCl_4 was present in these experiments because of incomplete stirring of the suspension in the optical cells. Stirring was not a problem when treating the suspension in the larger chamber (*i.e.*, Figure 1).

The infrared bands observed in all these experiments are listed in Table I along with the corresponding bands observed for Cabosil *in vacuo*, the molecular assignments that have been given these bands, and the appropriate references.

Discussion

The results in Table I indicate that with the exception of the isolated ≥SiOH and ≥SiOD bands the correspondence between the SiO_2–CCl_4 and the SiO_2–vacuum bands was nearly exact. The frequency of the H-bonded molecular water bond obtained here is given as a range between 3370 and 3400 cm^{-1} because

Table I: Infrared Band Frequencies and Assignments

Frequency, cm^{-1}			
SiO_2–CCl_4	SiO_2–vacuum	Group assignment	Ref
3700	3750	Isolated ≥SiOH	9, 10
3660	3660	Adjacent H-bonded ≥SiOH	10
3370–3400	3400	H-bonded H_2O	10
2725	2760	Isolated ≥SiOD	10, 11
2660	~2690	Adjacent ≥SiOD	11
2510	2520	H-bonded D_2O	11

it appears at 3400 cm^{-1} in the spectra of the suspensions (Figure 3) but at 3370 cm^{-1} in the differential spectrum (Figure 7). The 3400-cm^{-1} value may reflect overlap with the 3700-cm^{-1} band and so the lower value of 3370 cm^{-1} is probably closer to the true frequency.

The shift of the ≥SiOH (or ≥SiOD) bands from 3750 to 3700 cm^{-1} (or 2760 to 2725 cm^{-1}) is undoubtedly due to a relatively weak interaction of these surface groups with CCl_4. Gas-phase adsorption of CCl_4 on silica produced a comparable shift.[5] Low and Hasegawa[6] observed the isolated ≥SiOH band at 3686 cm^{-1} for pressed Cabosil plates immersed in CCl_4. The fact that the band at 3660 cm^{-1}, which corresponds to adjacent hydroxyl interaction

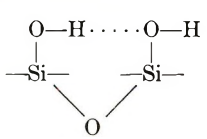

and the band at 3370 cm^{-1} for H-bonded water are not displaced in CCl_4 compared to vacuum indicates that these interactions are stronger than the hydroxyl–CCl_4 interaction. Indeed, the shift of the 3750-cm^{-1} band for the latter is only 50 cm^{-1} whereas the shift due to adjacent hydroxyl H-bonding and the water H-bonding are 90 and 380 cm^{-1}, respectively.

The good correlation between the band frequencies of the SiO_2–CCl_4 and the SiO_2–vacuum systems demonstrates that the infrared spectroscopy of water adsorption on silica can be conveniently studied using SiO_2–CCl_4 suspensions. The handling of these suspensions is relatively easy and free of the encumbrances of working with pressed silica disks in gas adsorption systems. Initially there was some concern about water pickup from the atmosphere during manipulation of the samples. However, the H_2O band (3400 cm^{-1}) in the spectrum of the deuterated SiO_2 suspension (Figure 6) was very weak but would not have been so had there been any significant water uptake.

The spectral changes that occurred when the dried silica was rehydrated allow an estimate of the molar absorptivity of adsorbed water and also give some insight into how the water is held on the silica.

The molar absorptivity (α) of the 3400-cm^{-1} band of the adsorbed water was computed from the Beer–Lambert plot (Figure 4). A value of 53 M^{-1} cm^{-1} was obtained if the following assumptions are made: (a) the water film thickness was 3 Å, *i.e.*, a monolayer of water; and (b) the cell thickness was 0.8×10^{-3} cm. This latter value was obtained by taking the thickness of Cabosil as 2% of the cell thickness (1 cm), the path length through the water film to be 6 Å, and the SiO_2 particle size as 150 Å. All considered, the value for α of 53 M^{-1} cm^{-1} is surprisingly close to the values of 55–95 M^{-1} cm^{-1} reported for bulk water.[7]

It was somewhat surprising to find in the differential spectra that there had been no change in the intensity of the ≥SiOH band at 3700 cm^{-1}. There is general agreement that adsorbed molecular water is held on the surface of silica by H bonding to the surface hydroxyls. For example, Kiselev has shown that the heat of adsorption of water on silica is lowered by dehydroxylation of the silica surface.[8] In fact, he argued that the intensity of the free O–H is progressively reduced with increased adsorption of molecular water. This would seem to be the case in Figure 3 where the intensity of the 3700-cm^{-1} band in the spectrum of the rehydrated sample is reduced relative to the dried silica by subtraction of the background due to the broad 3400-cm^{-1} water band. However, this subtraction involves assuming a shape for the high-frequency region of the 3400-cm^{-1} band.

Closer examination of the problem reveals that failure to observe a major decrease in intensity at 3700 cm^{-1} by differential spectroscopy does not mean the water is not H bonded to the surface hydroxyls. In fact, it is difficult to visualize a H-bonded configuration which does not leave at least one free O–H bond. For example, on a sparsely hydroxylated surface

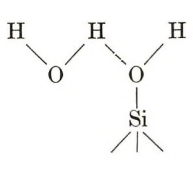

II

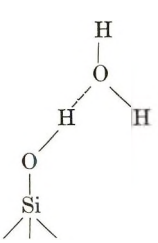

III

there would be two free hydroxyls for each silanol–water pair. If the silanols are close enough (<6 Å) to permit the water molecule to bridge between them, the ratio of H bond to free O–H would be 1:1.

(5) W. Hertl and M. L. Hair, *J. Phys. Chem.*, **72**, 4676 (1968).

(6) M. J. D. Low and M. Hasegawa, *J. Colloid Interface Sci.*, **26**, 95 (1968).

(7) R. E. Kagarise, "Intensity Measurements of Some Fundamental Absorption Bands at H_2O, D_2O, and CS_2," NRL Report 6394, Naval Research Laboratory, Washington, D. C., May 27, 1966.

(8) V. Ya. Davydov and A. V. Kiselev, *Kolloid. Zh.*, **30**, 265 (1968).

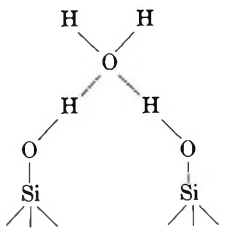

IV

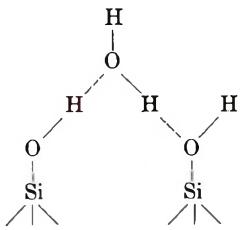

V

In these experiments the level of water coverage was rather low, about one water per 100 Å. At greater coverages large changes in the 3700-cm^{-1} band are to be expected and were in fact observed by Kiselev.[8]

The final point to be made is that in addition to hydration there was some rehydroxylation of the silica after treatment by wet helium. The most obvious evidence for hydroxylation is the appearance of the band at 3660 cm^{-1} in the differential spectra (*e.g.*, Figure 7). In silica–vacuum spectra this band has been assigned to adjacent, H-bonded ≥SiOH groups[9,10] and is the most likely product if a surface siloxane group is hydrolyzed. Treatment of the silica with D_2O produced a band of 2660 cm^{-1} (Figure 6) which may be due to adjacent ≥SiOD groups. This band has been reported to be at about 2700 cm^{-1} by McDonald[10] and 2690 cm^{-1} by Kiselev and coworkers.[11]

The 3660-cm^{-1} band appeared in the differential spectra within 5 min of wet He treatment and continued to increase in intensity for about 15 min, after which the intensity remained constant. The immediate appearance of this band implies the presence of surface sites highly susceptible to hydrolysis, presumably strained siloxane groups. The fact that the band reached a limiting intensity does not necessarily mean there was no further hydroxylation. The relatively weak H bonding between adjacent hydroxyls may be disrupted by stronger H bonding with molecular water so that the limiting intensity could represent a steady state achieved between the formation of adjacent H-bonded hydroxyls and their dissociation by adsorbing water. The simultaneous hydroxylation and hydration of silica is discussed in a recent paper by Deitz and Turner.[12]

(9) R. S. McDonald, *J. Amer. Chem. Soc.*, **79**, 850 (1957).

(10) R. S. McDonald, *J. Phys. Chem.*, **62**, 1168 (1958).

(11) G. A. Galkin, A. V. Kiselev, and V. I. Lygin, *Russ. J. Phys. Chem.*, **42**, 765 (1968).

(12) V. R. Deitz and N. H. Turner, *J. Phys. Chem.*, **75**, 2718 (1971)

Hydrolysis of Triethylethoxysilane at the Silica–Carbon Tetrachloride Interface[1]

by Willard D. Bascom*

Surface Chemistry Branch, Chemistry Division, Naval Research Laboratory, Washington, D. C. 20390

and Richard B. Timmons

Chemistry Department, Catholic University of America, Washington, D. C. 20017 *(Received April 5, 1972)*

Publication costs assisted by the Office of Naval Research

It was discovered that $(C_2H_5)_3SiOC_2H_5$ is hydrolyzed to $(C_2H_5)_3SiOH$ and C_2H_5OH by adsorbed water on silica in CCl_4. The hydrolysis kinetics were determined in an effort to establish the mechanism of this surface reaction. The results suggest that for the hydrolysis to occur there must be enough adsorbed water to H bond between silanols to form an adsorbed, hydrated network. Hydrolysis of alkoxysilanes proceeds by protonization of the Si–O bond and the hydrated network facilitates proton transfer from the acidic surface silanols. At the lower reactant concentrations the amount of adsorbed reactant is determined by adsorption equilibrium with the solution and the rate is first order but when the hydrated network is saturated with reactant the rate is zero order. Increasing the reaction temperature tends to disrupt the ≥SiOH–H_2O network and thereby decrease the reaction rate. The rate-determining step appears to be a slow orientation of the adsorbate reactant preceding the hydrolysis step.

Introduction

Alkoxysilanes and chlorosilanes having the general formulas, $R_nSi(OR')_{4-n}$ and R_nSiCl_{4-n}, are widely used as treating agents to modify the surfaces of glass, clay, and metal oxides.[2] These agents form tenacious films on the inorganic substrates and by the proper choice of the R group, will render the surface hydrophobic[2,3] or even oleophobic.[3] They are also used to

(1) Taken in part from the Ph.D. Thesis of W. D. Bascom, Catholic University of America, Washington, D. C.

treat resin reinforcements such as glass fiber, in which case an R group is selected that will react with the resin.[4]

The technical use of these silicon compounds as surface treating agents has stimulated fundamental studies of their interaction with siliceous surfaces.[5-9] Almost all of these investigations have been concerned with the chemical adsorption of the alkoxy- or chlorosilane by surface hydroxyl groups. Recently, Hertl and Hair[7,8] studied the kinetics of the chemisorption of the methyl-, methoxy-, and methylchlorosilanes on amorphous silica from the gas phase. They demonstrated a condensation of the silane derivative with the surface silanols (≥Si–OH) as, for example, in reaction I. The temperatures required for detectable reaction were

$$(CH_3)_3SiOCH_3 + HOSi\leq \longrightarrow (CH_3)_3Si{-}O{-}Si\leq + CH_3OH \quad (1)$$

200° and higher and the activation energies were found to be about 20 kcal/mol for the chlorosilanes and 20–30 kcal/mol for the methoxysilanes. However, it seems questionable whether reactions such as (1) are important in forming tenacious films with alkoxysilanes since in technical practice they can be applied successfully at room temperature.[10]

As an alternate explanation for the tenacity of the adsorbed alkoxy- and chlorosilanes it has been suggested that they form siloxane polymer films on the surface.[2,3,9] Such high molecular weight polymer films resist desorption because of their low solubility and their ability to form multiplet attachments to the surface. Direct evidence of polysiloxane film formation by trialkoxy- and trichlorosilanes on glass and silica has been obtained from ellipsometer measurements,[3,11] radioactive labeled adsorbates,[12,13] and infrared[14] and Raman spectroscopy.[15]

Further evidence of the importance of silane hydrolysis in their interaction with silica is presented here in a study of the hydrolysis of triethylethoxysilane at the hydrated SiO_2–CCl_4 interface. It was possible to

$$(C_2H_5)_3SiOC_2H_5 + H_2O(\text{adsorbed}) \xrightarrow{\geq SiOH} (C_2H_5)_3SiOH + C_2H_5OH \quad (2)$$

study the kinetics of reaction 2 without interference by side reactions. It will be shown that (a) the reactant is not hydrolyzed in the CCl_4 phase, (b) there is no detectable disiloxane, $(C_2H_5)_3Si{-}O{-}Si(C_2H_5)_3$, formed by the reactant or by the triethylsilanol product, and (c) that neither the reactant nor the products were chemisorbed by the surface silanols (*i.e.*, reactions such as (1)). As in any surface study, it was necessary to characterize the silica surface. In this case infrared spectroscopy was used to monitor the surface hydroxyl groups and adsorbed water. The details of this infrared study have been reported elsewhere.[16]

Experimental Section

Materials. The silica used in this work was a nonporus aerosil (Cabosil, Cabot Corp., Boston, Mass.) having a surface area of 202 $m^2\ g^{-1}$ after outgassing at 80° for 20 hr to a residual gas evolution of $\ll 0.1$ $\mu mol\ hr^{-1}\ m^{-2}$. The carbon tetrachloride was percolated through a 6 in. long column of dried Florisil to remove water. The triethylethoxysilane (Pierce Chem. Co., Rockford, Ill.) and triethylsilanol (Peninsular Chemresearch Inc., Gainesville, Fla.) were used as received. The ethoxysilane was analyzed by gas chromatography and contained less than 1 mol % of the silanol. The other contaminants detected constituted less than 0.05% of the sample and could not be removed by distillation. The triethylsilanol contained about 0.01 mol % of the triethylethoxy compound.

Pretreatment of the Silica. The SiO_2 was dried at 10^{-3} mm pressure and 750° (or in some experiments at 550°) for 24 hr. Details of the procedure are given elsewhere.[16] The dried silica was dispersed into CCl_4 by first cooling the cell containing the powder and then bringing it to atmospheric pressure with dried He gas. A Teflon-covered stirring bar, held out of the heated section of the cell by a magnet, was allowed to fall into the silica powder. An appropriate amount of CCl_4 was added through a long, wide-bore (1.5 mm) hypodermic needle that extended from a septum inlet to the powder. Stirring for about 2 hr gave a clear suspension containing 2.00 ± 0.04% silica. The suspension was transparent because of the close match between the refractive indices of SiO_2 and CCl_4. The hypodermic needle was left in the cell and used for additions and withdrawals to or from the suspension. To rehydrate the silica, wet helium gas was bubbled through the suspension using the hypodermic needle as a gas inlet tube.

(2) R. L. Bass and M. R. Porter, "Waterproofing and Water Repellency," J. L. Molliet, Ed., American Elsevier, New York, N. Y., 1963, p 136.

(3) W. D. Bascom, *J. Colloid Interface Sci.*, **27**, 789 (1968).

(4) S. Sterman and J. G. Marsden, *Ind. Eng. Chem.*, **58**, 33 (1966).

(5) V. Ya. Davydov, L. T. Zhuravlev, and A. V. Kiselev, *Zh. Fiz. Khim.*, **38**, 2047 (1964).

(6) C. G. Armstead and J. A. Hockey, *Trans. Faraday Soc.*, **63**, 2549 (1967).

(7) W. Hertl, *J. Phys. Chem.*, **72**, 1248, 3993 (1968).

(8) M. L. Hair and W. Hertl, *ibid.*, **73**, 2372 (1969).

(9) W. J. Herzberg and W. R. Erwin, *J. Colloid Interface Sci.*, **33**, 172 (1970).

(10) J. Sidlovsky, *Proc. SPI (Soc. Plast. Ind.) Reinf. Plast. Div. Tech. Conf., 14th, 1959, Sect. 13F* (1959).

(11) D. J. Tutas, R. Stromberg, and E. Passaglia, *SPE (Soc. Plast. Eng.) Trans.*, **4**, 256 (1964).

(12) F. O. Stark, O. K. Johannson, G. E. Vogel, R. G. Chaffee, and R. M. Lacefield, *J. Phys. Chem.*, **72**, 2750 (1968).

(13) M. E. Schrader, *J. Adhes.*, **2**, 202 (1970).

(14) W. D. Bascom, *Macromolecules*, in press.

(15) J. L. Koenig and P. T. K. Shih, *J. Colloid Interface Sci.*, **36**, 247 (1971).

(16) W. D. Bascom, *J. Phys. Chem.*, **76**, 3188 (1972).

Infrared Spectroscopy of the Silica. Aliquots of 2.5 ml of the suspension were withdrawn using a gas-tight syringe and were injected into an Infrasil optical cell (1-cm path length) for spectroscopic examination in the 4000–2500-cm^{-1} region. The spectrometer was a double-beam Perkin-Elmer 457 Model operated at a spectral slit width of about 4 cm^{-1}. Compensation for solvent absorption was achieved by placing a matched Infrasil cell containing CCl_4 alone in the reference beam. In order to obtain the spectra of the CCl_4 phase and the SiO_2 separately, the suspension was filtered using microporous Teflon (Mitex, 5.0 ± 1.5 μ mean pore size, Millipore Corp., Bedford, Mass.) mounted in a Millipore filter assembly. In this assembly the SiO_2 is caught within a Teflon O-ring held against the filter disk. The SiO_2 was left slightly wet with CCl_4 so that the SiO_2 and the enclosing O-ring could be lifted from the filter and placed between NaCl plates for spectroscopic examination. Keeping the SiO_2 wet with CCl_4 also lessened beam scattering.

Chemical Analysis of the Suspension Filtrate. Aliquots of the suspension (1–2 ml) were withdrawn and filtered using microporous Teflon. The filtrate was analyzed by injecting 1 μl into a Varian Aerograph (Model 600) gas chromatograph with a flame ionization detector. The column was paraffin oil (Fisher Scientific) on Chromosorb G (Johns-Manville, Manville, N. J.) at a 1:5 weight ratio. This column gave good separation of the reactant, solvent, and products of reaction 2 on a single chromatogram. Three chromatograms were obtained for each aliquot and the amounts of products and reactants were determined by comparing peak heights with chromatograms of standard solutions.

Determination of the Adsorbed Water. In an earlier publication[16] it was shown that a band at 3400 cm^{-1} in the infrared spectra of SiO_2 in CCl_4 can be assigned to adsorbed molecular water and that the absorbance of this band plotted against moles/g (or molecules/100 $Å^2$) of water followed the linear, Beers–Lambert law. In the present study the amount of adsorbed water was determined from the 3400-cm^{-1} absorbance and this linear plot.

Results

Adsorption at the Dehydrated SiO_2–CCl_4 Interface. Triethylethoxysilane (TEES) was added to CCl_4 suspensions of Cabosil that had been dried at 750°. There was evidence that the silane was adsorbed (H bonded) by the surface silanols but no evidence that it had been chemisorbed according to reaction 1 or had been hydrolyzed according to reaction 2. For example, upon addition of 2.25 m*M* TEES to the suspension there was a 7% decrease in the ethoxy concentration in the first 15 min with no further change over the next 24 hr. (*Note.* The concentration units, millimoles/l., refer to the solution concentration. It will be useful at times to refer to the concentration per gram of Cabosil and, since the solids content (2.00 ± 0.04%) was the same in all the experiments, the conversion to millimoles/gram can be made by multiplying millimoles/l. by 0.05. Alternatively, for area units; (millimoles/l.) × 0.149 = molecules/100 $Å^2$).

The infrared spectra of the suspension 24 hr after the reactant addition showed the 3700-cm^{-1} band due to the surface silanol groups and the strong alkyl C–H stretching bands between 3000 and 2800 cm^{-1} attributable to the added ethoxysilane. In addition there was a weak band between 3500 and 3000 cm^{-1} probably due to H bonding of the ethoxysilane to some of the surface silanols. The filtrate spectrum showed only the alkyl C–H stretching bands but no evidence of O–H stretching vibrations from ethanol or triethylsilanol.

To show that the adsorbed alkoxysilane could be rinsed from the silica and thus was not chemically bound, 2 ml of the suspension was taken 250 and 1200 min after the addition of alkoxysilane and filtered using the Millipore filter. The spectra of the filtered SiO_2 were obtained and showed the expected surface silanol band (3700 cm^{-1}) and the C–H bands of the reactant (~3000 cm^{-1}). However, the C–H stretching bands could be eliminated from the spectra by simply rinsing the silica with 1 ml of dry CCl_4.

These experiments were repeated at 0 and 45° but again there was no evidence of any hydrolysis or chemisorption of the TEES.

Adsorption and Hydrolysis at the Hydrated SiO_2–CCl_4 Interface. Upon addition of triethylethoxysilane to a CCl_4 suspension of *rehydrated* SiO_2 there was a gradual disappearance from the liquid phase of the ethoxysilane and the simultaneous appearance of triethylsilanol and ethanol. A typical example of the change in solute concentration with time is given in Figure 1. The triethylsilanol (TES) and the ethanol were identified by gas chromatography.

To determine if the SiO_2 was actually necessary for the hydrolysis, solutions of the reactant (TEES) in water-saturated CCl_4 were prepared and allowed to stand at ~25° for as long as 6 months. No detectable hydrolysis was observed. Evidently, the role of the rehydrated Cabosil is more than just a source of water for the homogeneous reaction.

Attempts were made to detect the siloxane dimer, $(C_2H_5)_3Si–O–Si(C_2H_5)_3$, in the reaction mixture. Filtrate samples as large as 25 μl were taken after 24-hr reaction time and chromatographed on a column of 5% silicone (SE-30) on Chromosorb W. No evidence of the dimer was observed even though this column was found, using prepared solutions of the dimer, to be capable of detecting as little as 10^{-4} *M* of this siloxane compound.

The infrared spectra of the suspension and filtrate are given in Figure 2. Note in the spectrum of the 36-

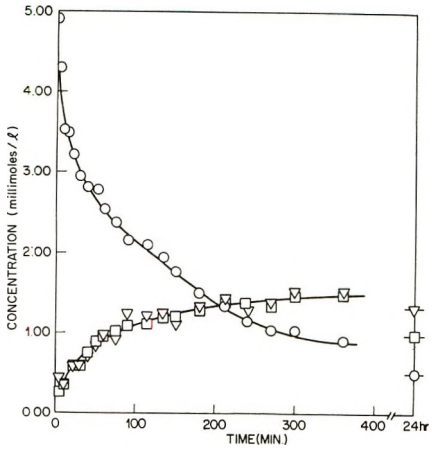

Figure 1. Time–concentration data for TEES (○) disappearance and TES (□) and ethanol (△) appearance in a rehydrated SiO_2–CCl_4 suspension. Initial concentration of TEES was 4.91 mM and the initial water content of the SiO_2 was 1.82 molecules/100 Å^2.

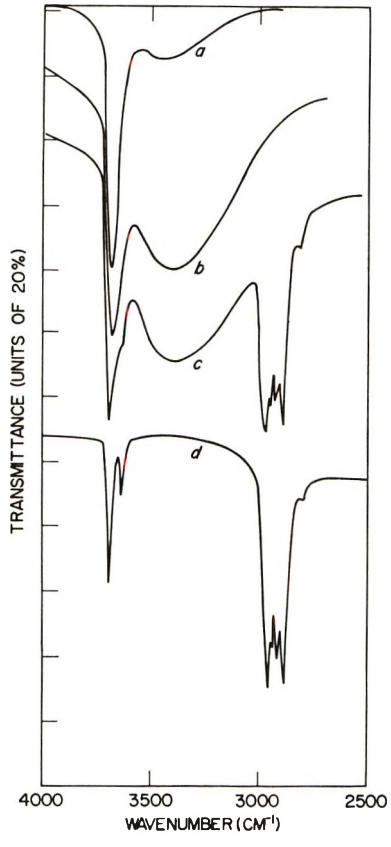

Figure 2. Infrared spectra of a CCl_4 suspension of rehydrated SiO_2: (a) dried (750°) SiO_2; (b) rehydrated; (c) 36 hr after TEES addition; (d) filtrate of c.

hr filtrate (Figure 2) the sharp bands at 3700 and 3620 cm^{-1} which correspond to the O–H stretching vibration of $(C_2H_5)_3SiOH$ and C_2H_5OH, respectively.

Effect of Adsorbed Water Concentration. In this study it was discovered that in order for the hydrolysis to proceed at a detectable rate, a minimum amount of adsorbed water was required. This important ob-

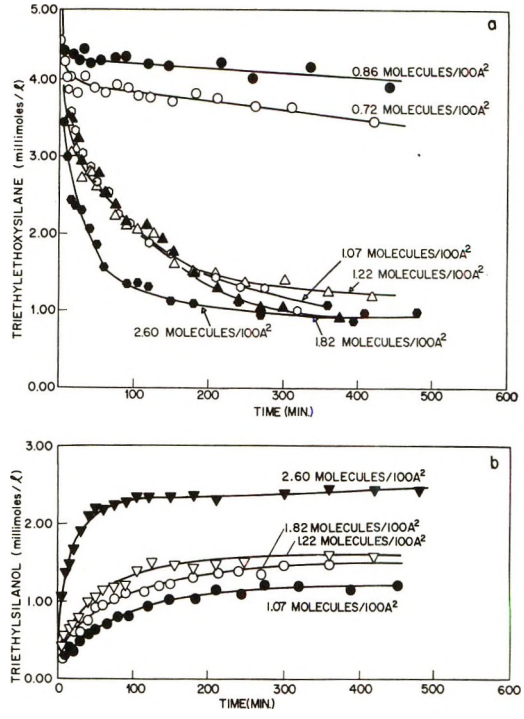

Figure 3. Effect of adsorbed water content on the time–concentration data of (a) TEES and (b) TES.

servation is evident from Figure 3 in which the time–concentration curves are given for different water coverages. The data suggest that the amount of adsorbed water necessary for reaction is between 0.9 and 1.0 molecules/100 Å^2. At water contents of less than 0.9 molecules/100 Å^2 only traces ($<10^{-4}$ M) of triethylsilanol or ethanol could be detected in the liquid phase after 24 hr.

It would appear that the reaction rate is not significantly altered by increasing the adsorbed water content from 1.0 to 1.8 molecules/100 Å^2, *i.e.*, Figure 3. The reaction did go faster when the adsorbed water was 2.60 molecules/100 Å^2 (Figure 3) but this effect was not pursued since at these high water contents the suspension tended to gel, possibly because of water molecules bridging the silica particles.

Effect of Reactant Concentration. Time–concentration data were obtained for initial reactant concentrations of 3.51, 4.91, 7.70, 10.36, 15.25, and 20.90 mM. The data were tested for zero-, one-half-, first-, and second-order kinetics. At the high starting concentrations, $[TEES]_0$ = 10.36, 15.25, and 20.90 mM, the data followed zero-order kinetics from 50 min to at least 200 min (Figure 4). Also, product formation was essentially independent of reactant concentration, *i.e.*, filled points in Figure 5. At the lower concentration, $[TEES]_0$ = 3.51, 4.91, and 7.70 mM, the data gave reasonably linear first- and one-half-order plots but in both cases the rate constants differed significantly. The best agreement in rate constants was obtained from the first-order plots (Figure 6) and these values,

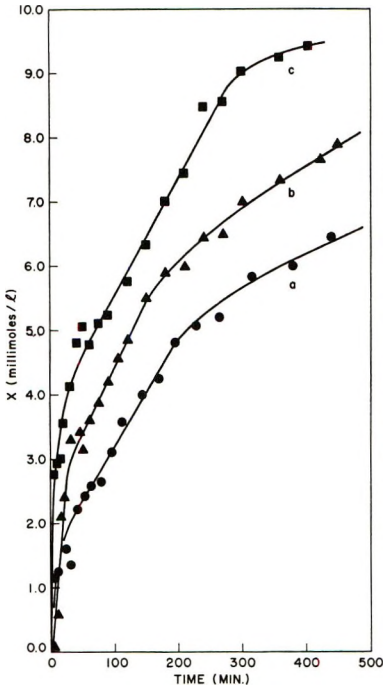

Figure 4. Zero-order plots of the data for $[TEES]_0$ = (a) 10.36, (b) 15.25, and (c) 20.90 mM.

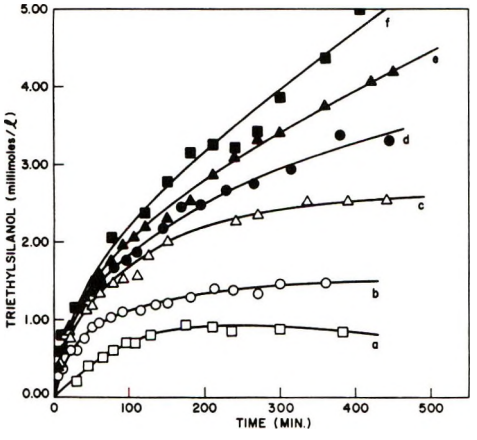

Figure 5. Effect of varying the initial concentration of TEES on the time–TES concentration data: $[TEES]_0$ = (a) 3.51, (b) 4.19, (c) 7.70, (d) 10.36, (e) 15.25, and (f) 20.90 mM.

k_1, are compiled along with the zero-order constants, k_2, in Table I. Also listed in Table I are the values of $[H_2O]_0{}^a$, the amount of adsorbed water at t_0, and estimated values for the amount of adsorbed reactant at t_0, *i.e.*, $[TEES]_0{}^a$. These latter values were obtained by plotting the combined amount of adsorbed TEES and TES against time. Fortuitously, this plot was essentially linear at early reaction times (Figure 7) and could be extrapolated back to zero time. The combined amount of TEES plus TES adsorbed was obtained by subtracting the moles of TEES plus TES in the CCl_4 phase at time t from the moles of TEES initially added.

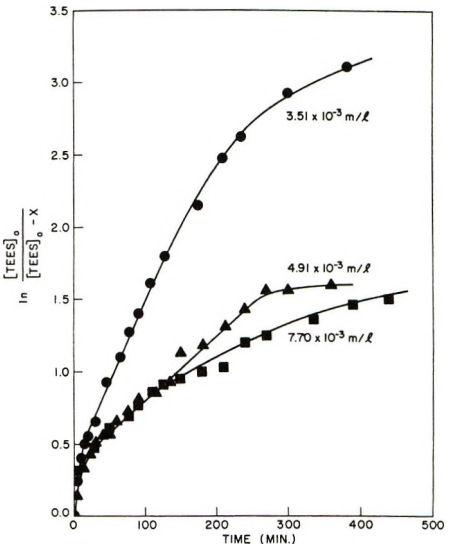

Figure 6. First-order plots of the data for the indicated values of $[TEES]_0$.

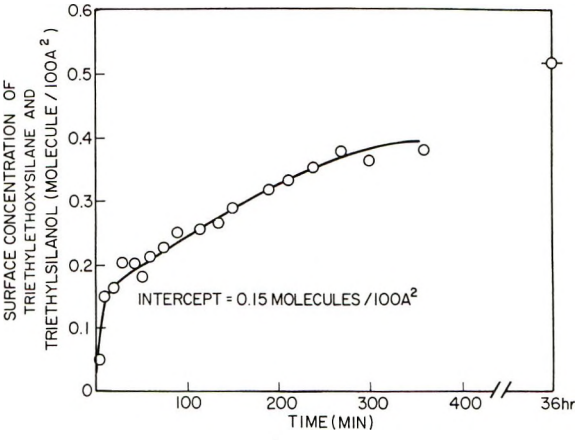

Figure 7. Combined adsorption of TEES and TES on rehydrated SiO_2.

An effort was made to increase the concentration of silanol groups [Si–OH] on the SiO_2 surface and determine the effect on the hydrolysis reaction. The temperature at which the SiO_2 powder was dried was decreased from 750 to 550° which, according to Kiselev and coworkers,[17] should increase the silanol surface concentration from a range of 1.0–1.5 OH/100 Å^2 at 750° to 1.5–2.0 OH/100 Å^2 at 550°.

The time–concentration curves for the triethoxysilane hydrolysis by the 550° SiO_2 are given in Figure 8 for different levels of adsorbed water. Just as observed for the more intensely dried silica, there was a minimum amount of water necessary for significant hydrolysis to occur. However, the minimum appears to be between 1.1 and 1.3 molecules/100 Å^2, which is slightly greater than for the silica dried at 750°.

(17) A. A. Agzamkhodzhaev, L. T. Zhuravlev, and A. V. Kiselev, *Izv. Akad. Nauk SSSR, Ser. Khim.*, **6**, 1186 (1968).

Table I: Effect of Reactant Concentration $[TEES]_0$ on Reaction Order and Rate Constant

$[TEES]_0$, mM	Order	k_1, sec^{-1}	k_2, M sec^{-1}	$[H_2O]_0$[a,c] molecules/100 Å^2	$[TEES]_0$[a,b] Molecules/100 Å^2	$[TEES]_0$[a,b] % coverage[c]
3.51	1	19.2×10^{-6}		1.57	0.159	9
4.91	1	7.47×10^{-6}		1.82	0.150	9
7.70	1	3.53×10^{-6}		1.52	0.249	16
10.36	0		2.83×10^{-7}	1.58	0.225	13
15.25	0		3.11×10^{-7}	1.67	0.353	21
20.90	0		3.02×10^{-7}	2.08	0.551	33
			D–H Exchange			
15.18	0		3.00×10^{-7}	~1.2	0.670	40

[a] Surface concentration of adsorbed water at t_0. [b] Surface concentration of adsorbed reactant at t_0. [c] Per cent of surface area covered by TEES at t_0.

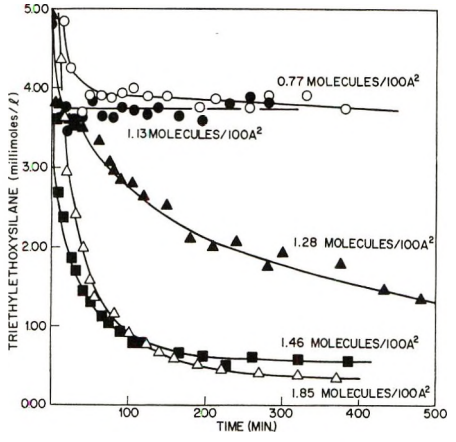

Figure 8. Time–concentration data for TEES in CCl_4 suspensions of SiO_2 dried at 550° and rehydrated to the indicated levels of adsorbed water.

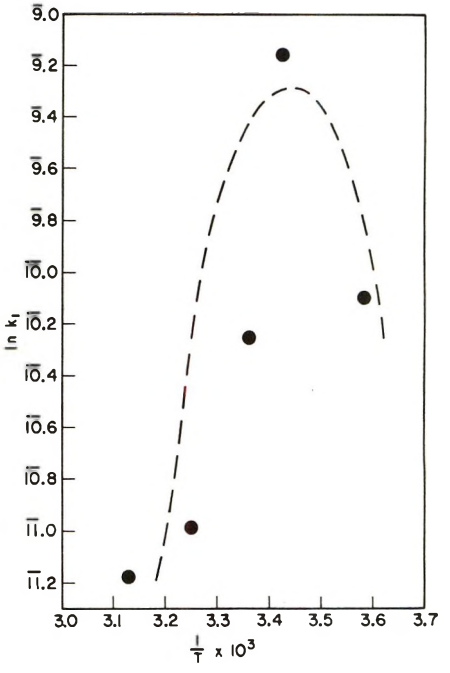

Figure 9. Arrhenius plot of the first-order rate constants.

Unfortunately, meaningful experiments at rehydration levels of 1.5 molecules/100 Å^2 or higher were not possible with the 550° dried silica. These suspensions had a strong tendency to gel thus making it impossible to take representative aliquots from the reaction mixture.

Isotope Exchange. The hydrolysis kinetics were determined using D_2O-exchanged SiO_2. In ref 16 it was shown that essentially all of the ≥Si–OH and adsorbed H_2O on silica could be exchanged with D_2O. The time–concentration data for $[TEES]_0$ = 15.18 mM followed zero-order kinetics over 100-min reaction time. Also, the rate constant was 3.00×10^{-7} M sec^{-1}. Clearly the D–H exchange did not affect the hydrolysis rate since this is essentially identical with the rate constant for the unexchanged silica. These results and other pertinent data for the isotope study are given in Table I. The amount of adsorbed D_2O (column 5) was estimated by comparing the transmittance ratio of T_{OD}/T_{D_2O} with the T_{OH}/T_{H_2O} ratio of spectra of SiO_2 in CCl_4 with known amounts of adsorbed H_2O. This comparison of ratios was necessary since the D_2O peak (2510 cm^{-1}) and the H_2O peak (3400 cm^{-1}) have different molar absorptivities.

Temperature Dependence of k. Experiments were conducted over a temperature range of 7 to 46° and with initial reactant concentrations of 7.0 and 15.0 mM. In all cases the silica was dried at 750° and rehydrated to a level of about 1.5 molecules/100 Å^2. The data for the reactions with $[TEES]_0$ = 7.0 mM followed first-order kinetics and for $[TEES]_0$ = 15.0 mM the data were zero order. Arrhenius plots of ln k *vs.* $1/T$ for both the first- and zero-order results went through a maximum (Figures 9 and 10).

Discussion

The results most pertinent to the mechanism of the surface hydrolysis are (a) the abrupt increase in rate with increasing water coverage, (b) the change from

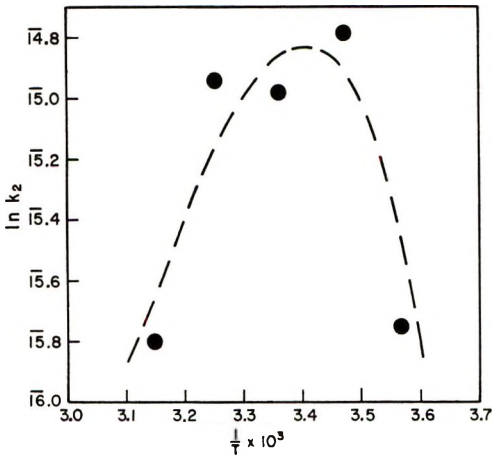

Figure 10. Arrhenius plot of the zero-order rate constants.

first- to zero-order kinetics with increasing solution concentration of reactant, and (c) the unusual temperature dependence of the rate constants.

Consider first the change in kinetics with water coverage. It would appear that this abrupt change occurs when the number of adsorbed water molecules and surface hydroxyls are approximately equal. This 1:1 correspondence appeared to be true for the silica dried at 750 and 550°. The fact that the reaction rate increases abruptly at a particular water coverage implies that the adsorbed water assumes some specific arrangement highly favorable to the hydrolysis and that this arrangement does not exist at lower water coverages. Some insight into this "arrangement" of the hydrated silica surface can be derived from the work of Fripiat, *et al.*,[18] in their study of the thermodynamic and electrical properties of adsorbed water on silica. They determined the entropy loss (ΔS_a) for the adsorbed water (relative to the gas phase) between a fractional coverage (θ) of 0.2 (ΔS_a = 50 eu) and 1.2 (ΔS_a = 38 eu). In the region of θ = 0.9–1.2 the entropy changed from that characteristic of a localized (immobile) to a delocalized (mobile) film. In this same region of coverage, which for their silica corresponds to a $\geqslant$SiOH/H_2O mole ratio of about unity, there was an abrupt increase in surface conductivity. They conclude that the charge carrier is protonic (H^+ or H_2O^+) and that proton migration proceeds by a chain of exchange reactions

$$H_3O^+ + H_2O \longrightarrow H_2O + H_3O^+ \qquad (3)$$

The abrupt change in conductivity in the work of Fripiat, *et al.*, and the abrupt increase in hydrolysis rate observed here may occur because at a $\geqslant$SiOH/H_2O ratio of about 1:1 a H-bonded network develops as in structure I. This sudden formation of a network is analogous to the abrupt development of structure in the gelation of colloidal dispersions or in the curing of thermosetting resins.

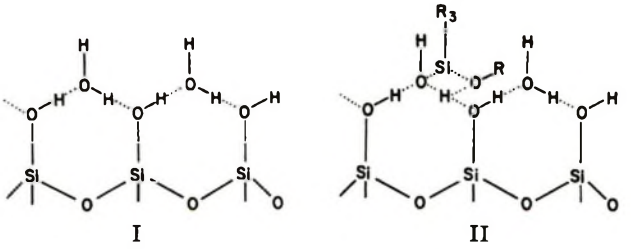

Although the adsorbed water could be held in configurations other than I, this particular arrangement allows adsorption of the triethylethoxysilane in a manner that strongly favors hydrolysis *via* a cyclic four-center intermediate (structure II). According to this model, there is a nucleophilic (OH^-) attack at the silicon and an electrophilic (H^+) attack at the alkoxy oxygen. Attack at the Si position by the nucleophilic reagent is generally believed to be the preferred mechanism for the cleavage of alkoxysilanes and other silane derivatives.[19a] The theoretical basis for this mechanism is the availability of the d orbitals of silicon. There is experimental evidence for cleavage of the Si–O bond in the acid hydrolysis of alkoxysilanes.[19b] The cyclic four-membered intermediate has been proposed by Eaborn[19a] and Sommer[20] and the latter found that the predominate reaction path in nonpolar media is a "flank" rather than a backside approach by the attacking agent relative to the leaving group. He argues for a cyclic intermediate (rather than ion formation) in nonpolar media since it would minimize charge separation.

The need for the hydroxyl–water network before any sensible hydrolysis occurs is probably that it makes the protons of the more acidic surface silanols available to all the reactant sites along the network. The first step of the acid-catalyzed hydrolysis of alkoxysilanes in homogeneous solution is believed to be the protonization of the alkoxy oxygen.[19b] However, the "acid sites" on silica (*i.e.*, $\geqslant$Si–OH) are not equivalent in their ability to donate protons. One indication of this is the change in the isosteric heat of adsorption of water with surface coverage. For example, at a fractional monolayer coverage of 0.15 the heat of adsorption is about 20 kcal/mol but a a coverage of 0.9 it is only 11 kcal mol.[17] The interconnecting of the surface silanols by H-bonded water serves to make the protons of the more "active" silanols available to all the reactant sites by proton transfer (reaction 3) along the network.

If this model is correct, then the integrity of the hydroxyl–water network is a critical factor in determining the hydrolysis rate. This integrity will be progressively lost as the reaction temperature is in-

(18) J. J. Fripiat, A. Jelli, G. Poncelet, and J. Andre, *J. Phys. Chem.*, 69, 2185 (1965).

(19) C. Eaborn, "Organosilicon Compounds," Academic Press, New York, N. Y., (a) p 86, (b) p 103.

(20) L. H. Sommer, "Stereochemistry, Mechanism, and Silicon," McGraw Hill, New York, N. Y., 1965, p 48.

creased due to thermal weakening and even dissociation of the H bonds. Disruption of the adsorbed water reasonably explains the decrease in the rate constants with increasing temperature (Figures 9 and 10). There is abundant evidence for a large decrease in the association of H-bonded systems with a temperature change of only 10–20°,[21] so it is not unreasonable that association in the hydroxyl–water network changed significantly over the 40° temperature range studied here.

A consistent interpretation of the kinetic data can be derived by assuming that during the early stages the surface hydrolysis is *pseudo*unimolecular with respect to the alkoxysilane. This assumption is reasonable since the initial amount of adsorbed water is large compared to the amount of adsorbed silane and the water removed from the surface was not enough to significantly alter the hydrated network. From Table I the ratio of $[H_2O]_0^a/[TEES]_0^a$ was as high as 10 and never less than 4. As for the removal of water from the surface, the depletion was 30% or less during the 200 min through which the pseudounimolecular kinetics is assumed. However, the amount of adsorbed water always exceeded the level needed to maintain a H-bonded network (structure I) by at least 30%.

The absolute rate theory predicts for a unimolecular surface reaction that the reaction should be first order at low adsorbate concentrations (low surface coverage) and zero order at higher concentrations (surface saturated). Although, just such a change in reaction order with concentration is observed, the data in column 5 of Table I are in apparent contradiction since the surface concentration increased continuously over the entire range of solution concentrations. However, the data in the last column of Table I indicate that the reaction order changed to zero when the surface coverage reached 15–20%. Since the hydroxyl–water network covers about 15% of the surface it would appear that the reaction becomes zero order when the hydrated or "active" portion of the surface is saturated with reactant.

At the lower reactant concentrations, before the active sites are saturated, the data fit first-order kinetics but the rate constant decreased with increasing reactant concentration (Table I). Actually, this variation in k_1 with $[TEES]_0$ is not unexpected since among the factors that directly influence the first-order rate constant of a unimolecular surface reaction are the number or "availability" of the surface sites.[22] As the surface becomes crowded there may be a decrease in the availability of sites and thus a decrease in k_1.

The failure to observe any effect of the deuterium–hydrogen exchange on the zero-order rate indicates that the rate-determining step does not involve proton transfer. If activation proceeds by a concerted attack of H on the alkoxy oxygen and OH on the silicon (structure II), the addition of the heavier deuteron will be more demanding energetically than protonization and the rate will be slower in the deuterated system by as much as a factor of 10.[22] Since the D–H exchange had no such effect, some process other than the attack by H and OH must be rate determining. Possibly the slow step is an orientation of the adsorbed reactant from one or more nonreactive configurations or sites to a precise configuration (*e.g.*, structure II) which is followed immediately by activation. If this is the case then the adsorption–orientation reactive sequence can be expressed by

$$R_{solution} \underset{k_{-1}}{\overset{k_1}{\rightleftharpoons}} R_a \underset{k_{-2}}{\overset{k_2}{\rightleftharpoons}} R_a^* \longrightarrow \text{products}$$

where R_a is adsorbed reactant and R_a^* is the activated adsorbate. This argument implies that the activation energy for the hydrolysis step is so low that activation is fast compared to orientation. It is more likely that in the orientation step the translational and/or rotational energy of the adsorbate is immediately available as part of the activation energy. Thus, the effective activation energy is the true activation energy for hydrolysis less the energy of adsorption for R_a.

In addition to being adsorbed on the hydrated sites, the TEES is undoubtedly adsorbed on the intervening nonhydrated siloxane network. This reactant on the nonhydrated surface is not involved in the hydrolysis, but it is probably responsible for the low adsorption equilibrium during the first 50 min of the reaction. One reason for such a long equilibration time is the slow rate of diffusion through the liquid. More important is the fact that the solute must compete with solvent molecules for surface sites. This competition is probably not important for adsorption onto the active surface since the TEES is capable of stronger H bonding to the hydrated sites than is the CCl_4. However, the interaction energies of the TEES and CCl_4 with the siloxane network would be comparable. Additional evidence that adsorption equilibrium on the hydrated sites is fast is the immediate appearance in the solution phase of the triethylsilanol (and ethanol) and the fact that throughout the initial 50 min their formation follows the expected first- or zero-order kinetics with respect to the solution concentration of reactant (see Figure 5). Evidently, adsorption–reaction on the hydrated sites and simple adsorption on the nonhydrated regions occur simultaneously but independently.

The absorption of the products, triethylsilanol and ethanol, undoubtedly influence the reaction kinetics. However, at early reaction times the effect is probably slight because the small amount of products formed is partitioned between the surface and the solvent phase with the solvent being favored because the product

(21) G. C. Pimentel and A. L. McClellan, "The Hydrogen Bond," W. H. Freeman, San Francisco, Calif., 1960, p 76.

(22) K. J. Laidler, "Chemical Kinetics," 2nd ed, McGraw-Hill, New York, N. Y., 1965, p 256.

molecules must compete for surface sites with a relatively high reactant concentration. At long reaction times (>200 min) adsorption of the products should be more important and in fact may be the primary factor for the reaction to deviate from first- or zero-order kinetics.

Acknowledgment. The authors wish to express their appreciation to Professor Paul Emmett, Oregon State University, for many helpful discussions during the course of this work. Also, thanks are extended to Dr. C. R. Singleterry, Dr. Victor R. Deitz, and Mr. Albert J. Fryar for their encouragement and help.

Ketyl Radicals of Benzoylpyridines

by D. A. Nelson*[1] and E. Hayon

Pioneering Research Laboratory, U. S. Army Natick Laboratories, Natick, Massachusetts 01760 *(Received May 18, 1972)*

Publication costs assisted by the U. S. Army Natick Laboratories

The absorption spectra, extinction coefficients, decay kinetics, and dissociation constants of the ketyl radicals and the radical anions of 2-, 3-, and 4-benzoylpyridines have been observed and determined. These radicals were produced from the reaction with hydrated electrons in aqueous 1.0 *M tert*-butyl alcohol, using the technique of pulse radiolysis. The ketyl radicals have high extinction coefficients and absorption bands in the visible and uv regions. The pK_a's are 12.3 ± 0.2, 9.2 ± 0.2, and 12.0 ± 0.2 for 2-, 3-, and 4-benzoylpyridine, respectively. A second dissociation constant of the ketyl radicals for the corresponding benzoylpyridinium ions is observed with pK_a's of 3.1 ± 0.1, 4.1 ± 0.2, and 4.2 ± 0.2, respectively. Identical spectra were observed from the reaction of acetone ketyl radicals $(CH_3)_2\dot{C}OH$ with these benzoylpyridines (BP), indicating a quantitative electron transfer to form the corresponding ketyl radicals. The rate constants of reactions of $(CH_3)_2\dot{C}OH$ radicals with BP were found to be dependent on the pK_a of the BP. The ketyl radical and radical anions of 3-benzoyl-*N*-methylpyridinium ion were found to be distinctly different from those of 3-BP and a pK_a = 5.9 ± 0.2 was determined. The absorption spectra of the H atom adducts to benzoylpyridinium ions were also determined and are compared with those of the ketyl radicals. Analogies between the photochemistry and radiation chemistry of benzoylpyridines and benzophenone are discussed.

Introduction

Relatively little work appears to have been carried out on the photochemistry of nicotinamide and its de-

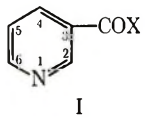

I

rivatives. Studies on nicotinamide[2,3] (X = NH_2) and nicotinic acid (X = OH), on 3-acetylpyridine[4a] (X = CH_3), and on dipyridyl ketone[4b] have been performed. The mechanism leading to the observed photoproducts has not been established. Since a considerable amount of work has been done on the photochemistry of benzophenone, it seemed of interest to consider the photochemistry of benzoylpyridine (X = C_6H_5). Work on both the flash photolysis[5] and steady-state photolysis[6] of benzoylpyridines is in progress. In the course of trying to identify the transient species observed[5] in the flash photolysis, it appeared necessary to produce by some independent method the ketyl radicals and radical anions of benzoylpyridines since these have not been previously observed or reported. The reaction of solvated electrons with aromatic ketones has been found[7] to be a convenient way of generating ketyl radicals for the purpose of determining their absorption spectra, dissociation constants, and extinction coefficients.

$$e^-_{solv} + C_6H_5COR \longrightarrow C_6H_5\overset{O^-}{\overset{|}{\dot{C}}}R \qquad (1)$$

(1) Permanent address: Chemistry Dept., University of Wyoming, Laramie, Wyoming.

(2) A. D. McLaren and D. Shugar, "Photochemistry of Proteins and Nucleic Acids," Pergamon Press, New York, N. Y., 1964.

(3) S. Y. Wang, *Biochemistry*, **7**, 3740 (1968); F. Takenchi, *et al.*, *Bull. Chem. Soc. Jap.*, **43**, 3637 (1970).

(4) (a) W. L. Bencze, C. A. Burckhardt, and W. L. Yost, *J. Org. Chem.*, **27**, 2865 (1962); (b) F. L. Minn, C. L. Trichilo, C. R. Hurt, and N. Filipescu, *J. Amer. Chem. Soc.*, **92**, 3600 (1970).

(5) D. A. Nelson and E. Hayon, to be submitted for publication.

(6) M. R. Kegelman and E. W. Brown, *J. Amer. Chem. Soc.*, **75**, 4649 (1953); P. Traynard and J.-P. Blanchi, *C. R. Acad. Sci.*, **267**, 1381 (1968); D. A. Nelson, *et al.*, to be submitted for publication.

(7) E. Hayon, T. Ibata, N. N. Lichtin, and M. Simic, *J. Phys. Chem.*, **76**, 2072 (1972).

$$C_6H_5\dot{C}R(O^-) + H_3O^+ \rightleftharpoons C_6H_5\dot{C}R(OH) + H_2O \quad (2)$$

$$C_6H_5\dot{C}R(O^-) + H_2O \rightleftharpoons C_6H_5\dot{C}R(OH) + OH^-$$

In this work, we report results on the absorption spectra, extinction coefficients, dissociation constants, and decay kinetics of the ketyl radicals and radical anions of 2-, 3-, and 4-benzoylpyridines, their corresponding pyridinium ions, and of *N*-methyl-3-benzoylpyridinium ion. The technique of pulse radiolysis was used to produce the solvated electrons. In addition, the rate constants of the reaction of acetone ketyl radicals, $(CH_3)_2\dot{C}OH$, with these benzoylpyridines as a function of the pK_a of the benzoylpyridines and of the acetone ketyl radicals have been determined. For comparison with the absorption spectra of the ketyl radicals, the absorption spectra of the H-atom adducts to 2-, 3-, and 4-benzoylpyridines were obtained.

Experimental Section

The pulse radiolysis set-up used has been described elsewhere.[8] Single pulses of 2.3-MeV electrons and ~30 nsec duration were used. The 450-W xenon lamp monitoring light source was boosted for ~1 msec thus increasing the total light output 25-fold. A double monochromator (two high-intensity Bausch & Lomb monochromators placed in series) was used to obtain better wavelength resolution and reduce the scattered light. Various solution and glass filters were positioned between the monitoring light and the solution containing the benzoylpyridines in order to minimize possible photochemical changes induced by the monitoring light. In addition, a synchronized shutter was used which opened for a total time duration of $\leq$5 msec.

The benzoylpyridines (Aldrich Chemical Co.) after purification by three recrystallizations from isopropyl alcohol–water and by two sublimations were kept in the dark.

Aqueous solutions containing 1–2 *M* *tert*-butyl alcohol or isopropyl alcohol were used to scavenge the OH radicals produced from the radiolysis of water. In argon-saturated aqueous t-BuOH solutions, the solvated electrons e^-_{aq} reacted with the benzoylpyridines according to reaction 1, and the *tert*-butyl alcohol radicals were found *not* to react with the benzoylpyridines (BP). This was established on saturation of the solution with nitrous oxide when the transient absorptions of the ketyl radicals disappeared, and no other transients could be observed above 300 nm. In N_2O-saturated solutions, all the e^-_{aq} ($\geq$98%) produce OH radicals according to reaction 3

$$e^-_{aq} + N_2O \longrightarrow OH + N_2 + OH^- \quad (3)$$

with $k_3 = 6 \times 10^9\ M^{-1}\ sec^{-1}$ (ref 9). The acetone ketyl radical was found to react quantitatively with BP to produce exclusively the corresponding ketyl radicals.

$$OH + (CH_3)_2CHOH \longrightarrow (CH_3)_2\dot{C}OH + H_2O \quad (4)$$

$$(CH_3)_2\dot{C}OH + PyCOC_6H_5 \longrightarrow Py\dot{C}(OH)C_6H_5 + CH_3COCH_3 \quad (5)$$

The pH of the solutions was adjusted using perchloric acid, potassium hydroxide, and ~2 m*M* phosphate and borate buffers.

Extinction coefficients were derived taking $G(e^-_{aq}) = G(OH) = 2.8$ and $G(H) = 0.6$.

Products produced subsequent to the initial formation of the ketyl radicals were observed under some conditions. In neutral aqueous 2 *M* isopropyl alcohol solutions, a permanent product with λ_{max} ~355 nm was observed with 3-BP. The 4-BP formed an intermediate ($\tau_{1/2}$ ~30 sec) with λ_{max} ~390 nm. No intermediate was observed from 2-BP. Considerable care was taken to eliminate possible photochemical effects from the analyzing light. However, products with essentially the same characteristics were observed both in the flash and steady-state photolysis of 3- and 4-BP. Similar intermediates have been observed in the photochemistry of benzophenone[10] and di(4-pyridyl) ketone,[4b] and various structures have been suggested. Since it has been definitely determined that these intermediates are formed subsequent to the initial formation of ketyl radicals in the pulse radiolysis experiments, they are not of concern to the major conclusions of this work. The decay kinetics of the ketyl radicals, however, might be affected.

Hydrogen atoms were produced from the reaction $e^-_{aq} + H^+ \rightarrow H$ in acid solutions at pH $\leq$1, under conditions that all the e^-_{aq} formed H atoms. *tert*-Butyl alcohol was added to scavenge the OH radicals; its rate constant for reaction with H atoms is ~$10^5\ M^{-1}\ sec^{-1}$.

Results

In order to determine the extinction coefficients of the ketyl radicals of the benzoylpyridines all the electrons must react quantitatively with the benzoylpyridines. It was necessary, therefore, to determine the rate constants of reaction 1. This was done by following the pseudo-first-order decay of e^-_{aq} at 700 nm. The rates of reaction for 2-, 3-, and 4-BP were found to

(8) (a) M. Simic, P. Neta, and E. Hayon, *J. Phys. Chem.*, **73**, 3794 (1969); (b) J. P. Keene, E. D. Black, and E. Hayon, *Rev. Sci. Instrum.*, **40**, 1199 (1969); E. Hayon, *J. Chem. Phys.*, **51**, 4881 (1969).

(9) M. Anbar and P. Neta, *Int. J. Appl. Radiat. Isotopes*, **18**, 493 (1967).

(10) N. Filipescu and F. L. Minn, *J. Amer. Chem. Soc.*, **90**, 1544 (1968), and references cited therein.

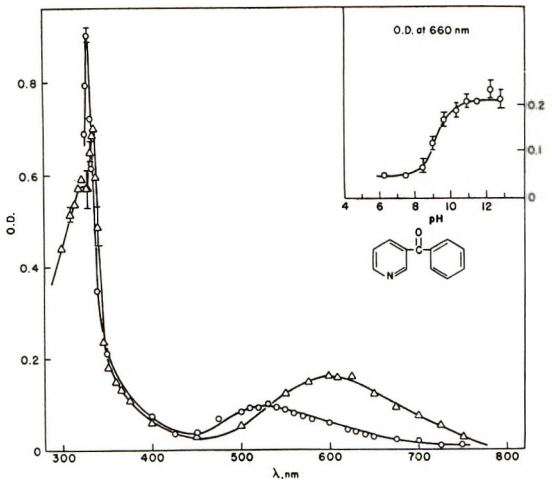

Figure 1. Optical absorption spectrum of the ketyl radical (O, pH 5.1) and radical anion (Δ, pH 12.0) of 3-benzoylpyridine in 1.0 M aqueous *tert*-butyl alcohol. Insert shows the absorbance of ketyl radical at 660 nm *vs.* pH.

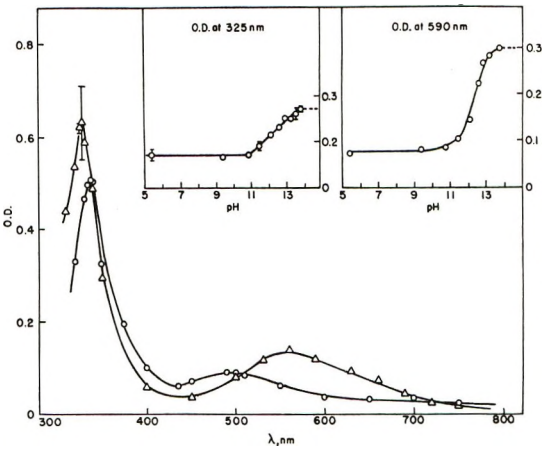

Figure 2. Optical absorption spectrum of the ketyl radical (O, pH 5.1) and radical anion (Δ, pH 13.4) of 2-benzoylpyridine in 1.0 M aqueous *tert*-butyl alcohol. Insert shows the absorbance of ketyl radical at 590 and 325 nm *vs.* pH.

be the same within experimental error, namely, $k_1 \sim 3 \times 10^{10}\ M^{-1}\ \text{sec}^{-1}$, see Table I. The electron rate constants were very close to those obtained[7] for a number of aromatic ketones and quinones. The rate of reaction of e^-_{aq} with 3-benzoyl-*N*-methylpyridinium ion was higher, $k = 5.5 \times 10^{10}\ M^{-1}\ \text{sec}^{-1}$, as expected for a positively charged pyridinium ion.

Table I: Reaction Rate Constants of Hydrated Electrons and Hydrogen Atoms with Benzoylpyridines in Aqueous Solution

System	$k(e^-_{aq} + S)$, $M^{-1}\ \text{sec}^{-1}$ [a]	$k(H + S)$, $M^{-1}\ \text{sec}^{-1}$ [b]
2-Benzoylpyridine	$2.5 \pm 0.3 \times 10^{10}$	$2.3 \pm 0.4 \times 10^{9}$
3-Benzoylpyridine	$3.0 \pm 0.3 \times 10^{10}$	$3.7 \pm 0.6 \times 10^{9}$
4-Benzoylpyridine	$2.8 \pm 0.3 \times 10^{10}$	$2.4 \pm 0.3 \times 10^{9}$
3-Benzoyl-*N*-methyl-pyridinium ion	$5.5 \pm 0.7 \times 10^{10}$	

[a] Determined at pH 9.0, following the decay of e^-_{aq} at 700 nm. [b] Determined at pH 1.0, following the formation of the H atom adduct at 348, 400, and 375 nm for 2-, 3-, 4-benzoylpyridines, respectively.

Absorption Spectra of Ketyl Radicals. The optical absorption spectrum of the ketyl radical of 3-BP produced from the reaction with e^-_{aq} in 1.0 M aqueous t-BuOH is shown in Figure 1. Absorption maxima at 530 and 330 nm with extinction coefficients of 3.4×10^3 and $3.2 \times 10^4\ M^{-1}\ \text{cm}^{-1}$, respectively, were obtained. In alkaline solutions at pH 12.0, a significant change in the absorption spectra of the transient is observed (Figure 1) with λ_{max} at 605 and 336 nm, and is assigned to the ketyl radical anion of 3-BP. By monitoring the change in absorbance at a fixed wavelength (660 nm) a "titration curve" is obtained (see insert in Figure 1), from which the dissociation constant $pK_a = 9.2 \pm 0.2$ of the ketyl radical can be derived.

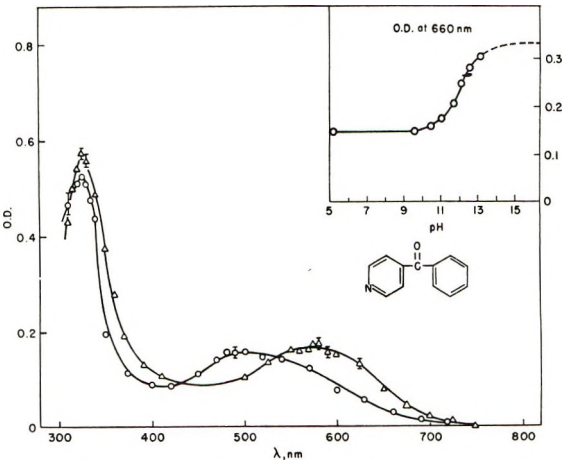

Figure 3. Optical absorption spectrum of the ketyl radical (O, pH 5.1) and radical anion (Δ, pH 13.0) of 4-benzoylpyridine in 1.0 M aqueous *tert*-butyl alcohol. Insert shows the absorbance of ketyl radical at 660 nm *vs.* pH

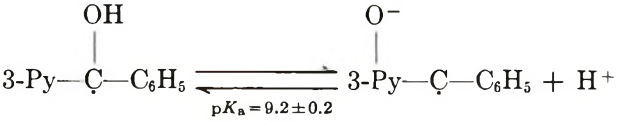

(6)

By following the same procedure, the optical absorption spectra and dissociation constants of the ketyl radicals of 2-BP and 4-BP were obtained, see Figures 2 and 3 and Table II. It is to be noted that the pK_a of the 2-PyĊ(OH)C_6H_5 radical is 12.3 ± 0.2, and that of the 4-PyĊ(OH)C_6H_5 radical is 12.0 ± 0.2. Both of these ketyl radicals have dissociation constants which are significantly higher than that of 3-BP. In addition, there are distinct differences in the absorption

Table II: Absorption Maxima, Extinction Coefficients, and Dissociation Constants of the Ketyl Radicals and Radical Anions of Benzoylpyridines

System	Radical	pK	γ_{max}, nm	ϵ_{max}, M^{-1} cm^{-1} [a]
2-Benzoylpyridine	2-PyĊ(O$^-$)C$_6$H$_5$		560, 328	4.8×10^3, 2.3×10^4
	⇃↾	12.3 ± 0.2		
	2-PyĊ(OH)C$_6$H$_5$		495, 338	3.0×10^3, 2.0×10^4
	⇃↾	3.1 ± 0.1		
	2-PyH$^+$Ċ(OH)C$_6$H$_5$		540, 350	2.3×10^3, 3.7×10^4
3-Benzoylpyridine	3-PyĊ(O$^-$)C$_6$H$_5$		605, 336	5.6×10^3, 2.5×10^4
	⇃↾	9.2 ± 0.2		
	3-PyĊ(OH)C$_6$H$_5$		530, 330	3.4×10^3, 3.2×10^4
	⇃↾	4.1 ± 0.2		
	3-PyH$^+$Ċ(OH)C$_6$H$_5$		695, 503, 375, 331	1.2×10^3, 3.4×10^3, 2.8×10^3, 3.1×10^4
4-Benzoylpyridine	4-PyĊ(O$^-$)C$_6$H$_5$		575, 325	5.9×10^3, 2.0×10^4
	⇃↾	12.0 ± 0.2		
	4-PyĊ(OH)C$_6$H$_5$		500, 325	5.6×10^3, 1.8×10^4
	⇃↾	4.2 ± 0.2		
	4-PyH$^+$Ċ(OH)C$_6$H$_5$		510, 395, 322	5.8×10^3, 1.5×10^4, 1.7×10^4
3-Benzoyl-*N*-methylpyridinium	3-PyCH$_3$$^+$Ċ(O$^-$)C$_6H_5$		555, 395, 318	5.2×10^3, 2.0×10^3, 1.9×10^4
	⇃↾	5.9 ± 0.2		
	3-PyCH$_3$$^+$Ċ(OH)C$_6H_5$		520, 385, 332	3.2×10^3, 3.2×10^3, 2.0×10^4

[a] Values to ±10%.

Table III: Decay Kinetics of Ketyl Radicals of Benzoylpyridines in Aqueous Solution

System	pH	Radical	λ, nm	$2k$, M^{-1} sec^{-1} [a]
2-Benzoylpyridine	5.9	2-PyĊ(OH)C$_6$H$_5$	500	1.8×10^8, 1.2×10^8
	13.3	2-PyĊ(O$^-$)C$_6$H$_5$	550	1.6×10^8, 1.2×10^8
	1.1	2-PyH$^+$Ċ(OH)C$_6$H$_5$	550	7.9×10^8
			350	7.1×10^8
3-Benzoylpyridine	5.1	3-PyĊ(OH)C$_6$H$_5$	530	5.1×10^8, 7.6×10^8
	13.0	3-PyĊ(O$^-$)C$_6$H$_5$	605	5.3×10^7
	0.9	3-PyH$^+$Ċ(OH)C$_6$H$_5$	505	6.2×10^8,[b] 7.8×10^8
4-Benzoylpyridine	5.2	4-PyĊ(OH)C$_6$H$_5$	500	9.6×10^7
	13.2	4-PyĊ(O$^-$)C$_6$H$_5$	575	1.6×10^8, 1.7×10^8
	0.8	4-PyH$^+$Ċ(OH)C$_6$H$_5$	505	1.1×10^9
			390	1.2×10^9
			340	1.1×10^9
3-Benzoyl-*N*-methylpyridinium ion	4.7	3-PyCH$_3$$^+$Ċ(OH)C$_6H_5$	530	1.1×10^9, 1.2×10^9
			332	1.2×10^9
	10.1	3-PyCH$_3$$^+$Ċ(O$^-$)C$_6H_5$	555	1.2×10^9
			318	1.3×10^9

[a] Rate values determined in aqueous 1.0 M *tert*-butyl alcohol and 2.0 M isopropyl alcohol, respectively. [b] Measured at pH 3.1.

maxima of the ketyl radicals and radical anions of the three benzoylpyridines.

The decay kinetics of the ketyl radicals are presented in Table III.

Reaction of Acetone Ketyl Radicals with Benzoylpyridines. In the photochemistry of aromatic ketones, the triplet excited state has been shown to abstract an H atom efficiently from isopropyl alcohol (for review see ref 11).

(11) J. G. Calvert and J. N. Pitts, Jr., "Photochemistry," Wiley, New York, N. Y., 1966, p 366.

$$^3C_6H_5COR + (CH_3)_2CHOH \longrightarrow C_6H_5\dot{C}(OH)R + (CH_3)_2\dot{C}OH \quad (7)$$

The subsequent reactions of the $(CH_3)_2\dot{C}OH$ radical have been disputed. While reaction 8 has been sug-

$$(CH_3)_2\dot{C}OH + C_6H_5COR \longrightarrow C_6H_5\dot{C}(OH)R + CH_3COCH_3 \quad (8)$$

gested to occur in most cases, leading to a doubling of the quantum yield of primary decomposition of the ketone, a range of quantum yields have been obtained for the same aromatic ketones by various workers. In only a few cases has the rate of reaction 8 been determined, and it is suggested that the discrepancy in the quantum yields could be due to incomplete scavenging of the $(CH_3)_2\dot{C}OH$ radicals since a range of ketone concentrations was used by the different investigators. For complete scavenging $k_8[C_6H_5\dot{C}OR] \geq 50k_9[(CH_3)_2\dot{C}OH]$

$$2(CH_3)\dot{C}OH \longrightarrow \text{products} \quad (9)$$

where $k_9 = 1.4 \times 10^9\ M^{-1}\ \text{sec}^{-1}$ (ref 8a). In order to interpret certain aspects of the photochemistry of the benzoylpyridines in isopropyl alcohol, it was necessary to know the rate of reaction 5. These were determined by pulse radiolysis in 2.0 M aqueous isopropyl alcohol solutions saturated with nitrous oxide. Under these conditions all the e^-_{aq} are converted to OH radicals (reaction 3) and all the OH radicals and H atoms are converted to $(CH_3)_2\dot{C}OH$ radicals *via* reactions 4 and 10. By monitoring the ketyl radicals formed *via* reac-

$$H + (CH_3)_2CHOH \longrightarrow (CH_3)_2\dot{C}OH + H_2 \quad (10)$$

tion 5 at the wavelengths of maximum absorption, k_5 was determined from the pseudo-first-order rate of formation of the ketyl radical. These rate constant values are given in Table IV. In neutral solutions, the values for k_5 are ~ 1–$2 \times 10^8\ M^{-1}\ \text{sec}^{-1}$ for 2-, 3-, and 4-benzoylpyridines.

In alkaline solutions, beyond the $pK_a = 12.2$[12] of

$$(CH_3)_2\dot{C}OH \rightleftharpoons (CH_3)_2\dot{C}O^- + H^+ \quad (11)$$

the acetone ketyl radical, the rate of electron transfer from the $(CH_3)_2\dot{C}O^-$ radical to BP was found to be higher by about a factor of 10–20 (see Table IV),

$$(CH_3)_2\dot{C}O^- + PyCOC_6H_5 \longrightarrow PyC(O^-)C_6H_5 + CH_3COCH_3 \quad (12)$$

compared to k_5. This increase in k_{12} compared to k_5 is to be expected, since an electron transfer process from a radical anion should be more favorable.

Table IV: Reaction Rate Constants of the Acetone Ketyl Radicals, $(CH_3)_2\dot{C}OH$ and $(CH_3)_2\dot{C}O^-$ with Benzoylpyridines in 2.0 M Aqueous Isopropyl Alcohol Solutions

System	pH	λ (monitored), nm	k, $M^{-1}\ \text{sec}^{-1}$ [a]
2-Benzoylpyridine	5.9	500	$1.5 \pm 0.2 \times 10^8$
	13.2	550	$2.3 \pm 0.2 \times 10^9$
	1.0	500	$3.0 \pm 0.3 \times 10^9$
	1.0	330	$3.0 \pm 0.3 \times 10^9$
3-Benzoylpyridine	5.1	530	$1.0 \pm 0.2 \times 10^8$
	13.0	605	$2.0 \pm 0.2 \times 10^9$
	13.0	341	$2.0 \pm 0.2 \times 10^9$
	0.9	500	$1.7 \pm 0.2 \times 10^9$
	0.5	330	$2.3 \pm 0.3 \times 10^9$
4-Benzoylpyridine	7.7	500	$2.4 \pm 0.4 \times 10^8$
	13.2	575	$2.5 \pm 0.2 \times 10^9$
	0.7	510	$2.5 \pm 0.2 \times 10^9$
3-Benzoyl-*N*-methylpyridinium ion	5.0	530	$2.3 \pm 0.3 \times 10^9$
	1.0	530	$2.3 \pm 0.3 \times 10^9$
Benzophenone	13.1	605	$1.6 \pm 0.2 \times 10^9$

[a] In alkaline solution, radical is dissociated, $(CH_3)_2\dot{C}O^-$.

The dissociation constants of benzoylpyridines have been measured, and pK_a of 3.18 and 3.35 for 3-BP and 4-BP, respectively, have been reported.[13] The pK_a of 2-BP has apparently not been determined. The

$$(CH_3)_2\dot{C}OH + PyH^+\text{—}CO\text{—}C_6H_5 \longrightarrow PyH^+\text{—}C(OH)\text{—}C_6H_5 + CH_3COCH_3 \quad (13)$$

rate constant for reaction 13 in acidic solution was determined and values of $\sim 2 \times 10^9\ M^{-1}\ \text{sec}^{-1}$ were obtained, for 2-, 3-, and 4-benzoylpyridines, almost identical with the values of k_{12}. This high value for k_{13} (see Table IV) would appear to support an electron transfer mechanism to the benzoylpyridinium ion, followed by rapid protonation at pH values lower than the pK_a of the BP ketyl radicals.

In order to ascertain that the observed values of k_{13} were indeed associated with the protonated forms of benzoylpyridines, these rate constants were determined as a function of pH, and are presented in Figure 4. It can be seen that these rates decrease with increase in pH, and from the curves in Figure 4 one can derive pK_a values of 2.6 ± 0.2, 3.3 ± 0.2, and 3.8 ± 0.2 for 2-, 3-, and 4-benzoylpyridines, respectively. The pK_a for 3-BP is in good agreement with the literature value[13] of 3.18. The pK_a of 4-BP was redetermined

(12) K. D. Asmus, A. Henglein, A. Wigger, and G. Beck, *Ber. Bunsenges. Phys. Chem.*, **70**, 756 (1966).

(13) A. Fischer, W. J. Galloway, and J. Vaughan, *J. Chem. Soc.*, 3591 (1964).

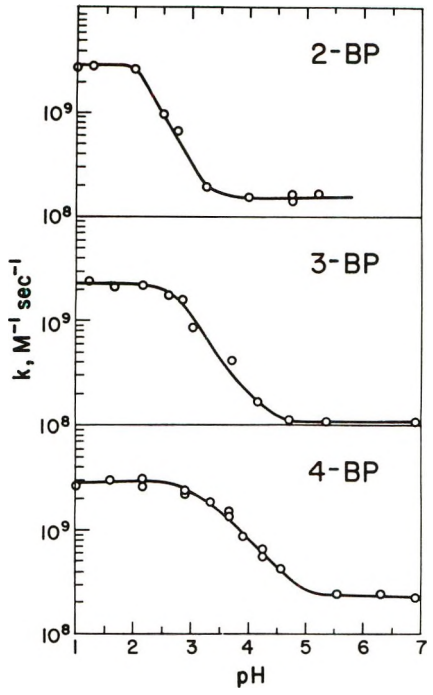

Figure 4. pH dependence of the rate constant of reaction of the acetone ketyl radical, $(CH_3)_2\dot{C}OH$, with benzoylpyridines in 1–2 *M* aqueous isopropyl alcohol solutions.

(spectrophotometrically by following the change in absorbance with pH at 250 nm) and a value of 3.6 ± 0.1 was obtained, compared to 3.35.[13] The pK_a of 2-BP was determined for the first time (by following ΔOD at both 250 and 320 nm) and a value of 2.15 ± 0.1 was derived. In view of the larger experimental error involved in determing the value of k_{13}, the results shown in Figure 4 are considered to be in reasonably good agreement with the pK_a's of the parent molecules.

Concomitant with the change in the rate constant for reaction of $(CH_3)_2\dot{C}OH$ with $PyH^+COC_6H_5$, different optical absorption bands of the corresponding ketyl radicals were observed, see Figures 5 and 6 and Table II. For 3-$PyH^+COC_6H_5$, the absorption spectrum of the ketyl radical has maxima at 695, 503, 375, and 331 nm (Figure 5). In order to demonstrate that the intermediate produced *via* reaction 13 is the ketyl radical, 3-$PyH^+COC_6H_5$ was allowed to react with e^-_{aq} in presence of 2.0 *M* t-BuOH

$$e^-_{aq} + \text{3-PyH}^+\text{—CO—C}_6\text{H}_5 \xrightarrow{H^+} \text{3-PyH}^+\text{—}\underset{\displaystyle OH}{\overset{|}{C}}\text{—C}_6\text{H}_5 \quad (14)$$

An identical spectrum and extinction coefficient were obtained (see Figure 5), indicating a quantitative formation of the ketyl radical *via* reaction 13. Furthermore, the flash photolysis of 3-BP in 2.0 *M* aqueous isopropyl alcohol at pH 1.6 produced a similar spectrum, which has been normalized with the pulse radiolysis results, see Figure 5.

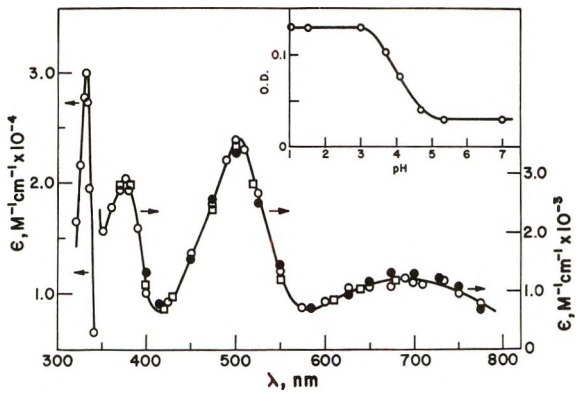

Figure 5. Optical absorption spectrum of the ketyl radical of 3-benzoylpyridinium ion produced from (a) the reaction of $(CH_3)_2\dot{C}OH$ radicals at pH 0.88 in aqueous 2 *M* isopropyl alcohol (○), and (b) the reaction of e_{aq}^- at pH 3.1 in 1 × 10^{-2} *M* 3-BP, 2.2 *M* *tert*-butyl alcohol, and N_2O (1 atm) (□). The spectrum of the ketyl radical of 3-benzoylpyridinium ion (10^{-4} *M*) produced by flash photolysis at pH 1.6 in 2.0 *M* aqueous isopropyl alcohol is also shown (●).

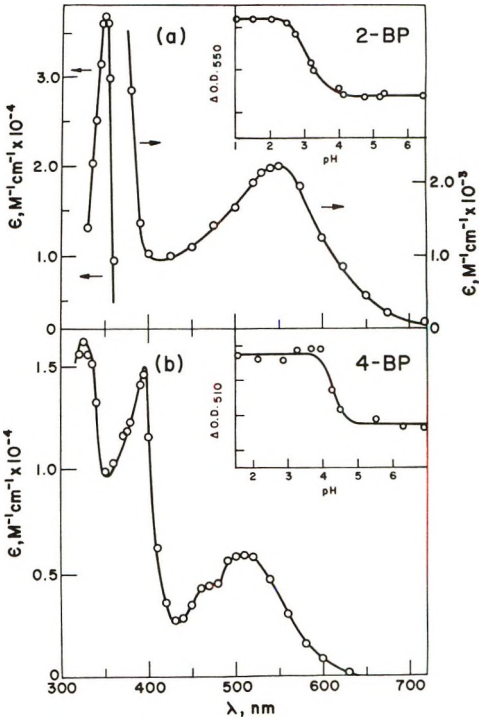

Figure 6. Optical absorption spectrum of the ketyl radical of benzoylpyridinium ion produced in aqueous 2.0 *M* isopropyl alcohol from the reaction of $(CH_3)_2\dot{C}OH$ radicals with (a) 2-benzoylpyridine at pH 1.2 and (b) 4-benzoylpyridine at pH 0.8. Inserts show the absorbances of ketyl radicals of benzoylpyridinium ions *vs.* pH.

The dissociation constants of the ketyl radicals of benzoylpyridinium ions were found to be different from the pK_a's of the corresponding parent compounds. From the inserts in Figures 5 and 6, the pK_a's of the ketyl radicals were determined to be 3.1 ± 0.1, 4.1 ± 0.2, and 4.2 ± 0.2 for the 2-, 3-, and 4-benzoylpyri-

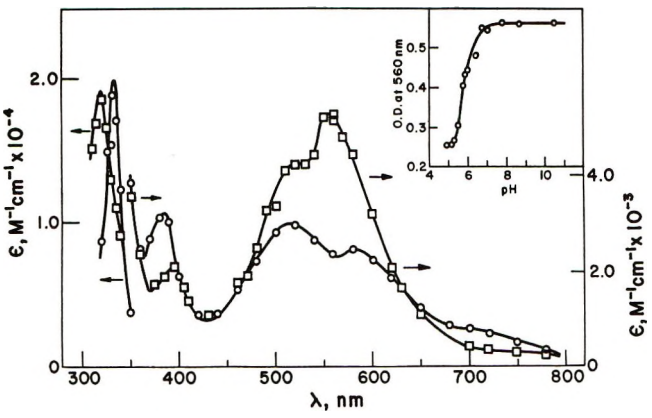

Figure 7. Optical absorption spectrum of the ketyl radical (○, pH 5.0) and radical anion (□, pH 10.1) of 3-benzoyl-*N*-methylpyridinium chloride in 1.0 *M* aqueous *tert*-butyl alcohol. Insert shows the absorbance of ketyl radical at 560 nm *vs.* pH.

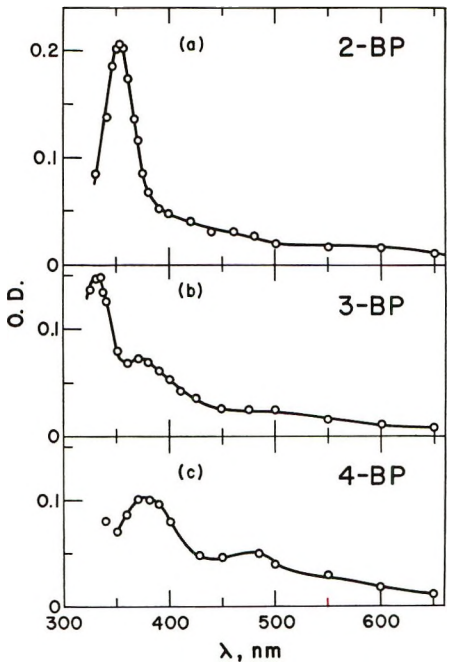

Figure 8. Absorption spectra of the H atom adducts of 2-, 3-, and 4-benzoylpyridinium ions obtained at pH 0.8–1.0 in 1.0 *M* aqueous *tert*-butyl alcohol.

dinium ions, respectively. It is to be noted that in all these cases, the pK_a of the ketyl radical is higher than that of the parent compounds.

The decay rates of the ketyl radicals of benzoylpyridinium ions are given in Table III.

Ketyl Radicals of Benzoyl-N-methylpyridinium Ions. The optical absorption spectrum of the ketyl radical of 3-benzoyl-*N*-methylpyridinium chloride(3-PyCH_3^+CO-C_6H_5) in 1.0 *M* aqueous t-BuOH can be seen to be distinctly different from that of the corresponding radical of 3-benzoylpyridine, compare Figure 7 with Figures 1 and 5. The spectrum is more structured, and an additional band is observed at ~385 nm. In the wavelength region 350–420 nm, and subsequent to the initial formation of the ketyl radical at pH 4.7, the "build-in" of a new absorbing species can be seen with a rate of formation of $\sim 4.0 \times 10^4$ sec^{-1}. This new species has an absorption maximum in this region and appears to be a permanent product (no decay could be seen in oxygen-free solutions after 5 min). A similar effect was observed for the corresponding band at pH 10.1.

In alkaline solutions, the absorption spectrum of the ketyl radical anions undergoes similar changes to those observed for the benzoylpyridines, and from the change in absorbance with pH at 560 nm, a pK_a = 5.9 ± 0.2 was determined for the equilibrium

$$3\text{-Py}CH_3^+\text{—}\underset{\displaystyle \underset{\displaystyle OH}{|}}{\dot{C}}\text{—}C_6H_5 \rightleftharpoons 3\text{-Py}CH_3^+\text{—}\underset{\displaystyle \underset{\displaystyle O^-}{|}}{\dot{C}}\text{—}C_6H_5 + H^+ \quad (15)$$

This acid dissociation constant compares with the pK_a = 9.2 ± 0.2 for the ketyl radical of 3-benzoylpyridine. The strong inductive effect of the *N*-methylpyridinium ion can be seen to influence the acid–base properties of the ketyl radical of the 3-substituted benzoyl derivative.

Similar spectra were produced from the reaction of $(CH_3)_2\dot{C}OH$ radicals with 3-PyCH_3^+COC_6H_5 at pH 4.7 and 10.1. At pH 1.0, the spectrum was found to be unchanged from that observed at pH 4.7. It is interesting to note (see Table IV) that $k_{16} = 2.3 \pm 0.3 \times 10^9\ M^{-1}$ sec^{-1} at pH 5.0 and 1.0, and that it is the same

$$(CH_3)_2\dot{C}OH + 3\text{-Py}CH_3^+\text{—}CO\text{—}C_6H_5 \longrightarrow CH_3COCH_3 + 3\text{-Py}CH_3^+\text{—}\underset{\displaystyle \underset{\displaystyle OH}{|}}{\dot{C}}\text{—}C_6H_5 \quad (16)$$

as the rate constant of reaction 13. This indicates that it is the pyridinium ion which enhances the rate of reaction with the acetone ketyl radical, indicating that the reaction presumably takes place *via* an electron transfer from $(CH_3)_2\dot{C}OH$, followed by rapid protonation.

The extinction coefficients and decay kinetics of these radicals are given in Tables II and III.

Hydrogen Atom Adducts to Benzoylpyridines. The reactions of hydrogen atoms with aromatic carbonyl compounds are quite different from the reactions of electrons with the same ketones. The reaction rate constants, the site(s) of addition, and the transient optical absorption spectra of the resulting intermediates all attest to this difference. Recent work[7] has demonstrated quite clearly that the solvated electrons add to aromatic ketones, quinones, and β diketones to produce exclusively the ketyl radicals and radical

anions of the corresponding carbonyl compounds. Interaction of the odd electron with the aromatic and pyridine rings gives rise to various resonating structures. The H atoms, however, are much less selective and add to the aromatic ring at presumably more than one position on the ring.[7]

Similar effects and observations are found for the reactions of H atoms with benzoylpyridinium ions. The rate constants of the reaction (Table I) are $\sim 3 \times 10^9\ M^{-1}\ \text{sec}^{-1}$, similar to the rate constants found[7] for other aromatic ketones. Figure 8 shows the absorption spectra of the H atom adducts to 2-, 3-, and 4-benzoylpyridinium ions. These were obtained at pH 0.8–1.0 in presence of 1.0 *M* *tert*-butyl alcohol to scavenge all the OH radicals. The decay rates of these adducts and their extinction coefficients are given in Table V. The difference in the spectra of the H atom adducts compared to the spectra of the ketyl radicals supports the conclusion reached above that the reaction of $(CH_3)_2\dot{C}OH$ radicals with benzoylpyridines produces radicals which are identical with those formed directly from the reaction of e^-_{aq} with BP.

Table V: Absorption Maxima, Extinction Coefficients, and Decay Kinetics of the Hydrogen Atom Adducts of Benzoylpyridines Determined at pH ~1.0 in 1–1.5 *M* Aqueous *tert*-Butyl Alcohol

System	λ_{max}, nm	ϵ_{max}, $M^{-1}\ \text{cm}^{-1}$	$2k$, $M^{-1}\ \text{sec}^{-1}$
2-Benzoylpyridine	350	7.0×10^3	$3.0 \pm 0.4 \times 10^8$
3-Benzoylpyridine	395	4.8×10^3	$3.2 \pm 0.5 \times 10^8$
	332	7.9×10^3	
4-Benzoylpyridine	375	3.6×10^3	
	335	2.9×10^3	$2.9 \pm 0.4 \times 10^8$

Discussion

The results and mechanism presented above indicate that in some respects the chemistry of benzoylpyridines is similar to that of benzophenone, *e.g.*, even though the pyridine ring has a greater electron affinity than the benzene ring, all the solvated electrons appear to lead to the formation of the corresponding ketyl radical anions. The odd electron on the carbonyl carbon atom subsequently interacts with both benzene and pyridine rings. Furthermore, the pK_a of the ketyl radical of 3-BP, $pK_a = 9.2 \pm 0.2$, is the same as that of benzophenone, 9.25 ± 0.1.[7] However, the pK_a of the ketyl radicals of 2-BP and 4-BP are distinctly higher, 12.3 ± 0.2 and 12.0 ± 0.2, respectively. These results indicate that the electronegative nitrogen atom on the ring plays an important role in determining the acid–base properties of these ketyl radicals. It would appear that its effect is strongest for substituents at positions 2 and 4.

The pyridine ring also influences the rate constant for reaction of $(CH_3)_2\dot{C}OH$ radicals with benzoylpyridines. These rates are $\sim 1\text{–}2 \times 10^8\ M^{-1}\ \text{sec}^{-1}$ for 2-, 3-, 4-benzoylpyridines and $2.3 \times 10^9\ M^{-1}\ \text{sec}^{-1}$ for 3-benzoyl-*N*-methylpyridinium ion, while the rate of $(CH_3)_2\dot{C}OH$ radicals with benzophenone at pH 6.0 is $< 10^7\ M^{-1}\ \text{sec}^{-1}$. At pH 1.0, the $(CH_3)_2\dot{C}OH$ radicals react much faster with the corresponding benzoylpyridinium ions (see Table IV), but the rate constant with benzophenone is still $< 10^7\ M^{-1}\ \text{sec}^{-1}$. In alkaline solutions, the rate of reaction of $(CH_3)_2\dot{C}O^-$ radicals with benzophenone becomes similar to those for the benzoylpyridines (see Table IV), $k \sim 2.0 \times 10^9\ M^{-1}\ \text{sec}^{-1}$.

A very interesting observation in this work is that the pK_a of the ketyl radical of 3-benzoyl-*N*-methylpyridinium ion is about three units lower than that of 3-benzoylpyridine, 5.9 ± 0.2 and 9.2 ± 0.2, respectively. This can be attributed to an inductive effect of the pyridinium ring. Methylation of the nitrogen considerably affects the electron distributions of the ketyl radical, making it a stronger acid. Furthermore, protonation, like alkylation, produces a hyperchromic effect, *i.e.*, an increase in absorbance particularly at longer wavelengths. This result is potentially of considerable interest in the understanding of electron transfer processes in NAD–NADH reactions. Work on nicotinamide, NAD^+, and NADH is in progress.

The decay kinetics of the ketyl radicals presented in Table III all follow second-order processes, and show certain general similarities. The $PyH^+\dot{C}OHC_6H_5$ radicals of 2-, 3-, and 4-BP decay with $2k \sim 7\text{–}12 \times 10^8\ M^{-1}\ \text{sec}^{-1}$. The decay rates of the $Py\dot{C}(OH)C_6H_5$ radical of 2- and 4-BP are $\sim 10^8\ M^{-1}\ \text{sec}^{-1}$, while the corresponding 3-BP radical decays faster with $2k \sim 7 \times 10^8\ M^{-1}\ \text{sec}^{-1}$. The decay kinetics of the ketyl radical anions ($P\cdot^-$) were all determined at pH ~13. For 3-BP, the decay rate was found to be lower by a factor of about 10, $2k \sim 5 \times 10^7\ M^{-1}\ \text{sec}^{-1}$, presumably due to the slower termination of two negatively charged radicals, $P\cdot^-$. In the cases of 2-BP and 4-BP, the observed decay rates of the corresponding $P\cdot^-$ are not significantly different from those of PH· radicals. Since the pK_a of the ketyl radicals is 12.3 and 12.0, respectively, at the pH used to determine these rates some 10% or more of the radicals are present as PH·, and the observed rates are therefore probably due to $P\cdot^- + PH\cdot$ reactions, as well as to $P\cdot^- + P\cdot^-$ reactions.

Argon Matrix Raman and Infrared Spectra and Vibrational Analysis of Ozone and the Oxygen-18 Substituted Ozone Molecules

by Lester Andrews* and Robert C. Spiker, Jr.

Chemistry Department, University of Virginia, Charlottesville, Virginia 22901 *(Received May 30, 1972)*

Raman spectra of argon matrix-isolated ozone and oxygen-18 enriched ozones were obtained using reduced power argon ion laser excitation. Photodecomposition of ozone was sufficiently moderated to obtain excellent Raman spectra, with the following $^{16}O_3$ assignments: ν_1, 1104 cm^{-1}, very strong; ν_2, 701 cm^{-1}, strong; ν_3, 1038 cm^{-1}, weak. Infrared spectra provided complementary data: ν_1, 1105 cm^{-1}, very weak; ν_2, 704 cm^{-1}, weak; ν_3, 1040 cm^{-1}, very strong. Potential constants were calculated using vibrational fundamentals for six isotopic ozone molecules. An ozone valence angle of 116.3 ± 4° was calculated from four isotopic ν_3 assignments, in excellent agreement with the microwave value.

Introduction

Although there have been many infrared studies of the vibrational fundamentals of ozone, only one Raman spectrum has been reported to date. Gas-phase infrared measurements have yielded the fundamentals 1103.1, 1042.1, and 701.0 cm^{-1} for ν_1, ν_3, and ν_2, respectively.[1,2] Infrared observations of O_3 in solid oxygen[3,4] and liquid argon[5] have been recently compared to krypton and xenon matrix frequencies of ozone produced upon passing O_2 matrix samples through a microwave discharge.[6]

The primary difficulty with Raman studies of ozone has been its sensitivity to photodecomposition by the excitation source. Nevertheless, Selig and Claassen[7] have obtained the Raman spectrum of gaseous ozone at pressures of 2 to 4 atm using a He–Ne laser. These workers assigned ν_1 and ν_2 of $^{16}O_3$ to 1103.3 and 702.1 cm^{-1}, respectively; polarization data confirmed these assignments. However, this approach is less practical for isotopic ozone species. Deglise and Giguere[8] erroneously attributed bands to the Raman spectrum of ozone in studies of electrical discharge products of hydrogen–oxygen systems condensed at 93°K. Giguere has recently clarified these results and privately communicated[9] values of 1106, 703, and 1037 cm^{-1} for ν_1, ν_2, and ν_3 of $^{16}O_3$, respectively, in a solid hydroxylic medium.

The present study[10] was undertaken to observe Raman spectra of isotopic ozone molecules isolated in argon matrices at 16°K. Matrix trapping may retard the photodecomposition of the ozone molecule; furthermore, small quantities of oxygen-18 enriched ozone species can be studied using the matrix technique.

In recent infrared studies[11] of alkali metal atom–ozone reactions, infrared spectra of isotopic ozone molecules in argon matrices at 15°K were observed. These data will be reported here for comparison between infrared and Raman argon matrix spectra of ozone isotopes.

Experimental Section

The cryogenic apparatus (Cryogenic Technology, Inc., Waltham, Mass.) and vacuum vessel used for obtaining laser-Raman matrix spectra has recently been described by Hatzenbühler and Andrews.[12] Ozone was synthesized by tesla coil discharge of oxygen at low pressures in a Pyrex finger partially immersed in liquid nitrogen as described by Spiker and Andrews.[11] Samples of ozone ($^{16}O_3$, $^{18}O_3$, or $^{16,18}O_3$) were outgassed at 77°K, expanded into a stainless steel bulb, and diluted with argon in ratios ranging from argon/ozone = M/R = 50/1 to 200/1. Matrix samples were condensed on a polished, tilted copper wedge at 16°K for 4 hr at the rate of 2.5 mM/hr.

Raman spectra were recorded using a Coherent Radiation Model 52 G argon ion laser (5145 and 4880 Å) and a Spex Model 1 Ramalog spectrometer. The technique used for obtaining Raman matrix spectra has recently been described.[12,13] Laser power was reduced in these studies using neutral density filters. Dielectric long-wavelength pass filters (5145 and 4880 Å, Corion Instrument Corp.) were used in the regions above 900 cm^{-1} to suppress reflected laser light and thus eliminate grating ghosts. Spectra were calibrated by a technique

(1) D. J. McCaa and J. H. Shaw, *J. Mol. Spectrosc.*, **25**, 374 (1968).
(2) S. A. Clough and F. X. Kneizys, *J. Chem. Phys.*, **44**, 1855 (1966).
(3) K. B. Harvey and A. M. Bass, *J. Mol. Spectrosc.*, **2**, 405 (1958).
(4) J. L. Brumant, A. Barbe, and P. Jouve, *C. R. Acad. Sci., Ser. B*, **268**, 549 (1969).
(5) A. Barbe and P. Jouve, *ibid.*, **268**, 1723 (1969).
(6) L. Brewer and J. L-F. Wang, *J. Chem. Phys.*, **56**, 759 (1972).
(7) H. Selig and H. H. Claassen, *Isr. J. Chem.*, **6**, 499 (1968).
(8) X. Deglise and P. A. Giguere, *Can. J. Chem.*, **49**, 2242 (1971).
(9) P. A. Giguere, personal communication, 1972.
(10) Taken in part from the thesis submitted by Robert C. Spiker, Jr., to the Graduate School of the University of Virginia in partial fulfillment of the Ph.D. degree requirements.
(11) R. C. Spiker, Jr., and L. Andrews, *J. Chem. Phys.*, in press.
(12) D. A. Hatzenbühler and L. Andrews, *ibid.*, **56**, 3398 (1972).
(13) L. Andrews, *ibid.*, **57**, 51 (1972).

of superimposing argon fluorescence lines[14] on each side of a particular Raman band during a scan, which provides a frequency accuracy and reproducibility of ± 1 cm^{-1} for the most intense bands and ± 2 cm^{-1} for the weaker lines. Polarization measurements were carried out with the use of a polarization analyzer followed by a quartz polarization scrambler.

Infrared spectra were recorded during and after sample deposition on a Beckman IR-12 filter-grating infrared spectrophotometer in the 200–4000-cm^{-1} spectral region. Deposition times for infrared experiments ranged from 12 to 22 hr. The instrument was calibrated using vibration–rotation bands of standard molecules.[15] High-resolution spectra were taken using either 8 or 3.2 cm^{-1} per min scanning speeds and either 20 or 10 cm^{-1} per in. scale expansions. Wave number accuracy is ± 0.5 cm^{-1}.

Results and Discussion

Raman and infrared spectra were recorded for isotopic ozones in argon matrices. The observed vibrational fundamentals were used to calculate potential constants and the ozone valence angle.

Raman Spectra. Four Raman investigations were performed on natural isotopic ozone–argon matrix samples. Excellent Raman spectra were obtained from samples using approximately 100 mW of 5145-Å excitation and approximately 15 mW of 4880-Å excitation. Comparable Raman intensities for ozone were observed under these two sets of conditions. Since photodecomposition of the ozone sample was a major concern, the relative Raman intensities of O_2 and O_3 were monitored at intervals throughout the time of recording and calibrating spectra. As expected, the intensity ratio (O_2/O_3) increased gradually during the sample illumination period. After 70 min of illumination with 15 mW of 4880-Å excitation, the 1104-cm^{-1} ozone fundamental decreased to two-thirds of its original value while the 1553-cm^{-1} oxygen fundamental doubled its intensity. Fortunately, the ozone photodecomposition proceeded slowly enough to facilitate recording Raman spectra of argon matrix isolated ozone.

A sample of ozone ($Ar/O_3 = 100$) was studied extensively using approximately 15 mW of 4880-Å excitation. The initial Raman spectrum showed the O_2 fundamental to be one-third as intense as the strong $^{16}O_3$ fundamental at 1104 cm^{-1}. Three Raman bands were observed at 1104, 701, and 1038 cm^{-1} using blue excitation; the spectrum was almost identical with the one in Figure 1 using green excitation. These frequencies, which were calibrated against argon fluorescence lines, are appropriate for the ν_1 (symmetric O–O stretch), ν_2 (valence angle bend), and ν_3 (antisymmetric O–O stretch) fundamentals of $^{16}O_3$. Relative Raman intensities of the ozone fundamentals were approximately 7/3/1, respectively. The 1038-cm^{-1} band was observed using a dielectric long-wavelength pass filter

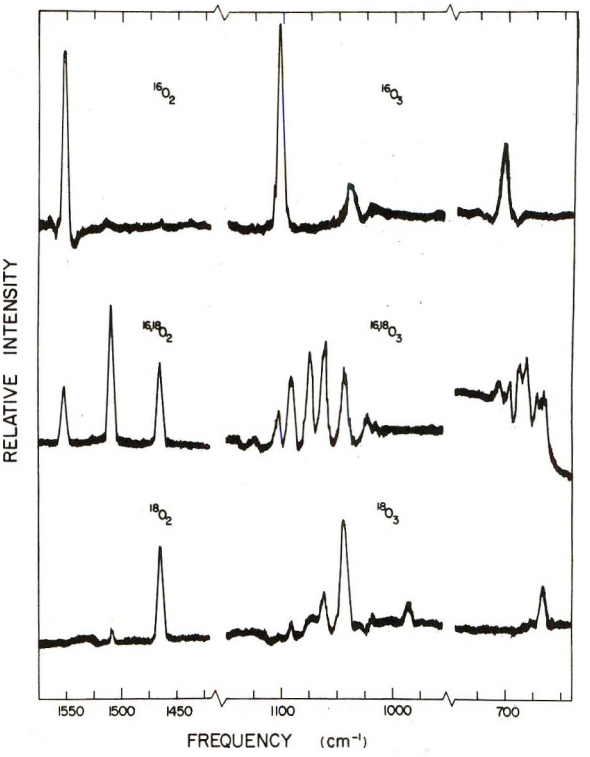

Figure 1. Raman spectra of isotopic oxygen molecules in the 1420–1575-cm^{-1} region and isotopic ozone molecules in the 640–745- and 955–1150-cm^{-1} regions at 16°K: all spectra approximately 100 mW of 5145-Å excitation at the sample, 10 cm^{-1}/min scanning speed, 5 cm^{-1} resolution, suppression 0–1 $\times 10^{-9}$ A; top spectrum, 61 μM of O_3 deposited, Ar/O_3 = 135/1, rise time 10 sec, range 0.3 $\times 10^{-9}$ A; middle spectrum, 166 μM of $^{16,18}O_3$ deposited (55% ^{18}O), Ar/O_3 = 50/1; 955–1150- and 1420–1575-cm^{-1} regions, rise time 3 sec, range 0.3 $\times 10^{-9}$ A; 640–745-cm^{-1} region, rise time 10 sec, range 0.1 $\times 10^{-9}$ A; bottom spectrum, 41 μM of $^{18}O_3$ deposited (93% ^{18}O), Ar/O_3 = 200/1, rise time 10 sec, range 0.1 $\times 10^{-9}$ A.

to eliminate the possible interference of grating ghosts observed using higher laser power in this spectral region. The ν_3 fundamental was not observed in the gas-phase Raman spectrum of ozone; however, the ν_1 and ν_2 fundamentals were very strong.[7] The matrix may enhance the Raman intensity of ν_3. A similar strengthening of ν_3 was observed in the Raman spectrum[13] of matrix isolated OF_2.

Depolarization ratios were measured for ozone and oxygen in this frosty argon matrix sample using 4880-Å excitation. Three measurements of ρ, the depolarization ratio, for O_2 ranged from 0.55 to 0.60; ρ for O_2 in frosty argon matrices has been previously[16] reported as 0.52. For ozone the following depolarization ratios were determined: ρ_1, 0.64; ρ_2, 0.78; ρ_3, 0.89. Clearly,

(14) A. R. Striganov and N. S. Sventitskii, "Tables of Spectral Lines of Neutral and Ionized Atoms," Plenum Data Corp., New York, N. Y., 1968, pp 354–356.

(15) E. K. Plyler, A. Danti, L. R. Blaine, and E. D. Tidwell, *J. Res. Nat. Bur. Stand.*, **64**, 1 (1960).

(16) R. R. Smardzewski and L. Andrews, *J. Chem. Phys.*, **57**, 1327 (1972).

ρ_1 and ρ_2 are much higher than expected for symmetric modes. This discrepancy can be attributed to the scrambling effect of the frosty matrix. Hence, these ρ values do not represent true values for ozone; they are a function of the matrix environment. However, a trend is apparent; the lowest depolarization ratio was determined for the diatomic species O_2. ρ's for the symmetric stretch, symmetric bend, and antisymmetric stretch progressively increased. The same trend has been reported for the depolarization ratios of OF and the OF_2 fundamentals in argon matrices[13] and for the OF_2 fundamentals in liquid OF_2.[17]

The Raman spectrum of matrix isolated ozone using approximately 100 mW of 5145-Å excitation is illustrated in the top trace of Figure 1. Oxygen produced by ozone photolysis was observed at 1553 cm^{-1} after scanning the spectrum. The very strong band observed at 1104 cm^{-1} is assigned to ν_1 of argon matrix-isolated $^{16}O_3$, the medium intensity signal at 703 cm^{-1} is ν_2, and the weak feature at 1039 cm^{-1} is attributed to ν_3. The relative Raman intensities of $\nu_1/\nu_2/\nu_3$ were respectively 6/2/1 in this green laser experiment.

The third trace of Figure 1 shows Raman spectra of oxygen-18 substituted (93% ^{18}O)O_2 and O_3 (Ar/O_3 = 200/1) using approximately 100 mW of green excitation. The band at 1465 cm^{-1} is due to $^{18}O_2$ while the much weaker feature near 1510 cm^{-1} is due to a trace of $^{16}O^{18}O$. In the ozone region of the spectrum, the intense feature at 1042 cm^{-1} is assigned to ν_1 of $^{18}O_3$, since this band shows the appropriate isotopic shift from $^{16}O_3$. Two depolarization ratio measurements were obtained for this band, the first yielded a value of 0.50 and the second 0.55. These values add further evidence that the 1042-cm^{-1} feature is ν_1 of $^{18}O_3$. Weaker isotopic bands, due to 7% oxygen-16 in the sample, were observed near 1062, 1075, and 1091 cm^{-1}. The ν_2 and ν_3 vibrations of $^{18}O_3$ appeared at 665 and 983 cm^{-1}, respectively, as is shown in Figure 1.

The second trace displays green laser spectra of isotopically scrambled oxygen (20% $^{16}O_2$, 50% $^{16}O^{18}O$, 30% $^{18}O_2$) and ozone molecules (55% ^{18}O enriched). The 2/5/3 relative intensity triplet at 1465, 1510, and 1553 cm^{-1} is due to $^{18}O_2$, $^{16}O^{18}O$, and $^{16}O_2$, respectively. In the ozone portion of the spectrum, two multiplets were seen, the higher frequency one contained five bands and the lower frequency multiplet showed six partially resolved bands. The two outermost components of the first multiplet at 1042 and 1104 cm^{-1} are assigned to ν_1 of $^{18}O_3$ and $^{16}O_3$, respectively, since both of these features match with bands observed in individual $^{18}O_3$ and $^{16}O_3$ Raman spectra. The following intensities are predicted from statistics for the six isotopic ozone molecules: 16–16–16, 0.091; 16–16–18, 0.222; 18–16–18, 0.136; 16–18–16, 0.111; 18–18–16, 0.272; 18–18–18, 0.166. Referring to the statistical weights, the band at 1061 cm^{-1}, which is almost twice as intense as its 1042-cm^{-1} counterpart, is assigned to ν_1 of 18–18–16. The same reasoning applies to the 1091-cm^{-1} band which is undoubtedly due to ν_1 of 16–16–18. The remaining feature at 1074 cm^{-1} is due to the unresolved 18–16–18 and 16–18–16 components, whose statistical weights, when added, compare favorably with the observed intensity of the 1074-cm^{-1} signal. The partially resolved multiplet in the 670–710-cm^{-1} ν_2 region of ozone is more difficult to analyze because of the changing background and high noise level. This feature contains six partially resolved components; the peaks at 682 and 688 cm^{-1} are the most intense features. Referring to the above statistical weights, the 682- and 688-cm^{-1} signals must be assigned to the unsymmetrical ozone isotopes 18–18–16 and 16–16–18, respectively. The outside peaks at 664 and 704 cm^{-1} are respectively assigned to ν_2 of $^{18}O_3$ and $^{16}O_3$. The remaining weaker features at 671 and 698 cm^{-1} are attributed to ν_2 of the symmetrical mixed isotopes 18–16–18 and 16–18–16, respectively.

The frequencies assigned to ν_1 and ν_2 of isotopic ozones listed in Table I were taken from the scrambled isotopic experiment where these frequencies were measured relative to each other, hence isotopic shifts are more accurate than absolute frequency accuracy.

Table I: Raman and Infrared Frequencies (cm^{-1}) Observed for the Fundamental Vibrations of Isotopic Ozone Molecules in Argon Matrices at 16°K[a]

Isotopic assignments	Obsd frequencies		Calcd frequencies
	Raman	Infrared	
ν_2, 18–18–18	664[b]	664.3	664.7[c]
ν_2, 18–16–18	671	671.8	672.9
ν_2, 18–18–16	682	681.5	680.7
ν_2, 16–16–18	688	688.7	688.9
ν_2, 16–18–16	698	697.4	695.8
ν_2, 16–16–16	704[b]	704.5	705.2
ν_3, 18–18–18	983	982.8	981.7
ν_3, 18–18–16	*d*	992.0	991.2
ν_3, 16–18–16	*d*	1006.5	1006.5
ν_3, 18–16–18	*d*	1017.1	1017.5
ν_3, 16–16–18	*d*	1026.2	1026.2
ν_3, 16–16–16	1039	1040.0	1041.4
ν_1, 18–18–18	1042	1044	1041.3
ν_1, 18–18–16	1061	*d*	1061.7
ν_1, 18–16–18	1074	*d*	1070.8
ν_1, 16–18–16	1074	*d*	1077.1
ν_1, 16–16–18	1091	*d*	1091.4
ν_1, 16–16–16	1104	1105	1104.7

[a] Frequencies calculated using C_s potential function are listed for comparison. [b] Frequency measurements from 55% ^{18}O enriched ozone sample. Raman ν_2 of pure $^{16}O_3$ measured at 701 (4880 Å) and 703 cm^{-1} (5145 Å). [c] Input data for frequency calculations were infrared bands for ν_2 and ν_3 and Raman bands for ν_1, see text. [d] Too weak to be observed.

(17) D. J. Gardiner and J. J. Turner, *J. Mol. Spectrosc.*, **38**, 428 (1971).

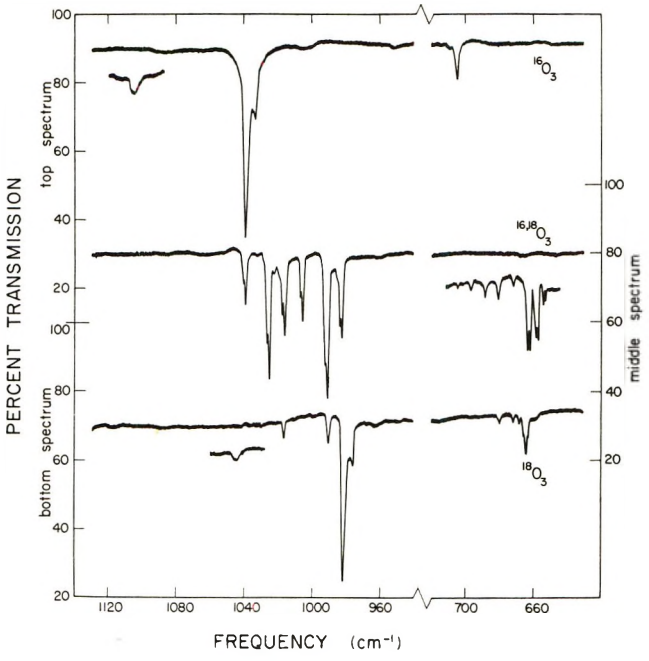

Figure 2. Infrared spectra recorded in the 630–720- and 940–1130-cm^{-1} spectral regions for isotopic samples of ozone in argon (Ar/O_3 = 200/1) deposited at 15°K: top spectrum $^{16}O_3$; middle spectrum $^{16,18}O_3$, 55% oxygen-18; bottom spectrum, $^{18}O_3$, 93% oxygen-18. Inset spectra were recorded from thicker samples.

The Raman assignments to ν_3 were measured in the pure isotopic experiments.

Infrared Spectra. Typical infrared spectra for three isotopic ozone samples in argon matrices (M/R = 200) are illustrated in Figure 2. The sharp, intense ν_3 of $^{16}O_3$ is immediately obvious at 1039.6 cm^{-1} as the most prominent feature of the infrared spectrum; a weak shoulder is resolved at 1033.5 cm^{-1}, which is probably due to a matrix site splitting. The weaker band at 704.4 cm^{-1} is assigned to ν_2; the very weak, broader feature at 1105 cm^{-1} in the indented spectrum recorded from a thicker sample is likely the argon matrix ν_1 fundamental of $^{16}O_3$. An estimate of the relative infrared intensities of $\nu_3/\nu_2/\nu_1$ is 70/7/1.

Similarly, the very intense, sharp band in the $^{18}O_3$ spectrum at 982.8 cm^{-1} and the resolved shoulder at 976.8 cm^{-1} are assigned to ν_3 of $^{18}O_3$. Great care was taken to minimize CO_2 in this experiment to avoid ambiguity with ν_2 of $^{18}O_3$; the weaker band at 664.3 cm^{-1} is assigned to ν_2 of the $^{18}O_3$ species. The very weak, broad feature at 1044 cm^{-1} in the indented trace is attributed to ν_1 of $^{18}O_3$.

The middle spectrum in Figure 2 was recorded of an ozone sample prepared from 55% oxygen-18 enriched O_2. The sharp six-component multiplet is appropriate for a nondegenerate vibration of a three oxygen atom species, with two equivalent oxygen atoms, namely, C_{2v} ozone. The relative intensities of the six bands are appropriate for the statistical weights of the isotopes as assigned in Table I. The spectra of 55% ^{18}O enriched ozone clearly shows that the 1017-cm^{-1} absorption is more intense than the 1006-cm^{-1} band; since the 18–16–18 isotope has a greater statistical weight, the 1017-cm^{-1} band is assigned to ν_3 of 18–16–18 ozone and the 1006-cm^{-1} band to ν_3 of 16–18–16 ozone. Further statistical evidence supporting this assignment is seen in the 93% ^{18}O enriched ozone spectrum, where the 1017-cm^{-1} feature was the only one of these two bands detected, as is shown in the bottom spectrum of Figure 2. Note that the 18–18–16 component is double the intensity of the 18–16–18 feature.

The present spectra show six clearly resolved ν_3 isotopic components for the scrambled ozone isotopes as expected. In recent discharge experiments, Brewer and Wang[6] passed xenon containing $^{16}O_2$ and $^{18}O_2$ through a microwave discharge and trapped the effusing products at 20°K. These workers resolved only four isotopic bands; the 18–16–18 and 18–18–16 ν_3 components were missing. Clearly, matrix deposition of presynthesized ozone, as in the present work, produces better resolved, sharper spectra.

The bending mode region was examined after depositing more $^{16,18}O_3$ sample; the spectrum is inset from the middle spectrum of Figure 2. Also present in this scan are traces of $C^{16,18}O_2$ causing the trio of doublets centering at 663, 658, and 653 cm^{-1}. The CO_2 doublet at 663 obscures ν_2 of $^{18}O_3$ in this spectrum. The five remaining bands are assigned to ν_2 of the scrambled ozone isotopes in Table I. It is important to note that the two central features are the most intense components; hence, these bands must be assigned to the most abundant isotopes, the unsymmetrical species 16–16–18 and 16–18–18.

Weak bands in the $^{16}O_3$ spectrum at 2109 cm^{-1} and in the $^{18}O_3$ spectrum at 1997 cm^{-1} (not shown in Figure 2) are assigned to the $\nu_1 + \nu_3$ combination band of $^{16}O_3$ and $^{18}O_3$, respectively.

The same ozone isotopic species were studied in nitrogen matrices. For the $^{16}O_3$ isotope ν_1, ν_2 and ν_3 were observed at 1109, 704.5, and 1042.5 cm^{-1}, respectively. In the $^{16,18}O_3$ nitrogen matrix spectrum, the ν_3 components were observed 3.0 cm^{-1} higher than the corresponding argon matrix isotopic frequencies.

Potential Constants. The vibrational assignments listed in Table I provide ample basis for normal coordinate calculations for the isotopic ozone molecules. The force constant adjustment program FADJ written by Schachtschneider was used for matrix calculations which were performed in the usual Wilson FG-matrix format.

First, the four symmetrical isotopes were analyzed in C_{2v} symmetry by factoring the secular equation accordingly. Since the ν_1 Raman band at 1074 cm^{-1} was not resolved into 16–18–16 and 18–16–18 isotopic components, frequencies of 1078 and 1070 cm^{-1}, respectively, were used for these assignments. Raman bands for ν_1 and infrared frequencies for ν_2 and ν_3

were used as input data to calculate potential constants. The potential constants obtained in symmetry coordinates are listed in Table II; their internal coordinate counterparts are readily obtained to be F_{O-O} = 5.829 ± 0.100, $F_{O-O,O-O}$ = 1.664 ± 0.100, and $F_{O-O,\alpha}$ = 0.565 ± 0.054. These numbers can be compared to the results of the C_s calculations to follow.

Table II: Vibrational Potential Constants and Potential Energy Distribution for Isotopic Ozone Molecules[a]

Potential constants		Potential energy distribution, $^{16}O_3$ ν_1	ν_2	ν_3
	C_{2v} Symmetry. Four Isotopes			
F_{sym}	= 7.493 ± 0.091[b]	0.988[c]	0.054	0.000
$F_{sym,\alpha}$	= 0.800 ± 0.050	−0.169	0.086	0.000
F_{α}	= 2.036 ± 0.015	0.181	0.860	0.000
$F_{antisym}$	= 4.166 ± 0.010	0.000	0.000	1.000
$\Delta\nu$	= 0.8 cm^{-1}			
	C_s Symmetry. Six Isotopes			
F_{O-O}	= 5.879 ± 0.098[b]	0.409[c]	0.015	0.684
$F_{O-O,O-O}$	= 1.662 ± 0.039	0.219	0.012	−0.398
$F_{O-O,\alpha}$	= 0.483 ± 0.076	−0.092	0.038	−0.006
F_{O-O}	= 5.778 ± 0.074	0.360	0.029	0.713
$F_{O-O,\alpha}$	= 0.520 ± 0.054	−0.078	0.048	−0.006
F_{α}	= 2.038 ± 0.012	0.182	0.860	0.001
$\Delta\nu$	= 0.7 cm^{-1}			

[a] R_{O-O} = 1.278, O–O–O angle = α = 116.8°. [b] Units: stretching, mdyn/Å; stretch–bend, mdyn/rad; bend, mdyn Å/rad^2; error limits provided by program FADJ. [c] Fraction of ν_1 in indicated force constant.

Second, calculations were done for all six ozone isotopes using intenal coordinates in C_s symmetry. The six force constants determined are given in Table II; calculated frequencies are listed in Table I for each isotopic assignment. The frequency fit is excellent ($\Delta\nu$ = 0.7 cm^{-1}) for 18 vibrational frequencies. Anharmonicity is likely the major contribution to this discrepancy. When average isotopic force constants are used to calculate isotopic frequencies, the effect of normal cubic contributions to anharmonicity is to make calculated lighter isotopic values exceed the observed while calculated heavier isotopic values fall below the observed. Such is the case for these isotopic ozone calculations. It is of interest to compare the two F_{O-O} force constants and the two $F_{O-O,\alpha}$ force constants which, by symmetry, should be the same. These force constants agree, within the error limits of the calculations, for the ozone molecule with two equivalent oxygen–oxygen bonds. In fact, the average of the two F_{O-O} force constants obtained for C_s symmetry agrees exactly with the F_{O-O} obtained from symmetry coordinates.

In the only other report of ozone potential constants, Pierce determined vibrational potential constants from centrifugal distortion effects by requiring compatibility between the infrared vibrational and microwave rotational spectra for the $^{16}O_3$ isotope.[18] The potential constants of Pierce are in excellent agreement with the present values calculated from isotopic data. Pierce's values (converted to Table II units) were reported as follows: F_{O-O} = 5.70, $F_{O-O,O-O}$ = 1.52, $F_{O-O,\alpha}$ = 0.424, F_{α} = 2.09. The observed frequencies for the 16–18–16 and 16–16–18 isotopes are in good agreement with the values calculated by Pierce.[18]

Potential energy distributions, the fraction of each frequency contributing to each force constant, are also given in Table II for each potential function. It is clear that ν_1 contains a small amount of bending character; as would be expected, the symmetric ν_1 and ν_2 modes interact to a small degree. This is particularly evident in the unsymmetrical isotopes, which causes a rearrangement of mixed ozone ν_2 frequencies from the order predicted from diagonal valence angle bending G-matrix elements alone. Consistent with symmetry, ν_3 has negligible bending character, even for the unsymmetrical ozone isotopes.

Ozone Valence Angle. Matrix frequencies for antisymmetric vibrational fundamentals of C_{2v} molecules have been widely used in recent years to calculate bond angles for these molecules. Since ν_3 is alone in its antisymmetric irreducible representation, in principle the valence angle can be calculated directly from the fundamental frequencies. The ν_3 assignments reported here for the four symmetrical ozone isotopes provide a good test of the angle calculation procedure, since the ozone valence angle is accurately known from microwave spectra.

The 16–16–16/18–18–18 isotopic frequency ratio cannot be used to calculate the ozone valence angle because the G-matrix elements contain a single isotopic mass, and hence, the angular dependence cancels, leaving a frequency ratio depending only on mass. Using the four combinations of symmetrical isotopes 16–18–16/16–16–16, 18–16–18/18–18–18, 18–16–18/16–16–16, 16–18–16/18–18–18, the ν_3 assignments listed in Table I produce the ozone valence angle cosines −0.32188, −0.30987, −0.55349, and −0.56827, respectively. These cosine values place the ozone valence angle lower limit at 108.4 ± 0.4° and the upper limit at 124.1 ± 0.5° with an average value of 116.3°. As has been discussed previously for SO_2 isotopic calculations, the upper limit and lower limit average represents an excellent determination of the bond angle for isotopes whose anharmonicities are nearly the same.[19] The 116.3 ± 4° bond angle for ozone determined from

(18) L. Pierce, *J. Chem. Phys.*, **24**, 139 (1956).

(19) M. Allavena, R. Rysnik, D. White, V. Calder, and D. E. Mann, *ibid.*, **50**, 3399 (1969).

argon matrix isotopic ν_3 frequencies is in excellent agreement with the 116.8 ± 0.5° microwave value.[20]

Hence, reliable angles can be calculated from ν_3 matrix frequencies. Clearly, the precision of these calculations depends upon accurate frequency measurement and isotopic anharmonicities being nearly the same. It is also helpful to have data for both terminal and central atom isotopic substitutions.

Conclusions

The vibrational fundamentals of ozone in argon matrices are in very good agreement with gas-phase values. The intense infrared mode ν_3 is two wave numbers lower in the matrix phase; the bending mode ν_2 occurs 2–3 cm^{-1} higher. The intense Raman active fundamental ν_1 agrees within one wave number with gas-phase values. It is interesting to note the extraordinary infrared intensity of ν_3 and weakness of ν_1 of ozone and the complete reversal of this intensity relationship in the Raman spectrum.

The technique of laser-Raman matrix isolation spectroscopy is useful for obtaining Raman spectra of relatively small amounts of sample molecules. For photolytically unstable molecules such as ozone, the matrix cage apparently retards photodecomposition such that excellent Raman spectra of the trapped molecule can be obtained.

Acknowledgments. The authors gratefully acknowledge financial support for this research by the National Science Foundation under Grant No. GP-28582 and a Governor's Fellowship for R. C. S., Jr. We acknowledge helpful discussions with Dr. Alfred Arkell on ozone synthesis.

(20) R. H. Hughes, *J. Chem. Phys.*, **24**, 131 (1956).

Influence of Internal Motion on the Carbon-13 Relaxation Times of Methyl Carbons

by James R. Lyerla, Jr., and David M. Grant*

Department of Chemistry, University of Utah, Salt Lake City, Utah 84112 *(Received May 1, 1972)*

Publication costs assisted by the National Institutes of Health

The carbon-13 spin–lattice relaxation times, T_1, and $^{13}C-\{^1H\}$ nuclear Overhauser enhancements have been determined at 38° for 14.1 and 23.5 kG fields for various methyl carbons subject to internal reorientational motion. The contributions of the C–H dipolar and spin–rotation mechanisms to T_1 have been separated from the overall relaxation rate. The influence of methyl internal rotation on the C–H dipolar and spin–rotation relaxation rates has been discussed and C–H dipolar rates have been used to estimate the magnitude of methyl rotational barriers.

Introduction

The use of nuclear magnetic relaxation times as a means of investigating molecular dynamics in liquid systems has been well established.[1,2] Although the precise details of the microdynamic behavior of the liquid are not readily available from these relaxation data,[3] the results do allow semiquantitative evaluation of the molecular motion. While the majority of reports relating relaxation times to a system's dynamics have been carried out *via* proton magnetic resonance, several recent studies have focused on the determination of carbon-13 spin–lattice relaxation times (T_1).[4-12] In particular, work from this laboratory[7-12] has concentrated on simple molecular systems with the purpose of elucidating the relaxation mechanisms governing ^{13}C relaxation. By separating the C–H dipolar part from the overall ^{13}C relaxation rate, these workers have

(1) N. Bloembergen, E. M. Purcell, and R. V. Pound, *Phys. Rev.*, **73**, 679 (1948).

(2) J. S. Waugh in "Molecular Relaxation Processes," Academic Press, London, 1966.

(3) W. T. Huntress, Jr., *J. Phys. Chem.*, **73**, 103 (1969).

(4) K. T. Gillen, M. Schwartz, and J. H. Noggle, *Mol. Phys.*, **20**, 899 (1971).

(5) D. Doddrell and A. Allerhand, *J. Amer. Chem Soc.*, **93**, 1558 (1971).

(6) H. Jaeckle, U. Haeberlen, and D. Schweitzer, *J. Magn. Resonance*, **4**, 198 (1971).

(7) K. F. Kuhlmann, D. M. Grant, and R. K. Harris, *J. Chem. Phys.*, **52**, 3439 (1970).

(8) T. D. Alger, S. W. Collins, and D. M. Grant *ibid.*, **54**, 2820 (1971).

Table I:

Molecule	T_1 (14 kG), sec	T_1 (23 kG), sec	η_{CH} (14 kG)	η_{CH} (23 kG)	T_{1d}, sec	T_{1o}, sec
$(CH_3)_2SO$	6.4 ± 0.4	6.7 ± 0.3	1.68 ± 0.07	1.69 ± 0.10	7.8 ± 0.6	42.9 ± 3.1
$(^{13}CH_3)_2CO$	17.3 ± 0.8	17.3 ± 1.0	0.73 ± 0.06[a]	0.78 ± 0.05[a]	45.3 ± 3.4	28.1 ± 2.1
$^{13}CH_3CCl_3$	11.5 ± 0.8	11.5 ± 0.9	1.60 ± 0.12	1.62 ± 0.09	14.3 ± 1.4	59.1 ± 6.0
$(^{13}CH_3)_3CCl$	11.6 ± 1.1	12.9 ± 0.5	1.70 ± 0.13	1.82 ± 0.15	13.7 ± 1.6	104 ± 12.5
$^{13}CH_3COOCH_3$[b]					51.4 ± 8.0	24.6 ± 3.7
$CH_3COO^{13}CH_3$[b]					37.6 ± 4.2	33.1 ± 3.7

[a] This value of η_{CH} is in agreement with that reported ($\eta \cong 0.7$) by G. LaMar [*J. Amer. Chem. Soc.*, **93**, 1040 (1971)] using a different technique. [b] Results taken from ref 12.

discussed the correlation times obtained in terms of motional features of these liquid systems.[9-12] Herein are reported ^{13}C proton-decoupled spin–lattice relaxation times and nuclear Overhauser enhancements (NOE) for the methyl carbons of molecules in which the methyl group is restricted in its internal reorientation. From this information the rotational barriers may be determined.[10-11]

Experimental Section

The compounds under study (methyl sulfoxide, acetone, *tert*-butyl chloride, and methylchloroform) were spectral quality and used without further purification. Samples were degassed using standard freeze–pump–thaw cycles before being sealed. T_1 and NOE values were determined on a Varian AFS-60 spectrometer operating at 14.1 kG equipped with noise-modulated proton decoupling. In order to investigate any field dependence of the relaxation rate, T_1 and NOE values were also determined on a Varian XL-100-15 spectrometer operating at 23.5 kG and also equipped with noise-modulated proton decoupling. Operating temperature of the AFS-60 probe under the experimental conditions was 38 ± 2° and the XL-100-15, equipped with variable-temperature controller, was adjusted to have the same probe temperature. NOE determinations and relaxation measurements made *via* adiabatic fast passage techniques have been previously described.[7-9]

Results

Reported in Table I are the ^{13}C T_1 values and $^{13}C-\{^1H\}$ NOE enhancement factors,[9] η_{CH}, of the various methyl carbons. The data represent an average of at least three determinations of each parameter. The close agreement of both parameters at the two different fields indicates negligible contributions from field-dependent mechanisms to the ^{13}C relaxation process. The average values of T_1 and η_{CH} at the two fields were used in the analysis which follows. While T_1 and NOE values individually provide some qualitative information, their combination allows separation of the relaxation mechanisms into the dipole–dipole and all other processes and these separate contributions may then be treated quantitatively in accordance with the approach of Kuhlmann, Grant, and Harris,[7] *i.e.*

$$\frac{1}{T_1} = \frac{1}{T_{1d}} + \frac{1}{T_{1o}} \tag{1}$$

$$T_{1d} = \gamma_H T_1 / 2\gamma_C \eta_{CH} \tag{2}$$

where in the extreme narrowing limit γ_H and γ_C are the respective magnetogyric ratios of the proton and carbon. The relaxation times corresponding to the C–H dipolar mechanism is given by T_{1d}, and T_{1o} characterizes the time for all other mechanisms which in the cases studied here appear to be dominated by the spin–rotation term. T_{1d} and T_{1o} have been evaluated and are reported in Table I. Also included are the T_{1d} and T_{1o} values for the methyl and methoxy carbons of methyl acetate as determined elsewhere.[12] As both of these carbons are subject to energy barriers to internal motion, they are pertinent to the subsequent discussion.

Discussion

A. Dipolar Relaxation. Assuming that intermolecular C–H dipolar interactions are negligible, the value of T_{1d} characterizes the time scale for the C–H intramolecular dipolar interaction.[8] Neglect of the intermolecular contributions is an excellent approximation in considering the relaxation of carbons with directly attached protons owing to the r_{CH}^{-6} distance dependence of the dipolar coupling.[7,13] Formalistic treatment of the C–H intramolecular dipolar interaction for a methyl carbon yields

$$1/T_{1d} = \frac{3\gamma_H^2\gamma_C^2\hbar^2}{r_{CH}^6}\tau_{eff} \tag{3}$$

where τ_{eff} is an effective correlation time for molecular

(9) J. R. Lyerla, Jr., D. M. Grant, and R. K. Harris, *J. Phys. Chem.*, **75**, 585 (1971).

(10) K. F. Kuhlmann and D. M. Grant, *J. Chem. Phys.*, **55**, 2998 (1971).

(11) T. D. Alger, D. M. Grant, and R. K. Harris, *J. Phys. Chem.*, **76**, 281 (1972).

(12) T. D. Alger, D. M. Grant, and J. R. Lyerla, Jr., *ibid.*, **75**, 2539 (1971).

(13) A. J. Jones, D. M. Grant, and K. F. Kuhlmann, *J. Amer. Chem. Soc.*, **91**, 5013 (1969).

reorientation. While the τ_{eff} parameter is readily calculated once T_{1d} is known, separation of axial reorientation times from τ_{eff} requires an assumed model of molecular reorientation in the liquid. The model usually assumed is that of a sphere undergoing small-step angular diffusion.[14,15] However, more recent treatments by Woessner[16,17] and others[3,18] have accounted for the motional anistropy of most molecular systems by considering small-step diffusion of a rigid ellipsoid. Furthermore, Woessner[19] has considered the effects of internal motion upon the T_1 of a nucleus attached to a molecule of ellipsoidal shape.

One model of methyl internal reorientation is that of a methyl top undergoing random jumping among its three equivalent positions.[19,20] The ^{13}C relaxation rate arising from the C–H dipolar interaction for such a methyl carbon attached to a molecule whose symmetry is C_{3v} or greater is given in the Woessner construct by

$$1/T_{1d} = \frac{3\gamma_H^2\gamma_C^2\hbar^2}{2r_{CH}^6} D_\perp^{-1}\left[\frac{A_1}{6} + \frac{(A_2 + A_3)}{6 + R/D_\perp} + \frac{B_1}{5 + \sigma} + \frac{(B_2 + B_3)}{5 + \sigma + R/D_\perp} + \frac{C_1}{4\sigma + 2} + \frac{(C_2 + C_3)}{4\sigma + 2 + R/D_\perp}\right] \quad (4)$$

where $D_\perp$ is the rotational diffusion constant perpendicular to the symmetry axis, σ the ratio of the parallel to perpendicular diffusion parameters, the geometric constants A, B, and C are defined in ref 19, and R is $^3/_2$ the total jumping rate of the methyl from any of its three equivalent positions. Provided T_{1d}, $D_\perp$, and σ are available, eq 4 can be used to compute R; however, $D_\perp$ and σ are not known for most molecules and indeed for C_{2v} or lower symmetries an additional diffusion parameter must also be known to account for the nonequivalence in reorientational rates about all three principal axes. Nevertheless, estimates of R can be made provided certain simplifying assumptions are allowed. If the molecules are assumed to undergo isotropic reorientation (*i.e.*, $\sigma = 1$) then eq 4 reduces to

$$1/T_{1d} = \frac{3\gamma_H^2\gamma_C^2\hbar^2}{2r_{CH}^6} D^{-1}\left[\frac{A_1 + B_1 + C_1}{6} + \frac{A_2 + A_3 + B_2 + B_3 + C_2 + C_3}{6 + R/D}\right] \quad (5)$$

where D is now the overall isotropic diffusion rate. Values of D can be estimated from microviscosity theory[21] using temperature dependent density and viscosity data or from dielectric relaxation times. Values of D at approximately 38° have been calculated for the molecules under consideration and are given in Table II. Based on these D values and the T_{1d} times given in Table I, R values are then computed using eq 5 and are reported in Table II. It is acknowledged that eq 4 and 5 neglect coupling between the overall molecular motion and the internal process and also ignores the intermolecular effects on the internal vibrational modes.

Table II: Calculated Values of Methyl Internal Rotational Barriers from ^{13}C Dipolar Relaxation Rates

Molecule	$D \times 10^{-11}$, sec^{-1}	$R \times 10^{-11}$, sec^{-1}	V_0 (eq 6), kcal/mol	V_0 (lit),[e] kcal/mol
$(CH_3)_2SO$	0.35[a]	4.0	2.2[i]	3.07,[f] 2.87
$(CH_3)_2CO$	1.6[b]	29.9	0.92	0.76,[g] 0.78
$(CH_3)CCl_3$	1.3[c]	1.2	2.9	2.91
$(CH_3)_3CCl$	1.4[c]	0.5	3.5	4.3[h]
$(CH_3)COOCH_3$	1.4[d]	49.4	0.67	0.48
$CH_3COO(CH_3)$	1.4[d]	21.0	1.1	1.19[i]

[a] Value calculated using microviscosity calculations on density and viscosity data from H. L. Schläfer and W. Schaffernicht, *Angew. Chem.*, **72**, 618 (1960). [b] From microviscosity calculations using data from E. Hatscheck, "The Viscosity of Liquids," Van Nostrand, New York, N. Y., 1928, and also from ^{17}O nmr relaxation results: E. V. Goldammer and H. G. Hertz, *J. Phys. Chem.*, **74**, 3734 (1970). [c] Values from interpretation of dielectric relaxation results of S. Mallikarjun and N. E. Hill, *Trans. Faraday Soc.*, **61**, 1389 (1965). [d] Microviscosity calculations from data of W. J. Jones and S. T. Bouden, *Phil. Mag.*, **36**, 705 (1945). [e] Values represent gas-phase data and unless otherwise noted derive from W. Gordy and R. L. Cook in "Technique of Organic Chemistry," Vol. IX, A. Weissberger, Ed., Interscience, New York, N. Y., 1970, p 477. [f] H. Dreizler and G. Dendl, *Z. Naturforsch. A*, **20**, 1431 (1965). [g] J. D. Swalen and C. C. Costain, *J. Chem. Phys.*, **31**, 1562 (1959). [h] This is the value for *tert*-butyl fluoride to be compared with the value reported here for *tert*-butyl chloride. [i] This is the value for OCH_3 in formic acid to be compared with the value reported here for acetic acid. [j] This value is probably too low due to the larger value of R which results from the rather small D value, and the error in the estimate is probably greater than in the remaining entries.

The values of R can be related to methyl internal rotational barrier using a conventional relationship[10,11] of the form

$$R = R_0 e^{-V_0/RT} \quad (6)$$

where R_0 is $^3/_2$ the rate of reorientation for zero barrier and V_0 is the potential barrier in cal/mol. A convenient measure of R_0 is the rate of rotation of a methyl fragment in the gas phase $(kT/I_{Me})^{1/2}$ multiplied by the $^3/_2$ degeneracy factor. Using this calculated R_0 (1.3×10^{13} sec^{-1}) and the value of R from eq 5, one

(14) W. T. Huntress, Jr., *Advan. Magn. Resonance*, **4**, 1 (1970).
(15) N. Bloembergen, E. M. Purcell, and R. V. Pound, *Phys. Rev.*, **73**, 679 (1948).
(16) D. E. Woessner, *J. Chem. Phys.*, **37**, 647 (1963).
(17) D. E. Woessner, B. S. Snowden, Jr., and E. T. Strom, *Mol. Phys.*, **14**, 265 (1968).
(18) T. T. Bopp, *J. Chem. Phys.*, **47**, 3621 (1967).
(19) D. E. Woessner, B. S. Snowden, Jr., and G. H. Meyer, *ibid.*, **50**, 719(1969).
(20) N. Bloembergen, *Phys. Rev.*, **104**, 1542 (1956).
(21) K. T. Gillen and J. H. Noggle, *J. Chem. Phys.*, **53**, 801 (1970).

may obtain V_0 from eq 6. These calculated barriers are also reported in Table II. For comparative purposes some gas-phase microwave values of the barriers are also given. The agreement between the microwave values and those determined from T_{1d} measurements is generally quite good in view of the several approximations used in making the calculations. This result indicates a close relationship between methyl rotational barriers and ^{13}C spin–lattice relaxation times.

In all cases but that of DMSO, the D values from microviscosity and dielectric data are quite similar, thus the majority of differences in the $1/T_{1d}$ rates should arise from internal rotational effects on τ_{eff}. The effect of internal motion is to shorten τ_{eff} resulting in a less efficient C–H dipolar process and a larger value for T_{1d}. Indeed, acetone and the two carbons of interest in methyl acetate have longer T_{1d} values while the values in *tert*-BuCl and CH_3CCl_3 with their higher barriers are much reduced and their T_{1d} values are largely determined by the overall rotational motion. The T_{1d} in DMSO is also consistent with this model as its more efficient dipolar process relative to *tert*-BuCl and CH_3CCl_3 arises in its slower overall reorientation rate. Thus, these results provide evidence of a relationship between T_{1d} times for methyl carbons and the respective methyl internal barriers. Furthermore, the applicability of the method to liquids when most other methods are restricted to gases, further emphasizes the importance of this technique.

B. Spin–Rotation Mechanism. On the basis of previous studies[22] exhibiting negligible chlorine effects on carbon relaxation and as no field dependence of the T_1 results are discernible, the relaxation rate represented by the T_{1o} times is ascribed to the spin–rotation mechanism. This relaxation mechanism has not received the same attention as devoted to the dipolar process because of the paucity of data on spin–rotation interaction constants. The spin–rotation interaction arises from the coupling between the nuclear magnetic moment vector and the magnetic field associated with the angular momentum of the molecular system.[23–26] The coupling depends on the magnitude of the field generated and on a correlation time that governs the decay of the molecular angular momentum.

As in the case of τ_{eff} for the dipolar process, τ_{sr} must be regarded as some composite average decay time but is affected by internal motion in a manner which is opposite from that of τ_{eff}. To a first approximation it is necessary to consider only the effects of internal motion on the T_{1o} relaxation times. A lower barrier to methyl rotational motion will yield a comparatively longer spin–rotation correlation time and greater angular velocities thereby increasing the importance of the spin–rotation mechanism. Hence the lower the barrier to internal reorientation, the more efficient the spin–rotation process and the smaller the value of T_{1o}. Examination of the T_{1o} data in Table I and the corresponding barrier in Table II calculated from the T_{1d} values show exact correspondence to this anticipated trend. Furthermore, where the barrier is high, the T_{1o} relaxation time is inefficient compared to T_{1d}. This qualitative discussion stresses the significance of internal motion upon both the magnitude of relaxation times and the relative importance of various relaxation mechanisms.

One further result also supports the relative importance of the spin–rotation mechanism in low-barrier methyls. A very low nuclear Overhauser enhancement factor was found in nitromethane ($\eta_{CH} = 0.10$), in which the internal methyl barrier is only 6 cal/mol. Here the methyl governed by a sixfold barrier is for all practical purposes a free rotor. Thus, the spin–rotation interaction should dominate the relaxation process as the η_{CH} value for CH_3NO_2 indicates.

The above results demonstrate the degree to which rotational barriers influence the relative efficiencies of the C–H dipolar and spin–rotational relaxation processes in small molecules. Furthermore, this study indicates the significance of separating the contributions of the various relaxation mechanisms to T_1 in discussing molecular dynamics and illustrates how quantitative treatment is possible in the case of the dipolar data. As spin–rotation interaction constants become available similar information can be obtained from the spin–rotation data, which at this point can be treated only qualitatively.

Acknowledgment. This research was supported by the National Institutes of Health under Grant No. GM-08521.

(22) J. R. Lyerla, Jr., D. M. Grant, and R. D. Bertrand, *J. Phys. Chem.*, **75**, 3936 (1971).

(23) C. Deverell, *Mol. Phys.*, **18**, 319 (1970).

(24) D. K. Green and J. G. Powles, *Proc. Phys. Soc., London*, **85**, 87 (1965).

(25) C. H. Wang, D. M. Grant, and J. R. Lyerla, Jr., *J. Chem. Phys.*, **55**, 4674 (1971).

(26) J. R. Lyerla, Jr., D. M. Grant, and C. H. Wang, *ibid.*, **55**, 4676 (1971).

Chemical Ionization Mass Spectrometry Using Tetramethylsilane

by T. J. Odiorne, D. J. Harvey, and Paul Vouros*

The Institute for Lipid Research, Baylor College of Medicine, Houston, Texas 77025 *(Received April 4, 1972)*

Publication costs assisted by the National Institutes of Health

The use of tetramethylsilane [$Si(CH_3)_4$] as a reagent gas for chemical ionization mass spectrometry is described. The high-pressure spectrum of tetramethylsilane is dominated by the ion of mass 73 [$(CH_3)_3$–Si^+] which reacts as a Lewis acid with sample molecules. The high reactivity of the alkyl siliconium cations coupled with a low-energy release upon reaction results in most cases in the formation of an abundant quasimolecular ion (M + 73). Chemical ionization mass spectra of several types of compounds in tetramethylsilane are discussed and compared with the spectra obtained in other reagent gases.

The utility of chemical ionization for the identification of organic compounds has stimulated research into the use of a variety of reagent gases and gas systems. Different types of structural information can be obtained depending on the energetics of reaction between the reagent gas ions and the sample. For example, the ions from methane are considered to be strongly acidic and sufficient energy is available during the reaction of reagent ions with the sample to form a multiplicity, not only of quasimolecular ions (M + 1, M + 29, etc.), but also of fragment ions.[1] By contrast to this isobutane with its lower acidity releases less energy into vibrational modes upon reaction and consequently tends to produce predominantly quasimolecular ions and much less fragmentation.[2] In an extreme of low-energy release ammonia has been used to produce only the quasimolecular M + 1 ion,[3] but in many cases, due to the weak acidity of the ammonium cation, no chemical ionization spectra could be observed.

In an attempt to obtain spectra resulting from reactant ions of high reactivity and therefore increased sensitivity, but with moderate energy release, we have considered the use of alternative reagents. In recent years the expanded usage of trimethylsilyl derivatives has led to the detection of a variety of intramolecular rearrangement reactions involving the trimethylsilyl moiety.[4] Many of those intramolecular reactions have been shown to proceed *via* the interaction of a positively charged alkyl siliconium center with an electronegative site in the molecule.[5] Furthermore, in this laboratory we have also reported intermolecular vapor-phase reactions of trimethylsilyl positive ions with various compounds in the ion source of an LKB-9000 mass spectrometer. These reactions were observed under pressure conditions sufficient for the occurrence of bimolecular collisons.[6] The apparent high reactivity of the trimethylsiliconium ion has prompted us to pursue further investigations of this type of reaction under better controlled pressure conditions suitable for chemical ionization.

Experimental Section

Tetramethylsilane [$Si(CH_3)_4$], in view of previous evidence,[6] appeared to be a suitable choice as a precursor for the generation of trimethylsilyl cations. Its high volatility simplified introduction into the ion source of a modified CEC 21-110B mass spectrometer.[7] The ion source was connected to both a heated and an unheated glass inlet system. The tetramethylsilane was introduced *via* the latter. All spectra were recorded at source temperatures of ~180°, a repeller field of 10 V/cm, and ion accelerating voltage of 8 kV. The total filament emission current was 100 μA and the electron energy 400 V. The ion beam was focussed for maximum secondary ion intensity at m/e 131. Ion intensity data were collected in a source pressure range of 0.025–0.625 Torr.

High-resolution mass measurements were made for all the reported reagent gas ions at a source pressure of 0.15 Torr by mixing perfluorokerosene with the tetramethylsilane. The ions were photographically recorded and the photoplates processed and evaluated by standard techniques.

The samples were introduced *via* the standard solid probe inlet provided with the CEC 21-110B high-resolution mass spectrometer. Sample spectra were taken at a source pressure of 0.15–0.20 Torr. Spectra recorded

(1) M. S. B. Munson, *Anal. Chem.*, **43**, 13, 28A (1971), and references cited therein.

(2) F. H. Field, *J. Amer. Chem. Soc.*, **92**, 2627 (1970).

(3) M. S. Wilson, I. Dzidic, and J. A. McCloskey, *Biochim. Biophys. Acta*, **240**, 623 (1971).

(4) G. H. Draffan, R. N. Stilwell, and J. A. McCloskey, *Org. Mass Spectrom.*, **1**, 669 (1968).

(5) (a) J. Diekman, J. B. Thomson, and C. Djerassi, *J. Org. Chem.*, **34**, 3147 (1969); (b) P. D. Woodwate, R. T. Gray, and C. Djerassi, *Org. Mass Spectrom.*, **4**, 257 (1970); (c) E. White, S. Tsuboyama, and J. A. McCloskey, *J. Amer. Chem. Soc.*, **93**, 6340 (1971).

(6) D. J. Harvey, M. G. Horning, and P. Vouros, *Org. Mass Spectrom.*, **5**, 599 (1971).

(7) (a) J. H. Futrell and L. H. Wojcik, *Rev. Sci. Instrum.*, **42**, 244 (1971); (b) I. Djidic, D. M. Desiderio, M. S. Wilson, P. F. Crain, and J. A. McCloskey, *Anal. Chem.*, **43**, 1877 (1971).

Chart I

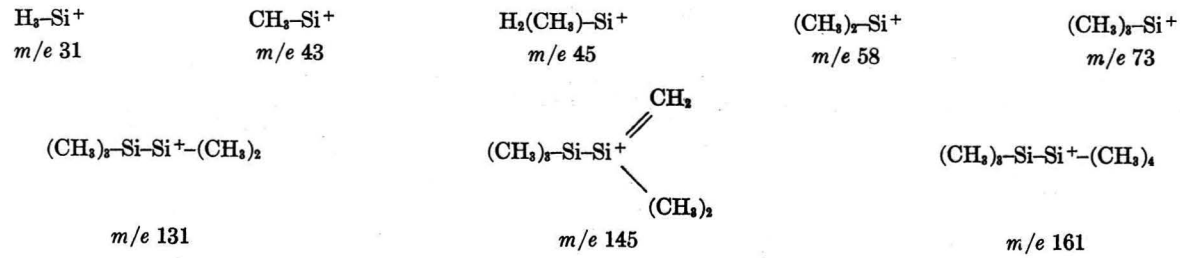

at higher source pressures up to 0.40 Torr exhibited no significant differences in relative ion intensities.

Results and Discussion

Ion Intensity Curves. The relative intensities of the primary and secondary fragment ions of tetramethylsilane as a function of pressure are shown in Figures 1 and 2, respectively. The abundances of all ions except for those of m/e 73 and 131 have been multiplied by a factor of 10. Ion curves below 0.025 Torr are simple extrapolations to zero and the extent of error in the measurements is $\pm 1\%$ Σ. The ion of m/e 73 dominates the spectrum of tetramethylsilane, in agreement with the data of Potzinger and Lampe,[8] and its relative abundance approaches 80% of the total ion current at source pressures between 0.100 and 0.300 Torr.

The elemental compositions of the principal ions found in the high-pressure spectrum of tetramethylsilane were determined by high-resolution mass measurements. Plausible structures corresponding to these compositions are shown in Chart I. The depiction of ions containing a pentavalent silicon (m/e 145 and 161) is analogous to the occurrence of ions containing a pentavalent carbon center (*e.g.*, CH_5^+) in the high-pressure spectrum of methane. In the case of silicon the pentavalent state is further stabilized by the availability of the d orbitals. Metastable evidence indicates the following transitions: m/e 73 → m/e 43; m/e 58 → m/e 31; m/e 73 → m/e 58; m/e 73 → m/e 45; m/e 45 → m/e 43; m/e 88 → m/e 73; m/e 161 → m/e 73; m/e 131 → m/e 73. The intensities of the metastable peaks followed the same pressure dependence as the abundances of the corresponding reactant ions.

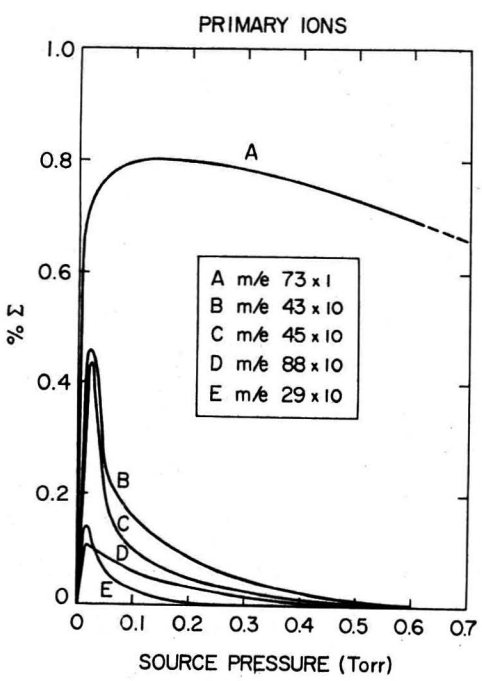

Figure 1. Ion intensity curves for primary ions in the mass spectrum of tetramethylsilane (relative abundance *vs.* source pressure).

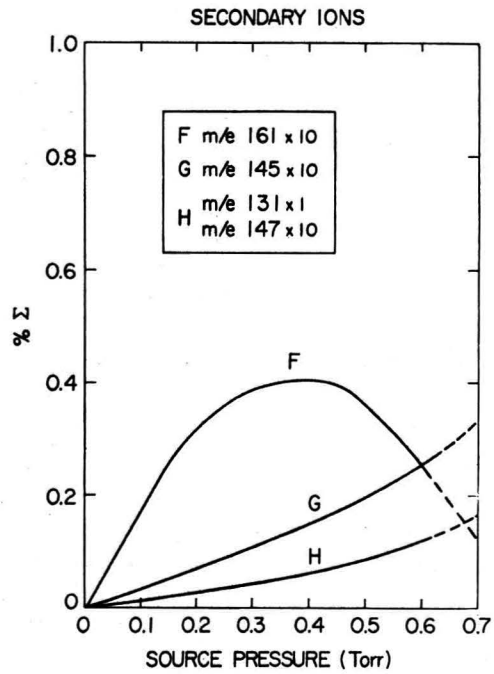

Figure 2. Ion intensity curves for secondary ions in the mass spectrum of tetramethylsilane (relative abundance *vs.* source pressure).

Chemical Ionization Mass Spectra in Tetramethylsilane. In an effort to evaluate the characteristics of tetramethylsilane as a reagent gas in chemical ionization mass spectrometry we have chosen a series of compounds containing a range of functional groups. Representative mass spectra for two of the compounds are shown in Figures 3 and 4. The general features of the mass spectra of the other compounds are summarized in Table I according to quasimolecular and fragment ions, and are discussed below in comparison to the spectra obtained with other commonly used reagent gases.

(8) B. Potzinger and F. W. Lampe, *J. Phys. Chem.*, **75**, 13 (1971).

Table I: Fragment Ion Intensities (% Σ)

Compound	$(M - 17)^+$	$(M)^+$	$(M + 1)^+$	$(M + 73)^+$	$(M + 131)^+$	$(M + 145)^+$	Total % Σ shown
Octadec-1-ene		3	2	81	2	1	89
5α-Androstan-17-one	12		3	74	4	4	97
5-Indanamine				73	3	18	94
Naphthalene		3	34	54	8		99
Quinoline			11	85	3		99

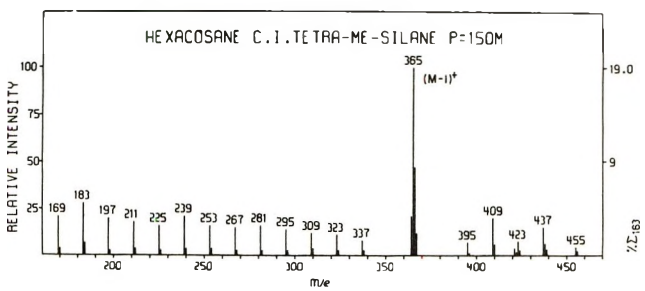

Figure 3. Chemical ionization mass spectrum of *n*-hexacosane with tetramethylsilane.

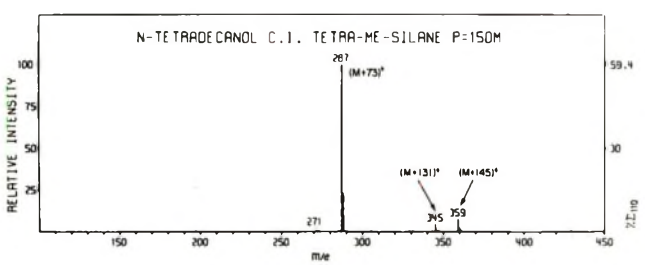

Figure 4. Chemical ionization mass spectrum of 1-tetradecanol with tetramethylsilane.

The spectrum of the hydrocarbon ($C_{26}H_{54}$) shown in Figure 3 is virtually identical with those obtained with methane and isobutane. The high abundance of the $(M - 1)^+$ ion (m/e 365) may be noted as well as the stepwise losses of methylene groups. The ions of mass greater than m/e 365 are quasimolecular ions corresponding to addition products.

The presence of an olefinic function (octadec-1-ene, Table I) results in a significant increase in the relative abundance of the quasimolecular ion when using tetramethylsilane rather than methane as the reagent gas. The relative abundance of $(M + 73)^+$ in tetramethylsilane is more than an order of magnitude higher than the $(M + 1)^+$ ion from either a C_{16} or C_{20} olefin in methane.[9] This is apparently due to the lower energy release during the reaction of the $(CH_3)_3$–Si^+ rather than the CH_5^+ ion with the olefin. The advantage of tetramethylsilane in chemical ionization mass spectra is reflected again in the abundance of the quasimolecular ion of a long chain alcohol as shown in Figure 4. The $(M + 73)^+$ ion constitutes ~75% of the total ion current whereas Field reports[10] that in the spectra of long-chain alcohols with isobutane the total ion current is distributed among a variety of fragment ions and principally those at $(M + 57)^+$, $(M - 1)^+$, and $(M - 17)^+$. When the spectrum of tetradecanol was recorded using methane as the reagent gas even more fragmentation was evident, with the principal peak occurring at m/e 197 [$(M - 17)^+$; 20% Σ].

In order to determine the utility of tetramethylsilane as a reagent gas for chemical ionization mass spectrometry of complex biological molecules we examined the mass spectrum (Table I) of 5α-androstan-17-one (**1**) whose structure is shown. The $(M + 73)^+$ ion constitutes 65% of the total ion current as compared to ~20% of the total ion current for the analogous (M

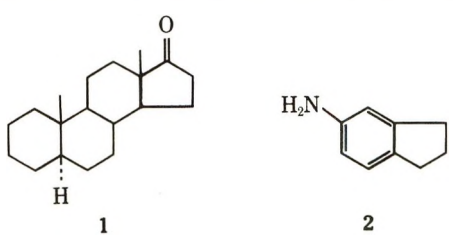

1 **2**

$+ 1)^+$ ion in methane. The $[(M + 1)–H_2O]^+$ ion is predominant (53% Σ) in the methane spectrum of this compound. An analogous ion at m/e 257 is also present (5% Σ) in the tetramethylsilane spectrum of **1** and it corresponds mainly to the elimination of trimethylsilanol $[(CH_3)_3SiOH]$ from $(M + 73)^+$. These fragmentations have been confirmed by metastable transitions and ^{18}O labeling of the carbonyl oxygen.

The overall stability of aromatic ring systems virtually excludes the possibility of fragmentation and as a result essentially all of the ion current is found in the quasimolecular ions. In that respect the mass spectra of naphthalene and quinoline are similar in tetramethylsilane (Table I), methane, and isobutane.[11] The nitrogen atom in quinoline further enhances the stability of $(M + 73)^+$ (85% Σ in quinoline *vs.* 54% Σ in naphthalene) by formation of a quaternary ammonium ion. The nitrogen atom may also be responsible for an increased reactivity which is furthermore reflected in the intensity (73% Σ) of the $(M + 73)^+$ peak in the spectrum of 5-indanamine (**2**). In the latter case we can

(9) F. H. Field, *J. Amer. Chem. Soc.*, **90**, 5649 (1968).
(10) F. H. Field, *ibid.*, **92**, 2672 (1970).
(11) M. S. B. Munson and F. H. Field, *ibid.*, **89**, 1047 (1967).

also see the formation of an appreciable amount of an $(M + 145)^+$ ion which presumably arises from the addition of two alkyl siliconium moieties.

Conclusions

The brief survey of compounds discussed above shows that tetramethylsilane, when used as a chemical ionization reagent gas, exhibits the advantageous properties of a high reactivity coupled with a low-energy release upon reaction. This low-energy release is evident in the similarity of spectra of compounds with different functional groups which are dominated by an abundant $(M + 73)^+$ quasimolecular ion. On the other hand in the absence of a well-defined reaction site the spectra obtained in tetramethylsilane are very similar to those obtained in methane or isobutane. It is significant to note here that it has been reported[12] that tetramethylsilane has been used successfully to study the chemical ionization mass spectra of trimethylsilyl derivatives of prostaglandins whereas neither ammonia or methane produced useable spectra. One disadvantage of tetramethylsilane is the large number of intense reagent ion peaks up to approximately mass 200. While this may effectively limit the sample molecular weight range which can be investigated, it may also be utilized to an advantage by serving as an internal mass marker which is in contrast to the difficulty of counting when using a reagent gas such as ammonia.

Acknowledgments. Financial assistance by the National Institutes of Health (Grants No. GM-13901, GM-16216, and GM-02055) is gratefully acknowledged.

(12) P. A. Leclercq, K. Hagele, B. Middleditch, R. Thompson, and D. M. Desiderio, 20th Annual Conference on Mass Spectrometry and Allied Topics, Dallas, Tex., June 1972, paper K4.

Correlation of Spectral Data for Halogen Atom Complexes with the Electron Donors Involved

by Rolf E. Bühler

Laboratory for Physical Chemistry, Swiss Federal Institute of Technology, 8006 Zürich, Switzerland
(Received December 28, 1971)

With the known data for transient charge-transfer complexes (CT complexes) with chlorine, bromine, and iodine atoms, the correlation of the CT energy (E_{CT}) with the ionization potential, I_D, of the electron donors is studied. It is shown that the pseudolinear dependency with slopes much less than one can be explained by the nonlinear, general solution for the simple resonance structure model $E_{CT} = (\gamma_0 I_D^2 - \gamma_1 I_D + \gamma_2)^{1/2}$. With an estimated value for the overlap integral S_{01} this correlation can be fitted to experimental data by the least-squares method, which then permits calculation of the resonance integral β_0 and an energy term C_1, which contains the electron affinity. From these three values (S_{01}, β_0, and C_1) I_D dependency of characteristic data for the ground state and excited state of the complexes can be derived. The resonance energies, the enthalpy of formation, the ionic character, and the dipole moments show strong dependences on I_D, but the derived transition moments, the oscillator strengths, and the extinction coefficients ϵ_{max} have little correlation with I_D. The calculated ϵ_{max} is compared to experimental values. It is found that the rather small differences are most likely due to the neglected environmental and structural effects.

1. Introduction

In recent years a large number of transient absorptions detected by pulse radiolysis and flash photolysis were interpreted as being due to charge-transfer complexes (CT complexes) with halogen atoms.[1] These absorption bands are quite broad and without structure (*e.g.*, ref 2–4). Their lifetimes cover the range from milliseconds to microseconds. To confirm these band assignments it was common to test the energy of maximum absorption (CT energy) for a linear dependence on the ionization potential I_D of the presumptive donors.[2–5] This test was derived from a two-structure resonance model calculated by second-order pertur-

(1) R. E. Bühler, *Radiat. Res. Rev.*, **4**, 233 (1972).

(2) T. A. Gover and G. Porter, *Proc. Roy. Soc., Ser. A*, **262**, 476 (1961).

(3) R. E. Bühler, *Helv. Chim. Acta*, **51**, 1558 (1968).

(4) J. M. Bossy, R. E. Bühler, and M. Ebert, *J. Amer. Chem. Soc.*, **92**, 1099 (1970).

(5) R. E. Bühler and M. Ebert, *Nature (London)*, **214**, 1220 (1967).

bation.[6-8] Although the correlations for the halogen atom complexes were close to linear, their slopes were as low as 0.51, 0.37, and 0.29 for the iodine, bromine, and chlorine atom complexes, respectively,[2-4] in contrast to the expected slope of one. Similar but less dramatic deviations are known for molecular complexes. It will be shown for the halogen atom complexes that the simple two-structure resonance model is still capable of explaining the apparent weaker dependency on I_D if the general solution of the secular determinant is used.[8,9] Since the quantum chemical terms involved correspond to estimated values, several I_D dependencies of complex properties were deduced: resonance energy, ionic character, dipole and transition moments, and extinction coefficients. The latter corresponds surprisingly well with the experimental values. The validity of such data will be discussed.

2. Correlation Formula from the Resonance Structure Theory

The simplified resonance model for a 1:1 complex originally introduced by Mulliken[6] describes the ground and excited electronic state (ψ_N and ψ_E) of a CT complex as a linear combination of a no-bond wave function (ψ_0) and a dative wave function (ψ_1): $\psi_N = a_0\psi_0 + a_1\psi_1$ and $\psi_E = b_0\psi_1 - b_1\psi_0$. Calculation by the second-order perturbation method yields the following, well-known correlation for the CT energy ($E_{CT} = E_E - E_N$) with the ionization potential of the donor I_D[7,8,10]

$$E_{CT} = I_D - C_1 + \frac{C_2}{I_D - C_1} \quad (1)$$

$C_1 = E_A - H_{11}' + H_{00}'$ and $C_2 = \beta_0^2 + \beta_1^2$[11] are assumed to be constant for a given electron acceptor, irrespective of the choice of donors. The condition for near linearity is

$$C_2 \ll (I_D - C_1)^2 \quad (2)$$

This implies a slope of one. Apparent linear dependency with slopes substantially smaller than one cannot be explained by eq 1. For some molecular complexes such deviations were explained by the general solution of the secular determinant[8]

$$E_{CT}^2 = (E_E - E_N)^2 = \frac{1}{(1 - S_{01}^2)^2}[(I_D - C_1)^2 + 4\beta_0\beta_1] \quad (3)$$

S_{01} is the overlap integral. The resonance integrals β_0 and β_1 are related through

$$\beta_1 = \beta_0 - S_{01}(I_D - C_1) \quad (4)$$

For the halogen atom complexes they differ at most by about 20% (calculated from the values in Table I).[12a] They therefore cannot be set equal. But for most cases it is acceptable to arbitrarily assume β_0 as constant. The following correlation formula then results

$$E_{CT}^2 = \gamma_0 I_D^2 - \gamma_1 I_D + \gamma_2 \quad (5)$$

with

$$\gamma_0 = (1 - S_{01}^2)^{-2} \quad (6)$$

$$\gamma_1 = (2C_1 + 4\beta_0 S_{01})\gamma_0 \quad (7)$$

$$\gamma_2 = (C_1^2 + 4\beta_0^2 + 4\beta_0 S_{01} C_1)\gamma_0 \quad (8)$$

The square of the CT energy therefore should be quadratically dependent on I_D.

Table I: Least-Squares Adjustment of Eq 5 to the CT Energy of Halogen Complexes

Complexes	S_{01}	β_0, eV	C_1, eV
Cl–π	0.1	−1.04	7.7
Br–π	0.1	−0.94	7.8
I–π[a]	0.1	−1.02	8.0
I–π,RX,ROH	0.1	−1.12	8.6
Br_2–π	0.1	−1.17	5.7
I_2–π	0.1	−0.78	5.2
I_2–n[b]	0.3	−2.14	8.2
Estimated error	±0.1	±0.03	±0.3

[a] Person[9] found similar data: $S_{01} = 0.2 \pm 0.1$, $\beta_0 = -1.0 \pm 0.1$ eV, and $C_1 = 8.0 \pm 0.5$ eV. [b] The values from Person[9,10] ($S_{01} = 0.3$, $\beta_0 = -2.5$ eV, and $C_1 = 6.9$ eV) differ from these values and do not fit the data by Yada, *et al.*[21]

If it is possible to fit a curve as given by (5) to the experimental data, then the three values S_{01}, β_0, and C_1 derived from such optimized curves will allow calculation of some characteristic properties of the complexes.[8]

(a) The resonance energies X_0 for the ground state and X_1 for the excited state are given by

$$X_{0,1} = \frac{1}{2(1 - S_{01}^2)}\{(I_D - C_1) \mp 2\beta_{0,1}S_{01} - [(I_D - C_1)^2 + 4\beta_0\beta_1]^{1/2}\} \quad (9)$$

(b) The ionic character of the CT band in the ground

(6) R. S. Mulliken, *J. Amer. Chem. Soc.*, **74**, 811 (1952).

(7) G. Briegleb, "Elektronen-Donator–Akzeptor Komplexe," Springer-Verlag, West Berlin, 1961.

(8) W. B. Person and R. S. Mulliken, "Molecular Complexes: A Lecture and Reprint Volume," Wiley, New York, N. Y., 1970.

(9) W. B. Person, *J. Chem. Phys.*, **38**, 109 (1963).

(10) R. S. Mulliken and W. B. Person, *Ann. Rev. Phys. Chem.*, **13**, 107 (1962).

(11) H_{00}', and H_{11}', are the bond energies of the hypothetical no-bond and dative structure, respectively; β_0 and β_1 are the corresponding resonance integrals; E_A = electron affinity of the electron acceptor.

(12) (a) R. E. Bühler, "Halogenatom-Charge-Transfer Komplexe, Vergleichende und theoretische Diskussion Pulsradiolytischer Resultate," Habilitationsschrift, Eidgenoss. Technische Hochschule, Zürich, 1970. (b) R. Foster, "Organic Charge-Transfer Complexes," Academic Press, New York, N. Y., 1969.

state ($\xi_N = a_1^2/(a_0^2 + a_1^2)$) and excited state ($\xi_E = b_0^2/(b_0^2 + b_1^2)$) can be calculated from the coefficient ratios of the linear combination of the wave functions ψ_0 and ψ_1.

$$a_1/a_0 = (2\beta_1)^{-1}\{(I_D - C_1) - [(I_D - C_1)^2 + 4\beta_0\beta_1]^{1/2}\} \quad (10a)$$

$$b_0/b_1 = (2\beta_1)^{-1}\{-(I_D - C_1) - [(I_D - C_1)^2 + 4\beta_0\beta_1]^{1/2}\} \quad (10b)$$

(c) The dipole moment of the CT complex in the ground state (μ_N) and excited state (μ_E) and the transition moment (μ_{EN}) can be calculated from μ_0 (the dipole moment of the no-bond structure) and μ_1 (the dipole moment of the dative structure).

$$\mu_N = (a_1^2 + a_0a_1S_{01})\mu_1 + (a_0^2 + a_0a_1S_{01})\mu_0 \quad (11)$$

$$\mu_E = (b_0^2 - b_0b_1S_{01})\mu_1 + (b_1^2 - b_0b_1S_{01})\mu_0 \quad (12)$$

$$\mu_{EN} = [a_1b_0 + (S_{01}/2)(a_0b_0 - a_1b_1)](\mu_1 - \mu_0) \quad (13)$$

with

$$\mu_1 = \mu_0 + e_0r_{AD} \quad (14)$$

(d) Assuming that the oscillator strength[7,12b] $f_{th} = (2\pi^2m_e/h^2e_0)E_{CT}\mu_{EN}^2$ [13] is identical with the optically defined one, the maximum extinction coefficient of the CT band can be calculated from the transition moment[7]

$$\epsilon_{max} = \frac{4\pi^2N_Le_0}{2.3\ 10^3hc}\frac{E_{CT}}{E_R - E_L}\mu_{EN}^2 \quad (15)$$

$E_R - E_L$ denotes the full half-width of the absorption band, which must be taken from the experiment.

3. CT Data

The correlation formula 5 was tested with all published CT energies on halogen atom π complexes in liquid systems. The data used are given in Tables II–IV.[14–20] For the purpose of comparison the following additional sets of data were analyzed in exactly the same way: (a) iodine atom complexes with mixed donors, including π donors, alkyl halides, and alcohols (Table II, this is based on the fact that for *molecular* iodine complexes these additional donors are found to

Table II: Experimental Data for Chlorine Atom CT Complexes in CCl_4 Solution

Donor = Solute	I_D, eV	λ_{max}, nm	E_{CT}, eV	Method[a]
Benzene	9.25	490	2.53	PR
Chlorobenzene	9.07	490	2.53	PR
o-Dichlorobenzene	9.06	485	2.56	PR
Bromobenzene	8.98	510	2.43	PR
Toluene	8.82	475	2.61	PR
Cumene	8.69	480	2.58	PR
tert-Butylbenzene	8.68	480	2.58	PR
o-Xylene	8.56	505	2.46	PR
Biphenyl	8.31	540	2.30	PR
Naphthalene	8.12	540	2.30	PR
1-Methylnaphthalene	7.96	550	2.26	PR
Anthracene	7.38	605	2.05	PR
Naphthacene	6.88	620	2.00	PR

[a] PR = pulse radiolysis, see ref 3 and 5

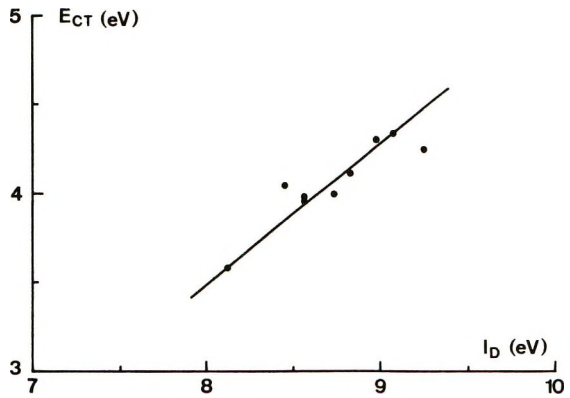

Figure 1. Br_2–π complexes. The following donors, taken from Table XII in ref 7 and listed with increasing I_D, were used: naphthalene, *p*-, *o*-, and, *m*-xylene, iodobenzene, toluene, bromobenzene, chlorobenzene, and benzene.

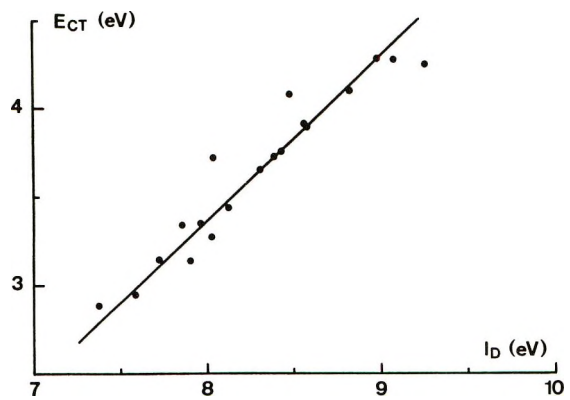

Figure 2. I_2–π complexes. The following donors, taken from Table XI in ref 7 and listed with increasing I_D, were used: anthracene, pyrene, chrysene, hexamethylbenzene, triphenylene, 1-methylnaphthalene, phenenantrene, durene, naphthalene, biphenyl, mesitylene, *p*-, *o*-, and *m*-xylene, toluene, styrene, bromobenzene, chlorobenzene, and benzene.

(13) e_0 and m_e are the charge and mass of an electron.

(14) (a) R. L. Strong, *J. Phys. Chem.*, **66**, 2423 (1962); (b) J. S. Bartlett, "Flash Photolysis of Bromine in Benzene," Thesis, Rensselaer Polytechnic Institute, 1962.

(15) J. M. Bossy, "Die Radiolyse von Brombenzol," Thesis No. 4490 Eidgenoss. Technische Hochschule, Zürich, manuscript in preparation.

(16) N. Yamamato, T. Kajikawa, H. Sato, and H. Tsubomura, *J. Amer. Chem. Soc.*, **91**, 265 (1969).

(17) V. I. Vedeneyev, L. V. Gurvich, V. N. Kondrat'yev, V. A. Medvedev, and Ye. L. Frankevich, "Bond Energies, Ionization Potentials, and Electron Affinities," E. Arnold, London, 1966.

(18) S. J. Rand and R. L. Strong, *J. Amer. Chem. Soc.*, **82**, 5 (1960).

(19) R. L. Strong, S. J. Rand, and J. A. Britt, *ibid.*, **82**, 5053 (1960).

(20) R. L. Strong and J. Perano, *ibid.*, **89**, 2535 (1967).

Table III: Experimental Data for Bromine Atom CT Complexes

Donor	I_D, eV	Solvent	Solute	λ_{max}, nm	E_{CT}, eV	Method[a]
Benzene	9.25	Benzene	Br_2	560	2.21	FP[c]
Benzene	9.25	Benzene	Br_2	560	2.21	FP[d]
Benzene	9.25	Benzene	Br_2	555	2.24	FP[e]
Benzene	9.25	Benzene	CBr_4	550	2.25	PR[d,f]
Benzene	9.25	Benzene	$CHBr_3$	540	2.30	PR[d,f]
Benzene	9.25	Benzene	CCl_3Br	535	2.32	PR[d,f]
Bromobenzene	8.98	Bromobenzene		560	2.21	PR[d,f]
Bromobenzene	8.98	Bromobenzene	Br_2	560	2.21	FP[d]
Toluene	8.82	Toluene	Br_2	575	2.15	FP[e]
Biphenyl	8.31	$CHBr_3$	Biphenyl	640	1.94	PR[d,f]
Naphthalene	8.12	$CHBr_3$	Naphthalene	680	1.82	PR[d,f]
Bromocyclohexane	9.9[b]	Bromocyclohexane		480	2.58	PR[d,f]

[a] PR = pulse radiolysis; FP = flash photolysis. [b] Estimated value by analogy to 1-bromobicyclo[2.2.1]hexane.[17] [c] Reference 14. [d] Reference 15. [e] Reference 16. [f] Reference 4.

Table IV: Experimental Data for Iodine Atom CT Complexes

Donor	I_D, eV	Solvent	Solute	λ_{max}, nm	E_{CT}, eV	Method[a]
Benzene	9.25	Benzene	I_2	500	2.48	FP[b]
Benzene	9.25	Benzene	I_2	495	2.50	FP[c,d]
Benzene	9.25	Benzene	I_2	465	2.67	FP[e]
Toluene	8.82	Toluene	I_2	520	2.39	FP[b]
Toluene	8.82	Toluene	I_2	515	2.41	FP[c]
o-Xylene	8.56	*o*-Xylene	I_2	570	2.18	FP[c,f]
p-Xylene	8.44	*p*-Xylene	I_2	520	2.39	FP[c]
Mesitylene	8.39	Mesitylene	I_2	590	2.10	FP[c]
Methanol	10.85	Methanol	I_2	390	3.18	FP[b]
Ethanol	10.50	Ethanol	I_2	390	3.18	FP[b]
Ethyl bromide	10.29	Ethyl bromide	I_2	395	3.14	FP[b]
Ethyl iodide	9.33	Ethyl iodide	I_2	490	2.54	FP[b]
Ethyl iodide	9.33	Cyclohexane	I_2 + ethyl iodide	475	2.60	FP[b]

[a] FP = flash photolysis. [b] Reference 2. [c] References 14a and 19. [d] Reference 18. [e] Reference 16. [f] Reference 20.

fit the π dependency[7]); (b) Br_2–π complexes, a selection of data taken from Table 12 in ref 7 (see Figure 1); (c) I_2–π complexes, a selection of data taken from Table 11 in ref 7 (see Figure 2); (d) I_2–n complexes, a set of primary, secondary, and tertiary amines as n donors from ref 21 (see Figure 2).

For all complexes the resulting values for S_{01}, β_0, and C_1 were used to calculate the characteristic complex data (eq 9–15).

4. Results and Discussion

4.1 CT Energy. In principle the correlation formula 5 should be fitted to the data by the least-squares method. Because the data are close to a linear dependence, the calculation of a quadratic regression involves small differences of very large numbers. The optimized values for γ_0, γ_1, and γ_2 therefore have very large errors, and it is impossible to give a reasonable interpretation. Instead, the overlap integral S_{01} (and γ_0) was estimated by simple quantum chemical method, and the problem of determining the best fit of eq 5 is reduced to a least-squares fit with two coefficients only. The resultant values for γ_1 and γ_2 then allow calculation of the energy term C_1 and the resonance integral β_0 for the various sets of data, with errors of a few per cent only (see below).

Person estimated the overlap integral S_{01} to be 0.1 for weak CT complexes (*e.g.*, I_2–π complexes) and 0.3 for strong complexes (I_2 complexes with amines).[9,22] In the present calculation for halogen atom complexes it was found that the fit to eq 5 is better for smaller values of S_{01}. The overlap integral was therefore

(21) H. Yada, J. Tanaka, and S. Nagakura, *Bull. Chem. Soc. Jap.*, **33**, 1660 (1960).

(22) R. S. Mulliken, C. A. Rieke, D. Orloff, and H. Orloff, *J. Chem. Phys.*, **17**, 1248 (1949).

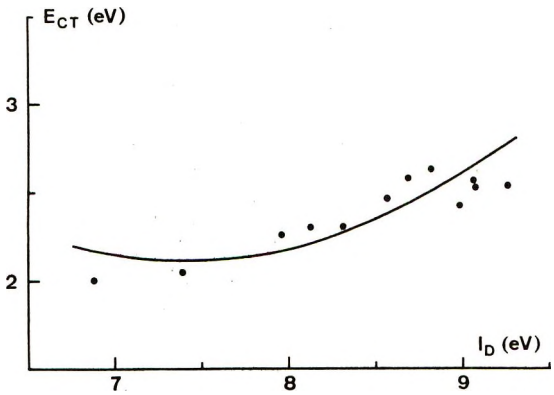

Figure 3. Chlorine atom CT complexes.

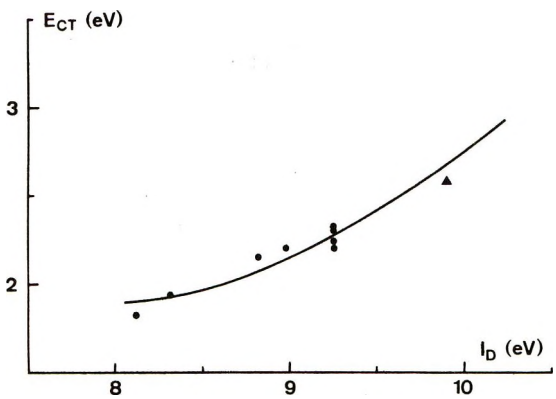

Figure 4. Bromine atom CT complexes. (The effect from the difference with and without bromocyclohexane, a non-π donor (▲), is negligible on the curve fitting.)

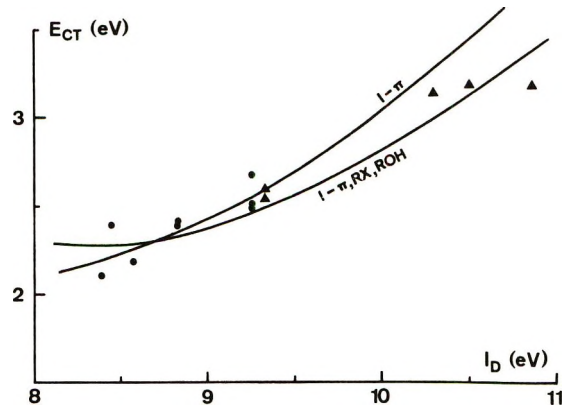

Figure 5. Iodine atom CT complexes. (● denotes the π donors).

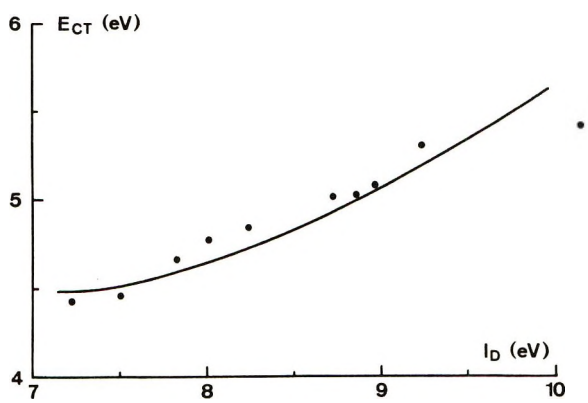

Figure 6. I_2–amine complexes. The following donors, taken from ref 21 and listed with increasing I_D, were used: tri-*n*-propylamine, triethylamine, trimethylamine, diethylamine, dimethylamine, *n*-butylamine, ethylamine, methylamine, pyridine, and ammonia.

chosen to be 0.1 ($\pm$0.1). The terms C_1 and β_0 are not very sensitive to S_{01}: the error limit of $\pm$0.1 affects the values for β_0 and C_1 by a few per cent only (Table V).

Table V: Sensitivity of β_0 and C_1 for Variations of S_{01}

Energy term affected	Effect[a] of ΔS_{01} = 0.1 for π complexes with Cl atoms	Br atoms	I atoms
β_0	0.02	0.02	0.03
C_1	0.23	0.22	0.27

[a] Measured in eV.

The results of the least-squares calculations are given in Table I. The corresponding curves for the halogen atom–CT complexes are shown in Figures 3–5 and for the halogen molecule complexes in Figures 1, 2, and 6. It is seen that the correlation formula 5 is able to explain the low I_D dependency of the experimental data.

The scatter of points relative to the theoretical curve is roughly comparable to the results with *molecular* complexes (see Figures 1 and 2 and also ref 7). For the weak *molecular* complexes (Figures 1 and 2) the optimized curve (eq 5) corresponds exactly to the usual linear relationship based on eq 1.

The three curves for halogen atom π complexes (Figures 3–5) are almost parallel. For a fixed donor the CT energy is decreasing from Cl complexes to I complexes to Br complexes. This unexpected sequence is primarily due to the low value of β_0 for bromine atom complexes.[12a] Often the resonance integral β_0 is considered representative of the complex strength. Consequently the Br complexes should be weaker than the Cl and I complexes. Such conclusions are based on the experience that the enthalpy of formation (ΔH_f) is often paralleled by the value of β_0.[7] But since ΔH_f is dependent on the donor (Table VI), contrary to β_0, the statement is relatively weak. From Table I and the definition of C_1 it can be seen that there are two main reasons for large values of C_1: (1) the electron affinity is large (as for the halogen atom complexes) or (2) strong complexes are involved, where the much smaller mean distance between the complex charge centers produces a large Coulomb term for $-H_{11}'$ (*e.g.*, I_2–n complexes). It is possible to estimate the value of C_1 by analogy to a

discussion by Person[9] by calculating the basic terms which define C_1 (*cf.* Table VII). The electron affinities are taken from the literature.[23,24] The energy H_{00}' must be derived from

$$\Delta H_f = H_{00}' + X_0 \qquad (16)$$

Known values for the enthalpy of formation are summarized in Table VI,[25] together with calculated values for X_0 (see Section 4.2). The mean values for H_{00}' from Table VI, are assumed to be valid for all similar complexes (see Table VII). The term $-H_{11}'$ is the sum of the Coulomb energy E_C and the valence energy E_V in the dative structure. E_V is estimated on the base that it must be smaller than the equivalent covalent bond energy by a fraction related to the differences between the covalent bond length and the complex distance r_{AD} (see Table VII). E_C can be calculated if the mean charge separation r_{AD} is known. r_{AD} was evaluated from the van der Waals distance and the few known values for solid-state complexes (Table VIII).[26-29] The average value for weak complexes was used to calculate E_C. If no solid-state values are known, a correction from the van der Waals distance of about -5% was chosen. For the strong complexes, where r_{AD} for the solid-state complexes is much smaller than the van der Waals value, a $+5\%$ correction was applied to the solid-state value. Table VIII lists the values used to calculate E_C. The sum of all the energy terms discussed so far yields the calculated values $C_{1,\text{calcd}} = E_A + E_C + E_V + H_{00}'$. In Table VII they are compared with the values $C_{1,\text{expt}}$ from the fit to the experimental data. It is seen that correspondence is within estimated error limits.

Table VI: H_{00}' from Experimental ΔH_f and Calculated X_0 (see Section 4.2)

Complexes	ΔH_f, eV	X_0, eV	H_{00}', eV	$\overline{H_{00}'}$, eV
		I_2–π		
Benzene	−0.06[b]	−0.14	0.08	
Chlorobenzene	−0.05[b]	−0.14	0.09	
Toluene	−0.08[b]	−0.15	0.07	
p-Xylene	−0.09[b]	−0.17	0.08	0.08 ± 0.02
Naphthalene	−0.08[b]	−0.18	0.10	
Hexamethyl-benzene	−0.16[b]	−0.20	0.04	
		I_2–n		
Ammonia	−0.22[b]	−1.08	0.86	
Pyridine	−0.35[b]	−1.31	0.96	
Ethylamine	−0.33[b]	−1.41	1.08	1.0 ± 0.2
Dimethylamine	−0.43[b]	−1.63	1.20	
Diethylamine	−0.43[b]	−1.45	1.02	
Triethylamine	−0.53[b]	−1.17	0.64	
		I–π		
Benzene	−0.09[c]	−0.53	0.44	0.48 ± 0.2[a]
o-Xylene	−0.19[d]	−0.71	0.52	

[a] Estimated error. [b] Reference 7. [c] Reference 25. [d] Reference 20.

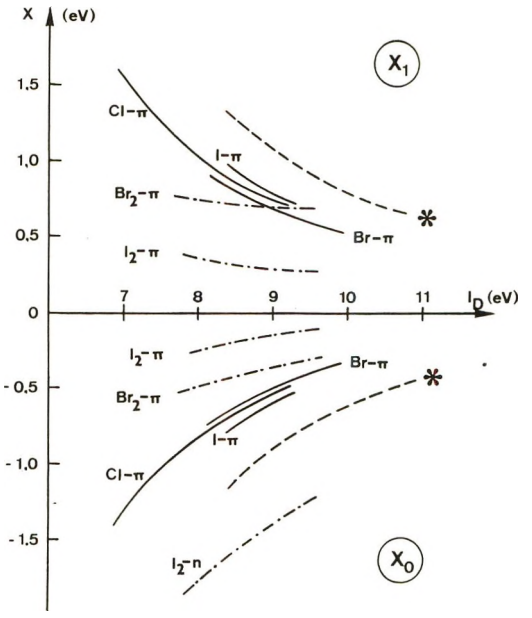

Figure 7. I_D dependence of the resonance energies for the halogen *atom* complexes in comparison with halogen *molecule* complexes: (*) denotes the dependence for iodine atom complexes with mixed donors (π, RX, and ROH); estimated relative error ±10%.

4.2. Resonance Energy and Enthalpy of Formation. The resonance energies X_0 and X_1 as calculated by eq 9 are shown in Figure 7. They have an estimated relative error of ±10%. The resonance energies for all halogen atom complexes are strongly dependent on I_D. They are intermediate between the weak π complexes of the halogen molecules and the strong complexes of I_2 with the amines (I_2–n). A comparison of the curves for (I–π) and (I–π, RX, ROH) demonstrate that it is not acceptable to relate different classes of donors. The same is true for the ionic character (Figure 8). The enthalpy of formation, ΔH_f, is related to the resonance energy X_0 by eq 16. H_{00}' was calculated from a number of known ΔH_f in Table VI. If one assumes that H_{00}' is not (or very little) dependent on I_D (see Table VI), then the mean values H_{00}' from Table 6 can be used to estimate ΔH_f through eq 16 and X_0. The results in Table IX demonstrate that the halogen atom complexes with donors of higher I_D (*e.g.*, benzene) do form weak

(23) B. L. Moiseiwitsch, *Advan. At. Mol. Phys.*, **1**, 61 (1965).
(24) J. J. DeCorpo and J. L. Franklin, *J. Chem. Phys.*, **54**, 1885 (1971).
(25) G. Porter and J. A. Smith, *Proc. Roy. Soc., Ser. A*, **261**, 28 (1961).
(26) O. Hassel and Chr. Rømming, *Quart. Rev., Chem. Soc.*, **16**, 1 (1962).
(27) O. Hassel and K. O. Strømme, *Acta Chem. Scand.*, **13**, 1781 (1959).
(28) O. Hassel and K. O. Strømme, *ibid.*, **12**, 1146 (1958).
(29) H. A. Bent, *Chem. Rev.*, **68**, 587 (1968).

Table VII: Comparison of Calculated and Experimental Values for C_1 (All Data in eV)

Complex	E_A	E_C (±0.1)	E_V	H_{00}'	$C_{1,calcd}$ (±0.5)	$C_{1,expt}$ (±0.3)
Cl–π	3.613 ± 0.003[a]	4.2	0.2	0.4 ± 0.2	8.4	7.7
Br–π	3.363 ± 0.003[a]	4.0	0.2	0.4 ± 0.2	8.0	7.8
I–π	3.063 ± 0.003[a]	3.7	0.2	0.4 ± 0.2	7.4	8.0
I_2–amine	2.6 ± 0.1[b]	3.9	1.0	1.0 ± 0.2	8.5	8.2
I_2–π	2.6 ± 0.1[b]	2.8	0.2	0.1 ± 0.02	5.7	5.2
Br_2–π	2.9 ± 0.1[b]	3.0	0.2	0.1 ± 0.02	6.2	5.7

[a] Reference 23. [b] Reference 24.

Table VIII: Mean Distance between Charge Centers of the Dative Structure

Complex	r_{AD}, Å (solid state)	r_{AD}, Å (van der Waals)	r_{AD}, Å[a] (liquid phase)
Cl–π	3.28[d,e]	3.65	3.45
Br–π	3.36[d,f]	3.80	3.60
I–π	3.7[g]	4.0	3.85
Br_2–π	4.57[d,f]	4.94	4.75
I_2–π	5.1[d,g]	5.3	5.2
I_2–amine	3.7[d]	5.0	3.9
Cl–RCl		3.80/3.60[b]	3.50
Cl–RBr		3.80/3.75[b]	3.55
Br–RBr		3.95/3.90[b]	3.70
I–RI		4.15/4.30[b]	4.00
I–RBr		4.15/4.10[b]	3.90
I–ROH	2.90[c]	3.55	3.20

[a] Estimated values as discussed in text. [b] First number for σ donor, second number for n donor. [c] Estimated value by analogy to values for similar O···X complexes.[26] [d] Reference 26. [e] Reference 27. [f] Reference 28. [g] Reference 29.

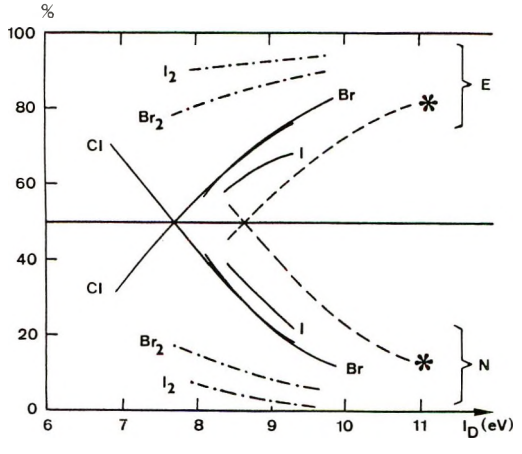

Figure 8. I_D dependence of the ionic character, ξ, for halogen *atom* and halogen *molecule* complexes with π donors: (*) denotes the dependence for iodine atom complexes with mixed donors (π, RX, and ROH); estimated relative error ±20%; N = ground state; E = excited state.

complexes, but with donors of low I_D they are much stronger. Here too, the I_D dependence of ΔH_f is weak for X_2–π complexes, intermediate for X–π complexes, and strong for the I_2–n complexes.

Table IX: Enthalpy of Formation (ΔH_f)

Complex	H_{00}', eV[a]	ΔH_f, eV: Benzene (I_D = 9.25 eV)	ΔH_f, eV: Naphthalene (I_D = 8.12 eV)
X–π	0.4 ± 0.2	0 to −0.1	∼−0.3
I_2–π	0.08 ± 0.02	∼−0.06	∼−0.1
Br_2–π	0.08 ± 0.02	∼−0.25	∼−0.34
		Pyridine (I_D = 9.23 eV)	$(C_2H_5)_2NH$ (I_D = 8.01 eV)
I_2–n	1.0 ± 0.2	∼−0.30	∼−0.7

[a] Values from Table VI.

4.3. Ionic Character. There is a very strong I_D dependence visible for the ionic character ξ_N and ξ_E as calculated by eq 10 for the X–π complexes (Figure 8). Contrary to the molecular X_2–π complexes the percentage of ionic character in the ground state can be very high. The fact that the curves for ξ_N and ξ_E even cross each other is related to the resonance model used and has already been explained by Mulliken for a similar case of $BF_3 \cdot NR_3$.[6] The crossover point is apparent if C_1 is larger than the lowest I_D of the donors involved.

4.4. Dipole Moments. With eq 10 and the normalizing conditions for a_0, a_1, b_0, and b_1 the dipole moments μ_N and μ_E are calculated by eq 11 and 12. The necessary mean distances between charge centers in the dative structure (eq 14) are given in Table VIII. The relative orientation of $\boldsymbol{\mu}_0$ and $\boldsymbol{\mu}_1$, or $\boldsymbol{\mu}_0$ and $\mathbf{r}_{AD}$ must be derived from the complex structure (μ_0 values are taken from ref 30), and can be discussed as follows.

(a) For *aromatic hydrocarbons* it is assumed that X (and X_2 with its axis) lies vertically above the ring plane. Since it is known that the X_2 axes are actually oblique to the ring planes, the derived values for molecular complexes will be slightly too large.

(b) The structure of complexes with *alkyl halides* is not known. RX can act as a n or σ donor. For the following calculation $\boldsymbol{\mu}_0$ and $e_0\mathbf{r}_{AD}$ are assumed to be parallel (with a right angle, the values would be about 10% smaller).

(30) R. D. Nelson, Jr., D. R. Lide, Jr., and A. A. Maryott, *Nat. Bur. Stand. (U. S.)*, NSRDS-NBS-10 (1967).

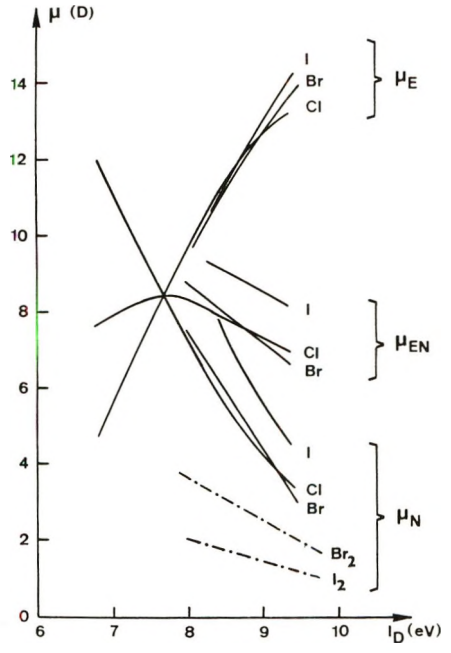

Figure 9. I_D dependence of the dipole and transition moments for π complexes: estimated relative error $\pm 20\%$.

(c) *Alcohols* are n donors. From known solid-state structures the angle between $\boldsymbol{\mu}_0$ and $e_0\mathbf{r}_{AD}$ must be assumed to be close to tetrahedral.[31,32]

The resulting dipole moments μ_N and μ_E are given in Figure 9. Obviously their principal I_D dependence is closely related to the ionic character and is again much steeper than for X_2–π complexes. Neither induced dipole moments nor solvent effects are included in these results. Particularly the latter can be large through dielectric screening. Weiss[33] proposed to correct any dipole moment by a factor ϵ_s^{-1} (ϵ_s = dielectric constant of the system). For most solvents this probably would overestimate the solvent effect.[34,35]

4.5. Transition Moments and the CT Band. The transition moments, calculated by eq 13 for the three halogen atom complexes, are also shown in Figure 9. Their dependences on I_D are relatively weak and do not differ very much from molecular halogen complexes (μ_{EN} for X–π complexes cover the range of *ca.* 6–9 D, for X_2–π complexes *ca.* 5–7 D, and for I_2–n complexes *ca.* 9–10 D). The solvent effect must be similar to the effect on the dipole moment. The calculated values therefore represent upper limits. The calculated oscillator strengths f_{th} and the extinction coefficients $\epsilon_{max,th}$, calculated from eq 15, are given in Tables X and XI. There is little I_D dependence, and the values for π complexes (atomic and molecular) are all very close. The calculated oscillator strength for the strong I_2–n complexes are abnormally high: *e.g.*, for I_2–pyridine, f_{th} = 1.4 and for I_2–diethylamine, f_{th} = 1.3. Both values are too large by definition and indicate that most calculated f_{th} values are too large. It is not surprising therefore that the calculated values for ϵ_{max} are also larger than the experimental values (Table XI). They differ by factors of 3–5. If a correction for the solvent effect could be applied, the correspondence of experimental and theoretical values for ϵ_{max} would be surprisingly good.

Table X: A Selection of Oscillator Strengths, f_{th}, for CT Bands of π Complexes

	Acceptor				
Donor	Cl	Br	I	Br_2	I_2
Benzene	0.37	0.32	0.49	0.44	0.33
Chlorobenzene	0.39				
o-Dichloro-benzene	0.39				
Bromobenzene	0.43	0.31			
Toluene	0.40		0.51		
Cumene	0.40				
o-Xylene	0.42		0.51		
Biphenyl	0.42	0.38			
Naphthalene	0.44	0.39		0.47	0.35
Mesitylene			0.52		

5. Conclusions

The correlation formula (eq 5) based on the very simple model with two-resonance structures is able to reproduce the experimental data within expected accuracy. Also, the derived extinction coefficients are in reasonable agreement with the experiments. It is concluded that for all halogen atom CT complexes the simple model is adequate enough to describe the correlation between the CT energy and the ionization potential of the donors, as it is for the molecular CT complexes. A generalized resonance structure theory[8] or some other improved theory probably does not improve such correlation studies, since the scatter of the experimental data, as it appears in Figures 1–6, is large and is mostly due to unknown factors like change of structure and influence of environment. To include such factors in the theory would make it impossible to derive a simple correlation of the CT energy with one variable only. Nevertheless, such E_{CT}–I_D correlation tests as discussed with eq 5 remain quite useful in kinetic spectroscopy as a test for assignments of transient absorptions to radical CT complexes with donors of a particular class. The calculated properties of the complexes are expected to be meaningful as in-

(31) P. Groth and O. Hassel, *Mol. Phys.*, **6**, 543 (1963).

(32) P. Groth and O. Hassel, *Acta Chem. Scand.*, **18**, 402 (1964).

(33) J. J. Weiss, *Phil. Mag.* [8], **8**, 1169 (1963).

(34) There are measurements[35] known, which indicate a solvent effect for benzene (ϵ_s = 2.28) of about 10%, whereas the ϵ_s^{-1} method would correct by about 50%.

(35) H. A. Stuart, "Molekülstruktur," Springer Verlag, West Berlin, 1967.

Table XI: ϵ_{max} for Halogen Atom CT Complexes

Complexes	Solvent	Dielectric constant	Full band width, cm^{-1}	ϵ_{max}, calcd, M^{-1} cm^{-1}	ϵ_{max}, expt, M^{-1} cm^{-1}
Cl–					
Benzene	CCl_4[f]	2.24[f]	6600 ± 600[a]	8,300 ± 30%	
Chlorobenzene			6700 ± 500[a]	8,600 ± 30%	
o-Dichlorobenzene			4000 ± 800[a]	14,000 ± 40%	
Bromobenzene			6500 ± 600[a]	9,800 ± 30%	
Toluene			6000 ± 500[a]	9,900 ± 30%	
Cumene			6000 ± 1000[a]	9,900 ± 35%	
o-Xylene			6400 ± 500[a]	9,700 ± 30%	
Biphenyl			4000 ± 1000[a]	15,000 ± 45%	
Br–					
Benzene	Benzene–bromoform	~2.9	5400 ± 500[c]	8,800	
Bromobenzene	Bromobenzene	5.40	5500 ± 500[d]	8,300	2600 ± 500[d]
Biphenyl	Bromoform	4.39	6000 ± 500[d]	9,400 ± 30%	
Naphthalene	Bromoform	4.39	7500 ± 500[d]	7,700	
Bromocyclohexane	Bromocyclohexane	~8	7500 ± 500[d]	5,300	
I–					
Benzene	Benzene	2.28	5700 ± 500[e]	12,700	2450[b]
Toluene	Toluene	2.39	7000 ± 500[e]	10,800 ± 30%	1950[b]
o-Xylene	*o*-Xylene	2.57	7000 ± 800[e]	10,800	2500[b]
Mesitylene	Mesitylene	2.28	5300 ± 500[e]	14,500	2900[b]

[a] Reevaluation of the data in ref 3. [b] These are mean values of all published data[19,12b,14a] (*cf.* ref 1). [c] Reference 3. [d] Reference 4. [e] Reference 19. [f] Solvent for all Cl complexes; value for all Cl complexes.

dicated by their relative error limits. The absolute values must be used critically. They are probably affected by systematic errors.

Acknowledgment. The author wishes to express his gratitude for the financial support by the Swiss National Funds.

Structure of Liquid Water. Statistical Thermodynamic Theory[1a,b]

by Arnold T. Hagler,[1c] Harold A. Scheraga,*

Department of Chemistry, Cornell University, Ithaca, New York 14850

and George Némethy

Rockefeller University, New York, New York 10021 *(Received February 16, 1972)*

A statistical thermodynamic treatment is given for a model of liquid water, which consists of a continuous distribution of cluster sizes in equilibrium. A partition function is written for this model, and the distribution of cluster sizes, the median cluster size, and the mole fraction of unbroken hydrogen bonds are calculated. The median cluster size is 11.2 at 0°, and at no temperature is there a significant number of large clusters (>60). The approximations made in the theory are analyzed in terms of their effects on the results and in relation to similar approximations made in other theories. The inapplicability of a two-state model to liquid water is also discussed in terms of the results obtained here.

I. Introduction

The purpose of this paper is twofold. The first is to propose and treat a model for the structure of liquid water in order to learn more about this substance. The second is to analyze and evaluate the nature and effects of the standard approximations which occur in both this and other theories of water.[2]

In this paper, we present a model for liquid water and formulate a partition function for this model. The partition function takes into account contributions from the shift in intramolecular frequencies associated with the breaking of hydrogen bonds, the volume dependence of the background potential which results in a volume-dependent hydrogen bond energy, and the internal entropy of clusters, which have been omitted from previous theories. In addition, the Percus–Yevick equation is used to calculate the configurational (translational) entropy of the liquid, which has caused great difficulty previously.

By making several simplifying assumptions, the partition function is evaluated and the thermodynamic properties and distribution of cluster sizes are calculated. The various contributions to the free energy, energy, and entropy are also calculated, enabling one to evaluate the importance of these terms as a function of temperature.

An analysis and evaluation is made of the nature of the approximations and of their effect on the results and of the range of applicability of the theory. The inapplicability of a two-state model to liquid water is also discussed in terms of the results obtained here, and a possible resolution of the difference between discrete and continuum theories is suggested in terms of this discussion.

Finally, other properties such as the radial distribution function, volume, and intermolecular spectrum are accounted for qualitatively in terms of the theory.

II. The Model

In the model for liquid water proposed here, it is assumed that water consists of a continuous distribution of all possible cluster sizes in equilibrium. We take cognizance of the views of Longuet-Higgins and Widom[3a] and Widom[3b] that the structure of liquids near the triple point is determined mainly by the repulsive forces and that the attractive forces give rise to a uniform background potential which in no way influences the molecular configuration but serves merely to keep the molecules together. With this view, these authors were successful in accounting for several observed thermodynamic properties of the inert gases at the triple point, although they could not account for the second derivative of the free energy. This approach alone is, of course, clearly not applicable without modification to water where the attractive forces (*i.e.*, basically a tetrahedral hydrogen-bonding potential) are very dependent on orientation and play a major role in determining the structure of water. However, we assume that this orientation-dependent hydrogen-bonding potential function results in cluster formation; *i.e.*, the effect of the hydrogen-bonding potential is taken into account by the assumption of the existence of clusters. We then assume that the overall structural arrangement of clusters in the liquid

(1) (a) This work was supported by research grants from the National Science Foundation (GB-28469X1) and from the National Institute of General Medical Sciences of the National Institutes of Health, U. S. Public Health Service (GM-14312); (b) presented, in part, before the Division of Colloid Chemistry at the 157th National Meeting of the American Chemical Society, April 1969, Minneapolis, Minn.; (c) NIH predoctoral fellow, 1966–1970.

(2) In general, other theories of water have a large number of adjustable parameters and treat the combinatorial factor in the partition function incorrectly; a review of these theories has been presented by A. Hagler, H. A. Scheraga, and G. Némethy, *Ann. N. Y. Acad. Sci.*, in press.

(3) (a) H. C. Longuet-Higgins and B. Widom, *J. Mol. Phys.*, **8**, 549 (1964); (b) B. Widom, *Science*, **157**, 375 (1967).

is determined mainly by the repulsive forces, with a uniform background potential serving to keep the clusters together as a liquid. In this way, we can evaluate the configurational integral and determine the configurational entropy.

The background potential will effectively reduce the energy of formation of the hydrogen bond in the liquid from its value in the vapor. To illustrate this, consider the rupture of all the bonds in ice and the conversion of the system to a vapor, on the one hand, and to a hypothetical liquid in which all bonds are broken, but in which there is a uniform background potential, on the other hand. If we attribute the total energy changes for both of these processes to the breaking of hydrogen bonds, we see that the difference in energy between breaking a bond in the liquid and in the vapor is just the background potential. The geometrical aspects of this cluster model are essentially the same as those proposed by Frank and Wen,[4,5] who assumed that water consists of a continuous distribution of "flickering clusters" in equilibrium.

A canonical partition function, $Z(N,V,T)$ is written for this model, where N, V, and T are the number of molecules in the system, the volume, and temperature, respectively, and the thermodynamic functions [the Helmholtz free energy F (taken here to be the same as the Gibbs free energy G), the internal energy U (taken here to be the same as the enthalpy H), the entropy S, and the constant-pressure heat capacity c_p] are computed from the usual statistical mechanical relations.[6-10]

III. The Partition Function[11]

For the present model of all possible cluster sizes in equilibrium, the canonical partition function is given by the sum over all coordinates and momenta characterizing the external and internal degrees of freedom of the clusters and over all possible distributions of cluster sizes subject to the constraint that the total number of molecules is equal to 1 mol. Thus, the partition function can be written as

$$Z(N_0,V,T;\{N_j\}) = \sum_{\{N_j\}} Q_{\text{ext}}(N_0,V,T;\{N_j\})Q_{\text{int}}(N_0,T,V;\{N_j\}) \quad (1)$$

at constant T and V, where N_0 is Avogadro's number, N_j is the number of clusters containing j water molecules, and $\{N_j\}$ is a vector (representing a distribution function of cluster sizes) whose jth component is N_j, with the constraint that $\Sigma_j jN_j = N_0$, and where Q_{ext} and Q_{int} are the partition functions for the external and internal degrees of freedom of the clusters, respectively. By definition (see section IVB), the hydrogen bond energy, which appears in Q_{int}, is dependent on volume, and hence we have written Q_{int} in eq 1 as a function of volume.

If the sum in eq 1 is replaced by its maximum term with respect to the distribution, we obtain

$$Z(N_0,V,T;\{N_j^*\}) = Q_{\text{ext}}(N_0,V,T;\{N_j^*\})Q_{\text{int}}(N_0,V,T;\{N_j^*\}) \quad (2)$$

where $\{N_j^*\}$ is the distribution of cluster sizes which maximizes the partition function and is, in fact, the equilibrium distribution sought here. For convenience, the asterisk will be omitted, but it should be understood that hereafter $\{N_j\}$ is the equilibrium distribution.

IV. Internal Partition Function

The internal partition function may be written as

$$Q_{\text{int}}(N_0,V,T;\{N_j\}) = \prod_{j=1}^{N_0} [Q_{\text{vib},j}Q_{\text{HB},j}Q_{\text{entropy},j}]^{N_j} \quad (3)$$

where $Q_{\text{vib},j}$ is the vibrational partition function, $Q_{\text{HB},j}$ is the contribution from the hydrogen bonding energy, and $Q_{\text{entropy},j}$ is the configurational entropy contribution, all for a j-size cluster. The product over N_0 terms in eq 3 can be replaced by one over a smaller number of terms if the convergence is fast enough. We have taken a product of 100 terms, with negligible error from the omission of clusters larger than 100, as will be justified in section VIII. The choice of a larger number of terms did not change the results.

A. Vibrational Partition Function.[11] We obtain $Q_{\text{vib},j}$ as an Einstein partition function, by assuming that the normal modes of the clusters are harmonic. Since the intramolecular frequencies are not excited in the temperature range of interest, their characteristic temperatures being one at ~2300°K and two at ~4600°K, we can ignore these vibrations. However, we do take into account the change in the zero point

(4) H. S. Frank and W. Y. Wen, *Discuss. Faraday Soc.*, **24**, 133 (1957).

(5) H. S. Frank, *Proc. Roy. Soc., Ser. A*, **247**, 481 (1958).

(6) A discussion of the statistical mechanical relations used in this paper can be found in any standard book on statistical mechanics, such as that of Hill.[7]

(7) T. L. Hill, "An Introduction to Statistical Thermodynamics," Addison-Wesley, Reading, Mass., 1960.

(8) An error was made previously[9,10] in the interpretation of the calculated heat capacity. The actual calculation gives the heat capacity at constant pressure [from the relation $c_p = (\partial H/\partial T)_p \simeq (\partial U/\partial T)_p$] instead of that at constant volume, because the heat capacity is not calculated by closed-form differentiation of the partition function, but is obtained from numerical differentiation of the theoretical energy with respect to temperature; since the energy at each temperature was calculated at 1 atm, the derivative of the energy is the constant *pressure* heat capacity. This derivative has previously been incorrectly interpreted as the constant *volume* heat capacity and compared with this experimental quantity.[9,10]

(9) G. Némethy and H. A. Scheraga, *J. Chem. Phys.*, **36**, 3382 (1962).

(10) V. Vand and W. A. Senior, *ibid.*, **43**, 1878 (1965).

(11) An expanded version of this paper, giving details of the formulation and evaluation of the partition function, and further discussion of the results, has been deposited as Document No. NAPS-01916 with the ASIS National Auxiliary Publication Service, c/o CCM Information Corp., 909 3rd Ave., New York, N. Y. 10022. A copy may be secured by citing the document number and by remitting $4.00 for microfiche or $9.10 for photocopy. Advance payment is required. Make checks or money orders payable to CCMIC-NAPS.

energy, associated with the shift in the intramolecular frequencies upon breaking a hydrogen bond, including it in the value used for E_H (see sections IVC and D).

It is only reasonable to expect that the frequencies of the intermolecular vibrations will depend on the size and shape of a cluster. This size and shape dependence of the frequency, together with the frequency distribution corresponding to the various vibrational modes for a cluster of a given size and shape, accounts qualitatively for the relative broadness of the intermolecular peaks. Unfortunately, we have no way of taking these effects into account without introducing more adjustable parameters. Therefore, we will neglect the dependence of the frequency on these factors and assign the same six frequencies, corresponding to the six degrees of freedom lost by each molecule, to each molecule in the cluster. These frequencies (60, 175, 175, 450, 550, 722 cm^{-1}, the 175-cm^{-1} frequency being a degenerate one) are those observed by Walrafen[12,13] for the liquid at 25°.[14] Thus, the vibrational partition function for a cluster of size j is given by

$$Q_{vib,j} = \left(\prod_{l=1}^{6} [\exp(-h\nu_l/2kT)] \times [1 - \exp(-h\nu_l/kT)]^{-1}\right)^{j-1} \quad (4)$$

with the six ν_l's being given above; h and k are the Planck and Boltzmann constants, respectively. There are six degrees of freedom per molecule in the cluster corresponding to the three translational and three rotational degrees of freedom of the molecules (intramolecular degrees of freedom are ignored here as discussed above). Since the cluster has six external degrees of freedom, there remain $6j - 6$ intermolecular modes.

B. Hydrogen Bond Energy. The energy of the hydrogen bond is calculated from the minimum of the intermolecular potential function for a four-bonded molecule (A in Figure 1). This differs from a definition, in which the ground state is taken as ice at 0°K (B in Figure 1), by the *inter*molecular zero point energy, E_{ZPE}, which is given by Whalley[15] as 3513 cal/mol.

To calculate the difference in energy $2E_H'$, between the minimum and the asymptotic limit of the potential curve (process A–D) from experimental data, it is necessary to take into account the contribution of the change in the *intra*molecular zero point energies to the sublimation energy at 0°K.

The sublimation energy at 0°K is the energy absorbed when a water molecule is transferred from its lowest intermolecular and intramolecular quantum levels in ice to its lowest intramolecular quantum level in the vapor. The intramolecular zero point energy in the vapor is 1400 cal higher than the intramolecular zero point energy in ice.[15] Thus, to calculate the energy for the process A–D one simply subtracts 1400 cal from the sublimation energy which yields the energy for the process B–D and adds the energy for the process A–B, *i.e.*, the intermolecular zero point energy.

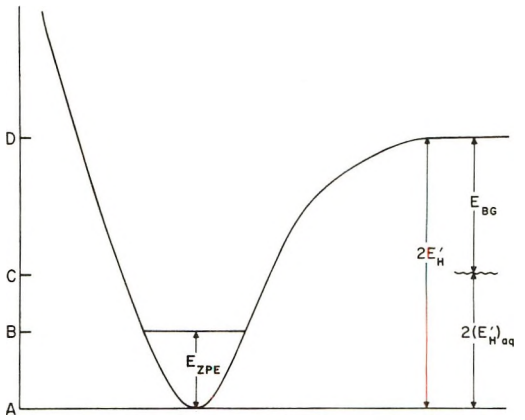

Figure 1. Schematic representation of the *inter*molecular hydrogen-bonding potential; in this diagram only, the intramolecular zero point energies in the vapor and in the solid have been omitted. A is the minimum of the potential function and corresponds to the zero of the energy scale. B is the lowest intermolecular quantum state. D is the energy of infinitely separated water molecules (at rest) in the vapor. Without trying to imply anything about a distance dependence, the wavy energy level at position C corresponds to the energy of infinitely separated water molecules at rest in the liquid. A–B represents the *inter*molecular zero-point energy E_{ZPE}. A–D represents $2E_H'$, since there are two moles of hydrogen bonds per mole of water in ice. E_{BG} and $(E_H')_{aq}$ are also indicated.

$$2E_H' = E_{subl}(0°K) - 1400 + 3513 \quad (5)$$

Since $E_{subl}(0°K) = 11{,}300$ cal,[16] we obtain

$$E_H' = 6706 \text{ cal/mol} \quad (6)$$

This is one-half the energy required for the *imaginary* process of transferring a water molecule at rest from ice to the ideal vapor at 0°K with no change in the frequency of intramolecular vibrations. By definition, it is independent of temperature and volume.

If, instead of taking the final state in the above process as the ideal vapor, we take it as the liquid (C in Figure 1), the energy needed will be smaller because of the existence of a background potential, E_{BG}, as mentioned in the discussion of the model. As discussed below (see section VA), we take E_{BG} to be inversely proportional to the volume, V, *viz.*, as

$$E_{BG} = -2c/V \quad (7)$$

(12) G. E. Walrafen, *J. Chem. Phys.*, **47**, 114 (1967).

(13) G. E. Walrafen, *ibid.*, **40**, 3249 (1964).

(14) These frequencies are taken here as independent of temperature.

(15) E. Whalley, *Trans. Faraday Soc.*, **53**, 1578 (1957).

(16) See, for example, D. Eisenberg and W. Kauzmann, "The Structure and Properties of Water," Oxford University Press, London, 1969.

where c is some positive constant. We then define the energy to break a hydrogen bond in the liquid as one-half the energy for process A–C

$$2(E_H')_{aq} = 2E_H' - E_{BG}$$

or

$$(E_H')_{aq} = 6706 - c/V \text{ cal/mol} \quad (8)$$

C. Shift in Intramolecular Zero Point Energies. We have referred above to the fact that there is a change of 1400 cal/mol in the intramolecular zero point energies when a four-bonded molecule is transferred from ice to the vapor at 0°K.[15] We attribute this change to the breaking of the hydrogen bond and assume that the shift in intramolecular frequency on breaking a hydrogen bond in the liquid will depend on the background potential. We take the shift in intramolecular zero point energy as linear with respect to the background potential, *viz.*

$$(E_{ZPE,\,unbonded} - E_{ZPE,\,4\text{-bonded}})_{intra(aq)} =$$

$$1400 - b(2c/V) = 1400 - 2b'/V \text{ cal/mol} \quad (9)$$

where V is the volume of the liquid as in eq 7, and b and b' are constants.

D. Hydrogen-Bonding Partition Function. Since both the hydrogen bond energy and the shift in the intramolecular zero point energy in the liquid have the same inverse volume dependence, it is convenient to combine them. Combining eq 8 and 9, we obtain

$$(E_H)_{aq} = (E_H')_{aq} + (1/2)(E_{ZPE,\,unbonded} -$$

$$E_{ZPE,\,4\text{-bonded}})_{intra(aq)} = 6706 - c/V + 700 -$$

$$b'/V = 7406 - a/V \text{ cal/mol} \quad (10)$$

where $a = c + b'$. This is the energy necessary to break a hydrogen bond in the liquid, including the difference in *intra*molecular zero point energies in the bonded and unbonded states, referred to the minimum of the curve of Figure 1. Equation 10 is intended to hold in the range of volumes encountered for the liquid. It should also be noted that it is consistent with the experimental sublimation energy (*i.e.*, it gives the correct result in the limit $V \to \infty$).

Having defined $(E_H)_{aq}$ by eq 10 and introducing the assumption that $(E_H)_{aq}$ is independent of the cluster size and of the connexity of the bonds (*e.g.*, all trimers in Figure 2 are assumed to have the same energy), we can immediately write the hydrogen-bonding partition function for a cluster of size j as

$$Q_{HB,j} = \exp[-(E_H)_{aq}N_{Bj}/kT] \quad (11)$$

where N_{Bj} is the number of broken hydrogen bonds. We assume that the clusters are as spherical as possible, so that a maximum number of hydrogen bonds can form. In accordance with this, we make the simplifying assumption that, for clusters larger than $j = 7$,

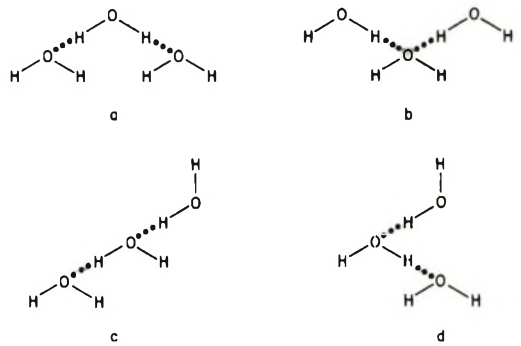

Figure 2. Illustration of the four distinguishable ways of forming a two-bonded trimer. See text for discussion of these forms.

for which it is geometrically possible, all the molecules will be two-, three-, or four-bonded, and they will contain no one-bonded molecules. To calculate N_{Bj}, we make use of the empirical equations for the numbers of four-, three-, and two-bonded molecules in a cluster of given size, given by Némethy and Scheraga[17] for clusters of more than 15 molecules; *i.e.*, $N_{Bj} = (j/2)(4 - \Sigma_i i y_i)$, where $i = 2$, 3, and 4, and y_i = fraction of i-bonded molecules in a cluster of size j. For smaller clusters, models were built, and the number of each bonded species (including one-bonded molecules) in the cluster was counted directly. Values of y_i as a function of j are given in Table I.

Table I: Dependence of y_i and j

Cluster size, j	Mole fraction y_i: One-bonded	Two-bonded	Three-bonded	Four-bonded
2	1.0	0	0	0
3	0.67	0.33	0	0
4	0.75	0	0.25	0
5	0.80	0	0	0.20
6	0	1.0	0	0
7	0.14	0.72	0.14	0
8	0	0.75	0.25	0
9	0	0.77	0.23	0
10	0	0.60	0.40	0
15	0	0.47	0.45	0.08
20	0	0.42	0.46	0.12
25	0	0.37	0.48	0.15
30	0	0.33	0.50	0.17
50	0	0.22	0.52	0.26
100	0	0.10	0.56	0.34

In this theory, a will be treated as an adjustable parameter, to be determined by fitting experimental data.

E. Internal Cluster Entropy. The term $Q_{entropy,j}$ in Q_{int} is required to account for the configurational entropy of the clusters, *i.e.*, for the fact that there is more than one way of achieving a given energy state of

(17) Equations 3–5 of ref 9.

a cluster of size j defined by the vibrational and hydrogen-bonding terms. There are at least two types of configurational entropy which must be considered.

The first type of configurational entropy is best described by an example. As can be seen from Figure 2, there are four distinguishable ways of forming a two-bonded trimer.[18-21] In (a) both hydrogens of the center molecule are bonded, in (b) both orbitals are bonded, and in (c) and (d) one hydrogen and one orbital are involved in bonds, there being two ways to accomplish this because of the asymmetric nature of the tetrahedral structure. This type of configurational entropy, which is related to the residual entropy of ice, also arises in ring structures as can be seen in Figure 3.

The second type of configurational entropy arises from the possible variation in the "quasicrystalline" structure of the clusters (including a deviation from spherical shape). There are many possible structures involving interconnected networks of five- and six-membered rings which will form roughly spherical clusters. These are possible because the clusters are not infinite in extent but contain a relatively small number of molecules and are therefore not restricted to structures which propagate an infinite lattice.

Both types together constitute a configurational entropy of a j-size cluster, and the internal partition function for a j-size cluster must contain a factor $Q_{\text{entropy},j}$ which is a measure of the total number of isoenergetic configurations of a cluster of size j. Since there is no way to calculate the total number of configurations for the larger clusters, $Q_{\text{entropy},j}$ will have to be treated empirically.

The equation

$$Q_{\text{entropy},j} = (j^{\omega})! \qquad (12)$$

is suggested by the fact that the largest number of ways of ordering j distinguishable particles is $j!$. Since $j!$ is obviously not the correct quantity required here, we take ω as an adjustable parameter which is expected to be less than one; indeed, this turns out to be so (see section VIII). We would expect the configurational entropy per molecule to vary qualitatively with j as shown in Figure 4 (curve a). The configurational entropy of the monomer is zero, and the entropy of very large clusters approaches $R \ln {}^3/_2$, the residual entropy of ice. The maximum occurs because of the added "quasicrystalline" entropy of medium-sized clusters. For $\omega < 1$, the entropy per molecule, which results from eq 12 ($S_{\text{entropy},j} = k \ln Q_{\text{entropy},j}$), has the functional form shown in Figure 4 (curve b). It is also zero for $j = 1$, and goes through a maximum; however, its limiting value for $j \to \infty$ is zero rather than $R \ln {}^3/_2$. Equation 12 is used as an approximation to represent the expected form of curve a of Figure 4 because the behavior of the two curves deviates appreciably only for very large values of j (>100), which are outside the range of interest since the distributions computed here have

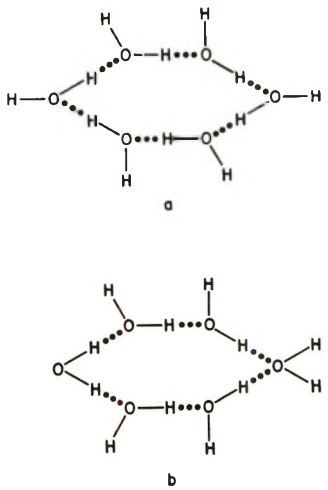

Figure 3. Illustration of two of the possible distinguishable ways of forming a six-membered ring. These diagrams are only schematic, since the ring structures are not planar.

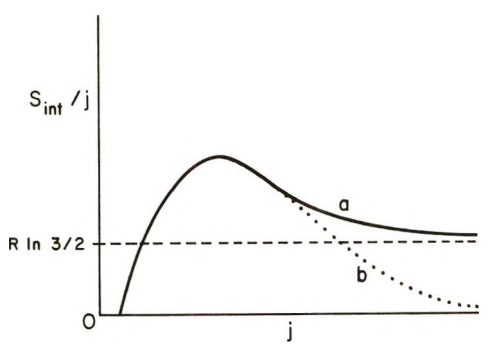

Figure 4. A schematic plot of the variation of the configurational entropy per molecule as a function of j (curve a). Curve b represents the configurational entropy per molecule resulting from the function $R \ln [(j^{\omega})!]$ (for $\omega < 1$); *cf.* eq 12.

negligible numbers of clusters larger than 60 or 70 even at 0°; further, eq 12 involves only one adjustable parameter.

V. External Partition Function[11]

The external partition function may be expressed in terms of the translational and rotational contributions

(18) Quantum mechanical calculations[19] indicate that all four species of Figure 2 do not have the same energy. In fact, species a and b are anticooperative. This does not affect the qualitative argument here, since there is still more entropy than if there were only one possible trimer (but less than the maximum if all structures were of equal energy), and this entropy must be taken into account. Since the total number of configurations cannot be counted in any case, it will be taken as an adjustable parameter.

(19) J. Del Bene and J. A. Pople, *Chem. Phys. Lett.*, **4**, 426 (1969); *J. Chem. Phys.*, **52**, 4858 (1970).

(20) This source of configurational entropy resembles somewhat that suggested by Vand and Senior.[21] However, the latter concentrated on bonded species and therefore made an error in the counting. For example, they said that a one-bonded molecule could be made in four ways, and a two-bonded one in six ways. Hence, they would have counted $4 \times 6 \times 4 = 96$ ways of making a two-bonded trimer instead of four.

(21) V. Vand and W. A. Senior, *J. Chem. Phys.*, **43**, 1869 (1965).

$$Q_{ext}(N_0,V,T;\{N_j\}) = Q_{trans}(N_0,V,T;\{N_j\})Q_{rot}(N_0,V,T;\{N_j\}) \quad (13)$$

A. Translational Partition Function. The translational partition function may be written as

$$Q_{trans}(N_0,V,T;\{N_j\}) = \frac{1}{h^{3\Sigma N_j}\prod_j N_j!}\int_{\{q\}}\cdots\int_{\{p\}} \times \exp\left[-\sum_{j=1}^{100}\sum_{i=1}^{N_j}(p_{ij}^2/2m_jkT) - V(\{q\})/kT\right] d\{p\}d\{q\} \quad (14)$$

where $\{q\}$ and $\{p\}$ are vectors representing the coordinates and momenta, respectively, of the centers of mass of all the clusters in the liquid, m_j is the mass of a cluster of size j, p_{ij} is the momentum of the ith cluster of size j, and $V(\{q\})$ is the potential energy of the system.

In general, it is impossible to carry out the integration over the coordinates, which is the essential difficulty in the theory of liquids. However, we can obtain an approximate expression for Q_{trans} by introducing the assumption that the overall configurations of the clusters are determined mainly by the hard-sphere repulsion, in line with the views of Longuet-Higgins and Widom, as discussed in section II; *i.e.*, we separate $V(\{q\})$ into a sum of two terms, a hard-sphere repulsive potential and a uniform background potential

$$V(\{q\}) = V_{HS}(\{q\}) + V_{BG} \quad (15)$$

where $V_{HS}(\{q\})$ is the potential energy of a system of hard spheres and is, of course, a function of all the coordinates, and V_{BG} (the same as E_{BG}) is a uniform background potential independent of the coordinates and inversely proportional to the volume[22,23] (as anticipated in eq 7–10). As mentioned in the discussion of the model, we assume that the effect of the orientation-dependent, hydrogen-bonding potential has been taken into account by the assumption of the existence of clusters. Since V_{BG} is independent of coordinates, it can be taken out of the integral and combined with the energy of breaking a hydrogen bond in the vapor to give the hydrogen bond energy in liquid water.

Since V_{BG} has been taken out of the integral in eq 14, the remaining part becomes

$$Q_{trans} = \frac{1}{h^{3\Sigma N_j}\prod_j N_j!}\int_{\{q\}}\cdots\int_{\{p\}} \times \exp\left[-\sum_{j=1}^{100}\sum_{i=1}^{N_j}(p_{ij}^2/2m_jkT) - V_{HS}(\{q\})/kT\right] d\{q\}d\{p\} \quad (16)$$

But this is just the canonical partition function for a mixture of hard spheres, whose distribution of diameters corresponds to that of the clusters. Furthermore, Lebowitz has solved the generalized Percus–Yevick equation for a mixture of hard spheres, and his results are in good agreement with machine calculations of the pressure.[24] The thermodynamic properties follow from these results and are given by Lebowitz and Rowlinson[25] as

$$(\mu_j)_{HS}/kT = \ln\left[\frac{\rho_j h^3}{(2\pi m_j kT)^{3/2}}\right] - \ln(1-\xi) + (\pi/6)\frac{P_{HS}}{kT}R_j^3 + \frac{R_j^2}{(1-\xi)^3}[3Y - 6\xi Y + (9/2)X^2 - (9/2)\xi X^2 + 3\xi^2 Y] + \frac{R_j}{(1-\xi)^3}[3X - 6\xi X + 3\xi^2 X] \quad (17)$$

$$P_{HS}/kT = \frac{1}{(1-\xi)^3}\left[\sum_j \rho_j(1+\xi+\xi^2) - \frac{18}{\pi}\sum_{i<j}\eta_i\eta_j(R_i-R_j)^2(R_i+R_j+R_iR_jX)\right] \quad (18)$$

where

$$\eta_j = (1/6)\pi\rho_j \qquad \xi = \sum_j \eta_j R_j^3 \qquad X = \sum_j \eta_j R_j^2 \qquad Y = \sum_j \eta_j R_j \quad (19)$$

and μ_j, R_j, and ρ_j are the chemical potential, diameter, and number density, respectively, of component j, and P_{HS} is the hard-sphere pressure. Hence, the translational partition function is given by

$$-kT\ln Q_{trans}(N_0,V,T;\{N_j\}) = F_{HS}(N_0,V,T;\{N_j\}) = \sum_{j=1}^{100}N_j(\mu_j)_{HS} - P_{HS}V \quad (20)$$

where F_{HS} is the Helmholtz free energy of a mixture of hard spheres.

It should be pointed out that there is no problem in

(22) Widom[23] has shown that thermodynamic consistency requires that this relation be satisfied for a system of hard spheres. However, this assumes that the total volume of the hard spheres is independent of temperature, a condition which is not satisfied in our model because the distribution of cluster sizes changes with temperature (and the volume of a cluster depends nonlinearly on j, as discussed at the end of section VA). Nevertheless, we will take the background potential as inversely proportional to the volume since it reduces to the correct result as $V \to \infty$, and would be expected to hold reasonably well over the range of temperatures and volumes treated here.

(23) B. Widom, *J. Chem. Phys.*, **39**, 2808 (1963).

(24) J. C. Lebowitz, *Phys. Rev.*, **133**, A895 (1964).

(25) J. C. Lebowitz and J. S. Rowlinson, *J. Chem. Phys.*, **41**, 133 (1964). There is a misprint in this paper. The sign of the term $\ln(1-\xi)$ should be negative, as shown in eq 17, not positive as was given in the reference [see N. Snider and T. H. Herrington, *ibid.*, **47**, 2248 (1967)].

substituting hard spheres for the hypothesized "flickering clusters" which are continually breaking apart and re-forming. The quantity that is sought is the configurational entropy, which arises from the various possible arrangements of clusters in the liquid for a given $\{N_j\}$. This quantity does not depend on whether the clusters are flickering or not. However, since it does depend on the shape of the clusters, an error is made in replacing the clusters by spheres in order to carry out this calculation (see section X).

Before the value of Q_{trans} can be computed, it is necessary to specify the diameter, R_j, of the clusters. The effective diameter[26] per molecule will vary from a small value characteristic of the monomer to larger values, approaching that for ice, as the cluster increases in size. Rather than introduce one or more additional adjustable parameters into the theory, the hard-sphere diameters are approximated as follows. To obtain the diameter of the monomer, we make use of Kamb's observation[27] that, in ice VII, which is an interpenetrating lattice in which each oxygen has eight nearest neighbors (four to which it it bonded and four others), the nearest-neighbor distance increases from 2.86 Å at 25 kbars to 2.95 Å at atmospheric pressure. Since the lattice expands as the pressure is reduced, it follows that the overall potential is repulsive at these distances. The repulsion is presumably due to the four nonbonded neighbor–neighbor interactions since the hydrogen-bonded interaction is attractive at these distances (*e.g.*, the O–O distance in ice I is approximately 2.76 Å). Since the diameter of an unbonded monomer is used in the partition function to tell essentially what volume is excluded to other molecules, it makes sense to choose a diameter which corresponds to some point in the repulsive part of the potential for non-hydrogen-bonded molecules. This diameter should probably correspond to a repulsive energy of the order of kT and therefore be temperature dependent; however, we ignore this factor since the potential function is not known to this accuracy and take the diameter of the monomer to be 2.9 Å (midway between 2.86 and 2.95 Å) at 1 atm and independent of temperature (all the properties calculated here being at 1 atm).

For a molecule in ice I, division of the molar volume by N_0 leads to an effective diameter per molecule of 4.0 Å. Therefore, the effective diameter increases from approximately 2.9 Å for a monomer to 4.0 Å for a very large cluster. We arbitrarily assume that this increase is linear in the diameter and take the effective diameter in a j-sized cluster as $2.89 + 0.01j$ Å, which assigns the effective diameter of a water molecule in ice to one in a cluster of size ~100.

B. Rotational Partition Function. The rotational partition function is taken as

$$Q_{rot} = \prod_{j=1}^{100} \left[\frac{\pi^{1/2}}{\sigma_j \sigma'} \left(\frac{8\pi^2 kT}{h^2} \right)^{3/2} (I_A I_B I_C)_j^{1/2} \right]^{N_j} \quad (21)$$

where $(I_A I_B I_C)_j$ and σ_j are the product of the moments of inertia and symmetry factor, respectively, of a j-sized cluster, and σ' is a parameter.

The moments of inertia were approximated by those of compact ice I clusters of the same size and were calculated from the coordinates of the atoms in an ice I cluster. For $j \leq 19$, the results of such a computation were used directly while, for clusters larger than 19, the results were expressed in terms of an empirical linear dependence of $\ln I_j$ on j, the linear function being a sufficiently accurate representation of the data, since the three rotational degrees of freedom make a smaller relative contribution to the partition function with increasing cluster size. The symmetry factors were all taken as 1 except for the monomer which has a symmetry factor of 2.

As expected, preliminary calculations (with $\sigma' = 1$) yielded values of the entropy which were too high because of the free rotation initially allowed for the clusters. The number of rotational states, like the total number of translational configurations, should depend on the excluded volume; *i.e.*, all values of the Eulerian angles of a given cluster should not be allowed, since there will be overlap for some values of these. Since it is not possible to compute the reduced number of rotational configurations in the liquid, σ' has been introduced as a parameter[28] into the denominator of eq 21, where

$$\sigma' = 1 + d/V \quad (22)$$

We take this volume dependence since, as the volume increases, there should be less overlap and therefore more allowed rotation (in the limit of infinite volume, $\sigma' = 1$, which corresponds to completely free rotation). Since we are considering liquid volumes only at 1 atm, there is no problem with the limit $V \to 0$ where eq 22 does not hold.

VI. Summary of the Partition Function

The partition function of liquid water is expressed as the product of the external and internal partition functions. The internal partition function is composed of a vibrational partition function for which a harmonic approximation was used, a hydrogen-bonding partition function which involves the energy of a broken hydrogen bond in the liquid relative to the minimum of the hydrogen bond potential (including the change in intramolecular zero point energy which accompanies the rupture of a hydrogen bond), and a configurational entropy which reflects the different ways that a cluster

(26) If the total vloume of the cluster is divided by the number of molecules in the cluster, V_1 is obtained, *i.e.*, the volume per molecule in the cluster. The diameter of a sphere having volume V_1 is defined as the effective diameter per molecule for a cluster of a given size.

(27) B. Kamb, *J. Chem. Phys.*, **43**, 3917 (1965).

(28) Actually, σ' should also depend on j. However, to avoid the introduction of too many adjustable parameters, σ' was taken as independent of j.

of a given size and energy can be formed. The external partition function consists of a hard-sphere term which enables the configurational (translational) entropy to be calculated, a cohesive energy term which was combined with the hydrogen-bonding partition function, and a rotational partition function (reduced to account for the restricted rotation in the liquid). Collecting the various contributions, we obtain the following expression for the complete partition function

$$Z(N_0,V,T;\{N_j\}) = \left\{\prod_{j=1}^{100}\left[\left(\prod_{l=1}^{6}[\exp(-h\nu_l/2kT)]\times[1-\exp(-h\nu_l/kT)]^{-1}\right)^{j-1}\right]^{N_j}\times[\exp\{-(E_H)_{aq}N_{Bj}\}]^{N_j}[(j^\omega)!]^{N_j}\times\left[\frac{\pi^{1/2}}{\sigma\sigma'}\left(\frac{8\pi^2kT}{h^3}\right)^{3/2}(I_AI_BI_C)_j^{1/2}\right]^{N_j}\right\}\times\exp\left[-\left\{\sum_{j=1}^{100}N_j(\mu_j)_{HS}-P_{HS}V\right\}\Big/kT\right] \quad (23)$$

The three adjustable parameters in this partition function are a (in E_H), ω, and d (in σ').

VII. Computational Procedures

The negative logarithm of the partition function must be a minimum with respect to $\{N_j\}$, at each temperature, for given values of a, ω, and d. (This is just the condition that the partition function must be a maximum at equilibrium.) Thus, in principle, the minimization is carried out with respect to the $\{N_j\}$ for $j = 1$ to 100, for various values of a, ω, and d until the thermodynamic data are fit.

In practice, this minimization is very difficult to carry out, since it involves the minimization of a function with respect to 100 variables. To make the problem tractable, some of the properties that the distribution of N_j's must have are taken into account.

The first property is that, as j approaches infinity, the number of clusters of size j, *viz.*, N_j, must approach zero, or otherwise ice would be favored. (This condition also has an experimental basis in the results of small angle X-ray scattering[29] which rule out very large clusters.) In addition, the distribution would not be expected to exhibit any minima or irregularities, especially in the region of large clusters (for example, one would hardly expect to find a large number of clusters of, say, size 40, a few of size 41 and a large number of size 42). We thus expect the distribution to have a form similar to one of those given in Figure 5, *i.e.*, the distribution function would be expected to be either a monotonically decreasing function or else to exhibit a single maximum on a skewed curve.[30] The

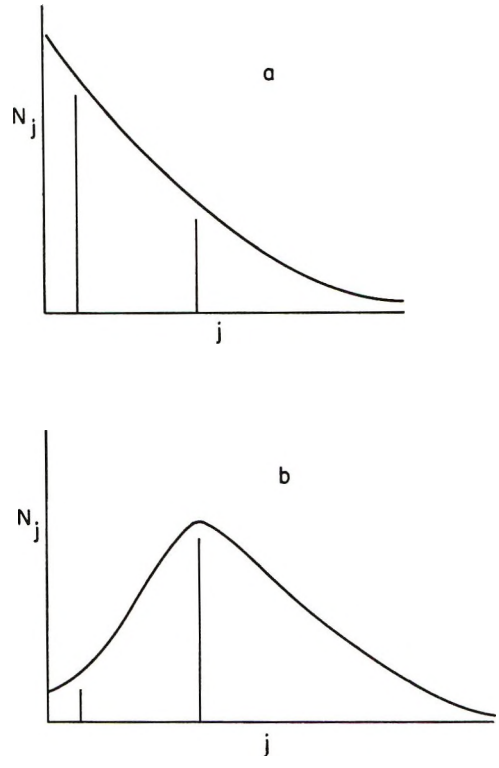

Figure 5. The two expected forms of the distribution function of cluster sizes. The vertical lines in a and b represent the distribution assumed in some two-state theories.

γ distribution has just these qualitative properties[31] and is given in terms of two constants, α and β, by

$$N_j = kj^{\alpha-2}\exp(-j\beta) \quad (24)$$

where k is a normalizing factor determined by the condition

$$\sum_{j=1}^{100} jN_j = N_0 \quad (25)$$

If we assume that the distribution of cluster sizes can be represented by a γ distribution, then we have only two variables (α and β), instead of the 100 N_j's, with respect to which we must maximize the partition function. The use of eq 24 will not discriminate against either small or large clusters; if a distribution of large clusters minimizes the free energy, the minimum will occur at large α and small β, and *vice versa* for small clusters.

In practice, a nested minimization is used in which the free energy is first minimized with respect to α and β at 11 temperatures between 0 and 100° for some spec-

(29) A. H. Narten and H. A. Levy, *Science*, **165**, 447 (1969).

(30) This approximation has been justified in the text. The much more extreme approximation of the distribution (*viz.*, δ functions), implicitly assumed in some two-state theories, is represented schematically in Figure 5. From this figure, it can be seen how unrealistic the two-state distribution is compared to the expected one.

(31) (a) A. M. Mood and F. A. Graybill, "Introduction to the Theory of Statistics," 2nd ed, McGraw-Hill, New York, N. Y., 1963; (b) W. Feller, "An Introduction to Probability Theory and Its Applications," Vol. II, Wiley, New York, N. Y., 1966, p 46.

ified set of a, ω, and d, and then the deviation between the experimental and calculated free energy and energy at these temperatures (calculated with the α's and β's determined by the first minimization) is minimized with respect to a, ω, and d. The point here is that every time that a, ω, and d are changed in the minimization procedure, the free energy must again be minimized to determine the equilibrium distribution of clusters for these parameters.

The final values of α and β at each temperature, for the resultant values of a, ω, and d, are checked by contour diagrams; where the minimization procedure has not reached the absolute minimum with respect to α and β, these values are then taken from the contour diagrams.

VIII. Quantitative Results

The values of the parameters, determined as described in section VII, are a = 87,670 cal cm³/mol, ω = 0.827, and d = 32,500 cm³/mol. Using these parameters, and the values of α and β determined by minimization at each temperature, we obtain the computed thermodynamic data (compared with experimental ones)[32] shown in Table I of the expanded version[11] of this paper for seven temperatures between 0 and 60°. Above 60°, the distribution consists mainly of clusters smaller than 6-mers. Since the calculated number of small clusters is in error at all temperatures, the approximations in the theory render it inapplicable above 60°, as will be discussed in section X. The deviations of the calculated values from the experimental ones, and the trends, can be seen in Figures 6–8. In this range, the largest deviations in the free energy, energy, and entropy are approximately 4.3, 4, and 2.4%, respectively. The errors in the experimental data are of the order of 2–3%.[32] Because of the nature of the approximations that must be made at this time in a theory of water (see section X), the magnitude of the deviation between the calculated and observed values is considered minimal. A significantly better fit of the data, at this stage, would require the use of an excess of adjustable parameters. As usual,[9,33] the error in the heat capacity,[11] which depends on the second derivative of the free energy, is much larger, being approximately 20%.

The various contributions to the free energy, energy, and entropy are given in Tables II–IV. It should be noted that the experimental values of F and U are relative to ice at 0°K; therefore, the intermolecular zero point energy of 3513 cal has been subtracted from the sum of the free energy and energy terms in Tables II and III, respectively, to compare them with experimental values. Also, the observed values of F and S include the residual entropy of ice. It can be seen from these tables that the contribution from the internal configurational entropy, S_{int}, which was ignored in previous theories, is quite significant, accounting

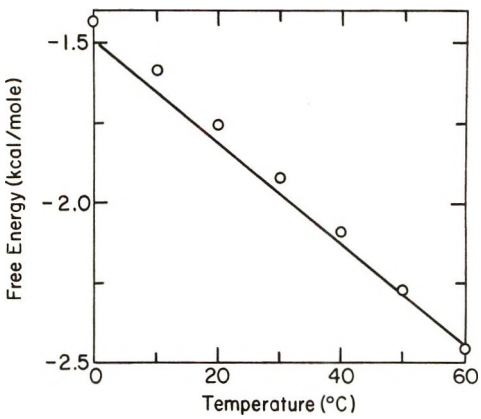

Figure 6. Comparison of the calculated and experimental values of the Helmholtz free energy F (having essentially the same value as the Gibbs free energy G) as a function of temperature. The points are experimental values,[32] and the curve is a theoretical one.

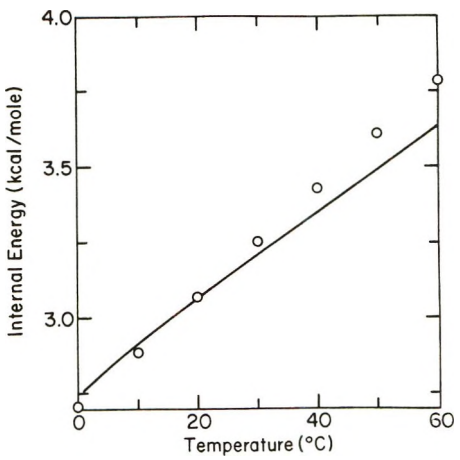

Figure 7. Comparison of the calculated and experimental values of the internal energy U (having essentially the same value as the enthalpy H) as a function of temperature. The points are experimental values,[32] and the curve is a theoretical one.

for over 10% of the entropy at 0°. The relaxational heat capacity (that part of c_p arising from the change in the distribution of cluster sizes with temperature) is given in Table V. It can be seen that this accounts for over 50% of the heat capacity at 0° but falls off rapidly. It is basically this factor which accounts for the fact that the calculated heat capacity is low.[11]

The volume-dependent hydrogen bond energy (see eq 10), β and α, the constants in the γ distribution, the median of the distribution, and the mole fraction of unbroken hydrogen bonds, X_{HB}, are given in Table VI. The median cluster size (which is the cluster size

(32) (a) W. E. Sharp, Report of the Lawrence Radiation Laboratory, University of California UCRL 7118 (1962); (b) N. E. Dorsey, "Properties of Ordinary Water Substance," ACS Monograph No. 81, Reinhold, New York, N. Y., 1940.

(33) M. S. Jhon, J. Grosh, T. Ree, and H. Eyring, *J. Chem. Phys.*, **44**, 1465 (1966).

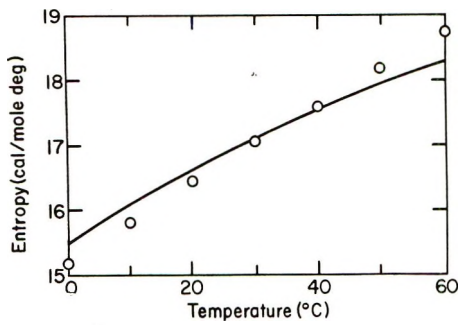

Figure 8. Comparison of the calculated and experimental values of the entropy S as a function of temperature. The points are experimental values,[32] and the curve is a theoretical one.

Table II: Contribution of Various Terms to the Total Free Energy[a] (units of all free energies: cal/mol)

t, °C	F_{trans}	F_{rot}	F_{vib}	F_{int}	F_{HB}	F_{total}[b]
0	−923	−302	1443	−427	2227	−1496
10	−1079	−360	1323	−409	2384	−1654
20	−1200	−398	1214	−403	2487	−1813
30	−1310	−435	1110	−401	2576	−1972
40	−1411	−472	1009	−401	2657	−2132
50	−1508	−510	909	−403	2731	−2293
60	−1629	−552	805	−399	2834	−2456

[a] Obtained from the partition function as derived above. [b] 3513 cal has been subtracted from the sum of the free energies to obtain F_{total}.

Table III: Contribution of Various Terms to the Total Energy[a] (units of all energies: cal/mol)

t, °C	U_{trans}	U_{rot}	U_{vib}	U_{HB}	U_{total}[b]
0	120	120	3785	2227	2739
10	142	142	3765	2384	2920
20	160	160	3772	2487	3066
30	176	176	3792	2576	3207
40	190	190	3822	2657	3345
50	203	203	3859	2731	3483
60	221	221	3876	2834	3638

[a] Obtained from the partition function as derived above. [b] 3513 cal has been subtracted from the sum of the internal energies to obtain U_{total}.

for which 50% of the molecules are in larger clusters and 50% in smaller clusters) decreases from 11.2 at 0° to 5.6 at 60° while X_{HB} [which is $1 - (\Sigma N_{Bj} N_j)/2N_0$] decreases from 0.565 to 0.460 between these same two temperatures. The increase in $(E_H)_{aq}$ with increasing temperature is in accord with eq 10. The distributions of cluster sizes (mole fraction of water molecules in clusters of size j as a function of j) from 0 to 60° are given in Figure 9. It can be seen from these curves that there is no problem in making a cutoff at a cluster

Table IV: Contribution of Various Terms to the Total Entropy[a] (units of all entropy terms: cal/mol deg)

t, °C	S_{trans}	S_{rot}	S_{vib}	S_{int}	S_{total}
0	3.82	1.55	8.58	1.57	15.51
10	4.31	1.77	8.63	1.44	16.16
20	4.64	1.90	8.73	1.38	16.65
30	4.90	2.01	8.85	1.32	17.09
40	5.12	2.12	8.99	1.28	17.50
50	5.30	2.21	9.13	1.25	17.88
60	5.56	2.32	9.22	1.20	18.30

[a] Obtained from quantities in Tables II and III.

Table V: Relaxational Heat Capacity

t, °C	$c_{p,relax}$, cal/mol deg
0	10.7
10	7.7
20	4.9
30	4.7
40	3.6
50	3.0
60	2.8

size of 100, since there are essentially no water molecules in clusters larger than this. A larger cutoff does not change the results. The free energy, energy, and entropy, as well as β and α and the mole fraction of unbroken hydrogen bonds, for the temperature range 70–100°, are given in Table VII of the expanded version[11] of this paper to show the effect of the approximations at these temperatures (see section X).

Table VI: Structural Parameters of Liquid Water

t, °C	V, cm³/mol	$(E_H)_{aq}$, cal/mol	β	α	Median of distribution	X_{HB}
0	18.018	2541	0.11	1.60	11.2	0.565
10	18.021	2541	0.17	1.90	8.8	0.531
20	18.048	2549	0.21	2.05	7.8	0.512
30	18.093	2561	0.25	2.20	7.0	0.497
40	18.157	2578	0.29	2.35	6.5	0.485
50	18.234	2598	0.33	2.50	6.1	0.474
60	18.324	2622	0.39	2.70	5.6	0.460

It can also be seen from the distribution functions that there are approximately 3% monomers present at all temperatures. This number is not very accurate, however, because of the seriousness of the approximations in the region of small clusters ($j < 6$) at all temperatures. While the "dense species" in most two-state theories has been considered to be the monomer, the latter plays no special role in the present

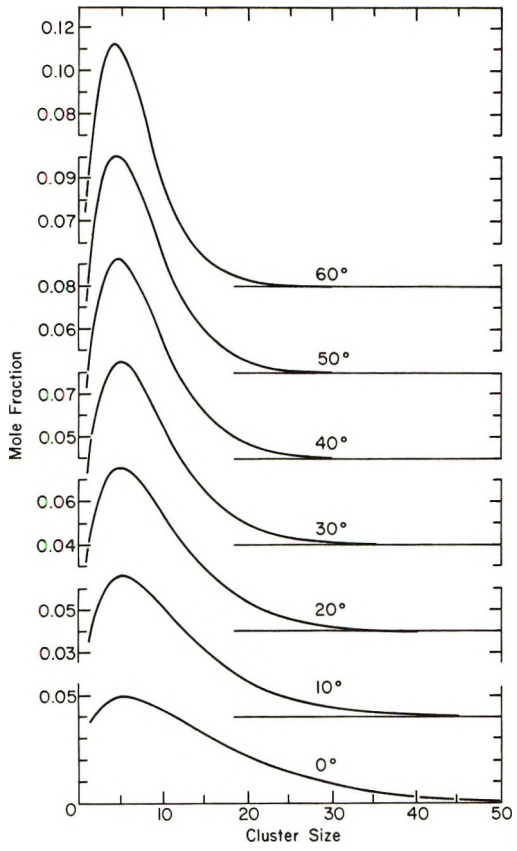

Figure 9. Calculated distribution of the mole fraction of water molecules in a cluster of size j as a function of j, for various temperatures.

theory since it is simply one out of many j-mers; the amount of monomer actually present in water has been the subject of some controversy.[34]

IX. Qualitative Results

In addition to the quantitative thermodynamic results presented in section VIII, the theory can also account for other characteristic properties of water in a qualitative way. We consider here the radial distribution function, the volume, and the intermolecular spectrum.

The radial distribution function[35] of water at 4° is characterized by a sharp peak at 2.82 Å, corresponding to approximately 4.4 nearest neighbors, and by additional maxima at 4.5 and 7 Å, corresponding to second and third neighbors. These peaks also appear in the radial distribution function of ice I, although the first peak occurs at 2.76 Å for ice I at 0°.[36] In addition, there is a small peak (for the liquid) at ~3.7 Å, but the data of Narten[37] indicate that this may be an artifact arising from the Fourier inversion of the scattering data. The position of the maximum of the first peak shifts from 2.82 to 2.94 Å as the temperature is increased from 4 to 200°.[35] In addition, the peaks at 4.5 and 7 Å gradually disappear with increasing temperature. These features can be accounted for qualitatively by our model. The peak at ~2.82 Å is, of course, the primary evidence for the existence of hydrogen-bonded nearest neighbors and hence, presumably, of tetrahedral arrangements in liquid water. This peak would arise from the existence of clusters in the model. In addition, non-hydrogen-bonded nearest neighbors, arising from molecules in neighboring clusters, would contribute to this peak, thereby explaining why the number of nearest neighbors is greater than four, and also why the maximum occurs at a larger distance than in ice. As the temperature increases, the number of hydrogen-bonded molecules decreases and the distribution of cluster sizes shifts to one in which smaller clusters predominate. Thus, a molecule in a cluster will have fewer second and third neighbors *within the cluster*, thereby accounting for the gradual disappearance of the peaks at 4.5 and 7 Å with increasing temperature. The broadening of the peak at 2.82 Å and its shift to larger distances with increasing temperature also reflects the increasing distance between non-hydrogen-bonded nearest neighbors (ordinary thermal expansion of a nonbonded liquid).

The temperature-dependent values of the volume were used in the partition function, and thus the liquid is constrained to have a volume equal to the experimental one. However, as is the case with "mixture models," in general, the minimum in the temperature dependence of the molar volume at 4° is rationalized in terms of a balance between the volume decrease accompanying the decrease in the average cluster size and the volume increase due to normal thermal expansion as the temperature increases.

As is the case with the volume, the values of the intermolecular frequencies have been used in the partition function, and thus the liquid is constrained to exhibit an intermolecular spectrum consisting of these experimental frequencies. Nevertheless, the qualitative features of the intermolecular spectrum, such as the broadness of the peaks, the decrease in intensity of these peaks with increasing temperature,[12] and the shift of the maximum frequency to lower values with increasing temperature,[38] can be accounted for in terms of the distribution of cluster sizes and the shift in the distribution with temperature. Broadness of the peaks arises from a distribution of cluster sizes and shapes, and the intensity decreases because of a decrease in the total number of vibrational degrees of freedom as the number of small clusters increases. The frequency shift is accounted for qualitatively by

(34) H. S. Frank, *Science*, **169**, 635 (1970).

(35) A. H. Narten, M. D. Danford, and H. A. Levy, *Discuss. Faraday Soc.*, **43**, 97 (1967).

(36) B. Kamb in "Structural Chemistry and Molecular Biology," A. Rich and N. Davidson, Ed., W. H. Freeman, San Francisco, Calif., 1968, p 507.

(37) A. H. Narten, Oak Ridge National Laboratory Report No. ORNL-4578, July 1970.

(38) D. A. Draegert, N. W. B. Stone, B. Curnutte, and D. Williams, *J. Opt. Soc. Amer.*, **56**, 64 (1966).

the fact that, at higher temperatures, smaller clusters become more numerous, and these would be expected to have lower frequencies. However, despite the qualitative consistency, it should be recalled that these effects were not taken into account quantitatively, the spectrum being approximated by six discrete, temperature-independent frequencies. From Tables II–IV, it can be seen that the vibrational contribution to the thermodynamic properties of water is a very important one, and the values used for the frequencies are the primary reason for the inapplicability of the theory above 60° (see section X).

X. Discussion and Criticism of Theory

While a perfect theory would contain no approximations or adjustable parameters, this is not the case for the foregoing one, which should be regarded as a first approximation to a theory of water structure. Hence, we discuss here some of the implications of the approximations and also the prospect of eliminating the need for adjustable parameters.

The most serious approximation is the assumption that the frequencies are independent of cluster size, j. It appears, in one form or another, in most theories. For example, in all two-state theories, one state is taken as a dense species (usually unbonded water) and the other as a bulky species (usually icelike). Each state is then assigned a set of properties which are independent of the extent (size) of the given species; this is equivalent to the assignment of the same frequencies to all bulky species. The assumption that the frequencies are independent of j is especially bad for small clusters (as will be demonstrated below) and leads to a breakdown of the theory above ~60° where small clusters are predicted to predominate. While the librational frequencies in the range of 450–725 cm^{-1}, observed in ice and in the liquid, are properly assignable to large clusters in the liquid, since they contain three- and four-bonded molecules, these frequencies are not applicable to small clusters such as dimers, trimers, etc. On the contrary, we would expect the frequencies to decrease with decreasing cluster size in the region of small j since, *e.g.*, the libration of a molecule having four hydrogen bonds resisting the libration would be expected to occur at a higher frequency than the libration of a molecule having only one hydrogen bond. As mentioned in section IX, such a variation of frequency with j would account for the broadness of the peaks in the intermolecular spectrum and also for the shift to lower frequencies as the temperature is increased (leading to a larger number of smaller-sized clusters).

By having assigned overly high frequencies to small clusters, we have made their energy too positive because of the large zero-point energies associated with these frequencies and have therefore decreased the probability of, say, two monomers forming a dimer. This is illustrated by a calculation of the energy of dimerization, which appears in the expanded version[11] of this paper. If the error (in which the monomer is favored relative to small clusters) caused by the use of an overly high frequency for small clusters were not otherwise compensated, we would have obtained a distribution of cluster sizes with a minimum at some low value of j (>1), a maximum at some higher value of j, and an asymptotic approach to zero as $j \rightarrow \infty$.[39] However, such a behavior, in which the monomer is favored, does not actually appear because this error, arising from the assignment of overly high frequencies to clusters of small j, is partially compensated by other factors (especially the rotational partition function) which tend to lower the concentration of monomers; *i.e.*, the parameter d of the rotational partition function has adjusted itself, during the course of the nested minimization, to reduce the rotational entropy and consequently the number of monomers. In other words, the parameter d becomes very large, which would imply that rotation is very restricted. However, as suggested above, this large value of d may reflect not so much the hindrance to rotation, but rather the need to decrease the number of monomers, especially since the effect of the parameter d in reducing the number of j-mers is greatest for the monomer, because of its small moment of inertia and also because the relative contribution of the rotational partition function decreases with increasing j (there being relatively fewer rotational degrees of freedom for larger j). In summary, the rotational partition function partially compensates the effect of the high frequencies and reduces the relative number of monomers; the remaining error in the number of clusters decreases with increasing j.

One would expect the free energy to be a minimum at a given set of values of α and β (the constants of the γ distribution (see eq 24)) and increase monotonically as α and β depart from their values at the minimum. Actually, a second minimum in the free energy appears (at values of α and β corresponding to distributions of *small* clusters ($j \leq 6$)) and becomes the one of lowest free energy at ~60°. As discussed in the Appendix of the expanded version[11] of this paper, this second minimum is an artifact and arises because the energies of all j-mers (for $j < 6$) are roughly equal (because of the high vibrational energy assigned to clusters of low j). At the temperature where this second minimum becomes the lower one, we consider the theory to be inapplicable and do not try to fit the thermodynamic

(39) The use of eq 24 could conceivably impose a reduction in the number of monomers, thereby artificially preventing the occurrence of this type of distribution of cluster sizes. However, the absence of such a distribution is *not* due to the use of eq 24. Even if the latter is not used, *i.e.*, if the number of monomers is not restricted to a value determined by the γ distribution but varies independently, there is no tendency for the concentration of monomers to increase; in fact, in a numerical test, they were found to decrease without any change in the general features of the distribution.

properties in Figures 6–8; the data above 60° are presented in Table VII of the expanded version[11] of this paper. If one used the values for the thermodynamic properties obtained from this second minimum, one would find that the free energy is continuous but that a discontinuity appears in the energy at the temperature where the two minima have equal free energies.

Despite the appearance of the second minimum as an artifact and the resultant inapplicability of the theory above 60°, we acquire some information about the liquid above this temperature. We have shown that the calculated distribution function is in error at all temperatures (in that the number of small clusters is undercounted) because of the use of overly high frequencies at small j. Thus, if anything, the actual distribution functions should show a greater preponderance of small clusters than those calculated here; therefore, one of the main conclusions of the theory (*viz.*, that there is an insignificant number of very large clusters, of the order of $j = 60$ or 70 at *all* temperatures) is unaffected by the error in the frequency assignments at low j. Furthermore, it follows that above 60° we would expect liquid water to be composed mainly of small clusters, with a negligible number of clusters larger than $j = 15$ or 20 at these temperatures (see Figure 9).

While the frequencies have been taken as independent of j in the foregoing theory, the form of the partition function (eq 23) would not change if the approximation were eliminated by using frequencies which depend on j; only the numerical values of ν_l would change, but the Einstein vibrational partition function and the overall partition function would remain the same in form, for all cluster sizes.

From the above discussion of the frequencies and the results presented in Tables II–IV, it becomes clear that a two-state theory is inadequate to describe the structure of liquid water. This follows from the fact that the properties of the clusters change continuously as j increases from $j = 1$ to $j \rightarrow \infty$, and one property (the configurational or translational entropy) is a nonadditive function of the entire distribution of cluster sizes. Those properties (*viz.*, the internal configurational entropy of a cluster, the number of hydrogen bonds per molecule in a cluster, the intermolecular vibrational frequencies, and the number of external (translational and rotational) degrees of freedom per molecule), all of which change continuously as a function of cluster size, all make significant contributions to the partition function. As we have seen in connection with the intermolecular vibrational partition function, one cannot represent the properties of a continuous distribution of cluster sizes by just one set of numbers (frequencies, in this case) representing a "bulky" state, which is the error committed of necessity in two-state theories. Likewise, the other properties, and the change in these properties with a change in the distribution of cluster sizes, cannot be reproduced by just two states.

Another approximation made in the theory (which is also of necessity made in two-state theories) is the use of only one value of $(E_H)_{aq}$; *i.e.*, $(E_H)_{aq}$ is taken to be independent of both cluster size and connexity. As already pointed out, recent quantum mechanical calculations[18,19] indicate that the hydrogen bond energy depends on both of these factors.[40] The error in the cluster energy, introduced by this approximation, is probably larger for small clusters, since these contain a larger fraction of one-, two-, and three-bonded molecules. It is probably a better approximation to regard $(E_H)_{aq}$ as an average energy per bond, in the *larger* clusters, because of the larger number of hydrogen bonds per molecule.[40]

Like the similar approximation made about the frequencies, the form of the partition function (eq 23) would not change if this approximation were eliminated by using a relationship giving the dependence of $(E_H)_{aq}$ on size (*i.e.*, on j). The dependence of $(E_H)_{aq}$ on connexity could be taken into account by a partition function of the same form as eq 23, if the differences in energy among, say, the four trimers of Figure 2 were known. In such a case, the partition function would be maximized with respect to the number of each of the trimers in addition to the other cluster sizes (in which case the configurational entropy of each trimer would be zero because there is only one way to form each trimer). In practice, however, it would be extremely difficult to account for structures of all types of connexity in clusters containing more than eight or nine molecules, and the number of variables with respect to which the partition function would have to be maximized would be very large. Because of this and because the dependence of the hydrogen-bond energy on connexity in the liquid is not known, we have used an "average" value of $(E_H)_{aq}$.

It should be noted that many of the arguments presented here against two-state theory are very similar to the same arguments made by proponents of continuum theory.[16] Essentially what is being said is that there is a wide distribution of environments for a water molecule and not just two distinct environments. This argument arose here from a discrete treatment of water (albeit of a continuous distribution of cluster sizes) and may help to resolve the controversy as to whether water is a continuum or a mixture.

A further approximation is the use of the Percus–Yevick theory, from which the configurational (translational) entropy of the clusters was obtained. While the Percus–Yevick theory applies only to spheres and the clusters are not perfect spheres, it is felt that this treatment of the translational degrees of freedom does

(40) For example, it seems[18,19] to be more favorable for a two-bonded molecule to have one bond on an orbital and one on a hydrogen.

not introduce a significant error, since the number of ways that the centers of mass of the clusters can be arranged in the given volume (without rotating them, since the rotation is accounted for in the rotational partition function) is mainly a function of the excluded volume and should not be too sensitive to deviations from spherical shape of the clusters.

A measure of the effect of all the approximations discussed above on the properties of water is obtained from a comparison of the calculated and observed thermodynamic properties (see Figures 6–8), and from the fact that the theory is inapplicable above 60°. It is clear, from the existence of deviations which could not be reduced by further variation of the adjustable parameters, that the theory does not contain an excess of parameters. Although there would be no adjustable parameters in a perfect theory, the use of only three parameters here compares favorably with previous theories.[2] Conceivably, the foregoing theory could be improved by elimination of adjustable parameters if configurations could be counted properly (to determine ω or, more properly, a better alternative to eq 12), if a better quantum mechanical treatment of the hydrogen bond as a function of j could be developed (thereby providing a proper substitute for eq 10), and if a theory of hindered rotation of nonspherical particles in a liquid could be developed (thereby circumventing the necessity of using the rotational parameter d); because the shapes of the clusters are not known, the prospects are not bright for eliminating some parameter equivalent to d to treat rotation.

A limitation of the theory is its inapplicability at high pressures. Unlike the foregoing difficulties (*e.g.*, the inapplicability at high temperatures), which can be removed, *e.g.*, by introducing a dependence of the frequencies on cluster size, the functional form of the potential energy in the translational partition function (eq 15) would have to be changed to apply it at high pressures. Since the hard-sphere repulsion contains no volume-dependent energy term, the energy decreases much too rapidly (because of the background potential) as the pressure is increased and the volume is decreased. To obtain the correct energy at small volumes or high pressures, a softer repulsive potential would be required.

XI. Summary and Conclusions

The main purpose of this paper is to obtain information about the structure of liquid water. Thus, despite the introduction of approximations, which make this treatment only a first step toward a theory of water, the analysis of these approximations in section X has provided insight into the structure, the inadequacies of the theory, and the directions in which it can be improved. For example, it is clearly seen how important the vibrational frequencies (and their dependence on cluster size) are for an understanding of the thermodynamic data and the intermolecular spectrum.

In the form presented here, the computed thermodynamic properties fit the experimental ones reasonably well, considering the nature of the approximations made, and the theory also accounts qualitatively for the radial distribution function, volume, and intermolecular spectrum, all as a function of temperature. Thus, if we accept a cluster model for liquid water, then we can say that water consists of a continuous distribution of cluster sizes, a *negligible number* of which contain more than 60 or 70 molecules. The median cluster size of the distribution decreases with increasing temperature, thus accounting for many of the properties of water, such as the minimum in the molar volume and the decrease in the intensity of intermolecular vibrations.

The thermodynamic properties (Figures 6–8) and the various contributions to these properties (Tables II–IV) were calculated as a function of temperature, using three adjustable parameters. The approximations made in this theory, and commonly made in other theories, were evaluated in terms of these contributions. The internal configurational entropy of the clusters, which had been omitted from previous theories of water, was shown to account for between 1 and 2 entropy units or roughly 10% of the entropy of the liquid. The volume dependence of the background potential, and therefore of the hydrogen bond energy, and the contribution to the energy from the shift in the intramolecular vibrational frequencies on breaking a hydrogen bond, also omitted in previous theories, were included here in the hydrogen-bonding term (Table VI). The error arising from the approximation made in the assignment of the frequencies was discussed in terms of the vibrational energy contribution, and it was pointed out that an equivalent error is made of necessity in all two-state theories (since they cannot represent a distribution of properties, but must approximate the distribution by two values corresponding to the two states, and these values cannot always represent a proper average). The inadequacy of a two-state theory was also discussed in terms of the translational entropy, which constitutes roughly 15–30% (Table IV) of the total entropy and is a nonadditive function of the entire distribution of cluster sizes, and cannot be represented by the mixing of only two states. It was pointed out that these arguments against two-state theory are very similar to those presented by proponents of continuum theories and that this treatment may resolve the differences between the continuum and discrete points of view. Other approximations, such as the use of a hydrogen bond energy independent of cluster size and connexity and the representation of the clusters by spheres for the sake of the translational partition function, were also discussed in section X.

Finally, the analysis of the approximations in this

theory provides some insight into the nature and significance of some approximations frequently made in theories of water structure.

At the present time, we are attempting to extend the theory to take into account the cooperativity of hydrogen bonding (using quantum mechanical results) and to make a better approximation for the dependence of the frequencies on cluster size.

Acknowledgment. We are indebted to Professor B. Widom and Mr. Barry Lentz for fruitful discussions and to Mr. Robert Tuttle for help with the computing.

Appendix

In anticipation of two possible misconceptions about the model used in this paper, we discuss them here.

1. One possible misconception is the idea that the structure of liquid water must be an overall connected lattice (rather than a mixture of small disconnected clusters) because an ice I lattice has been shown[41] to maintain overall connectivity when 38.8% of the bonds are intact.

In such connectivity calculations, it is assumed (a) that bond breaking is a random process, and it is implicitly assumed (b) that the translational degrees of freedom are frozen-in in a fixed lattice.

It is clear that neither of these assumptions obtains in liquid water.

First of all, recent quantum mechanical calculations all conclude that hydrogen bond formation is a cooperative[19,42] and not a random process. In fact, Del Bene and Pople[19] were led to suggest that small clusters consisting of hydrogen-bonded rings (which are unable to form an extended network) may contribute significantly to the structure of water.

Secondly, water molecules are not restricted to a lattice. Hence, by forming near-spherical type clusters, the number of hydrogen bonds per molecule is increased, and at the same time the cluster gains translational and rotational entropy relative to a connected lattice.

These two effects are not taken into account in random statistics calculations on a lattice (which have been used to treat other subjects); thus, the results of these calculations cannot be taken over indiscriminately and applied to water.

2. A second possible misconception is the idea that low-angle X-ray diffraction studies indicate that clusters do not exist.

While the conclusions that can be drawn from X-ray scattering are the subject of some controversy,[43,44] some facts seem indisputable. At room temperature, the structure is essentially random beyond 8 Å; *i.e.*, "a water molecule located at the center of a sphere with a radius of 8 Å "sees" approximately $(4/3)\pi 8^3\rho \sim 70$ other molecules in positions which are on the average nonrandom."[29] This fact rules out the existence of *very large* clusters or nonrandom regions but obviously not clusters of the sizes predicted by our theory (see Figure 9), which are in good agreement with the experimental results.

It should also be pointed out that, when fluctuation theory calculations are carried out to find the maximum allowable cluster size in water,[29,45] the density assumed for the clusters is usually taken to be that of ordinary ice. However, the density of small clusters is much higher than that of ice since the clusters consist mostly of surface molecules (*e.g.*, there is only one "hole" in a cluster of size 12 compared to one "hole" per two water molecules in ice; the low density of ice results from its open structure, *i.e.*, from the fact that there are so many "holes" per water molecule). If a higher density were used for the clusters in the fluctuation theory calculations, larger cluster sizes would be obtained. However, even with the lower density used in the calculations,[29,45] the maximum cluster size (*viz.*, an upper limit of 20 or so to the size of frequently occurring clusters in water) obtained from the low-angle X-ray data is in good agreement with our computed distributions of cluster sizes (see Figure 9). Thus, the concept that low-angle X-ray scattering experiments rule out clusters is erroneous; such experiments rule out only the existence of *very large* clusters or any *large* ordered region in water.

(41) V. A. Vyssotsky, S. B. Gordon, H. L. Frisch, and J. Hammersley, *Phys. Rev.*, **123**, 1566 (1961).

(42) D. Hankins, J. W. Moskowitz, and F. Stillinger, *J. Chem. Phys.*, **53**, 4544 (1970).

(43) B. Kamb, *Science*, **167**, 1520 (1970).

(44) A. H. Narten and H. A. Levy, *ibid.*, **167**, 1521 (1970).

(45) H. J. C. Berendsen, "Theoretical and Experimental Biophysics," Vol. 1, A. Cole, Ed., Marcel Dekker, New York, N. Y., 1967, p 1.

Fluidity and Conductance in Aqueous Electrolyte Solutions. An Approach from the Glassy State and High-Concentration Limit. I. $Ca(NO_3)_2$ Solutions

by C. A. Angell* and R. D. Bressel

Department of Chemistry, Purdue University, Lafayette, Indiana 47907 *(Received January 14, 1972)*

Publication costs assisted by the Department of the Interior, Office of Saline Water

This paper is concerned with a treatment of aqueous electrolyte solution transport properties which differs from conventional approaches by the absence of any initial assignment of separate solute and solvent roles to the constituent particles of the solution. In this approach the embarrassments met by conventional theory on passing to compositions at which there is no longer any recognizable bulk solvent may be avoided. To provide the experimental basis for the treatment, a study of electrical conductance and fluidity of $Ca(NO_3)_2$–water solutions in the composition range 0–26 mol % (0–20 *m*) and temperature range +80 to −60° has been performed. Results are analyzed utilizing concepts and expressions for relaxation processes in glass-forming liquids, of which aqueous solutions provide many excellent examples. The data provide the basis for quasi-empirical expressions in which the composition dependence of the transport properties can be expressed in simple form incorporating the parameters which describe the transport temperature dependence. A simple general form which describes the isothermal composition dependence of viscosity in these solutions as it varies over four orders of magnitude between infinite dilution and extreme concentration is $\eta^{-1} = A \exp[-B/(x_0 - x)]$, where x is the solution composition in mole per cent salt and x_0, B, and A are constants. This form is shown to be almost the equivalent of the Vand equation which has previously been invoked to describe the η composition dependence of highly viscous solutions. In the viscous region, solution equivalent conductances are described by the same form of equation with almost the same value of x_0. From our analysis we conclude that the behavior of this type of electrolyte system may be described in terms of the following three composition regions: (i) a relatively simple high-concentration region in which it is suggested there is no "bulk" water present and all modes of motion are presumed to be strongly coupled (the cohesive energy, indicated by the glass temperature, T_g, and "ideal" glass temperature, T_0, decreases in simple linear fashion with composition as the ionic charges are diluted by intervening oriented water molecules); (ii) a complex intermediate region in which the solution structure is probably inhomogeneous on a microscopic scale ("worm-hole" structure) due to cooperative overlap of oppositely charged (ion–solvent cosphere) complexes, and is subject to increasingly large water-rich and hydrated salt-rich composition fluctuations with decreasing temperature; and (iii) a dilute region in which, as normally conceived, the ions plus their solvent cospheres are dispersed in a bulk water continuum.

Introduction

The attempt to interpret properties of electrolyte solutions at concentrations far from the very dilute region to which the Debye–Hückel theory applies has been one of the celebrated failures of physical chemistry. The concentration region in which the Debye–Hückel theory is rigorously valid is assessed differently by different authors, some estimates putting the limit of validity as low as 0.001 *m*.[1] Even with the more commonly accepted limit of 0.01 *m*, the grim fact remains that a theoretical description, free of adjustable parameters, is at hand only for the first 0.02 mol % of the binary system water–salt, of which homogeneous solutions ranging up to 35 mol % salt may be available for study at room temperature.

There are, of course, a number of famous refinements of both the equilibrium and nonequilibrium expressions of Debye–Hückel theory which extend the description to somewhat higher concentrations, but it seems that these must founder before the 1–10 *m* concentrations of common practical interest are reached because the electrostatic interactions become so large with respect to kT that the "charge-cloud" concept becomes quite untenable. At concentrations beyond the valid charge-cloud domain, it is expected in principle that the charges will tend to arrange themselves on a regular lattice to minimize the electrostatic energy. It is easily shown[2] that under these conditions a $C^{1/3}$ concentration dependence is to be expected for the salt activity coefficient. Indeed Lietzke, Stoughton, and Fuoss[3] recently utilized this idea in constructing a two-structure model for moderately concentrated solutions. They found thermodynamic data for NaCl solutions up to 2 *M* concentrations could be accurately described, using the Madelung constant appropriate to the energy-minimizing rock salt arrangement of the ions. However, it seems that any such "homogeneous"

(1) H. S. Frank, *J. Chem. Phys.*, 31, 1086 (1959).

(2) G. Kortum, "Treatise on Electrochemistry," 2nd ed, Elsevier, Amsterdam, 1965, p 175.

(3) M. H. Lietzke, R. W. Stoughton, and R. M. Fuoss, *Proc. Nat. Acad. Sci. U. S.*, 59, 39 (1968).

or "continuum" model must have strict limitations on its usefulness in view of the marked changes in cohesion-indicating properties which are commonly found near concentrations of 4–6 *m*. Such breaks are particularly pronounced in studies performed at low (subzero) temperatures at which thermal disordering effects are minimized.[4]

It is clear from the success of Gurney's interpretation of activity coefficient and viscosity *B* coefficient data[5] that no progress can be made in understanding more concentrated solutions without properly accounting for the consequences of the specific interactions occurring between ions and solvent molecules. From these interactions result ion-plus-reorganized-solvent complexes, the reorganized solvent shell being called by Gurney, the "cosphere." Under these circumstances, important effects must be anticipated in the composition region where the cospheres begin to overlap. For solutions of cations capable of reorientating two sheaths of water molecules,[6] this composition region will fall somewhat before 7 mol % salt or 4 *m* salt concentration. In a system such as $Ca(NO_3)_2$–water, in which solutions containing up to 30 mol % of salt may be studied at room temperature, solutions in some 75% of the measurable composition range, therefore, lack any recognizable solvent in the sense of a molecular continuum which exhibits properties essentially those of the pure molecular component.

At these higher concentrations the composition and temperature dependences of solution viscosity and conductance become so great that logarithmic graphs are required to display them adequately. Attempts have been made to understand such rapid changes within a classical solute–solvent *theoretical* framework by Vand[7] who utilized the concept of variably hydrated solute species (single solvation sheath) distorting the "lines of flow" of the solvent. The equations derived by Vand, or equations of similar form based on them, have been applied with some success to describe viscosity–composition relations in electrolyte solutions.[8] Recently similar applications have been made to rare earth chloride solutions up to 3.9 *m*[9] and to some 72 electrolyte solutions to concentrations as high as 8 *m*.[10] However, it seems to us that the Vand approach collapses completely with the finding (this paper and ref 4) that solution properties vary quite smoothly through to, and even beyond, salt hydrate compositions at which there is, of course, no solvent, hence no flow lines to distort. The conclusion is reached that a new type of interpretation must be found. A similar conclusion, concerning the usefulness of the classically based Wishaw–Stokes equation for the electrical conductance of concentrated solutions, was reached in a previous paper.[11] The limitations of the latter equation have also been brought out by Molenat[12] in connection with recent studies of uni-univalent salt solutions up to saturation concentrations.

Attention has recently been directed to the fact that the great majority of solutions which reach concentrations greater than 4–5 *m* (7–8 mol % salt) become very viscous on cooling to their liquidus temperatures and may commonly be supercooled into the vitreous state with little difficulty.[4,11,13] This has suggested the application of the concepts and equations being developed for the understanding of relaxation processes in other glass-forming liquids to bring new insight to the nature of transport processes in concentrated solutions and to provide new empirical descriptions of the composition dependence of transport constants.

A start in this direction was made by one of us[11] when it was demonstrated that the temperature dependence of conductance in $Mg(NO_3)_2$ and $Ca(NO_3)_2$ solutions followed the empirical Vogel–Tammann–Fulcher (VTF)[14] equation which describes the transport properties $W(T)$ (*e.g.*, conductance and fluidity) of a variety of glass-forming liquids

$$W(T) = AT^{-1/2} \exp(-B/(T - T_0)) \qquad (1)$$

where A, B, and T_0 are constants.[15] T_0 in this expression represents the temperature at which ionic mobilities would appear to fall to zero and has been attributed thermodynamic significance in the theoretical interpretations of eq 1 by Cohen and Turnbull,[16] Adam and Gibbs,[17] and Angell and Rao.[18] Equation 1 has been transformed into an isothermal form[11] by taking into account the composition variation of the three constants. The similarity of its functional form with that of the Vand equation[7] provides an alternative explanation of the relative success of the latter, as will be discussed in detail below.

Proper evaluation of the utility of this new general approach, however, has been hampered by the lack of data covering a sufficiently extensive range of composi-

(4) C. A. Angell and E. J. Sare, *J. Chem. Phys.*, **52**, 1058 (1970).

(5) R. W. Gurney, "Ionic Processes in Solutions," Dover Publications, New York, N. Y., 1953.

(6) R. A. Robinson and R. H. Stokes, *J. Amer. Chem. Soc.*, **70**, 1870 (1948).

(7) (a) V. Vand, *J. Phys. Chem.*, **52**, 277 (1948); (b) *ibid.*, **52**, 314 (1948).

(8) R. H. Stokes in "The Structure of Electrolytic Solutions," W. J. Hamer, Ed., Wiley, New York, N. Y., 1959, p 298.

(9) F. Spedding and M. Pikal, *J. Phys. Chem.*, **70**, 2430 (1966).

(10) B. Breslau and I. Miller, *ibid.*, **74**, 1056 (1970).

(11) C. A. Angell, *ibid.*, **70**, 3988 (1966).

(12) J. Molenat, *J. Chim. Phys.*, **66**, 825 (1969).

(13) (a) C. A. Angell, *J. Phys. Chem.*, **69**, 2137 (1965); (b) *J. Chem. Phys.*, **46**, 4673 (1967); (c) G. Vuillard, *Ann. Chim. (Paris)*, **2**, 233 (1957).

(14) (a) H. Vogel, *Physik. Z.*, **22**, 645 (1921); (b) V. G. Tammann and W. Hesse, *Z. Anorg. Allg. Chem.*, **156**, 245 (1926); (c) G. S. Fulcher, *J. Amer. Ceram. Soc.*, **8**, 339 (1925).

(15) The original VTF equation did not contain the $T^{-1/2}$ factor (see ref 11).

(16) M. H. Cohen and D. Turnbull, *J. Chem. Phys.*, **31**, 1164 (1959).

(17) G. Adam and J. H. Gibbs, *ibid.*, **43**, 139 (1965).

(18) C. A. Angell and K. J. Rao, *ibid.*, **57**, 470 (1972).

tions and temperatures. The present study on the $Ca(NO_3)_2$–H_2O solution is intended to fill this data gap and to demonstrate the extent to which the apparent complexity of concentrated solution behavior can be reduced by interpretation in these new terms.

Experimental Section

Mallinckrodt analytical reagent grade calcium nitrate tetrahydrate from a single bottle was used in making up all the solutions. The water used was distilled, deionized conductivity water with a specific resistance greater than 10^6 Ω cm. The concentrations were gravimetrically determined by vacuum dehydration of 2–5-g samples at 140°. Evolution of HNO_3 was not detectable at 140°. Absence of water in the dehydrated samples was confirmed by addition of the dry sample to Karl Fisher reagent at its end point with no subsequent change. Analyses were reproducible to 0.01% by weight.

The viscosities were measured using a Haake falling ball viscometer to 0.1%. The particular feature of this viscometer is that the solution is sealed in the viscometer, thus preventing the condensation of water vapor at low temperatures and the loss of water at high temperatures. The viscometer tube was jacketed with a larger tube through which a 50:50 ethanol–methanol bath was circulated by a Haake circulator. The temperature of the fluid in this outer jacket was measured with a Hewlett-Packard quartz thermometer. The temperature remained stable to ±0.02° during the course of viscosity measurements at a given nominal temperature.

The specific conductivities were measured with a Wayne Kerr B331 autobalance bridge capable of accuracy of 0.01%. The conductivity cells were of the glass capillary dipping type with platinized platinum electrodes. The cell constants (l/A) for the four cells used were 40.05, 92.52, 108.74, and 96.85 cm^{-1}. Cells were immersed in ≈10 ml of solution contained in a 20 × 150 mm test tube and the assembly thermostated in either a Pt resistance-thermometer-controlled constant temperature bath or an aluminum block "furnace." The aluminum block was 3 in. in diameter and 6 in. in height and was bored to the test tube dimension. The temperature of the block was controlled with a Melabs Model CTC-1A proportional temperature controller employing a platinum resistance sensor and two 6-in. 250-W Firerod cartridge heaters. The mass of the aluminum block was large enough to damp out any thermal fluctuations originating at the heating elements.

The temperature of the solution was measured with a precision of 0.02° using copper–constantan thermocouples located next to the capillary in the cell, in conjunction with a Leeds & Northrup K-3 potentiometer and null detector. The cell was designed so that when the thermostat setting was changed both the thermocouple and solution in the conductance path changed temperature at the same rate, thus permitting precise measurements using either equilibrium conditions or continuous slow cooling or heating schedules. The latter permit many more temperature *vs.* conductance readings and lead ultimately to more precise temperature coefficients (which were of primary interest in this study), and this method of data taking was extensively used. However, check equilibrium measurements were always included in any given run. A Melabs Model C1111 temperature programmer was used with two rates of temperature change, 0.3 and 0.75°/min. The direction of change was usually from higher to lower temperatures.

Measured conductances using both programmed rates and equilibrium temperatures agree to 0.5% for all temperatures. While this error among the three methods may seem large, it must be remembered that the conductance is a very sensitive function of temperature in the concentration range where programming was used, and the error corresponds to a difference in temperature of only 0.05° on average.

The densities used were for the most part taken from the data of Ewing and Mikovsky.[19] For cases where linear extrapolations of these data to lower temperatures was unreliable because of nonlinear temperature dependences, new data, accurate to 0.01%, were acquired using a calibrated glass dilatometer.

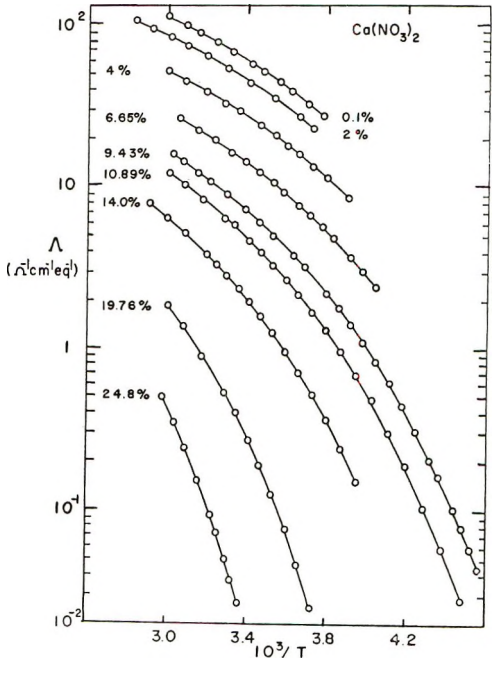

Figure 1. Arrhenius plots of equivalent conductance, Λ, for calcium nitrate solutions. Compositions indicated in mol % $Ca(NO_3)_2$.

(19) W. W. Ewing and R. J. Mikovsky, *J. Amer. Chem. Soc.*, **72**, 1390 (1950).

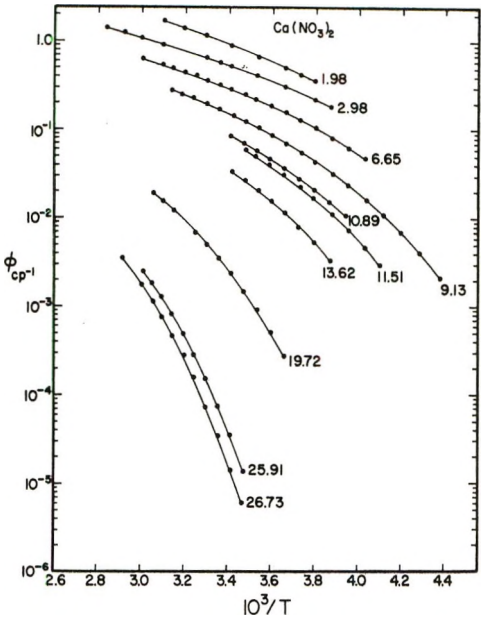

Figure 2. Arrhenius plots of fluidity, ϕ, (= reciprocal viscosity) for calcium nitrate solutions. Compositions indicated in mol % $Ca(NO_3)_2$.

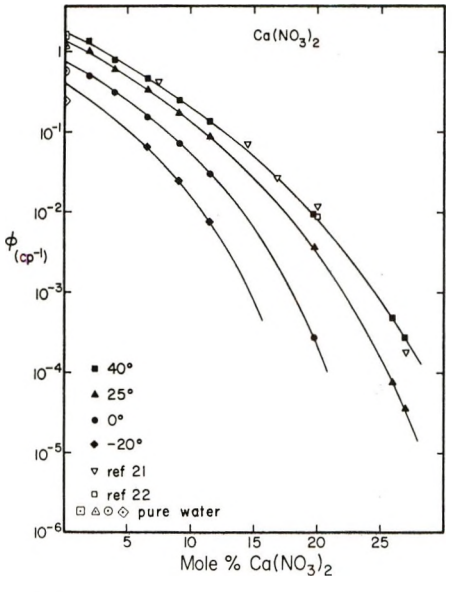

Figure 3. Fluidity isotherms for calcium nitrate solutions. The lines through the experimental points are plots of eq 3 using computed least-squares best fit values of the parameters. The best fit x_0 values lie on a linear extrapolation of the $T_{0(\phi)}$ *vs.* x plot and hence are wholly consistent with the derivation of eq 3. At higher temperatures, where the water structure is considerably disrupted, eq 3 is evidently valid to low salt concentrations.

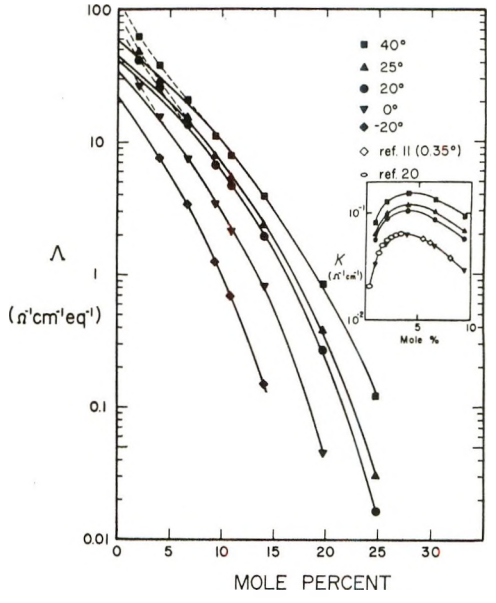

Figure 4. Equivalent conductance isotherms for calcium nitrate solutions. Inset shows specific conductance isotherms in the region of the conductance maximum. The lines through the experimental equivalent conductance points are plots of eq 3 using computed least-squares best fit values of the parameters. These best fit values of x_0 do not fall exactly on the extension of the linear $T_{0(\Lambda)}$ *vs.* x plots. However, plots of eq 3 using values of x_0 which do lie on such an extension are barely distinguishable from the best fit plots and hence have been omitted.

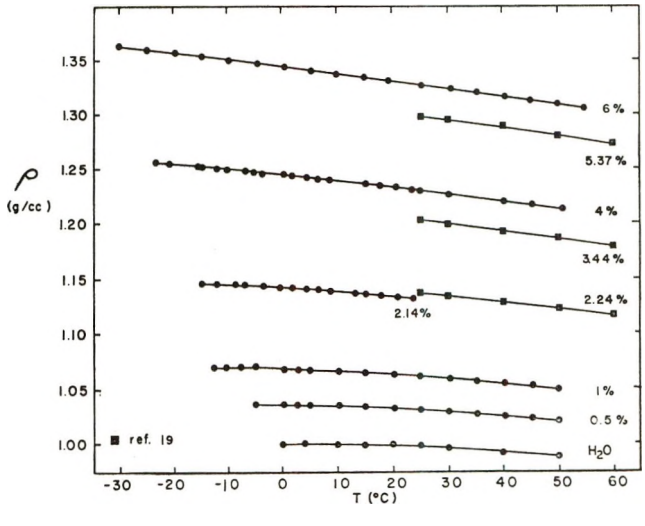

Figure 5. Nonlinear density–temperature relations for calcium nitrate solutions. Densities of all solutions richer than 6 mol % $Ca(NO_3)_2$ are quite linear (see ref 19).

Results

The transport properties measured in this work describe the responses of the solution to perturbations from their equilibrium states brought about by the imposition of electric field and shear stresses. To facilitate comparison of these responses it is desirable that the response constants change in the same direction with change of the experimental variables, temperature and composition. Accordingly, we present our data as equivalent conductances, Λ, and fluidities, ϕ, ($\phi = 1/\eta$) rather than equivalent conductances and viscosities, η, as is more commonly done. In Figures 1 and 2, equivalent conductance and fluidity data covering as much as four orders of magnitude in the

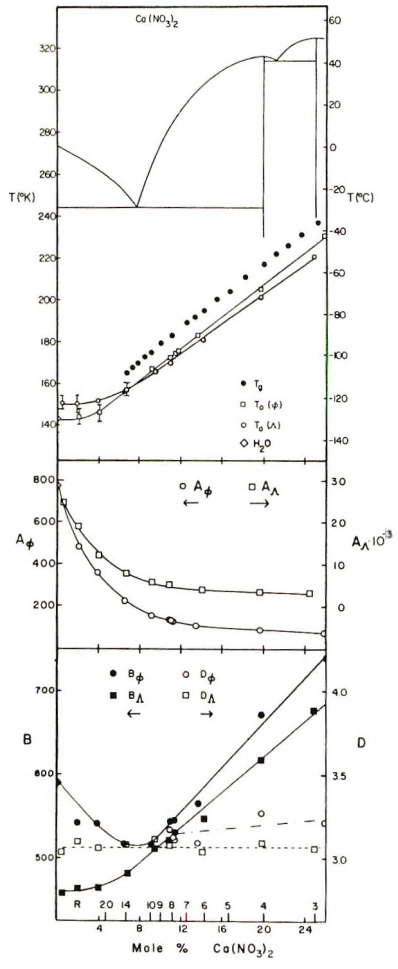

Figure 6. Phase equilibrium diagram, best fit values of the parameters of eq 1 and 2 ($T_{0(\phi)}$, $T_{0(\Lambda)}$, A_ϕ, A_Λ, B_ϕ, B_Λ, D_ϕ, and D_Λ), and experimental glass transition temperatures, T_g, for the system calcium nitrate–water (D_ϕ, –·–; D_Λ, - - - -). Fluidity parameters for water are derived from the data of L. Korsan, *et al.*, *J. Phys. Chem.*, **73**, 34 (1969). R values are units of moles of water/moles of salt.

transport coefficient are displayed in the form of Arrhenius plots.[20] From these data we have constructed fluidity and conductance isotherms for temperatures ranging from −20 to +50°. These are shown in Figures 3 and 4. Some results of previous studies of $Ca(NO_3)_2$–H_2O solutions[11,21] are included for comparison.

Density data for solutions with nonlinear density temperature relations are shown in Figure 5.

After conversion of specific conductance, κ, to equivalent conductance, Λ, the data were computer fitted to eq 1 by an iterative least-squares technique. The best choice of parameters fit eq 1 with standard deviations of better than 0.5% and in many cases better than 0.1%. Choices of confidence limits have been discussed before[22] and are manifested in the choice of the parameter T_0. The best fit parameters are shown in Figure 6 for equivalent conductance and fluidity. The experimental glass transition temperatures, T_g, determined by DTA[4] are also included, together with the equilibrium phase diagram. Compositions are given both in mole per cent $Ca(NO_3)_2$ and in R units, where R = moles of water/moles of salt. This composition scale is very useful in discussion of composition regions in which all or most solvent molecules are immobilized in solvation sheaths.

Discussion of Results

Empirical Aspects. In view of the enormous variations of conductance and fluidity seen in this work compared with those normally reported in aqueous solution studies, the simple, linear composition dependence of the parameters $T_{0(\Lambda)}$ and $T_{0(\phi)}$ of eq 1, for $R < 14$, is impressive. For each process the parameters T_0 have similar composition dependences (Figure 6), and differ by only 5°K in absolute value. The same difference was found by Moynihan[22] in his study of the composition $R = 4$. These T_0 values are also very closely correlated with the experimental glass transition temperature which is commonly believed to occur when $\phi \approx 10^{-15}$ cP^{-1} at the time scale of the T_g determination.[23] The ratio $T_g/T_{0(\phi)}$ remains constant at the value 1.11 over the entire composition range for which the comparison can be made. The similarity of T_0 values for the different processes, and their relation to T_g, is expected from theories giving T_0 thermodynamic significance as the temperature at which the liquid in principle settles into a configurational ground state[16,17] (see below).

The empirical description of the conductance data is made even simpler when it is realized that the composition dependence of the B parameter, B_Λ, is exactly that of T_0 at high concentration, so that B_Λ may be written as $D_\Lambda T_0$ with D_Λ independent of composition (Figure 6). Following eq 1, the entire composition and temperature variation of the conductance process in this high-concentration region may, therefore, be expressed by three-parameter equations of the form

$$\Lambda = A_\Lambda T^{-1/2} \exp(-D_\Lambda T_0/(T - T_0)) \qquad (2)$$

in which (disregarding barely significant changes in A_Λ) only T_0 is composition dependent. Furthermore, the composition dependence of T_0 is a simple linear one. For the fluid flow process B of eq 1 decreases somewhat more rapidly with composition than does T_0. Never-

(20) A complete tabulation of the data presented in Figures 1, 2, and 5 will appear following these pages in the microfilm edition of this volume of the journal. Single copies may be obtained from the Business Operations Office, Books and Journals Division, American Chemical Society, 1155 Sixteenth St., N.W., Washington, D. C. 20036, by referring to code number JPC-72-3244. Remit check or money order for $3.00 for photocopy or $2.00 for microfiche.

(21) (a) H. Jones and C. Stine, *Am. Chem. J.*, **39**, 313 (1908); (b) B. V. Bak, *Russ. J. Phys. Chem.*, **13**, 534 (1939).

(22) C. T. Moynihan, *J. Phys. Chem.*, **70**, 3399 (1966).

(23) Recent experiments (C. T. Moynihan, private communication) suggest the appropriate fluidity may be nearer to 10^{-13} cP^{-1}, when T_g is determined by DTA methods at scanning rates of ~10°/min.

theless, eq 2 with A_ϕ and D_ϕ constant and T_0 linearly dependent on composition will still represent the data with little error. It must be expected that not all concentrated solutions will be as simply behaved as the present one, though many cases of long linear variations of T_g, (hence, presumably of T_0) with composition have been observed.[4]

In a separate article,[24] it is shown that the pressure dependence of conductance in this system can be described with equal simplicity through a pressure dependence of T_0 alone.

Since most interest in solution transport has been devoted to accounting for isothermal composition dependences, we now consider whether any useful empirical descriptions of such a dependence can be derived from the foregoing results. A previous attempt in this direction,[11] made in the absence of data, was based on developing eq 1 with the use of the simplest possible assumptions: (a) a linear dependence of T_0 on charge concentration, N, (equiv $l.^{-1}$), and (b) no composition dependence of the parameters, A and B. These lead to an equation in which a parameter, N_0, the concentration at which particle mobilities would fall to zero at the temperature of the chosen isotherm, played a role analogous to that of T_0 in eq 1. The present results show that, while these assumptions were inadequate, the actual composition dependence of the eq 1 parameters is such that an equally simple form of transport composition dependence can be derived.

We obtain the isothermal composition dependence corresponding to eq 1 and 2 by using the fact (Figure 6) that T_0 is linear in mole per cent, x, of salt

$$T_0(x) = T_0(x = 0) + Qx \qquad \text{(A)}$$

Since $T_0(x = 0)$ is not a meaningful quantity to this discussion, it can be replaced by defining x_0 as the composition at which T_0 equals the temperature under consideration. Consequently

$$T_0(x) = T - Q(x_0 - x) \qquad \text{(B)}$$

Also, since the B parameters are constant (B_Λ) or nearly constant (B_ϕ) multiples of T_0 [see eq 2], substitution into eq 2 with a further substitution of eq B for $T_0(x)$ produces

$$W(x) = AT^{-1/2} \exp -\left[\frac{D_\Lambda T}{Q(x_0 - x)} + D_\Lambda\right] \qquad \text{(C)}$$

which under isothermal conditions, can be expressed as

$$W(x) = A'T^{-1/2} \exp[-B'/(x_0 - x)] \qquad (3)$$

where A', B', and x_0 are constants at any temperatures.[25]

This notably simple equation (*cf.* eq 1), because of the dominance of the exponential term, performs very well in describing high-concentration solution behavior in spite of the small composition dependence of A_Λ, A_ϕ, and D_ϕ of eq 2. This is shown in Figures 3 and 4 in which the solid lines are plots of eq 3 with appropriate parameters (see caption to Figure 3). This is a significant achievement because, on replacing mole per cent x with the molar concentration c

$$x = 1800c/(1000\rho - [M_{salt} - 18]c) \qquad (4)$$

one obtains from eq 3 an equation

$$W(c) = A' \exp -\frac{D_1 + D_2c}{D_3 - c} \qquad (5)$$

the form of which is very similar to that of Vand as used successfully by Spedding and Pikal[9] for lanthanide solution viscosities

$$W(c) = A'' \exp \frac{-A_3c}{1 - Q'c} \equiv A'' \exp \frac{-D_4c}{D_5 - c}$$

Since, as Spedding and Pikal point out, Vand's theory cannot be expected to apply rigorously to electrolyte solutions in general, much less to those of extreme concentration, an alternative origin for this successful mathematical form for the composition dependence of transport is welcome. On the basis of Breslau and Miller's correlation[10] of the Jones–Dole viscosity B parameter and the "effective flowing volume" parameter V_e of the Vand theory, we may anticipate a correlation of B with x_0^{-1} (eq 3) for different salts. A closely related correlation between B and T_g at constant R value has already been demonstrated elsewhere.[4] The theoretical basis for eq 1–3 is considered in a following section.

The specific conductance maximum, characteristic of electrolyte solutions (inset of Figure 4) is also predicted by eq 3 when modified to describe specific conductance by the relation

$$\Lambda = \frac{10^3\kappa}{c} = \frac{\kappa[1800 + (M_{salt} - 18)x}{\rho x}$$

The modified eq 3 contains the composition x in both preexponential and exponential factors. Differentiation predicts a maximum value for κ at the value of x satisfying the relation

$$\frac{d\kappa}{dT} = 0 = \frac{1}{(S + x)} - \frac{x}{(S + x)^2} - \frac{B'x}{(S + x)(x_0 - x)^2}$$

where $S = 1800/(M_{salt} - 18)$ (eq 4), and B' and x_0 are the constants of eq 3. Substituting best fit experimental values for the constants, we obtain $x_{\kappa_{max}} = 4.6\%$ $Ca(NO_3)_2$ for the 0° isotherm compared with the experimental value of 3.5% (Figure 4). The discrepancy arises because eq 3, which was derived for the high-concentration region, does not take account of the changes in dT_0/dx and A found at low concentrations (Figure 6).

(24) C. A. Angell, L. J. Pollard, and W. Strauss, in press.
(25) R. D. Bressel, Ph.D. Thesis, Purdue University, 1972.

In summary, eq 2 and 3 allow us to describe the behavior of solution conductances and fluidities which vary over some five orders of magnitude in value. We will show in our interpretation section that the values of T_0 obtained from the transport analysis are quite consistent with the configurational entropy zero-point temperature $T_{0(cal)}$, obtained from an independent analysis of equilibrium (calorimetric) data. This is an important consistency because of the dominant role we allow the T_0 parameter to play in our analysis.

The validity of our equations, and of the correlation of their parameters with $T_{0(cal)}$, has limits which should be noted. Between normal fluidities and the glass temperature, T_g, no less than 15 orders of magnitude of fluidity change occur. Not surprisingly, eq 2 does not apply over this entire range without changes in parameters. In a current low-temperature study of the present system, Ambrus, *et al.*,[26] have found, for instance, that between the 6th and 10th decade below normal fluidities the best fit $T_{0(\Lambda)}$ and $T_{0(\phi)}$ values agree neither with each other nor with $T_{0(cal)}$. In fact, $T_{0(\Lambda)} < T_{0(\phi)} < T_{0(cal)}$. Similar behavior at very low fluidities is also found for pure molecular substances[27] and anhydrous ionic liquids.[28] We believe, however, that the fluidity region investigated in the present study, in which calorimetric and mass transport T_0 values are all in accord, is that of greatest immediate interest to the development of concentrated solution transport theory.

Theoretical Interpretation

On passing from the liquid into the glassy state very substantial decreases in solution heat capacities, C_p, are observed. These decreases, which are utilized in the experimental determination of T_g,[4] result from the loss of the configurational degrees of freedom. This implies that at lower temperatures the potential energy of the system determined by the relative positions of the particles remains essentially constant. The changes in C_p occur at T_g because structural relaxation times become too long for internal structural equilibrium to be maintained on the time scale of the cooling process. Hence, as observed in the laboratory, the transition is a relaxational phenomenon. However, from thermodynamic arguments utilizing additional data from crystalline phases[29] it can be seen that the decrease in heat capacity must occur as an equilibrium phenomenon at slightly lower temperatures, in order that the liquid total entropy does not become less than that of the crystal. For instance, calorimetric data for $Ca(NO_3)_2 \cdot 4H_2O$ liquid (*i.e.*, the 20 mol % solution) and crystal phases[30] place a lower limit for the maintenance of the observed liquid heat capacity at ~203°K. This is obviously very close to the value of T_0 extracted from the present transport data ($T_{0,\phi} = 205°$ and $T_{0,\Lambda} = 200°$), and since similar results are found for many other liquids,[18] it seems clear that the mass transport, or structural relaxation, rates are closely related to the extent of excitation of the system's configurational degrees of freedom. This is not only very important conceptually but it also provides the means whereby, at least at the compositions of crystalline compounds, one of the adjustable parameters of the transport equation, eq 1, can be removed.

Seeking such a connection between equilibrium and relaxation properties Adam and Gibbs[17] developed an expression for the fundamental transition probability for a cooperative mass transport process which had the form

$$W(T) \propto \exp \frac{-C}{TS_c} \tag{6}$$

where the constant C contains among other invariables a free energy, $\Delta\mu$, which distinguishes the "rearrangeable" subsystems from all the others. S_c is the total configurational entropy.

S_c can be evaluated by integration of the configurational heat capacity, ΔC_p (the difference between the supercooled liquid and extrapolated glass heat capacities), from T_0 to some temperature T. Adam and Gibbs assumed this ΔC_p to be constant and obtained

$$S_c = \int_{T_0}^{T} \frac{\Delta C_p}{T} \, dT = \Delta C_p \ln T/T_0 \approx \Delta C_p \left[\frac{T - T_0}{T}\right] \tag{7}$$

which when substituted into eq 6 yields the VTF equation with the restriction that T be very close to T_0. The condition ΔC_p = constant is, however, a rather poor description of the temperature dependence of the configurational heat capacity as defined above. A simple relation in much better accord with experiment is ΔC_p = constant/T. Use of this form in the evaluation of S_c by integration from T_0 to T gives an expression which, on substitution into eq 6, yields the VTF equation (eq 1) as an exact relation

$$W(T) \propto \exp(-C'T_0/(T - T_0)) = \exp(-B/(T - T_0)) \tag{8}$$

Note that B of eq 1 is now proportional to T_0, as is found empirically for the present solutions. Hence, the Adam–Gibbs theory provides a possible theoretical basis for the empirically determined transport expressions. One of the constants determining the value of C' in eq 8 may be obtained from suitable heat ca-

(26) J. H. Ambrus, C. T. Moynihan, and P. B. Macedo, *J. Electrochem. Soc.*, **119**, 192 (1971).

(27) D. R. Uhlmann in "Amorphous Solids," R. W. Douglas and B. Ellis, Ed., Wiley, New York, N. Y., 1971.

(28) H. Tweer, N. Laberge, and P. B. Macedo, *J. Chem. Phys.*, **54**, 121 (1971).

(29) (a) W. Kauzmann, *Chem. Rev.*, **43**, 219 (1948); (b) C. A. Angell, *J. Chem. Educ.*, **47**, 583 (1970).

(30) C. A. Angell and J. Tucker, to be submitted for publication (results included in ref 18).

pacity studies but the remainder cannot be independently determined.

Notwithstanding the useful finding that T_0, the key parameter of eq 1 and 2, may be obtained from an independent thermodynamic experiment at certain compositions, the theory of the transport phenomena is little advanced without a theory for T_0 itself.

For chain-polymer liquids and systems with some cross linking, T_0 can be related to chain stiffness and hole energy parameters by a theory by Gibbs and DiMarzio.[31] However, this approach does not seem adaptable to the present solutions which are more closely related to the three-dimensional networks to which Gibbs and DiMarzio's theory could not be extended. Indeed, if the solutions are considered as networks in which the variably hydrated cations are bound together through hydrogen bonds to the nitrate anions,[4] then the recent "bond lattice" model of Angell and Rao[18] may provide the more relevant basis for discussion.

The bond lattice model, which has already been shown to reconcile thermodynamic and mass transport aspects of the behavior of water with a hydrogen bonded network structure,[32] leads in zero-order approximation to an expression for the degree of configurational excitation of a liquid in terms of the fraction, N_x, of "bonds," which are broken at temperature T

$$N_x = \left[1 + \exp \frac{\Delta H - T\Delta S}{RT}\right]^{-1} \tag{9}$$

In this expression ΔH is an average value of the (noncooperative[18,32]) energy per mole required to produce each elementary configurational excitation (broken bond) of the lattice, while ΔS is the average molar change of lattice entropy[33] associated with the excitation.

According to eq 9 the liquid only settles into its configurational ground state ($N_x = 0$) at 0°K. However, the form of eq 9 is such that, in the temperature range in which our measurements are made, N_x varies almost linearly with T, tending by extrapolation to vanish at a finite temperature, T_0. This suggests that the correlation of mass transport rates and degree of configurational excitation implied by the coincidence of calorimetric and eq 1 T_0 values may involve the broken bond fraction, N_x. In fact, if mass transport occurs *via* cooperative redistributions of molecules at sites of abnormal fluctuations in the local concentration of randomly distributed broken bonds, then an exponential relation between the mass transport probability and the reciprocal broken bond fraction is expected. Previous free volume fluctuation theories[16] and free energy fluctuation theories[17] have yielded similar exponential relations between relaxation time and appropriate macroscopic configurational quantities.

Thus, we write

$$W(T) = \frac{1}{Z} \exp - \zeta/N_x \tag{10}$$

where Z and ζ are constants of order unity. Since the VTF B_ϕ and B_Λ parameters differ (Figure 6), experiment requires that ζ depend somewhat ($\sim$20%) on the transport process under study. Substituting eq 9 into eq 10, and for empirical purposes absorbing ζ into the other parameters in the exponential,[34] we obtain a new quasi-empirical expression for the temperature dependence of mass transport processes

$$\Lambda,\phi \propto W(T) = AT^{-1/2} \times \exp -\left(1 + \exp\frac{\Delta H - T\Delta S}{RT}\right) = AT^{-1/2} \exp -\left(1 + \exp\left(\frac{B}{T} - C\right)\right) \tag{11}$$

This three parameter transcendental equation is capable of representing the experimental data with essentially the same precision (Δ = 0.1–0.5%) as the three parameter VTF equation, eq 1. Although not of as simple form as the VTF equation, eq 11 has the advantage of not requiring or implying a sharp (second order) transition at a finite temperature T_0 to a configuration ground state.

The parameters B ($= \Delta H/R$) and C ($= \Delta S/R$) in eq 11 contain the information necessary to approximately determine the configurational heat capacity of the liquid. In a case such as water, in which the number of possible "bonds" per mole of substance is generally agreed upon as $2N$, (N = Avogadro's number) the measured configurational heat capacity can actually be used to predict the temperature dependence of mass transport processes.[32] In more complicated multicomponent liquids, however, the configurational heat capacity per mole of liquid can be measured, but it will not be clear how many moles of "bonds" are involved. In this case, it may be useful to work backward from the transport parameters to estimate the configurational heat capacity per mole of bonds and, thence, by comparison with experimental heat capacities, the number of bonds per mole of liquid. By thus defining something analogous to Wunderlich's "beads,"[35a] such

(31) J. H. Gibbs and E. A. DiMarzio, *J. Chem. Phys.*, **38**, 373 (1958).

(32) C. A. Angell, *J. Phys. Chem.*, **75**, 3698 (1971).

(33) Such an entropy change can arise through a shift in density of states to lower frequencies, through an increase in anharmonic character of existing modes, or through a local configurational degeneracy following the breaking of a bond.

(34) Differences in ζ will show up principally as differences in the ΔS or C parameter in eq 11.

(35) (a) B. Wunderlich, *J. Phys. Chem.*, **64**, 1052 (1960). Wunderlich defined a bead as the smallest unit of the structure whose motion could affect the hole–phonon equilibrium in the Hirai–Eyring hole theory for polymers (N. Hirai and H. Eyring, *J. Appl. Phys.*, **29**, 810 (1958); *J. Polymer Sci.*, **37**, 51 (1959)). (b) E. J. Sare, C. T. Moynihan, and C. A. Angell, *J. Phys. Chem.*, submitted for publication.

determinations (although tentative in view of the quasi-empirical nature of eq 10) may help clarify some molecular details of transport in these solutions. For instance, fitting the data for the $R = 4$ solution to eq 11 we find $\Delta H = 2560$, and 2450 cal/mol and $\Delta S = 5.25$ and 5.08 eu from the fluidity and conductance data, respectively. Using relations given elsewhere,[18] these parameters yield a maximum configurational heat capacity of 5.3 cal deg^{-1} per mole of bonds near 350°K, whereas experiment[28] yields ΔC_p at the melting point (316°K) = $C_{p(\text{configuration})}$ = 48 cal deg^{-1} per mole of $Ca(NO_3)_2 \cdot 4H_2O$. It is implied that, as a gross average (two state approximation), there are $9N$ equivalent disruptable points of interaction per mole of $Ca(NO_3)_2 \cdot 4H_2O$ (*cf.* $2N$ per mole of pure water). This figure could be interpreted as reflecting the number of hydrogen bonds between solvated H_2O and NO_3^- ions (there are $8N$ protons per mole). On the other hand, it seems certain that the reorientation of the asymmetric NO_3^- ions in the hydrated cation force field must contribute independently to the measured value of ΔC_p; hence any simple description of what constitutes a "bond" in a system as complex as this present one is probably not possible. For comparison, Wunderlich[35a] would suggest $Ca(NO_3)_2 \cdot 4H_2O$ contains 11 "beads" per mole based on the number of oxygen atoms and the calcium ion, although in this case the change in heat capacity per bead at T_g, 5.0 cal deg^{-1}, is much greater than his "universal" value of 2.7 cal deg^{-1}. Clearly some systematic studies of heat capacity and its increase at T_g in different glass-forming solutions are needed before the relation between thermodynamic properties and mass transport temperature dependence in arbitrary solutions can be clarified.

Processing of data at other compositions using eq 11 shows that ΔH, like T_0 of eq 1, increases linearly with mole per cent $Ca(NO_3)_2$. This is consistent with increasing average hydrogen bond strength (*cf.* results of proton chemical shift studies[35b]) and increasingly inhibited NO_3 reorientation with increasing concentration of ions.

Structural Interpretations

The foregoing should establish the usefulness and potential of approaching the concentrated solution problem from the high-concentration limit by application of current ideas on viscous liquids and the glass transition phenomenon. Little attention actually has so far been paid in our discussion to the presence of charged particles and water molecules in the liquids studied (although, of course, it is the interactions between these particles which determine the magnitude and composition dependence of the parameters of eq 1, 3, and 11).

In the present section we give brief attention to those features of our data which invite some structural interpretation.

We pointed out earlier that the specific conductance maximum, which has in the past been attributed structural significance, is expected to arise naturally from the balancing of carrier density and mobility factors which may change smoothly through all concentration ranges. Therefore, the existence of a conductance maximum at a particular composition (3.5% $Ca(NO_3)_2$ in this case) is itself not of structural significance. However, the changes of slope in the A, B, and T_0 parameters in the same general composition region (Figure 6) certainly do require some discussion, particularly since it is this behavior which prevents us from extending our empirical description to dilute solutions.[36]

First, we should note that the differences in behavior of conductance and viscosity parameters may not be significant. The B and T_0 parameters, which jointly determine the transport temperature dependence, are closely correlated, and if B_Λ were constrained to follow the composition dependence of B_ϕ, then $T_{0(\Lambda)}$, like $T_{0(\phi)}$, would not show a change in composition dependence until ~4 mol % $Ca(NO_3)_2$. The experimental T_g, which should provide a good guide to the behavior of T_0, cannot be determined in this range unfortunately, but it is interesting to note that, if 17% of the water in the solutions is replaced by dioxane (a 50:50 wt % solution), T_g for the solutions is found to become suddenly independent of composition at 4 mol % $Ca(NO_3)_2$ ($T_g = -110$°K).[37] This behavior, which is observed in a number of purely aqueous electrolyte systems,[4] is actually intermediate between that of $T_{0(\Lambda)}$ and $T_{0(\phi)}$ seen in Figure 6 although the T_g arrest is much more abrupt. Together, these observations suggest that some sort of structural transition, which is naturally much better defined at the lower thermal excitation levels characteristic of the glass transition temperature, occurs within the solution between 4 and 8 mol % $Ca(NO_3)_2$.

Below 6 mol % $Ca(NO_3)_2$ the density *vs.* temperature relations become nonlinear (Figure 5), a characteristic of water and a relatively few other highly structured liquids. This, and other considerations,[4] suggests to us that the transition region probably has its origin in an incompatibility of the network water structure with an ionic liquid structure involving anions and hydrated cations which we believe is formed at high salt concentrations (and/or low temperatures) by cooperative association of solvent separated ion pairs. In some cases, it seems that the interactions involved in these processes may actually lead to liquid–liquid phase separation when the solution temperature is sufficiently lowered. Such a phenomenon, initially envisaged by

(36) Despite the behavior of the best fit eq 1 parameters for fluidity, eq 3 describes the fluidity composition dependence satisfactorily to low salt concentration (Figure 3 and Figure 3 ref 13b), due to the compensation of the varying parameters.

(37) E. J. Sare, Thesis, Purdue University, 1971.

Angell and Sare,[4] was recently demonstrated rather directly for the LiCl–H_2O system by the low-temperature light scattering studies of Hsich, *et al.*[38]

In this case it may be possible to make useful comparisons of the behavior of the A and B parameters seen in Figure 6 with the behavior of these parameters in other systems in which an ionic solute dissolves endothermically in a solvent of network structure to yield a solution which phase separates at lower temperatures.[39] However, since the manifestations of this structural reorganization are not particularly pronounced in the present system, further discussion of this important and interesting region of aqueous solution behavior will be deferred to a subsequent publication.

Summary and Concluding Remarks

We have presented transport data for aqueous salt solutions extending to unusually high concentrations and low temperatures and have shown that these may be described over much of the composition range by quasi-empirical three-parameter equations of very simple form.

Our analysis has suggested the existence of three distinguishable concentration regions of behavior in these systems. The very high concentration region, in which water molecules are being added to the first or second hydration shells of the cation, may be relatively straightforward to interpret since the cohesive energy appears to vary linearly with water mole fraction and to dominate the liquid properties. The very dilute region is well understood, but the intermediate composition region, in which a structural transition from classical aqueous solution to liquid salt hydrate occurs, appears very complex in character possibly due to "structural" microheterogeneity of the solutions.

It is possible to obtain more information on the characteristics of these regions from transport measurements in which the time or frequency dependence of the system response to the perturbation from equilibrium is studied. By revealing details of the conductance or viscous flow relaxation time distribution function, such measurements give insight into the mechanism by which the applied stress is dissipated and indirectly reveal the structural character of the relaxing medium.

Attempts to explore the viscous flow response of the more viscous of the present solutions by studying the dissipation of ultrasonic energy in the medium have been reported.[40] Unfortunately, the frequency range needed to explore the interesting structural transition region is currently inaccessible to ultrasonic investigation. However, the conductivity relaxation[26,41] process in the temperature range of this study is accessible to dielectric relaxation techniques. By utilizing the supercooling ability of these solutions, on the other hand, the transport process relaxation times can be increased at will to match any experimentally convenient range (including the audio frequencies of the present conductance measurements). This possibility has motivated conductivity and viscous relaxation studies on various salt–water systems including the present one some of which are currently being reported.[26,41] The combination of the present type of survey with low-temperature frequency dependence studies, aimed particularly at the structural transition region, should make possible substantial improvements in the understanding of moderately concentrated electrolyte solutions.

Finally, we will note that, because of the deviations from eq 1 commonly found at extreme viscosities, eq 3 cannot be expected in principle to describe the composition dependence of transport at the limit of $x \rightarrow x_0$ even if this limit could be realized experimentally (in practice a glass transition would be encountered at a lower salt content, $x_g < x_0$). Thus, the form of eq 3 should not be regarded as a high-concentration limiting law in the sense that the Debye–Hückel equation describes limiting behavior in the dilute region. There is reason to believe, however, that solution thermodynamic properties, unlike the transport properties, do not become irregular as T_g is approached, and that simple high-concentration limiting laws for configurational contributions to the solution thermodynamic properties will be formulable.

Acknowledgments. Support of this research by a grant from the Department of the Interior, Office of Saline Water, is gratefully acknowledged. The authors have benefitted from many helpful discussions with Professor C. T. Moynihan.

(38) S.-Y. Hsich, R. W. Gammon, P. B. Macedo, and C. J. Montrose, *J. Chem. Phys.*, **56**, 1663 (1972).

(39) A. J. Easteal and C. A. Angell, *J. Phys. Chem.*, **74**, 3987 (1970).

(40) G. S. Darbari and S. Petrucci, *ibid.*, **73**, 921 (1969); J. H. Ambrus, C. T. Moynihan, and P. B. Macedo, *ibid.*, in press.

(41) C. T. Moynihan, R. D. Bressel, and C. A. Angell, *J. Chem. Phys.*, **55**, 4414 (1971).

Potential-Dependent Chronoamperometry. Disproportionation Followed by an Irreversible Chemical Reaction

by Lynn Marcoux

Department of Chemistry, Texas Tech University, Lubbock, Texas 79409 *(Received April 5, 1972)*

It has been suggested that anodic substitution reactions proceed *via* an ECE reaction pathway, *i.e.*, $A - e \rightleftarrows B$, $B + Z \xrightarrow{k} C$, $C - e \rightleftarrows D$; however, the possibility exists that the reaction might instead involve disproportionation leading to the sequence $A - e \rightleftarrows B$, $2B \underset{}{\overset{K_{dispro}}{\rightleftharpoons}} C + A$, $C + Z \xrightarrow{k'} D$. In addition to these possibilities, the ECC variation of the ECE mechanism which includes provision for the solution equilibrium, $A + D \underset{}{\overset{K_{ECC}}{\rightleftharpoons}} B + C$, must also be considered. A potential-dependent form of double-step chronoamperometry is shown to be diagnostically valuable for distinguishing between these alternative mechanisms.

The ECE reaction sequence which is most commonly notated in the following fashion

$$A - e \rightleftarrows B \qquad E^\circ_1 \tag{1}$$

$$B + Z \xrightarrow{k} C \tag{2}$$

$$C - e \rightleftarrows D \qquad E^\circ_2 \tag{3}$$

has been the subject of a great deal of recent comment due to the fact that several related combinations of reactions give rise to similar electrochemical responses. The first of these variant mechanisms was described by Feldberg,[1-3] who noted that an oxidation–reduction equilibrium of the type

$$A + D \underset{}{\overset{K_{ECC}}{\rightleftharpoons}} B + C \tag{4}$$

$$K_{ECC} = \exp\left[\frac{F}{RT}(E^\circ_2 - E^\circ_1)\right] \tag{5}$$

existed in solution and that its presence must be taken into account when deriving equations for voltammetric responses. This complication was dubbed the ECC mechanism, and its existence was theoretically described and experimentally confirmed. For both the organic oxidations and reductions to which ECE behavior has been ascribed, species C is quite often an aromatic free radical which is oxidized (reduced) at potentials much less positive (negative) than species A. This, in addition to the fact that electron transfer reactions of this type are normally quite rapid in solution, would lead one to believe that the ECC case should be more prevalent than the ECE. This refinement has unfortunately been ignored by several investigators.

Disproportionation pathways also give rise to overall reactions indentical to ECC or ECE mechanisms, and several of the possibilities have been described.[4-9] The goal of these authors was to find means by which the several alternative mechanisms could be distinguished. The following very specific mechanism

$$A - e \rightleftarrows B \tag{6}$$

$$2B \underset{}{\overset{K_{dispro}}{\rightleftharpoons}} C + A \tag{7}$$

$$C + Z \xrightarrow{k'} D \tag{8}$$

has recently been suggested as a possible route for anodic substitution reactions.[10] In both of these sequences Z is an electroinactive nucleophile and is usually assumed to be present in excess in order to permit the reaction to be treated as pseudo-first order. The disproportionation mechanism assumes the presence of a second electron transfer step

$$B - e \rightleftarrows C \qquad E^\circ_3 \tag{9}$$

Consequently, K_{dispro} may be written

$$K_{dispro} = \exp\left[\frac{F}{RT}(E^\circ_1 - E^\circ_3)\right] \tag{10}$$

This suggestion was based on the observation of Shine[11-13] and coworkers that this mechanism was the

(1) M. D. Hawley and S. W. Feldberg, *J. Phys. Chem.*, **70**, 3459 (1966).
(2) R. N. Adams, M. D. Hawley, and S. W. Feldberg, *ibid.*, **71**, 851 (1967).
(3) S. W. Feldberg, *ibid.*, **75**, 2377 (1971).
(4) S. W. Feldberg, *ibid.*, **73**, 1238 (1969).
(5) M. Mastragostino, L. Nadjo, and J. M. Saveant, *Electrochim. Acta*, **13**, 721 (1968).
(6) M. Mastragostino and J. M. Saveant, *ibid.*, **13**, 751 (1968).
(7) L. Nadjo and J. M. Saveant, *ibid.*, **16**, 887 (1971).
(8) L. Nadjo and J. M. Saveant, *J. Electroanal. Chem.*, **33**, 417 (1971).
(9) C. P. Andrieux and J. M. Saveant, *ibid.*, **33**, 453 (1971).
(10) L. Marcoux, *J. Amer. Chem. Soc.*, **93**, 537 (1971).
(11) H. J. Shine and Y. Murata, *ibid.*, **91**, 1872 (1969).
(12) Y. Murata and H. J. Shine, *J. Org. Chem.*, **34**, 3368 (1969).

most likely explanation for the disappearance kinetics of some chemically prepared cation radicals. This proposal is contrary to the results of other investigators.[14,15] The reason for disagreement as to mechanism stems from the fact that the previously published diagnostic methods are somewhat equivocal. The purpose of this work is to present an electroanalytical approach which permits a less ambiguous assignment of mechanism.

Results

The approach chosen is a chronoamperometric method in which the potential is not necessarily stepped into the region of diffusion control. This technique has been named potential-dependent chronoamperometry, and it has been shown to be a useful approach to the EC reaction sequence.[16] It was pointed out[16] that this potential program accomplished the same result as other methods but possessed several experimental advantages. It should also be noted that this type of experiment is easily extended to the chronocoulometric[17] and double-step[18] methods. Variation of the applied potential permits the systematic variation of the concentration ratios of the reactants within the diffusion layer. This, of course, may affect different reaction mechanisms to different extents, and this is the origin of the diagnostic value of this technique.

Although the EC case[16] was simple enough to allow an analytical solution, this was not the most expedient approach to the present problem; consequently, the working curves were generated by digital simulation.[19] To introduce potential dependence into these calculations one assumes Nernstian behavior and the boundary condition at the electrode surface becomes

$$C_B = C_A \exp\left[\frac{F}{RT}(E_{app} - E^\circ)\right] \qquad (11)$$

when $t > 0$ and $x = 0$ and where E_{app} is the applied potential. For all three calculations the follow-up reactions, eq 2 and 8, were assumed to be pseudo-first order. In the case of disproportionation, it was assumed that the equilibrium, eq 7, was rapid and that there existed a very small steady-state concentration of species C. The rate law for this situation is

$$-\frac{dC_B}{dT} = \frac{k' K_{dispro} C_B^2}{C_A} \qquad (12)$$

To carry out calculations for the ECC mechanism, it is necessary to know the value of the equilibrium constant K_{ECC} since the shape of this curve varies extensively with this parameter.[1] For the present case it was assumed that the second electrode reaction, eq 3, took place at a potential much less positive than that of eq 1. This approaches the $K = 0$ limiting case of Feldberg.[1] This assumption is consistent with previous findings,[20] but it must be borne in mind that the actual chemical cases are probably much more complicated than these models. To treat the ECE and ECC sequences by a double-potential step program, it is necessary to assume a relationship between the final applied potential and E°_1 and E°_2. For those pur-

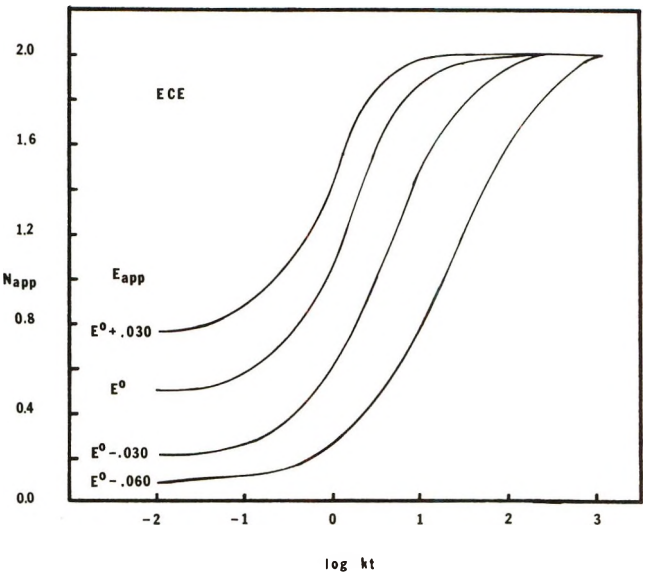

Figure 1. Single-step potential dependent working curves for the ECE reaction; E° refers to E_1° in this and other figures.

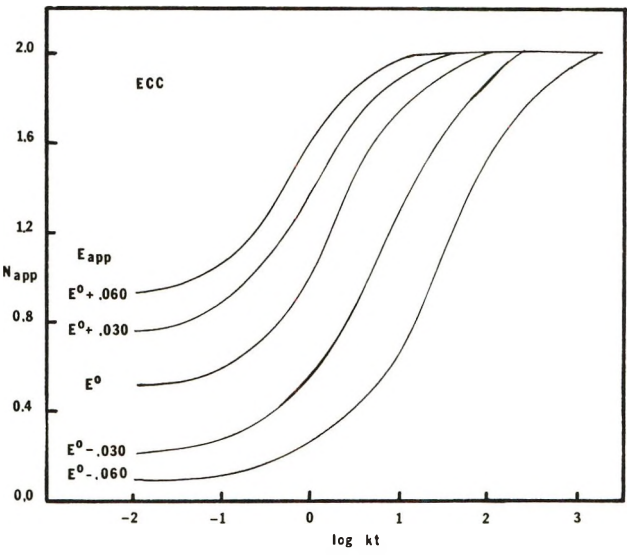

Figure 2. Single-step potential-dependent working curve for the ECC, $K = 0$ reaction.

(13) J. J. Silber and H. J. Shine, *J. Org. Chem.*, **36**, 2923 (1971).
(14) G. Manning, V. D. Parker, and R. N. Adams, *J. Amer. Chem. Soc.*, **91**, 4584 (1969).
(15) V. D. Parker and L. Eberson, *ibid.*, **92**, 7488 (1970).
(16) L. Marcoux and T. J. P. O'Brien, *J. Phys. Chem.*, **76**, 1666 (1972).
(17) J. H. Christie, *J. Electroanal. Chem.*, 13, 79 (1967).
(18) W. M. Schwarz and I. Shain, *J. Phys. Chem.*, **69**, 30 (1965).
(19) S. W. Feldberg in "Electroanalytical Chemistry, A Series of Advances," Vol. 3, A. J. Bard, Ed., Marcel Dekker, New York, N. Y., 1969.
(20) R. Dietz and B. E. Larcombe, *J. Chem. Soc. B*, 1369 (1970).

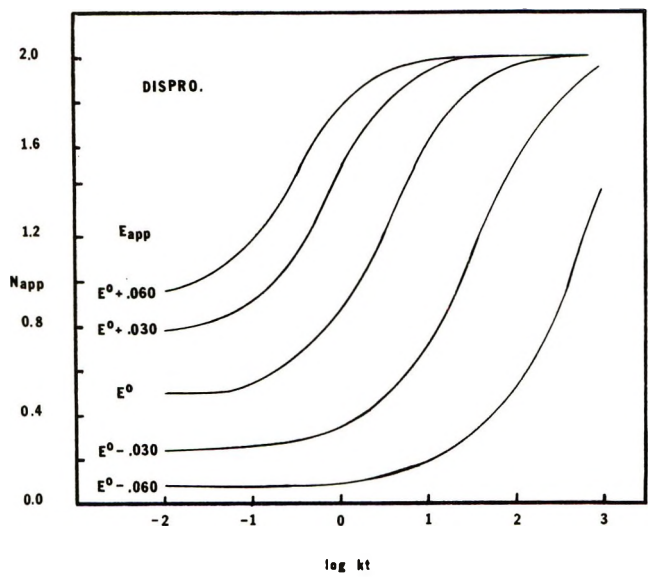

Figure 3. Single-step potential-dependent working curve for the disproportionation mechanism.

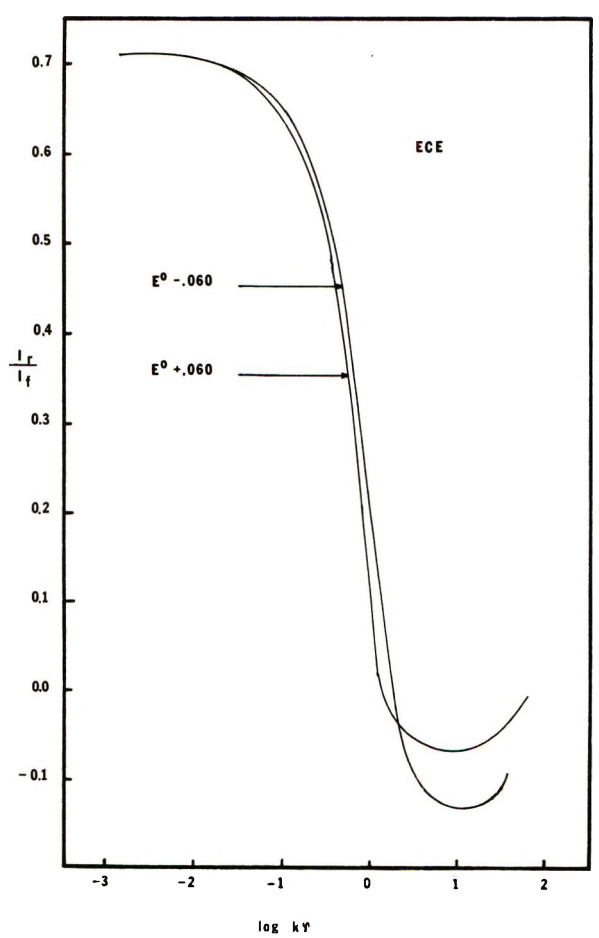

Figure 4. Double-step potential-dependent working curve for the ECE reaction.

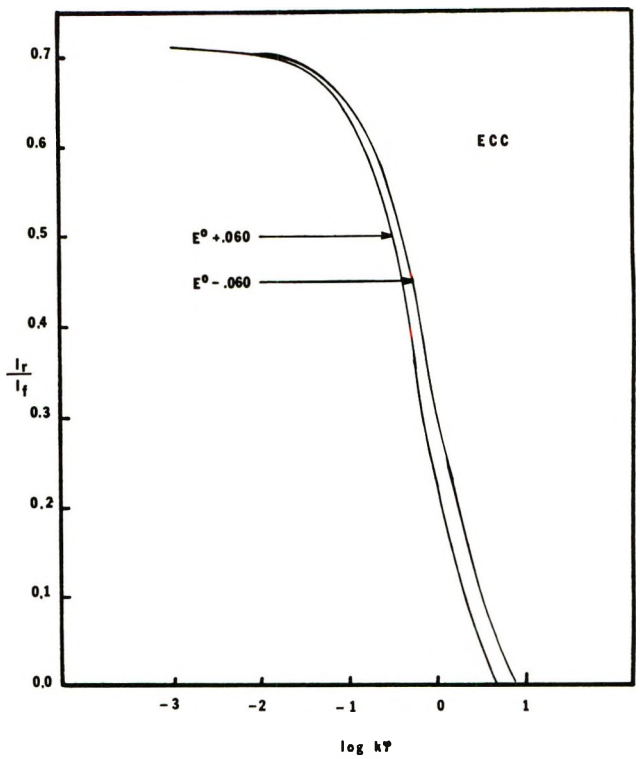

Figure 5. Double-step potential-dependent working curve for the ECC reaction.

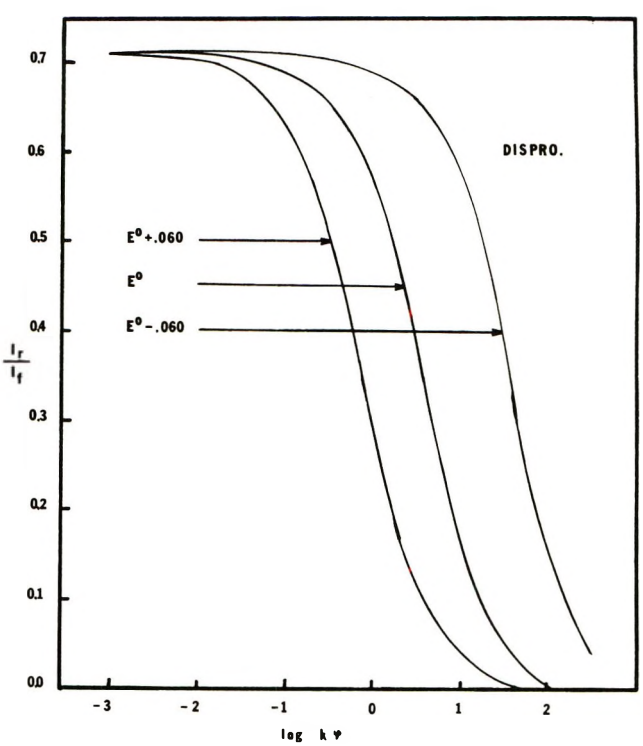

Figure 6. Double-step potential-dependent working curve for the disproportionation mechanism.

poses the final potential was assumed to be such that the reaction

$$B + e \rightleftarrows A \qquad (13)$$

was diffusion controlled and that the reaction

$$D + e \rightleftarrows C \qquad (14)$$

could not take place.

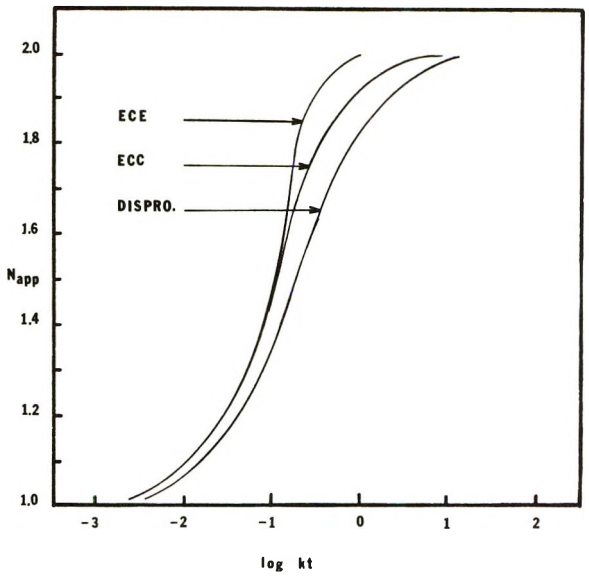

Figure 7. Single-step diffusion-controlled working curves for all three mechanisms. The abscissa has been shifted to facilitate comparison.

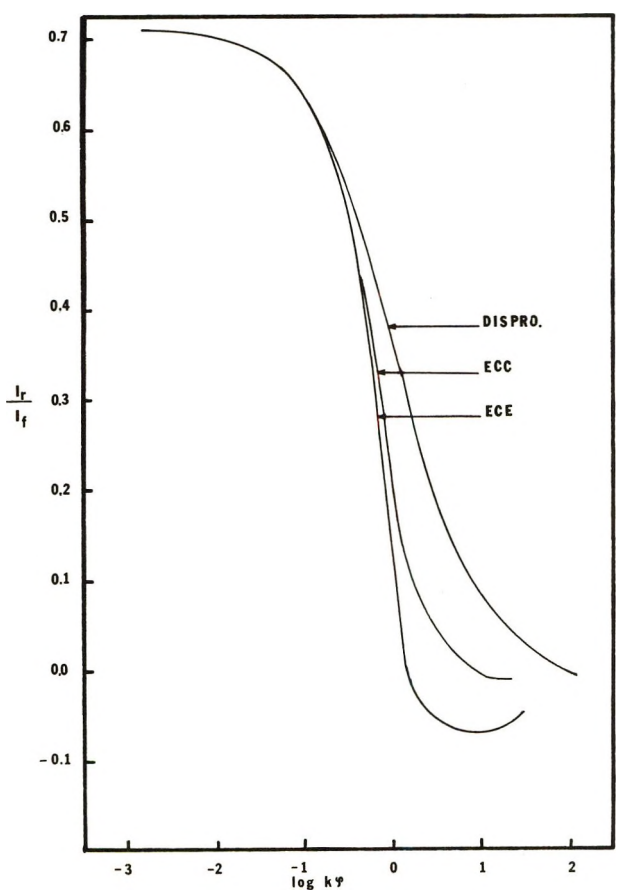

Figure 8. Double-step diffusion-controlled working curves for all three mechanisms. The abscissa has been shifted to facilitate comparison.

Figures 1, 2, and 3 represent the results for the single-step experiment at a variety of E_{app} values for the ECE, ECC, and disproportionation cases, respectively. These plots are the same format previously used.[1,4,10] The working curves for the double-step experiments are shown in the same order in Figures 4, 5, and 6. These data are presented in the same manner as Schwarz and Shain.[18] The curves shown represent the ratio of the current for the reverse step to that of the forward step as a function of rate constant and reversal time, τ. The cases shown are appropriate to experiments in which the currents are measured at a time corresponding to one-tenth of the time of the forward step, *i.e.*, in the notation of Schwarz and Shain[18] $(t - \tau)/\tau = 0.1$. For example, for an experiment with a reversal time $\tau = 100$ msec, the forward current would be measured 10 msec after the experiment was initiated and the reversal current at 110 msec after initiation. For the purposes of comparison the results for the diffusion-controlled single-step method are shown in Figure 7, and Figure 8 shows the results for the corresponding double-step experiment also at $(t - \tau)/\tau = 0.1$.

Discussion

The diagnostic approach is made clear by the accompanying figures. To differentiate the disproportionation possibility from the ECE and ECC mechanisms, one need only carry out the appropriate experiment at several different applied potentials. Both the single-step and double-step methods distinguish between the disproportionation and ECE–ECC pathways; however, the difference is more pronounced in the case of the reversal experiment. It is also clear from these figures that it is unlikely that one could distinguish the ECE from the ECC mechanism by this method. These latter two mechanisms are fortunately fairly easily distinguished from one another by the conventional diffusion-controlled chronoamperometric techniques shown in Figures 7 and 8. The two results are therefore complimentary. The computed values of E_{app} were selected arbitrarily, but they encompass the most likely experimental range since current magnitudes would be quite small and consequently irreproducible in the region below $E_{app} = E^\circ - 0.060$.

Philosophically this technique is not unlike that of Saveant[5-9] in which the variation of the peak potential of single-sweep stationary electrode voltammograms is observed as a function of scan rate. The predicted shifts vary on the order of 10–20 mV per decade of sweep rate. These shifts are reproducibly observable and diagnostically meaningful as Saveant has convincingly demonstrated; however, it must be noted that the work cited was carried out on mercury electrodes and one could not anticipate data of this quality with solid electrodes. The present results should also be compared with the cyclic voltammetric method which has previously been suggested.[15] The cyclic voltammetric method was more specifically directed at the region between the two electron transfers, *i.e.*,

$E^\circ_1 < E < E^\circ_2$. This method was presented in a qualitative fashion, and the solution equilibrium between the cation, dication, and parent molecule was ignored. In actual fact, this method should be effective in the region $E^\circ_1 \pm 0.060$; however, it suffers from the drawback that the best diagnostic region falls prior to the voltammetric peak on the steeply rising portion of the wave. This, of course, renders difficult the accurate and reproducible measurement of current. The cyclic voltammetric method is quite analogous to the previously proposed step-sweep technique[21] which was developed for EC reactions. It must be emphasized that the difference between the present method and the others discussed herein is purely operational. The experimental variable in this case is more easily measured and also varies to a greater extent from one mechanism to another.

The experimental restraints to the present method are not severe; nonetheless, one must be certain that the initial electron transfer reaction is rapid. This is normally true for organic molecules in nonaqueous solvents. Because the exact value of the applied potential is an essential quantity in this experiment, high quality potential control is assumed. Uncompensated resistance[22] therefore cannot be tolerated, and this is a serious consideration in nonaqueous media. This complication must also be considered when utilizing the sweep method so it is not a unique disadvantage.

To ascertain the limits of certainty within which this technique could be applied the following approach was taken. The experimental limitations were first determined from potential-dependent chronocoulometric measurements of an uncomplicated system, and then calculations were made to establish the effect of this uncertainty upon the calculated working curves. Table I shows the value of the product $Qt^{-1/2}$ obtained at a series of times and at various values of applied potential for a 1.85 mM solution of phenothiazine in acetonitrile which contained 0.148 M tetraethylammonium perchlorate as supporting electrolyte. The reversibility of this system has been previously established.[23-25] A PAR Model 170 electrochemistry system was used; the Pt working electrode was 0.024 cm^2, and an Ag/Ag$^+$ (acetonitrile) reference electrode was employed.

Table I: Chronocoulometric Data ($Q\tau^{-1/2}$) for the Oxidation of Phenothiazine at Various Applied Potentials

τ, sec	E_{app}, V, vs. Ag/Ag$^+$			
	0.500[a]	0.320	0.290	0.260
0.020	6.56	5.53	4.25	2.55
0.030	6.64	5.40	4.31	2.49
0.040	6.70	5.35	4.25	2.44
0.050	6.65	5.48	4.24	2.46
0.060	6.55	5.32	4.28	2.44
0.070	6.65	5.40	4.26	2.45
0.080	6.78	5.40	4.38	2.41
0.090	6.65	5.46	4.24	2.50
0.100	6.76	5.42	4.27	2.53
0.040	6.70	5.50	4.30	2.50
0.060	6.55	5.51	4.34	2.37
0.080	6.72	5.48	4.38	2.37
0.100	6.70	5.48	4.34	2.52
0.120	6.75	5.40	4.35	2.48
0.140	6.68	5.54	4.38	2.42
0.160	6.75	5.54	4.38	2.50
0.180	6.64	5.48	4.35	2.43
0.200	6.60	5.86	4.28	2.38
0.100	6.76	5.64	4.27	2.53
0.150	6.65	5.55	4.26	2.33
0.200	6.60	5.52	4.20	2.37
0.250	6.68	5.55	4.26	2.44
0.300	6.55	5.48	4.20	2.39
0.350	6.67	5.48	4.19	2.42
0.400	6.60	5.85	4.22	2.38
0.450	6.60	5.45	4.23	2.44
0.500	6.65	5.85	4.25	2.35
Av	6.66 ± 0.06	5.47 ± 0.05	4.28 ± 0.05	2.44 ± 0.05

[a] Region of diffusion control.

Based upon the average deviations shown in Table I, data obtained on the wave are no more subject to scatter than those obtained in the region of diffusion control. A more important criterion might be how accurately these data compare with the known value of E° for this system. From cyclic voltammetry using the relationship[26] $E_{1/2} = E_{p/2} + 0.0285$ one finds that $E_{1/2} = 0.28$ V for this particular reference electrode. Since the system in question is reversible, the approximation $E^\circ \cong E_{1/2}$ is valid. The relationship

$$N_{app} = \frac{Qt^{-1/2}}{Qt^{-1/2}\,(\text{diffusion control})} = \frac{10^\phi}{1 + 10^\phi}$$

$$\phi = \frac{E_{app} - E^\circ}{0.059}$$

may be easily obtained and applied to the data in Table I. For the applied potentials of 0.320, 0.290, and 0.260 V one obtains E° values of 0.281, 0.275, and 0.277 V, respectively.

Using these data pessimistically and assuming that E_{app} is uncertain, ±5 mV, disproportionation working curves were obtained for E_{app} values of $E^\circ - 0.025$, $E^\circ - 0.030$, $E^\circ - 0.035$. The maximum total uncertainty in the log ktC axis was found to be 0.2 unit. This is the amount of uncertainty that one normally encounters with solid electrodes in the region of diffusion control.[10] Since most experimental data are obtained from oscilloscope traces, the source of this uncertainty

(21) W. M. Schwarz and I. Shain, *J. Phys. Chem.*, **70**, 848 (1966).
(22) E. R. Brown, T. G. McCord, and D. D. DeFord, *Anal. Chem.*, **38**, 1117 (1966).
(23) J. P. Billon, *Bull. Soc. Chim. Fr.*, 1784 (1961).
(24) J. P. Billon, *ibid.*, 1923 (1961).
(25) J. P. Billon, G. Cauquis, J. Combrisson, and A. Li, *ibid.*, 2062 (1960).
(26) R. S. Nicholson and I. Shain, *Anal. Chem.*, **36**, 706 (1964).

is as likely to arise in the mode of data presentation as it is from electrochemical sources. Based upon these estimates it can be seen that the working curves for the ECE and ECC cases will be as far as experiment is concerned essentially invariant with potential. Furthermore it is clear that a 30-mV variation in potential will probably reflect disproportionation behavior and that a 60-mV increment certainly will.

A fact more discomforting than possible experimental difficulties is that the usefulness of these calculations is ultimately limited by the validity of the model. In most cases anodic substitution reactions are probably much more complicated than they are herein portrayed. In spite of the several complications mentioned above, potential-dependent chronoamperometry appears, thus far, to be the best experimental approach to the question of the role of disproportionation in anodic substitution reactions.

Acknowledgment. This work was partially supported by Research Corporation in the form of a Frederick Gardner Cottrell grant-in-aid.

Effect of Temperature on Wetting of High- and Low-Energy Solid Surfaces

by Elaine G. Shafrin* and W. A. Zisman

Laboratory for Chemical Physics, Naval Research Laboratory, Washington, D. C. 20390 *(Received May 30, 1972)*

Publication costs assisted by the Naval Research Laboratory

Various investigators have extended to high-energy surfaces the concept of the critical surface tension of wetting (γ_c) and its method of measurement at constant temperature, developed from earlier contact-angle investigations of low-energy surfaces. Recently, Rhee proposed and applied an alternate approach to obtaining a critical tension (γ_{cs}) for a high-energy surface by increasing the temperature (T) to the critical value (T_{cs}) at which a previously nonspreading liquid metal just spreads on a metal or ceramic surface. Using literature data on the effect of increasing T on the wetting of low-energy surfaces by organic liquids, we demonstrate the following: (a) Rhee's γ_{cs} is equal to γ_c for the specific temperature T_{cs}; (b) when interpreted and used correctly, the variable-temperature method is applicable to low- as well as high-energy surfaces; and (c) values of γ_c obtained by the constant- and the variable-temperature methods agree. Literature data have been processed to obtain γ_c values at various constant temperatures. A graphical summary of results for seven solid organic polymers revealed that a straight-line relation of small negative slope characterized the γ_c *vs.* T data for these surfaces at least up to 125°, and the overall effect of T on γ_c for organic solids approximated that on the liquid surface tension of organic liquids. A proper basis now exists for more extended use of the variable-temperature method and for the correct interpretation of the results so obtained in terms of a γ_c which is measured at constant T; thus, two separate but complementary methods for determining γ_c are now available. The concepts of γ_c and T_{cs} and the recognition that γ_c is a linearly decreasing function of temperature provide a sound foundation for knowledge of wettability.

Introduction

The concept of the critical surface tension of spreading (γ_c) as an empirical parameter characterizing the wettability of a solid surface at a constant temperature was developed by our laboratory originally from research on the equilibrium contact angle (θ) of a wide variety of pure organic and inorganic liquids in contact with well-defined low-energy solid surfaces including organic polymers[1,2] and crystals.[2,3] The concept later proved equally applicable to the wettability of high-energy surfaces such as metals, metal oxides, sapphire, and various glasses when these had been modified, either deliberately or inadvertently, by the presence of adsorbed films of organic molecules[2,4-6] or of water.[7-9]

In view of the technological as well as theoretical significance of the wetting of unmodified high-energy surfaces, there has been increasing interest in deter-

(1) H. W. Fox and W. A. Zisman, *J. Colloid Sci.*, **5**, 514 (1950).
(2) W. A. Zisman, *Advan. Chem. Ser.*, **No. 43**, 1 (1964).
(3) H. W. Fox and W. A. Zisman, *J. Colloid Sci.*, **7**, 428 (1952).
(4) E. G. Shafrin and W. A. Zisman, *ibid.*, **7**, 166 (1952).
(5) H. W. Fox, E. F. Hare, and W. A. Zisman, *J. Phys. Chem.*, **59**, 1097 (1955).
(6) W. A. Zisman, *J. Paint Technol.*, **44**, No. 564, 41 (1972).
(7) E. G. Shafrin and W. A. Zisman, *J. Amer. Ceram. Soc.*, **50**, 478 (1967).
(8) M. K. Bernett and W. A. Zisman, *J. Colloid Interface Sci.*, **29**, 413 (1969).
(9) M. K. Bernett and W. A. Zisman, *ibid.*, **28**, 243 (1968).

mining if the γ_c concept can be extended to characterize the wetting of inorganic and metallic high-energy solid surfaces by liquids of high surface tension (γ_{LV}) such as salt solutions, liquid nonmetallic and metallic elements, and liquid alloys.

Thus, Olsen and Osteraas[10] reported values of γ_c for Pyrex glass (Corning Code 7740), lead glass (Corning Code 0120), fused silica, and soda-lime glasses. When the liquids used were concentrated aqueous solutions of pure potassium carbonate or calcium chloride, the plot of values of cos θ *vs.* γ_{LV} at 20° and 20% RH revealed that γ_c = 73 dyn/cm. When the liquids were low-melting metals, from 20 to 156° under vacuum, they obtained the straight-line graph redrawn here in Figure 1 (curve F) with $\gamma_c = 75 \pm 10$ dyn/cm. The authors concluded the values of γ_c obtained were characteristic of tightly bound surface water. Using the contact angles of 70 and 110° for mercury and gallium, respectively, on baked, outgassed glass reported by Good, Givens, and Tucek[11] and also their surface tensions of 485 and 700–735 dyn/cm, respectively, Olsen and Osteraas[10] estimated values of γ_c for the glass of 260 dyn/cm from which they inferred that at least some of the adsorbed moisture had been removed.

Olsen, Moravec, and Osteraas[12] used a variety of organic and inorganic liquids at 20° to obtain values of γ_c of 30, 30.5, and 31.5 dyn/cm for orthorhombic, monoclinic, and amorphous sulfur, respectively. Similar measurements on freshly cleaved surfaces of selenium and tellurium led to γ_c values of 32 and 35.5 dyn/cm. Finally, they also showed that γ_c of these elements plotted as a direct rectilinear function of the atomic radii.

Eberhart[13] showed that a rectilinear plot of cos θ *vs.* γ_{LV} resulted upon using recent literature data on the contact angles on sapphire exhibited by various liquid transition metals at 1500° under vacuum. Curve A in Figure 1 shows his results and the estimated value of $\gamma_c = 1050 \pm 100$ dyn/cm at 1500°.

A straight-line relation between cos θ and γ_{LV} was reported recently by Rhee[14] for a series of related metal alloys of graded surface tensions on a high-energy surface. Using θ and γ_{LV} data drawn from recent metallurgical and ceramic literature, he reported a value of 440 dyn/cm for the γ_c of sapphire at 1230° (curve B, Figure 1) and 230 dyn/cm for graphite (Graphatite "A") using θ data[15] at 600–650° and γ_{LV} values from the literature at 700–740° (curve E). Reference 15 also provides limited contact angle data for the same series of metal alloys on two additional high-energy surfaces. When these data are treated in a way identical with that Rhee used for graphite, a value of γ_c of 340 dyn/cm is obtained for boron carbide (curve D) and approximately 350 dyn/cm for beryllium (curve E) for the same elevated temperatures as the graphite data.

A critical surface tension for high-energy surfaces was also obtained by Rhee[16–20] by employing a convenient and novel approach he had developed. Contact angles of liquid aluminum were measured on each of the solid ceramics, AlN, TiB_2, TiN, and TiC;[16] liquid lead was observed on solid AlN and TiC;[17] liquid silver and liquid copper were each observed on solid AlN and TiC[18] and TaC.[20] The temperature dependence of θ and γ_{LV} was determined for each molten pure metal within a limited temperature range generally corresponding to large values of θ. Plots of cos θ *vs.* γ_{LV} for each liquid metal on each ceramic surface were found to be rectilinear. Rhee proposed that the intercept of that straight line extrapolated to the cos $\theta = 1$ axis be used to characterize the critical surface tension of that solid substrate. Since he had designated as T_{cs} the temperature which corresponded to the critical surface tension when γ_{LV} was varied by changing the temperature of the system,[19] we will use the corresponding symbol γ_{cs} adopted in ref 20 to denote every critical surface tension value obtained by his variable-temperature method and thus distinguish it from the symbol γ_c which we (and many others) have used for many years to denote the value determined at a constant temperature by using liquids of different surface tensions, *i.e.*, by a wetting isotherm.

The results through 1971 of Rhee's variable-temperature method were reported in his papers,[16–19] and plots of cos θ *vs.* γ_{LV} he made from recent literature concerning other ceramic and liquid metal systems are collected and discussed in ref 19. The major difficulty is that, for any given solid, Rhee's values of γ_{cs} differ depending on the liquid metal used as the sessile drop. Other difficulties arise from experimental restrictions and approximations introduced to avoid the severe high-temperature requirements involved in the use of liquid metals. These approximations had to be reviewed critically before interpreting Rhee's temperature-dependent method for obtaining his γ_{cs} values and then relating them to our definition and results on γ_c.

Finally, we have determined γ_{cs} from data for an experimentally more tractable system, namely, one involving the wetting of a low-energy surface by an organic liquid over a wide range of temperatures. By that approach we have revealed those aspects of Rhee's data treatment which are valid and useful for both high-

(10) D. A. Olsen and A. J. Osteraas, *J. Phys. Chem.*, **68**, 2730 (1964).
(11) R. J. Good, W. G. Givens, and C. S. Tucek, *Advan. Chem. Ser.*, **No. 43**, 211 (1964).
(12) D. A. Olsen, R. W. Moravec, and A. J. Osteraas, *J. Phys. Chem.*, **71**, 4464 (1967).
(13) J. G. Eberhart, *ibid.*, **71**, 4125 (1967).
(14) S. K. Rhee, *J. Amer. Ceram. Soc.*, **54**, 376 (1971).
(15) C. R. Manning, Jr., and T. B. Gurganus, *ibid.*, **52**, 115 (1969).
(16) S. K. Rhee, *ibid.*, **53**, 386 (1970).
(17) S. K. Rhee, *ibid.*, **53**, 426 (1970).
(18) S. K. Rhee, *ibid.*, **53**, 639 (1970).
(19) S. K. Rhee, *ibid.*, **54**, 332 (1971).
(20) S. K. Rhee, *ibid.*, **55**, 157 (1972).

Table I: Physical Properties and Wetting Behavior of Liquid Metals on High-Energy Ceramic Surfaces

	Physical properties				Wetting of TiC			Wetting of AlN		
Metal	Mp, °C	Bp, °C	Liquid surface tension $\gamma_{LV} = a + b(T)$, dyn/cm (T, °C) a	b	γ_{cs}, dyn/cm	T_{cs}, °C	Vapor pressure of metal at T_{cs}, Torr	γ_{cs}, dyn/cm	T_{cs}, °C	Vapor pressure of metal at T_{cs}, Torr
Pb	327	1740	547	−0.26	93	1764	>760	2	2096	≫760
Al	660	2467	893	−0.202	725	831	10^{-3}	664	1133	10^{-1}
Ag	961	2212	1092	−0.14	873	1564	9	783	2207	~730
Cu	1083	2595	1462	−0.27	1083	1404	6×10^{-2}	880	2155	60

and low-energy solid surfaces. We have then applied these conclusions to data already available in the literature on the effect of temperature on the wetting of low-energy surfaces, and as a result we have been able to draw sound conclusions concerning the relation of γ_{cs} to γ_c.

Despite the attractiveness of Rhee's experimental approach, the values of the cos $\theta = 1$ intercept (γ_{cs}) which he obtained for liquid metal ceramic systems (Table I) proved difficult to interpret. These difficulties arose (a) from limitations in the range of values of cos θ to well below 1 which he used to exemplify the variable-temperature method and (b) insufficient emphasis on the temperature-dependent nature of the critical surface tension (γ_c), especially since such large temperature ranges were involved. Rhee used his own observations[16-20] of the effect of temperature (over a limited range of T) on θ and γ_{LV} and also the data published by other authors to support his conclusion that cos θ increased linearly with increasing T in liquid metal–ceramic systems. The linear relation was discontinuous, however, if the surface energy of the solid varied discontinuously with respect to T or if the system did not come to equilibrium.[19] To avoid ambiguities arising from the approximately linear relation of cos θ to θ in the range $\theta = 40$–$140°$, he elected to examine the possible linear temperature dependence of cos θ (as distinct from θ) by selecting experimental conditions favorable to the development of contact angles in the range of 20 to 60° or of 120 to 160°, generally the latter. As a result of this consideration and also of the experimental difficulties inherent in the high-temperature measurements on liquid metals, Rhee did not attempt to heat his systems to temperatures such that the liquid metal would actually exhibit a zero contact angle! Indeed, only for one liquid metal (Al) did he observe contact angles less than 90° and even then the experiments were terminated before $\theta < 45°$.

Rhee's Definition of the Critical Temperature of Wetting

The basic premise of Rhee's variable-temperature method of characterizing the wettability of a solid[16-20] is as follows: for a given liquid–solid system in which the liquid exhibits a nonzero contact angle, if increasing the temperature (T) results in a decrease in θ, it should be possible to increase T to some critical value (T_{cs}) where the liquid just spreads (*i.e.*, exhibits a zero contact angle). At this temperature, the surface tension of the liquid (γ_{LV}) should be equal to the critical surface tension (γ_c) for spreading characterizing the solid *at that specific temperature*. Of course, the usual restrictions would have to apply: there must be no dissolving, alloying, or chemical interaction between the two phases, and the surface of the solid should not be modified by adsorbed films (including adsorbed vapors of the wetting liquid).

Rhee's use of temperature to alter the γ_{LV} of the sessile liquid is roughly analogous to Bernett and Zisman's use[21,22] of solute concentration to alter γ_{LV}. With a series of sessile liquids comprising solutions of increasing solute concentration in a single solvent they obtained from the graph of cos θ *vs.* γ_{LV} and its intercept at cos = 1 a value of γ_c in agreement with that obtained from measurements on a series of related pure liquids.

Over the limited range of T which Rhee employed for any given liquid metal–substrate combination, his sessile drop measurements indicated a linear temperature dependence of γ_{LV} for each liquid metal, with both the intercept constants and the temperature coefficients (Table I, column 4) in good agreement with similar equations derived by other experimental techniques. Moreover, Rhee was able to establish that cos θ increased linearly with increasing T or with decreasing γ_{LV} over the temperature range investigated (usually within some 100 to 200° above the melting point of the metal). Postulating that these relations would persist rectilinearly to even higher temperatures (or lower values of γ_{LV}), he made a graphical extrapolation of the straight-line portion of the cos θ *vs.* γ_{LV} chart to obtain the intercept of the graph with the cos $\theta = 1$ axis.[19] The resulting plot of the data thus resembles the conventional treatment for the cos θ *vs.* γ_{LV} data obtained at constant temperature for a homologous series of liq-

(21) M. K. Bernett and W. A. Zisman, *J. Phys. Chem.*, **63**, 1241 (1959).

(22) M. K. Bernett and W. A. Zisman, *ibid.*, **63**, 1911 (1959).

uids on a low-energy surface. It differs, however, in that the data are obtained for a single liquid by varying the temperature, so that the intersection of the straight-line graph with the $\cos\theta = 1$ axis (denoted here as γ_{cs}) is equivalent to γ_c only for the single temperature (T_{cs}) to which that value of γ_{LV} corresponds for that particular liquid.

For a given single high-energy surface, a different value of γ_{cs} (Table I, columns 5 and 8) was reported by Rhee for each of the liquid metals he used as the sessile drop, but the fact that the temperature to which each value corresponded also was different was generally not stated explicitly. In columns 6 and 9 of Table I the appropriate values of T_{cs} for each liquid metal–ceramic system have been determined by using the equivalence of γ_{cs} to γ_{LV} at the temperature T_{cs} and calculating back from Rhee's experimentally derived equations for the temperature dependence of γ_{LV}. The results are presented in the order of increasing melting point of the liquid metals; for the metals shown, this is also the order of their increasing surface tension. Comparison of the fifth and eighth columns of Table I shows that this is also the order of increasing γ_{cs} values for the wetting of TiC and of AlN, a correlation already pointed out by Rhee with respect to γ_{LV}. As shown by the data of Table I, no simple correlation exists between γ_{cs} and T_{cs} for either TiC or AlN.

If the metals are put in the order of their ascending values of T_{cs}, the sequence is different for TiC (Al, Cu, Ag, and Pb) than for AlN (Al, Pb, Cu, and Ag). Exclusion of the data for Pb, however, leads to an identical order of the remaining three metals on both substrates. Finally, it is noted that, for some liquid metal–ceramic systems, the values of T_{cs} calculated from γ_{cs} correspond to temperatures at or above the boiling point of the metal (*cf.* column 3, Table I). Where this occurs, notably in the case of Pb, it provides internal evidence that the assumption of a continuous straight-line $\cos\theta$ *vs.* T relation is not warranted, even though the data of Livey and Murray[23] quoted by Rhee[19] show that the $\cos\theta$ *vs.* T graph for Pb on TiC remains linear through 700°; at this temperature, however, the contact angle is still large (80°). Although Rhee did not include his earlier wetting data for Pb[17] in his subsequent comparison of the effect of the liquid metal on γ_{cs} for AlN and TiC,[18] no reason for the exclusion is indicated in the latter paper.

Rhee also discussed[18] the possibility of complications arising in the variable-temperature method from the adsorption of metallic vapors on the ceramic surface. In this connection, ref 17 points out that the low critical surface tension in the Pb–TiC system suggests that the surface energy of TiC is substantially reduced by adsorption of Pb vapor. That explanation is not advanced for the AlN surface. Moreover, the vapor pressure of Pb in the temperature range 350–550° studied by Rhee[17] is less than 10^{-4} Torr, and, even at the temperature of 700° reached by Livey and Murray, the vapor pressure is 10^{-2} Torr.

To see if vapor adsorption on the ceramic surfaces might account for the lack of a direct or obvious relation between γ_{cs} and T_{cs}, handbook values for the vapor pressure of each metal at its T_{cs} have been included in Table I. The corresponding values cover a wide range of pressures and differ by orders of magnitude from one ceramic substrate to the other at T_{cs}. More significant, however, was the fact that the temperature range over which θ was observed experimentally was far below that corresponding to either T_{cs} or the boiling point. Therefore, the effect of vapor pressure on the data which were obtained from the experimental observations and on which the subsequent extrapolations were based should be small and an unlikely source for the lack of regularity in the γ_{cs} *vs.* T_{cs} relation.

Rhee's sets of γ_{cs} values for a single ceramic substrate indicate that γ_{cs} depends on the liquid metal used as the sessile drop. The resulting multiplicity of values for a single substrate is difficult to reconcile with the widely accepted concept of γ_c as an empirical parameter characteristic of the solid surface, with only minor variations possible when the wetting liquid interacts with the solid surface.

To determine how consistent the wetting data are with Rhee's conclusion that, for a given ceramic, γ_{cs} increases with the surface tension of the liquid metal used,[18] his wetting data for AlN were compared at the arbitrarily chosen temperature of 1100°. Rhee's equations (column 4, Table I) were used to calculate γ_{LV} for the four liquid metals and his $\cos\theta$ *vs.* γ_{LV} graphs to obtain $\cos\theta$ at that temperature. Although the results show that γ_{cs} does, indeed, increase with increasing γ_{LV} at a single temperature, no correlation is observed between γ_{LV} and $\cos\theta$ for the four metals. Thus, the four $\cos\theta$ *vs.* γ_{LV} data points do not result in a rectilinear wetting isotherm from which γ_c could be determined directly, as has been done for other high-energy surfaces (Figure 1). Therefore, it is not possible to use presently available wetting data for high-energy surfaces to show directly the consistency of γ_{cs} and γ_c for a specific temperature.

Applicability of the Variable-Temperature Approach to Low-Energy Surfaces

Inasmuch as the isothermal method for determining the wettability of low-energy surfaces proved applicable to high-energy surfaces (Figure 1), it is of interest to determine whether the variable-temperature method developed by Rhee for high-energy surfaces can also be used to obtain γ_{cs} for low-energy surfaces. Experimentally, the method is convenient for the study of low-energy surfaces because of the low temperatures characterizing the melting and boiling of the organic liquids

(23) D. T. Livey and P. Murray, *Plansee Proc., Pap. Plansee Semin., "de Re Metal.,"* 2nd, *1955*, 375 (1956).

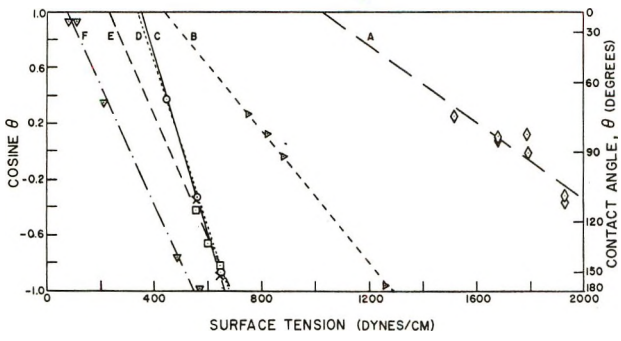

Figure 1. Wetting of high-energy surfaces by liquid metals or alloys: (A) ◇, sapphire at 1500°;[13] (B) ▷, sapphire at 1230°;[14] (C) ×, beryllium at 650–750°;[15] (D) ⊙, boron carbide at 650–750°;[15] (E) ⊡, graphite at 650–750°;[14] (F) ▽, silica or pyrex at 20–156°.[10]

normally used to study low-energy surfaces. This circumstance favors the direct experimental observation of the θ *vs.* T relation up to T_{cs}, thus eliminating the necessity for assuming the nature of the relation.

Considerable information now is available in the literature concerning the effect of temperature on θ for selected organic liquids on various solid surfaces, including both bulk polymers[24-29] and thin films of polymers (silicone-treated glass).[30] But only the investigation of Johnson and Dettre[27] had been pursued to temperatures sufficiently high that fresh, advancing, sessile drops of a liquid which had not spread at lower temperatures began to exhibit spreading behavior (*i.e.*, zero contact angle). The temperature dependence of θ was found to be curvilinear (Figure 2a) for both of the organic liquids studied on the low-energy surface. Such curvature is at variance with the rectilinear relation postulated by Rhee for the liquid metal–high-energy surface, and it effectively precludes any attempts to extrapolate to $\theta = 0$ the θ *vs.* T data from those studies of low-energy surfaces which were not heated high enough for the investigated liquid to spread. Therefore, only ref 27 could be used to obtain values of T_{cs} and their corresponding values of γ_{cs}.

Johnson and Dettre's observations[26,27] of two *n*-alkanes in contact with a tetrafluoroethylene–hexafluoropropylene copolymer of unspecified per cent composition showed θ to be essentially temperature-independent over an extended, well-defined range of lower temperatures (Figure 2a); at the higher temperatures, the θ–T graph began to curve and develop a large negative slope, intercepting the $\theta = 0$ axis at a temperature (here defined as T_{cs}) only a few degrees below the boiling point of the respective wetting liquid. Thus, the hexadecane contact angle, which had been constant over the interval T = 25–120°[26] and had increased only 4° over the next 40° interval, decreased some 48° in the final 70° interval. Johnson and Dettre remarked,[27] "The most probable explanation for this is an increase in surface diffuseness with a corresponding reduction of interfacial tension."

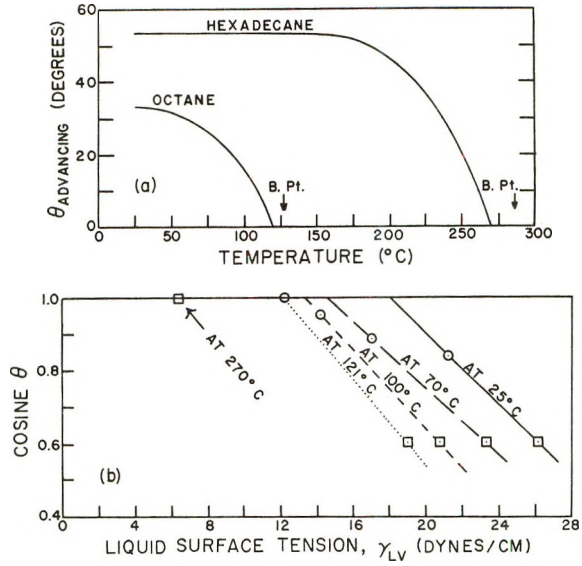

Figure 2. Wettability of fluorinated ethylene–propylene copolymer by hexadecane (squares) and octane (circles): (a) advancing contact angles as a function of temperature,[26,27] and (b) cosine of the advancing contact angle as a function of the liquid surface tension at selected temperatures.

Values of the advancing contact angles for both alkanes have been estimated from the smooth curves of Figure 2a (redrawn from ref 27) and tabulated (Table II) for three arbitrarily chosen temperatures as well as for the two values of T_{cs}. The variable-temperature method has been applied to the latter data and a value of γ_{cs} assigned to each T_{cs} by obtaining the appropriate alkane liquid surface tension by extrapolating the γ_{LV} *vs.* T data of Vogel.[32] The values of γ_{cs} (12.2 dyn/cm at 121° and 6.4 dyn/cm at 270°) are both well below the literature values for γ_c around 18 dyn/cm at 25°.[28,29,33] Since a decrease in critical surface tension had been found for high-energy surfaces with increasing temperature, the present decrease for a low-energy surface indicated the desirability of obtaining γ_c values over a range of T. This has been done, using a limited selec-

(24) F. D. Petke and B. R. Ray, *J. Colloid Interface Sci.*, **31**, 216 (1969); *erratum*, *ibid.*, **33**, 195 (1970).

(25) A. W. Neumann, G. Haage, and D. Renzow, *ibid.*, **35**, 379 (1971).

(26) R. E. Johnson, Jr., and R. H. Dettre, *ibid.*, **20**, 173 (1965).

(27) R. E. Johnson, Jr., and R. H. Dettre, "Surface and Colloid Science," Vol. 2, E. Matijević, Ed., Wiley-Interscience, New York, N. Y., 1969, p 144.

(28) C. L. Sutula, R. Hautala, R. W. Dalla Betta, and L. A. Michel, Abstracts, 153rd National Meeting of the American Chemical Society, Miami Beach, Fla., Apr 1967.

(29) R. A. Dalla Betta, C. L. Sutula, R. Hautala, and L. A. Michel, Abstracts, 153rd National Meeting of the American Chemical Society, Miami Beach, Fla., Apr 1967.

(30) A. W. Neumann and D. Renzow, *Z. Phys. Chem.* (*Frankfurt am Main*), **68**, 11 (1969).

(31) F. R. Driesbach, *Advan. Chem. Ser.*, **No. 33**, 166 (1959).

(32) A. I. Vogel, *J. Chem. Soc.*, 133 (1946).

(33) M. K. Bernett and W. A. Zisman, *J. Phys. Chem.*, **64**, 1292 (1960).

Table II: Effect of Temperature on the Wettability of Fluorinated Ethylene–Propylene Copolymer

	n-Octane (bp 126°)			*n*-Hexadecane (bp 286°)			Critical surface tension, dyn/cm	
T, °C	Liquid surface tension[a] γ_{LV}, dyn/cm	Contact angle[b] θ, deg	Vapor pressure[c] p, Torr	Liquid surface tension[a] γ_{LV}, dyn/cm	Contact angle[b] θ, deg	Vapor pressure[c] p, Torr	By variable-temperature method[d] γ_{cs}	From wetting isotherm[e] γ_c
25	21.2	33	14	27.1	53			18.1
70	17.0	28	119	23.3	53			14.5
100	14.2	18	351	20.8	53			13.4
121	12.2	Just spreads	666	19.0	53	$\ll 1$	12.2	
270				6.4	Just spreads	521	6.4	

[a] Extrapolated from data of ref 31. [b] From θ_{adv} *vs.* T curves of Johnson and Dettre, ref 26 and 27. [c] Calculated from Antoine vapor pressure equation using constants from ref 31. [d] From intercept with $\theta = 0$ axis of θ_{adv} *vs.* T curve of Figure 2a. [e] From intercept with $\cos\theta = 1$ axis of isotherms of Figure 2b, where data points corresponding to each indicated temperature had been read off the θ *vs.* T curves of Figure 2a.

tion from the suitable data of ref 26 and 27. Because both alkanes exhibited nonzero contact angles at temperatures below 121°, it is possible to assign to each a value of θ determined from Figure 2a and a value of γ_{LV} from ref 31 corresponding to any given temperature, $T < 121°$. The resulting $\cos\theta$ *vs.* γ_{LV} data points can then be used to locate the isotherm for that specific temperature (Figure 2b) so that the intercept of the isotherm with the $\cos\theta = 1$ axis can provide the value of γ_c characterizing the surface at that particular temperature.

Although each such value of γ_c is based on the behavior of only two liquids, the results are in good agreement, at least at the lower temperatures, with literature values based on more extensive measurements. Thus, the intercept value of 18.1 dyn/cm based on the two data points at 25° (Figure 2b) compares favorably with the range of values of 18.5 to 17.8 dyn/cm reported in 1960 by Bernett and Zisman[33] for a series of fluorinated copolymers with increasing mole per cent of the hexafluoropropylene constituent up to 23%, these values having been determined from data for seven members of the homologous series of *n*-alkane liquids at 25°. Similarly, the agreement is also excellent with the γ_c = 18.2 dyn/cm quoted in ref 24 from a personal communication of Sutula for the fluorinated copolymer of unspecified per cent composition identified as "*x*-100."

Similar treatment of the data for octane and hexadecane at two other arbitrarily chosen temperatures (70 and 100°) leads to the corresponding values of γ_c listed in the final column of Table II. How well these values for intermediate temperatures agree with those obtained at either room or high temperatures is illustrated in Figure 3 where the three γ_c values (open circles) and the two γ_{cs} values (closed circles) of Table II have been plotted as a function of temperature. A good straight line of slope −0.061 dyn/cm deg describes the γ_c values for the lower temperatures as well

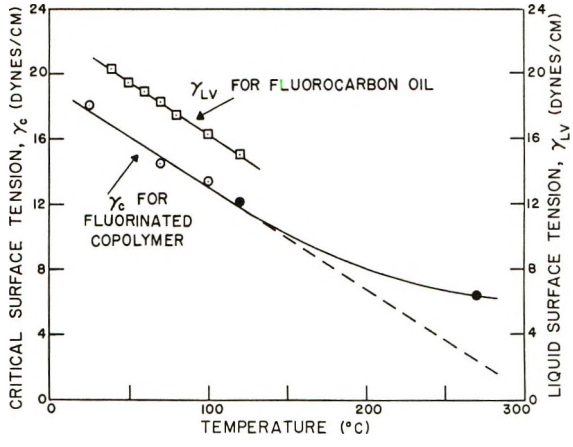

Figure 3. Effect of temperature on the critical surface tension of a low-energy solid (γ_c, open circles; γ_{cs}, filled circles) and a comparison with the effect of temperature on the surface tension of a chemically related liquid.

as the γ_{cs} value at T_{cs} = 121° for *n*-octane. This indicates the consistency of our interpretation of the relation between the γ_c from wetting isotherms and the γ_{cs} from the variable-temperature approach. Additional confirmation is provided by the temperature coefficient of −0.08 dyn/cm deg reported by Sutula, *et al.*,[28] for γ_c values determined by contact angle measurements on a homologous series of *n*-alkanes from hexane through hexadecane on "*x*-100" at temperatures up to 150°.

Extrapolation of the straight-line portion of the lower graph of Figure 3 by an additional 150% (to 270°) indicates a critical surface tension some 3.8 dyn/cm lower than the γ_{cs} obtained experimentally for hexadecane at its T_{cs}. The deviation from linearity could be due to alkane deposition or adsorption from the vapor phase, since T_{cs} is close to the boiling point of the hexadecane. A similar effect would then be expected, however, for octane, since its vapor pressure is also high at its T_{cs} (Table II). This is not the case,

and the octane datum point is consistent with the γ_c *vs.* T data obtained at temperatures sufficiently low that the vapor pressure of the several alkane liquids used to define γ_c remained relatively inconsequential.

The effect of temperature on γ_c of the fully fluorinated, chain-branched polymeric solid strongly parallels that on γ_{LV} of a fully fluorinated, partially chain-branched liquid which is highly viscous at 25°. This is evident in Figure 3 where the γ_{LV} data for an oil of average composition $C_{21}F_{44}$[34] have been plotted as a function of T to the same scale as the critical surface tension data for the related solid polymer. A good straight line describes the γ_{LV} *vs.* T data up to the highest temperature reported (120°). Moreover, the slope of this graph (−0.064 dyn/cm deg) is close to that of the γ_c *vs.* T graph. This finding is in keeping with the general observation of Petke and Ray[24] that the temperature coefficients of their γ_c values for several different polymers all fell within the values of $d\gamma_{LV}/dT$ for organic liquids.

These results are consistent with a model in which (a) γ_c is related monotonically to the surface energy (γ_s) of the low-energy solid; and (b) the change in γ_s with temperature for a solid of given chemical composition, configuration, and weak intermolecular force will not differ greatly from the change in the γ_{LV} of a liquid with similar chemical, steric, and interactive properties.

Effect of Temperature on γ_c of Low-Energy Surfaces

The effect of temperature on the critical surface tension of the solid fluoropolymer can also be compared with the effect for other low-energy solids, since the literature provides considerable information on the effect of temperature on the contact angles of organic liquids on a variety of polymers. Thus, values of γ_c at different temperatures are available either from direct determination of the wetting isotherms for specific temperatures by the original investigators or by subsequent construction of $\cos\theta$ *vs.* γ_{LV} isotherms from published θ *vs.* T data from wetting studies and γ_{LV} values from the surface tension literature.

Petke and Ray[24] used the isotherm method to determine γ_c values at seven different temperatures for five nonhalogenated polymers, using measurements of the advancing contact angles for the same group of high surface tension liquids on each solid. Their results are summarized graphically by the continuous-line plots in Figure 4, where the length of each graph reflects the temperature range covered by the original investigators. The data for the nonhalogenated polymers are well described by straight-line graphs of γ_c *vs.* T with slopes between −0.03 and −0.06 dyn/cm deg. Although the temperature coefficients ($d\gamma_c/dT$) do not vary greatly from one polymer to another, there is some crossing of the lines. Therefore, the curves have been labeled in an alphabetical sequence which reflects the order of decreasing γ_c at 25°: (A) poly(ethylene terephthalate), 40.0 dyn/cm; (B) polyoxymethylene (Polyacetal), 38.0 dyn/cm; (C) polyethylene, 36.0 dyn/cm; (D) polycarbonate, 34.5 dyn/cm; and (E) polystyrene, 33.0 dyn/cm.

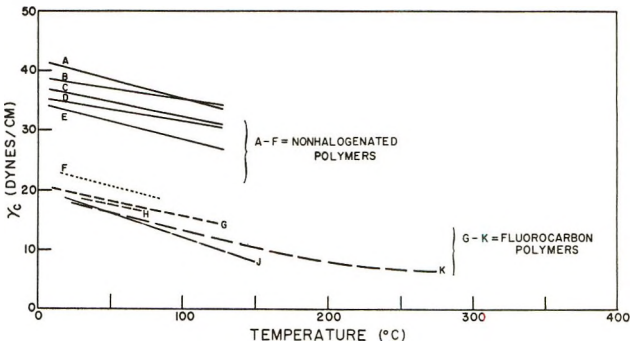

Figure 4. Effect of temperature on the critical surface tension for spreading on low-energy surfaces: (A) poly(ethylene terephthalate); (B) polyoxymethylene; (C) polyethylene; (D) polycarbonate; (E) polystyrene; (F) silicone; (G) and (H) polytetrafluoroethylene; and (J) and (K) polytetrafluoroethylene–hexafluoropropylene copolymer.

Neumann and Renzow[30] had studied the effect of temperature on the wetting of a methyl-rich polysiloxane (Silikonöl 350, Schuchardt) in the form of a thin film polymerized on a glass substrate. Capillary rise measurements on four liquid alkanes against a vertical, silicone-coated, glass plate resulted in calculated values of θ leading to γ_c = 22.7 dyn/cm at 20°, in excellent agreement with γ_c = 23.5 dyn/cm obtained from sessile drop measurements for a much larger number of liquids at the same temperature.[35] By applying Neumann and Renzow's values of $d\theta/dT$ to their γ_c at 20°, a value of γ_c = 19.4 dyn/cm is obtained for 70°, the highest temperature they observed. The resulting dotted-line graph (curve F) has a slope, $d\gamma_c/dT$ = −0.066 dyn/cm deg, which agrees well with the slopes of the other nonhalogenated polymers of Figure 4. These slopes all indicate temperature coefficients about half as large as the coefficients for the liquid surface tensions of many hydrocarbon liquids.[36]

The effect of temperature on the wettability of polytetrafluoroethylene has been studied by both the sessile drop[24] and the capillary rise methods;[25] the results are shown in Figure 4 where the same pattern of dashed lines has been used to represent both sets of data. Curve G corresponds to the data of Petke and Ray[24] for a specimen of polytetrafluoroethylene (inadvertently identified by the manufacturer as a fluorinated ethylene–propylene copolymer and so cited in the original publication). The results of their γ_c measurements at seven different temperatures are well represented by a straight-line graph. In contrast, there is much un-

(34) R. H. Dettre and R. E. Johnson, Jr., *J. Phys. Chem.*, **71**, 1529 (1967).

(35) E. G. Shafrin and W. A. Zisman, *Advan. Chem. Ser.*, **No. 43**, 145 (1964).

(36) O. Quayle, *Chem. Rev.*, **53**, 439 (1953).

certainty about the assignment of γ_c values to the data of Neumann, Haage, and Renzow[25] because of the difficulties encountered in fitting a conventional straight-line isotherm to their cos θ *vs.* γ_{LV} data, particularly at the higher temperatures where their data are best described by progressively more curved isotherms. If reasonable curvilinear extrapolations of these isotherms are made to the cos $\theta = 1$ axis, the resulting values of γ_c do plot as a straight-line function of T (curve H) which is both close and parallel to the graph describing the data of Petke and Ray.

The bottom two curves of Figure 4 correspond to the data of Johnson and Dettre (curve K) and of Sutula (curve J) for the fluorinated copolymer which was discussed earlier.

The graphical summary in Figure 4 emphasizes how similar the effect of temperature on critical surface tension is for low-energy surfaces, whether the latter are primarily hydrocarbon-type or fluorocarbon-type polymers. As a result, the relative positions of the γ_c *vs.* T curves are maintained despite large increases in temperature so that, even at high temperatures, fluorine-rich surfaces remain far less wettable than nonfluorinated surfaces. The strong similarity in the several graphs of Figure 4 and the conformity of curve K (derived from both γ_c and γ_{cs} data) to curve J for the same kind of polymer and to the remaining curves for the other polymers reinforces the conclusion that the value of γ_{cs} obtained by the variable-temperature method on a low-energy surface is, indeed, equivalent to γ_c for the temperature T_{cs}.

Discussion

Because the contact angle data were available for some organic liquids on at least one low-energy surface at temperatures up to and including the temperature of spreading, T_{cs}, we were able to prove for the low-energy surfaces what Rhee had postulated for high-energy surfaces, namely, that the value of the surface tension of a liquid at the temperature at which it just spreads on a given solid is equivalent to the critical surface tension of that solid at T_{cs}.

Thus, if Rhee's variable-temperature method is interpreted and used correctly, it can be applied to high-energy surfaces as Rhee has done for various metals and ceramics[16-20] or it can be applied to low-energy surfaces, as we have shown using the data of Johnson and Dettre for a fluorinated copolymer.[26,27] In either application, however, it is imperative that wetting behavior be observed at temperatures up to and including T_{cs}. The variable-temperature method could permit γ_c determinations to be extended to cryogenic temperature ranges or wherever it would be difficult to find a sufficient number of nonspreading liquids to permit the construction of a conventional cos θ *vs.* γ_{LV} wetting isotherm.

Despite the attractiveness of the variable-temperature method, it has some important limitations. For example, it is often desirable for technical or theoretical reasons to determine the γ_c of a solid surface at some specific temperature; if the variable-temperature method is employed, it may be necessary to observe a variety of liquids to determine empirically which particular liquid has a value of T_{cs} in the temperature regime of interest. Moreover, because T_{cs} will generally differ from one liquid to another, it will be difficult to make direct comparisons of the effect of changes in the wetting liquid on γ_c at a single temperature. Reliance on a γ_c value obtained for only a single liquid increases the risk of allowing specific liquid–solid interactions to remain unrecognized. In the case of liquid metals in contact with the high surface energy ceramics, Rhee recognized this danger and took the precaution of examining the interface by various electron-optical techniques to see if phase interpenetration or compound formation had occurred. Low-energy surfaces would be less amenable to such examination. Yet, we know from the results of studies at constant temperature using a variety of organic and aqueous liquids that specific liquid–solid interactions can profoundly affect wetting. Examples of such effects include hydrogen bonding[37] and possible changes in surface molecular conformation.[6]

There are also limitations to the constant-temperature method. The critical surface tension of the solid may lie in a region where it is difficult to find liquids with sufficiently high surface tensions to be nonspreading or where the chemical compositions required to impart sufficiently high γ_{LV} values will be such that liquid–solid interactions cannot be avoided. This has been a serious difficulty, for example, in determining γ_c values much above 45 dyn/cm at room temperature for low-energy surfaces which are potential proton acceptors, since most organic liquids with $\gamma_{LV} > 45$ dyn/cm are capable of hydrogen-bond formation. In the case of high-energy surfaces, the limitation is more severe since the determination of γ_c for a specific, constant temperature would depend on the availability of a series of related liquids (such as liquid metal alloys) having the right range of γ_{LV} values to be useful in the temperature range of interest.

Therefore, one conclusion from the present study is that there are now available two separate, but complementary, techniques for obtaining γ_c. The judicious application of each may greatly extend our ability to determine the wettability of surfaces, whether of high or low energy, and may provide a route to circumvent experimental limitations encountered when only a single technique is employed.

Clearly, from our past work and the collateral work of others by the constant-temperature method and from Rhee's exploratory work with liquid metals on

(37) A. H. Ellison and W. A. Zisman, *J. Phys. Chem.*, **58**, 503 (1954).

ceramic surfaces by the variable-temperature method, it is safe to say that the analysis of contact angle behavior as a function of solid surface composition and liquid surface tension is now essentially consistent for a large variety of surfaces over a wide range of temperatures. We have shown the similarity of the temperature effect on γ_c for a variety of low-energy surfaces. As yet this cannot be done for high-energy surfaces because the results are not couched in a language which we can presently handle. The concepts of γ_c, γ_{cs}, and T_{cs}, and the recognition that γ_c is essentially a function of surface composition and a linear decreasing function of temperature appear adequate to provide a sound foundation and a framework on which to broaden the whole field concerned with the contact angle, spreading, and wetting.

Experimental Study of the Relation between Contact Angle and Surface Roughness

by Y. Tamai and K. Aratani*[1]

Chemical Research Institute of Non-Aqueous Solutions, Tohoku University, Sendai, Japan *(Received November 15, 1971)*

Publication costs assisted by the Research Laboratories of Kawasaki Steel Corporation

The effect of surface roughness on the contact angle of a liquid was studied for the silica glass–mercury system using the sessile drop method. Silica glass plates were roughened in three different ways and classified in three groups. Considering the roughness profiles and the electron micrographs of these surfaces, a model of roughened surface was proposed. Assuming Wenzel's relation, the parameters of the model were estimated from the experimental data of one group. The experimental data of the other two groups were explained satisfactorily by this model, proving Wenzel's theory to hold.

Introduction

It is a well-known fact that the contact angle of a sessile liquid drop on a plane surface of a solid depends largely on the roughness of the plane. To explain the effect of roughness, Wenzel[2] proposed a theory in which the increase in the surface area of a roughened plane is shown to be responsible for the change of the contact angle. After Wenzel, Cassie and Baxter,[3] Deryagin,[4] Shuttleworth and Bailey,[5] Good,[6] and Johnson and Dettre[7] have tried to derive Wenzel's relation by thermodynamic treatments. Several investigators have compared the experimental results with Wenzel's equation. However some of the comparisons were of qualitative nature,[8] and others were not successful in comparing the results with the theory.[9]

The present work was planned to examine the relation between the measured contact angle and the roughness of a surface on the basis of Wenzel's equation, by making an approximate model of surface geometry consistent with experimental observation and by introducing the roughness factor based on this model into Wenzel's equation.

For this purpose the advancing contact angle was measured with a sessile drop of mercury on the surface of silica glass which was roughened to various extents.

Experimental Section

Preparation of the Specimen. The silica glass plates used were of 10 × 10 × 1 mm in size and roughened in three different ways. The first way was to abrade the specimen with carborundum abrasive followed by successive polishings for different times with diamond paste. In this way the prepared specimens had different surface finishes ranging from a maximum

(1) Research Laboratories of Kawasaki Steel Corp., Chiba, Japan.

(2) R. N. Wenzel, *Ind. Eng. Chem.*, **28**, 988 (1936).

(3) A. B. D. Cassie and S. Baxter, *Trans. Faraday Soc.*, **40**, 546 (1944).

(4) B. V. Deryagin, *Dokl. Akad. Nauk USSR*, **51**, 357 (1946).

(5) R. Shuttleworth and G. L. J. Bailey, *Discuss. Faraday Soc.*, **3**, 16 (1948).

(6) R. J. Good, *J. Amer. Chem. Soc.*, **74**, 5041 (1952).

(7) R. E. Johnson, Jr., and R. Dettre, *Surface Colloid Sci.*, **2**, 85 (1969).

(8) R. E. Johnson and R. H. Dettre, *Advan. Chem. Ser.*, **No. 43**, 112 (1963).

(9) F. E. Bartell and J. W. Shepard, *J. Phys. Chem.*, **57**, 211, 455, 458 (1953).

roughness to a mirror finish. The second way was to abrade the specimen plates with abrasives of different powder size. The first group of specimens was therefore expected to have a different surface geometry from that of the second. The specimens of the third group were abraded in the same way as the second and then polished with diamond paste.

The specimens were cleaned by ultrasonic radiation for 1 hr in an aqueous solution of soap and then by immersion for 10 hr in a chromic acid mixture at room temperature. After these treatments, the specimens were rinsed with running tap water and distilled water and kept in a clean desiccator until used.

Contact Angle Measurement. The contact angle was measured on these specimens at 20° and 60% relative humidity by the sessile drop method. The advancing contact angle of mercury was observed with a goniometer telescope. In this way, we measured the advancing contact angle at various drop sizes from 2 to 10 mm in diameter on the as-abraded and mirror-finished specimens, and it was found that the contact angle changed little with drop size in each case. Therefore, the measured contact angle was regarded as the equilibrium advancing contact angle. The reproducibility of the angle was within ±3°.

Observation of the Surface Roughness. A surface profilometer of the tracer stylus type was employed. It was also possible to measure the center line average height h_{av} by means of a built-in electronic device. Each specimen was observed in several different directions drawn on the surface, and the scatter of h_{av} was within 10%.

In addition, an electron microscopic examination was made by the double replica method.

Results and Discussion

Surface Roughness. Figure 1 shows the representative profiles of the first group specimens in different stages of polishing. Profile a is the surface as-abraded which is denoted by RA0, and profile d is the mirror-finished surface, M. As the polishing proceeded, the profiles changed from b to c. They are denoted by RA3, RA5, and so on, respectively. It is evident from Figure 1 that polishing cuts the tops of roughened hills and makes them flat. To specify the surface geometry, a parameter was introduced to represent this characteristic, that is, the ratio x of the length of flat portions to the length of the base line. The value of x is, for example, zero for profile a in Figure 1 and 1 for profile d. The x's were measured for a number of profiles on one specimen. The scatter of x was about 10% at each stage of polishing. As to the second group of specimens, the profiles were essentially the same as RA0 in the first group, but h_{av} decreased as the size of the abrasive power used got smaller.

The electron microscopic pictures are shown in Figure 2. These suggest that the pattern is rather homogeneous and the orientation effect by abrasion is not seen. In Table I, the resultant contact angle, θ, x, and h_{av} for the first group are shown.

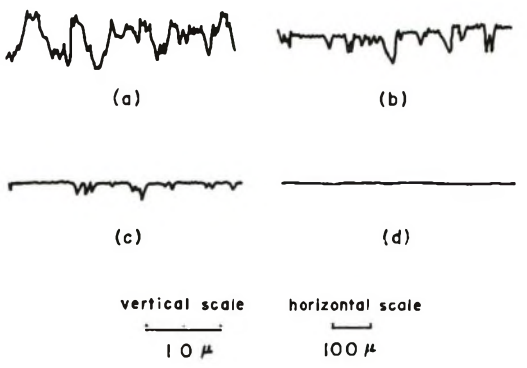

Figure 1. Representative roughness profiles of the first group; a, as abraded by SiC abrasive (specimen RA0); b and c, after abraded by the same size of abrasive as RA0, polished by diamond paste step by step (specimens RA3 and RA5); d, mirror finished (specimen M).

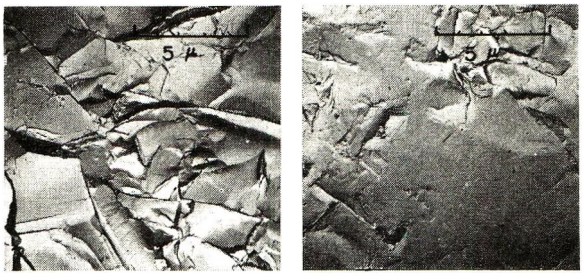

Figure 2. Electron micrographs of the plates of the first group: a, as abraded by SiC abrasive (specimen RA0); b, after abraded, polished by diamond paste (specimen RA3).

Table I: Experimental Values of the Results of Contact Angle, θ, Ratio of the Length of Top-Flat Portions, to Base Length x, and Center Line Average Height, h_{av}, for the First Group in Different Stages of Polishing

Specimen	θ, deg	x^a	h_{av}, μ
RA0	160.1	0.0	1.47
RA1	152.3	0.21	1.33
RA2	145.0	0.35	1.09
RA3	141.5	0.42	0.92
RA4	136.6	0.55	0.71
RA5	132.5	0.77	0.32
RA6	130.5	0.93	0.06
M	129.1	1.00	0.00

[a] Observed from roughness profiles.

Model Surface, Roughness Factor, and Average Height. From Figure 1, we can see a relatively smaller number of deep large valleys and a larger number of shallow subvalleys which are located mostly at the top

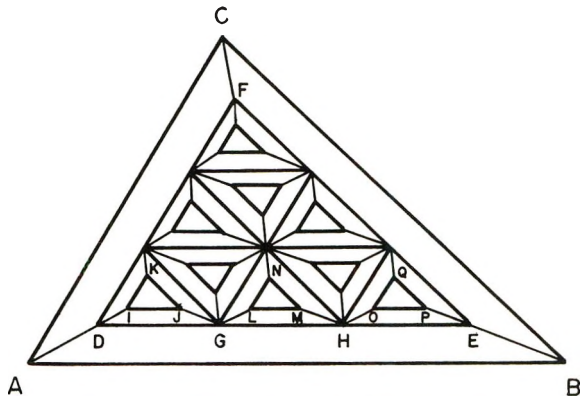

Figure 3. Upper view of the model.

of the large hills. From Figure 2, the pattern of hills and valleys seems homogeneous.

Considering these characteristics, a model surface may be approximately proposed as in Figure 3, which illustrates a unit portion of surface and is composed of a large basic trigonal pyramid and of smaller top-cut pyramids on it. As a basic trigonal ABC, any shape or any size is acceptable. The upper pyramids are assumed to be all in the same shape and size and similar to ABC. It is also assumed that each side plane of a single pyramid makes the same angle with the basic plane, and that the cut surfaces DEF, IJK, and so on are parallel to ABC.

With this model, the roughness factor, r, is readily calculated; that is

$$r = \frac{1 - y^2}{\cos \alpha} + \frac{y^2 - x^2}{\cos \beta} + x^2 \qquad (1)$$

where α and β are the angles of the side planes of the lower and upper pyramids, respectively, against the basal plane, and x and y are ratios of lengths of the upper edges to the parallel base line of the pyramids, *i.e.*, for example, AB = a, DE = ya and IJ + LM + OP = xa. In the case where the upper pyramids are absent, which corresponds to the well-polished surface, the second term of eq 1 vanishes and y in the first term should be read x.

The center line average height, h_{av}, depends on the direction in which the probe stylus traversed. The larger scatter of the data shows this dependence and, as can be seen from the roughness profiles, the cross section of the hill is roughly represented in Figure 4. By definition, the center line average height, h_{av}, is shown to be

$$h_{av} = \frac{a}{8 \tan \alpha'}\left[\frac{1}{n}(y^2 - x^2) \tan \beta' + (1 - y^2) \tan \alpha'\right]^2 \qquad (2)$$

where, as shown in Figure 4, α' and β' are the inclinations of the upper and lower hills, respectively, a is the length of the base line, and n is the number of small hills.

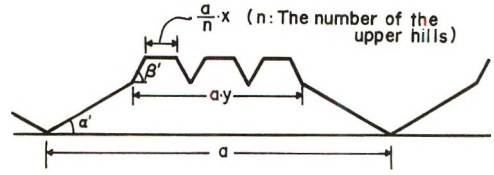

Figure 4. Representative cross section of one unit of the characteristic hill of the model.

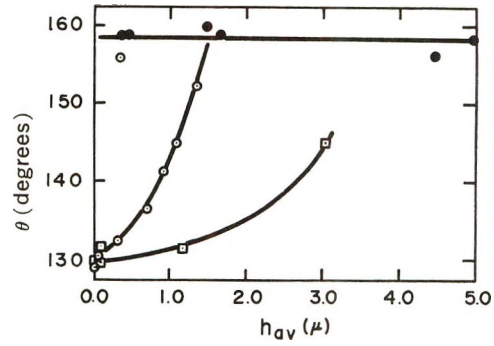

Figure 5. Plots of contact angle θ *vs.* center line average height h_{av}: ⊙, for the first group in different stages of polishing; ●, for the second group in different states of abrasion; ⊡, for the third group in different states of abrasion and polishing.

Equations 1 and 2 can be applied to other composed polyhedral truncated cones provided that the conditions for the above model are satisfied

Contact Angle and Average Height. The contact angles of mercury were plotted against the observed h_{av} in Figure 5 for the first group, *i.e.*, different degrees of polishing, and for the second and third group, *i.e.*, different degrees of abrasion and polishing.

In the case of the second group, it is evident that the observed angle is not dependent on h_{av}. On the other hand, the angles change markedly with h_{av} for the polished groups.

Comparison of the Results with the Model. Now we assume that Wenzel's relation holds for the present surface, that is

$$\cos \theta = r \cos \theta^\circ \qquad (3)$$

where θ° is the contact angle for the smooth surface and θ for the roughened surface.

As given by eq 1, r is independent of a and n, and as far as the shape is similar, that is, as far as α, β, y, and x are constant, r should be the same in each specimen. In the second group, a will differ in each specimen because of the abrasions by the different sizes of abrasives, but the x's are considered to be zero, because the specimens were only roughened and not polished. The other parameters are considered to be constant. Therefore, although in this group h_{av} will change with a and n according to eq 2, r will not change in each

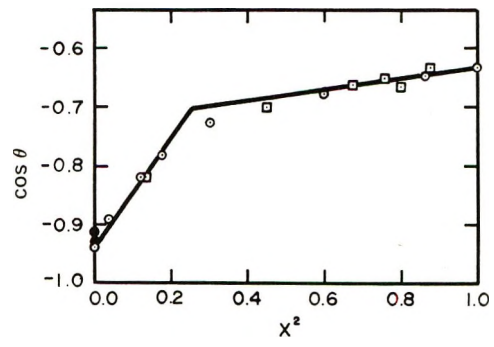

Figure 6. Plots of cos θ *vs.* x^2 for the first, second, and third group: ○, for the first group in different stages of polishing; ●, for the second group in different states of abrasion; ⊡, for the third group in different states of abrasion and polishing.

specimen, and if Wenzel's relation is assumed to be reasonable, cos θ will not change even if the h_{av} vary. The results for this group in Figure 5 may be explained on this basis.

For the first group of polished specimens the situation is very much complicated. To determine the parameters which appear in the model, the observed contact angles were applied to the assumed Wenzel's relation.

For the mirror-finished surface, the contact angle is 129° (M in Table I), and this angle should be the true contact angle $\theta°$ in eq 3. By plotting cos θ against x^2, y is determined as equal to x at the point where the straight line deflects, because as x decreases from unity, the small hills would disappear at the point $x = y$. To plot this relation, x^2 were taken as obtained from roughness profiles, because even though x obtained from the profiles show a large amount of scatter, x in eq 1 would still be within the total range of the experimental values.

The plot is shown in Figure 6. From this figure, y is found to be 0.5. Putting this value and some data for the first group into eq 1 and 3 and combining them, α and β are 29.5 and 66.5°, respectively.

As for the value of α, α' evaluated from the observed profile ranges from 26 to 31°. In general, α' is expected to be a little smaller than α, and the agreement between the calculated and observed values is fairly good.

The present model can be further examined using the experimental values of x and h_{av} given in Table I. The obtained numerical values of α, β, and y are introduced into eq 2, in which α', and β' are assumed equal to α and β, respectively. As mentioned before, α', and β' are a little smaller than α and β, but the difference is small and they can be considered to be nearly equal. Then, using the data of h_{av} for $x = 0$ and $x = 0.42$ (RA0 and RA3 in Table I), we can evaluate a and n by solving eq 2. Thus a is found to be 19 μ and n to be 3.3. As the sample plates in this group were roughened by the same size of SiC abrasive, a and n should be constant, and so, if these a and n values and the α and β obtained before are put into eq 2, x^2 can be calculated from observed h_{av} for the other samples in this group. In Table II, x^2 calculated by the above method are compared with x^2 obtained from roughness profiles. In the table, r calculated using eq 1 are also shown for reference. From this table, it can be seen that the calculated and observed values agree very well with each other. This agreement shows the model to be reasonable. Conversely, as the reasonableness of the model was shown above by h_{av} and α measured, respectively, the plots of x^2 and cos θ in Figure 6 show the reasonableness of Wenzel's relation, because the parameters of the model were decided by assuming Wenzel's relation to hold.

Table II: Comparison of x^2 Calculated from h_{av} and That Observed from Roughness Profiles for the First Group in Different Stages of Polishing; r Calculated from x^2 Is Shown for Reference

Specimen	x^2		r^a	
	Calcd	Obsd	Calcd	Obsd
RA0	0.00	0.00	1.49	1.49
RA1	0.04	0.04	1.43	1.43
RA2	0.12	0.12	1.31	1.31
RA3	0.18	0.18	1.22	1.22
RA4	0.28	0.30	1.11	1.10
RA5	0.52	0.60	1.07	1.06
RA6	0.79	0.86	1.03	1.02
M	1.00	1.00	1.00	1.00

[a] r is calculated from eq 1 or 2 using x^2 calculated or observed, respectively.

The specimens in the third group have various a and x values. In Figure 6, plots of cos θ *vs.* x^2 for this group and for the second group are also shown, and it can be seen that they agree very well with the theoretical line derived from the model and Wenzel's relation.

From these considerations, the Wenzel equation was verified experimentally. Of course, when the size of the hills on the surface is large such as in the literature,[7] Wenzel's relation would not be satisfied, and the size effect should be introduced. But at least within the size in this experiment—the size of the hill is as large as about one-hundredth of the size in the literature,[7] and the roughness factors are below 1.5—Wenzel's relation was found to be reasonable. As shown in eq 1, the roughness factor is independent of the size of hills a, and so, even if the roughness factor is large, Wenzel's equation would be satisfied if the size of the hills is small. The upper limit of the size of hills which satisfy Wenzel's equation is now unknown.

Thus, it can be concluded that the change of solid surface area affects the contact angle of liquid on it according to Wenzel's relation, at least in the range of

roughness that was used in this experiment. This is because the change in surface area of the solid by roughening it causes a change in surface energy of the solid and in interface energy of the solid–liquid interface and brings about a new energy balance in the Young–Dupré equation.

Conclusion

From the observed surface profiles and electron micrographs, a simplified model was proposed. Then Wenzel's relation between contact angle and roughness was applied to the observed contact angle and the calculated roughness.

For the second group, the contact angles were constant regardless of h_{av}. This could be explained reasonably by the proposed model and Wenzel's relation.

For the first group, from the experimental relation of x^2 and cos θ, the parameters α, β, and y of the model were determined. On the other hand, from some experimental values of h_{av} and x, a and n were estimated. Putting the obtained parameters into eq 2, x^2 for differing degrees of roughness was calculated and compared with the observed x^2. The agreement between them was very good, showing that the model was acceptable, and conversely, Wenzel's theory was shown to be reasonable.

Specimens of the third group were prepared in a different way from the other groups. In this group, Wenzel's relation was also well explained by the proposed model.

Thus, Wenzel's relation was verified experimentally, and it can be concluded that the contact angle should be decided in terms of surface energy of the solid, the liquid, and the solid–liquid interface at least in the range of roughness in this experiment.

Acknowledgment. We should like to express our gratitude to Professor Takanashi and Dr. Sato, Research Institute for Scientific Measurements, Tohoku University, who kindly facilitated our using the profilometer.

Mass Spectrometric Study of the Vaporization of Cuprous Bromide

by D. W. Schaaf and N. W. Gregory*

Department of Chemistry, University of Washington, Seattle, Washington 98195 *(Received April 7, 1972)*

Publication costs assisted by the National Science Foundation

An effusion-mass spectrometric study of cuprous bromide indicates that in the vicinity of 700°K the trimer is the dominant molecular species in the saturated vapor, along with substantial amounts of tetramer. Heats of vaporization for these two species are derived.

Vaporization characteristics of cuprous bromide have recently been studied by spectrophotometric[1] and effusion methods.[2] We now report results of a mass spectrometric study in which intensities of mass peaks, generated by ionization of molecules in a beam issuing from a Knudsen effusion cell containing a condensed sample of cuprous bromide, were observed as a function of the temperature of the cell. Heats of vaporization for Cu_3Br_3 and Cu_4Br_4 have been derived and results compared with the earlier studies on the bromide as well as with recently reported mass spectrometric work on cuprous chloride.[3]

Experimental Section

Cuprous bromide was prepared by reaction of copper and bromine.[1] Samples were placed in a cylindrical glass effusion cell *ca.* 30 mm long and 25 mm in diameter with a knife-edged orifice *ca.* 1 mm in diameter. The cell was heated by a quartz-lined nichrome element mounted in a stainless steel vacuum chamber. Most of the effusate was trapped immediately above the cell on a copper plate, cooled with liquid nitrogen. An orifice in this plate permitted a beam of molecules to move without interference through two additional collimating orifices (1 mm diameter), inserted in the portals of a gate valve, into the ionizer of a Spectroscan 750 mass analyzer probe. Temperatures of the cell at the top, side, and bottom were measured with calibrated

(1) D. L. Hilden and N. W. Gregory, *J. Phys. Chem.*, **76**, 1632 (1972).

(2) R. A. J. Shelton, *Trans. Faraday Soc.*, **57**, 2113 (1961).

(3) M. Guido, G. Balducci, G. Gigli, and M. Spoliti, *J. Chem. Phys.*, **55**, 4566 (1971).

chromel–alumel thermocouples and were controlled within ±1–2° by independent heating elements. Background pressures in the probe chamber were in the 10^{-7} Torr range; those in the effusion chamber were in the range of 10^{-6} Torr.

Results

Ions observed and their relative intensities, as indicated by the ion current for the most abundant isotope, are shown in Table I. While the instrument is capable of unit mass resolution in the range of interest, the signal intensity was low relative to background and all peaks were not fully resolved into isotopic components. Ion identification was made on the basis of mass range (instrument calibrated with perfluorokerosene) and in the cases where resolution was sufficient ($Cu_3Br_3^+$, Cu^+) by isotopic distribution. Correction for background was made by subtracting the ion current measured with a shutter intercepting the beam. The relative intensities shown were measured with the effusion sample at 700°K and the ionization voltage at 70. Appearance potentials, also measured with the sample source at 700°K, were derived by extrapolation of the ion current plotted as a function of ionization voltage, with the latter varied by 2-V intervals up to 40 V. Voltage readings were calibrated by observation of appearance potentials for N_2^+, H_2O^+, and O_2^+ in the background spectrum.[4] Appearance potentials for the cuprous bromide ions are similar to those reported for corresponding ions in the cuprous chloride system[3] and indicate that $Cu_4Br_4^+$ and $Cu_3Br_3^+$ are the only simple parent ions produced in significant quantities. Thus we assume that the effusion beam consists principally of Cu_4Br_4 and Cu_3Br_3, with smaller ions resulting from fragmentation of these molecules.

Table I: Mass Spectral Data for CuBr Vapor

Ionic species	Rel intensities	AP, eV	$-Rd(\ln I^+T)/d(1/T)$, kcal/mol
$Cu_4Br_4^+$	4.4	9.2	35.3
$Cu_4Br_3^+$	5.9	10.4	36.1
$Cu_3Br_3^+$	100	9.7	28.5
$Cu_3Br_2^+$	74	12.4	28.9
$Cu_2Br_2^+$	8.4	16.8	32.2
Cu_2Br^+	32	15.0	30.8
$CuBr^+$	21	17.1	30.9
Cu^+	25	16.7	31.2

A plot of I^+T (log scale) *vs.* $1/T$, where T is the absolute temperature of the Knudsen cell containing the vapor in equilibrium with CuBr(β) and I^+ is the ion current, is shown for each of the ions in Figure 1. Transitions in solid CuBr, γ (zincblend) → β (hexagonal) at 385° and for β to α (body centered cubic) at 470° have been reported;[5] the $\beta \rightarrow \alpha$ transition temperature appears slightly above the upper limit of the molecular flow range for the vapor pressure.[2] The range of our study has been confined to the region of stability of the β phase as, in general, a good quantitative measure of ion intensity was not practical over a significant temperature range for the γ phase.

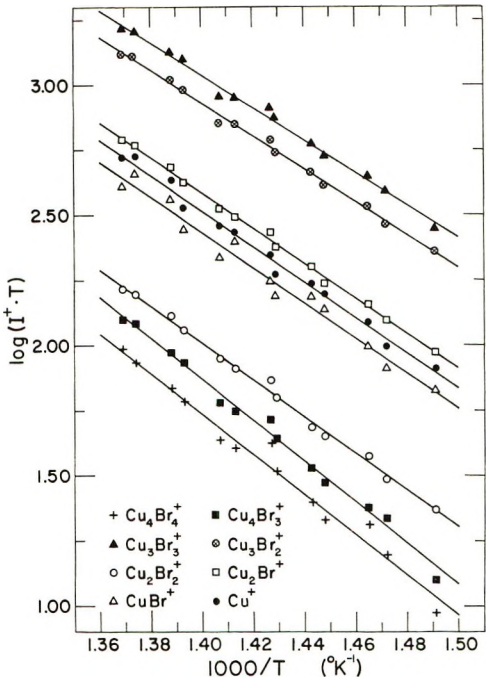

Figure 1. Plot of I^+T (log scale) *vs.* $1/T$ for various ions generated from a molecular beam of cuprous bromide vapor. Ion currents (A × 10^7, after subtraction of the background current) represent values for the most abundant isotopic species.

Linear least-squares lines are shown for each ion in Figure 1 and the corresponding slopes listed in Table I. Several independently prepared samples were studied with concordant results. If ionization efficiencies and instrumental constants are assumed independent of the temperature of the sample source, values of $-R\,d(\ln I^+T)/d(1/T)$ for ions which arise from a single neutral molecule may be taken as a measure of the heat of sublimation of that species. Since masses higher than the parent ion of the tetramer were not observed, slopes for $Cu_4Br_4^+$ and $Cu_4Br_3^+$ may be associated with the heat of sublimation of Cu_4Br_4 (from CuBr(β)); the average value for these two ions is 35.7 kcal mol^{-1}. From the relative ion currents and estimated fragmentation ratios (discussed below) it appears that Cu_3Br_3 is the dominant species in the effusion beam. Hence this species is believed to be the major source of $Cu_3Br_3^+$; the temperature dependence of the intensity of the mass peak of this species gives an apparent heat of sublimation of 28.5 kcal mol^{-1} for Cu_3Br_3, slightly larger than

(4) R. W. Kiser, "Introduction to Mass Spectrometry and Its Applications," Prentice-Hall, Englewood Cliffs, N. J., 1965.

(5) S. Hoshino, *J. Phys. Soc. Jap.*, **7**, 560 (1952).

the value based on spectrophotometric measurements (27.8 kcal),[1] and somewhat less than the apparent heat based on Shelton's total rate of effusion (30.9 kcal).[2] The heat predicted by the slope in Figure 1 is expected to be slightly larger than the true value if Cu_4Br_4 contributes significantly to the formation of $Cu_3Br_3^+$; however, the difference between the mass spectral and spectrophotometric values is probably not beyond the combined experimental errors.

The conclusion that the smaller ions arise principally from fragmentation of the trimer and tetramer receives further support from the observation that the slopes observed (Figure 1 and Table I) for these species are intermediate between those for $Cu_3Br_3^+$ and $Cu_4Br_4^+$. If two source molecules contribute to the formation of a given ion, the line (Figure 1) should not be strictly linear, though the deviation from linearity over the small temperature interval of the experiment is expected to be small; curvature cannot be detected within experimental error. Hence the linear least-squares slopes have been used to make a rough estimate of the fractional contribution from Cu_4Br_4 and Cu_3Br_3, respectively, in each case, assuming the fragmentation ratios to be independent of temperature. Each ion current was corrected by the appropriate isotopic distribution factor; however, no allowance could be made for possible differences in detection efficiencies for the various ions or ionization efficiencies for the parent molecules. This treatment indicates that the Cu_3Br_3:Cu_4Br_4 ratio in the original beam is roughly 5:1, a value considerably greater than found in the chloride system (1.4:1).[3] These comparative values are generally consistent with conclusions based on the spectrometric study, where absorbance attributed to the tetramer in the vapor of the chloride was clearly evident, but a similar effect in the bromide system was not detected.[1]

An independent estimate of P(trimer)/P(tetramer) in the equilibrium vapor of the bromide can be made by comparison of the temperature dependence of the total rate of effusion measured by Shelton[2] with the temperature dependence of the parent ion currents found in the present work. This gives a pressure ratio of 3.6 at 686°K, which together with Shelton's effusion rate indicates standard entropies of vaporization of 36 and 28 cal mol^{-1} deg^{-1} for tetramer and trimer, respectively. The calculation neglects contribution of tetramer to the trimer parent ion peak; the concentration ratio is determined by a ratio of differences of similar slopes, with attendant large uncertainty. When compared with the relative ion currents, the derived concentration ratio suggests that in ionization the fraction of tetramer converted to $Cu_4Br_4^+$ is much smaller than the fraction of trimer converted to $Cu_3Br_3^+$.

If one assumes that the standard entropy change at 700°K for the reaction

$$^4/_3Cu_3X_3(g) = Cu_4X_4(g)$$

is the same for the bromide and the chloride, respectively, then the values of $\Delta H°$ derived, -2.3 ± 1 kcal for the bromide and -10.3 ± 1.8 kcal for the chloride,[3] may be used to estimate the ratio of the equilibrium constants in the two cases. The experimental uncertainty in the heats is large. This calculation, together with vapor pressure data,[2,3] predicts that only between 0.1 and 2.5% (the range based on the indicated uncertainties in the heats) of the molecules in saturated cuprous bromide vapor at 700°K are tetramer. This estimate appears low in comparison with the relative intensities shown in Table I.

Acknowledgment. This work was carried out with financial support from the National Science Foundation, Grant No. 6608X, which is acknowledged with thanks.

Electron Spin Resonance Study of γ-Irradiated Single Crystals of Ammonium Oxalate Monohydrate

by P. I. Premović,*[1a] K. J. Adamić,[1b] and J. N. Herak[1b]

Institute "Boris Kidrič," Vinča, Yugoslavia, and Institute "Rudjer Bošković," Zagreb, Yugoslavia
(Received November 30, 1971)

Free radicals produced in a single crystal of ammonium oxalate monohydrate by γ irradiation have been investigated with the method of electron spin resonance. At 77°K three different species are found: B, $^{-}O_2C\dot{C}O_2$; C, $[HOOCCO_2^{-}]\cdot^{-}$; and radical pairs (D). The spin–spin interaction comes from different radicals B and C. On heating, the radical pairs vanish first. At temperatures above 190°K concentration of species C decays. At room temperature, two radical species are detected: A, $^{-}O_2CCOH^{-}$, and B. Radicals denoted as A are more stable than species B.

Introduction

Dicarboxylic acids and their salts are suitable model systems for studying the influence of hydrogen bonds in the radiation damage processes in solids. Particular interest in oxalic acid arises from the fact that it is a parent compound of many derivates and metal salts and that it is the first member of a homologous series of dicarboxylic acids. This interest is enhanced by the fact that both chemical forms of oxalic acid (anhydrous and dihydrated) and many oxalate salts can be readily obtained as pure crystals of known structure.

Radiolytic behavior of oxalic acid in aqueous solution is a useful tool for large-dose dosimetry, and to some extent this is also the case with solid oxalic acid and oxalates. These compounds in the solid state can be used even in the more difficult dosimetric conditions (multimegarad doses of mixed-pile radiations), although the chemistry of the solid compounds is less studied, and also less understood, than that of their aqueous solution.

Our earlier esr work[2] was concerned with the general considerations on the radiation processes in oxalates. Several authors have already studied single crystals of some of these substances, like oxalic acid, anhydrous and dihydrate,[3a] urea oxalate,[3b,4] sodium hydrogen oxalate,[5] and hydrazinium hydrogen oxalate.[6] The present work is an attempt to understand better the paramagnetic species formed in ammonium oxalate monohydrate (Am-Ox) and the processes in this substance upon irradiation.

Experimental Section

Single crystals of Am-Ox were grown from aqueous solution by slow evaporation at room temperature. Deuterated crystals were obtained by the same procedure from a heavy water solution. A typical configuration and crystal axes are shown in Figure 1. The crystal is orthorhombic with space group $P2_12_12$, the unit cell dimensions being $a = 8.06$, $b = 10.27$, and $c = 3.82$ Å.[7] A right-handed set of the orthogonal crystallographic axes a, b, and c is used as the reference coordinate system for the esr measurements. The axes have been identified by optical goniometer and X-ray diffraction analysis. The crystals were irradiated with a ^{60}Co γ source at liquid nitrogen and room temperature. Absorbed doses were between 1 and 15 Mrads. Esr spectra at both temperatures were recorded using a Varian E-3 (X-band) spectrometer.

The esr parameters were evaluated by the procedure of Schonland[8] and Lund and Vanngard.[9] Calculations were made by a CDC 3600 computer.

Results

Low-Temperature Measurements. Three distinct paramagnetic species, denoted for convenience as B, C, and D, were observed at 77°K after irradiation at the same temperature. Species B and C have a single-line resonance, while species D shows a doublet with a strong anisotropic splitting. Essentially the same spectra were observed for the crystals grown from regular and heavy water solutions. The esr parameters were measured on a deuterated crystal, because in this case the lines were sharper, particularly that belonging to species C.

(1) (a) Institute "Boris Kidrič"; (b) Institute "Rudjer Bošković."

(2) B. Radak, Lj. Petković, and P. Premović, Proceedings of the 10th Czechoslovakian Annual Meeting on Radiation Chemistry, Marianske Lazne, Czechoslovakia, 1970, pp 580–588.

(3) (a) G. C. Moulton, M. P. Cernansky, and D. C. Straw, *J. Chem. Phys.*, **46**, 4292 (1967); (b) B. L. Bales, Ph.D. Thesis, University of Colorado, 1968.

(4) D. V. Rao and W. Gordy, *J. Chem. Phys.*, **35**, 362 (1961).

(5) O. Edlund, A. Lund, and H. Tellegren, *Proc. Colloq. AMPERE*, 1968, **15**, 293 (1969).

(6) O. Edlund, A. Lund, and A. Nilsson, *J. Chem. Phys.*, **49**, 749 (1968).

(7) S. B. Hendricks and M. E. Jefferson, *ibid.*, **4**, 102 (1936).

(8) D. S. Schonland, *Proc. Phys. Soc.*, 73 (1959).

(9) A. Lund and T. Vanngard, *J. Chem. Phys.*, **42**, 2979 (1965).

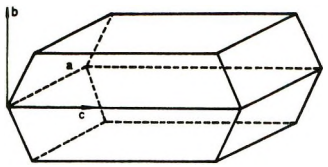

Figure 1. The appearance of the single crystal of ammonium oxalate monohydrate and the crystallographic and coordinate axes.

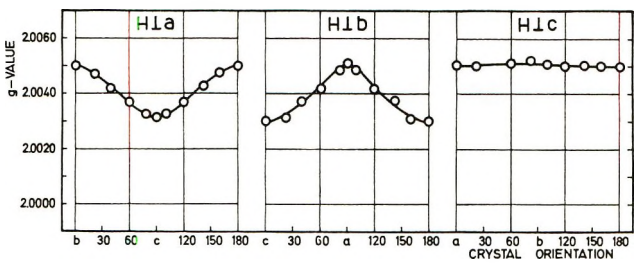

Figure 2. Variation of the g value for radical B in the three perpendicular coordinate planes.

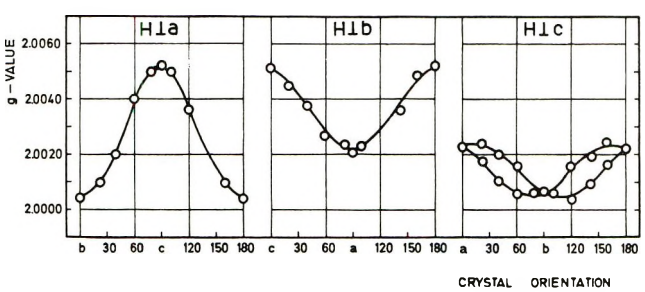

Figure 3. Variation of the g value for radical C in the three perpendicular coordinate planes.

Figures 2 and 3 give the variations of the g factor in the three planes for species B and C, respectively. Table I gives principal values of the g tensor and the direction cosines for the species. In Figure 3 the g value as a function of angle in the ab plane shows two magnetically unequivalent sites per unit cell (site splitting) for species C. The magnetically unequivalent sites of species B in the same plane cause unresolved site splitting. Here only "average" g values (Figure 2) are observed.

The separation $D = 2(H - H_0)$ of the doublet of species D (Figure 4) follows the equation $D = D_0(3\cos^2\theta - 1)$. This behavior is characteristic of the dipolar magnetic coupling between two like spins, and species D can be identified as radical pairs with the average distance R between the two unpaired electrons[10]

$$R = \frac{3}{D}\beta(3\cos^2\theta - 1)^{1/3}$$

where θ is the angle between R and H. The maximum value $D_{||}$, obtained for H parallel to a, gives $R = (6\beta/D_{||})^{1/3} = 8.5$ Å.

After heating the samples, the radical pairs D vanish

Table I

Species	Principal values	Direction cosines a	b	c
A				
A_1, G(−)	6.2	±0.77	∓0.64	0
A_2, G(−)	22.0	±0.64	±0.77	0
A_3, G(−)	12.8	0	0	1
g_1	2.0058	±0.50	∓0.87	0
g_2	2.0048	±0.87	±0.50	0
g_3	2.0028	0	0	1
B				
g_1	2.0050	1	0	0
g_2	2.0052	0	1	0
g_3	2.0026	0	0	1
C				
g_1	1.9995	±0.94	±0.33	0
g_2	2.0021	∓0.33	±0.94	0
g_3	2.0051	0	0	1
D				
$D_{||}$, G	90.0	1	0	0
$D_\perp$, G	44.0			

first. At temperatures above 190°K the concentration of species C decays with a simultaneous change of the spectrum. This process has not been studied in detail.

Room-Temperature Measurement. The room-temperature spectrum obtained immediately after irradiation at room temperature consists of a singlet and a doublet. The same is true for the crystal irradiated at 77°K if the spectrum is recorded at 300°K. The singlet attributed to species B remains unchanged after heating. At room temperature the radical species denoted as A, corresponding to the doublet, is more stable than species B (Figure 5). Figure 6 gives the variation of the doublet splitting in the three crystallographic planes. The principal value of the hyperfine splitting tensor, g tensor, and the direction cosines are listed in Table I. The variation of the splitting and g factor in the ab plane indicates two magnetically unequivalent sites of species A. For the crystal grown from heavy

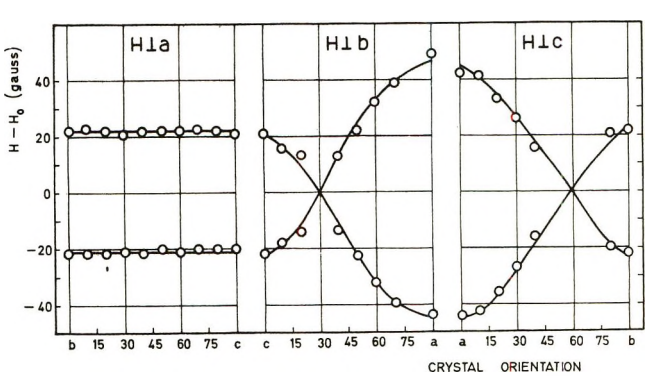

Figure 4. The angular variation of the spin–spin coupling for radical pairs (species D).

(10) Y. Kurita, *Nippon Kagaku Zasshi*, **85**, 842 (1964).

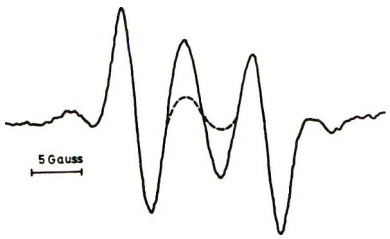

Figure 5. The room-temperature esr spectra (first derivative) recorded immediately after irradiation (—) and after several weeks (– – –).

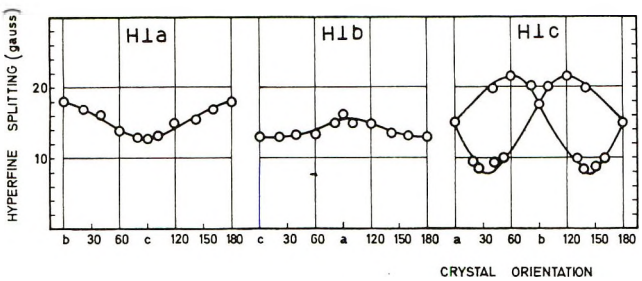

Figure 6. Angular variation of the hyperfine splitting for radical species A.

water the doublet is replaced by a 1:1:1 triplet with the hyperfine splitting smaller than that of the doublet by a factor of about 6.5.

Discussion

A great deal of the primary effect of γ radiation is ionization of either cation or anion species, or both. The high-energy secondary electrons make further ionizations until they reach thermal energies; then they are trapped. Thus, as a consequence of irradiation, one might expect species bearing one electron more or less than in the undamaged crystal. One can also expect species formed by the breaking of some of the covalent bonds in either cation or anion.

Unfortunately, species B and C detected at 77°K are characterized only by the g values. This fact makes the identification of the radicals more difficult. However, there exist already a number of precise measurements both of the principal values and direction cosines of g tensor for similar radicals in other matrices, and a comparison of the present values with those reported earlier offers a possibility for identification of the radical species in the present system.

In oxalates one expects to observe the CO_2^- radicals upon irradiation. In the present case, we have to exclude that possibility, because the observed g values of the present radicals (Table I) differ significantly from the known values of CO_2^-.[11]

For species B the direction of the minimum principal value of the g tensor is perpendicular to the *ab* plane, and the g value in that plane varies very little. We assume radical B to be planar, in the *ab* plane, although in the undamaged crystal the strong hydrogen bonds cause twisting of carboxyl groups out of the *ab* plane.[7] The g values of radical B agree very well in size and direction with respect to the parent molecule with those reported for the radical.[12]

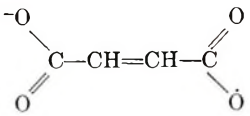

It has been shown both theoretically and experimentally that the direction of the minimum value of the g tensor in such a radical is perpendicular to the plane of the radical. Based on the above considerations and on the fact that this kind of radical is expected to be formed as a primary event upon irradiation, radical species B is assumed to be

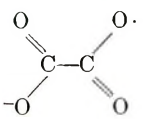

A rough calculation in the Hückel approximation indicates that for such a radical about 80% of the spin density should be localized on oxygen atoms. The presence of considerable spin density on oxygen explains the somewhat higher principal values of the g tensor for radical B than for the radicals in dicarboxylic acids.[13-15] The larger g value is due to the larger spin–orbit coupling constant of oxygen ($\lambda \approx 139$ cm^{-1}) in comparison to that of carbon ($\lambda \approx 28$ cm^{-1}).[16]

For species C the direction of the minimum g value is in the C–C direction, *i.e.*, in the *ab* plane, while the direction of the maximum value is perpendicular to the *ab* plane. We propose radical C to be of the form

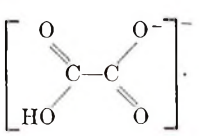

The reasons are as follows.

(a) The Hückel calculation for this radical indicates a higher spin density on the carbon atoms than on the oxygen atoms. In this case one expects the direction of the C–C bond to be prefered in esr parameters. That is really the case: the C–C bond is the direction of the minimum principal value of the g tensor.

(b) The narrowing of the resonance line of this radical upon the H → D replacement is much more pronounced than that for radical B. Such a change of the line width is due to the change of the hyperfine coupling of the unpaired electron with the paramag-

(11) P. W. Atkins and M. C. R. Symons, "The Structure of Inorganic Radicals," Elsevier, Amsterdam, 1967, p 132.

(12) H. C. Heller and T. Cole, *J. Amer. Chem. Soc.*, **84**, 4448 (1962).

(13) H. M. McConnell, C. Heller, and T. Cole, *ibid.*, **82**, 766 (1960).

(14) C. Heller and H. M. McConnell, *J. Chem. Phys.*, **32**, 1535 (1960).

(15) D. Pooley and P. H. Whiffen, *Mol. Phys.*, **4**, 81 (1961).

(16) E. H. Radford, *Phys. Rev.*, **122**, 114 (1961).

netic nuclei (protons or deuterons). Since for radical B one expects much larger spin density on oxygens than on carbons, and for radical C the opposite, the observation that radical C is much more sensitive to the hydrogen isotope present suggests that the hyperfine interaction responsible for the line width must be intramolecular rather than intermolecular. That is in accordance with the suggested radical structures. The small spin density on oxygens for radical C is the reason that one does not see a resolved hyperfine coupling. Besides, two magnetically distinct species make it even more unresolved.

A possible mechanism for the formation of radicals B and C is

(B)

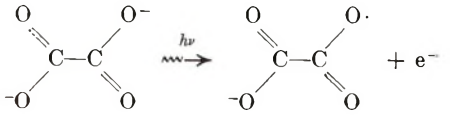

(C)

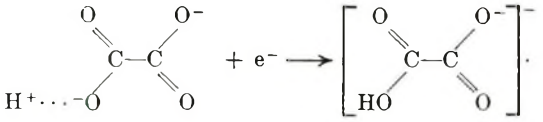

Radical species B is formed by the loss of an electron from the oxalate anion in the crystal. Radicals C are formed by trapping an electron with a subsequent transfer of a proton. The above mechanism corresponds to the primary radiolytic process[2] in which the ionic precursors of the more stable secondary radicals are formed. While radical C disappears before room temperature is reached, the half-life of radical B at room temperature is several days.

The nature of the radical pairs (species D) remains unexplained. From the direction of $D_{||}$ and from the calculated distance of 8.5 Å between the spins, it is obvious that the spin–spin coupling comes from two neighboring radicals in the a direction. The separation between the molecules in that direction is 8.06 Å.[7] From the spin–spin coupling of delocalized identical radicals one expects to get an" effective" interspin distance smaller than the crystallographic value of 8.06 Å. For two different radicals, like B and C in our case, the "effective" interspin distance is expected to be larger than the actual intermolecular distance. That is the only argument in support of the assumption that in ammonium oxalate the spin–spin interaction comes from two different radicals, namely radicals B and C.

For radical species A the hyperfine splitting tensor, as presented in Table I, is characteristic for an α-proton coupling. In elucidating the nature of this radical we may rule out any structure associated with the ammonium cation, since such a structure would give a much more complex resonance pattern. Also, the observed proton coupling cannot be due to a hydroxyl proton, because such a proton would have the principal values of the coupling tensor not all of the same sign,[17-19] which is in contrast to the present observation. Therefore, we conclude that we deal with the C–H fragment in radical species A.

The actual structure of the radical is not easily determined. We considered two structures, AI and AII.

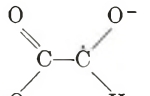

AI

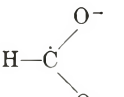

AII

AI is in much better agreement with the observed tensor parameters. The principal g values (Table I) are almost the same as those reported for very similar radicals HOĊH–COOH[4,17] and HOĊH–COO⁻.[15] The directions of the principal elements are very similar with respect to molecular skeleton in all of these radicals. The coupling parameters for radical A are slightly smaller than those for the HOĊH–COOH and HOĊH–COO⁻ radicals, but the relative magnitudes of the components are similar in all of these radicals. The orientation of the smallest value of the coupling, A_3, is ±39° from the a axis. If one supposes that the orientation of the radical in the crystal matrix is the same as the orientation of the undamaged molecule, this direction is exactly in the sp^2 hybrid orbital of carbon in the oxalate ion. That is, again, in accordance with the expectation for radical AI.

Slightly larger g values and smaller proton coupling components for radical species A as compared with the values for similar oxalate radicals[4,17,18] can be justified by the fact that in the present case both hydroxyl protons are missing. The tendency of increasing g values and decreasing coupling parameters with the removal of these protons can be noticed from the data reported by Atherton and Whiffen.[17,18]

The only problem with structure AI is the lack of an obvious way of its formation. At present we are unable to visualize any reasonable mechanism leading to structure AI. Similar reasons led Bales[3b] to assume that in some oxalates a structure of type AII rather than AI was present. In our case structure AII seems less probable. By assuming that serious reorientation of the $-COO^-$ group does not take place upon radical formation, for radicals AII one expects minimum proton coupling in the former C–C direction, *i.e.*, ±19° from the a axis, which is far from the observed direction. In addition, the stability observed for radical species A is strongly against the doubly charged structure AII. All the above considerations make us be-

(17) N. M. Atherton and D. H. Whiffen, *Mol. Phys.*, **3**, 1 (1960).
(18) N. M. Atherton and D. H. Whiffen, *ibid.*, **3**, 103 (1960).
(19) M. Kashiwagi, *J. Mol. Spectrosc.*, **20**, 190 (1966).

lieve that we deal with radical AI. The observation that these radicals are not detectable at low temperatures, but only at room temperature, may account for a rather complicated mechanism which must be involved in the radical formation.

Acknowledgments. We are grateful to Dr. B. Radak and Dr. I. Draganić for their interest during the progress of the work. We are also indebted to Dr. R. Herak and Mr. B. Prelesnik for checking the unit cell dimensions of our crystal.

The Electrode Reduction Kinetics of Carbon Dioxide in Aqueous Solution

by J. Ryu, T. N. Andersen, and H. Eyring*

Department of Chemistry, University of Utah, Salt Lake City, Utah 84112 *(Received December 8, 1971)*

Publication costs assisted by the National Institutes of Health, the National Science Foundation, and the Army Research Office–Durham

The electrolytic reduction of CO_2 in neutral, aqueous solution at a mercury pool cathode has been studied to establish the mechanism and to obtain the kinetic parameters by the steady-state galvanostatic method. The log current *vs.* potential curves show two Tafel regions of different slope which is indicative that different, *i.e.*, consecutive, steps are rate determining in the two regions. The most plausible steps considered are (1) $CO_2 + H_2O + e \rightleftarrows HCO_2\cdot(ads) + OH^-$ and (2) $HCO_2\cdot(ads) + e \rightarrow HCO_2^-$. Reaction orders with respect to the partial pressure of the CO_2 and the Tafel slopes are considered as the criteria for the proposed mechanism. The Langmuir and Temkin conditions for the adsorption of the reaction intermediate are considered and compared. The experimental results show that the Temkin condition is the more suitable and hence there is an appreciable change in the heat of adsorption with the surface coverage of the reaction intermediate.

Introduction

The cathodic reduction of carbon dioxide in an aqueous solution has been the subject of investigations by several authors.[1-13] Through the above works, the principal reaction product in aqueous solution has been found to be the formate ion. Although some of the previously published papers[10-13] have proposed mechanisms for the reaction, certain salient points have been overlooked and it is necessary to reconsider and clarify some aspects of the kinetics. Therefore we have proposed and formulated a mechanism, as was done in some previous papers,[10-13] but have more carefully considered the form of the rate equations in order to apply reaction order differentials as a criteria of our mechanism. In particular, the influence of the partial pressure of CO_2 on the pH and the reversible potential, and thus on the form of the rate equations, has been taken into account. Also the adsorption of the reaction intermediate and its influence on the rate equations have been more fully and explicitly investigated than had been previously. Finally, the effect of temperature on the rate has been studied.

Experimental Section

The details of the experimental setup can be found elsewhere.[14] An H-type cell was used which consisted of an anode and cathode compartment in a thermostated jacket. The cathode, which was separated by a glass frit from the anode, consisted of a pool of polarographic grade mercury of 2.98-cm diameter which was connected by a tube of Hg to a Pt wire lead located

(1) M. E. Royer, *C. R. Acad. Sci.*, **70**, 73 (1870).

(2) A. Cohen and S. Jahn, *Ber. Deut. Chem. Ges.*, **37**, 2836 (1904).

(3) R. Ehrenfeld, *ibid.*, **38**, 4138 (1905).

(4) F. Fisher and O. Prziza, *ibid.*, **47**, 256 (1914).

(5) M. Rabinowitsch and A. Maschowetz, *Z. Elektrochem.*, **36**, 846 (1930).

(6) T. E. Teeter and P. Van Rysselberghe, *J. Chem. Phys.*, **22**, 759 (1954).

(7) Proceedings of the Sixth Meeting of the International Committee on Electrochemical Thermodynamics and Kinetics, Butterworths, London, 1955, p 538.

(8) T. E. Teeter, Ph.D. dissertation, University of Oregon, Eugene, Ore., June 1954.

(9) M. Hong, Ph.D. dissertation, University of Utah, Salt Lake City, Aug 1969.

(10) W. Paik, T. N. Andersen, and H. Eyring, *Electrochim. Acta*, **14**, 1217 (1969); W. Paik, Ph.D. dissertation, University of Utah, Salt Lake City, Utah, Aug 1968.

(11) L. V. Haynes and D. T. Sawyer, *Anal. Chem.*, **39**, 332 (1967).

(12) J. L. Roberts, Jr., and D. T. Sawyer, *J. Electroanal. Chem.*, **9**, 1 (1965).

(13) J. Jordan and P. T. Smith, *Proc. Chem. Soc.*, 246 (1960); P. T. Smith and J. Jordan, "Polarography 1964, Proceedings of the Third International Congress," G. J. Hills, Ed., Macmillan, London, 1966, pp 407–418.

(14) J. Ryu, Ph.D. dissertation, University of Utah, Salt Lake City, Utah, June 1971.

above the solution level. The anode consisted of a Pt wire. The solution was stirred during the experiment. The potential of the cathode was measured with respect to a saturated calomel electrode (sce) at room temperature (25 ± 0.5°), which was separated from the cathode by a glass Luggin tube and capillary.

The electrolytes used were aqueous solutions of sodium bicarbonate and sodium formate prepared from water doubly distilled from a basic permanganate solution. Reagent grade nitrogen gas and commercial CO_2 were metered together, after purification, to give the desired composition. Purification consisted of passing them through a wash bottle containing an acidic solution of 0.1 *M* vanadous sulfate and amalgamated zinc granules and then through a presaturator which contained the electrolyte under investigation. The partial pressure of CO_2 was varied from 95.6 to 616 mm at a temperature of 30 ± 0.2°. The upper limit of the CO_2 pressure corresponded to only CO_2 in the bubbling gas and differed from atmospheric pressure (of about 645 mm) by the vapor pressure under the experimental conditions. For temperature variation, experiments were run at 0.2, 10, 20, 30, 40, 50, and 60° under a constant P_{CO_2} of 489 ± 4 mm.

The solution was pre-electrolyzed between a Hg pool cathode and Pt anodes at 10^{-4} A/cm² for about 24 hr under purified N_2 gas at room temperature. After pre-electrolysis, the used mercury was replaced for the kinetic measurements. The range of the current density studied was from 5×10^{-7} to about 10^{-3} A/cm². The current–potential relations were studied by the steady-state galvanostatic method with stirring. The stable potentials in the Tafel region did not change significantly (±2 mV) after waiting several hours.

The potentials were measured with a recorder hooked to an electrometer amplifier or with a potentiometer, and the currents were measured with meters accurate to within 2%. The pH of the solution was recorded following each experiment.

Results and Discussion

A. Proposed Mechanism. To postulate the reaction steps we consider previous studies on the subject in light of our own results.

The reduction of carbon dioxide in the neutral pH region has been found to give the formate ion as the principal product. The current efficiency for the formation of formate ions tends to decrease with increasing acidity of the solution because of the competition from hydrogen evolution.[9,10] The current efficiency also decreases at very high current densities because of amalgam formation.

Van Rysselberghe and coworkers[6,15] demonstrated that HCO_3^- and CO_3^{2-} ions are not reduced but that CO_2 must be present. Smith and Jordan[13] confirmed the above results and also showed that the electroreductive species is dissolved CO_2 rather than H_2CO_3

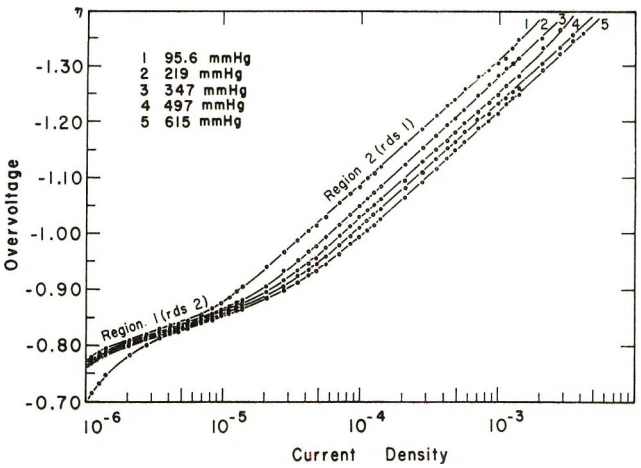

Figure 1. The log current–overvoltage polarization curves under various partial pressures of carbon dioxide at 30°: 1, 95.6 mm; 2, 219 mm; 3, 347 mm; 4, 497 mm; 5, 615 mm. Current density in amps cm^{-2}; η in volts.

(which either exists in solution or is formed by the rapid combination of CO_2 and H_2O prior to the charge transfer). These authors[13] also obtained polarographic diffusion currents which substantiated the idea that CO_2 molecules are the primary reactants rather than one of the hydrated CO_2 species, of which there are several in low concentration under the present conditions.[16-19]

The rate of CO_2 reduction is so slow that it can only be studied in the high overvoltage range. A revealing feature of this reaction on Hg in neutral aqueous media is the occurrence of two Tafel regions—one at lower current densities having a slope of approximately 91 mV and another at high current densities with a slope of approximately 224 mV at 30° (see Figure 1). These Tafel lines are independent of stirring. The diagnostic tests for the reaction products and the current efficiencies in the present work were carried out in the low current region (region 1), with 0.1 *M* $NaHCO_3$ solution at room temperature under 625 mm Hg of pure carbon dioxide. The resulting solutions gave positive results for the chromotropic acid test[20] and, hence, the reaction product was confirmed to be the formate ion. Titration of the solution with a permanganate solution showed that the current efficiency was 98% which is in good agreement with results of previous research.[10] The two Tafel lines with their relative respective slopes

(15) P. Van Rysselberghe, *J. Amer. Chem. Soc.*, 68, 2050 (1946).

(16) E. L. Quinn and C. L. Jones, "Carbon Dioxide," Reinhold, New York, N. Y., 1936.

(17) W. Heinpel and J. Seidel, *Ber.*, 31, 2997 (1898).

(18) P. Villard, *C. R. Acad. Sci.*, 119, 368 (1894); P. Villard, *Ann. Chim. Phys.*, 11, 355 (1879).

(19) R. M. Barrer and D. J. Ruzicka, *Trans. Faraday Soc.*, 58, 2239 (1962); R. M. Barrer and D. J. Ruzicka, *ibid.*, 58, 2253 (1962).

(20) F. Feigl, "Spot Test in Organic Analysis," 6th English ed, Eisenia, New York, N. Y., 1960, p 368.

lead us to believe that the reaction occurs in two consecutive steps, which we conclude are

$$CO_2 + H_2O + e^- \longrightarrow HCO_2\cdot(ads) + OH^- \quad (I)$$

$$HCO_2\cdot(ads) + e^- \longrightarrow HCO_2^- \quad (II)$$

The overall reaction is hence written as

$$CO_2 + H_2O + 2e \longrightarrow HCO_2^- + OH^- \quad (III)$$

In region 1 of the Tafel curves (Figure 1) step II is considered to be rate controlling while in region 2 step I is rate controlling. Several past studies[10,11,13] have also proposed an initial step which involves electron transfer. The present mechanism, however, suggests that water is involved in the initial step and that an adsorbed formate radical intermediate ($HCO_2\cdot(ads)$) is formed in this step. In support of water participating in the first step, it has been observed[11] that the chronopotentiograms and potentials for the reduction of CO_2 in dimethyl sulfoxide containing various concentrations of water change with the water content.

Previous work[10] has provided evidence for the existence of the reaction intermediate in region 1 from galvanostatic charging curves and from the difference exhibited by these curves in CO_2- and N_2-saturated solutions. The charge necessary to produce this intermediate was found to be 32 $\mu C/cm^2$. From spectroscopic data[21] the area of the adsorbed formate radical is calculated to be 11.3 $Å^2$.[14] Assuming close-packed coverage is present when $\theta = 1$, one calculates that the 32 $\mu C/cm^2$ corresponds to $\theta \simeq 0.23$. The open-circuit potential decay curves, which were measured in the present work (*cf.* Figure 2), are also consistent with this general range of values for θ. In this case if one considers reaction II to be the predominant means of desorbing the intermediate, then one obtains θ from the total charge passed by step II in changing the potential by the amount shown in Figure 2.

The remainder of this paper serves to substantiate and quantify the proposed mechanism. Equations are derived for the rate of reaction III under different conditions for the heat of adsorption of the intermediate, and the experimental results are compared with these formulations.

B. Langmuir Adsorption of Intermediate. 1. Rate Equations. If we apply absolute reaction rate theory[22] to the proposed mechanism and derive the standard electrochemical free energy of activation in the usual way,[23,24] rate equations 1–6 in Chart I are obtained (see ref 24 for the detailed derivations of similar equations). The notation in Chart I is as follows: α's are the transfer coefficients, κ's are the transmission coefficients and will be taken as equal to unity throughout this paper, η equals the overvoltage, a's are the activities; $\Delta G^{\pm}_1$ and $\Delta G^{\pm}_{-1}$ are the chemical part (non-voltage-dependent part) of the standard electrochemical free energies of activation for the forward and reverse process I while $\Delta G^{\pm}_2$ and $\Delta G^{\pm}_{-2}$ are those for reaction II; f represents the partial pressure of the CO_2 in the gas phase; θ is the surface coverage of the adsorbed reaction intermediate (the formate radical, $HCO_2\cdot(ads)$); R's are the rates for the appropriate reactions for which the specific rate constants are denoted by k° with the proper subscript; ϕ_2 is the potential of the outer Helmholtz plane, the position at which the reactants of step I are assumed to be located. The reaction order with respect to CO_2 is denoted by n. If the presently proposed mechanism is correct, n should equal one, but we leave it unspecified in the equations to be determined as a criterion of the mechanism. The reaction orders of the other species (OH^-, H_2O, HCO_2^-, and θ) in the steps 1, −1, and 2 are assumed to be equal to one, in accordance with the proposed mechanism. The present study does not specifically serve to determine such values. W is defined by

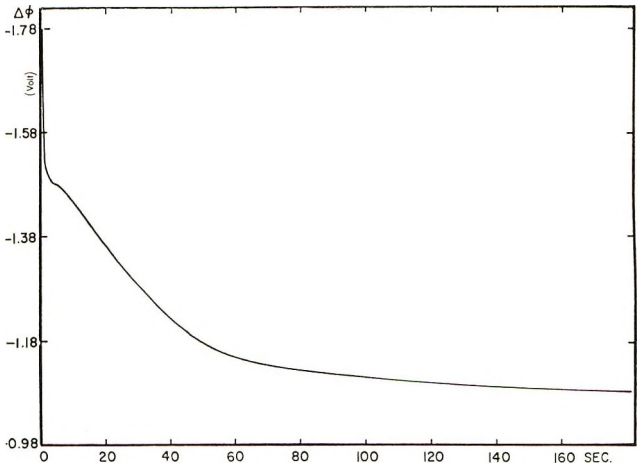

Figure 2. Open circuit potential decay curve at 30° and f_{CO_2} = 497 mm.

$$W = \frac{K_a K_b (K_w + a_{OH^-} K_c)}{0.02 K_c K_w \left[0.1 + \frac{K_w}{a_{OH^-}} - a_{OH^-} - \frac{0.02 K_c a_{OH^-}}{K_w + a_{OH^-} K_w}\right]} \quad (7)$$

where K_w is the ionization constant of water and the numbers 0.02 and 0.1 appear since our solution contained 0.02 M formate and 0.08 M bicarbonate. K_a, K_b, and K_c are the equilibrium constants for the following reactions: $CO_2(gas) + H_2O(l) \overset{K_a}{\rightleftarrows} H_2CO_3$ (in solution) $\overset{K_b}{\rightleftarrows} H^+ + HCO_3^-$ and $HCO_2H \overset{K_c}{\rightleftarrows} HCO_2^- + H^+$. $\Delta\phi_0$ is the inner potential difference between the elec-

(21) G. Herzberg, "Molecular Spectra and Molecular Structure," D. Van Nostrand, Princeton, N. J., 1966.

(22) S. Glasstone, K. J. Laidler, and H. Eyring, "Theory of Rate Processes," McGraw-Hill, New York, N. Y., 1940.

(23) P. Delahay, "Double Layer and Electrode Kinetics," Wiley, New York, N. Y., 1965.

(24) B. E. Conway, "Theory and Principles of Electrode Processes," Ronald Press, New York, N. Y., 1965.

Chart I: The Rate Equations for Reactions I and II under Langmuir Adsorption for the Intermediate

$$R_1 = k^\circ_1 \exp(-\alpha_1 F\eta/RT) \tag{1}$$

$$k^\circ_1 = \kappa_1 \frac{kT}{h} a_{H_2O} f^n (1-\theta)[W(a_{H_2O}f)^2/a_{OH^-}]^{-\alpha_1/2} \exp[-(\Delta G^{\pm}_1 - \alpha_1 F\phi_2 + \alpha_1 F\Delta\phi_0)/RT] \tag{2}$$

$$R_{-1} = k^\circ_{-1} \exp[(1-\alpha_1)F\eta/RT] \tag{3}$$

$$k^\circ_{-1} = \kappa_{-1} \frac{kT}{h} a_{OH^-}\theta[W(a_{H_2O}f)^2/a_{OH^-}]^{(1-\alpha_1)/2} \exp\{-[\Delta G^{\pm}_{-1} - (1-\alpha_1)F\Delta\phi_0 - \alpha_1 F\phi_2]/RT\} \tag{4}$$

$$R_2 = k^\circ_2 \exp(-\alpha_2 F\eta/RT) \tag{5}$$

$$k^\circ_2 = \kappa_2 \frac{kT}{h}\theta[W(a_{H_2O}f)^2/a_{OH^-}]^{-\alpha_2/2} \exp[-\Delta G^{\pm}_2 - \alpha_2 F\phi_2 + \alpha_2 F\Delta\phi_0/RT] \tag{6}$$

Table I: The Standard Reversible Potential of Reaction III Compared to the Standard Hydrogen Electrode at Several Temperatures

Temp, °C	2	10	20	25	30	40	50	60
Rev. potential (E°_h)	−0.699	−0.708	−0.718	−0.723	−0.728	−0.739	−0.750	−0.760

trode and solution at standard state. The other symbols in Chart I have their usual meanings.

The overvoltage is defined by $\eta = E_h - E_h^r$ where E_h is the potential of the working electrode and E_h^r is the reversible or Nernst potential with respect to the standard hydrogen electrode. The reversible potential of the Hg electrode can be written in the form

$$E_h^r = E^\circ_h - \frac{RT}{2F} \ln\left(\frac{a_{OH^-}a_{HCO_2^-}}{f a_{H_2O}}\right) \tag{8}$$

The reaction is too slow for E_h^r to be measured directly, but the values of E°_h (eq 8) at various temperatures were computed from thermodynamic data[25] and are tabulated in Table I. The rates for R_{-2} are not formulated as there was no indication that HCO_2^- ions influenced the overall rate.

2. Reaction Orders Using Langmuir Adsorption Condition. a. Reaction I as the Rate-Determining Step. At high overvoltage the net current density is given by

$$i = 2i_{1,c} \simeq 2i_{0,1} \exp(-\alpha_1 F\eta/RT) \tag{9}$$

where $i_{0,1}$ is the exchange current density for reaction I which is given by $i_{0,1} = Fk^\circ_1$. From Figure 1 log $i_{0,1} = -8.81$ at $f = 497$ mm and $T = 30°$; $\alpha_1 = 0.27$ independent of f at 30°.

From eq 9 with the aid of eq 1 and 2 in Chart I we can derive the reaction order differentials in the forms

$$\left(\frac{\partial\eta}{\partial \ln f}\right)_{T,i_{1,c}} = \frac{RT}{\alpha_1 F}\left(n - \alpha_1 + \frac{\alpha_1}{2}\frac{d \ln a_{OH^-}}{d \ln f} - \frac{\alpha_1}{2}\frac{d \ln W}{d \ln f}\right) \tag{10a}$$

$$\left(\frac{\partial \ln i_{0,1}}{\partial \ln f}\right)_T = \left(\frac{d\eta}{d \ln f}\right)_{T,i_{1,c}}\left(\frac{\alpha_1 F}{RT}\right) \tag{10b}$$

$$\left(\frac{\partial E}{\partial \ln f}\right)_{T,i_{1,c}} = \frac{nRT}{\alpha_1 F} \tag{11}$$

by assuming that $\theta \ll 1$, where E is the electrode potential with respect to a constant reference electrode (*e.g.*, sce). The value of d ln a_{OH^-}/d ln f was obtained experimentally and found to be −0.69 (*cf.* ref 14). The term d ln W/d ln f (= −1.12) was obtained from W (eq 7) and d ln a_{OH^-}/d ln f. The plots made of η and ln $i_{0,1}$ *vs.* ln f, using the data of Figure 1, region 2, are linear (*cf.* 14) and yield values which are listed in Table II. The plot of E *vs.* ln f is linear and gives a value of $n = 0.82$ (using the data at $i \simeq 10^{-4}$ cm^{-2}). It is clear that the results are in close harmony with those anticipated for $n = 1$ and hence with reaction I which is first order with respect to CO_2.

b. Reaction II as the Rate-Determining Step. i. Quasiequilibrium Condition for Reaction I. At high overvoltage the net cathodic current is expressed by

$$i = 2FR_{c,2} = 2i_{c,2} \simeq 2i_{0,2} \exp(-\alpha_2 F\eta/RT) \tag{12}$$

The term $i_{0,2}$ is the exchange current density of reaction II and is found from the extrapolation of the Tafel line in Figure 1 to be $10^{-13.8}$ at 30° and 616 mm. $\alpha_2 = 0.66 \pm 0.1$ independent of f at 30°. From $R_1 = R_{-1}$ we obtain θ, which increases as the overvoltage increases cathodically. If θ is substituted into eq 6, the resulting rate expression for reaction II is rather complex. Therefore the two limiting cases in which $\theta \to 0$ and $\theta \to 1$ will be considered.

For $\theta/(1-\theta) \simeq \theta$ we obtain at high overvoltages

(25) W. M. Latimer, "The Oxidation State of the Elements and Their Potential in Aqueous Solutions," Prentice-Hall, Englewood Cliffs, N. J., 1938.

Table II: The Tafel Slope and Reaction Order Differentials Calculated for Different Conditions (Top) and Observed from the Experimental Data of Figure 1 (Bottom)

Conditions	Tafel slope	$(\partial\eta/\partial \ln f)_{T,i_1}$, mV	$(\partial \ln i_0/\partial \ln f)_T$
	Calculated		
Reaction I as rds[a]	$2.3RT/\alpha_1F$	76 ($n = 1$)	0.79 ($n = 1$)
Reaction II as rds			
Langmuir absorption			
Step I, quasiequilibrium			
$\theta \to 0$	$2.3RT/(1 + \alpha_2)F$	44	1.16
$\theta \to 1$	$2.3RT/\alpha_2F$	−21	−0.53
Steps I and II, steady-state			
$\theta \to 1$	$2.3RT/\alpha_2F$	−21	−0.53
$\theta \to D_1/D_2$ ($\to 0$)	$2.3RT/\alpha_1F$	77	0.79
Temkin adsorption (activated)			
Step I, quasiequilibrium	$2.3RT/2\alpha_2F$	2	0.04
	Observed		
Reaction I as rds	$2.3RT/(0.27F)$	50[b] ($n = 0.80$)	0.65 ($n = 0.86$)
Reaction II as rds	$2.3RT/(0.66F)$	7[c]	0.39

[a] rds = rate-determining step. [b] $i = 10^{-4}$ A cm^{-2}. [c] $i = 5 \times 10^{-6}$ A cm^{-2}.

$$i_{c,2} = F\frac{kT}{h}\left[\frac{1}{(a_{H_2O}f)^{\alpha_2}a_{OH^-}{}^{(1-\alpha_2)/2}W^{(1+\alpha_2)/2}}\right] \times \exp\left[\frac{\Delta G^{\ddagger}{}_2 + \Delta g - \alpha_2F(\phi_2 - \Delta\phi_0) + F\Delta\phi_0}{RT}\right] \times \exp\left[-\frac{(1 + \alpha_2)F\eta}{RT}\right] \quad (13)$$

where $(\Delta G^{\ddagger}{}_1 - \Delta G^{\ddagger}{}_{-1})$ is replaced by g, the free energy change of reaction I. From eq 13 we obtain the reaction order differential in the form

$$\left(\frac{\partial\eta}{\partial \ln f}\right)_{T,i_{c,2}} = \frac{-RT}{(1 + \alpha_2)F} \times \left[\alpha_2 + \frac{(1 - \alpha_2)}{2}\frac{d \ln a_{OH^-}}{d \ln f} + \frac{(1 + \alpha_2)}{2}\frac{d \ln W}{d \ln f}\right] \quad (14)$$

and

$$\left(\frac{\partial \ln i_{0,2}}{\partial \ln f}\right)_T = -\left[\alpha_2 + \frac{(1 - \alpha_2)}{2}\frac{d \ln a_{OH^-}}{d \ln f} + \frac{(1 + \alpha_2)}{2}\frac{d \ln W}{d \ln f}\right] \quad (15)$$

where we assume that $d\phi_2/d \ln f \simeq 0$. Using the experimental values of α_2, $d \ln a_{OH^-}/d \ln f$, and $d \ln W/d \ln f$, we calculate values for eq 14 and 15 of 44 mV and 1.16, respectively, which are compared to the experimental values in Table II.

When θ approaches unity, the net cathodic current is given from eq 5 and 6 by

$$i_{c,2} = F\frac{kT}{h}\left[\frac{W(a_{H_2O}f)^2}{a_{OH^-}}\right]^{-\alpha_2/2} \times \exp\left(-\frac{\Delta G^{\ddagger}{}_2 - \alpha_2F(\phi_2 - \Delta\phi_0)}{RT}\right)\exp\left(-\frac{\alpha_2F\eta}{RT}\right) \quad (16)$$

The reaction order differentials are then given by

$$\left(\frac{\partial\eta}{\partial \ln f}\right)_{T,i_{c,2}} = -\frac{RT}{2F}\left(2 + \frac{d \ln W}{d \ln f} - \frac{d \ln a_{OH^-}}{d \ln f}\right) \quad (17)$$

and

$$\left(\frac{\partial \ln i_{0,2}}{\partial \ln f}\right)_T = -\frac{\alpha_2}{2}\left(2 + \frac{d \ln W}{d \ln f} - \frac{d \ln a_{OH^-}}{d \ln f}\right) \quad (18)$$

assuming that $(d\phi_2/d \ln f)_T \simeq 0$. The calculation using the experimental data gives a value of −21 mV and −0.53 for $(d\eta/d \ln f)_{T,i_{c,2}}$ and $(d \ln i_{0,2}/d \ln f)_T$, respectively (*cf.* Table II).

From Table II one can see for $\theta \to 0$ that the values of the reaction order differentials are larger than the experimental values and that α_2 is less than zero which is incompatible with its definition. For $\theta \to 1$ α_2 is positive (0.68), but the reaction order differentials assume negative values which are unreasonable. Therefore, neither of the two conditions gives satisfactory results, but it appears that the reaction system may be located between $\theta \to 0$ and $\theta \to 1$.

ii. Steady-State Condition for the Intermediate. Under this circumstance we assume that

$$\frac{d\theta}{dt} = R_1 - R_{-1} - R_2 \simeq 0 \quad (19)$$

Also $i = 2i_{c,2}$. From eq 1–6 and 19 we obtain

$$\theta = \frac{D_1}{D_1 + D_{-1} + D_2} \quad (20)$$

where

Chart II: Rate Equations for Reactions I and II under General Temkin Condition for Activated Adsorption[a]

$$R_1 = \kappa_1 \frac{\bar{k}T}{h} a_{H_2O} f(1-\theta)\left[\frac{W(a_{H_2O}f)^2}{a_{OH^-}}\right]^{-\alpha_1/2} \exp\left[-\frac{\Delta G^{\ddagger}_1 + \alpha_1 F(\Delta\phi_0 - \phi_2)}{RT}\right] \exp\left[-\frac{\alpha_1 F\eta}{RT}\right] \exp[-\gamma g(\theta)] \quad (24)$$

$$R_{-1} = \kappa_{-1} \frac{\bar{k}T}{h} a_{OH^-}\theta\left[\frac{W(a_{H_2O}f)^2}{a_{OH^-}}\right]^{(1-\alpha_1)/2} \exp\left[-\frac{\Delta G^{\ddagger}_{-1} - (1-\alpha_1)F\Delta\phi_0 - (1+\alpha_1)F\phi_2}{RT}\right] \exp\left[\frac{(1-\alpha_1)F\eta}{RT}\right] \exp[(1-\gamma)g(\theta)] \quad (25)$$

$$R_2 = \kappa_2 \frac{\bar{k}T}{h} \theta\left[\frac{W(a_{H_2O}f)^2}{a_{OH^-}}\right]^{-\alpha_2/2} \exp\left[-\frac{\Delta G^{\ddagger}_2 + \alpha_2 F(\Delta\phi_0 - \phi_2)}{RT}\right] \exp\left[-\frac{\alpha_2 F\eta}{RT}\right] \exp[(1-\gamma)g(\theta)] \quad (26)$$

[a] $\gamma \simeq \alpha_1$ for reaction I and $\gamma \simeq 1 - \alpha_2$ for reaction II (see ref 14).

$$D_1 = R_1/(1-\theta);\ D_{-1} = R_{-1}/\theta;\ D_2 = R_2/\theta \quad (21)$$

If we substitute θ from eq 20 into i, the resulting equation is still somewhat complex. Therefore the two extreme cases will be considered.

iia. Case 1, $D_1 \gg D_{-1}, D_2$. In this case it is clear from eq 20 that $\theta \simeq 1$ and $i_{c,2}$ is equivalent to eq 16. This result gives the reaction order differentials equivalent to those in the case of the quasiequilibrium condition for $\theta \to 1$ (eq 17 and 18).

iib. Case 2, $D_2 \gg D_1$, D_{-1} or $\theta = D_1/D_2 \to 0$. Taking $i = 2i_{c,2}$, we obtain for the reaction order differentials

$$\left(\frac{\partial\eta}{\partial \ln f}\right)_{T,i_{c,2}} = \frac{RT}{\alpha_1 F}\left(1 - \frac{\alpha_1}{2}\frac{\mathrm{d}\ln W}{\mathrm{d}\ln f} + 2 - \frac{\mathrm{d}\ln a_{OH^-}}{\mathrm{d}\ln f}\right) \quad (22)$$

and

$$\left(\frac{\partial \ln i_{0,2}}{\partial \ln f}\right)_T = 1 - \frac{\alpha_1}{2}\left(\frac{\mathrm{d}\ln W}{\mathrm{d}\ln f} + 2 - \frac{\mathrm{d}\ln a_{OH^-}}{\mathrm{d}\ln f}\right) \quad (23)$$

The calculated results for eq 22 and 23 are tabulated in Table II as are those for the case of $D_1 \gg D_{-1}, D_2$. From these results we anticipate that the surface coverage, θ, is in the intermediate range. As we treat this condition with the Temkin isotherm in the following section, we shall not attempt to go into more detail with the Langmuir adsorption, steady-state treatment.

C. Temkin Adsorption of the Intermediate. The results of the previous sections indicate that the surface coverage, θ, by the reaction intermediate falls into the intermediate range. In this case the heat of adsorption may change with θ. We will here consider the general Temkin condition[26] for activated adsorption[22,26,27] and nonactivated adsorption.[26]

1. Rate Equations for Activated Adsorption. If there is a change of standard free energy of activation with a change in θ, the rate equations for the proposed mechanism can be derived in the forms which are tabulated in Chart II (see ref 24 for a detailed derivation of analogous equations for a different system). The term $g(\theta)$ which appears in Chart II is defined in eq 27 as

$$g(\theta) = \frac{1}{RT}\frac{\mathrm{d}(\overline{\Delta G^\circ}_\theta)}{\mathrm{d}\theta} \quad (27)$$

Here $\overline{\Delta G^\circ}_\theta$ is the standard free energy of adsorption at surface coverage (θ); γ is the proportionality factor between the change of activation energy and the change of coverage ($0 < \gamma < 1$).

2. Reaction Order for Activated Adsorption. a. Reaction I as the Rate-Determining Step. If reaction 1 is rate controlling, $\theta \simeq 0$; hence, the last terms involving $g(\theta)$ in eq 24 and 25 are approximately equal to unity. Then the resulting equations are identical with those obtained from the Langmuir condition (*cf.* eq 10 and 11).

b. Reaction II as the Rate-Determining Step: Quasiequilibrium Condition for Reaction I. By considering θ to be in the intermediate range we can neglect the changes in $1 - \theta$ and in θ compared to those in the exponents containing $g(\theta)$. Then, by solving for $g(\theta)$ from eq 24 and 25 and substituting this function into eq 26, we obtain

$$R_2 = \frac{\bar{k}T}{h}\left(\frac{1}{a_{H_2O}fW}\right)^{\alpha_2} \times \exp\left[-\frac{\Delta G^{\ddagger}_2 + \alpha_2\Delta g + \alpha_2 F(\Delta\phi_0 - \phi_2)}{RT}\right] \times \exp\left(-\frac{2\alpha_2 F\eta}{RT}\right) \quad (28)$$

The experimental value of the Tafel slope (91 mV) gives a value for α_2 of 0.34. From eq 28 we obtain the reaction order differentials

$$\left(\frac{\partial\eta}{\partial \ln f}\right)_{T,i_{c,2}} = -\frac{RT}{2F}\left(1 + \frac{\mathrm{d}\ln W}{\mathrm{d}\ln f}\right) \quad (29)$$

and

$$\left(\frac{\partial \ln i_{0,2}}{\partial \ln f}\right)_T = -\alpha_2\left(1 + \frac{\mathrm{d}\ln W}{\mathrm{d}\ln f}\right) \quad (30)$$

The calculated values from experimental data are compared with the observed values in Table II. Although

(26) E. Gileadi and B. E. Conway, "Modern Aspects of Electrochemistry," Vol, 3, J. O'M Bockris and B. E. Conway, Ed., Butterworths, Washington, D. C., 1964.

(27) A. F. H. Ward, *Trans. Faraday Soc.*, **28**, 399 (1932).

the calculated values are somewhat smaller than the observed values, they do predict that the reaction rate is nearly independent of the partial pressure of CO_2 which is borne out experimentally by Figure 1. Hence, the experimental results can be explained with the derived rate equations without some of the qualifications which were necessary with the Langmuir adsorption condition.

c. Reaction II as the Rate-Determining Step: Steady-State Condition for the Intermediate. From the steady-state condition, $d\theta/dt = R_1 - R_{-1} - R_2 \simeq 0$, and with the assumption of $R_{-1} \ll R_1$ and R_2, $g(\theta)$ may readily be obtained. When this function is substituted into eq 26, we obtain the net cathodic current density in the form

$$\frac{i}{2} = i_{c,2} = F\frac{\bar{k}T}{h}(a_{H_2O}f)^{\alpha_2/(\alpha_1+\alpha_2)} \times \left(\frac{W(a_{H_2O}f)^2}{a_{OH^-}}\right)^{-\alpha_1\alpha_2/(\alpha_1+\alpha_2)} \times \exp\left(-\frac{\alpha_2\Delta G^{\ddagger}_1 + \alpha_1\Delta G^{\ddagger}_2}{RT}\right) \times \exp\left[-\left(\frac{2\alpha_1\alpha_2}{\alpha_1+\alpha_2}\right)\frac{F(\Delta\phi^{\circ}_0 - \phi_2)}{RT}\right] \times \exp\left[-\left(\frac{2\alpha_1\alpha_2}{\alpha_1+\alpha_2}\right)\frac{F\eta}{RT}\right] \quad (31)$$

at high overvoltage. This equation gives $2.3RT/(2\alpha_1\alpha_2/(\alpha_1 + \alpha_2))F$ as the Tafel slope; the observed value is about 91 mV. If we use the value of 0.29 for α_1 (from the Tafel slope of region 2) and then calculate α_2 from eq 31, the value of α_2 turns out to be a negative number. This is in contradiction with the definition of α_2. Therefore, we consider that the steady-state approximation is not suitable for the reaction system using our model.

3. Nonactivated Adsorption of the Reaction Intermediate. R_2 can be written in the form

$$R_2 = \kappa_2\frac{\bar{k}T}{h}\exp\left[-\frac{\Delta G^{\ddagger}_2 + \alpha_2F(\Delta\phi^{\circ}_h - \phi_2)}{RT}\right] \times \exp\left(-\frac{\alpha_2F\eta}{RT}\right)\exp[g(\theta)] \quad (32)$$

(see ref 14 for the detailed derivation of eq 32). Under the quasiequilibrium condition we have

$$i_{c,2} = \alpha_2F\frac{\bar{k}T}{h}\left[\frac{W(a_{H_2O}f)^2}{a_{OH^-}}\right]^{-\alpha_2/2}\frac{1}{(Wa_{OH^-})^{1/2}} \times \exp\left(-\frac{\Delta G^{\ddagger}_2 + \Delta g}{RT}\right) \times \exp\left[-\frac{(1+\alpha_2)F\Delta\phi^{\circ}_0 - \alpha_2F\phi_2}{RT}\right] \times \exp\left[-\frac{(1+\alpha_2)F\eta}{RT}\right] \quad (33)$$

This gives a Tafel slope of $2.3RT/(1 + \alpha_2)F$. The calculation with the experimental Tafel slope gives a negative value for α_2 which is in contradiction with the definition of α_2.

If we substitute $g(\theta)$ for the steady-state condition into eq 32, the formula for the net cathodic current density ($i_{c,2}$) involves α_1 but not α_2 in the overvoltage term. Because this is incompatible with the assumption that R_2 is rate determining, we may disregard the steady-state approximation. Hence the cases of nonactivated adsorption of the intermediate appear untenable.

D. The Effect on Rate of Temperature. 1. Reaction I as the Rate-Determining Step. In this circumstance $\theta \simeq 0$ for i for either the Langmuir or Temkin condition is virtually the same. Thus, from eq 1 and 2 or from eq 24 we write

$$\ln i_{1,c} = \ln B_1 - \frac{\Delta H^{\ddagger}_1 + \alpha_1F\Delta\phi^{\circ}_0}{RT} - \frac{\alpha_1F\eta}{RT} \quad (34)$$

where

$$B_1 = F\frac{\bar{k}T}{h}\frac{(a_{H_2O}f)^{1-\alpha_1}a_{OH^-}{}^{\alpha_1/2}}{W^{\alpha_1/2}}\exp\left(\frac{\alpha_1F\phi_2 + T\Delta S^{\ddagger}_1}{RT}\right) \quad (35)$$

and where $\Delta H^{\ddagger}_1$ and $\Delta S^{\ddagger}_1$ are the heat and entropy of activation, respectively, for reaction I at zero field strength across the double layer. If we neglect the temperature effect on the B_1 term and on α_1, we obtain

$$\left(\frac{\partial \ln i_{0,1}}{\partial(1/T)}\right)_f = -\frac{\Delta H^{\ddagger}_1}{R} - \frac{\alpha_1F}{R}\frac{d(\Delta\phi_0/T)}{d(1/T)} = -\frac{\Delta H^{\ddagger}_1}{R} + \frac{\alpha_1}{2R}\Delta H_0 \quad (36)$$

Here ΔH_0 is the standard enthalpy of reaction III. Equation 36 has been derived and discussed previously[24,28,29] and, because ΔH_0 is unknown (*i.e.*, only the difference between ΔH_0 and the corresponding heat for the standard hydrogen electrode is calculable), one can go no further than to obtain $[\partial \ln i_{0,1}/\partial(1/T)]_f$ or $\Delta H^{\ddagger}_1 - \alpha\Delta H_0/2$ which is termed "the apparent heat of activation."[24,29] The values of $i_{0,1}$ at various temperatures were obtained by extrapolating the Tafel lines of Figure 3 to zero overpotential. The plot of $\ln i_{0,1}$ *vs.* $1/T$ is essentially linear (*cf.* ref 14) and yields a value for $\Delta H^{\ddagger}_1 - \alpha_1\Delta H_0/2$ of 18.8 kcal/mol.

2. Reaction II as the Rate-Determining Step. Because the experimental findings are best described by the condition in which the intermediate obeys the Temkin isotherm with activated adsorption, and in which reaction I is in quasiequilibrium, we shall only consider this case. The net current is then given by $2FR_2$ where

(28) J. H. Baxendale, Comment on Randels' paper, *Discuss. Faraday Soc.*, **No. 1**, 46 (1947).

(29) M. I. Temkin, *Zh. Fiz. Khim.*, **22**, 1081 (1948).

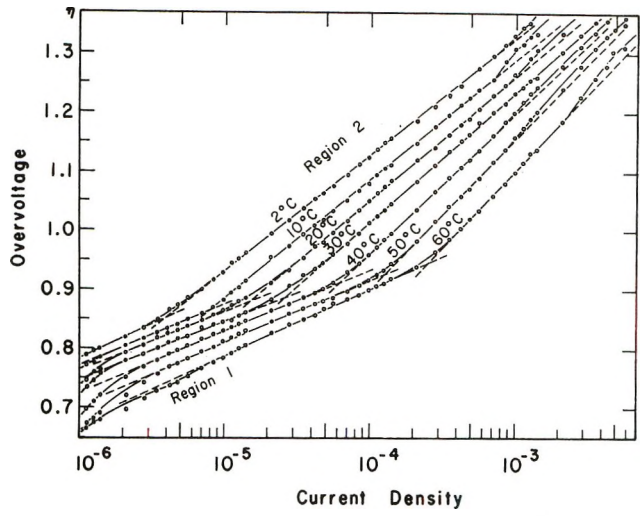

Figure 3. The log current–overvoltage polarization curves at various temperatures under a constant partial pressure (497 mm) of CO_2. Current density in amps cm^{-2}; η in volts.

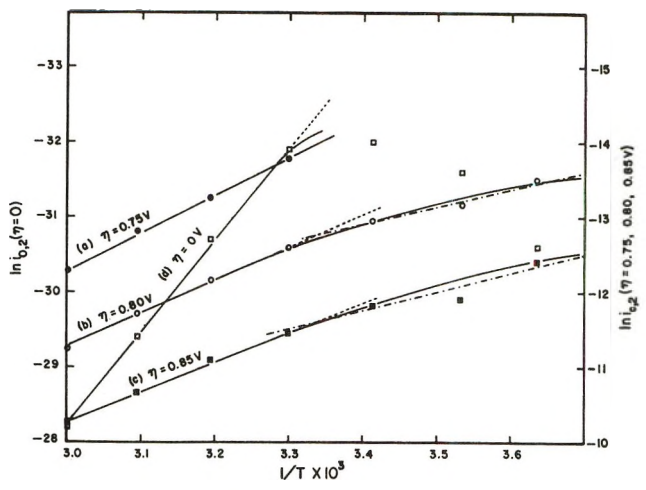

Figure 4. The temperature dependence of $i_{0,2}$ and $i_{c,2}$ at various overpotentials.

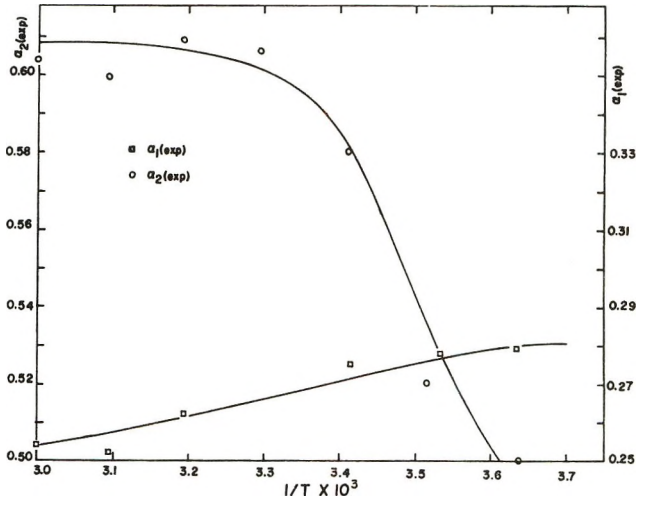

Figure 5. The dependence of the experimental transfer coefficients (α) on the reciprocal of the absolute temperature.

R_2 is given by eq 28. If we neglect the temperature dependence of the pre-exponential terms in eq 28 as well as that of Δg, α_2, $\Delta S^{\ddagger}_2$ and ϕ_2/T, we obtain

$$\left[\frac{\partial \ln i_{0,2}}{\partial(1/T)}\right]_f = -\frac{\Delta H^{\ddagger}_2}{R} + \frac{\alpha_2}{2R}\Delta H_0 \qquad (37)$$

analogous to the case of eq 36. The plot of ln $i_{0,2}$ *vs.* $1/T$ obtained from extrapolating the lower Tafel lines of Figure 3 to zero overvoltage is shown in Figure 4. Also shown is the plot of ln $i_{c,2}$ *vs.* $1/T$ at constant overvoltage values of 0.75, 0.80, and 0.85 V. Not only do the apparent heats of activation decrease with a decrease in temperature, but the difference in these apparent heats for $\eta = 0$ and $\eta = 0.75$–0.85 V changes markedly with temperature. Some decrease in $\partial \ln i_0/\partial(1/T)$ with a decrease in temperature is understandable due to our neglecting the temperature dependence of such terms as T in the pre-exponential of i and ϕ_2/T in the exponential. However, the sharp effect of η on $\partial \ln i_{0,2}/\partial \ln (1/T)$ (which makes this term appear to change sign as the temperature is decreased) is believed to be due to the variation of the experimentally determined transfer coefficient with temperature. Thus the experimental value of the apparent heat of activation (for either reaction I or II) at zero overvoltage is related to that value at some fixed overvoltage η by

$$\left[\frac{\partial \ln i_0}{\partial(1/T)}\right]_{\text{exptl}} = \left[\frac{\partial \ln i}{\partial(1/T)}\right]_{\eta} + \frac{\alpha_{\text{exptl}} F\eta}{R} + \frac{F\eta}{RT}\frac{d\alpha_{\text{exptl}}}{d(1/T)} \qquad (38)$$

It is apparent that a variation in $d\alpha_2/d(1/T)$ with temperature can account for the great difference in the curves at $\eta = 0$ and $\eta = 0.75$–0.85 V in Figure 4. In Figure 5 are shown the variations of the experimental transfer coefficients with temperature for steps I and II. These were obtained by applying eq 39 to the appropriate Tafel line of Figure 3.

$$\alpha_{i(\text{exptl})} = \frac{RT}{F}\frac{\partial \ln i_{i,c}}{\partial \eta} \qquad (39)$$

It is observed that the experimentally determined α_1 and α_2 both vary with $1/T$ and that this rate of variation for α_2 changes with temperature in such a way as to cause $\partial \ln i_{0,2}/\partial(1/T)$ to vary with temperature as noted in Figure 4.

Variations of the experimental transfer coefficient or symmetry factor with temperature have been observed and discussed for some other reactions (*cf.*, *e.g.*, ref 30). [From the derivation of the rate equations in this paper it is apparent that the transfer coefficients, α_1 and α_2, have the same meaning as the symmetry factor β in some other works such as ref 30.] Variations in α_1 and/or α_2 with temperature may occur if

the position of the activated state compared to that of the initial state in the field of the double layer changes with temperature. This may occur if the thickness of the double layer, the relative orientation of water dipoles on the Hg surface, or the amount of specific adsorption of ions changes with temperature. While there is not likely to be anion specific adsorption in the present case, cation specific adsorption may play a role as evidenced from the different Tafel slopes for solutions containing Li^+, Na^+, and tetraethylammonium ions.[10] Furthermore, the differences in the Tafel slopes for these various cations are more pronounced in region 2, *i.e.*, at more negative cathode potentials. Conway, *et al.*,[30] also point out that the experimental transfer coefficient may vary with temperature if $\Delta S^{\pm}$ varies with potential, due to effects of the field on the solvent structure associated with the reactant. As reaction II involves an adsorbed intermediate, effects of T on θ may also influence the temperature coefficient of the reaction rate in such a way that the experimental value of α_2 in eq 28 appears to vary with temperature (*cf.* ref 30). Equation 28 is an approximation for intermediate fractional surface coverage (θ) but the exact expression for R_2 includes θ-containing terms.

Although possible reasons for a variation in the α's with temperature have been listed, the present work does not identify which factors are controlling in the cases of α_1 and α_2. However, these reasons do not directly bear upon the main thrust of this work—to investigate the pathway and kinetics of reaction III.

E. Conclusions. Previous work has identified the mechanism of the electroreduction of CO_2 on mercury as consisting of two consecutive charge-transfer steps. The reactant species have been identified as CO_2 molecules and water on the electrode. In the potential region for which the second step is rate determining an adsorbed intermediate has been detected on the mercury surface. In the present work the cathodic Tafel curves as well as the effect of the partial pressure of CO_2 on them have been analyzed. From this analysis the form of the rate equations for the consecutive steps have been detailed such as to include the adsorption characteristics of the intermediate. The observed Tafel slope and reaction order differentials with respect to P_{CO_2} are best rationalized by assuming that the intermediate undergoes activated adsorption according to the Temkin isotherm.

Acknowledgment. The authors wish to thank the National Institutes of Health, Grant GP 12862, National Science Foundation, Grant GP 28631, and the Army Research Office—Durham, Contract DA-ARO-D-31-124-72-G15, for support of this work.

(30) B. E. Conway, D. J. MacKinnon, and B. V. Tilak, *Trans. Faraday Soc.*, **66**, 1203 (1970).

Conductivity Relaxation in a Concentrated Aqueous Electrolyte Solution

by J. H. Ambrus,

Naval Ordnance Laboratory, White Oak, Silver Spring, Maryland 20910

C. T. Moynihan,* and P. B. Macedo

Vitreous State Laboratory, Catholic University of America, Washington, D. C. 20017 *(Received November 16, 1970)*

Publication costs assisted by the Office of Naval Research

Capacitance and conductance measurements were made in a highly concentrated aqueous $Ca(NO_3)_2$ solution (6.15 water:salt ratio, 9.03 m) as a function of frequency and temperature. The frequency range covered was 1–1 × 10^6 Hz; the temperature range was from −91.5 to −61.9°. The data were analyzed in terms of the electric modulus, M (= $1/\epsilon$, where ϵ is the complex permittivity). The frequency dependence of the electric modulus shows the presence of more than one relaxation. The relaxation process observed at the lowest frequencies has been identified with the conductance process involved in long-range charge transport and has been analyzed in terms of a log Gaussian distribution of relaxation times. The sources of the low-strength relaxation process observed at higher frequencies cannot be unambiguously identified, but may be water molecule reorientation or localized ion-jumping mechanisms.

Introduction

Previous studies of electric relaxation in aqueous electrolyte solutions have been confined to the high-fluidity region in the vicinity of room temperature. These include investigations of the relaxation of the ionic atmosphere in dilute solution (Debye–Falkenhagen effect),[1] the dielectric relaxation of the polar water molecules,[2,3] and dispersion effects connected with ionic association reactions.[3] In addition, it has been pointed out recently[4,5] that electric relaxation effects associated with the long-range ionic diffusion process may lead to an observable frequency dispersion in the dielectric constant and loss. As an initial effort in an investigation of electric relaxation in aqueous electrolytes at low temperatures and low fluidities, we report below the results of a study of a glass-forming[6] concentrated solution of calcium nitrate in water. We begin, however, with a summary of the phenomenology of the frequency dependence of admittance in ionic conductors.

Conductivity Relaxation

The complex permittivity, ϵ, of a system is defined

$$\epsilon = \epsilon' - i\epsilon'' = \epsilon' - i(\sigma/\omega e_0) \qquad (1)$$

where ω is the angular frequency, ϵ' the relative permittivity or dielectric constant, ϵ'' the dielectric loss, σ the specific conductance, and e_0 the permittivity of free space (8.854 × 10^{-14} F cm^{-1}). An alternative parameter of considerable utility in the analysis of electrical relaxation phenomena in conducting materials has been termed[4] the *electric modulus*, M.

$$M \equiv \frac{1}{\epsilon} = \frac{\epsilon'}{\epsilon'^2 + \epsilon''^2} + \frac{i\epsilon''}{\epsilon'^2 + \epsilon''^2} = M' + iM'' \qquad (2)$$

The electric modulus, M, and the complex permittivity, ϵ, bear the same relationship to one another as do the modulus and the compliance in mechanical relaxation experiments.

The simplest representation of the equivalent circuit of an ionic conductor is a simple parallel conductance and capacitance combination that exhibits a frequency independent conductivity, σ_0, and relative permittivity, ϵ_s. A characteristic time may be written for this system

$$\tau_\sigma = e_0\epsilon_s/\sigma_0 \qquad (3)$$

τ_σ has been termed the *conductivity relaxation time*[4] and characterizes the decay of the electric field E in the conductor to zero under the constraint of constant displacement vector *via* the dc conductance process

$$E = E_0 \exp(-t/\tau_\sigma) \qquad (4)$$

From eq 1–3, the electric modulus may then be shown to be[4]

$$M = M_s\left(\frac{i\omega\tau_\sigma}{1 + i\omega\tau_\sigma}\right) = M_s\left[\frac{(\omega\tau_\sigma)^2}{1 + (\omega\tau_\sigma)^2}\right] + iM_s\left[\frac{\omega\tau_\sigma}{1 + (\omega\tau_\sigma)^2}\right] \qquad (5)$$

(1) H. Falkenhagen, "Electrolytes," Clarendon Press, Oxford, 1934, p 182 ff.

(2) (a) J. B. Hasted, D. M. Ritson, and C. H. Collie, *J. Chem. Phys.*, **16**, 1 (1948); (b) G. H. Haggis, J. B. Hasted, and T. J. Buchanan, *ibid.*, **20**, 1452 (1952); (c) F. A. Harris and C. T. O'Konski, *J. Phys. Chem.*, **61**, 310 (1957).

(3) (a) R. Pottel, *Ber. Bunsenges. Phys. Chem.*, **71**, 135 (1967); (b) R. Pottel, "Chemical Physics of Ionic Solutions," B. E. Conway and R. G. Barradas, Ed., Wiley, New York, N. Y., 1966, pp 581–589; (c) R. Pottel, *Ber. Bunsenges. Phys. Chem.*, **69**, 363 (1965); (d) K. Geise, U. Kaatze, and R. Pottel, *J. Phys. Chem.*, **74**, 3718 (1970).

(4) V. Provenzano, L. P. Boesch, V. Volterra, C. T. Moynihan, and P. B. Macedo, *J. Amer. Ceram. Soc.*, in press.

where

$$M_s = 1/\epsilon_s \tag{6}$$

Hence, when treated in the modulus notation, the conducting material exhibits a Debye-like or single relaxation time dispersion, identical in form with that used to describe shear relaxation processes in liquids.[4,7] The limiting low- and high-frequency values of the real and imaginary parts of the modulus are

$$\lim_{\omega\tau_\sigma<<1} M' = 0, \quad \lim_{\omega\tau_\sigma>>1} M' = M_s$$
$$\lim_{\omega\tau_\sigma<<1} M'' = \lim_{\omega\tau_\sigma>>1} M'' = 0 \tag{7}$$

The imaginary part of the modulus passes through a maximum ($M'' = {}^1/_2 M_s$) at $\omega\tau_\sigma = 1$.

It is generally found[7] that for structural, shear, and dielectric relaxation processes in liquids in regions of high viscosity single relaxation time equations such as eq 5 are not adequate, but rather the dispersion effects are observed over a much broader range of frequencies than predicted by the single relaxation time equation. In these cases it is customary to invoke a spectrum of relaxation times, characterized by some appropriate distribution function, $g(\tau)$, to describe the phenomena. Where a distribution of relaxation times is needed, eq 5 is modified to read

$$M = M_s\int_0^\infty g(\tau_\sigma)\left(\frac{i\omega\tau_\sigma}{1 + i\omega\tau_\sigma}\right)d\tau_\sigma = M_s\int_0^\infty g(\tau_\sigma)\left(\frac{(\omega\tau_\sigma)^2}{1 + (\omega\tau_\sigma)^2}\right)d\tau_\sigma + iM_s\int_0^\infty g(\tau_\sigma)\left(\frac{\omega\tau_\sigma}{1 + (\omega\tau_\sigma)^2}\right)d\tau_\sigma \tag{8}$$

Equations 7 still hold for the limiting values of M' and M'', the effect of the distribution of relaxation times being primarily to broaden the dispersion region and lower the maximum in M''. The conductivity and dielectric constant, however, are no longer predicted to be frequency independent, but also exhibit dispersion effects due to the distribution of relaxation times. The limiting high- and low-frequency values of ϵ' and σ due to the conductivity relaxation may be shown to be[4]

$$\lim_{\omega\tau_\sigma>>1} \epsilon' = \epsilon_s = 1/M_s \tag{9}$$

$$\lim_{\omega\tau_\sigma<<1} \epsilon' = \epsilon_s\frac{\langle\tau_\sigma^2\rangle}{\langle\tau_\sigma\rangle^2} = \frac{1}{M_s}\frac{\langle\tau_\sigma^2\rangle}{\langle\tau_\sigma\rangle^2} \tag{10}$$

$$\lim_{\omega\tau_\sigma>>1} \sigma = e_0\epsilon_s\left\langle\frac{1}{\tau_\sigma}\right\rangle = \frac{e_0}{M_s}\left\langle\frac{1}{\tau_\sigma}\right\rangle \tag{11}$$

$$\lim_{\omega\tau_\sigma<<1} \sigma \equiv \sigma_0 = \frac{e_0\epsilon_s}{\langle\tau_\sigma\rangle} = \frac{e_0}{M_s\langle\tau_\sigma\rangle} \tag{12}$$

$\langle\tau_\sigma\rangle$ is the average conductivity relaxation time

$$\langle\tau_\sigma\rangle \equiv \int_0^\infty \tau_\sigma g(\tau_\sigma)d\tau_\sigma \tag{13}$$

and $\langle\tau_\sigma^2\rangle$ and $\langle 1/\tau_\sigma\rangle$ are defined similarly. (It should be noted that ϵ_s in eq 9, in the case of a distribution of conductivity relaxation times, no longer has its conventional meaning ($\epsilon_s = \lim_{\omega\to 0}\epsilon'$).)

The characteristics of a conductivity relaxation with a distribution of relaxation times can be reproduced by an electrical circuit consisting of a series connection of parallel RC elements, each element containing a conductance G_j shunted by a capacitance C.[8]

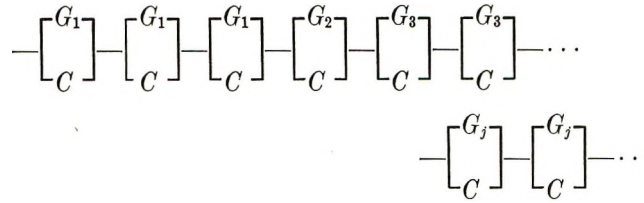

If there are n_j conductances with value G_j, and if the total number of conductances in the circuit is $N(=\Sigma_j n_j)$, the electric modulus M of the circuit is

$$M = \left(\frac{C_0 N}{C}\right)\sum_j \frac{n_j}{N}\left(\frac{i\omega\tau_j}{1 + i\omega\tau_j}\right) \tag{14}$$

where $\tau_j = C/G_j$, and C_0 is a circuit constant (C_0 = net capacitance of circuit when the dielectric material in each of the elements is replaced with a vacuum). The correspondence between eq 8 and 14 becomes clear if one makes the identifications

$$\tau_j \longleftrightarrow \tau_\sigma$$
$$\left(\frac{C_0 N}{C}\right) \longleftrightarrow M_s$$
$$\left(\frac{n_j}{N}\right) \longleftrightarrow g(\tau_\sigma)$$

and replaces the integration in eq 8 with a summation.

An equivalent circuit of the above type has been used previously to interpret the frequency dependence of the dielectric constant and loss of polycrystalline semiconductors.[8,9] The treatment suggests that the observation of a conductivity relaxation characterized by a distribution of relaxation times in a conducting liquid may be ascribed to a distribution of microregions of varying conductivity, the distribution presumably arising from local density or composition fluctuations, or, in alternative terms, to a distribution of free energy

(5) C. T. Moynihan, R. D. Bressel, and C. A. Angell, *J. Chem. Phys.*, **55**, 4414 (1971).
(6) C. A. Angell and E. J. Sare, *ibid.*, **52**, 1058 (1970).
(7) T. A. Litovitz and C. M. Davis in "Physical Acoustics," Vol. IIA, W. P. Mason, Ed., Academic Press, New York, N. Y., 1965, pp 281–349.
(8) J. Volger, *Progr. Semicond.*, **4**, 205 (1960).
(9) C. G. Koops, *Phys. Rev.*, **83**, 121 (1951).

barriers for the ionic diffusion or electron hopping process.[4]

Dielectric Relaxation

In the case in which a conducting dielectric may undergo a relaxation involving molecular mechanisms which do not contribute to the long-range conductance process (*e.g.*, reorientation of permanent dipoles), an additional term or terms must be added to the electric modulus expression for the conductivity relaxation. In the single relaxation time case in which there is only one dielectric relaxation, eq 5 would then become

$$M = M_s\left(\frac{i\omega\tau_\sigma}{1 + i\omega\tau_\sigma}\right) + (M_\infty - M_s)\left(\frac{i\omega\tau_D}{1 + i\omega\tau_D}\right) \quad (15)$$

The first term refers to the conductivity relaxation and the second term to the dielectric relaxation

$$M_s = 1/\epsilon_s$$

and

$$M_\infty = 1 \Big/ \lim_{\omega\tau_D >> 1} \epsilon'$$

τ_D is the dielectric relaxation time for constant displacement vector and is related to the conventional dielectric relaxation time for constant electrical field, τ_E, by

$$\tau_D = \frac{M_s}{M_\infty}\tau_E \quad (16)$$

In the more general case either or both terms in eq 15 may have to be modified to allow for a distribution of relaxation times; likewise, additional terms would need to be added in the event that there is more than one dielectric relaxation.

Since τ_σ in eq 15 is the time constant for the decay of the electric field to zero in the dielectric medium, only those dielectric relaxations which have $\tau_D \ll \tau_\sigma$ will be observable. Hence when data are represented in the electric modulus notation, the conductivity relaxation must always be the first (*i.e.*, the lowest frequency) relaxation process to be observed. In this regard, it is also important to note that, on the basis of the electric modulus data alone, it is in general not possible to distinguish the case of a conductivity relaxation coupled with a dielectric relaxation arising from non-charge-transporting mechanisms from the case of a conductivity relaxation characterized by a distribution of relaxation times, as may be seen from a comparison of eq 14 and 15.

Electrode Polarization Effects

A final element which must be considered as contributing to the frequency dependence of the admittance in a conducting dielectric is the presence of a capacitance in series with the equivalent circuit of the material. This is shown in the inset of Figure 1 as C_s,

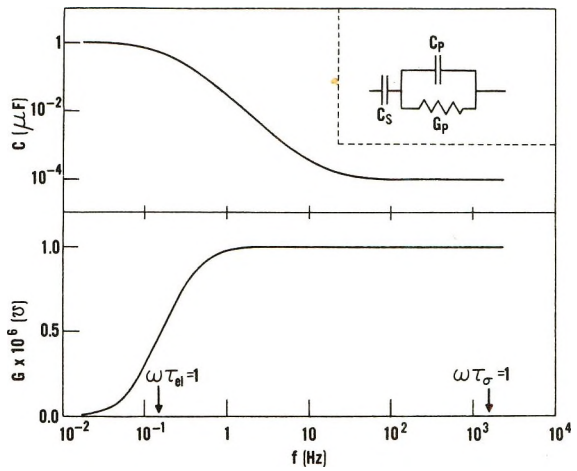

Figure 1. Frequency dependence of capacitance and conductance of model circuit for ionic conductor with blocking electrode capacitance. Component values for circuit in inset: $C_s = 1\ \mu F$, $C_p = 10^{-4}\ \mu F$, $G_p = 10^{-6}$ mho.

where the remainder of the circuit has been taken, for simplicity, as a parallel RC combination. For measurements on solid materials which are not electronic conductors and which do not allow the actual transport of charge across the material–electrode interface, C_s arises from a small air gap or layer of nonconducting oxide between the material and the electrode. In electrolyte solutions[10,11] C_s represents the ionic double layer capacitance at the solution–electrode interface and should rigorously be considered to be shunted by an additional impedance arising from charge transport across the interface by Faradaic processes. To a first approximation this Faradaic impedance may be neglected, particularly if the maximum amplitude of the alternating potential is kept below the decomposition potential of the solution.[10] For a typical conductance–capacitance cell used with electrolyte solutions the double layer capacitance, C_s, is quite large (>1 μF) in comparison to the capacitance, C_p, of the solution itself (10^{-4} μF or less). The admittance of the circuit of Figure 1 is

$$Y = \frac{\omega^2 C_s^2 G_p}{G_p^2 + \omega^2(C_s + C_p)^2} + \frac{i\omega[C_s G_p^2 + \omega^2 C_s C_p (C_s + C_p)]}{G_p^2 + \omega^2(C_s + C_p)^2} \quad (17)$$

For the case in which $C_s \gg C_p$, the high- and low-frequency limits of the net capacitance and net conductance of the circuit are

(10) (a) G. D. Robbins, *J. Electrochem. Soc.*, **116**, 813 (1969); (b) G. D. Robbins and J. Braunstein, "Molten Salts: Characterization and Analysis," G. Mamantov, Ed., Marcel Dekker, New York, N. Y., 1969, pp 443–478.

(11) R. A. Robinson and R. H. Stokes, "Electrolyte Solutions," 2nd ed, Butterworths, London, 1965, pp 93–95.

$$\lim_{\omega\to\infty} C \approx C_p, \lim_{\omega\to\infty} C \approx C_s$$

$$\lim_{\omega\to\infty} G \approx G_p, \lim_{\omega\to 0} G = 0 \qquad (18)$$

Hence at low frequencies the capacitance will commence a rather rapid increase from C_p to the much higher value, C_s, as the frequency is decreased, while the conductance will drop off from G_p to zero. Fortunately, for the case in which $C_s \gg C_p$, the time constant for the dispersion associated with the double-layer capacitance

$$\tau_{el} = (C_s + C_p)/G_p$$

will be much larger than the conductivity relaxation time

$$\tau_\sigma = C_p/G_p$$

Thus the dispersion due to the double layer capacitance will occur at much lower frequencies than the conductivity relaxation (and any subsequent dielectric relaxations) and will in general not obscure any effects of interest. This is shown in Figure 1, where the frequency dependence of the net conductance and capacitance of the circuit in the inset have been calculated using a set of component values typical for an experiment of the type presented here. It should be noted that an additional effect arising from the large difference in the magnitudes of C_s and C_p is that the measured value of G attains its high-frequency limit at much lower frequencies than does the measured value of C.

In the modulus notation the circuit of Figure 1 yields a particularly simple expression

$$M = \frac{C_0}{C_s} + \frac{C_0}{C_p}\left(\frac{i\omega\tau_\sigma}{1 + i\omega\tau_\sigma}\right) \qquad (19)$$

where C_0 is again a circuit constant corresponding to the vacuum capacitance of a dielectric cell. The double-layer capacitance thus makes a constant contribution to the real part of the modulus (which contribution may be reglected when $C_s \gg C_p$) and makes no contribution to the imaginary part.

Experimental Section

Reagent grade calcium nitrate tetrahydrate (Mallinckrodt AR) and deionized water were used to prepare a solution with a H_2O:$Ca(NO_3)_2$ mole ratio of approximately 6. The exact H_2O:$Ca(NO_3)_2$ mole ratio (6.15) was determined from the density (1.6033 g cm^{-3} at 30°) using the data of Ewing and Mikovsky.[12]

The dielectric cell was thermostated in a mechanically stirred methanol bath in a 4-qt dewar flask. Temperature was measured with a calibrated copper–constantan thermocouple. Above −78° the bath temperature was controlled to within ±0.05° by periodically adding small amounts of Dry Ice. Below −78° liquid nitrogen was used for temperature control (to within ±0.1°).

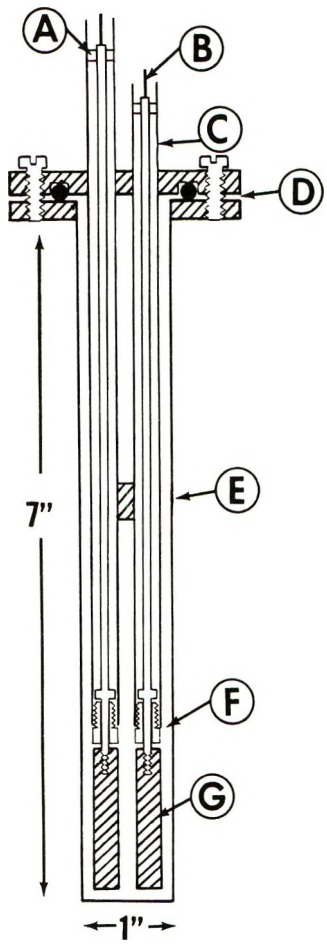

Figure 2. Dielectric cell: A, Teflon spacer; B, electrode lead, mates with female BNC connector; C, shield for electrode leads; D, O-ring joint; E, brace between electrode shields; F, Delrin insulator; G, cylindrical electrode, 3.8 cm long, 0.79 cm o.d.; electrode separation 0.3 cm.

The schematic of the dielectric cell is shown in Figure 2. Except for the plastic insulators and spacers and the rubber O ring, the cell is constructed entirely of nickel-plated stainless steel. The exterior of the cell and the electrode lead shields are connected to the neutral of the admittance bridge and serve to eliminate any stray capacitances due to fringing effects. The vacuum capacitance, C_0, of the cell was approximately 0.7 pF. The absence of stray capacitance in the cell and circuit was confirmed by the agreement between the C_0 values obtained using air and benzene as calibrating dielectric media in the cell. The C_0 value used in data reduction was determined by measuring the air capacitance of the assembled cell just before the experiment. C_0 was remeasured after the experiment, without disturbing the electrode assembly and found to agree with the initial value of C_0 within ±0.4%.

(12) W. W. Ewing and R. J. Mikovsky, *J. Amer. Chem. Soc.*, **72**, 1390 (1950).

Table I: Specifications for Admittance Bridges

Bridge	f range, Hz	C range, pF	G range, Ω^{-1}
Cole–Gross	500–1 × 10^6	0–100 ± 0.05	2 × 10^{-2} to 1 × 10^{-8} (±0.5%)
General Radio 1615A	500–1 × 10^5	0–10,000 ± 0.01	1 × 10^{-6} to 1 × 10^{-10} (±1%)
Berberian–Cole	1–500	0–100 ± 0.1	1 × 10^{-4} to 5 × 10^{-12} (±1%)

Depending on the frequency and conductance range, one of three different bridges was used to measure capacitance, C, and conductance, G: (1) a three-terminal transformer arm ratio bridge based on the design of Cole and Gross;[13] (2) a General Radio Model 1615A bridge used in the three-terminal mode; or (3) a three-terminal bridge designed by Berberian and Cole[14] for low-frequency measurements. The ranges and accuracies of these bridges are given in Table I. Frequencies of the oscillators used were accurate to ±1%.

During measurements, the dielectric cell containing the sample was first quenched in the precooled bath to a temperature in the vicinity of its glass transition temperature. The sample was annealed at this temperature for approximately 1 hr, then cooled to the lowest temperature at which measurements were to be made. A series of frequency–admittance measurements was then performed at increasingly higher temperatures. To ensure that the sample had come to thermal equilibrium at each temperature, we waited until the conductance and capacitance readings were constant at a given frequency for at least 10 min before commencing measurements. The measurements were terminated when the sample crystallized. Onset of crystallization was easily detected by the erratic behavior of the conductance.

Results and Discussion

The glass transition temperature for $Ca(NO_3)_2 \cdot 6.15H_2O$, determined at a heating rate of 15–17 deg/min, is −79°.[6] In our experiments 0.5–1 hr was required for heating and equilibration between successive temperatures, so that all measurements reported for temperatures above −79° may be considered to have been taken on a sample in internal equilibrium.

The relative permittivities, ϵ', and the conductivities, σ, were calculated from the measured conductances and capacitances *via* the equations

$$\epsilon' = C/C_0; \quad \sigma = e_0 G/C_0 \tag{20}$$

In Figures 3 and 4 the experimental values of ϵ' and σ are plotted as a function of frequency at various temperatures. The very rapid rise in ϵ' with decreasing frequency at the higher temperatures (−72.3° and up) and the lowest frequencies may be associated with electrode polarization, since the conductivity appears to be frequency independent in these regions (compare Figure 1). The frequency dependence of ϵ' and σ at frequencies higher than the polarization frequency at

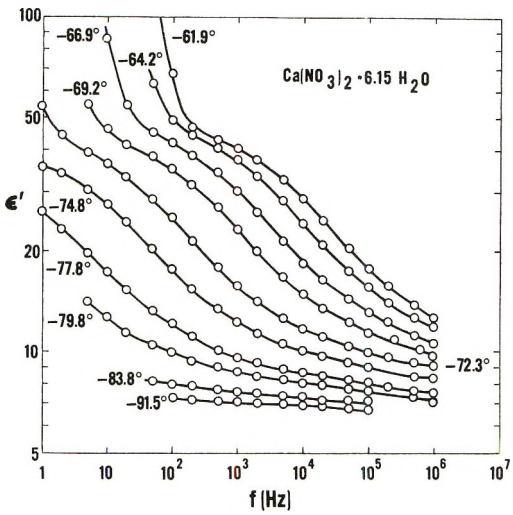

Figure 3. Relative permittivity, ϵ', of $Ca(NO_3)_2 \cdot 6.15H_2O$ as a function of frequency and temperature.

temperatures above −72.3° and at all frequencies below this temperature can then be associated with the conductivity or dielectric relaxations of the solution.

In Figures 5 and 6 the data of Figures 3 and 4 are shown plotted in the modulus form, where M' and M'' have been calculated from eq 2. At the higher temperatures M' approaches zero at low frequencies, indicating that the initial dispersions in M' and M'' are due to a conductivity relaxation. The fact that M' approaches zero at low frequencies also indicates that electrode polarization has a negligible effect on the data analysis in the modulus notation (*cf.* eq 19). M' does not level off, however, at higher frequencies, even at the lowest temperatures at which experiments were performed, so that the relaxation processes present are spread over a considerable range in frequency. The M'' plots of Figure 6 are somewhat more informative in this regard. The low-temperature M'' plots show the presence of at least two electrical relaxation processes, one associated with the large asymmetric low-frequency peak and a second associated with a smaller high-frequency peak, only part of which is visible in the frequency range available in this experiment.

As a first attempt at deciding what portion of the initial, low-frequency dispersion in M' and M'' should be associated with the conductivity relaxation, we com-

(13) R. H. Cole and P. M. Gross, *Rev. Sci. Instrum.*, **20**, 252 (1949).
(14) J. G. Berberian and R. H. Cole, *ibid.*, **40**, 811 (1969).

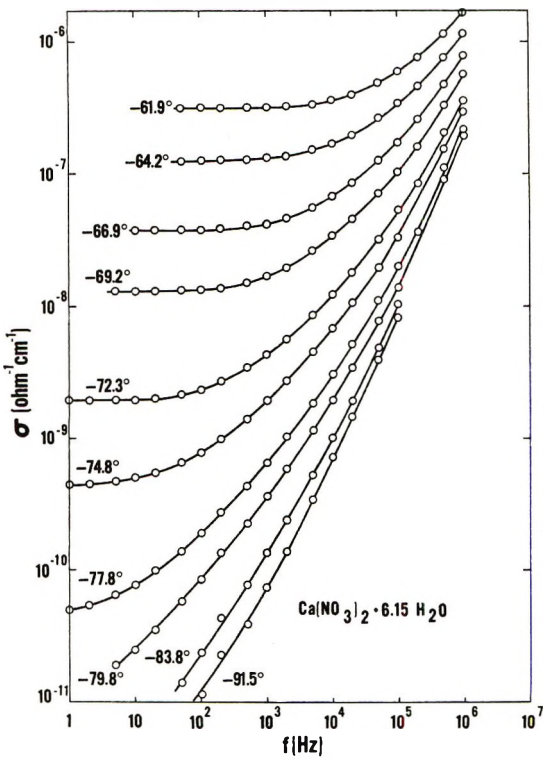

Figure 4. Conductivity, σ, of $Ca(NO_3)_2 \cdot 6.15H_2O$ as a function of frequency and temperature.

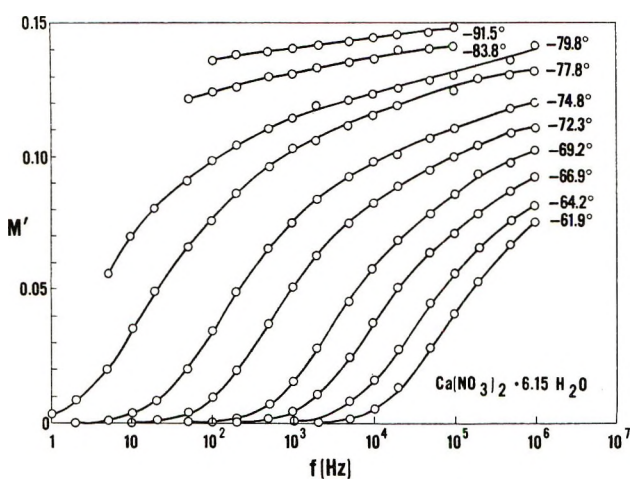

Figure 5. Real part of the electric modulus, M', of $Ca(NO_3)_2 \cdot 6.15H_2O$ as a function of frequency and temperature.

pared the experimental M' and M'' curves with those predicted on the assumption that the conductivity relaxation exhibited single relaxation time behavior. In this case the conductivity relaxation would make no contribution to the frequency dependence of ϵ', so that ϵ_s may be taken as the value of ϵ' in the vicinity of low-frequency shoulder in the plots of Figure 3. The relaxation time, τ_σ, may be calculated from eq 4, using the experimental value of the limiting low-frequency conductivity, σ_0. The single relaxation time curves for M' and M'', calculated from eq 5, are compared in Figure 7 with the experimental data for $-64.2°$.[15] If

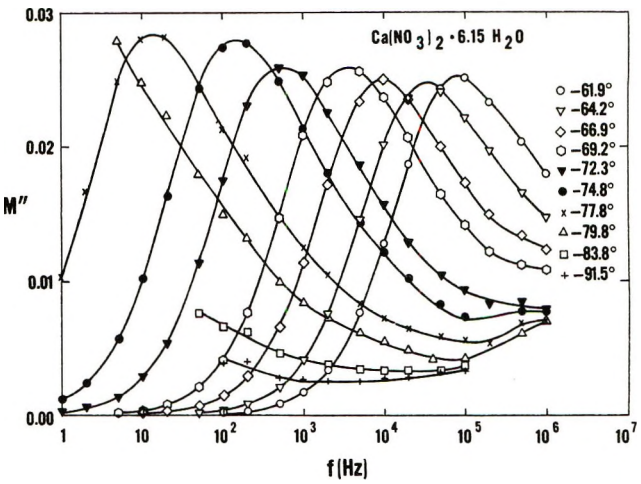

Figure 6. Imaginary part of the electric modulus, M'', of $Ca(NO_3)_2 \cdot 6.15H_2O$ as a function of frequency and temperature.

a single relaxation time treatment were adequate, one would expect the calculated M' curve to match the experimental data at low frequencies, but eventually to fall under the experimental curve as additional dielectric relaxations began to contribute to M'. As shown in Figure 7, however, the calculated curve for M' *exceeds* the experimental curve at low frequencies, showing that the single relaxation time treatment predicts too rapid an increase in M' and that the conductivity relaxation needs to be described in terms of a distribution of relaxation times.

As a second attempt at characterizing the initial conductivity relaxation, we have assumed that it may be described in terms of a log Gaussian distribution of relaxation times[7]

$$g\left(\ln \frac{\tau_\sigma}{\tau_\sigma'}\right) = \frac{b}{\sqrt{\pi}} \exp\left[-b^2 \ln^2 \left(\frac{\tau_\sigma}{\tau_\sigma'}\right)\right] \qquad (21)$$

τ_σ' is the most probable relaxation time, and b is a constant inversely proportional to the width of the distribution function at half-height. Using eq 21 for $g(\tau_\sigma)$ in the dispersion functions of eq 8, an iterative least-squares fit on the parameters b, M_s, and τ_σ' was performed simultaneously on the values of M' and M'' up to the peak frequencies in Figure 6 for each of the temperatures between -61.9 and $-77.8°$. The width parameter, b, was found to be virtually the same for each of the seven temperatures, the average value being 0.585 ± 0.010. The data therefore were fitted a second time to obtain M_s and τ_σ' values for the constant value $b = 0.585$. The least-squares values of M_s ($= 1/\epsilon_s$) and τ_σ' obtained in this fashion are given in Table II. The statistical uncertainties in M_s and τ_σ' were in

(15) As is evident from Figure 3, the value of ϵ_s for $-64.6°$ might be reasonably taken anywhere in the range 40–60. The single relaxation time plot for Figure 7 is for $\epsilon_s = 50$, but plots using ϵ_s anywhere in the 40–60 range lead to the same conclusion, that the single relaxation time treatment does not account for the data.

Table II: Parameters from Fit of Log Gaussian Distribution Functions to Initial Conductivity Relaxation in $Ca(NO_3)_2 \cdot 6.15H_2O$

T, °C	b	$10^2 M_s$	ϵ_s	τ_σ', sec	$\sigma_{0,calcd}$, Ω^{-1} cm^{-1}	$\sigma_{0,expt}$, Ω^{-1} cm^{-1}	$\epsilon_s\frac{\langle\tau_\sigma^2\rangle}{\langle\tau_\sigma\rangle^2}$ (calcd)
−61.9	0.585	7.3	13.8	2.05×10^{-6}	2.9×10^{-7}	3.2×10^{-7}	60
−64.2	0.585	7.2	13.9	5.0×10^{-6}	1.18×10^{-7}	1.27×10^{-7}	60
−66.9	0.585	7.4	13.5	1.62×10^{-5}	3.5×10^{-8}	3.8×10^{-8}	58
−69.2	0.585	7.6	13.2	4.7×10^{-4}	1.19×10^{-8}	1.30×10^{-8}	57
−72.3	0.585	7.8	12.8	2.9×10^{-4}	1.85×10^{-9}	1.95×10^{-9}	55
−74.8	0.585	8.3	12.0	1.16×10^{-3}	4.4×10^{-10}	4.3×10^{-10}	52
−77.8	0.585	8.4	11.8	1.13×10^{-2}	4.5×10^{-11}		51

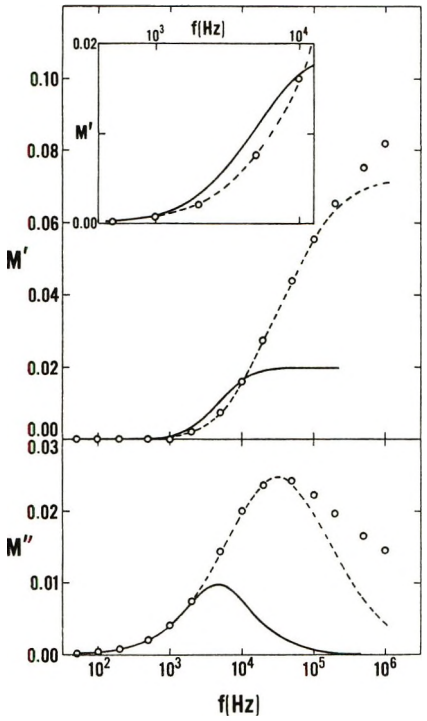

Figure 7. Comparison of experimental and calculated electric modulus dispersion curves for $Ca(NO_3)_2 \cdot 6.15H_2O$ at −64.2°: (——) single relaxation time curve for $\epsilon_s = 1/M_s = 50$, $\tau_\sigma = \epsilon_0\epsilon_s/\sigma_0 = 3.48 \times 10^{-5}$ sec; (- - - - - - -) fit using log Gaussian distribution function over frequency range 0.5–50 kHz; inset; blowup of M' plot in low-frequency dispersion region.

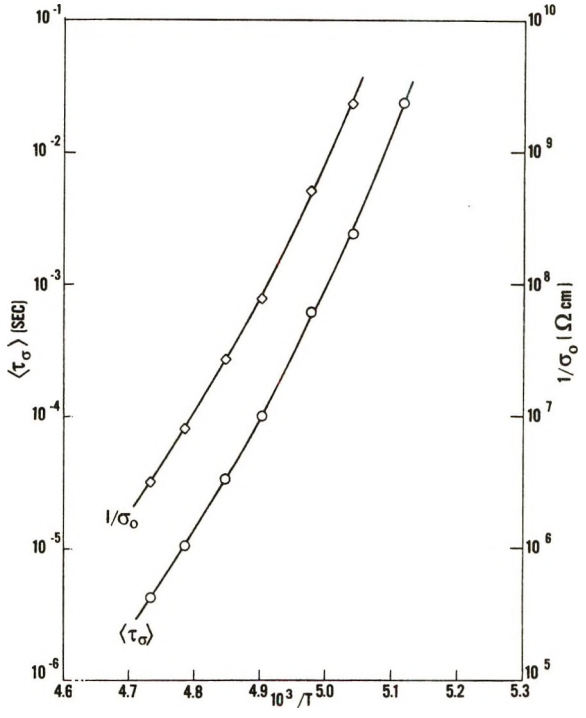

Figure 8. Arrhenius plots of dc conductivity, σ_0, and average conductivity relaxation time, $<\tau_\sigma>$, of $Ca(NO_3)_2 \cdot 6.15H_2O$.

the respective ranges 1–2 and 2–4%, except for the lowest temperature fitted (−77.8°), where they were 4 and 8%, respectively. The log Gaussian fit to the M' and M'' data for −64.2° is also shown in Figure 7.

A moderately sensitive test of this procedure in accounting for the initial conductivity relaxation is the ability to back-calculate (using eq 10 and 12) the limiting low-frequency values of the relative permittivity and conductivity, $\epsilon_s \langle\tau_\sigma^2\rangle/\langle\tau_\sigma\rangle^2$ and σ_0, from the parameters in Table II. (These parameters are obtained almost entirely from a fit to the data in regions where ϵ' and σ exhibit strong-frequency dependence and differ markedly from the limiting low-frequency values.) For a log Gaussian distribution of relaxation times, the average relaxation times needed in eq 10 and 12 are[16]

$$\langle\tau_\sigma\rangle = \tau_\sigma' \exp(1/4b^2) = 2.08\tau_\sigma' \qquad b = 0.585$$

$$\langle\tau_\sigma^2\rangle/\langle\tau_\sigma\rangle^2 = \exp(1/2b^2) = 4.33 \qquad b = 0.585$$

The calculated values of $\epsilon_s\langle\tau_\sigma^2\rangle/\langle\tau_\sigma\rangle^2$ and σ_0 are given in Table II, along with the experimental values of σ_0. The experimental and calculated values of σ_0 are in agreement within 10% or better, which is within the agreement expected from the statistical or experimental uncertainties in b, ϵ_s, τ_σ', and $\sigma_{0,exp}$. As shown in Figure 3, $\epsilon_s\langle\tau_\sigma^2\rangle/\langle\tau_\sigma\rangle^2$ cannot be measured precisely because of electrode polarization effects, but the values calculated in Table II can be seen to correspond closely

(16) J. H. Simmons and P. B. Macedo, *J. Chem. Phys.*, **53**, 2914 (1970).

Table III: Fulcher Equation Parameters for Transport Properties of $Ca(NO_3)_2 \cdot 6.15\ H_2O$ Solution

Property w	T range, °C	A	B	T_0	Std dev in ln w
$1/\sigma_0$, Ω cm	−61.9 to −74.8	−4.260	965.75	161	0.04
$\langle\tau_\sigma\rangle$, sec	−61.9 to −77.8	−30.929	933.18	161	0.05

to the limiting low-frequency values toward which the ϵ' plots appear to be headed just before the rapid rise due to electrode polarization.

In Figure 8 are shown Arrhenius plots of $\langle\tau_\sigma\rangle$ and $1/\sigma_0$. If one ignores the temperature dependence of ϵ_s, which is small compared to the temperature dependence of the relaxation time, $1/\sigma_0$ and $\langle\tau_\sigma\rangle$ are predicted from eq 12 to have identical activation energies. The Arrhenius plots in Figure 8 exhibit noticeable curvature, so that the apparent activation energies must be considered to be temperature dependent. The data for $1/\sigma_0$ and $\langle\tau_\sigma\rangle$ were fitted to the Fulcher equation

$$\ln w = A + \frac{B}{T - T_0} \tag{22}$$

where w is a transport property, and A, B, and T_0 are constants. It was found that within the statistical uncertainty of the fit, the same value of T_0 could be used for both $1/\sigma_0$ and $\langle\tau_\sigma\rangle$. The Fulcher equation parameters are given in Table III. (It should be noted that the Fulcher equation tends to give an incorrect description of the temperature dependence of transport properties when applied to data extending over many orders of magnitude.[17,18] Hence the parameters in Table III should not be used to extrapolate the data beyond the temperature limits indicated.) The activation energy, E, calculated from the Fulcher equation is

$$\frac{E}{R} = \frac{\partial \ln w}{\partial(1/T)} = \frac{BT^2}{(T - T_0)^2} \tag{23}$$

so that near equality of the B terms for $1/\sigma_0$ and $\langle\tau_\sigma\rangle$ indicates that the apparent activation energies are likewise nearly the same. The apparent activation energy for $\langle\tau_\sigma\rangle$ increases from 32.8 to 60.0 kcal/mol over the temperature range −61.9 to −77.8°.

Although our log Gaussian fit to the low-frequency portions of the M' and M'' curves of Figures 5 and 6 gives a satisfactory account of the low-frequency dispersion in ϵ' and σ due to the conductivity relaxation and yields an average conductivity relaxation time which exhibits the expected correlation with the dc conductivity, this is no guarantee that the distribution of conductivity relaxation times is in fact correctly described by a log Gaussian function. Rather, as is evident from eq 9–13, any distribution function which accounts for the low-frequency portion of M' and M'' plots will yield correct values of the average relaxation time, since only the long relaxation times (which give rise to the low-frequency dispersion in M' and M'') make any appreciable contribution to the average time.[5]

Inspection of Figure 6 shows that the smaller secondary relaxation peak which is evident in the megahertz region for the lower temperature curves is of considerable breadth and that the relaxation times associated with this peak have a much smaller temperature dependence than the conductivity relaxation time. In view of these complications, we feel that an attempt to accurately dissect the M' and M'' plots into contributions from the conductivity relaxation and contributions from other relaxation processes and hence to determine a genuine distribution function for the conductivity relaxation times would be premature. This high-frequency relaxation peak is similar in nature to the secondary peaks (β relaxations) which Johari and Goldstein[19] have found in a wide variety of simple molecular or ionic glass-forming liquids and which they suggest are endemic to the glassy state.

One possible source of the secondary relaxation peak in the $Ca(NO_3)_2 \cdot 6.15H_2O$ solution is the reorientation of polar water molecules. In this solution, however, one expects most of the water molecules to be bound up in the hydration spheres of the Ca^{2+} ions.[20] Previous dielectric relaxation studies for dilute aqueous electrolyte solutions (*cf.* for instance, ref 3d) indicate that the reorientation of water molecules bound in the hydration spheres of high-field cations cannot give rise to observable dielectric relaxations, since, if the metal ion–oxygen bond bisects the H–O–H angle, rotation of a water molecule about this bond involves no change in dipole orientation. Hence for the $Ca(NO_3)_2 \cdot 6.15H_2O$ solution water molecule reorientation may not be contributing to the observed high-frequency relaxation. A second possible source of the secondary relaxation are localized ion-jumping mechanisms similar to those which give rise to high-frequency electrical relaxations in doped alkali halide crystals.[21]

In the future we hope to report the results of similar

(17) (a) P. B. Macedo and A. Napolitano, *J. Chem. Phys.*, **49**, 1887 (1968); (b) R. Bose, R. Weiler, and P. B. Macedo, *Phys. Chem. Glasses*, **11**, 117 (1970).

(18) H. Tweer, N. Laberge, and P. B. Macedo, *J. Amer. Ceram. Soc.*, **71**, 121 (1971).

(19) (a) G. P. Johari and M. Goldstein, *J. Phys. Chem.*, **74**, 2034 (1970); (b) G. P. Johari and M. Goldstein, *J. Chem. Phys.*, **53**, 2372 (1970).

(20) C. T. Moynihan and A. Fratiello, *J. Amer. Chem. Soc.*, **89**, 5546 (1967).

(21) J. S. Dryden and R. J. Meakins, *Discuss. Faraday Soc.*, **23**, 39 (1957).

studies currently in progress for a number of concentrations in the glass-forming region of the $Ca(NO_3)_2$–H_2O system. These studies will hopefully clarify the role of water molecule reorientation in the observed electrical relaxation processes for these concentrated solutions.

Acknowledgments. The authors wish to thank F. Scott Howell, S. J., for assistance with computer calculations and bridge calibrations and V. Provenzano for assistance in the Berberian–Cole bridge measurements. This research was supported by the U. S. Naval Ordnance Laboratory's Independent Research Program and by a Themis Grant from the Office of Naval Research.

Molecular Structure and Shear Viscosity. Isomeric Hexanes

by Lawrence D. Eicher and Bruno J. Zwolinski*

Department of Chemistry, Thermodynamics Research Center, Texas A&M University, College Station, Texas 77843
(Received April 27, 1972)

Publication costs assisted by the American Petroleum Institute Research Project 44

Precise and accurate kinematic viscosity data are reported for four isomeric hexanes of certified purity at temperatures ranging from −18 to 65°. The experimental procedure utilized standard Cannon–Ubbelohde capillary viscometers, an electronic precision time-of-efflux technique, and platinum resistance thermometry. A generalized viscosity function reproduces the precision of data well within experimental uncertainty. Eyring's Significant Liquid Structures (SLS) theory, corrected for real gas viscosities, reproduces the hexane viscosity data in terms of three regression parameters which are internally consistent with the structural features of these isomers. The analysis was equally effective for literature data on neopentane and 2,3-dimethylbutane.

Introduction

The temperature coefficient of the viscosities of molecular liquids is of continuing theoretical and practical interest, from complex transition phenomena at one end of the spectrum to smoothing and predicting viscosities of simple liquids with temperature at the other extreme.[1-3] Earlier investigations identified viscosity–temperature relations for a variety of classes of organic and inorganic liquids.[4]

A second and more difficult problem is to relate viscosity magnitudes to chemical composition and structure, even at constant temperature. Although some progress has been made, still at the present time we do not have a reliable procedure for predicting viscosities of the higher members of a homologous series from the viscosity values for the first few members. The problem for isomeric but nonhomologous members is even more complex and thus more challenging. For these reasons, we selected the isomeric hexanes for our study to see whether any significant relationships could be found between shear viscosities, molecular structure, and other bulk liquid properties.

The nature of the problem is defined in Figure 1 on the basis of a reduced temperature diagram for the hexane isomers. It compares the temperatures at which the isomers have equal bulk property (vapor pressure, molar volume, and viscosity) values. The ratio of the "iso-property" temperature of the isomer to that of the normal or straight-chain member is plotted as ordinate *vs.* the isomers complexity. The normal boiling point, viscosity, and molar volume at 20° were used as reference values for *n*-hexane. Figure 1 illustrates that no simple relationships exist between these properties.

Experimental kinematic viscosities were measured for four of the five isomeric hexanes of well-defined purities and over the widest possible temperature ranges from −18 to 65°. The temperature coefficient data were analyzed successfully by the procedure proposed by the authors.[5] The effects of molecular structure on flow were determined in terms of Eyring's sig-

(1) G. L. Faerber, S. W. Kim, and H. Eyring, *J. Phys. Chem.*, **74**, 3510 (1970).

(2) A. J. Barlow, J. Lamb, and M. J. Matheson, *Proc. Roy. Soc., Ser. A*, **292**, 322 (1966).

(3) M. H. Cohen and D. Turnbull, *J. Chem. Phys.*, **31**, 1164 (1959).

(4) T. E. Thorpe and J. W. Rodgers, *Phil. Trans. Roy. Soc. London, Ser. A*, **185**, 397 (1894).

(5) L. D. Eicher and B. J. Zwolinski, *J. Phys. Chem.*, **75**, 2016 (1971).

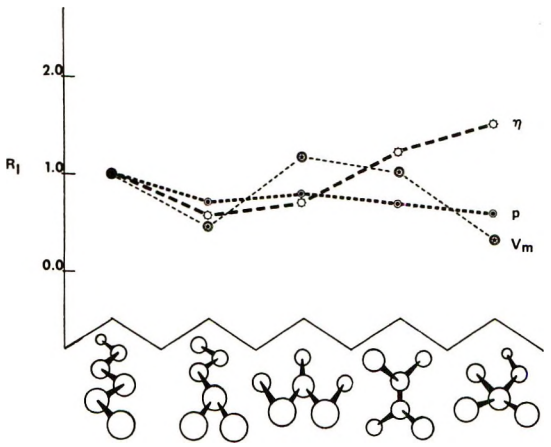

Figure 1. R_I is the temperature at which the property value for the isomer is equal to that of n-hexane divided by the corresponding n-hexane temperature: properties, p = vapor pressure, V_m = molar volume, and η = viscosity.

nificant liquid structures (SLS) theory which established a correspondence between shear viscosity magnitudes, solid-like volume parameters of the theory, and simple molecular geometry.

Experimental Section

The capillary viscometer, the sample and thermostat systems, and the efflux time measurements have been described previously.[5] To minimize sample contamination, the viscometer was cleaned with freshly prepared chromic acid solution, thoroughly rinsed with distilled deionized water, and dried under vacuum prior to the transfer of each sample. Each of the samples was transferred *in vacuo* to the viscometer from break-seal ampoules in an all-glass vacuum system with dry nitrogen purges as necessary. Temperatures were controlled to ±0.002°, fading off to ±0.01° in the lower temperature ranges. An NBS calibrated (IPTS-48) platinum resistance thermometer was used in all temperature measurements.

Sample Characterization

The four hexane samples were contributed by the Phillips Petroleum Co., Bartlesville, Okla. The purities of these samples (all in excess of 99.95 mol %), determined by freezing point determinations and gas–liquid chromatography, were accepted as specified by the supplier and are reported as supplemental data.[6] The remaining hexane isomer, 2,3-dimethylbutane, was not included in this study since the literature data were found to be reliable.

Results and Calculations

For the conversion of temperature and efflux time data to kinematic viscosities, eq 1 was used.

$$\nu_t = C[1 + \xi(t - t_c)]M_t\tau_t - \frac{E[1 + \xi(t - t_c)]^{5/2}}{\tau_t^2} \quad (1)$$

where ν_t is the kinematic viscosity at temperature t and efflux time τ_t. The C, E, ξ, and t_c symbols represent the viscometer constant, the kinetic energy correction constant, the mean linear thermal coefficient of expansion of the viscometer glass ($\xi = 3.25 \times 10^{-6}$ °C^{-1}), and the lower calibration temperature, respectively. For the Cannon–Ubbelohde suspended-meniscus viscometers, for which no appreciable correction for surface tension is needed, the factor M_t reduces to a correction for the gas density only at t.[7]

$$M_t = 1 + X_g \quad (1a)$$

$$X_g = \left(\frac{\rho_{gc}}{\rho_{lc}} - \frac{\rho_{gu}}{\sigma_{lu}}\right)\frac{\rho_{lc}}{(\rho_{lc} - \rho_{gc})}$$

In eq 1a, ρ_{gc}, ρ_{lc}, ρ_{gu}, and ρ_{lu} are the densities of the gas and liquid in the viscometer at calibration and use conditions, respectively. In the calculation of this factor, it was assumed that Dalton's law of mixtures was adequate for the sample-saturated nitrogen mixtures. E is assumed proportional to $V^{3/2}l^{-1/2}(Cr)^{-1/2}$ at t_c and determined experimentally *via* calibration at two temperatures.

Standard propagation of error considerations[8] for the case of uncorrelated fluctuations in the measured values of the independent variables, x_i, lead to the following expression for the estimated variance of the dependent variable y.

$$s_y^2 = \sum_{i=1}^{k} s_{x_i}^2\left(\frac{\partial y}{\partial x_i}\right)_{x_{j\neq i}} \quad (2)$$

where s_y^2 is the sample estimated variance of the dependent variable and the s_{x_i} factors are the experimentally determined variances of the ith measured independent variable. The viscometer calibration results with estimated variances based on the kinematic viscosities of water at 20 and 40° with a known accuracy of 0.2%[9] are also reported as supplementary data.[10]

The experimental results on the four liquid hexanes are presented in Table I. The uncertainties listed in Table I require an accurate numerical estimate of the temperature coefficient $(\partial\nu/\partial t)/t$. The empirical function selected for this purpose is discussed in the next section.

(6) A listing of mole per cent purity and the most probable impurities for each isomer will appear following these pages in the microfilm edition of this volume of the journal. Single copies may be obtained from the Business Operations Office, Books and Journals Division, American Chemical Society, 1155 Sixteenth St., N.W., Washington, D. C. 20036, by referring to code number JPC-72-3295. Remit check or money order for $3.00 for photocopy or $2.00 for microfiche.

(7) R. C. Hardy, *Nat. Bur. Stand. (U. S.), Monogr.* **No. 55** (1962).

(8) P. R. Bevington, "Data Reduction and Error Analysis for the Physical Sciences," McGraw-Hill, New York, N. Y., 1969.

(9) Throughout this paper the following units were used, and their conversions to SI units are as follows: cP (centipoise) = 10^{-3} N sec/m²; cSt (centistoke) = 10^{-6} m²/sec; ρ (g/cm³) = 10^3 kg/m³.

(10) A listing of calibration data, viscometer constants, and precision estimates are included in the microfilm edition; see ref 6.

Table I: Experimental Results for Four Isomeric Hexanes

Isomer	t, °C	ν, cSt[a]	% deviation (ν)[b]	ρ, g cm^{-3} [c]	η, cP[a]	% deviation (η)[b]
n-Hexane	−6.45	0.6087 ± 0.0004	0.15	0.6825	0.4154 ± 0.0007	0.32
t_m[d] = −95.348°	−2.379	0.5825 ± 0.0004	0.15	0.6790	0.3955 ± 0.0007	0.33
t_b[e] = +68.740°	+4.242	0.5457 ± 0.0005	0.18	0.6731	0.3673 ± 0.0007	0.40
$P_{t\text{-max}}$[f] = 340 Torr	20.910	0.4692 ± 0.0007	0.28	0.6586	0.3090 ± 0.0010	0.64
	23.117	0.4604 ± 0.0007	0.29	0.6565	0.3023 ± 0.0013	0.68
	36.876	0.4117 ± 0.0008	0.41	0.6440	0.2652 ± 0.0013	0.98
	45.234	0.3862 ± 0.0009	0.49	0.6361	0.2457 ± 0.0015	1.21
2-Methylpentane	−15.64	0.6178 ± 0.0004	0.13	0.6848	0.4230 ± 0.0006	0.29
t_m[d] = −153.670°	−9.727	0.5785 ± 0.0004	0.15	0.6797	0.3931 ± 0.0007	0.34
t_b[e] = +60.271°	−0.170	0.5263 ± 0.0005	0.20	0.6710	0.3531 ± 0.0008	0.45
$P_{t\text{-max}}$[f] = 767 Torr	+9.948	0.4795 ± 0.0006	0.26	0.6622	0.3175 ± 0.0009	0.60
	20.176	0.4392 ± 0.0007	0.34	0.6530	0.2868 ± 0.0011	0.79
	25.083	0.4219 ± 0.0008	0.38	0.6486	0.2736 ± 0.0012	0.90
	50.881	0.3476 ± 0.0012	0.66	0.6241	0.217 ± 0.002	1.71
	60.570	0.3247 ± 0.0013	0.81			
3-Methylpentane	−17.59	0.6635 ± 0.0004	0.11			
t_m[d] = −162.9°	−7.534	0.5934 ± 0.0004	0.15	0.6889	0.4088 ± 0.0006	0.31
t_b[e] = +63.282°	+0.362	0.5475 ± 0.0005	0.18	0.6820	0.3734 ± 0.0007	0.39
$P_{t\text{-max}}$[f] = 784 Torr	10.161	0.4984 ± 0.0006	0.23	0.6733	0.3356 ± 0.0009	0.52
	19.986	0.4563 ± 0.0007	0.30	0.6643	0.3031 ± 0.0010	0.68
	29.597	0.4210 ± 0.0008	0.38	0.6555	0.2760 ± 0.0012	0.89
	39.199	0.3902 ± 0.0009	0.47	0.6464	0.2522 ± 0.0014	1.13
	49.017	0.3624 ± 0.0011	0.59	0.6369	0.2308 ± 0.0017	1.45
	59.584	0.3356 ± 0.0012	0.73	0.6267	0.210 ± 0.0020	1.86
	64.290	0.3248 ± 0.0013	0.80			
2,2-Dimethylbutane	−13.72	0.8648 ± 0.0003	0.07			
t_m[d] = −99.870°	−3.857	0.7482 ± 0.0003	0.08	0.6707	0.5018 ± 0.0005	0.20
t_b[e] = +49.741°	+5.005	0.6666 ± 0.0004	0.11	0.6627	0.4417 ± 0.0006	0.25
$P_{t\text{-max}}$[f] = 770 Torr	14.051	0.5975 ± 0.0004	0.14	0.6546	0.3912 ± 0.0007	0.34
	22.724	0.5421 ± 0.0005	0.18	0.6466	0.3505 ± 0.0008	0.44
	46.952	0.4265 ± 0.0008	0.36	0.6236	0.2660 ± 0.0014	1.06
	50.162	0.4141 ± 0.0008	0.40			

[a] Uncertainty band is one sample standard deviation. [b] Per cent deviation calculated for a deviation equal to two sample standard deviations. [c] Density data from API Research Project 44 Tables, see ref 11. [d] Normal freezing point, see ref 11. [e] Normal boiling point, see ref 11. [f] Vapor pressure at highest viscosity measurement, see ref 11.

In Table I, the kinematic viscosities were converted to viscosities using the density data tabulated in the API Research Project 44 Tables.[11] The estimated uncertainty of these data was combined with that of the ν_t data to obtain the estimated uncertainty for the viscosity η_t values.

Analysis and Discussions of Experimental and Literature Data

The semiempirical equation, eq 3, introduced by the authors[5] for water was also selected for the hexane hydrocarbons. Since kinematic viscosities are measured directly, the reduced form of the equation

$$(\nu \text{ or } \eta) = AT^n \exp[B/(T - T_0)] \qquad (3)$$

$$\frac{\nu}{\nu'} = \left(\frac{T}{T'}\right)^n \exp\left[\frac{B(T' - T)}{(T' - T_0)(T - T_0)}\right] \qquad (3a)$$

was used to fit the hexane data in terms of the three parameters, n, B, and T_0.

Table II summarizes the results. It was found that the experimental data were reproduced well within experimental uncertainty for each of the four isomers at all temperatures. The values of the adjustable parameters listed in Table II were obtained by a nonlinear least-squares method.[5,12]

With these parameters, eq 3a was used as an interpolation tool to compare our reported values with literature data. A comparison of this kind is presented in the microfilm edition.[13-21] Reported values from the

(11) B. J. Zwolinski, *et al.*, "Selected Values of Properties of Hydrocarbons and Related Compounds," American Petroleum Institute Research Project 44, Thermodynamics Research Center, Texas A&M University, College Station, Tex. (loose-leaf data sheets, extant, 1972).

(12) D. Vogt and A. R. Buhl, "A Generalized Non-Linear Least Squares Data-Fitting Program," NDL-TM-55, U. S. Army Nuclear Defense Laboratory, Clearinghouse, Edgewood Arsenal, Md., 1969.

(13) A listing of literature data and comparison with eq 3 for references 4 and 14–21 is included in the microfilm edition; see ref 6.

(14) M. R. Cannon and J. M. Geist, *Ind. Eng. Chem., Anal. Ed.*, 18, 611 (1946).

literature were corrected to be consistent with our calibration data.[5] The distressing inconsistency of the literature data is apparent in this compilation. In general, the interpolated data of this work are most consistent with those of Cannon and Geist[14] and Giller and Drickamer.[15] In most of these cases, the deviation may be considered within the combined experimental uncertainty; however, systematic errors may be indicated by the consistent negative deviations. The remaining literature values give deviations which clearly exceed estimated experimental uncertainties. We regard the primary cause of these implied systematic errors to be variations in sample purity. However, no definitive experimental work in this area has ever been reported.

Table II: Parameters of Eq 3a for Isomeric Hexanes

	6H,[a] *n*-hexane	3Y,[a] 2-methylpentane	2Y2,[a] 3-methylpentane	2X,[a] 2,2-dimethylbutane
n	−2.24057	−2.09623	−1.96439	−1.97607
B	+4.78496	+8.82914	+29.4383	+74.59609
T_0	222.468	204.553	170.197	161.553
Rmsd[b]	0.00008	0.00024	0.00017	0.00023

[a] Wiswesser line notations. [b] Root-mean-square deviation.

Attention should be directed to the T_0 parameter value found for *n*-hexane. Ordinarily, T_0 is some fraction of the normal freezing point value, where here T_0 (222.468) is well above the melting point. This situation was remedied by combining the low-temperature data of Giller and Drickamer (extending through the normal freezing point) with our own data to obtain an extended temperature range data fit and parameter set. The Giller and Drickamer data were assigned uncertainties such that the estimated standard deviation was 1% of the reported kinematic viscosity, whereas our data were assigned the uncertainties reported in the previous section. Reciprocal variance weight factors were then used in the fitting calculations. The data of this investigation remain well represented by the extended range version of eq 3a. The value obtained for T_0 falls approximately 60° below the melting point, and the data of Giller and Drickamer near the melting point are well fitted within estimated experimental uncertainty. A small systematic divergence of the Giller–Drickamer data in the −20 to −40° range may be in excess of experimental uncertainty.[22]

Viscosity Structural Relations

A generalized phenomenological approach to molecular liquid theory has been developed by Eyring and his associates.[23] In this approach, absolute rate theory[24] is applied to a fluidizing vacancy liquid model to obtain eq 4 for Newtonian shear viscosity[25]

$$\eta = x_s\eta_s + x_g\eta_g \tag{4}$$

$$x_s = V_s/V \qquad x_g = (V - V_s)/V$$

$$\eta_s = \frac{V}{V_s}\left[\frac{(\pi mkT)^{1/2}N_A l}{2(V - V_s)\kappa}\right]\exp\left[\frac{Z\varphi(a)}{2kT}\left(\frac{a'V_s}{(V - V_s)}\right)\right]$$

The parameters which are particularly sample dependent are Z, κ, $\varphi(a)$, V_s, V, l, and η_g. These are, respectively, the number of nearest neighbors, the transmission coefficient, an intermolecular potential function, the molar volume of the solid-like liquid structures, the molar volume of the bulk liquid, a free length parameter associated with the activated state, and the gas viscosity.

In previous applications of eq 4 to simple molecular liquids,[23,25] the gas-like contribution, $x_g\eta_g$, to the total viscosity has been ignored. This has been justified on the basis that its contribution should be less than 2%, which for the cases treated were less than the experimental uncertainty.

In the following analysis of the high-precision data of the isomeric hexanes, the gas-like contribution is included in the following manner. The gas viscosity data of Pena, Esteban, and Sanchez[26] for the isomeric hexanes were fitted to an equation of the form

$$\eta_g = \frac{1}{\pi\sigma^2}\left(\frac{mkT}{\pi}\right)^{1/2} \tag{5}$$

with the added assumption

$$\sigma = \sigma_0 - \alpha T \tag{5a}$$

Equation 5 is the usual form of the kinetic theory gas viscosity.[27] To reproduce the real gas viscosity data, it was necessary to assume a temperature dependence for

(15) E. B. Giller and H. G. Drickamer, *Ind. Eng. Chem.*, **41**, 2067 (1949).

(16) K. Khalilov, *J. Exp. Theor. Phys. USSR*, **9**, 335 (1939).

(17) P. Drapier, *Bull. Acad. Sci. Belg.*, 626 (1911).

(18) H. Luther and H. Kolbel, *Brennst.-Chem.*, **30**, 362 (1949).

(19) E. N. Andrade and L. Rotherham, *Proc. Phys. Soc.*, **48**, 261 (1936).

(20) E. C. Bingham, G. F. White, A. Thomas, and W. Caldwell, *Z. Phys. Chem. (Frankfurt am Main)*, **83**, 641 (1931).

(21) G. Chavanne and H. Van Risseghem, *Bull. Soc. Chim. Belg.*, **31**, 87 (1922).

(22) A listing of the fitting parameters and per cent deviation as a function of temperature over the extended temperature range is included in the microfilm edition; see ref 6.

(23) H. Eyring and M. S. Jhon, "Significant Liquid Structures," Wiley, New York, N. Y., 1969.

(24) S. Glasstone, K. J. Laidler, and H. Eyring, "The Theory of Rate Processes," McGraw-Hill, New York, N. Y., 1941.

(25) M. S. Jhon, W. L. Klotz, and H. Eyring, *J. Chem. Phys.*, **51**, 3692 (1969).

(26) M. D. Pena, F. Esteban, and M. A. Sanchez, *An. Reale Soc. Espan. Fis. Quim., Ser. A*, **63**, 103 (1967).

(27) E. A. Moelwyn-Hughes, "Physical Chemistry," 2nd ed, Pergamon Press, New York, N. Y., 1961.

Table III: A Summary of Parameters Obtained from the Significant Liquid Structures Analysis of the Kinematic Viscosity Data of the Isomeric Hexanes and Neopentanes Using Eq 6

Liquid	Parameters adjusted by a least-squares analysis of data: V_s, cm³ g⁻¹	$-\alpha' Z\epsilon \times 10^{18}$, erg	$l/\kappa \times 10^{8}$, cm	Temp range, °C	Maximum deviation, %	Average deviation, %
6H, *n*-hexane	0.904351	1.94609	3.63254	−94.3, +45.5	1.04 at −94.3°	0.24
3Y, 2-methylpentane	0.81700	2.22619	3.56680	−15.6, +60.6	−0.69 at 60.6°	0.20
2Y2, 3-methylpentane	0.85500	2.09938	3.51916	−17.6, +50.2	−0.93 at 64.3°	0.23
2X, 2,2-dimethylbutane	1.05804	1.83471	3.40722	−13.7, +50.2	−0.16 at 50.2°	0.07
1Y&Y, 2,3-dimethylbutane	1.02720	1.66480	3.4994	0.0, +40	See text	
1X, neopentane	1.27367	1.62852	3.1719	−15.0, +20.0	1.1 at 20.0°	0.50

the collision diameter, σ, as given in eq 5, where σ_0 represents collision diameters at 0°K and infinite dilution. The values found for σ_0 are consistent with the degree of branching in the isomeric hexanes, that is, σ_0 was found to decrease with increasing compactness of the isomers.

Following Jhon, Klotz, and Eyring,[25] an approximation to the Lennard-Jones 6–12 potential function for $\varphi(a)$ was used.

$$\varphi(a) = \epsilon[1.0109(N_A\sigma^3/V_s)^4 - 2.4090(N_A\sigma^3/V_s)^2]$$
$$= \epsilon[1.0109(V_c/12V_s)^4 - 2.4090(V_c/12V_s)^2]$$

where V_c is the critical volume of the liquid.

In this analysis, eq 4 was recast in terms of the kinematic viscosity

$$\nu = \left(\frac{V}{V - V_s}\right)\left[\frac{(\pi mkT)^{1/2}}{2M\kappa} N_A l\right] \times \exp\left[\frac{a' Z\varphi(a)}{2kT}\left(\frac{V_s}{V - V_s}\right)\right] + \frac{(V - V_s)}{M}\eta_g \quad (6)$$

This cumbersome equation was reduced to a three-parameter equation by a judicious combination of certain of the theoretical parameters. The three chosen parameters, namely, V_s, $a'Z\epsilon$, and l/κ, were assumed temperature independent and were determined by a nonlinear least-squares procedure. In our regressions, it became apparent that there was a strong correlation between the l/κ parameter and the σ_0 constant in eq 5. The results reported in Table III were obtained based on $(l/\kappa)/\sigma_0$ = constant. In Table III, the *n*-hexane data of Giller and Drickamer near T_m were included in the least-squares calculations. The weighting procedures were identical with those described in the previous section. Table III summarizes the result of these calculations for the four isomeric hexanes studied and also for 2,3-dimethylbutane and neopentane which are discussed in the next section.[28]

The values obtained for the regression parameters appear to be reasonable. For example, assuming the transmission coefficient to be unity, the free length parameters, l, have values comparable to van der Waals molecular diameters.

The exponential terms, $\epsilon^{\mp} = a'Z\varphi(a)V_s[2(V - V_s)]^{-1}$, of the SLS theory assume values on the order of 1 kcal mol^{-1} in this treatment. V_s values fall between van der Waals volumes and volumes apparently accessible to the bulk liquid. They are generally smaller than packing volumes of the solid at the melting point. The numerical values obtained for the parameter product $a'Z\epsilon$ vary within a 22% range. This variation is reduced by division by kT_c (a corresponding states reduction) to 10%, which may be interpreted as consistent with the assumption that a' would be constant for the series,[1] with the effective near-neighbor parameter, Z, showing small variations.

A further comparison of the relative values of the parameters obtained for the homologous series is of interest. For this discussion, it is convenient to use the Wiswesser line formula notation[29] for the isomeric hexanes. They are 6H, 3Y, 2Y2, 1Y&Y, and 2X for *n*-hexane, 2-methylpentane, 3-methylpentane, 2,3-dimethylbutane, and 2,2-dimethylbutane, respectively.

The fitting of our experimental data and the literature data for 2,3-dimethylhexane was carried out assuming that $(l/\kappa)/\sigma_0 = 0.3795 \pm 0.0005$. This appears reasonable[1] in that a free length parameter associated with the flowing species should reflect structural effects, and the σ_0 parameters obtained from independent analysis of the gas viscosities are quite sensitive to structural differences in the isomeric series.

The relative kinematic viscosity magnitudes of these isomeric hexanes (*i.e.*, 2X > 6H > 2Y2 > 3Y) have not been easily explained. They do, however, correspond to the V_s parameters found for the series. For example, the kinematic viscosities at 20° of 2X, 6H, 2Y2, and 3Y are 0.5586, 0.4729, 0.4562, and 0.4399 cSt, respectively. The corresponding V_s parameters are 1.058, 0.9044 (note V_m = 1.137 at T_m), 0.8550, and 0.8170 cm³ g^{-1}. This trend would tentatively identify

(28) A complete listing of parameters, auxiliary data, calculated and observed kinematic viscosities, per cent deviations as a function of temperature, and per cent contribution of the gas-like kinematic viscosity is presented for each liquid in the microfilm edition; see ref 6.

(29) E. G. Smith, "The Wiswesser Line-Formula Chemical Notation," McGraw-Hill, New York, N. Y., 1968.

the packing efficiency of the solid-like liquid structures as reflecting the intermolecular interactions, which in turn are reflected in the kinematic viscosity magnitudes. With the exception of 6H, *n*-hexane, the above trend corresponds to increased branching in the molecular structure of the isomers.

Correlations of Literature Viscosity Data for Neopentane and 2,3-Dimethylbutane

Two other lines of evidence support the view that the relative kinematic viscosity magnitudes are directly related to packing efficiency, and therefore isomeric branching, in the solid-like structures. The first is that the fifth and final isomer of the series, 1Y&Y, is more branched than 2Y2, and less than 2X. Its kinematic viscosity would therefore be expected to fall between that of 2X and 2Y2. The reported literature value[14] at 20° is 0.508, as expected.

The second line of evidence comes from analysis of the gas and liquid viscosities of neopentane, 1X. If, as suggested above, packing efficiency in the solid-like structure decreases with increasing spherical symmetry or compactness, the maximum *specific* V_s should be obtained from analysis of the neopentane data regardless of the relative viscosity magnitudes. The liquid kinematic viscosities reported by Phibbs,[30] and the gas viscosities reported by Golubev,[31] were analyzed using the critical constants reported by Kudchadker, Alani, and Zwolinski.[32] The results, summarized in Table III, show that reported viscosities are again reproduced within experimental uncertainty (estimated at 1%) over the entire temperature range, and that the value of V_s for 1X is greater than 2X, as predicted.

As a final test, an attempt was made to calculate the kinematic viscosities of 1Y&Y, 2,3-dimethylbutane, at 0.0°. The relationship found above between σ_0 and l/κ, the gas viscosity parameters obtained from the data of Pena, *et al.*[22] (*i.e.*, $\sigma_0 = 9.221 \times 10^{-8}$ cm, $\alpha = 4.106 \times 10^{-11}$ cm °K^{-1}), and the kinematic viscosities reported by Cannon and Geist[11] for 1Y&Y at 20 and 40° were used to calculate the two remaining parameters, $a'Z\epsilon = -1.6648 \times 10^{-13}$ erg, and $V_s = 1.0272$ cm^3 g^{-1}. The kinematic viscosity is thus calculated from eq 6 as 0.629 cSt and compared with the reported value, 0.626 cSt. The deviation (0.6%) is within experimental uncertainty.

This extension of the theory indicates that the relationship found between l/κ and σ_0 is viable. The V_s parameter falls into the compactness sequences, as expected. The kinematic viscosity magnitude sequence for the total hexane isomeric set is as follows: 2X > 1Y&Y > 6H > 2Y2 > 3Y. The anomalous position of 6H in this series may be rationalized by considering it to be in less than a rod-like configuration in the normal state for the solid-like structures of the liquid, and therefore less efficiently packed.

Final Summary

The analysis of the small, thus subtle, effects of molecular structure on the kinematic viscosities of the isomeric hexanes within the framework of Eyring's significant liquid structures theory is very promising. A real test of this treatment resides in the prediction of shear viscosities for the higher isomeric alkanes. The fact that the empirical relation, eq 3, and the SLS theory, eq 6, are related functionally is not too surprising. If eq 6 is rewritten, regrouping temperature-independent terms, eq 6a is obtained.

$$\nu = A'\left(\frac{VT^{1/2}}{V - V_s}\right)\exp\left[\frac{B'}{T}\left(\frac{V_s}{V - V_s}\right)\right] \qquad (6a)$$

A rearrangement of terms in eq 3 gives

$$\nu = AT^n \exp\left[\frac{B}{T}\left(\frac{T}{T - T_0}\right)\right]$$

in which the similarity of temperature dependence becomes apparent. For example, if the exponential terms were considered proportional

$$\frac{T}{T - T_0} = A''\left(\frac{V_s}{V - V_s}\right)$$

or in the form

$$V = V_s\left[1 + A''\left(1 - \frac{T_0}{T}\right)\right]$$

then V is reasonably expressed as a slowly increasing function of T.

Previous work has shown that eq 4 can be used to successfully correlate the pressure dependence of liquid viscosities for selected normal alkanes and *cis*-decahydronaphthalene by considering the effect of pressure on V_s,[23] and also to predict glass transition temperatures for selected alkylbenzenes.[1] An appealing aspect of the SLS theory is that it can yield both the thermodynamic and transport properties of liquids in a unified treatment.[23]

Acknowledgment. This investigation was partially supported by the American Petroleum Institute Research Project 44 of the Thermodynamics Research Center at Texas A & M University.

(30) M. K. Phibbs, *J. Chem. Phys.*, **19**, 1420 (1951).

(31) I. F. Golubev, "Viscosity of Gases and Gas Mixtures," Gosudarstvennoe Izdatel'stvo, Fiziko Mathematichskoi Literatury, Moscow, 1959.

(32) A. P. Kudchadker, G. H. Alani, and B. J. Zwolinski, *Chem. Rev.*, **68**, 659 (1968).

COMMUNICATIONS TO THE EDITOR

Rate Constant for the Reaction of HO_2 with Carbon Monoxide

Publication costs assisted by the National Science Foundation

Sir: On the basis of an experimental determination of the relative rate constants, $k_a/k_b = 0.06$, for the reactions

$$HO_2 + CO \xrightarrow{k_a} CO_2 + OH \quad (1)$$

$$HO_2 + H \xrightarrow{k_b} OH + OH \quad (2)$$

Westenberg and deHaas[1] suggest that k_a may be as large or larger than the rate constant for the reaction of OH with CO. Because of the importance of these reactions with CO, particularly in the elucidation of photochemical reactions in contaminated atmospheres, we wish to present a contrary conclusion based on results we have obtained. Complete experimental details but not the discussion below are given in a forthcoming paper.[2]

We have studied the rate of CO_2 formation at 25° under constant illumination in the gaseous system H_2O_2–CO–O_2. The following reactions are pertinent.

$$H_2O_2 + h\nu(254\text{ nm}) \xrightarrow{I_a} 2OH \quad (3)$$

$$OH + H_2O_2 \xrightarrow{k_2} H_2O + HO_2 \quad (4)$$

$$HO_2 + HO_2 \xrightarrow{k_3} H_2O_2 + O_2 \quad (5)$$

$$OH + CO \xrightarrow{k_4} CO_2 + H \quad (6)$$

$$H + H_2O_2 \xrightarrow{k_5} H_2O + OH \quad (7)$$

$$H + H_2O_2 \xrightarrow{k_6} H_2 + HO_2 \quad (8)$$

$$H + O_2 + M \xrightarrow{k_7} HO_2 + M \quad (9)$$

$$HO_2 + CO \xrightarrow{k_a} CO_2 + OH \quad (10)$$

In the presence of sufficient O_2, the only reaction of H atom is given by eq 9. This is confirmed since hydrogen is not formed under these conditions. The rate expression for initial conditions is then

$$\left(\frac{d[CO_2]}{dt}\right)_0 = [CO]_0 \left\{k_4 \frac{2I_a + k_a[CO]_0(I_a/k_3)^{1/2}}{k_2[H_2O_2]_0 + k_4[CO]_0} + k_a\left(\frac{I_a}{k_3}\right)^{1/2}\right\} \quad (11)$$

In the absence of CO, the rate expression is

$$-\frac{d[H_2O_2]}{dt} = 2I_a \quad (12)$$

which, at the necessarily low concentration of H_2O_2, yields

$$-\frac{d[H_2O_2]}{dt} = 2I_0'[H_2O_2] \quad (13)$$

for a fixed illumination geometry with I_0' a function only of the incident light intensity.[3] In earlier work it was found that the photodecomposition of H_2O_2 was not affected by added oxygen,[3] and in the present work the same results were obtained with either H_2O_2 alone or with added CO_2. Consequently, we obtained I_0' from photodecomposition in the system H_2O_2–CO_2 using the integrated rate expression

$$\ln \frac{[H_2O_2]_0}{[H_2O_2]_0 - 2[O_2]} = 2I_0't \quad (14)$$

The yield of O_2 was determined and the rate expression was adhered to rigorously. Thus I_a in eq 11 can be replaced by $I_0'[H_2O_2]_0$ with $I_0' = 8.7 \times 10^{-4}$ sec^{-1}. Actinometry carried out with diethyl ketone yielded the same value of I_0'. The value of k_3 has been estimated[4] to be about 3×10^{-12} cm^3 molecule^{-1} sec^{-1}. However, the minimum rate derived from eq 11 will be given by the maximum value of k_3. If we assume reaction occurs on every collision, $k_3 \cong 1.0 \times 10^{-10}$. Other values used and our experimental conditions are $k_2 = 9.3 \times 10^{-13}$ cm^3 molecule^{-1} sec^{-1} at 298 K;[5] $k_4 = 1.5 \times 10^{-13}$ cm^3 molecule^{-1} sec^{-1} at 298 K;[6] $[H_2O_2]_0 = 3.0 \times 10^{16}$, $[O_2]_0 = 1.7 \times 10^{17}$, $[CO]_0 = 3.2 \times 10^{17}$ molecules cm^{-3} (0.94, 5.4, and 10.0 Torr, respectively).

If $k_a \cong k_4$, the calculated initial rate of CO_2 formation from eq 11 using the above values is 4.0×10^{16} while our experimentally determined rate based on CO_2 formation for a time interval during which the initial concentration of any reactant did not change by more than 1.5% is 2.8×10^{13} molecules cm^{-3} sec^{-1}.

(1) A. A. Westenberg and N. deHaas, *J. Phys. Chem.*, **76**, 1586 (1972).

(2) R. A. Gorse and D. H. Volman, *J. Photochem.*, 1, 1(1972).

(3) D. H. Volman, *J. Chem. Phys.*, **17**, 947 (1949).

(4) S. N. Foner and R. L. Hudson, *Advan. Chem. Ser.*, **No. 36**, 34 (1962).

(5) N. R. Greiner, *J. Phys. Chem.*, **72**, 406 (1968).

(6) D. L. Baulch, D. D. Drysdale, and A. C. Lloyd, High Temperature Reaction Rate Data Report No. 3, Leeds University, 1969.

Elimination of reaction 10 yields the expression

$$\left(\frac{d[CO_2]}{dt}\right)_0 = \frac{2I_0'k_4[CO]_0[H_2O_2]_0}{k_2[H_2O_2]_0 + k_4[CO]_0} \quad (15)$$

from which we obtain a rate of 3.3×10^{13} molecules cm^{-3} sec^{-1} in good agreement with our experimental results. The grossest error, say a factor of 10 too low, in our experimentally determined rate would lead to a calculated value of $k_4/k_a = 1.6 \times 10^2$ for eq 11 to give the presumed true rate. Therefore, we conclude that the rate constant for the reaction of HO_2 with CO is very much less than that for the reaction of OH with CO.

The above discussion has been limited to a single experimental value. We should, however, point out that we have successfully tested eq 15 by plotting $I_0'/(d[CO_2]/dt)_0$ *vs.* $1/[CO]_0$ for fixed initial O_2 and H_2O_2 concentrations, which should yield a straight line, with initial CO pressures from 3 to 30 Torr and with I_0' from 6.6×10^{-5} to 1.9×10^{-3} sec^{-1}.

Acknowledgment. Support for this research was received from the National Science Foundation.

DEPARTMENT OF CHEMISTRY
UNIVERSITY OF CALIFORNIA
DAVIS, CALIFORNIA 95616

DAVID H. VOLMAN*
ROBERT A. GORSE

RECEIVED JUNE 19, 1972

Journal of Chemical and Engineering Data

OCTOBER 1972, Vol. 17, No. 4

TABLE OF CONTENTS

There when you need them...

are the annual 700 pages of data published quarterly in the

Journal of Chemical & Engineering Data

This American Chemical Society journal is especially valuable in light of today's new instrumentation.

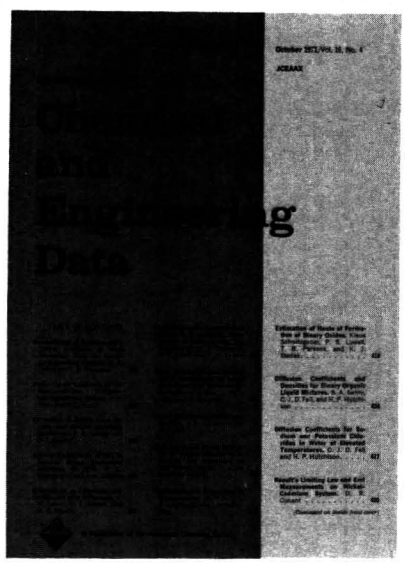

You'll find *four* clearly defined areas in JC & ED. They are:

☐ Experimental data relating to pure compounds of mixtures covering a range of states.

☐ Manuscripts based on published experimental information, which make tangible contributions through the reorganization or systematic presentation of such data . . . or which set forth a well documented method of prediction of properties as a function of state.

☐ Experimental data which aid in the identification or utilization of new organic or inorganic compounds.

☐ Papers relating primarily to newly developed or novel synthesis of organic compounds and their properties.

Sending for a subscription to the JOURNAL OF CHEMICAL & ENGINEERING DATA is so much easier than searching for data deposited in archives. Just fill in and return the form below. We'll do the rest.

American Chemical Society / 1155 Sixteenth Street, N.W., Washington, D.C. 20036

Please enter my subscription to **The Journal of Chemical & Engineering Data** at the rates checked below.

ACS Members: ☐ U.S. $15.00 ☐ Canada, PUAS $18.00 ☐ Other Nations $18.50

Nonmembers: ☐ U.S. $45.00 ☐ Canada, PUAS $48.00 ☐ Other Nations $48.50

☐ Bill me ☐ Bill employer ☐ Payment enclosed (Payable to American Chemical Society)

Name _____ Title _____

Employer _____

Address: ☐ Home ☐ Business _____

City _____ State/Country _____ Zip _____

Nature of employer's business? ☐ Manufacturing or processing ☐ Academic ☐ Government ☐ Other _____ (Please indicate)

Note: Subscriptions at ACS Member Rates are for personal use only.

☐ I am an ACS member ☐ I am not an ACS member

Payment must be made in U.S. currency, by international money order, UNESCO coupons, U.S. bank draft; or order through your book dealer.

T3A

THE RADIATION CHEMISTRY OF MACROMOLECULES

edited by MALCOLM DOLE, Department of Chemistry, Baylor Univ., Waco, Texas

Written by a number of experts in the field, these two volumes offer a complete and extensive survey of the chemical and physical effects of high energy radiations (including high speed electrons, gamma rays, and X-rays) on substances containing molecules of high molecular weight.

Volume 1 outlines the basic theory of radiation chemistry, which is applicable to all kinds of molecules. It presents the fundamentals of solid state phenomena, and includes discussions of the theory of solid state reactions, ion, electrons, free radicals, and energy transfer processes. Other chapters deal with the radiation chemistry of polyethylene, which can be considered as the prototype of all macromolecules.

Volume 2 describes other specific types of macromolecular systems, including substituted vinyl polymers, polyamides, polyesters, polysiloxanes, and biological macromolecules (such as nucleic acids, proteins, and polysaccharides). It also describes the effect of radiations on oxidation rates, mechanical properties, and on single crystals.

Volume 1/1972, 369 pp., $23.00
Set Price for Volume 1: $19.00
Volume 2/1972, about 375 pp., $25.00
Set Price for Volume 2: $21.00

NONAQUEOUS ELECTROLYTES HANDBOOK

Volume 1

by G. J. JANZ, and R. C. T. TOMKINS, Department of Chemistry, Rensselaer Polytechnic Inst., Troy, New York

This authoritative handbook provides quick and easy access to tabulated nonaqueous electrolyte data for over 200 solvents and 650 electrolytes in annotated form. The authors cover the literature to December 1971, make the significant comparisons of data, and indicate those areas which need further investigation.

1972, about 800 pp., in preparation

ADSORPTION-DESORPTION PHENOMENA

edited by F. RICCA, University of Turin, Italy

Proceedings of the II International Conference Held at Florence in April 1971.

This volume deals with fundamental problems in adsorption as distinct from catalysis and solid reactivity. They are structured in three subsections which are devoted to theoretical studies on physisorption, to particle beams, and to chemisorption of gases by metals. These subsections give particular attention to some of the most recent concepts and experimental results in adsorption studies.

1972, 478 pp., $20.50

INFRARED AND RAMAN SPECTRA OF CRYSTALS

by G. TURRELL, Professeur Associe, Laboratoire de Spectroscopie Infrarouge, Faculte des Sciences, Bordeaux, France

This guide to the interpretation of vibrational spectra and crystalline solids is the first work to discuss the subject in its entirety. The study reviews the dynamics and symmetry of molecular vibrations and introduces the matrix formulation that is used throughout the book. Following this is an examination of the dynamics of crystal lattices that provides the crystallographic basis for the interpretation of the vibrational spectra of solids. The final chapters are concerned with the applications of vibrational spectroscopy to the determination of potential constants and structures, and the study of polymer systems and impure crystals.

1972, 378 pp., $26.50

COMPUTERS IN CHEMICAL AND BIOCHEMICAL RESEARCH

Volume 1

edited by CHARLES KLOPFENSTEIN, Department of Chemistry, Univ. of Oregon, **and CHARLES WILKINS,** Department of Chemistry, Univ. of Nebraska

Here is a new serial publication that will be of interest to researchers in every phase of chemical and biochemical research. It is devoted to the application of real-time computer techniques to data-handling problems of all types in the experimental sciences and education. Contributors are recognized computer experts who describe in detail the work being done in both academic and industrial laboratories.

1972, 272 pp., $14.00

COMPUTER PROGRAMS FOR CHEMISTRY

Volume 4

edited by DeLOS F. DeTAR, Department of Chemistry and Inst. of Molecular Biophysics, Florida State Univ., Tallahassee

Computer Programs for Chemistry provides chemists with listings and descriptions of tested well-constructed FORTRAN programs-each of which performs a clearly defined calculation or other operation. The programs in Volume 4 are of interest to many chemists—e.g., LSKIN2; CDORD: and EQCENT. In addition, there are programs that can be applied by anyone working with computers—GENLSS, FRS3, and EDITQ and EDITID. This volume also includes a number of FORTRAN subroutines for conversion between binary coded numbers and their integer or real representation, as well as packing and unpacking routines. A tape copy of the program in Volume 4 contains over 15,000 card images of programs and test data. This tape copy can be obtained from the publisher.

1972, 296 pp., $15.00

MOLECULAR SPECTROSCOPY: Modern Research

edited by K. NARAHARI RAO, Department of Physics, The Ohio State Univ., Columbus, **and C. WELDON MATHEWS,** Department of Chemistry, The Ohio State Univ., Columbus

This volume contains reviews of current advances in several phases of research in high resolution molecular spectroscopy. Particular emphasis is placed on electronic, infrared, and microwave studies of molecular species in gas phase and in matrices. Included also are representative articles which feature discussions of such topics as: Techniques employed in high-resolution spectroscopy; Astrophysical aspects of molecular spectroscopy; Infrared molecular lasers; Applications of molecular spectroscopy in biophysics; An introduction to molecular lamb-dip spectroscopy.

1972, 422 pp.. $25.00

INTERATOMIC POTENTIALS

by IAN TORRENS, Centre d'Etudes Nucléaires de Saclay, France

Contents: The Nature of Interatomic Forces. Theoretical Models of the Atom. Interatomic Potentials Based on Thomas-Fermi Theory. Empirical Interatomic Potentials. Pseudopotential Theory. Pair Potentials Based on Pseudopotential Theory. Atomic Collision Theory and Interatomic Potentials. Experiments on the Scattering of Atoms and Ions. Liquid Metal Pair Interaction Potentials. The Application of Interatomic Potentials. Appendices: Table of Values of the Thomas-Fermi Screening Function $_{x}$ (x) and Its Derivative: Hartree Dielectric Screening of the Pseudopotential; The Cohesion of Ionic Crystals; Interatomic Potentials Derived from Planar Channeling Data.

1972, about 250 pp., in preparation